

# Thèse de Doctorat

**Javier MARTIN BLANCO**

*Mémoire présenté en vue de l'obtention du  
grade de Docteur de l'Université de Nantes  
sous le label de l'Université de Nantes Angers Le Mans*

**Discipline : Constituants élémentaires et physique théorique**  
**Spécialité : Physique nucléaire expérimentale**  
**Laboratoire : Laboratoire SUBATECH - UMR 6457**

**Soutenue le 29 Octobre 2015 à Nantes**

**École doctorale : 3MPL - Matière, Molecules, Matériaux en Pays de la Loire**  
**Thèse n° :**

**Study of  $J/\psi$  production dependence  
with the charged particle multiplicity  
in p-Pb collisions at  $\sqrt{s_{NN}} = 5.02$  TeV  
and pp collisions at  $\sqrt{s} = 8$  TeV  
with the ALICE experiment at the LHC**

## JURY

**Rapporteurs :** **M. Anton ANDRONIC**, Chercheur, GSI, Darmstadt (Allemagne)  
**M<sup>me</sup> Begoña DE LA CRUZ MARTINEZ**, Chercheur, CIEMAT, Madrid (Espagne)

**Examineurs :** **M. Andreas MORSH**, Chercheur, CERN, Genève (Suisse)  
**M. Christophe SUIRE**, Chargé de recherche CNRS, IPN, Orsay (France)  
**M. Kaus WERNER**, Professeur à l'Université de Nantes, SUBATECH, Nantes (France)

**Directeur de thèse :** **M. Ginés MARTINEZ GARCIA**, Directeur de recherche CNRS, SUBATECH, Nantes (France)

**Co-directeur de thèse :** **M. Laurent APHECETCHE**, Chargé de recherche CNRS, SUBATECH, Nantes (France)



Laboratoire SUBATECH  
4, rue Alfred Kastler  
La Chantrerie BP 20722  
44307 Nantes Cedex 3 FRANCE

École Doctorale 3MPL  
1, rue Gaston Veil  
BP 53508  
44035 NANTES CEDEX 1





## ABSTRACT

A suppression (relative to the measurement in pp collisions at the same energy) of the  $J/\psi$  production was found in Pb-Pb collisions at  $\sqrt{s_{\text{NN}}} = 2.76$  TeV, providing further evidence of the formation of a deconfined medium in ultra-relativistic heavy-ion collisions, the so-called Quark-Gluon Plasma. In addition, p-Pb collisions at  $\sqrt{s_{\text{NN}}} = 5.02$  TeV have been studied at the LHC to measure cold nuclear matter effects (e.g. gluon shadowing, energy loss, nuclear absorption). Understanding p-Pb collisions will help to disentangle hot and cold nuclear matter effects in Pb-Pb collisions. Surprisingly, some observables in p-Pb collisions behave as in heavy-ion collisions where it is understood as a result of a collective expansion of the medium.

This thesis analyses inclusive  $J/\psi$  production in p-Pb and pp collisions with the ALICE muon spectrometer. The  $J/\psi$  production rate, and its mean transverse momentum, have been measured at forward and backward rapidities as a function of the charged particle multiplicity. Measurements of particle production as a function of the event multiplicity in small size systems provide a way to sign the presence of collective final state effects like those observed in Pb-Pb collisions. In p-Pb collisions, the observed increase of the  $J/\psi$  production at backward rapidity with multiplicity is consistent with that observed in pp collisions. However, a deviation from this behavior in the  $J/\psi$  production at forward rapidity at high multiplicity has been measured. A trend towards saturation has also been observed in the  $J/\psi$  mean transverse momentum in p-Pb collisions. Whether these effects can be explained by cold nuclear matter effects or by the presence of further final state effects is currently under investigation.

### Keywords

Quark-Gluon Plasma,  $J/\psi$ , Cold Nuclear Matter, heavy-ions, quarkonium, p-Pb, pp, ALICE.



## RÉSUMÉ

Une suppression de la production de  $J/\psi$  a été mise en évidence lors les collisions Pb-Pb à  $\sqrt{s_{NN}} = 2.76$  TeV (relative à la mesure dans les collisions pp à la même énergie), fournissant une preuve supplémentaire de la formation d'un milieu déconfiné au cours des collisions d'ions lourds ultra-relativistes, appelé Plasma de Quarks et de Gluons. Par ailleurs, les collisions p-Pb à  $\sqrt{s_{NN}} = 5.02$  TeV ont été étudiées au LHC afin de mesurer les effets de la matière nucléaire froide (p. ex. écrantage des gluons, perte d'énergie, absorption nucléaire). La compréhension des collisions p-Pb aidera à dissocier les effets de la matière nucléaire chaude et froide dans les collisions Pb-Pb.

Cette thèse analyse la production inclusive de  $J/\psi$  dans les collisions p-Pb et pp avec le spectromètre à muons de l'expérience ALICE. Le taux de production de  $J/\psi$  et son moment transverse moyen, ont été mesurés pour des rapidités à l'avant et à l'arrière en fonction de la multiplicité des particules chargées. Des mesures de la production de particules en fonction de la multiplicité de l'évènement dans des systèmes de petite taille permettent de mettre en évidence des effets collectifs de l'état final, comme ceux observés dans les collisions Pb-Pb. En collisions p-Pb, l'augmentation observée avec la multiplicité, de la production de  $J/\psi$  aux rapidités à l'arrière est en accord avec celle mise en évidence en collisions pp. Cependant une déviation de ce comportement pour la production de  $J/\psi$  aux rapidités à l'avant à haute multiplicité a été mesurée. Une tendance à la saturation du moment transverse moyen du  $J/\psi$  en collisions p-Pb a aussi été observée. L'origine de ces comportements, qu'ils soient liés aux effets de la matière nucléaire froide ou à la présence d'autres effets à l'état final, n'est toujours pas connue.

### Mots clés

Plasma de Quarks et Gluons,  $J/\psi$ , Matière Nucleaire Froide, ions lourds, quarkonium, p-Pb, pp, ALICE.



## ACKNOWLEDGEMENTS

I would like to thank all the people who, in one way or another, have contributed to this thesis. Although I am possibly forgetting someone, my gratitude is equally big than for those mentioned here.

First of all a warm thanks to the members of the Dimuon group at SUBATECH laboratory for giving me the opportunity to work with them. I want to express my gratitude to Ginés Martinez, my thesis supervisor, for his support, hospitality and wise advices. I am specially thankful to Laurent Aphecetche, my thesis co-supervisor, for his guidance and infinite patience. He has always been available to discuss and solve my doubts, I have learnt a great deal from you. Thanks to both of you for all the knowledge you have transmitted to me, it was a great honour to work with you. I am grateful to Philippe Pillot and Diego Stocco, always there to help me at any time. Thanks for the many hours we spent discussing and the scientific rigorousness you taught to me. I would like to thank Guillaume Batigne and Patrice Pichot for introducing me '*la bête*' for the first time and the great time we had at CERN. I wish also to thank Laure Massacrier, Benjamin Audurier, Audrey Francisco, Alexis Mas, Astrid Morreal, Marie Germain, Alexandre Shabetai and Magali Estienne for this three years of very nice ambiance at the lab. Thanks to Antoine Lardeux for his hospitality and friendship, and Lucile Ronflette for the very nice times we had sharing office.

I am grateful to Bernt Grambow, director of SUBATECH, for allowing me to perform my thesis in this laboratory. Thanks to the administrative girls, the people of the informatics service and everyone I have met at the lab who has made my stay better just by being kind.

I want to thank to the members of my jury for accepting to be part of it. Thanks to my *rapporteurs*, Anton Andronic and Begoña de la Cruz for their patience reading this document, Klaus Werner for having accepted to preside the jury and my *examineurs* Andreas Morsh and Christophe Suire for the discussion before and during the defence.

During my thesis I have had the pleasure to meet many people of the ALICE collaboration. Roberta Arnaldi, Alberto Baldisseri, Javier Castillo, Zaida Conesa, Igor Lakomov, Marco Leoncino, Cynthia Hadjiakis, Lizardo Valencia... thank you for the moments we have shared and the fruitful discussions.

I wish to thank the group of Ph.D students at Subatech: Aurelien, Antoine, Alexandre<sup>2</sup>, Alexis, Benjamin<sup>3</sup>, Diego, Fanny, Guillaume, Grégoire, Kevin, Loïc, Loïck, Martin, Roland ... for all the nice moments at the lab and also outside. Special thanks to Florian, Charlotte, Lucile and Jose for being not only colleagues but also good friends. Thanks to Tatan, Rocio,

---

Jean Pascal and Sara for your friendship and being an anchor to life beyond physics. You have all made these years a very pleasant experience.

Thanks to my friends Alex, Julio, Santi, Ali... for being there even when I am far. Big thanks to my family for supporting me my whole life, you are too many to be mentioned here but you all have a place in my mind. To my father, who could not see the man I have become, I think you would be proud; and specially to my mother, thank you for your love, strength and all the sacrifices you have made for me. Finally I want to thank Lucía for being always by my side, for your support and your love. Thanks for making life a beautiful journey.

## INTRODUCTION

The Quark-Gluon Plasma (QGP), a deconfined state of partonic matter predicted by Quantum Chromodynamics (QCD), is expected to be formed in ultra-relativistic heavy-ion collisions, where nuclear matter reaches high temperatures and pressures. Heavy quarks are expected to be produced in the primary partonic scatterings, and therefore to experience the whole QGP evolution. As a consequence, quarkonium, bound states of heavy quark  $Q\bar{Q}$  pairs, thanks to its small size ( $< 1$  fm) and large binding energy (several hundred of MeV) are ideal probes of the strongly interacting QGP. It was predicted that in the presence of a QGP, the color-screening would lead to a sequential suppression of the quarkonium production [1]. However, other effects like charmonium regeneration in or at the QGP phase boundary may contribute to charmonium production, as supported by several  $J/\psi$  measurements at LHC energies (*e.g.* [2]).

However, in heavy ion collisions, other mechanisms related to initial-state effects and/or interaction of charmonia with cold nuclear matter (CNM) (*e.g.*  $p_T$  broadening, gluon shadowing, and partonic coherent energy loss) play a role in the charmonium suppression. The study of proton-nucleus collisions at the LHC is therefore essential to calibrate these effects, in order to allow a quantitative determination of the QGP-related suppression in nucleus-nucleus collisions. The measurements of the  $J/\psi$  nuclear modification factor in p-Pb collisions at  $\sqrt{s_{NN}} = 5.02$  TeV [3, 4] also support the QGP formation in Pb-Pb, since the models including gluon shadowing and partonic coherent energy loss are able to describe the p-Pb results, while they fail to explain the Pb-Pb results.

In this thesis, we study the evolution of the  $J/\psi$  production with the event charged particle multiplicity at mid-rapidity in p-Pb collisions at 5.02 TeV. The present study is complementary to that performed as a function of the collision centrality in [5]. We are able to study rare events, which represent a small fraction of the p-Pb nuclear cross-section and exhibit a very high charged particle multiplicity, up to 4 times the average charged particle multiplicity. The new results presented in this thesis may shed light on the interplay between the different CNM effects. Furthermore, measurements of soft probes in p-Pb collisions are in good qualitative agreement with hydrodynamical model calculations [6, 7], which were the natural explanation to the observations made in Pb-Pb collisions. Thus the presence of collective effects in p-Pb collisions cannot be excluded. Although inclusive  $J/\psi$  measurements do not show any evidence of collectivity in p-Pb collisions, measurements of particle production as a function of the charged particle multiplicity in small size systems provide a way to detect the possible presence of collective final state effects. The present analysis allows to search for these effects in events with a very high charged particle multiplicity. In this context, the  $J/\psi$  production in high multiplicity pp collisions at 8 TeV is also studied in the present thesis. The charged particle multiplicity is measured at mid-rapidity ( $|\eta| < 1$ ) by mean of the ALICE Silicon Pixel Detector, and the  $J/\psi$  mesons are reconstructed in the di-muon channel with the ALICE Muon Spectrometer in the laboratory pseudo-rapidity range  $-4 < \eta < -2.5$ .

---

Chapter 1 is devoted to an introduction of the experimental and theoretical background of quarkonium studies. We describe the hadronic matter phase diagram and the stages of the QGP formation in heavy ion collisions. The different models for quarkonium production in pp collisions are discussed. Then, we describe the effects that the QGP formation in heavy ion collisions has on quarkonium production. This allows to understand why the  $J/\psi$  production is a very important probe to study the QGP. Finally, the study of cold nuclear matter effects in quarkonium production is introduced. The discussion is supported by some quarkonium experimental results and their comparison with theoretical models.

The ALICE detector is described in Chapter 2. ALICE is a heavy-ion dedicated experiment located at the Large Hadron Collider at CERN. Its main goal is the study of the physics of strongly interacting matter in ultra-relativistic heavy-ion collisions. It also performs measurements in pp collisions as part of its physics program. In this chapter, we describe the different ALICE subsystems. Special attention will be given to the Muon Spectrometer, which is the detector used for the  $J/\psi$  measurements performed in this thesis.

In Chapters 3 and 4 we present the work done in this thesis for the development of two different methods to measure the charged particle pseudorapidity density,  $dN_{ch}/d\eta$ . This measurement is essential to study the global properties of pp, p-A and A-A collisions. In this thesis, an estimation of the event  $dN_{ch}/d\eta$  is used to sample the data for the study the  $J/\psi$  production dependence with the pseudorapidity density of charged particles. The improvements introduced in this thesis on the multiplicity computation for  $J/\psi$  studies, allow a better estimation of the multiplicity and a reduction of the systematic uncertainties with respect to previous measurements.

Chapter 5 presents the studies that we performed on the ALICE Muon Spectrometer tracking efficiency during the 2013 p-Pb data taking. The correction applied to the data taken by the spectrometer is computed by means of specific Monte Carlo (MC) simulations of the detector. The main purpose of the studies in this chapter is to ensure that these simulations reproduce the real conditions of the spectrometer during the data-taking and its evolution with time. A method to measure the tracking efficiency from the reconstructed tracks is used in real and MC events to cross-check the validity of the simulations, and to assign a systematic uncertainty to the detector simulations.

The Chapters 6 and 7 are devoted to the description of the  $J/\psi$  analyses in p-Pb collisions carried out in this thesis. The goal of the first one is to measure the  $J/\psi$  yield. We developed a novel approach to correct the data taken with the Muon Spectrometer by the detector acceptance and efficiency. This technique reduces the systematic uncertainty on the  $J/\psi$  yield measurement due to the correction determination. The second Chapter describes an innovative technique for the extraction of the  $J/\psi$  average transverse momentum ( $\langle p_T \rangle$ ), based on the study of the di-muon  $\langle p_T \rangle$  invariant mass spectrum. This technique, needs the correction method developed in the previous chapter. Using the same technique, the  $J/\psi$   $\langle p_T^2 \rangle$  is also extracted. The three measurements are performed as a function of the charged particle multiplicity.

In Chapter 8 a preliminary analysis of the  $J/\psi$  yield and  $\langle p_T \rangle$  as a function of the charged particle multiplicity is performed in pp collisions at 8 TeV. The main goal of this analysis is to provide a baseline for the interpretation of the results in p-Pb collisions. In addition, the charged particle multiplicities measured in high multiplicity pp collisions at 7 TeV were comparable to those measured in heavy ion collisions at lower energies, where effects ascribed to QGP formation were found [8, 9]. Therefore the search for heavy-ion-like collective effects at high multiplicities is also justified in high energy pp collisions at 8 TeV [10].

To conclude, in Chapter 9 we present and discuss the results obtained in pp collisions



---

at  $\sqrt{s} = 8$  TeV and p-Pb collisions at  $\sqrt{s_{\text{NN}}} = 5.02$  TeV, using the analysis techniques described in previous chapters. The results include the  $J/\psi$  yield and  $\langle p_{\text{T}} \rangle$  dependence with the charged particle multiplicity in pp and p-Pb collisions. We also show a preliminary measurement of the dependence of the  $J/\psi$   $\langle p_{\text{T}}^2 \rangle$  with multiplicity in p-Pb. Finally, we propose the measurement of the  $J/\psi$  nuclear modification factor using the  $dN_{\text{ch}}/d\eta$  event selector to determine the number of binary collisions ( $N_{\text{coll}}$ ). In this way, very high  $N_{\text{coll}}$  values are reached, allowing an extended range of the present ALICE  $J/\psi$  measurement.

**Disclaimer:** The results labeled as "ALICE Preliminary" were approved by the collaboration as official ALICE preliminary results. The rest of figures and results shown here, as well as the discussion and conclusions extracted from them, represent only the work and opinion of the author of this thesis. They must not be considered as official ALICE results. There is a paper preparation currently ongoing, which includes some of the results in p-Pb collisions. A part of the results presented here will become ALICE official results if approved in the next months.



# TABLE OF CONTENTS

	<b>Page</b>
<b>I Introduction</b>	<b>1</b>
<b>1 Theoretical and experimental context</b>	<b>3</b>
1.1 The standard model in a nutshell . . . . .	4
1.1.1 Basics of Quantum Chromodynamics . . . . .	5
1.2 QCD matter phase diagram and the Quark-Gluon Plasma . . . . .	7
1.3 The quest for the QGP in Heavy-Ion collisions . . . . .	9
1.3.1 Evolution of a heavy-ion collision: The Bjorken scenario . . . . .	9
1.3.2 Experimental probes to study the QGP . . . . .	11
1.4 Charmonium production in pp collisions . . . . .	12
1.4.1 Charmonium spectroscopy . . . . .	12
1.4.2 Theoretical models for quarkonium production . . . . .	14
1.4.3 Experimental results . . . . .	16
1.5 Charmonium production in A-A collisions: probing the Quark-Gluon Plasma	21
1.5.1 Color screening and charmonium sequential suppression . . . . .	21
1.5.2 Charmonium regeneration . . . . .	22
1.5.3 Experimental results . . . . .	24
1.6 Charmonium production in p-A collisions: Cold Nuclear Matter effects . . . .	27
1.6.1 Gluon shadowing . . . . .	28
1.6.2 Gluon saturation . . . . .	30
1.6.3 Coherent parton energy loss . . . . .	31
1.6.4 Nuclear absorption . . . . .	32
1.6.5 Experimental results . . . . .	33
<b>2 The ALICE experiment at the LHC</b>	<b>43</b>
2.1 The Large Hadron Collider (LHC) . . . . .	43
2.1.1 The LHC experiments . . . . .	43
2.2 The ALICE detector . . . . .	45
2.2.1 Global detectors . . . . .	45
2.2.2 Central barrel detectors . . . . .	48

2.2.3	Muon spectrometer . . . . .	52
2.3	ALICE Trigger system, Data Acquisition and Reconstruction . . . . .	57
2.3.1	Trigger system . . . . .	57
2.3.2	Data Acquisition (DAQ) . . . . .	59
2.3.3	Reconstruction . . . . .	59
2.4	Data sample selection . . . . .	59
2.5	Muon Tracks selection . . . . .	60
<b>II Charged particle multiplicity measurement</b>		<b>63</b>
<b>3</b>	<b>SPD acceptance<math>\times</math>efficiency multiplicity correction method</b>	<b>65</b>
3.1	SPD vertex and tracking . . . . .	66
3.2	SPD status and run variations . . . . .	67
3.3	Event selection for multiplicity determination . . . . .	69
3.4	SPD acceptance $\times$ efficiency correction . . . . .	72
3.5	Implementation of the correction method . . . . .	77
3.6	Charged particle pseudorapidity density distribution measurement . . . . .	79
3.7	Event selection efficiency correction . . . . .	83
3.8	Charged particle distribution measurement . . . . .	88
3.9	Use of the SPD $\mathcal{A}\times\epsilon$ corrected tracklets as multiplicity estimator . . . . .	93
3.10	Systematic uncertainties on $dN_{ch}/d\eta(\eta)$ measurement . . . . .	96
<b>4</b>	<b>Data-driven multiplicity correction method</b>	<b>99</b>
4.1	Basics of the correction method . . . . .	100
4.2	Choice of the reference value . . . . .	103
4.3	$dN_{ch}/d\eta/\langle dN_{ch}/d\eta \rangle$ axis construction from $N_{tr}^{corr}$ . . . . .	107
4.4	Equalization of p-Pb and Pb-p multiplicity estimation . . . . .	112
4.5	Considerations for the computation of the $\alpha$ factors in MC . . . . .	114
4.6	$\langle dN_{ch}/d\eta \rangle$ computation . . . . .	117
4.7	$\langle dN_{ch}/d\eta \rangle_i$ systematic uncertainty . . . . .	117
4.7.1	Event selection efficiency uncertainty . . . . .	118
4.7.2	Contribution from pile-up events . . . . .	119
4.7.3	Multiplicity bin-flow . . . . .	125
4.8	Multiplicity results . . . . .	127
<b>III J/<math>\psi</math> production measurement</b>		<b>129</b>
<b>5</b>	<b>Muon Spectrometer tracking efficiency</b>	<b>131</b>
5.1	Muon Spectrometer track reconstruction . . . . .	132
5.2	Muon Spectrometer acceptance and efficiency . . . . .	133

5.2.1	Acceptance . . . . .	133
5.2.2	Efficiency . . . . .	133
5.2.3	Acceptance $\times$ Efficiency determination . . . . .	134
5.3	Tracking efficiency estimation from reconstructed tracks . . . . .	135
5.4	Biases of the efficiency estimation from reconstructed tracks . . . . .	137
5.5	Efficiency studies for p-Pb data-taking periods . . . . .	138
5.5.1	Efficiency computation in data . . . . .	139
5.5.2	Comparison data-MC efficiency results . . . . .	141
5.5.3	Comparison data-MC efficiency results with reject list . . . . .	145
5.5.4	Single muon tracking efficiency systematic uncertainty estimation . . . . .	146
5.5.5	From single muon to $J/\psi$ tracking efficiency systematic uncertainty estimation . . . . .	146
<b>6</b>	<b><math>J/\psi</math> yield measurement</b>	<b>151</b>
6.1	$J/\psi$ yield measurement . . . . .	152
6.1.1	$J/\psi$ $\mathcal{A}\times\epsilon$ correction . . . . .	153
6.1.2	Computation of signal tails parameters . . . . .	154
6.1.3	$J/\psi$ signal extraction . . . . .	158
6.1.4	Di-muon trigger event normalisation . . . . .	160
6.2	Event selection efficiency correction . . . . .	164
6.3	Systematic uncertainties . . . . .	165
6.3.1	Signal extraction uncertainty . . . . .	166
6.3.2	Tails variation uncertainty . . . . .	168
6.3.3	Di-muon trigger event normalisation uncertainty . . . . .	169
6.3.4	Uncertainty on the input MC distributions for $\mathcal{A}\times\epsilon$ computation . . . . .	170
6.3.5	Bin-flow uncertainty. Combination of $\mathcal{A}\times\epsilon$ , bin-flow and signal extraction uncertainties . . . . .	173
6.3.6	Pile-up . . . . .	176
6.3.7	Combination of yield systematic uncertainties . . . . .	183
<b>7</b>	<b><math>J/\psi</math> mean transverse momentum measurement</b>	<b>185</b>
7.1	$J/\psi$ mean transverse momentum measurement . . . . .	186
7.1.1	$J/\psi$ mean transverse momentum extraction procedure . . . . .	187
7.2	Systematic uncertainties . . . . .	189
7.2.1	$\langle p_T \rangle$ extraction uncertainty . . . . .	189
7.2.2	$\mathcal{A}\times\epsilon$ -Bin-flow-extraction combined effect . . . . .	193
7.2.3	Di-muon $\langle p_T \rangle$ variation with invariant mass . . . . .	195
7.2.4	Propagation of signal extraction parameter errors to $\langle p_T \rangle$ extraction . . . . .	198
7.2.5	Pile-up contribution to $J/\psi$ $\langle p_T \rangle$ extraction . . . . .	200
7.2.6	Combination of $J/\psi$ $\langle p_T \rangle$ systematic uncertainties . . . . .	200
7.3	$J/\psi$ $\langle p_T^2 \rangle$ measurement . . . . .	203

<b>8</b>	<b><math>J/\psi</math> measurements in pp collisions</b>	<b>207</b>
8.1	Charged particle multiplicity estimation . . . . .	208
8.2	$J/\psi$ yield and $\langle p_T \rangle$ measurement . . . . .	211
8.3	Systematic uncertainties . . . . .	213
8.3.1	Yield uncertainties . . . . .	216
8.3.2	$\langle p_T \rangle$ uncertainties . . . . .	218
<b>IV</b>	<b>Results and discussion</b>	<b>221</b>
<b>9</b>	<b>Experimental results and discussion</b>	<b>223</b>
9.1	Relative $J/\psi$ production and $\langle p_T \rangle$ dependence with multiplicity in p-Pb collisions at 5.02 TeV . . . . .	224
9.2	Relative $J/\psi$ production and $\langle p_T \rangle$ dependence with multiplicity in pp collisions at 8 TeV . . . . .	227
9.3	Comparison of pp and p-Pb results . . . . .	228
9.4	$p_T$ broadening as a function of charged particle multiplicity . . . . .	230
9.5	$R_{FB}$ as a function of charged particle multiplicity . . . . .	231
9.6	Nuclear modification factor as a function of $\tilde{N}_{\text{coll}}^{mult}$ . . . . .	233
9.7	$p_T$ broadening as a function of $\tilde{N}_{\text{coll}}^{mult}$ . . . . .	236
	<b>Conclusions and outlook</b>	<b>239</b>
<b>A</b>	<b>Centrality determination in ALICE</b>	<b>243</b>
<b>B</b>	<b>Summary of uncertainties formulae</b>	<b>247</b>
<b>C</b>	<b>Comparison of <math>J/\psi</math> yield and <math>\langle p_T \rangle</math> with other analyses</b>	<b>249</b>
<b>D</b>	<b>Comparison of updated results with ALICE Preliminary</b>	<b>255</b>
<b>E</b>	<b><math>J/\psi</math> production dependence with forward rapidity multiplicity</b>	<b>261</b>
	<b>Résumé</b>	<b>265</b>
	<b>List of Tables</b>	<b>273</b>
	<b>List of Figures</b>	<b>277</b>
	<b>Bibliography</b>	<b>291</b>

## **Part I**

# **Introduction**





## THEORETICAL AND EXPERIMENTAL CONTEXT

A new state of matter, the so called Quark-Gluon Plasma (QGP), is predicted by Quantum Chromodynamics (QCD). QCD is a theory which describes the strong interaction, one of the four fundamental forces of nature. The QGP is a deconfined state of strongly interacting matter, which is expected to have been the state of the universe in the early stages of its evolution. The study of QGP is an intense research activity, both experimentally and theoretically. The production of charmonium, bound states of  $c$  and  $\bar{c}$  quarks, in heavy ion collisions is an ideal probe for QGP formation in the laboratory. This thesis is focused on the study of charmonium production in proton-proton and proton-lead collisions.

In this chapter we give the very basic notions of the Standard Model of particle physics and QCD. We also describe the hadronic matter phase diagram and QGP formation in heavy ion collisions. Among the many probes used to study the medium formed in heavy ion collisions, we focus on charmonium studies, since it is the main subject of this thesis. The different models for charmonium production in proton-proton collisions are reviewed, together with some of the available experimental results. The different effects of the QGP formation affecting charmonium production in heavy ion collisions are discussed, as well as several experimental results and its comparison with theoretical predictions. Finally, the study of cold nuclear matter effects in charmonium production is introduced. A summary of some of the latest results in proton-nucleus collisions with the ALICE detector at the LHC are presented and compared with cold nuclear matter models predictions.

## 1.1 The standard model in a nutshell

The Standard Model of particle physics is the theory that describes the electromagnetic, weak and strong interactions among the elementary particles which compose the matter in the universe <sup>1</sup>. From the formal point of view, the Standard Model is a quantum field theory based on the gauge symmetry  $SU(3)_C \times SU(2)_L \times U(1)_Y$ . This gauge group includes the symmetry group of the strong interactions ( $SU(3)_C$ ) and that of the electroweak interactions ( $SU(2)_L \times U(1)_Y$ ). The elementary particles are characterised by their masses and quantum numbers, such as the spin ( $S$ ), electric charge ( $Q$ ), baryon number ( $B$ ), lepton number ( $L$ ), color charge... A summary table is shown in Fig. 1.1. The spin allows to classify the elementary particles into two basic types, the fermions and the bosons.

The fermions are the basic building blocks of matter, having semi-integer spin. They are classified in three generations of quarks ( $u, d$ ), ( $c, s$ ), ( $t, b$ ) (with  $B \neq 0$ ,  $L = 0$ , color charge, fractional electrical charge and  $m > 0$ ) and three generations of leptons ( $e, \nu_e$ ), ( $\mu, \nu_\mu$ ), ( $\tau, \nu_\tau$ ) (with  $B = 0$ ,  $L \neq 0$ , no color charge, -1 electrical charge except for neutrino and  $m > 0$ ). These generations follow a mass hierarchy from lower to higher masses. The particles which build the stable matter belong to the first generation and the heavier ones quickly decay into the next most stable level. Each elementary particle has its corresponding anti-particle (anti-matter) which has the same mass but opposite quantum numbers.

The matter particles interact among them transferring discrete amounts of energy by means of bosons. The bosons have integer spin and they are the mediators of the fundamental interactions. The Standard Model includes the electromagnetic force, carried by the *photon* ( $\gamma$ ) and affects electrically charged particles; the weak force, carried by the electroweak bosons  $W^\pm$  and  $Z^0$  bosons, is responsible for nuclear decays; and the strong force, carried by the *gluon* ( $g$ ), which only involves color charged particles (quarks). The fourth fundamental interaction, the gravitation, is not yet described by the standard model.

The electromagnetic and weak interactions are unified in the electroweak theory [12–15]. The mechanism that breaks electroweak symmetry [16–21], implies the existence of a scalar particle, the Higgs boson  $H$ , which leads to the generation of the  $W^\pm$  and  $Z^0$  masses. The discovery at CERN’s Large Hadron Collider (LHC) of a new particle consistent with the Higgs boson was reported in [22, 23].

In our every day world the quarks are confined into colorless states called hadrons by means of the strong interaction [24–27]. They can be assembled in quark-anti-quark pairs ( $q\bar{q}$ ) named mesons, or three quark states (qqq) named baryons. The Quantum Chromodynamics (QCD) [28, 29] describes the strong interaction by means of the color charge. In the following we briefly describe the main properties of the strong interaction and its theoretical framework, the QCD.

---

<sup>1</sup>For a pedagogical introduction to the Standard Model see for example [11]

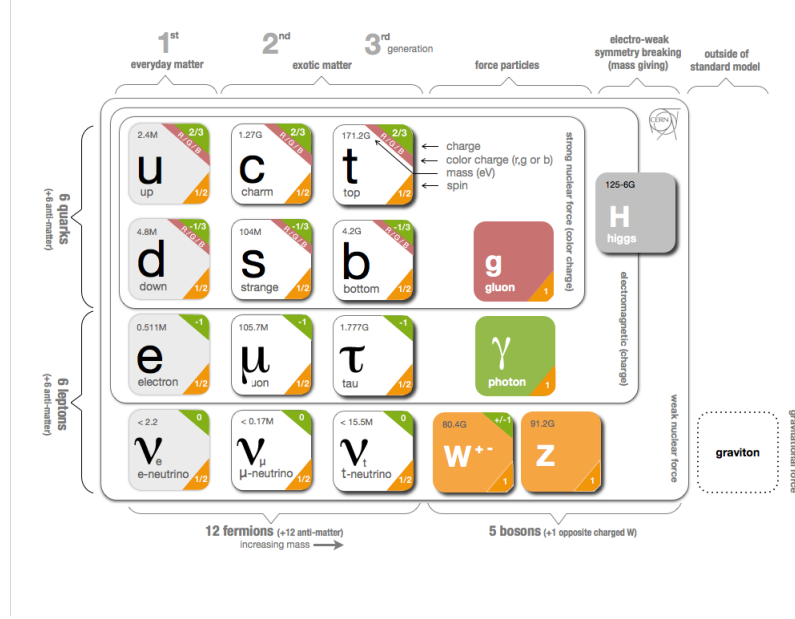


Figure 1.1: Summary table of the Standard Model elementary particles [30].

### 1.1.1 Basics of Quantum Chromodynamics

The QCD is a Quantum Field Theory (QFT) that describes the strong interactions of colored quarks and gluons. It results from the  $SU(3)_C$  gauge symmetry. For the purposes of this thesis, it is sufficient to recall the essential properties of the theory:

- Quarks carry color and electric charges. There are three possible color charge states *red*, *green* and *blue* and its corresponding anti-colors.
- Color is exchanged by eight bicolored gluons.
- The strength of the interaction is given by the strong coupling constant  $\alpha_s$ .

The fact that the gluons carry a color charge, allows them to interact with other gluons. This makes the strong interaction unique (non-abelian interaction) among the fundamental interactions. Two particularities of QCD are the confinement and asymptotic freedom, and chiral symmetry breaking at low energy.

#### 1.1.1.1 Confinement and asymptotic freedom

In QFTs the vacuum becomes a polarisable medium, as a result of quantum fluctuations. These fluctuations imply that a quark is not a quark alone, but as it propagates it can emit a gluon which subsequently annihilates into a  $q\bar{q}$  pair and so on. The quark is therefore surrounded by a cloud of color charges polarised with respect to it. If one wants to measure the force experienced by a test color charge, the result depends on the distance to the quark,

since the test charge penetrates more or less into the cloud that screens the quark's charge<sup>2</sup>. This is a result that we are familiar with from QED, and it is called *screening* (Fig. 1.2 **a**). However, unlike QED photons, in QCD the gluons can interact among themselves (since they are color charged), so another way of vacuum polarisation can happen involving gluons turning into pairs of gluons [31, 32]. This is called *anti-screening* (Fig. 1.2 **b**), and it results to be stronger than the *screening* effect.

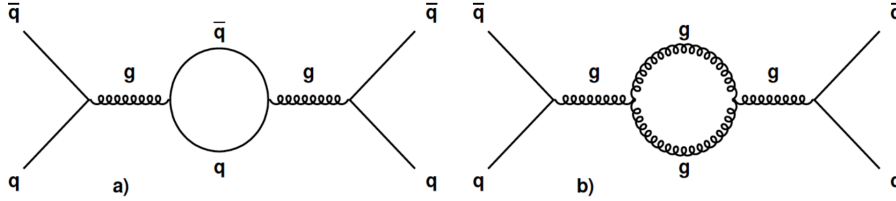


Figure 1.2: Vacuum polarization Feynmann diagrams in QCD. **a)** *screening*. **b)** *anti-screening*.

As a result of these possible vacuum polarisations, the dependence of the strong coupling constant with the momentum transferred in the interaction ( $Q^2$ ) can be written as:

$$(1.1) \quad \alpha_s(Q^2) = \frac{4\pi}{(11 - \frac{2}{3}n_f) \ln \frac{Q^2}{\Lambda_{QCD}^2}}$$

where  $n_f$  is the number of quark flavors and  $\Lambda_{QCD}$  ( $\approx 200$  MeV) is a constant which corresponds to the limit where, for smaller energy transfers, the perturbation theory is not applicable anymore to QCD calculations.

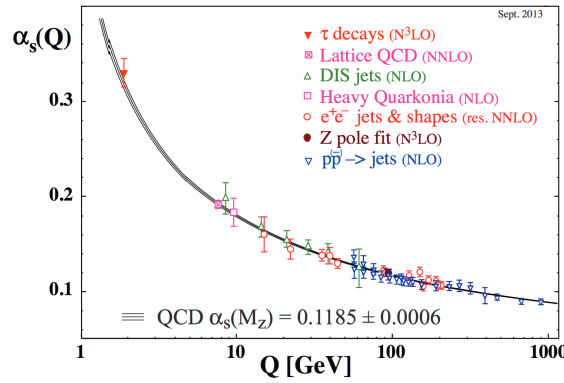


Figure 1.3: Summary of measurements of  $\alpha_s$  as a function of the energy scale  $Q$ . [33]

As illustrated in Fig. 1.3, the strength of the coupling constant  $\alpha_s$  decreases at short distances (high energy), allowing quarks to behave as quasi-free particles in this regime. This phenomenon is called *asymptotic freedom*. On the contrary, at long distances (low energy)

<sup>2</sup>The situation is analog to an electric charge in a dielectric medium.

the intensity of the coupling increases, explaining the fact that the quarks are confined in neutral color states. This property is called *confinement*.

### 1.1.1.2 Chiral symmetry breaking

The QCD Lagrangian, in absence of quark masses ( $m_q \approx 0$ ), is symmetric under helicity transformations of the quarks<sup>3</sup>. This is called chiral symmetry, and it implies that there is no interaction between quarks with different helicities. The quark fields can be decomposed in left- ( $\psi_L$ ) and right-hand ( $\psi_R$ ) quark fields. This symmetry can be characterised with the chiral condensate  $\langle \bar{\psi}\psi \rangle = \langle \bar{\psi}_L\psi_R + \bar{\psi}_R\psi_L \rangle = 0$ .

Nevertheless, the quark masses are not null and therefore  $\langle \bar{\psi}\psi \rangle \neq 0$ . We say that the chiral symmetry is spontaneously broken. The spontaneous breaking of the chiral symmetry in QCD, allows to explain the existence of 8 Goldstone bosons ( $\pi^0, \pi^\pm, K^0, K^\pm, \bar{K}^0, \eta_s$ ) [34]. At high energies ( $m_q \approx 0$ )<sup>4</sup> a restoration of the chiral symmetry is expected. A symmetry restoration represents a valid condition to predict the existence of a QCD phase transition.

## 1.2 QCD matter phase diagram and the Quark-Gluon Plasma

The phase diagram of strongly interacting matter is shown in Fig. 1.4 as a function of temperature and net baryon density ( $\mu_B$ ). At low temperature and low density, quarks and gluons are confined into hadrons. The matter can be described as an hadronic gas. At low temperatures and high densities, the matter can be described as a degenerated gas of neutrons, which is believed to exist in the neutron stars. For low temperatures, as  $\mu_B \rightarrow \infty$ , the quarks begin to form color Cooper pairs and a color superconducting state is expected to be formed [35].

Shortly after the discovery of the asymptotic freedom, the existence of a deconfined state of quarks and gluons was predicted at high temperatures [36, 37]. If the temperature is high enough the strength of the strong force becomes weak, and hence the quarks and gluons become deconfined. The deconfined state of matter is called Quark-Gluon Plasma (QGP).

Lattice QCD (lQCD)<sup>5</sup> at finite temperature allows to study the QCD equation of state, which can be used to characterize the transition of the hadronic matter to QGP. As mentioned in previous section, the chiral symmetry restoration allows to predict a phase transition. But the transition of hadronic matter to a deconfined state and whether the chiral transition is associated to deconfinement or not, can only be answered today from first principles with lQCD calculations. For a discussion on the description of the QCD phase diagram with a

---

<sup>3</sup>The helicity ( $h$ ) of a particle is the projection of its spin over the propagation direction. For particles with  $S = 1/2$ ,  $h = +1/2$  (right-handed) and  $-1/2$  (left-handed)

<sup>4</sup>This is valid only for low quark masses:  $u$ ,  $d$  and  $s$

<sup>5</sup>Lattice QCD is a very powerful technique which allows to explore the non-perturbative domain of QCD. lQCD is QCD formulated on a discrete Euclidean space-time lattice. When the spacing of the lattice points becomes infinitesimally small, the QCD continuum is recovered [38].

phenomenological model (MIT-Bag model [39]), a QCD effective model (NJL model [40, 41]) and lQCD see for example [42].

The results from lQCD calculations at  $\mu_B = 0$  show that the deconfinement transition occurs at a critical temperature  $180 \leq T_c \leq 200$  MeV [43]. The corresponding critical energy density has been determined to be about  $1 \text{ GeV/fm}^3$  [44]. Those results have also shown that the QGP does not behave as an ideal gas, since there is a residual interaction. Furthermore, the results in [43] also suggest that the deconfinement transition, reflected in the rapid increase of the system energy density; and the chiral phase transition, reflected on the sudden decrease of the chiral condensate, occur altogether at the same interval of temperatures.

lQCD results have shown that at small or vanishing values of  $\mu_B$  the deconfinement transition is not a phase transition but a continuous cross-over due to the non-zero mass of the  $u$ ,  $d$  and  $s$  quarks [44]. Model calculations [45, 46] as well as lQCD predict a critical point at  $\mu_B \sim 0.72$  MeV, where the cross-over becomes a second order phase transition [47, 48]. Beyond this critical point the transition becomes a first order phase transition.

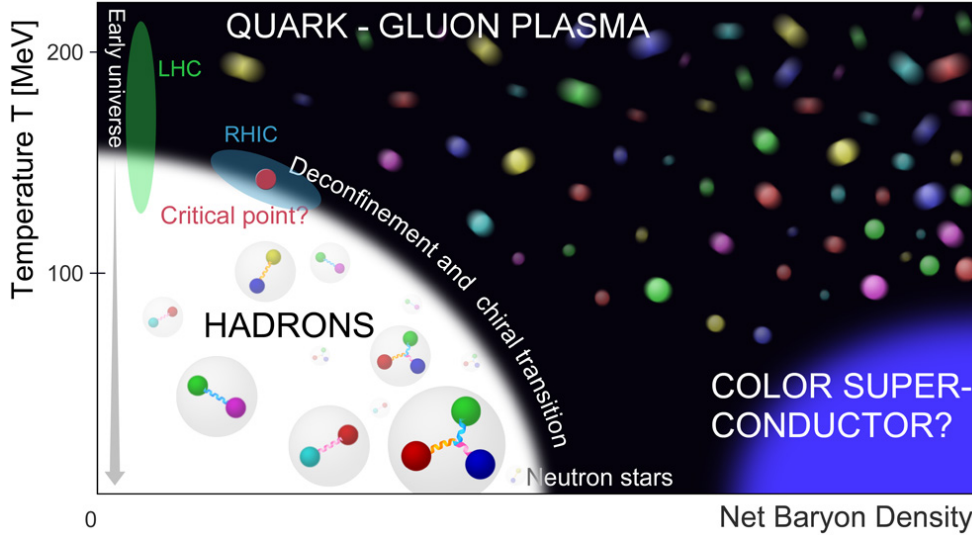


Figure 1.4: QCD phase diagram as a function of the baryon density and temperature.

As we have seen, the QCD phase diagram has been extensively studied theoretically by using models and lQCD calculations. The experimental validation of the QCD predictions is crucial. In the following section we focus on how to explore experimentally this diagram, and particularly how QGP can be studied in the laboratory.

### 1.3 The quest for the QGP in Heavy-Ion collisions

The experimental tool to study the strongly interacting matter in the laboratory consist on colliding heavy-ions at ultra-relativistic energies. When two nuclei collide, the multiple interactions among the participating nucleons leave behind an out-of-equilibrium system of partons<sup>6</sup>. For this to happen, the nuclei crossing time has to be much smaller than the characteristic time of the strong interaction  $\tau_{cross} \ll \tau_{strong} \approx 1/\Lambda_{QCD} \sim 1 \text{ fm}/c$ . If the energy density attained by the system is bigger than the critical energy density ( $\sim 1 \text{ GeV}/\text{fm}^3$ ), a drop of QGP might be formed. The dynamical evolution of such a system is very complicated. The initial energy density of the system formed in heavy-ion collisions and its evolution, can be modeled by the Bjorken scenario [49].

#### 1.3.1 Evolution of a heavy-ion collision: The Bjorken scenario

In the context of the Bjorken scenario, a picture of the space-time evolution of a heavy ion collision is given. The evolution of the formed system is treated with the Landau hydrodynamical model [50] in order to simplify the evolution of the system. The hypothesis assumed by Bjorken are:

- The nuclei crossing time is smaller than the characteristic time of the strong interaction. This assumption implies that the partons are created after the nuclei have crossed. In ultra-relativistic heavy-ion collisions, the two nuclei can be represented as pancakes in the center-of-mass system due to Lorentz contraction, and the crossing time can be estimated as  $\tau_{cross} = 2R/\gamma$ , where  $R$  is the nuclei radius and  $\gamma$  is the Lorentz factor. The condition  $\tau_{cross} \ll \tau_{strong}$  is therefore satisfied for  $\gamma > 12$ , which implies center-of-mass energies per nucleon above  $\sqrt{s_{NN}} > 25 \text{ GeV}$  (Note that in LHC Pb-Pb collisions  $\sqrt{s_{NN}} = 2760 \text{ GeV}$ ) [51]
- The particle production distribution presents a plateau at mid-rapidity. This implies a rapidity symmetry of the system which lead to simple solutions of the hydrodynamic equations.

In Fig. 1.5, the different stages of the space-time evolution of the collision described by the Bjorken scenario are shown. These stages are explained in the following:

1. **Pre-equilibrium** ( $0 < \tau < 1 \text{ fm}/c$ ): The collision of the nuclei takes place at  $\tau = 0$ . Right after the collision, the multiple interactions among the partons creates a pre-equilibrium phase. These partons re-scatter leading to thermalisation of the system.
2. **QGP formation and hydrodynamic expansion** ( $1 < \tau < 10 \text{ fm}/c$ ): If the energy density of the system is high enough the QGP is formed. Due to the pressure gradient

---

<sup>6</sup>In general the quarks and gluons are called partons

between the high density medium and the surrounding vacuum the system starts to quickly expand.

3. **Mixed state** ( $10 < \tau < 20 \text{ fm}/c$ ): The expanding system cools down. When the temperature drops below the critical temperature, the hadronization of quarks and gluons starts.
4. **Hadronic gas phase** ( $\tau \geq 20 \text{ fm}/c$ ): Once all the quarks and gluons are again confined, the system can be described by an expanding hadronic gas.
5. **Freeze-out** ( $1 < \tau < 20 \text{ fm}/c$ ): This stage is divided in two:
  - *Chemical freeze-out* : The relative abundances of hadrons is fixed when the inelastic collisions between hadrons cease.
  - *Kinetic freeze-out* : When the system further expands, the hadrons do not interact elastically anymore. The hadrons stream freely to the detectors.

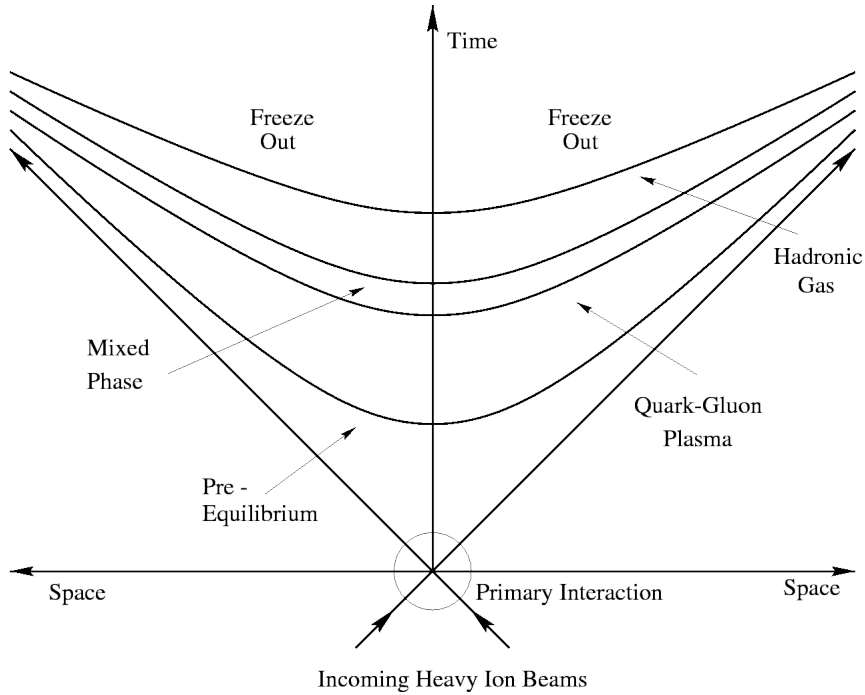


Figure 1.5: The space-time evolution of a heavy-ion collision. The collision stages, description of QGP formation and transition to ordinary matter are described in the text. Figure taken from [52].

As we have seen, the life-time of the QGP is so short that its direct experimental observation is not possible. In the following section the experimental probes that can be used to study the different phases of the system created in heavy-ion collisions are described.



### 1.3.2 Experimental probes to study the QGP

Due to the confinement property of the strong interaction we cannot observe directly the deconfined partons of a QGP. Only the indirect observation via the final products of the collision is possible. There is a large variety of probes, but here we just give a general classification and mention a few of them. Note also that the given references are not an exhaustive compilation.

First of all, the general properties of the collision can be measured through the study of the global observables. Furthermore, depending on the stage of the collision to be characterised, one can consider early and late signatures [53].

The global observables provide information about the initial energy density, geometrical aspects of the collision and expansion dynamics. The initial energy density can be estimated through the measurement of the transverse energy and charged particle multiplicity [49]. Besides, the measurements of the charged particle multiplicity give also geometrical information such as the impact parameter of the collision, number of participating nucleons and number of binary nucleon-nucleon collisions [54, 55]. Particle spectra and azimuthal anisotropies can be used to determine the pressure gradient of the expanding medium [56, 57]. In addition, the hadronic yield measurement also allows to infer the system temperature at chemical freeze-out using a statistical model [58].

The early signatures are those which are established early in the collision and their production is not affected by rescattering or system expansion. They can give information of perturbative QCD processes and also they serve to probe the QGP. Among these probes we find the electroweak bosons ( $\gamma$  (direct or di-lepton decay) and  $W^\pm$  and  $Z^0$  decaying into leptons), high transverse momentum ( $p_T$ ) particle production and hadrons made of heavy flavour quarks. Thermal photons<sup>7</sup> are directly emitted from the QGP and they do not interact strongly. They can give information about the initial temperature of the system [59, 60]. The  $W^\pm$  and  $Z^0$  bosons do not either interact strongly, thus their production can be used, for example, to study the parton distribution functions (PDF)<sup>8</sup> and nuclear effects on the PDFs [61–63]. Moreover, the energy loss suffered by hard-scattered partons passing through the QGP modify the yields (with respect to the yield without formed medium) of high momentum particles ("jet quenching") [64]. Heavy flavor quark pairs such as  $c\bar{c}$  pairs (or  $b\bar{b}$ ), due to its large mass can only be created in the primary nucleon-nucleon collisions. What can change due to interaction with the formed system, are the relative amounts of mesons with hidden ( $c\bar{c}$  bound states are called charmonium<sup>9</sup>) and open charm ( $c\bar{q}$  and  $q\bar{c}$ ). Charmonium states are formed during the QGP phase, so their production rates can be used as a QGP formation probe [1, 65]. The total charm production can also serve to test the perturbative QCD calculations [66]. Furthermore, the phase boundary and hadron gas stage can also be

<sup>7</sup>Note that there are other sources of photons like hadron scattering.

<sup>8</sup>The PDF is the momentum distribution functions of the partons in a nucleon. They represent the probability density to find a parton with a momentum fraction  $x$  of the nucleon at a given energy scale.

<sup>9</sup>In general, the  $q\bar{q}$  bound states are called quarkonium.

tested [67].

The strong interactions between the hadrons and partons before the freeze-out can fade the information of the early formed system in the collision. We consider as late signatures hadrons which are made of light quarks, since they can be produced and destroyed in all the phases of the system expansion. They provide information about the hadron gas and freeze-out stages [68, 69].

It is important to note, that in order to correctly characterise the QGP we need to study these probes in nucleus-nucleus (A-A)<sup>10</sup> collisions, but it is also crucial to determine its properties in collisions where the QGP is not (expected to be) formed like proton-proton (pp) and proton(deuteron)-nucleus (p(d)-A) collisions. Then, comparing the results in different collision systems the QGP properties can be inferred.

In this thesis, we focus on the study of charmonium production in p-Pb collisions, more specifically  $J/\psi$  ( $c\bar{c}$ ) production. The study of quarkonium production is experimentally interesting since, as we shall see, it allows to study confinement, and it is also a good probe to test the formation of the QGP. In addition, the study of quarkonium production can help to improve our understanding of the perturbative and non-perturbative aspects of QCD. During the following sections, we give a summary on the quarkonium production mechanisms, the expected effects on its production due to QGP formation in the collision or cold nuclear matter, and some of the related experimental results. For a recent comprehensive review on the different models and LHC results see [70].

## 1.4 Charmonium production in pp collisions

The first step to be able to use charmonia to probe heavy ion collisions is to know how they are produced in hadron-hadron collisions. In this section we briefly summarise the basis of charmonium spectroscopy and the theoretical models that try to explain the quarkonium production mechanism. Finally, a summary on some of the experimental results is given.

### 1.4.1 Charmonium spectroscopy

The quarkonia are bound states of heavy quark  $Q\bar{Q}$  pairs. In the following we discuss the charmonia case only. Since the mass of the charm quark is large ( $m_c \simeq 1.3$  GeV), its velocity on the quarkonium rest frame can be considered to be small. Therefore, quarkonium spectroscopy can be studied in non-relativistic potential theory [71]. The binding potential can be described by the "Cornell" potential [72]:

$$(1.2) \quad V(r) = \sigma r - \frac{\alpha}{r}$$

with a string tension  $\sigma \simeq 0.2$  GeV<sup>2</sup> (confinement) and a Coulomb-like term with a gauge coupling  $\alpha \simeq \pi/12$ . The solutions of the Schrödinger equation using this potential correspond

---

<sup>10</sup>A stands for the nucleus atomic number

to the different charmonia bound states. The charmonia masses and binding energies (defined as the difference between the charmonium mass and the open charm threshold) are summarised in Tab. 1.1 [73].

State	$\eta_c$	$J/\psi$	$\chi_{c0}$	$\chi_{c1}$	$\chi_{c2}$	$\psi(2S)$
Mass (GeV/ $c^2$ )	2.98	3.10	3.42	3.51	3.56	3.69
$\Delta E$ (GeV)	0.75	0.64	0.32	0.22	0.18	0.05

Table 1.1: Charmonium states and binding energies ( $\Delta E$ ) [73].

The charmonium resonances and the possible transitions between them are shown in Fig. 1.6. The fundamental state 1S contains the  $J/\psi$  vector meson, which was discovered in 1974 [74, 75]. The  $J/\psi$  decays, among other channels, into a di-lepton pair ( $J/\psi \rightarrow l^+ l^-$ ). In hadronic collisions, all the resonances are formed in the initial hard collisions. The higher mass states can decay into the  $J/\psi$ , which is called feed down effect. As a consequence, the  $J/\psi$  can be produced from the hadronization of a  $c\bar{c}$  pair (direct production), but it can also be produced by the decay of a  $\psi(2S)$  or a  $\chi_{cJ}(1P)$ . The  $J/\psi$  sample from these processes is called "prompt". In hadronic collisions, approximately the 60% of the prompt  $J/\psi$  sample comes from direct production, the 30% from  $\chi_{cJ}$  and the 10% from  $\psi(2S)$  decays [76–78]. The  $J/\psi$  or  $\psi(2S)$  can also be produced from weak decays of B mesons ( $b\bar{q}$  and  $q\bar{b}$ ). The  $J/\psi$  sample from these decays is called "non-prompt". We refer as inclusive production to the sum of prompt and non-prompt samples. About 9% of the inclusive  $J/\psi$  production comes from B meson decays [79].

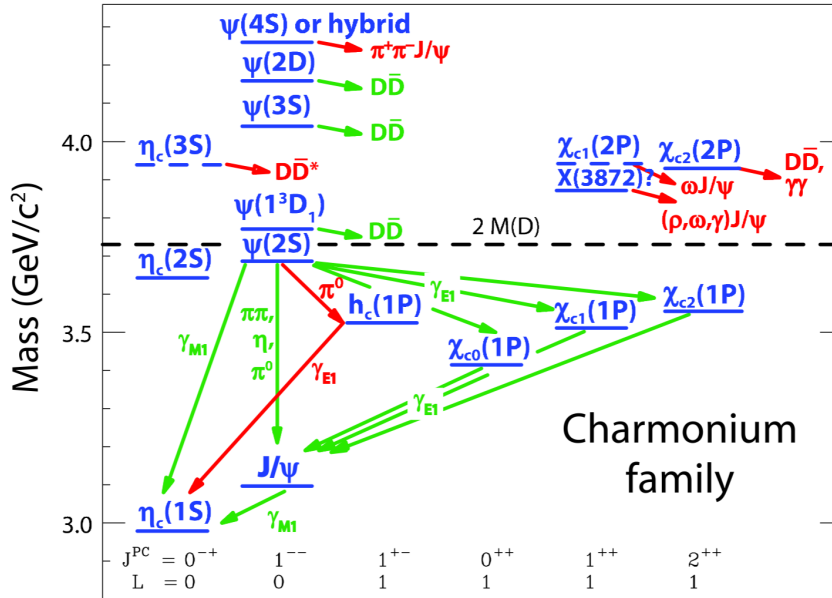


Figure 1.6: Spectroscopic diagram for charmonium family. The bottom row shows the spin, parity and charge conjugation quantum numbers associated with the states above it [80].

### 1.4.2 Theoretical models for quarkonium production

The production of a heavy  $Q\bar{Q}$  pair involves energy scales where the perturbative QCD is applicable ( $Q \geq 2m_q \gg \Lambda_{QCD}$ ). The leading order production processes are shown in Fig. 1.7<sup>11</sup>. However, the evolution of the  $Q\bar{Q}$  pair into the quarkonium state (hadronisation) involves energy scales of the order of the binding energy  $m_q v^2$  (where  $v$  is the heavy quark velocity in the quarkonium rest frame, which is considered to be small) so it is a non-perturbative process. A  $Q\bar{Q}$  pair can be created in 8 color states with a net color charge (color-octet state) and 1 state without color charge (color-singlet state). Therefore, the  $Q\bar{Q}$  pair is usually created in a color-octet state. In order to create a physical resonance (e.g.  $c\bar{c} \rightarrow J/\psi$ ) it is necessary to neutralize the charge of the pair. Neutralization of color charge occurs through interaction with the surrounding color fields.

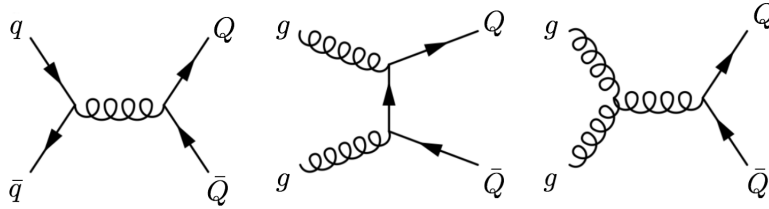


Figure 1.7: Heavy quark pair production at leading order through quark annihilation (left) and gluon fusion (middle and right).

From a theoretical point of view, the mechanism of color neutralisation is not yet fully understood. Most of the available theoretical models are based on the factorisation of the pair production and hadronization. In the following we summarise three models: *Color-Evaporation Model*, *Color-Singlet Model* and *Color-Octet Model*.

#### 1.4.2.1 The Color-Evaporation Model

The *Color-Evaporation Model* (CEM) is a simple phenomenological approach that describes the quarkonia formation probability in a statistical manner [83]. It is based on the assumption that the hadronisation is decorrelated from the  $Q\bar{Q}$  pair. This can be explained by the exchange of soft gluons by the pair with the collision-induced color fields, which destroys the correlation. This is what gives the name "*color evaporation*" to the model. Then, to obtain the cross section of a given quarkonium state, the  $Q\bar{Q}$  cross section is multiplied by a phenomenological factor which is related to the probability that the pair hadronizes into this state ( $F_{quarkonium}$ ). This factor is determined experimentally. The heavy quark pair mass is restricted to be smaller than the mass to create the lightest meson ( $m_M$ ) that can be

<sup>11</sup>Note that at the energy scales we deal with, the main mechanism is gluon fusion since gluon probability density in the nucleons is much bigger than that of quarks [81, 82] (see Fig. 1.19).

formed with the pair. Mathematically, this reads:

$$(1.3) \quad \sigma_{quarkonium} = F_{quarkonium} \int_{2m_Q}^{2m_M} \frac{d\sigma_{q\bar{q}}}{dm_{q\bar{q}}} dm_{q\bar{q}}$$

This calculation can be done at Leading Order (LO) (at  $\alpha_s^3$ ) in perturbation theory or at Next-to Leading Order (NLO) (at  $\alpha_s^4$ ) to account for the  $p_T$  dependence. This model is able to give correct predictions for the energy dependence and  $p_T$  distribution of the cross section in data [84, 85]. However, this model has several weak points. Among them are the fact that it is unable to give predictions of the quarkonium polarization and that also some discrepancies are found in the description of  $p_T$  spectra.

#### 1.4.2.2 The Color-Singlet Model

The *Color-Singlet Model* (CSM) was the first model for charmonia production and was proposed shortly after the discovery of the  $J/\psi$  [86–90]. In this model, the production of the bound state is completely correlated to the  $Q\bar{Q}$  production. In this way, the heavy quark pair has to be produced in a color-singlet state with the same quantum numbers as the charmonium. The non-perturbative factor of the quarkonium cross section is proportional to the bound state's wave function or its derivative, which can be extracted from data.

In Fig. 1.8, a diagram showing the  $J/\psi$  formation mechanism, via gluon fusion at order  $\alpha_s^3$ , is presented. The three diagrams can produce both color singlet and color octet states. In the left diagram, the state is produced with the same quantum numbers as the  $J/\psi$ , and therefore is the only diagram (the color singlet counterpart) which contributes to  $J/\psi$  formation in the CSM at LO.

As an example, the CSM successfully described the  $J/\psi$  and  $\Upsilon(b\bar{b})$  total cross sections as a function of the collision center-of-mass energy [91]. However, it failed on the predictions of  $\psi(2S)$  data in [92] by a factor 50. It has been shown that the NLO and Next-to-Next-to Leading Order (NNLO) (at  $\alpha_s^5$ ) corrections to the CSM are larger than the LO terms at mid and large  $p_T$  [93, 94].

#### 1.4.2.3 The Color-Octet Model

The *Color-Octet Model* (COM) [95] is based on a QCD effective theory called Non-Relativistic Quantum ChromoDynamics (NRQCD) [96]. The factorization in the COM uses NRQCD to separate the short-distance factors, which account for  $Q\bar{Q}$  creation, from the long-distance matrix elements, which account for the transition to a physical bound state and involves the non-perturbative scale  $v$  (velocity of heavy quark in the quarkonium rest frame). The COM calculations require an infinite sum of terms running over all possible quantum numbers of the heavy quark pair. In each term, the short distance coefficients are the perturbatively calculated (expansion in  $\alpha_s$ ) production rates of the heavy quark pair in the corresponding state  $n$  (color, spin and angular momentum), and the long-distance matrix elements are the

NRQCD matrix elements that give the probability of a heavy quark pair in the state  $n$  to form the bound state [97].

In the production cross section expressions, an infinite series of unknown matrix elements appear. However, the importance of each matrix element can be evaluated using the NRQCD velocity scaling rules [97, 98]. Each matrix element scales with a definite power of  $v$  so the cross section can be organised in a double expansion in powers of  $v^2$  and  $\alpha_s$ . For phenomenological applications the expansion is truncated at fixed order in  $v$ . The long-distance matrix elements can be determined from cross-sections fits in data [99, 100]. The transition of the intermediate  $c\bar{c}$  state into a physical  $J/\psi$  occurs through the emission of soft (non-perturbative) gluons, described by the long-distance matrix elements. Note, that the leading order term in  $v$  reduces to the CSM approach.

Although COM has successfully described many observables, a full proof of factorization does not yet exist. Furthermore it had problems describing polarisation results of  $J/\psi$  production in Tevatron  $p\bar{p}$  collisions at  $\sqrt{s} = 1.96$  TeV [101].

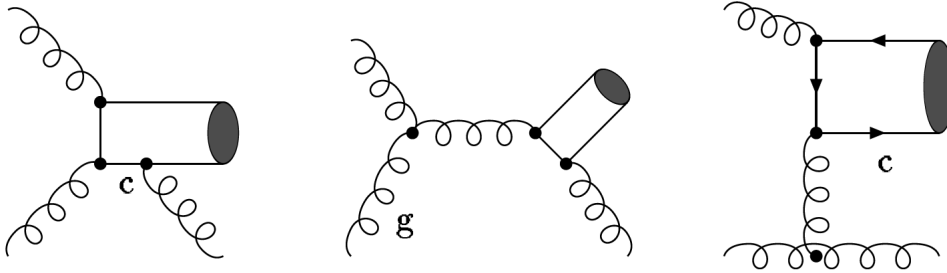


Figure 1.8: Diagrams that contribute to  $c\bar{c}$  hadroproduction via gluon fusion, at order  $\alpha_s^3$ . Figure taken from [102].

### 1.4.3 Experimental results

The quarkonium production measurements in pp collisions provide a crucial test for hadronisation models and QCD. They are also used as baseline for the measurements in heavy-ion collisions. In this section, we present a selection of charmonia and bottomonia experimental results in pp and  $p\bar{p}$  collisions performed at the LHC and Tevatron respectively. We briefly discuss the comparison of some results with the models explained before. For an extensive review of quarkonium results in pp collisions at the LHC see [70].

The inclusive  $J/\psi$  differential production cross section as a function of  $p_T$  in pp collisions at  $\sqrt{s} = 7$  TeV measured by ALICE [103] is presented in Fig. 1.9 (left). The result is compared to the theoretical calculations performed in the CSM at LO, NLO and NLO including the leading- $p_T$  contributions at NNLO (denoted as NNLO\*) [104]. The calculations were performed for direct production so they are scaled by a factor  $1/0.6$  to convert them to inclusive production. The LO calculation is not able to reproduce the  $p_T$  dependence of the

cross section. We can see how at NLO the  $p_T$  dependence is closer to the data behaviour but still underestimates the measurement. The addition of the leading- $p_T$  NNLO contributions further reduces the difference with respect to the experimental data.

In Fig. 1.9 (right) the same result of the ALICE  $J/\psi$  differential production cross section as a function of  $p_T$  are compared with NRQCD calculations for prompt  $J/\psi$  at NLO [105]. These calculations include the LO color-singlet contributions (the calculations in Fig. 1.9 (left)) and the color-octet contributions. The calculations show a reasonable agreement with the data. Note that in [103], the same comparison is performed for the  $\psi(2S)$  measurement obtaining also a reasonable agreement with the NRQCD calculations.

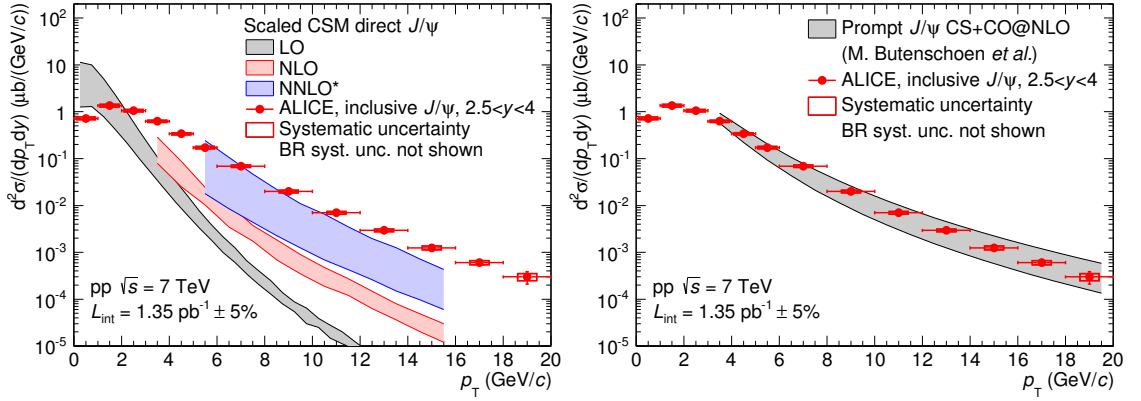


Figure 1.9: Left: Inclusive  $J/\psi$  production cross section as a function of  $p_T$  in pp collisions at  $\sqrt{s} = 7$  TeV. The bands correspond to several scaled CSM calculations for direct  $J/\psi$  [104]. Right: Inclusive  $J/\psi$  differential production cross section as a function of  $p_T$ . The band correspond to NRQCD calculations [105]. Figures taken from [103].

The results for the prompt  $J/\psi$  and  $\psi(2S)$  polarizations as a function of  $p_T$  in  $p\bar{p}$  collisions at  $\sqrt{s} = 1.96$  TeV measured by CDF [101] are presented in Fig. 1.10. The results are compared to NRQCD predictions in [106]. In data, the polarisation ( $\alpha$ ) information is extracted from the distribution of the muon decay angle (angle of the  $\mu^+$  in the rest frame of the vector meson with respect to the vector meson boost direction in the laboratory system). For fully transverse (longitudinal) polarisation  $\alpha = +1$  ( $-1$ ). As can be observed, the polarisations of both  $J/\psi$  and  $\psi(2S)$  become increasingly longitudinal as  $p_T$  increases beyond 10 GeV/c. The NRQCD calculations fail to describe the vector meson polarisation at high  $p_T$ .

$J/\psi$  polarisation measurements have also been performed at the LHC in pp collisions at  $\sqrt{s} = 7$  TeV. The results found by ALICE [108] and LHCb [109] are in good agreement, and predict a small or zero longitudinal  $J/\psi$  polarization.

The measurement of the  $\Upsilon(1S)$   $p_T$  differential production cross section were performed by ATLAS in pp collisions at  $\sqrt{s} = 7$  TeV [110] (Fig. 1.11). The results are compared with the theoretical predictions of the CEM and the NNLO\* CSM. From the comparison of the experimental results with the theoretical predictions, it can be extracted that both calculations have some problems in describing the spectra. Particularly, NNLO\* CSM

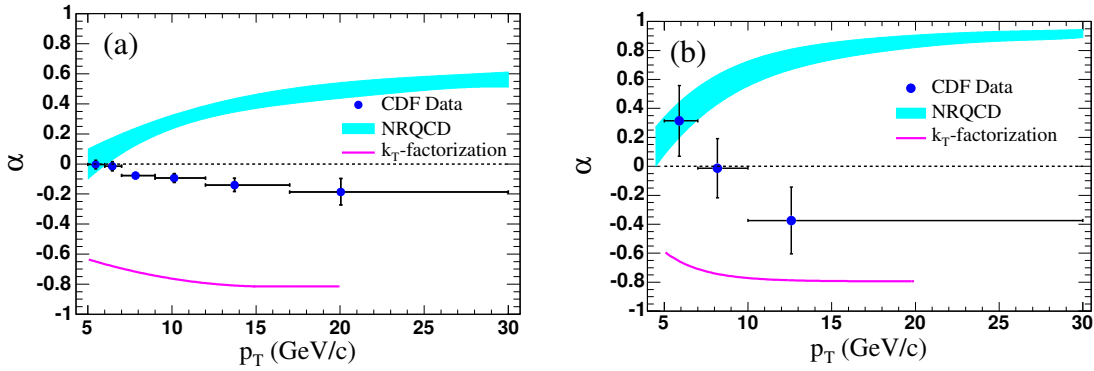


Figure 1.10: Prompt polarization as a function of  $p_T$  in  $p\bar{p}$  collisions at  $\sqrt{s} = 1.96$  TeV for: (a)  $J/\psi$  and (b)  $\psi(2S)$ . The line correspond to the  $k_T$  factorization model [107] and the band to the LO NRQCD prediction [106]. Figure taken from [101].

underestimates the rate at high  $p_T$ . In that region the agreement is better with the CEM calculations.

These results show that in spite of the success on reproducing some experimental measurements, further efforts towards the improvement of the theoretical description of the quarkonia formation mechanism are still needed.

The measured charged particle multiplicity in pp collisions at LHC energies reaches values comparable to those obtained in semi-peripheral Cu-Cu at RHIC at  $\sqrt{s_{NN}} = 200$  GeV [9]. It could be considered that the  $J/\psi$  yield can be modified in high multiplicity pp events due to collective phenomena, similar to those observed in heavy-ion collisions [10]. The measurement of the  $J/\psi$  yield as a function of multiplicity in pp was performed by ALICE in [8, 111]. In Fig. 1.12 we present the evolution of the relative  $J/\psi$  yield as a function of the relative charged particle multiplicity measured in pp collisions at  $\sqrt{s} = 7$  TeV. The measurement was performed at forward and mid rapidities, showing an approximately linear increase in both rapidity ranges.

Multiple-Parton Interactions (MPI)<sup>12</sup> are commonly used to describe the soft underlying event, but can also contribute on the hard and semi-hard scale at high energy collisions [112]. This introduces a correlation of the  $J/\psi$  production with the underlying event [113]. The observed rise of the  $J/\psi$  yield in pp collisions as a function of multiplicity could indicate that the  $J/\psi$  production is always connected with a strong hadronic activity, or that MPI affect also the hard scales relevant in quarkonium production [8, 114, 115].

In [116] the source interaction framework was proposed to explain the observed  $J/\psi$  yield behaviour in pp collisions. It was shown that the rise of  $J/\psi$  production with multiplicity could be explained as a consequence of string interaction or parton saturation. In this approach parton-parton collisions produce color strings, considered as the elementary sources of particle production. The number of parton-parton collisions is reflected as the number of

<sup>12</sup>MPI means several parton-parton interactions occurring in a single pp collision



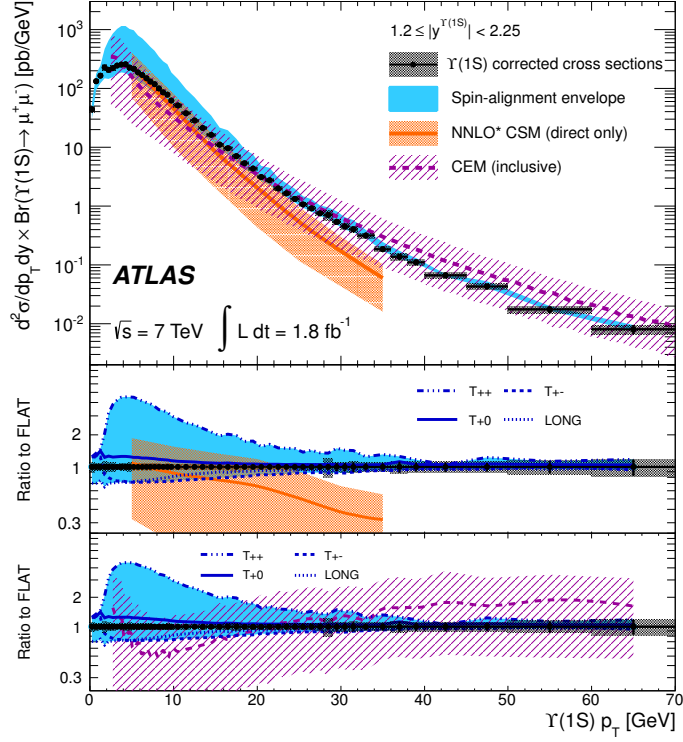


Figure 1.11:  $\Upsilon(1S)$   $p_T$  differential cross section multiplied by the di-muon branching ratio  $\text{Br}(\Upsilon \rightarrow \mu^+ \mu^-)$  in pp collisions at  $\sqrt{s} = 7$  TeV. The maximal envelope of variation of the results due to spin-alignment uncertainty is indicated by the solid band (see [110] for details). Predictions of direct production with CSM and inclusive production with CEM are also shown. The ratio to the data is shown in the middle (CEM) and bottom (CSM) panels. Figure taken from [110] .

produced strings. These strings can interact thus reducing the effective number of sources, specially those concerning soft particle production (charged particle multiplicity). The number of produced  $J/\psi$  behaves as the number of strings. The different dependence on the number of strings of the soft and hard interactions can explain the measurements. The model predicts a linear behaviour at low multiplicity and a quadratic one at higher multiplicities.

In Fig. 1.13, the results of this model are shown together with the  $J/\psi$  yield measurements as a function of multiplicity in [8]. The blue dots represent the measurement at forward rapidity, while the red ones are the one at mid rapidity. The dotted line represents the linear behaviour, the solid line the high multiplicity behaviour at forward rapidity and the dashed-dotted line the one at mid rapidity. As we can see, the model is able to reproduce the pp data. In addition, a prediction for the  $J/\psi$  yield in p-Pb collisions at 5 TeV was made, by assuming that the number of strings in p-Pb collisions is proportional to that in pp collisions. Note also that nuclear effects are not taken into account. The result is shown as the solid line.

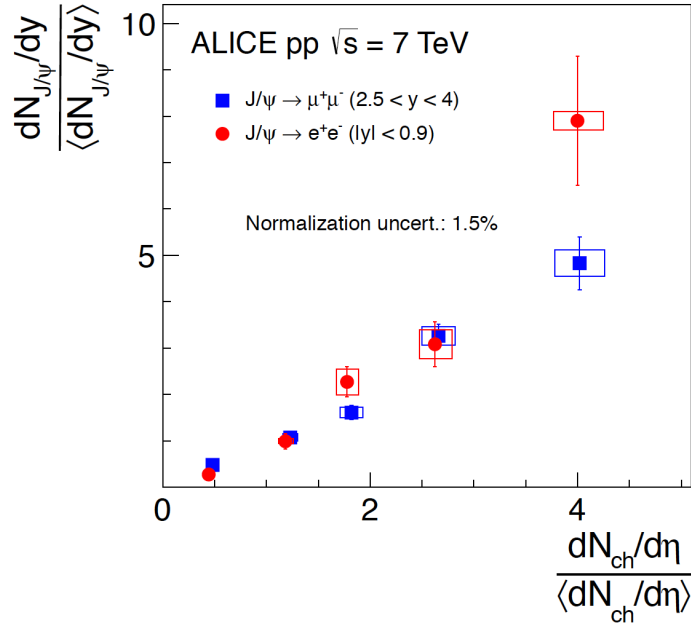


Figure 1.12:  $J/\psi$  relative yield as a function of relative charged particle multiplicity measured at mid-rapidity ( $|\eta| < 1$ ) in pp collisions at  $\sqrt{s} = 7$  TeV. Figure taken from [8].

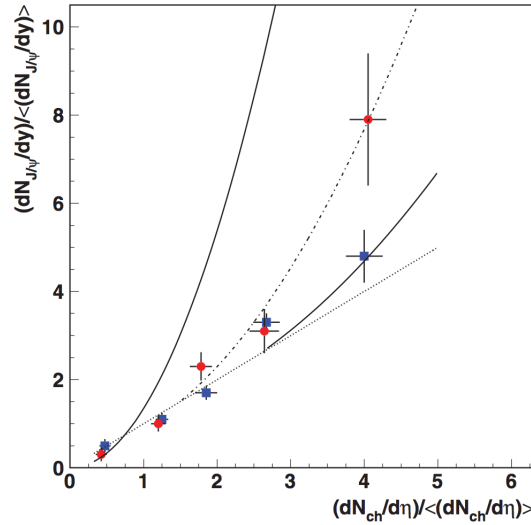


Figure 1.13:  $J/\psi$  relative yield as a function of relative charged particle multiplicity measured at mid-rapidity ( $|\eta| < 1$ ) in pp collisions at  $\sqrt{s} = 7$  TeV compared to prediction of the source interaction framework [116]. Figure taken from [116]

This result is the main motivation for this thesis to study the presence of collective phenomena in high multiplicity p-Pb collisions and higher energy pp collisions, by mean of  $J/\psi$  production measurements. In this thesis, the  $J/\psi$  yield as a function of charged particle multiplicity in p-Pb collisions at  $\sqrt{s_{NN}} = 5.02$  TeV and pp collisions at  $\sqrt{s} = 8$  TeV is studied.

## 1.5 Charmonium production in A-A collisions: probing the Quark-Gluon Plasma

As we mentioned earlier, charmonium production rates in heavy-ion collisions can be used to probe the formation of the QGP. The  $c\bar{c}$  pre-resonant state formation time can be roughly estimated to be about 0.05 - 0.15 fm/c. An approximative estimation of the time to form a bound state gives about 1-3 fm/c, and its decay into leptons is estimated to be about  $2.1 \cdot 10^3$  fm/c. This suggests that the pre-resonant state is produced while the QGP is formed, but the bound states are formed in coexistence with the QGP and may decay out of it [117].

The  $J/\psi$  suppression in heavy-ion collisions with respect to its production in pp collisions was proposed in 1986 by T. Matsui and H. Satz [1] as an indication of QGP formation. They argued that in the presence of a QGP the color screening would prevent the binding of the  $c\bar{c}$  pairs. In addition, other effects due to the formation of a hot medium can play also a role in the  $J/\psi$  production like quarkonium "regeneration" [118–120]. The "regeneration" mechanism is based on the possibility of the formation of charmonium states also from uncorrelated  $c\bar{c}$  pairs<sup>13</sup> in the hot medium. This is possible due to the increase of the  $c\bar{c}$  cross section with the energy [66]. This effect would compete with color screening. In this section we discuss the color screening mechanism and other effects that can be at play in quarkonium production due to the formation of a hot medium. Then, a selection of experimental results is presented.

### 1.5.1 Color screening and charmonium sequential suppression

When two charges are placed in a diluted charged medium, the binding potential between the charges is screened. The change in the binding potential is described by the Debye screening [121]:

$$(1.4) \quad \frac{1}{r} \rightarrow \frac{1}{r} e^{-\mu r}$$

where  $r_D = 1/\mu$  is the screening radius. Therefore the Cornell binding potential in Eq. 1.2 becomes:

$$(1.5) \quad V(r) \sim \sigma r \left( \frac{1 - e^{-\mu r}}{\mu r} \right) - \frac{\alpha}{r} e^{-\mu r}$$

where  $\mu = \mu(T)$  (T stands for the medium temperature) [122]. This potential qualitatively reproduce the essence of the mechanism. It converges to a finite value at long distances and, since  $\mu(T)$  increases with the medium temperature, it describes the decrease of the potential with increasing temperature. Note that this approach provides just a first insight into the problem. The quantitative description requires a more careful treatment (see [73]).

---

<sup>13</sup>  $c\bar{c}$  pairs from different hard parton-parton interactions

From this qualitative study it can be said that the effect of color screening makes the charmonium binding weaker as the temperature increases, and when the screening radius falls below the binding radius the bound state becomes dissociated. This effect depends on the states binding energy. Therefore the dissociation point of each state provides a way to measure the medium temperature. This effect is illustrated in Fig. 1.14 for  $J/\psi$  production. The different charmonium states sequentially become unbound with increasing medium temperature (or energy density) starting from the most loosely bound state. Consequently, they do not contribute anymore to the  $J/\psi$  production (by feed down or direct), producing the pattern shown in Fig. 1.14 of the  $J/\psi$  production dependence with the medium energy density.

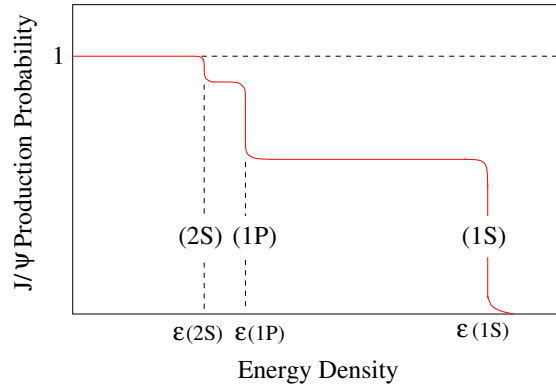


Figure 1.14:  $J/\psi$  sequential suppression due to Debye color screening in a QPG. Figure taken from [73] .

The quarkonium dissociation temperatures ( $T_d$ ) can be calculated with phenomenological binding potential models or lQCD (see [123] for a recent review). We have extracted from [123] the  $T_d$  values given for the  $J/\psi$  and  $\psi(2S)$  which are  $1.5 \cdot T_c$  and  $1.1 \cdot T_c$  respectively.

### 1.5.2 Charmonium regeneration

The picture of sequential suppression becomes blurred by other effects that may take place in the presence of a hot medium. It was proposed in [124] that the  $J/\psi$  could be statistically formed from uncorrelated  $c\bar{c}$  pairs from different initial hard collisions, if the charm density in the system is large enough. It has been observed that in A-A collisions the charm production grows with the number of binary nucleon-nucleon collisions ( $N_{coll}$ ). The light hadron production grows with the number of participant nucleons ( $N_{part}$ ), thus slower than the charm production. This makes the combination of uncorrelated  $c\bar{c}$  pairs more likely with increasing energy. This combination provides an "exogamous" charmonium production mechanism different from the  $J/\psi$  produced from  $c\bar{c}$  pairs from the same hard collision.

This new mechanism can compensate the suppression as it is illustrated in Fig. 1.15 (left). When the energy density increases, the suppression by color screening starts. At sufficiently high energy density the recombination begins to contribute, and even an enhancement might

be observed. The behaviour of the transverse momentum is also affected by this mechanism. In Fig. 1.15 (right) the difference of the average squared transverse momentum in AA and pp ( $\langle p_T^2 \rangle_{AA} - \langle p_T^2 \rangle_{pp}$ ) is shown. We observe how, while the 1S state survives, the  $\langle p_T^2 \rangle$  rises with centrality due to gluon multi-scattering in the initial state [125] and leakage effect (high  $p_T$   $J/\psi$  are less suppressed in the QGP) [126]. At high energy density, the dissociation of the 1S state leads also to the  $\langle p_T^2 \rangle$  suppression. The  $J/\psi$  production from recombination alone would remove the dependence with centrality, since in this mechanism the states are produced from uncorrelated pairs.

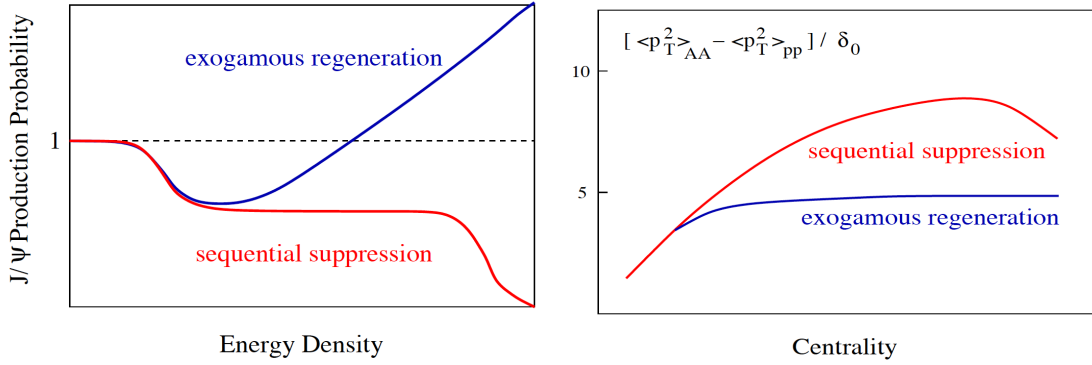


Figure 1.15:  $J/\psi$  sequential suppression vs. regeneration: Left:  $J/\psi$  survival probability. Right:  $J/\psi$  transverse momentum behaviour. Figure taken from [127] .

In the regeneration mechanism, the production of charmonia grows with the square of the number of charm quarks per unit of rapidity in the QGP. The production rate must be normalised by the number of interactions where a charm quark binds to light quarks to form an open charm hadron. The normalisation is taken to be proportional to the number of produced charged hadrons ( $N_{ch}$ ) leading to  $N_{J/\psi} \propto N_{c\bar{c}}^2 / N_{ch}$  [128]. This behaviour dominates over the color screening suppression, leading to the prediction of charmonia enhancement in a deconfined QGP at sufficiently large energy density.

Two different approaches to this mechanism can be found. In the statistical regeneration model [118, 129, 130] all the  $c\bar{c}$  pairs are deconfined and thermalised in the medium, and the  $J/\psi$  are formed at the QGP phase boundary. Charmed-hadron production is treated within the framework of canonical thermodynamics. The parameters needed in this approach are the chemical freeze out temperature, the baryochemical potential and the medium volume. These parameters are fitted in data of other hadrons (pions, kaons...), and can be parametrised as a function of the center-of-mass energy. While there are not explicit predictions of the momentum spectra with this model, one could expect a thermal distribution at the deconfinement temperature as shown in Fig. 1.15 (right). On the other hand, the transport models [119, 120, 131] are based on a kinetical approach where the charmonia are continuously formed and destroyed during the QGP phase. This kind of model is motivated by lattice calculations, which predict that the  $J/\psi$  may still be bound for temperatures above the

deconfinement temperature [132]. The evolution of the medium is treated with relativistic hydrodynamics. The charmonium distribution function evolution is given by a Boltzmann-type transport equation which includes a drift term, a dissociation term due to inelastic collisions between the charmonium and the medium constituents, and a regeneration term. In order to provide predictions, these models need as input the cross sections of quarkonium formation and dissociation in the medium. According to this model, the  $J/\psi$  momentum spectrum reflects the properties of initially produced charmonium and those related to modifications through interactions in the medium.

### 1.5.3 Experimental results

In this section we provide a small selection of some of the charmonium measurements that suggest strong evidence of the formation of a deconfined medium in heavy-ion collisions. A more extensive summary on the Pb-Pb results at the LHC is presented in [70].

A  $J/\psi$  anomalous suppression in Pb-Pb collisions at  $\sqrt{s_{NN}} = 158$  GeV was found by NA50 at the Super Proton Synchrotron (SPS) [133]. In Fig 1.16, the anomalous suppression for  $J/\psi$  (left) and  $\psi(2S)$  (right) is shown as a function of the distance of nuclear matter traversed ( $L$ ) (see [134]). At large values of  $L$  (central collisions), the  $J/\psi$  and  $\psi(2S)$  are further suppressed than expected from normal nuclear absorption (see Sec. 1.6.4) calculated with a Glauber fit of p-A data [135, 136].

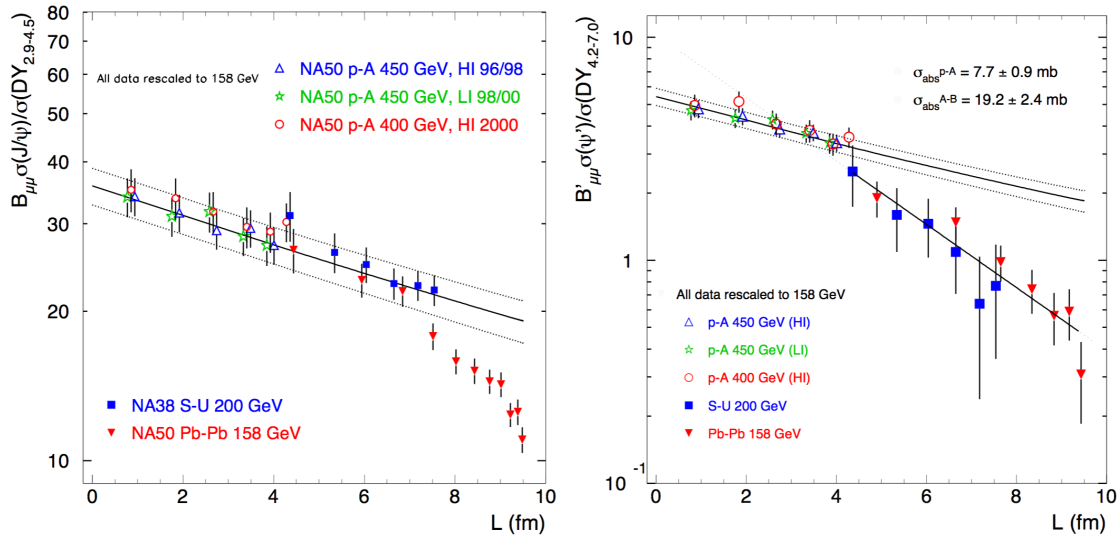


Figure 1.16: Left:  $J/\psi$  suppression pattern measured by NA38 and NA 50 collaborations in p-A, S-U and Pb-Pb collisions as a function of the distance of nuclear matter traversed by the charmonium. The band correspond to nuclear absorption estimates. Right:  $\psi(2S)$  suppression pattern. Figure taken from [134].

In the absence of medium effects, the charmonium production scale with the number of binary nucleon-nucleon collisions. An observable called nuclear modification factor ( $R_{AA}$ )

can be used to quantify deviations from this scaling. The  $R_{AA}$  is defined as:

$$(1.6) \quad R_{AA} = \frac{d^2 N_{AA}/dp_T dy}{\langle N_{coll} \rangle d^2 N_{pp}/dp_T dy}$$

where  $y$  is the rapidity<sup>14</sup>,  $\langle N_{coll} \rangle$  is the average number of binary nucleon nucleon collisions in A-A collisions and  $d^2 N_{AA(pp)}/dp_T dy$  denotes the charmonium differential yields in A-A (pp) collisions. Deviations from unity of  $R_{AA}$  indicate medium effects in the charmonium production in A-A collisions. However, since in pp collisions charmonium production is usually measured in terms of its cross section and not yields<sup>15</sup>, the nuclear modification factor is actually calculated as:

$$(1.7) \quad R_{AA} = \frac{d^2 N_{AA}/dp_T dy}{\langle T_{AA} \rangle d^2 \sigma_{pp}/dp_T dy}$$

where  $\langle T_{AA} \rangle$  is the average value of the nuclear overlap function, which can be calculated as  $\langle T_{AA} \rangle = \langle N_{coll} \rangle / \sigma_{NN}^{inel}$ . It represents the effective nucleon luminosity<sup>16</sup>.

The  $J/\psi$  nuclear modification factor was measured by PHENIX in Au-Au collisions at  $\sqrt{s_{NN}} = 0.2$  TeV as a function of the number of participant nucleons in the collision [138]. The result was compared to several theoretical models, concluding that the found suppression was beyond cold nuclear matter effects. The top panel of Fig. 1.17 shows the comparison of the  $J/\psi$   $R_{AA}$  in Au-Au collisions to that measured by ALICE in Pb-Pb collisions at  $\sqrt{s_{NN}} = 2.76$  TeV [65, 139]. As can be observed, the result in Pb-Pb collisions is less suppressed than the Au-Au result, which suggest a strong recombination component in  $J/\psi$  production at LHC energies.

In the bottom panel of Fig. 1.17, the  $R_{AA}$  in Pb-Pb collisions is compared to several theoretical models: the statistical hadronization model (SHM) [118], transport models (TM1) [120] and (TM2) [119] (the two calculations mainly differ in the rate controlling the  $J/\psi$  regeneration and dissociation), as well as a model including recombination, shadowing (see Sec. 1.6) and dissociation due to interaction with a co-moving medium (CIM) [140]. As can be observed, all models are able to reproduce reasonably well the measurement for  $\langle N_{part} \rangle > 70$ . All the models need to include a sizeable recombination component to the  $J/\psi$  production in order to reproduce the measurement.

The  $J/\psi$   $R_{AA}$  as a function of  $p_T$  measured for the 0-90% centrality class is shown in Fig. 1.18 compared with the transport models calculations. Both models reproduce reasonably well the trend of the data. It can be observed how in both cases the regeneration component

<sup>14</sup>The rapidity is defined as  $y = \frac{1}{2} \ln \frac{E+p_z}{E-p_z}$ , where  $E$  is the energy of the particle and  $p_z$  its longitudinal momentum

<sup>15</sup>Experimentally it is easier to measure the cross section  $\sigma_{pp}^{inel}$  of inelastic events [137] to calculate the charmonium cross section ( $d\sigma_{pp}^2/dp_T dy = dN_{pp}^2/dp_T dy \times \sigma_{pp}^{inel}$ ), than the trigger efficiency to correct the yields

<sup>16</sup>The luminosity ( $\mathcal{L}$ ) is the proportionality factor between the number of events per unit of time ( $dN/dt$ ) and the interaction cross section ( $\sigma$ ) ( $dN/dt = \mathcal{L} \cdot \sigma$ )

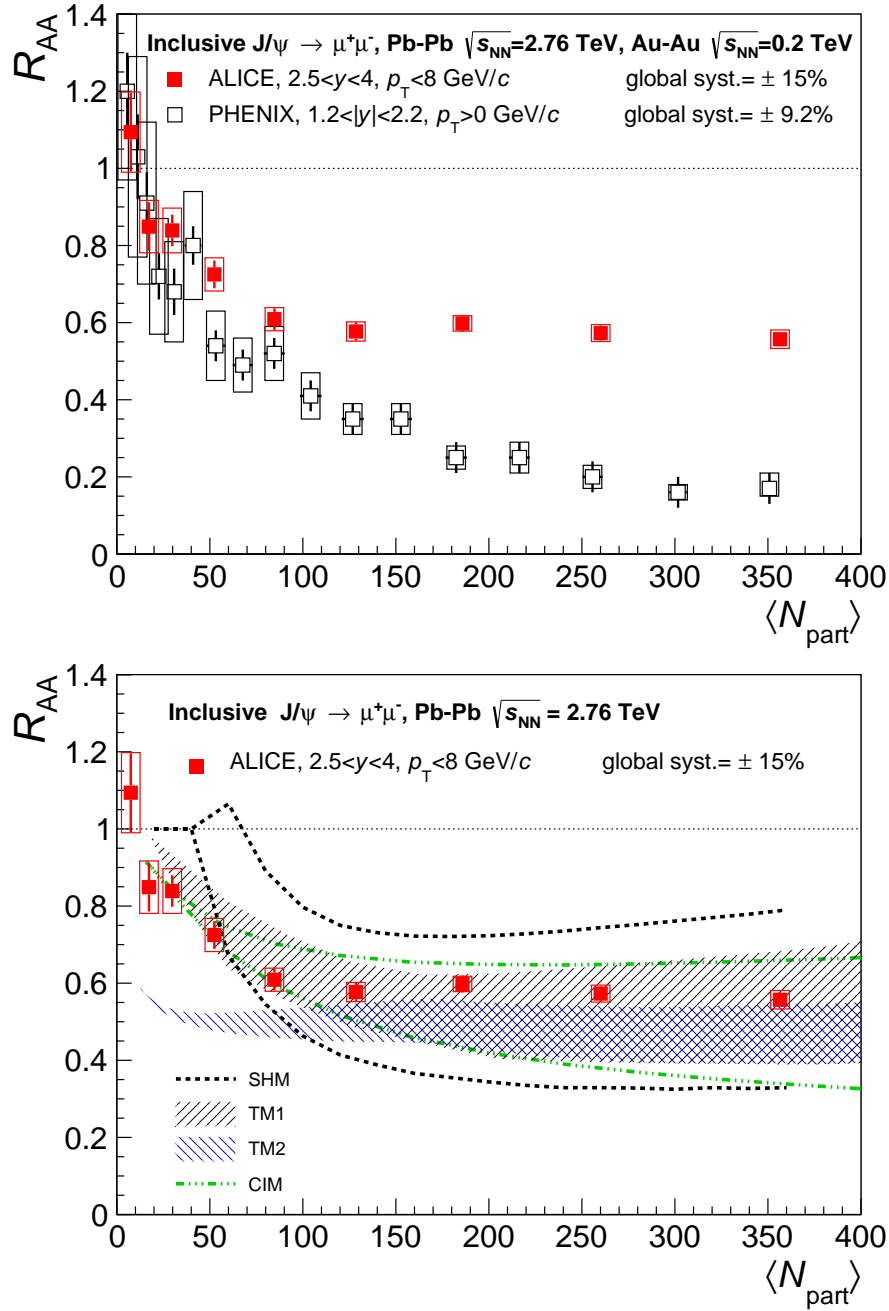


Figure 1.17: Inclusive  $J/\psi$   $R_{AA}$  as a function of  $\langle N_{part} \rangle$  measured in Pb-Pb collisions [65] compared to the measurement in Au-Au collisions [138]. The bottom figure shows only the ALICE (Pb-Pb) result compared to several theoretical models including recombination (see text). Figure taken from [139].

is more important at low  $p_T$ . However, the relative contributions of the primordial and regenerated components are different between the models (see [139] for further details).

These results provide strong evidence of the formation of a deconfined medium in heavy-ion collisions. They cannot be explained within the pure color screening suppression scenario,



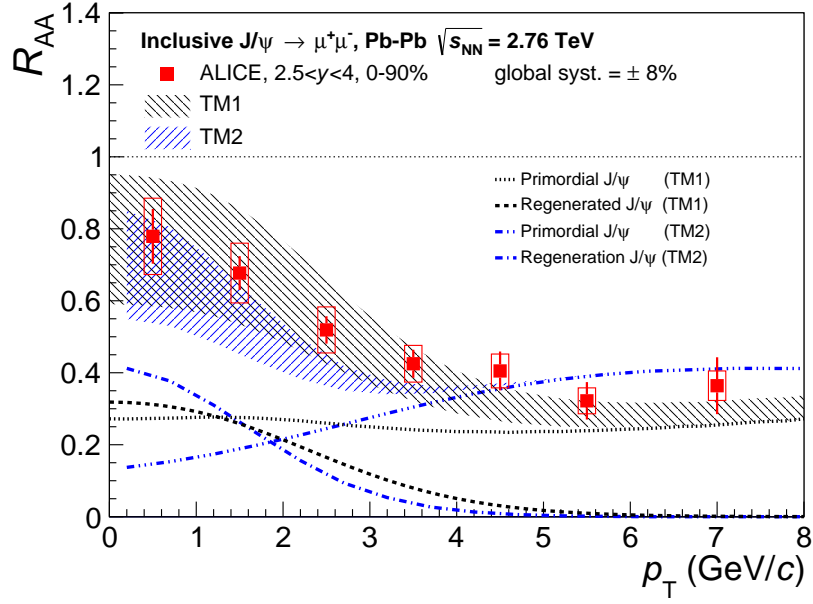


Figure 1.18: Inclusive  $J/\psi$   $R_{AA}$  as a function of  $\langle N_{part} \rangle$  measured in Pb-Pb collisions [139]. The measurement is compared to transport models (see text). Figure taken from [139].

and other effects like regeneration have been proposed to explain the observations. The study of cold nuclear matter effects affecting the quarkonia suppression are of crucial importance in order to be able to obtain a more quantitative description of hot matter effects.

## 1.6 Charmonium production in p-A collisions: Cold Nuclear Matter effects

The production of charmonium is affected in heavy-ion collisions already in absence of a hot medium, due to the presence of nuclear matter. These effects include the modification of the gluon densities in the colliding nucleons, coherent parton energy loss induced by the nuclear medium or nuclear absorption of the  $c\bar{c}$  pair or the resonance. Generally speaking, these effects are referred to as Cold Nuclear Matter (CNM) effects.

In order to disentangle the QGP formation related effects from the CNM ones, it is necessary to study charmonium production in collision systems where the QGP is not expected to be formed. At the beginning of 2013, p-Pb collisions at  $\sqrt{s_{NN}} = 5.02$  TeV were performed at the LHC in order to study CNM. As we see later, p-Pb collisions have also provided observations which are typically found in heavy-ion collisions and are understood as a result of a collective expansion of the medium. The study of  $J/\psi$  production in p-Pb collisions is the main subject of study in this thesis. In this section, a summary on the CNM effects from a theoretical point of view, some  $J/\psi$  results from PHENIX in d-Au collisions and some of the recent charmonium results obtained by ALICE in p-Pb collisions are given.

### 1.6.1 Gluon shadowing

The information of the parton structure of the nucleon is contained in the parton distribution functions (PDF). The PDF represent the probability density to find a parton  $i$  in a nucleon with a fraction  $x$  of the total momentum at an energy scale  $Q^2$  ( $f_i(x, Q^2)$ ). The cross section of an hadronic process can be factorized into a partonic cross section (which is calculable perturbatively) and the PDFs that characterize the hadronic bound states. The PDFs do not depend on the specific process (universality). This property allows to determine the PDF using the experimental cross sections in a particular set of processes, and then use them to make predictions for other processes. The knowledge of the PDF is essential in order to make theoretical predictions for any hadronic process. The PDFs are measured through the fits of experimental data in electron-proton and electron-nucleus collisions. An introduction to the theory and phenomenology of PDFs, and a recent review on the PDF determination are given in [141]. An example of the PDFs at two different energy scales is shown in Fig. 1.19.

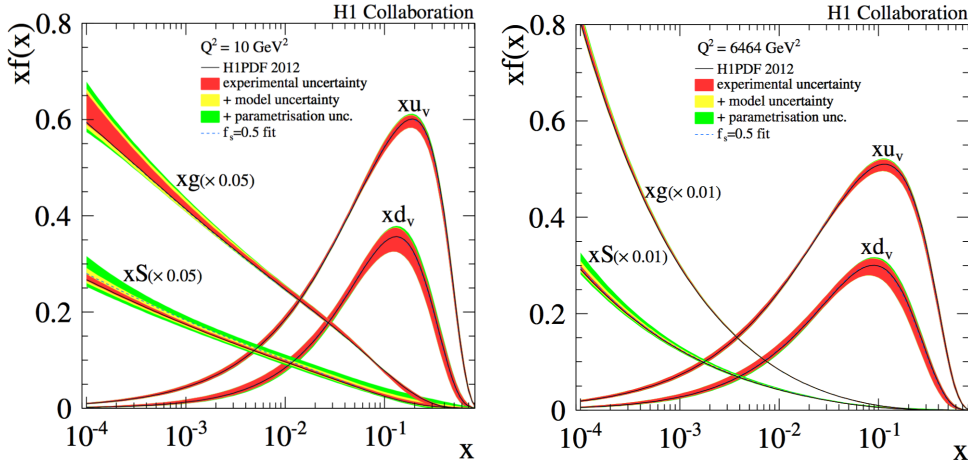


Figure 1.19: Parton distribution functions at two different energy scales. The gluon and sea quark distributions are scaled by a factor 0.05 (0.01) in the left (right) plot. Figure taken from [82].

In a nuclear environment, the partonic structure of the nucleons may be modified and hence the PDFs. The nuclear parton distribution functions (nPDFs) in a nucleus  $A$  ( $f_i^A(x, Q^2)$ ) are defined as:

$$(1.8) \quad f_i^A(x, Q^2) \equiv R_i^A(x, Q^2) f_i(x, Q^2)$$

where the information of the nuclear modification to the free proton PDF is encoded in the nuclear modification functions  $R_i^A(x, Q^2)$ . An illustration of the parametrisation of the nuclear effects  $R_i^A(x, Q^2)$  is given in Fig. 1.20. If there are no nuclear effects  $R_i^A(x, Q^2) = 1$ . We can distinguish several effects: at small  $x$  we find the shadowing effect, the parton probability density in the nucleon is smaller within the nuclear matter than for a free

nucleon; at higher  $x$  there is the antishadowing effect, which is the opposite effect; at even higher  $x$  we have the EMC effect [142], which consist again in a depletion of the quark distribution; and finally the Fermi motion.

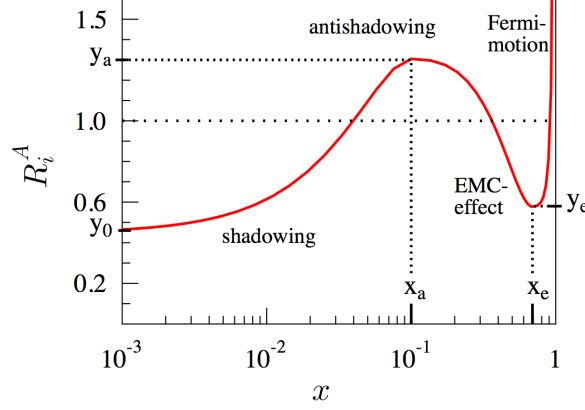


Figure 1.20: Illustration of  $R_i^A(x, Q^2)$  parametrisation. The different parameters used for the parametrisation are also indicated. Figure taken from [143].

The shadowing can be understood as an interaction of the partons of different nucleons. At small  $x$ , there can be a spatial overlap of the partons of different nucleons which may lead to gluon "recombination", producing a decrease in their density. Due to momentum conservation, the reduction of the number of partons at low  $x$  implies an enhancement at larger  $x$ , which explains anti-shadowing [144–147]. The origin of the EMC effect is still not well understood [148]. The behaviour in the Fermi motion region is mainly a kinematical effect due to the fact that the free nucleon PDFs vanishes for  $x \rightarrow 1$  and also due to the Fermi motion of the bound nucleons in the nucleus.

The nuclear modification functions on a lead nucleus obtained in [143] (EPS09 parametrisation), for the valence quarks ( $R_V^{Pb}$ ), sea quarks ( $R_S^{Pb}$ ) and gluons ( $R_G^{Pb}$ ) are shown in Fig. 1.21. The parametrisation is performed at the charm mass energy scale ( $Q_0^2 = 1.69 \text{ GeV}^2$ ) imposing the momentum and baryon sum rules for each nucleus separately. The  $R_i^{Pb}(x, Q^2)$  are evolved to energy scales  $Q^2 > Q_0^2$  using the DGLAP evolution equations [149–151] (see [143] for further details).

The nuclear modifications in the gluon PDFs affect the formation of  $c\bar{c}$  quarks. It is therefore needed to include the nuclear modification functions in the theoretical calculations in order to make correct predictions.

When measuring charmonium at a certain rapidity, if we consider that it has been produced in a " $2 \rightarrow 1$ "<sup>17</sup>, the momentum fractions of the incoming partons,  $x_1$  and  $x_2$  can be

<sup>17</sup>This is an oversimplification, since a final state gluon emission is necessary to produce the  $Q\bar{Q}$  pair with the quantum numbers of the vector meson

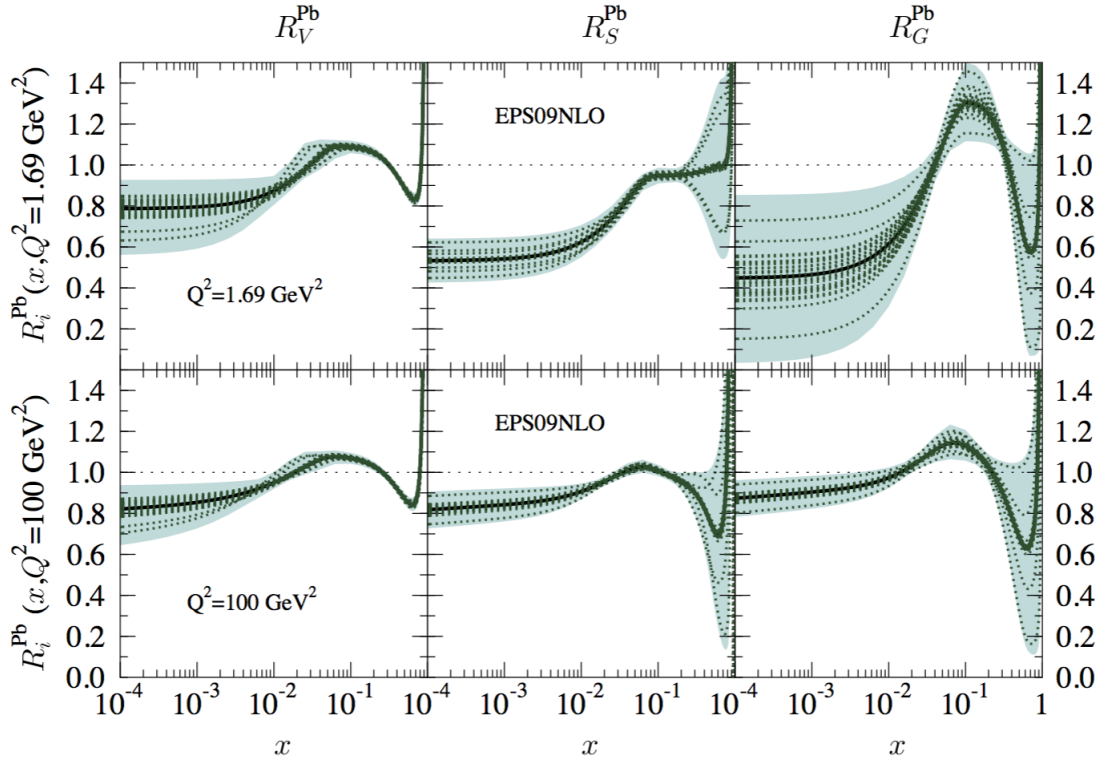


Figure 1.21: The nuclear modifications in lead for valence, sea quarks and gluons at the initial scale  $Q_0^2 = 1.69 \text{ GeV}^2$  and at  $Q_0^2 = 100 \text{ GeV}^2$ . The shaded areas represent the uncertainty. Figure taken from [143].

written as:

$$(1.9) \quad x_{1,2} = \frac{M_{c\bar{c}}}{\sqrt{s_{\text{NN}}}} e^{\pm y}$$

where  $M_{c\bar{c}}$  is the mass of the  $c\bar{c}$  pair state and  $\sqrt{s_{\text{NN}}}$  is the nucleon-nucleon center-of-mass energy. Therefore, measurements at different rapidities allow to explore different kinematical regions of the PDFs.

## 1.6.2 Gluon saturation

It can be seen in Fig. 1.19 how at low  $x$  values, the gluon density grows. Furthermore, at low  $x$  values, the gluon density increases with the energy. However the gluon density does not grow indefinitely, and it is expected to reach saturation. This saturation is characterised by the saturation scale  $Q_s(x)$ .

The Color Glass Condensate (CGC) [152, 153] is an effective theory that describes the properties of saturated gluons. As the gluon density increases, its typical separation become smaller and therefore  $\alpha_s$  is small. The maximal occupation of the phase space can be  $\sim 1/\alpha_s$ . When the maximal occupation is reached the system can be seen as a color condensate. We

can see in Fig. 1.19 that the density of valence partons is bigger at high  $x$  values. In the CGC framework, the low  $x$  gluons are described as the classical color fields radiated by color sources at higher  $x$  [152]. Therefore, due to Lorentz time dilation, the color configurations of the sources at large  $x$ , are "frozen" on the natural time scales of the strong interaction. The low  $x$  fields are coupled to the static color sources. A system which evolves slowly relative to natural time scales is called a glass. [154–156]

In the CGC approach the strength of the color field inside the nucleus is proportional to the saturation scale  $Q_s^2(x)$ . A "pocket formula" to estimate the energy and nuclear dependence of the saturation scale is  $Q_s^2 \sim A^{1/3} x^{-0.3}$  [157] (the  $A$  dependence comes from the Lorentz contraction of the nucleus). There are two different dynamical regimes of heavy quark production depending on the relation between the saturation scale and the quark mass  $m$  [158]. When  $Q_s^2 \ll m$  the heavy quark production is incoherent, since it is produced from the interaction of two nucleons. In this case the production can be treated within a conventional perturbative approach. On the other hand, when  $Q_s^2 \gg m$  the heavy quark production is coherent, meaning that the whole nucleus takes part in the process. In this case the production is sensitive to the CGC strong color field. This mechanism could be at play at the LHC. There are several approaches that use the CGC to describe  $J/\psi$  production and use different hadroproduction models [158–162]

### 1.6.3 Coherent parton energy loss

A high energy parton travelling in a medium can radiate gluons induced by the elastic scatterings with the constituents of the medium. This is called parton energy loss. The energy loss mechanism provide a powerful tool to study the properties of the hot and cold nuclear matter. As an example, the quenching of hadrons at large  $p_T$  in Pb-Pb collisions at the LHC [163, 164] could be explained in terms of parton energy loss in the QGP.

In general, energy loss models make several assumptions and approximations [165]:

- The partons produced in a hard collision undergo several gluon splittings
- The medium can be modelled in several ways. In the approach we discuss later, it is modelled as a collection of static scattering centres [166].
- Several approximations on the parton and gluon kinematics are made in all the calculations.

The basic picture of energy loss consists on a primary parton created in a hard interaction that radiates gluons. In [167] new scaling properties of the gluon radiation spectrum and associated energy loss of hard processes where a color charge undergoes small angle scattering through a static medium (cold matter or QGP), have been identified. The authors argued that the medium induced radiation cannot be strictly identified with the energy loss of a well defined parton for certain processes. These processes are those were the produced

parton is nearly collinear to one of the incoming partons (in the rest frame of the medium). Therefore, the gluon emission before and after the hard production is coherent.

In [167–170] the authors describe the suppression of the  $J/\psi$  production in p-A collisions from coherent energy loss in cold nuclear matter. They assume that the heavy quark pair (of mass  $M$ ) is produced in a compact color octet state in the time scale  $\tau_{Q\bar{Q}} \sim 1/M$ , and remains in that state during  $\tau_{octet} \gg \tau_{Q\bar{Q}}$ . This assumption holds independently of the quarkonium production model [169]. For sufficiently large quarkonium energy, and in nucleus rest frame, the hadroproduction can be considered as a small angle scattering of a color charge. Therefore, the associated gluon radiation depends on the amount of transverse momentum kick  $q_\perp$  to the charge. The spectrum is coherent, and it arises from the interference between the initial and final state emission amplitudes.

The average medium induced radiative loss scales as the quarkonium energy  $\Delta E \propto E$ . The amount of medium induced gluon radiation, and hence the strength of the  $J/\psi$  suppression in p-A collisions, depend on the transverse momentum nuclear broadening  $\Delta q_\perp^2$ . The  $\Delta q_\perp^2$  can be defined in terms of the path length  $L$  travelled across the target:

$$(1.10) \quad \Delta q_\perp^2(L) = \hat{q}_A L - \hat{q}_p L_p$$

where  $L = \frac{3}{2}r_0 A^{1/3}$  ( $r_0 = 1.12$  fm).  $\hat{q}_A$  and  $\hat{q}_p$  are the transport coefficients in the nucleus and proton respectively, which are related to the gluon distribution  $G(x)$  in a target nucleon. The transport coefficient can be expressed as  $\hat{q}(x) \propto \hat{q}_0$  [168], thus the only free parameter of the model is the transport coefficient  $\hat{q}_0$ . The transport coefficient can be obtained from a fit to data at a certain energy allowing to make predictions for different energies.

In [170], the centrality dependence of coherent parton energy loss is included by using the Glauber model<sup>18</sup> [171] to compute the average path length  $L$  in different centrality classes.

#### 1.6.4 Nuclear absorption

The interactions between the pre-resonant or bound  $c\bar{c}$  pair with the nucleus can lead to the dissociation of the state and consequently, a suppression of the charmonium production would be observed. Some authors refer to this effect as "normal nuclear absorption".

There are several approaches to treat nuclear absorption, from using the Glauber formalism to simpler parametrizations (exponential and linear) [172, 173]. In general, nuclear absorption depend on the amount of nuclear matter traversed by the  $c\bar{c}$  pair. Therefore the relationship between nuclei crossing times and the pair formation introduces a dependence with the collision center of mass energy, since the crossing time decreases for rising energy. In Fig. 1.22, the dependence of the  $J/\psi$  nuclear absorption with the collision energy in p-A collisions is presented. We can also see the fits with the nuclear absorption parametrizations, which indicate that at high energy, certainly at the LHC, this effect is negligible.

<sup>18</sup>The Glauber model is used to calculate geometric quantities such as impact parameter,  $N_{part}$  and  $N_{coll}$ .

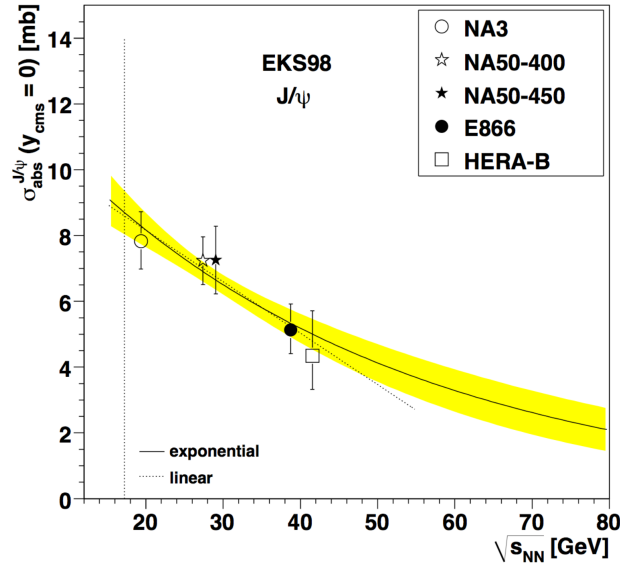


Figure 1.22:  $J/\psi$  nuclear absorption dependence with energy. The lines represent the fits to the different nuclear absorption parametrizations. The shaded areas represent the uncertainty. Figure taken from [173].

### 1.6.5 Experimental results

In order to understand if the suppression effects observed in Fig. 1.16 point to the formation of a deconfined medium, it is necessary to study the contribution of cold nuclear matter effects. For that, the  $J/\psi$  yields in d-Au collisions at  $\sqrt{s_{NN}} = 200$  GeV were studied by PHENIX and compared to the yields in pp collisions at the same energy per nucleon-nucleon collision [174].

In Fig. 1.23 we show the nuclear modification factor ( $R_{dAu}$ ) results obtained in peripheral (top) and central collisions (middle), and the ratio of the nuclear modification factors at central and peripheral events ( $R_{CP}$ ) (bottom) as a function of rapidity. The results in peripheral collisions seem consistent with a constant suppression with rapidity. In central collisions the suppression is stronger towards forward rapidity. The ratio allows to remove some systematic uncertainties, and shows a dramatic suppression of forward rapidity yields for central d-Au events compared to peripheral events.

The experimental results are compared to theoretical calculations. The first class of calculations include gluon shadowing through the EPS09 parametrisation [143] and nuclear break-up with a cross section  $\sigma_{br} = 4$  mb [175]. The model shows a reasonable agreement, within the uncertainties, for the  $R_{pAu}$  in central and peripheral collisions. However, it underestimates the suppression at forward rapidity in the  $R_{CP}$ . The second class of calculations incorporates gluon saturation effects at small- $x$  [176, 177]. The model describes the data at forward rapidity, but predicts an enhancement at mid-rapidity and peripheral collisions not observed in data.

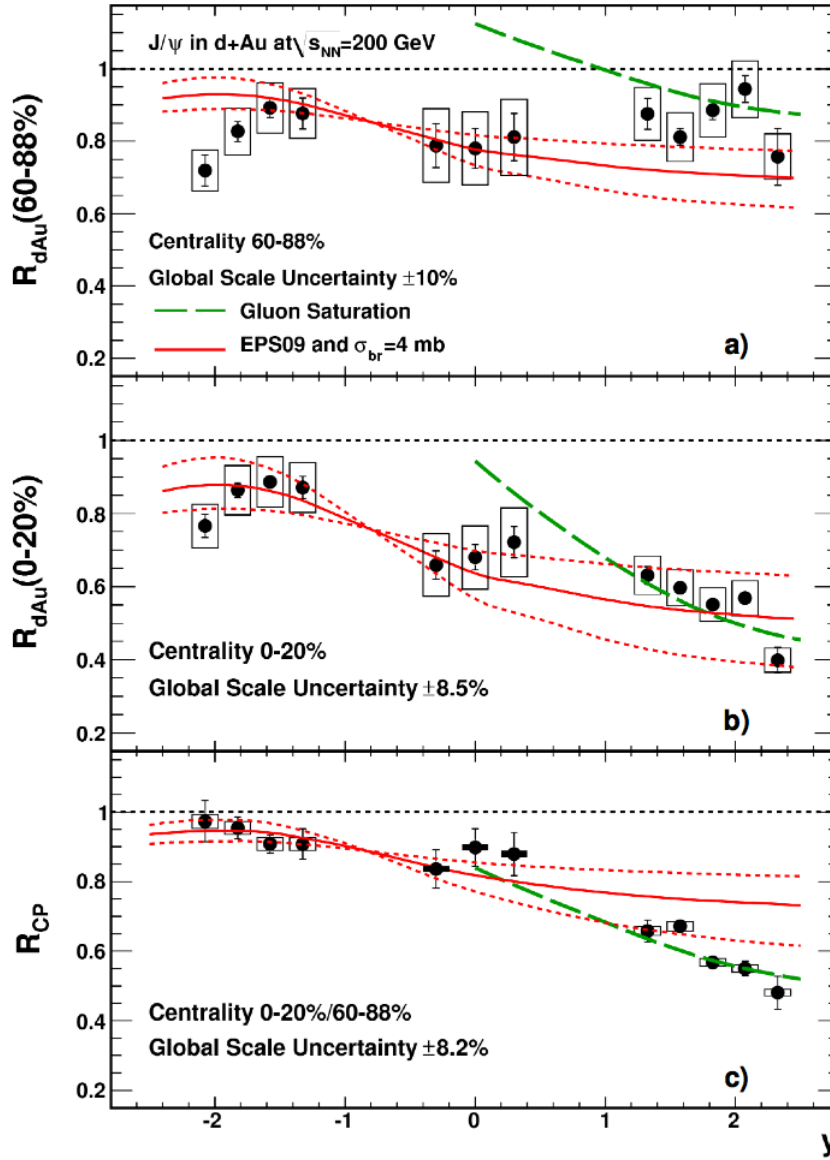


Figure 1.23:  $J/\psi$  nuclear modification factors ( $R_{dAu}$ ) in d-Au collisions at  $\sqrt{s_{NN}} = 200$  GeV for (a) peripheral, (b) central, and (c) ratio of nuclear modification factors of central and peripheral collisions ( $R_{CP}$ ) as a function of rapidity. The results are compared to shadowing with nuclear break-up [143, 175] and gluon saturation models [176, 177]. Figure taken from [174].

The measurement of the  $J/\psi$  production in d-Au collisions at  $\sqrt{s_{NN}} = 200$  GeV as a function of the transverse momentum at different rapidity ranges, was also performed by PHENIX [178]. In Fig. 1.24 the result of the  $R_{dAu}$  as a function of  $p_T$  for three rapidity ranges is shown. At backward rapidity (top), the  $R_{dAu}$  is suppressed only at the lowest  $p_T$ , with a rapid increase to  $R_{dAu} = 1$  at  $p_T \approx 1.5$  GeV/c. However, the mid- (middle) and forward rapidity data (bottom), exhibit a similar level of suppression at the lowest  $p_T$ , but a much



more gradual increase in  $R_{dAu}$  with  $p_T$ , increasing to  $R_{dAu} = 1$  only at  $p_T \approx 4$  GeV/c.

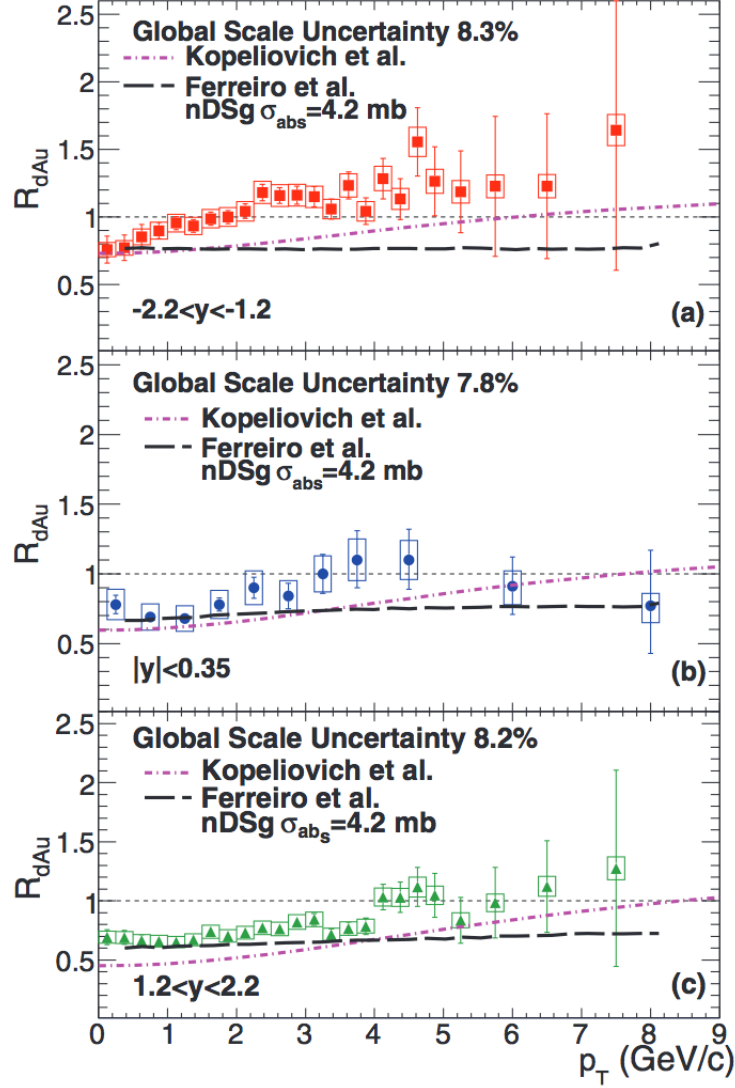


Figure 1.24:  $J/\psi$  nuclear modification factors ( $R_{dAu}$ ) as a function of  $p_T$  for (a) backward rapidity, (b) mid-rapidity, and (c) forward rapidity in 0-100% centrality integrated d-Au collisions at  $\sqrt{s_{NN}} = 200$  GeV. The results are compared to two theoretical models (see text). Figure taken from [178].

The results were also compared to two different models. Both models include a shadowing contribution using the nDSg nPDF parametrisation [179]. However, the  $J/\psi$  production kinematics are calculated differently, which leads to some differences in the shadowing contribution. The calculations from Kopeliovich et al. [180, 181] include the Cronin effect<sup>19</sup> [182], which provides a decrease in  $J/\psi$  production at low  $p_T$  and an increase at higher  $p_T$ . This leads to a  $R_{dAu}$  that exhibits less suppression at high  $p_T$  than at low  $p_T$ . The predicted

<sup>19</sup>The Cronin effect is produced by multiple scatterings of the incoming partons before the hard collision that produces a heavy quark pair

$p_T$  shape is in good agreement with the one observed in data at mid- and forward rapidity, but it shows a greater overall suppression than the data. At backward rapidity, there is a disagreement with the observed  $R_{pAu}$  dependence with  $p_T$ . The calculations from Ferreiro et al. [183, 184] do not include the Cronin effect, and therefore the  $p_T$  shape of  $R_{dAu}$  should be dominated by the effect of shadowing. The results of these calculations show reasonable agreement with the  $R_{pAu}$  at low  $p_T$  at mid- and forward rapidities. The predictions show a flatter distribution with increasing  $p_T$  than that seen in the data. The model predicts a different behaviour than the one observed in the data at backward rapidity.

In the following, some of the latest results on quarkonium measurements in p-Pb collisions at  $\sqrt{s_{NN}} = 5.02$  GeV at the LHC are briefly summarised. Note that the rapidity coverage of the ALICE Muon Spectrometer is  $-4.0 < y_{lab} < -2.5$  in the laboratory frame. However due to the LHC beam energy asymmetry in p-Pb collisions, the center of mass rapidity frame is displaced with respect to the laboratory one by  $\Delta y = 0.465$ . Consequently, the rapidity ranges covered by spectrometer in the p-Pb and Pb-p beam configurations are  $2.03 < y_{cms} < 3.53$  (forward- $y$ ) and  $-4.46 < y_{cms} < -2.96$  (backward- $y$ ) respectively.

The Muon Spectrometer tracking efficiency studies in p-Pb data taking periods performed in this thesis (Chap. 5), were a major part of the work done for the obtention of the ALICE p-Pb results that we discuss in the following.

In Fig. 1.25, the rapidity dependence of the  $J/\psi$  nuclear modification factor in p-Pb collisions  $R_{pPb}^{20}$  is presented [3]. At forward rapidity the  $J/\psi$  production is suppressed but remains unchanged at backward rapidity. The measurements are compared to several CNM models. A shadowing model using EPS09 shadowing parametrization [185] (denoted as "EPS09 NLO"), a model including coherent energy loss [169] ("Eloss"), and calculations in the CGC framework [161]. Within the data uncertainties only shadowing and coherent energy loss models describe the data. The CGC based model overestimates the suppression at forward rapidity.

The transverse momentum dependence of the  $J/\psi$  nuclear modification factor for two different rapidity ranges, forward and backward rapidity is shown in Fig. 1.26 [65]. At backward rapidity the result is consistent with a weak dependence of nuclear effects with  $p_T$ , while at forward rapidity the  $J/\psi$  production is more suppressed at low  $p_T$ . The different models predict also a weak  $p_T$  dependence at backward rapidity. At forward rapidity the CGC based model clearly overestimates suppression, while nuclear shadowing with or without an energy loss contribution is able to reproduce the data at high  $p_T$ . At low  $p_T$  the shadowing model has no prediction and the energy loss models predict a slightly more steeper behaviour than that observed in data.

In Fig. 1.27 the results of the  $Q_{pPb}$  as a function of the number of binary collisions  $\langle N_{coll}^{mult} \rangle$  is shown for several rapidity ranges [5]. Note that the nuclear modification factor is denoted by  $Q_{pPb}$ . This notation is used to make explicit the possible biases on the measurement due to centrality computation in p-Pb collisions. Also, the number of binary collisions is

<sup>20</sup>The nuclear modification factor in p-Pb collisions is defined in an equivalent way to the A-A one.

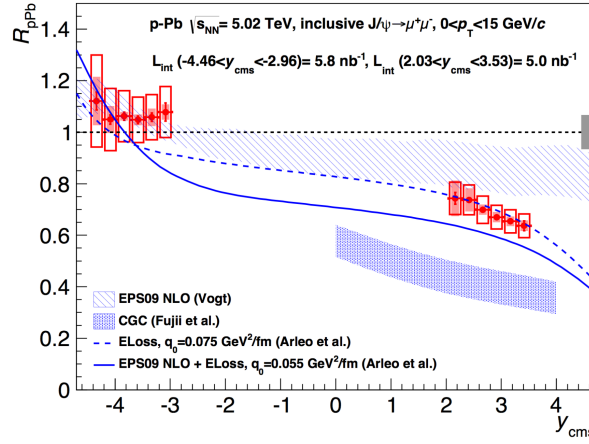


Figure 1.25:  $J/\psi$  nuclear modification factor ( $R_{pPb}$ ) as a function of rapidity. The results are compared with several CNM models (see text). Figure taken from [3].

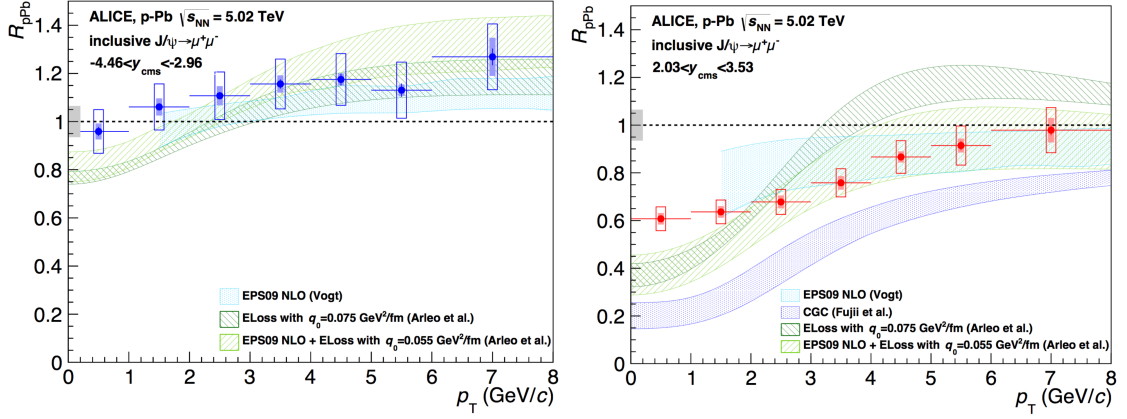


Figure 1.26:  $J/\psi$  nuclear modification factor as a function of  $p_T$  at backward (left) and forward (right) rapidity. The results are compared with several CNM models (see text). Figure taken from [4].

denoted as  $\langle N_{coll}^{mult} \rangle$ , due to the centrality computation method used in p-Pb collisions [55] (see App. A for a brief description of the ALICE centrality determination in p-Pb collisions). The  $Q_{pPb}$  is compatible within the uncertainties with binary collision scaling at backward rapidity. The result may suggest an increase of the  $J/\psi$  production with centrality when the uncertainties correlated over centrality are not considered. At forward rapidity, the  $J/\psi$  production is suppressed for all the considered centrality classes, exhibiting an increase of the suppression with centrality. The result at mid rapidity suggests a similar degree on the suppression of the  $J/\psi$  yield as at forward rapidity, but no conclusion can be drawn on the centrality dependence. The shadowing calculation (denoted as "CEM EPS09 NLO") [186] reproduce the data behaviour in all the rapidity ranges but its uncertainty is large. The model including shadowing with or without comovers interaction shows that the comover

effect is only important at mid and forward rapidity [187] ("EPS09 LO + comovers"). The energy loss model [170] reproduces shape and magnitude of the data in all the centrality ranges, except the increase at backward rapidity.

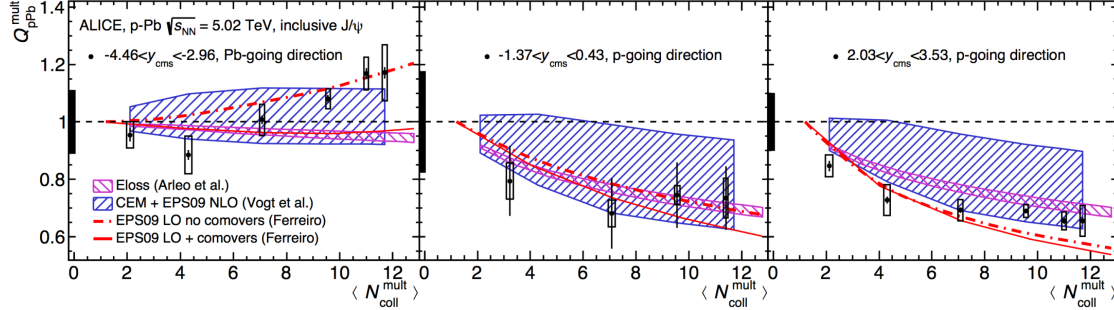


Figure 1.27:  $J/\psi$  nuclear modification factor ( $Q_{pPb}$ ) as a function of  $N_{coll}^{mult}$  at backward (left), mid (middle) and forward (right) rapidity. The results are compared with several CNM models (see text). Figure taken from [5].

The results obtained in [5] for the  $p_T$  broadening  $\Delta p_T$  are shown in Fig. 1.28. The  $\Delta p_T$  increases both at backward and forward rapidities with the number of binary collisions. For increasing number of collisions,  $\Delta p_T$  is bigger than that found in pp collisions. The result is compared with models including initial and final state multiple scattering of partons with the nuclear medium ("Mult. Scattering") [188, 189], which shows a good agreement with data. Also, a model including energy loss effects [170] describes the data at backward rapidity, while the predicted behaviour at forward rapidity is slightly steeper than the data.

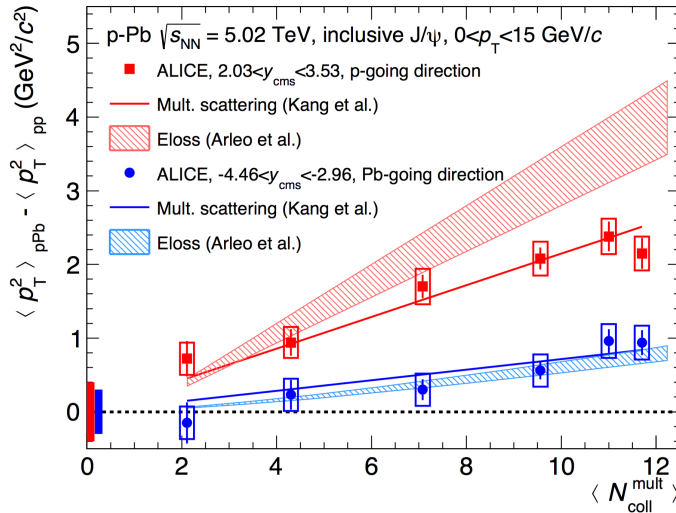


Figure 1.28:  $J/\psi$  transverse momentum broadening as a function of  $N_{coll}^{mult}$  at backward (blue dots) and forward (red dots) rapidity. The results are compared with theoretical calculations (see text). Figure taken from [5].

The comparison of the nuclear modification factor as a function of rapidity measured for  $J/\psi$  and  $\psi(2S)$  is shown in Fig. 1.29 [190]. As can be observed the measurement shows more suppression for  $\psi(2S)$  than for  $J/\psi$ . The results are compared with the CNM expectations, which do not predict this behaviour for  $\psi(2S)$ . Due to the similar kinematics of the  $c\bar{c}$  pairs producing a  $J/\psi$  or a  $\psi(2S)$  the shadowing effects are the same for both within 2-3%. These predictions are in disagreement with the data, which indicates that other mechanisms have to be taken into account to describe  $\psi(2S)$  suppression in p-Pb collisions.

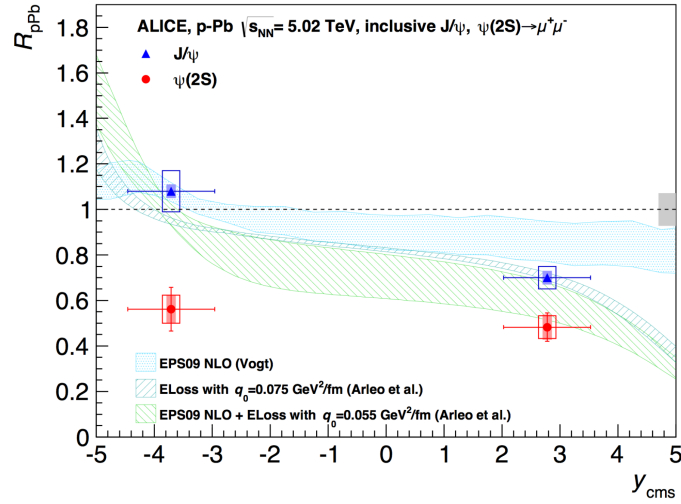


Figure 1.29:  $\psi(2S)$  nuclear modification factor compared to the  $J/\psi$  one. The theoretical model calculations for  $\psi(2S)$  produce identical values for the coherent energy loss mechanism and a 2-3% larger result for nuclear shadowing, so only calculations for  $J/\psi$  are shown. Figure taken from [190].

In this thesis, the same p-Pb data as that used in the previously presented results are used. However, the possible biases on the centrality determination in p-Pb collisions, provide a further incentive to study the event activity dependence of the  $J/\psi$  production in terms of the charged particle multiplicity. The  $J/\psi$  yield is studied as a function of the charged particle multiplicity measured at mid rapidity. This study is complementary to the one performed in [5]. The use of multiplicity to characterise event activity, also allows to explore high event activity regions not accessible with centrality analyses, where effects beyond CNM might be manifested.

Other studies of quarkonium production as a function of event activity in p-Pb collisions at the LHC have been performed. CMS has measured the  $Y$  production as a function of the event activity in pp and pPb collisions at the LHC [191]. In Fig. 1.30 we show the results of the cross section ratios  $Y(2S)/Y(1S)$  as a function of the number of measured tracks at mid rapidity  $|\eta| < 2.4$ , obtained pp collisions at a center-of-mass energy of 2.76 , Pb-Pb at 2.76 TeV and p-Pb at 5.02 TeV. The ratios were found to decrease with increasing tracks multiplicity. This is an unexpected dependence in pp and p-Pb collisions, which suggests novel phenomena

in quarkonium production. In [191] it is suggested that this dependence could arise from a larger number of charged particles being systematically produced with the ground state, or from a stronger impact of the growing number of nearby particles on the more weakly bound states. In addition, the double ratios  $[\Upsilon(nS)/\Upsilon(1S)]_{pPb}/[\Upsilon(nS)/\Upsilon(1S)]_{pp}$  were found to be smaller than unity, but larger than the corresponding double ratios measured for PbPb collisions. This suggests the presence of final-state suppression effects in the p-Pb collisions compared to pp collisions affecting strongly the excited states.

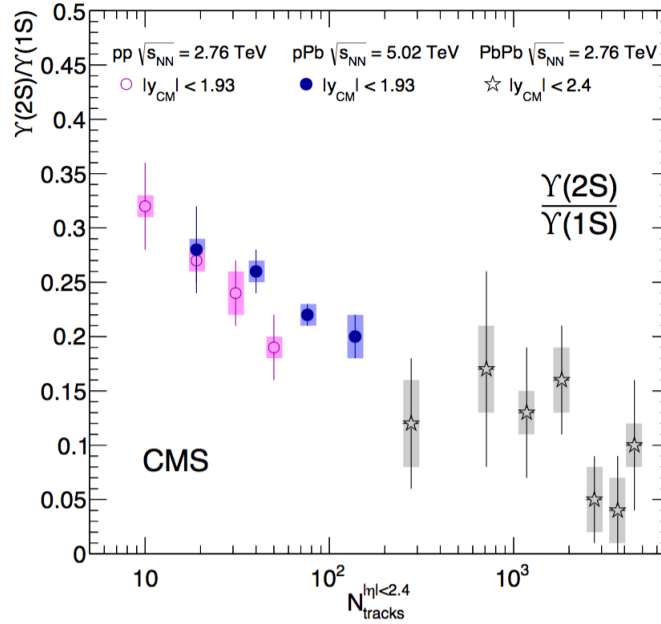


Figure 1.30: Cross section ratio  $Y(2S)/Y(1S)$  as a function of the number of measured tracks at mid rapidity  $|\eta| < 2.4$ . The results for pp at 2.76 Pb-Pb at 2.76 TeV and p-Pb at 5.02 TeV are shown. Figure taken from [191].

Also in [191], the relative  $Y(1S, 2S, 3S)$  cross sections as a function of relative number of measured tracks at mid rapidity  $|\eta| < 2.4$  was measured. The result is shown in Fig.1.31, for the three states in pp,Pb-Pb and p-Pb collisions. The relative cross sections increase with increasing multiplicity. The increase observed in p-Pb and Pb-Pb collisions can arise from the increase in the number of nucleon-nucleon collisions. The pp results reminds the  $J/\psi$  ALICE measurement at 7 TeV [8]. A possible interpretation of the increase observed in pp collisions is the occurrence of MPI in a single pp collision [114].

In addition, we are going to discuss a result which is not directly related with charmonium production but is one of the main motivations for the  $J/\psi \langle p_T \rangle$  measurements performed in this thesis. The result of the  $\langle p_T \rangle$  of charged particles, measured in the pseudorapidity<sup>21</sup> range  $|\eta| < 0.3$ , as a function of charged particle multiplicity, for pp, p-Pb and Pb-Pb collisions, is shown in Fig. 1.32 (left) [7]. In pp collisions, an increase of  $\langle p_T \rangle$  with multiplicity and a

<sup>21</sup> $\eta = -\ln \tan(\theta/2)$ , where  $\theta$  is the polar angle relative to the beam axis.

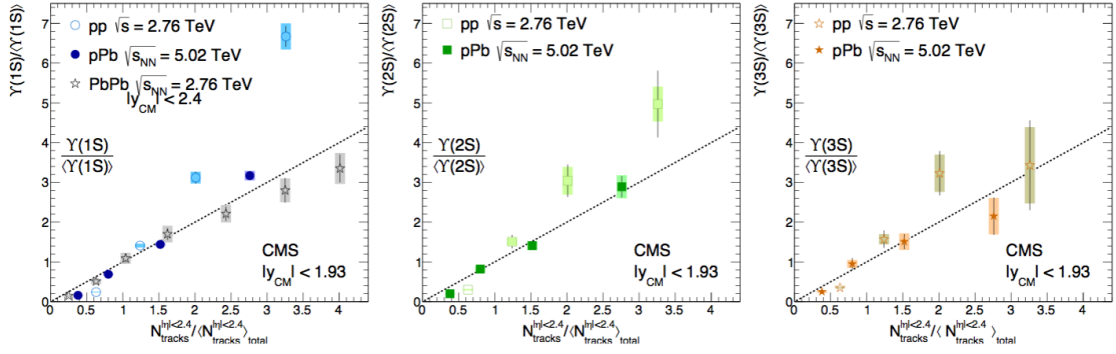


Figure 1.31: Relative  $\Upsilon(1S, 2S, 3S)$  cross sections as a function of relative number of measured tracks at mid rapidity  $|\eta| < 2.4$ . The results are shown for pp at 2.76 and p-Pb at 5.02 TeV collisions are shown for the three states. The measurement in Pb-Pb collisions at 2.76 is only shown for the ground state. The dotted line shows the linear behaviour. Figure taken from [191].

change of slope is observed. In p-Pb collisions at low multiplicity the  $\langle p_T \rangle$  increases as in pp collisions, while at higher multiplicities, the increase is softer in p-Pb than in pp collisions. The increase of  $\langle p_T \rangle$  in Pb-Pb collisions is rather weak. The p-Pb data have features of pp collisions at low multiplicity, while at high multiplicity it has a trend to saturation as in Pb-Pb collisions. The authors argued that the difference of  $\langle p_T \rangle$  at high multiplicity among the different collisions systems cannot be attributed to the different energies since the  $\langle p_T \rangle$  dependence with energy is weak.

In Fig. 1.32 (right), the results are compared to different model predictions. According to Monte Carlo (MC) generators, high multiplicity pp events are produced by multiple parton interactions (MPI). If high multiplicity pp events were just an incoherent superposition of parton-parton interactions, the  $\langle p_T \rangle$  would be constant at high multiplicities. PYTHIA models [192, 193] attribute the correlation of the  $\langle p_T \rangle$  with the color reconnection (CR) mechanism<sup>22</sup> [192]. As we can see, the model fairly describes the pp  $\langle p_T \rangle$  data. Whether the same mechanism is at play in p-Pb collisions is an open question. The models representing p-Pb collisions as an incoherent superposition of pp collisions are not able to reproduce the measurement. Only the EPOS model [194], which includes collective flow via parametrizations, is able to describe the trend of the p-Pb data. However, it is needed to study if initial state effects can also reproduce the data. Note that flow-like effects observed in pp collisions can be described with MPI and the CR mechanism [195]. The observed saturation of the  $\langle p_T \rangle$  in Pb-Pb collisions is ascribed to a redistribution of the spectrum due to rescattering of constituents, where most particles are part of a locally thermalized medium exhibiting collective hydrodynamic-type behavior. None of the presented models is able to reproduce

<sup>22</sup>In this mechanism, color strings from independent parton interactions do not hadronize independently, but fuse prior to hadronization. Each further MPI brings less and less additional  $N_{ch}$ , while still providing an equally big  $p_T$  kick from the interaction itself, to be shared among the produced hadrons. This leads to fewer hadrons, but more energetic.



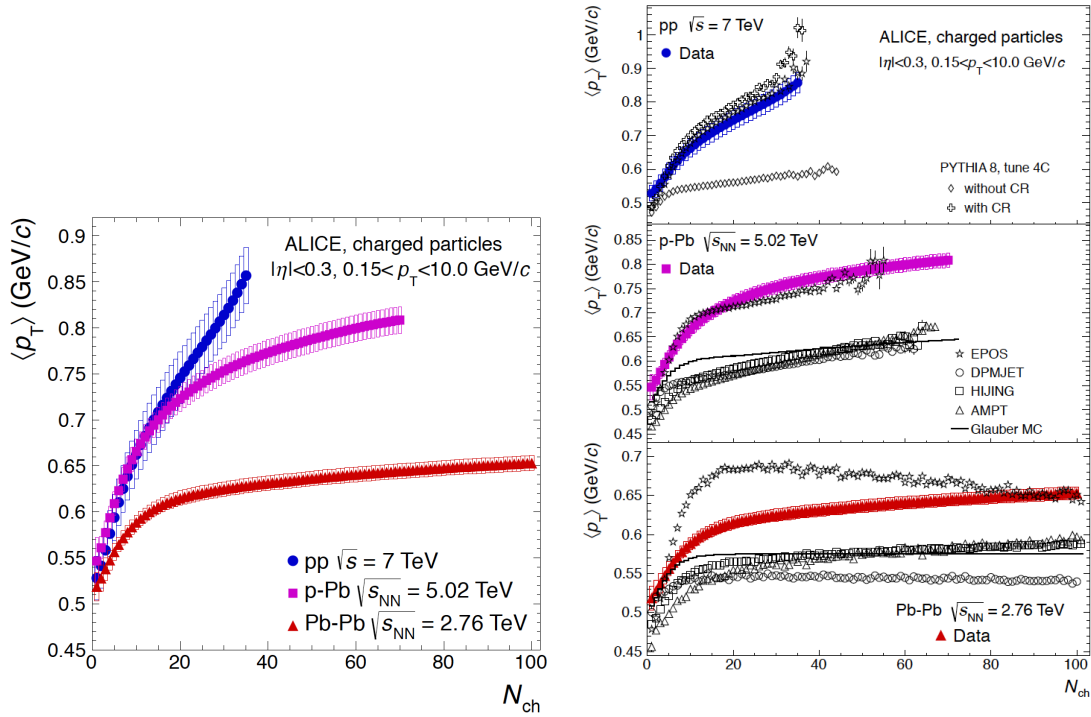


Figure 1.32: Average transverse momentum as a function of charged particle multiplicity ( $|\eta| < 0.3$ ). Boxes represent the systematic uncertainties, and the statistical ones are negligible. Left: experimental results only. Right: experimental results compared with model predictions. Figure taken from [7].

the charged particle  $\langle p_T \rangle$  trending in Pb-Pb collisions.

Regarding these results, it is very interesting to measure the dependence of the  $J/\psi$   $\langle p_T \rangle$  as a function of charged particle multiplicity to determine whether similar properties are observed or not. In this thesis, we perform the measurement of the  $J/\psi$   $\langle p_T \rangle$  as a function of charged particle multiplicity in pp collisions at  $\sqrt{s} = 8$  TeV and p-Pb collisions at  $\sqrt{s_{NN}} = 5$  TeV. In addition, a preliminary study of the multiplicity dependence of the transverse momentum broadening is presented for p-Pb collisions.



## THE ALICE EXPERIMENT AT THE LHC

In this chapter, the Large Hadron Collider (LHC) particle accelerator is briefly described. The main characteristics of the LHC and its experiments are mentioned in the first part of this chapter. The ALICE experiment is a heavy-ion dedicated experience located at the LHC. Its main goal is the study of the QGP formation in heavy-ion collisions. The data used for the analyses in this thesis were taken by ALICE detector. The second part of this chapter is focused on the description of the different ALICE subsystems. Special attention is given to the Muon Spectrometer, which is the detector used for the  $J/\psi$  measurements performed in this thesis.

### 2.1 The Large Hadron Collider (LHC)

The Large Hadron Collider (LHC) is the world's largest and most powerful particle accelerator and it is the latest addition to CERN's accelerator complex (Fig. 2.1) [196–198]. The accelerator complex is a succession of machines that accelerate particles to increasingly higher energies. The LHC consists of a 27-kilometres ring of superconducting magnets with a number of accelerating structures to boost the energy of the particles along their way. Two high-energy particle beams travel in opposite directions in separate ultrahigh vacuum beam pipes. These beams are made to collide at four locations around the accelerator ring, where four particle detectors are located: ATLAS, CMS, ALICE and LHCb.

#### 2.1.1 The LHC experiments

The experiments located at the LHC have several physics goals. Those include the search of the Higgs boson, searches for supersymmetric particles, matter anti-matter asymmetry and QGP studies.

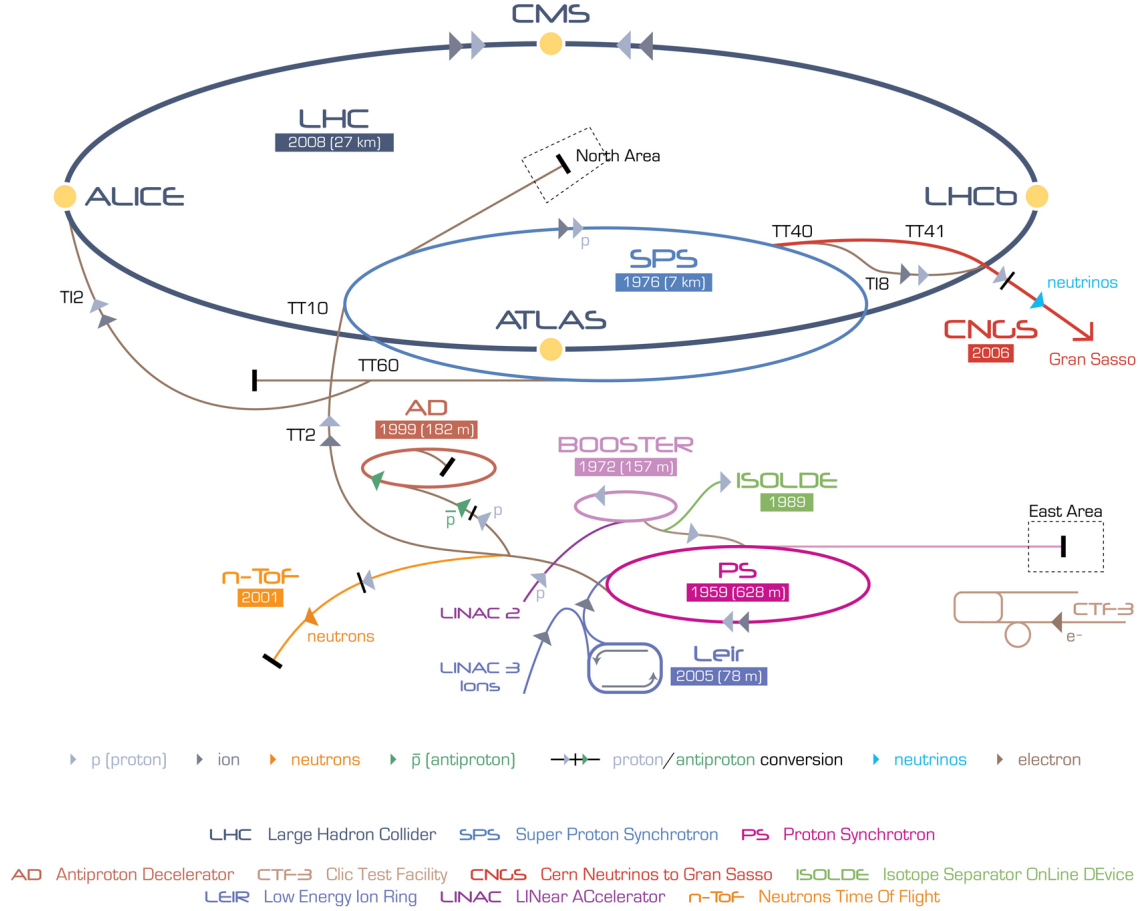


Figure 2.1: The CERN accelerator complex .

ATLAS [199] (A Toroidal AparatuS) is a general-purpose detector. The ATLAS detector has a large superconducting toroidal magnet. The detector surrounds entirely the collision point with an enclosed detector. It investigates a wide range of physics, from the search for the Higgs boson to supersymmetric particles and extra dimensions and particles that could conform the dark matter.

CMS [200] (Compact Muon Solenoid) is the second general-purpose detector at the LHC. The CMS detector is built around a huge solenoid magnet. It is also an enclosed detector. It has the same physics goals as the ATLAS experiment although they have different magnet system design.

LHCb [201] (Large Hadron Collider beauty) is specialised in the study of the matter anti-matter asymmetry, by measuring particles containing a beauty ( $b$ ) quark. The LHCb detectors are mainly situated in the forward direction to detect forward particles.

ALICE [202] (A Large Ion Collider Experiment) is the heavy-ion dedicated detector. It is mainly designed to study the physics of the QGP. The ALICE detector is further discussed in the following section.

## 2.2 The ALICE detector

The ALICE main physics goal is the study of the physics of strongly interacting matter in ultra-relativistic heavy-ion collisions. It also performs measurements in pp and p-Pb collisions as part of its physics program. The experiment has a high detector granularity to cope with the high particle densities in central Pb-Pb collisions, a low transverse momentum threshold ( $p_T \sim 0.15$  GeV/c), and a good particle identification up to 20 GeV/c. A summary on the physics topics covered by ALICE and the performance of its detectors in measuring different observables is given in [203–205]. The results obtained to date are available at [206].

The detector consist of three main parts. The central barrel detectors ( $\eta < 0.9$ ) which are embedded in a solenoid with magnetic field  $B = 0.5$  T, and are in charge of tracking and identifying charged particles (ITS, TPC, TRD, TOF, HMPID) and photons (PHOS and EMCAL). The global detectors (FMD, PMD, VZERO, TZERO, and ZDC), which are used for triggering, event characterisation (centrality, event plane...) and beam luminosity measurements. The Muon Spectrometer ( $-4.0 < \eta < -2.5$ ), which has its proper dipolar magnetic field of 3 T·m and is responsible for muon tracking and triggering. The detector is completed by an array of scintillators to trigger on cosmic rays (ACORDE). An schematic view of the ALICE subsystems is shown in Fig. 2.2.

The ALICE coordinate system is defined such as the system origin is located at the interaction point (IP). The  $z$ -axis is parallel to the beam line and is positive towards the A side of the detector (opposite tho the Muon Spectrometer which is in the C side), the  $x$ -axis is perpendicular to the beam line and points to the center of the LHC ring, and the  $y$ -axis points upwards.

The main characteristics of the different subsystems<sup>1</sup> are summarised in the corresponding subsections below.

### 2.2.1 Global detectors

#### 2.2.1.1 Forward Multiplicity Detector (FMD)

The FMD [208] consists of 5 rings perpendicular to the beam axis, made of Si semiconductor detectors with a total of 51200 individual strips (Fig. 2.3). The FMD system provides precise charged particle multiplicity information in the pseudorapidity range  $-3.4 < \eta < -1.7$  and  $1.7 < \eta < 5.0$ . It has a read-out time of about  $13 \mu\text{s}$ , which only allows it to participate in the ALICE trigger hierarchy at L2 and above (see Sec. 2.3.1). The FMD rapidity coverage is complementary to the ITS, so the combination of the information of the two detectors provide charged particle multiplicity distributions in a wide rapidity range  $-3.4 < \eta < 5.0$ . This detector also allows the study of multiplicity fluctuations and determination of event plane on an event by event basis, thanks to its azimuthal segmentation.

<sup>1</sup>As installed for the data taking periods considered in this thesis

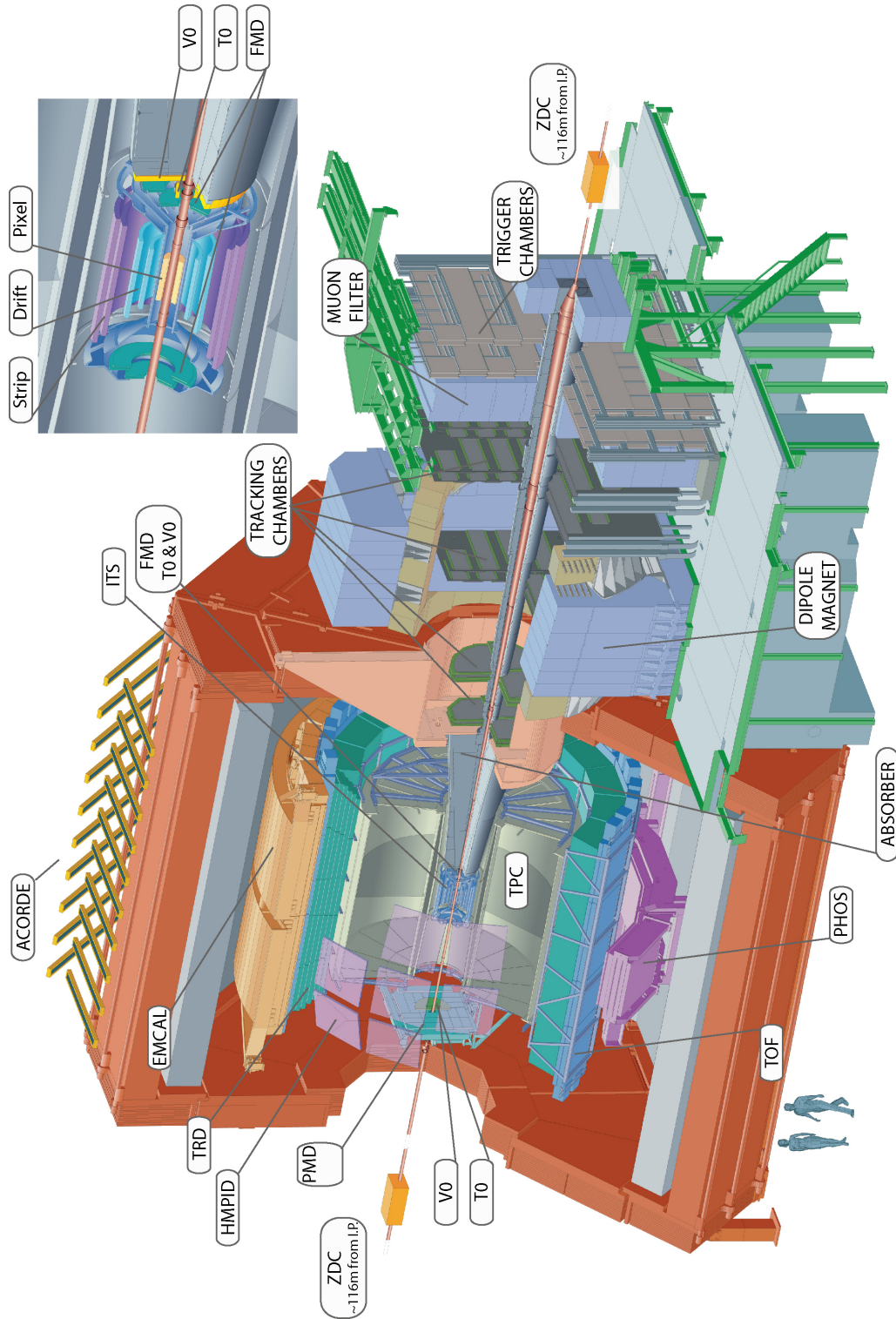


Figure 2.2: Schematic representation of the ALICE detector with all its sub detectors during Run1. Figure taken from [207] .

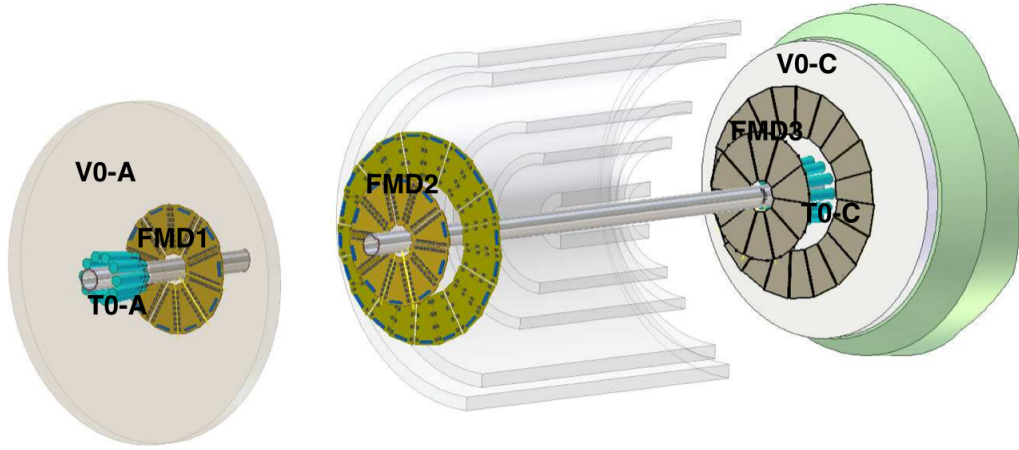


Figure 2.3: Schematic representation of the forward detectors. The 5 FMD rings (FMD1, FMD2 and FMD3) can be observed. The two V0 (A and C side) as well as the two T0 detectors are shown. The ITS is sketched in the centre of the figure as well as the front absorber of the Muon Spectrometer (green region). Figure taken from [208] .

### 2.2.1.2 Photon Multiplicity Detector (PMD)

The PMD [209, 210] is a preshower detector. The PMD has high granularity and full azimuthal coverage in the pseudorapidity region  $2.3 < \eta < 3.5$ . It is situated at 3.67 m from the interaction point on the opposite side of the Muon Spectrometer. The detector has two planes, one for charged particle veto and the other for preshower detection. Both planes have a honeycomb proportional chamber design. The detector measures the multiplicity and spatial distributions of photons on an event-by-event basis. The PMD is able to study event shapes and fluctuations as well as providing estimations of the transverse electromagnetic energy.

### 2.2.1.3 V0

The V0 [208] detector is a small angle detector which consists of two arrays of scintillator counters situated on both sides of the IP (Fig. 2.3). The counters cover the pseudorapidity ranges  $2.8 < \eta < 5.1$  (V0A) and  $-3.7 < \eta < -1.7$  (V0C) which partially overlap with the FMD acceptance. They are situated at 3.29 m and  $-0.88$  m from the IP. The V0 system can reject events arising from interaction of the beam particles with the residual particles in the beam pipe vacuum (beam-gas interaction) by measuring the difference of the time-of-flight between the two counters. Therefore, the V0 provides the online L0 (see Sec. 2.3.1) Minimum Bias (MB) trigger. It also measures charged-particle multiplicity distributions serving as an indicator of the centrality of the collision. The V0 detector is also used for luminosity measurements.

#### 2.2.1.4 T0

The T0 [208] detector consists of two arrays of quartz Cherenkov radiators optically coupled to photo-multiplier tubes (PMTs). The arrays cover the pseudorapidity ranges  $4.6 < \eta < 4.9$  (T0A) and  $-3.3 < \eta < -3.0$  (T0C) and are situated on the opposite sides of the IP at 3.70 m and  $-0.7$  m respectively (Fig. 2.3). The T0 supplies fast timing signals for L0 trigger (see Sec. 2.3.1) and gives a collision time reference for the TOF system (T0 time resolution is better than 50 ps). The T0 system can also provide the longitudinal position of the interaction, and a vertex trigger defined as the coincidence between the T0A and T0C with the requirement that the difference in their signal times corresponds to an interaction happening within 30 cm of the IP. This provides an excellent rejection of beam-gas interactions [205]. The T0 detector is also used as a luminometer.

#### 2.2.1.5 Zero Degree Calorimeter (ZDC)

The ZDCs [211] are two pairs of hadronic calorimeters with quartz fibres as active material. There are two systems of neutron (ZN) and proton (ZP) ZDCs located close to the beam pipe at 113 m on both sides of the IP. They cover the pseudorapidity ranges  $|\eta| < 8.8$  (ZP) and  $6.5 < \eta < 7.5$  (ZN). They are able to count spectator nucleons (nucleons not taking part in the collision) by measuring the deposited energy. They are therefore used for centrality estimation as well as reaction plane determination. The system is complemented by two electromagnetic calorimeters (ZEM) which cover the range  $4.8 < \eta < 5.7$  and are placed at 7.3 m at both sides of the IP. They are used to measure the energy carried by the photons (mainly from  $\pi^0$  decays) in the forward direction. This provides further information on the event centrality.

### 2.2.2 Central barrel detectors

#### 2.2.2.1 Inner Tracking System (ITS)

The ITS [212] consists of six cylindrical layers of silicon detectors (Fig. 2.3). The number and position of the layers are optimized for efficient track finding and vertex resolution. The outer radius is chosen to optimize the track matching with the TPC, while the inner one is the minimum compatible with the beam pipe. The silicon detectors feature a high granularity and excellent spatial precision required due to the high particle density. The system covers the central rapidity region  $|\eta| < 0.9$  for vertices located at  $\pm 10.6$  cm of the IP along the beam direction.

Due to the high granularity required for the innermost planes, silicon micro-pattern detectors are used: the first two layers are Silicon Pixel Detectors (SPD) and the two following are Silicon Drift Detectors (SDD). At larger radii, the density of particles is smaller so the last two layers are Silicon Strip Detectors (SSD). The dimensions and technology used for each detector layer are summarised in Tab. 2.1.

The SPD layers are fundamental in the determination of the position of the primary vertex and the measurement of the impact parameter of secondary tracks from the weak decays of strange, charm and beauty particles. The rest of the ITS layers provide also tracking and particle identification (SDD) of low momentum particles ( $p < 100 \text{ MeV}/c$ ). The ITS is able to measure the collision vertex with a resolution better than  $100 \mu\text{m}$ , it improves the position, angle and momentum resolution of the tracks measured by the TPC and it is able to recover particles missed by the TPC due to acceptance limitations.

Layer	Type	r (cm)	$ \eta $	$\pm z$ (cm)
1,2	Pixel	3.9, 7.6	2.0, 1.4	14.1
3,4	Drift	15.0, 23.9	0.9	22.2, 29.7
5,6	Strip	38, 43	1.0	43.1, 48.9

Table 2.1: ITS detector dimensions. From [213].

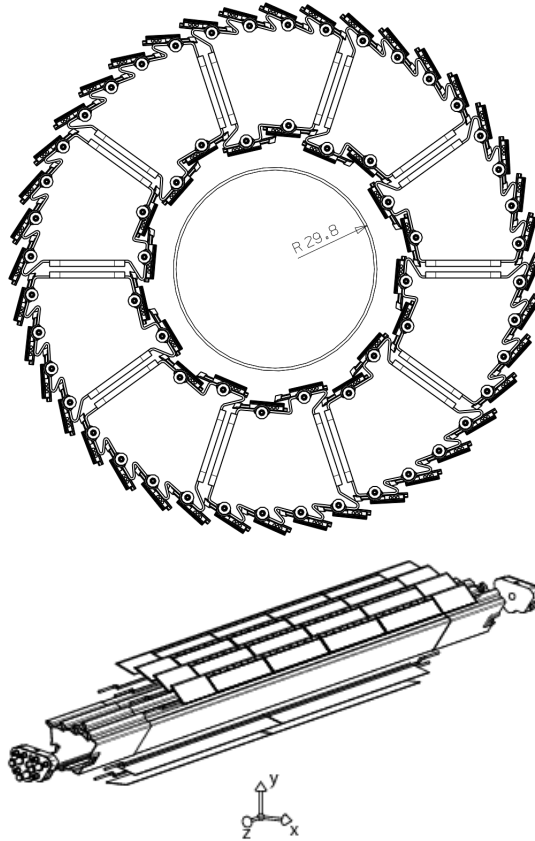


Figure 2.4: Top: Front view of the SPD barrel and the beam pipe radius (mm). Bottom: Carbon fibre support sector. Figure taken from [213] .

In the following we give some more details on the SPD detector geometry, since it is the one used for the charged particle multiplicity measurements in this thesis. The basic building block of the ALICE SPD is a module consisting of a two-dimensional matrix of

silicon pixel detector diodes. Two modules are mounted together along the  $z$  direction to form a 141.6 mm long half-stave. Two half-staves are attached, head-to-head along the  $z$  direction, to a carbon-fibre support sector which also provides cooling (Fig. 2.4 bottom). Each sector supports six staves: two on the inner layer and four on the outer layer.

### 2.2.2.2 Time Projection Chamber (TPC)

The TPC [214] is one of the main charged particle tracking detectors in the central barrel. The pseudorapidity range covered by the TPC is  $|\eta| < 0.9$ . It provides charged particle momentum measurement and vertex determination. In addition, the TPC provides particle identification via specific ionisation energy loss up to a particle momentum of 1 GeV/ $c$ .

The TPC has a cylindrical shape with an inner radius of about 85 cm and an outer radius of 250 cm. It has a length of 500 cm along the beam direction, divided by the central High Voltage (HV) electrode into two drift regions of 250 cm (Fig. 2.5). Each drift region has 18 sectors of read-out multi-wire proportional chambers mounted into the end plates. The detector is filled with a gas mixture of Ne, CO<sub>2</sub> and N<sub>2</sub>. The charged particles traversing the detector ionize the gas. Due to the influence of the electric field, the ionization electrons drift to the endplates of the cylinder, where their arrival point is precisely measured. With an accurate measurement of the arrival time, this allows to measure the complete trajectory of the particle with high precision.

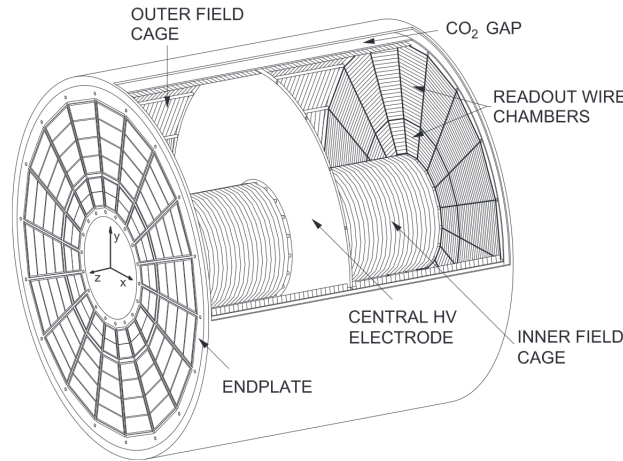


Figure 2.5: The TPC layout. Figure taken from [215] .

### 2.2.2.3 Transition Radiation Detector (TRD)

The TRD [216] detector consists of six individual layers of multi-wire proportional chambers (MWPC) filled with Xe-CO<sub>2</sub>, with a fiber/foam radiator in front of each chamber. It covers the pseudorapidity range  $|\eta| < 0.9$ . This detector provides charged-particle tracking, electron



identification via transition radiation<sup>2</sup>, pion rejection as well as triggering capability for high transverse momentum processes.

The radiator performance provides an increase of the pion rejection by a factor of 100 at 90% electron efficiency and  $p_T$  above 3 GeV/c. The TRD extends the PID particle momentum range of the TPC and TOF (see Sec. 2.2.2.4). Furthermore, combining the ITS, TPC and TRD detector's information, the momentum resolution in the central barrel tracking is good enough to measure high- $p_T$  tracks up to 100 GeV/c, with a mass resolution of about 100 MeV/c<sup>2</sup> at the  $\Upsilon$  mass. These characteristics enable the possibility to study light and heavy vector mesons as well as open charm and open beauty.

#### 2.2.2.4 Time Of Flight (TOF)

The TOF [217–219] is designed to identify charged particles. It extends the TPC PID capabilities for particles with a momentum from 1 GeV/c up to a few GeV/c. The TOF is a cylindrical detector with an inner radius of 3.7 m that covers the pseudorapidity interval  $|\eta| < 0.9$ . Due to the magnetic field, the momentum threshold for particles to reach the TOF is 300 MeV/c (up to 350 and 450 for kaons and protons respectively due to larger energy loss). The TOF exploits the Multigap Resistive Plate Chamber (MRPC) technology, which gives an intrinsic resolution better than 50 ps and an efficiency close to 100%. This allows a separation for  $\pi/K$  and  $K/p$  about  $2\sigma$  up to a particle momentum of 3 and 5 GeV/c respectively.

#### 2.2.2.5 High-Momentum Particle Identification Detector (HMPID)

The HMPID [220] has a single arm design consisting of seven proximity focusing type Ring Imaging Cherenkov Counter (RICH) modules. The detector covers the pseudorapidity  $|\eta| < 0.6$  and  $57.6^\circ$  in azimuth ( $\sim 5\%$  of the central barrel phase space). The HMPID performs inclusive measurements of identified hadrons at  $p_T > 1$  GeV/c. It is optimised to enhance the particle identification capabilities of ALICE. The HMPID can make  $\pi/K$  and  $K/p$  discrimination on a track-by-track basis up to 3 GeV/c and 5 GeV/c respectively. It can also perform identification of light nuclei and anti-nuclei (deuterium, tritium,  $^3\text{He}$  and  $\alpha$  particles) at high momenta.

#### 2.2.2.6 PHOTon Spectrometer (PHOS)

The PHOS [221] detector is a high resolution electromagnetic spectrometer of high granularity consisting of a highly segmented electromagnetic calorimeter of lead-tungstate crystals and a charged particle veto detector (a MWPC). It is positioned on the bottom of the ALICE set-up, and covers a pseudorapidity range  $|\eta| < 0.12$  and azimuthal angle of  $100^\circ$ . PHOS is

<sup>2</sup>When a highly relativistic charged particle traverses the boundary between two media of different dielectric constants it produces transition radiation. The average energy of the emitted photon is approximately proportional to the Lorentz factor of the particle, providing an excellent way for discriminating between electrons and pions for momenta of a few GeV/c and higher.

optimized for measuring photons and neutral mesons ( $\pi^0$  and  $\eta$ ) up to momenta about 10 GeV/c, through their decay into two photons .

#### 2.2.2.7 ElectroMagnetic CALorimeter (EMCAL)

The EMCAL [222] detector is a layered Pb-scintillator sampling calorimeter with alternating layers of 1.44 mm Pb and 1.76 mm polystyrene scintillator. It covers a pseudorapidity range of  $|\eta| < 0.7$  and  $107^\circ$  in azimuth.

The EMCAL enhances ALICE capabilities for jet quenching measurements. It enables the possibility for an unbiased L0 trigger (see Sec. 2.3.1) for high energy jets, improves jet energy resolution and extends the ALICE capabilities to measure high momentum photons, neutral hadrons and electrons.

#### 2.2.2.8 ALICE COsmic Ray DEtector (ACORDE)

ACORDE [223] is an array of doublets of plastic scintillator modules placed on the top sides of the central ALICE magnet. It provides a cosmic ray trigger, which is used for calibration and alignment of the TPD, TRD and ITS. Together with these detectors, ACORDE allows to study high energy cosmic rays through the detection of atmospheric muons.

### 2.2.3 Muon spectrometer

The Muon Spectrometer [224, 225] is designed to measure the production of quarkonia ( $J/\psi$ ,  $\psi(2S)$ ,  $\Upsilon$ ,  $\Upsilon'$ ,  $\Upsilon''$ , with a mass resolution good enough to separate the bottomonium states), and low mass vector mesons ( $\rho$ ,  $\omega$ ,  $\phi$ ) via their di-muon ( $\mu^+ \mu^-$ ) decay channel. It is also used to measure the production of single muons from decays of heavy flavor hadrons (D and B mesons) and the  $W^\pm$  and  $Z^0$  bosons. The detector is located at backward rapidity  $-4.0 < \eta < -2.5$ . It has a total length of about 17 m and consists of the following components: a system of passive absorbers, ten high granularity detection planes (arranged in five stations), a dipole magnet, a passive iron wall and four trigger chambers (arranged in four stations).

The different components of the Muon Spectrometer (Fig. 2.6) are discussed in more details in the following sections.

#### 2.2.3.1 System of absorbers

The large background environment in central Pb-Pb collisions requires to shield the Muon Spectrometer. The system of absorbers consists of four separated parts: the front absorber, the beam shield, the iron wall and the rear absorber.

- **Front absorber:** It is located inside the central barrel solenoid magnet at 90 cm from

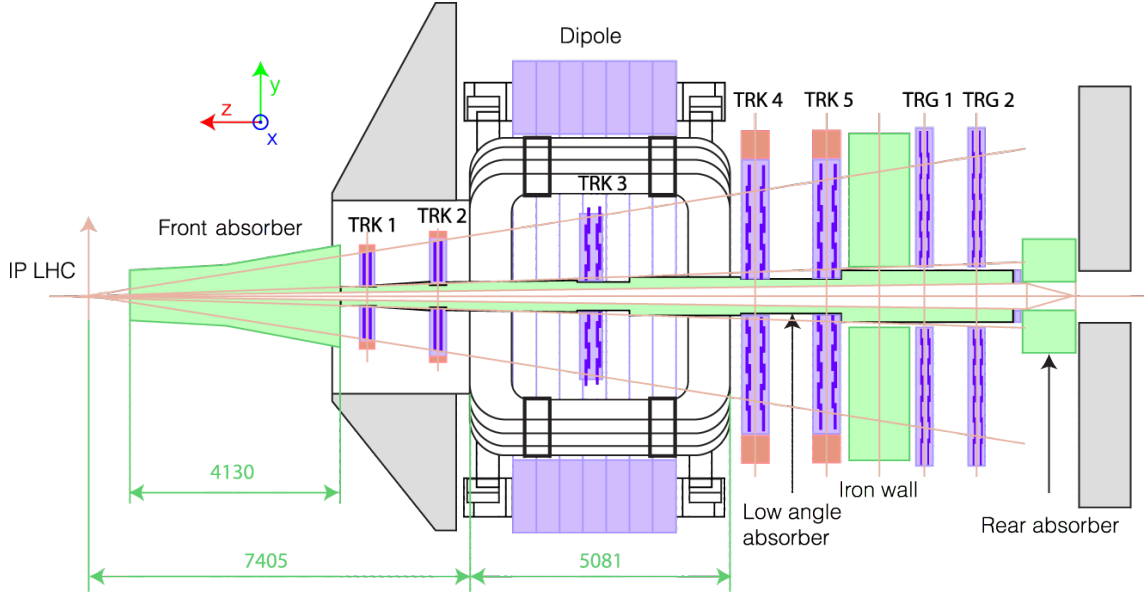


Figure 2.6: Layout of the ALICE Muon Spectrometer. Note that the front absorber and the two first stations are inside the ALICE solenoid magnet. Figure taken from [226].

the IP. The absorber has a length of 4.13 m ( $\sim 10 \lambda_{int}^3$  and  $\sim 60 X_0^4$ ). The absorber design is optimised to provide a good shielding from hadrons from the IP and from background muons from pion and kaon decays; and, at the same time, to limit the multiple scattering of the interesting muons. This is crucial to obtain the required resolution to separate the bottomonium states ( $\sim 100 \text{ MeV}/c^2$  at  $m \sim 10 \text{ GeV}/c^2$ ).

A layout of the front absorber is shown in Fig. 2.7. The region close to the IP is made of a low Z material, Carbon, in order to reduce multiple scattering effects. The rear part is made of concrete and several layers of lead and boronated polyethylene to absorb the secondary particles produced in the absorber and low energy protons and neutrons. The external coating of the absorber is made of lead and boronated polyethylene to avoid the recoil particles to reach the TPC. Finally there is an inner shield covering the beam, made of tungsten to absorb the background particles from beam-gas interactions.

- **Beam shield:** The beam pipe is shielded along the Muon Spectrometer to avoid background from interactions of low angle particles with the pipe or beam-gas interactions. The shield is made of tungsten, lead and stainless steel. It has a conical geometry along the length of the spectrometer to contain the further production of secondaries.
- **Iron wall:** The muon trigger need further shielding than that provided by the front absorber. A muon filter consisting of an iron wall of 1.2 m thick ( $\sim 7.2 \lambda_{int}$ ) is placed

<sup>3</sup>The nuclear interaction length,  $\lambda_{int}$  is the mean path length required to reduce the number of relativistic charged particles by the factor  $1/e$ , or 0.368, as they pass through matter

<sup>4</sup>The radiation length,  $X_0$ , is a characteristic of a material, and represents the mean distance over which a high-energy electron loses all but  $1/e$  of its energy.

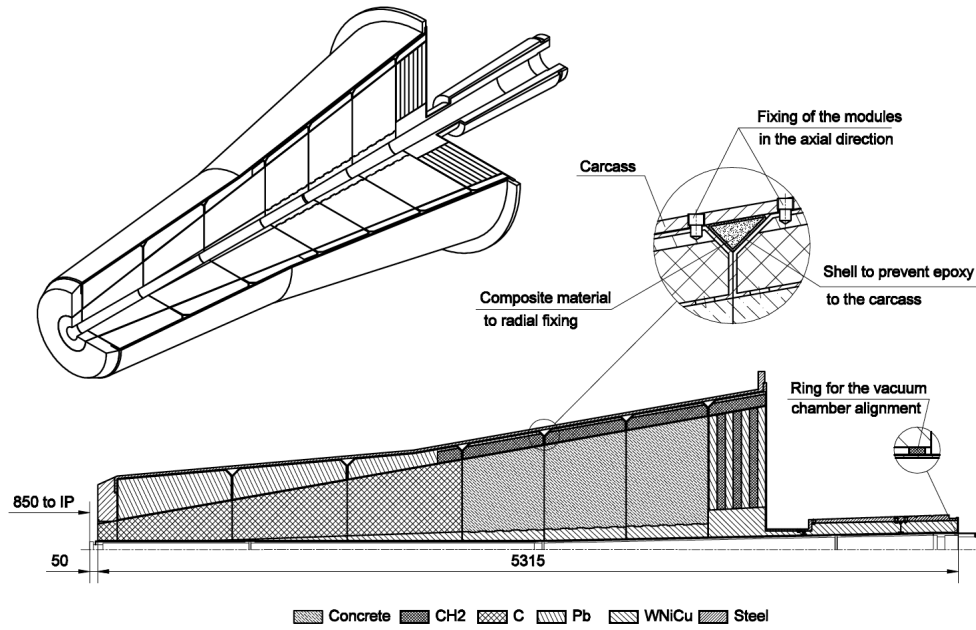


Figure 2.7: Layout of the Muon Spectrometer front absorber. Figure taken from [224].

between the last tracking chamber and the first trigger chamber. The muon filter stops energetic hadrons and secondary particles that traversed the absorber. The front absorber and the muon filter stop muons with momentum less than  $4 \text{ GeV}/c$ .

- **Rear absorber:** The back of the trigger chambers needs an additional shielding from beam gas interactions produced in the LHC beam pipe at the LHC tunnel. It is an ion wall which has been recently extended with respect to that seen in Fig. 2.6 to fully cover the tunnel aperture.

### 2.2.3.2 Dipole magnet

The dipole magnet of the Muon Spectrometer allows the measurement of the muon momentum and the determination of its electric charge. It is placed at 7 m from the IP and provides a central magnetic flux density of 0.67 T and an integrated value of  $3 \text{ T}\cdot\text{m}$  (from the IP to the muon filter). The direction of the field is perpendicular to the beam pipe in the horizontal plane. This defines the bending plane ( $zy$  plane) where the muons are deviated, and the non-bending plane ( $xz$  plane).

### 2.2.3.3 Muon tracking system

The muon tracking system (MCH) is in charge of reconstructing the muon trajectories. It consists of five stations of two Cathode Pad Chambers each. Given the magnetic field provided by the dipole, the tracking system is required to have a spatial resolution better than  $100 \mu\text{m}$  in the bending plane to achieve the mass resolution needed to separate the

bottomonium states. The resolution along the non-bending plane is better than 2 mm, which is enough to allow an efficient track finding.

The chambers are Multi-Wire Proportional Chambers (MWPC) with cathode pad readout. Each chamber consists of two planes of cathodes with a plane of anode wires in between. The space between the cathode planes is filled with a mixture of Ar and CO<sub>2</sub>. The anode wires are connected to high voltage while the cathode pads are grounded. A charged particle traversing the gas of the detector, produces ionization along its trajectory. The electrons drift towards the nearest anode wire where they generate an avalanche of secondary electrons (due to the intense electric field). The resulting ion cloud induces a charge distribution on the cathode pads close to the avalanche position. The distribution of charge in the pads of the bending and non-bending planes allow to determine the bidimensional position where the charged particle traversed the chamber. An sketch of the MWPC working principle is shown in Fig. 2.8.

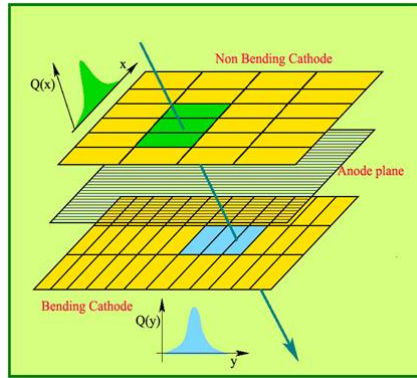


Figure 2.8: Sketch of the working principle of a MWPC. Figure taken from [227].

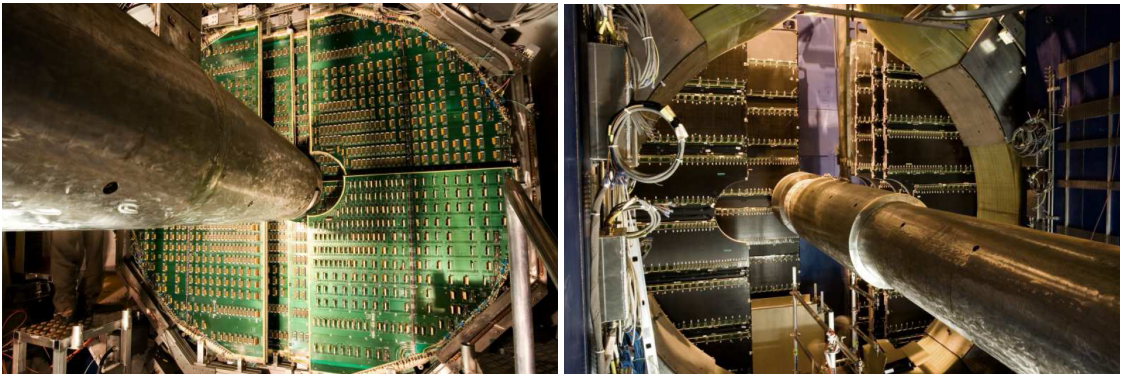


Figure 2.9: Left: Picture of a quadrant design chamber. Right: Picture of a slat design chamber. Pictures taken from [202].

Multiple scattering of the muons in the chamber is minimized by using a chamber thickness of only  $0.03 X_0$ . The size of the chambers in the first two stations is determined by the geometrical projection of the angular coverage of the spectrometer. They have a high

granularity and a quadrant design (Fig. 2.9 left). The chambers in stations 3 to 5 have higher dimensions to cope with the deviations of the muons in the magnetic field. Their granularity is more modest than that of the first chambers, and they have a modular design. In this case, each chamber is made of horizontal modules (slats) with different sizes (Fig. 2.9 right). In order to avoid dead zones, the quadrants or slats have a certain overlap. All the chambers have a smaller pad size close to the beam pipe, to cope with the higher density of particles.

#### 2.2.3.4 Muon trigger system

The ALICE Muon Spectrometer is equipped with a muon trigger. Its purpose is to select events with high  $p_T$  muons produced in heavy quarkonia or open charm decays, rejecting events with low  $p_T$  muons, which come mainly from pion and kaon decays. To this end, a  $p_T$  cut is applied at trigger level to each individual muon. In order to achieve this, the spatial resolution of the trigger chambers is better than 1 cm. The trigger front-end electronics (FEE) are specially designed to obtain a time resolution of 2 ns, which is necessary for the identification of the bunch crossing.

The muon trigger system (MTRG) consists of four Resistive Plate Chambers (RPC) planes arranged in two stations (MT1 and MT2) spaced 1 m apart, and located after the iron muon filter. The RPCs consist of two parallel plates made of a very high resistivity bakelite. The plates are separated by a 2 mm gas volume. The outside faces of the plates are painted with graphite and one is connected to high voltage and the other is grounded. An insulating film covers the graphite electrodes and aluminium strips are placed at the outside of the chamber (Fig. 2.10). The strips in one side are aligned with the  $x$ -axis of the ALICE reference system, and measure the deviation in the bending plane. The strips on the other side are aligned with the  $y$ -axis and measure the non-bending direction. The strips have a pitch and length increasing with their distance from the beam axis.

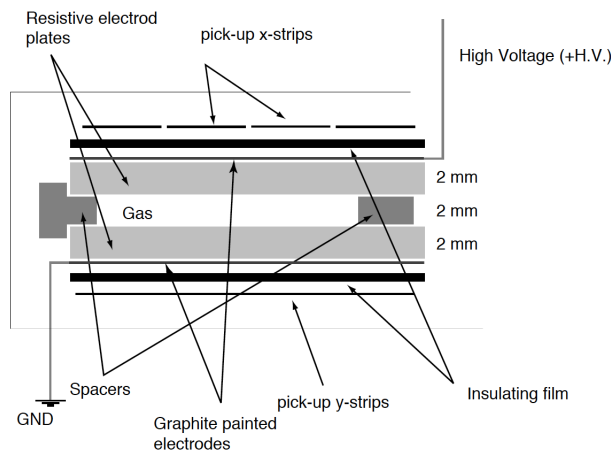


Figure 2.10: Schematic view of a RPC cross section. Figure taken from [202].

When a muon passes through the chamber it ionises the gas in the chamber. The

resulting electrons cause an avalanche of secondary electrons along the whole gas volume. The electrodes are transparent to these electrons, so they are picked up by the aluminium strips. The FEE gathers the signal from the strips, which consists of a pattern of hit strips. The signal is sent to the local trigger board which gives a quick measure of the muon momentum. It gives a trigger decision on the single track and is able to backup strip patterns to give a trigger decision on several tracks detected in sequence.

The momentum measurement for the trigger decision is based on the estimate of the deviation of the measured track, with respect to the track of a muon with infinite momentum (Fig. 2.11). The algorithm in the local board takes the measured track position on the first trigger station and build a straight line to the interaction vertex (muon with infinite momentum). Then it estimates the deviation of the track measured using the positions in the first and second trigger stations with respect to the straight line. The measured deviation on the  $(Y,Z)$  plane has to be smaller than a certain cut, which corresponds to the  $p_T$  cut.

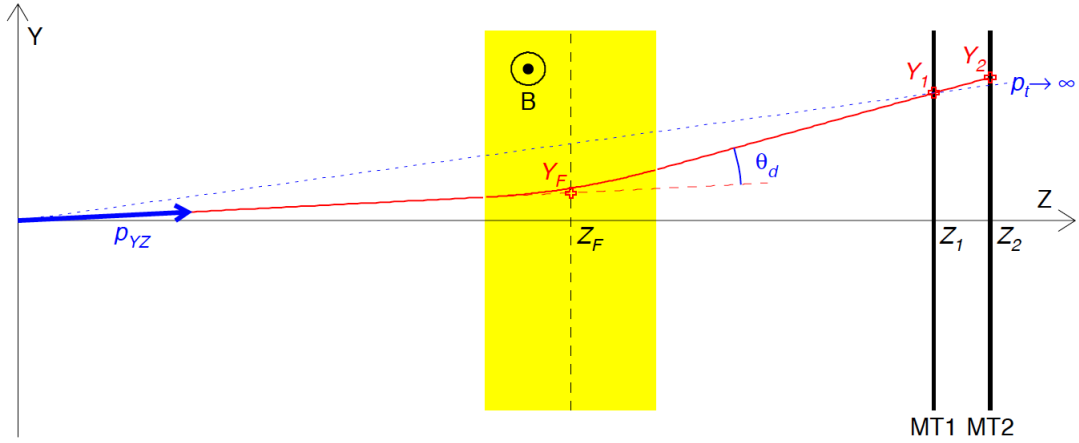


Figure 2.11: The Muon Spectrometer trigger principle. Figure taken from [224].

## 2.3 ALICE Trigger system, Data Acquisition and Reconstruction

### 2.3.1 Trigger system

Using the information of the detector signals and the LHC bunch filling scheme<sup>5</sup>, the ALICE Central Trigger Processor (CTP) generates the trigger decision [228]. It selects events with different features at rates which can be scaled down to suit physics requirements and the restrictions imposed by the bandwidth of the Data Acquisition (DAQ) system. Every machine

<sup>5</sup>The bunch filling scheme is the configuration of the beams in terms of time spacing between bunches, number of bunches in the beam...

clock cycle ( $\sim 25$  ns or one bunch crossing) the CTP evaluates the trigger inputs<sup>6</sup> from the detectors. Due to the different event processing speed of the detectors, the ALICE trigger is a 3-level system, level 0 (L0), level 1 (L1) and level 2 (L2).

The trigger classes define how the CTP handles the trigger inputs (a trigger class is made of the logical AND and OR of different trigger inputs and CTP vetoes (see later)). The read-out detectors can be grouped in trigger clusters, so more than one detector can measure the event. The CTP can send independent trigger signals to each cluster. In this way, while a slow detector is processing an event, another fast detector can process other events.

The basic scheme of the decision levels can be summarised as:

- The L0 trigger inputs (also called L0b, *b* for "*before* the CTP") are the first to arrive to the CTP. They are sent by detectors such as V0, T0, SPD, EMCAL (photon trigger signal), PHOS and MTR. The CTP can select an event by checking if the trigger inputs fulfil the logical conditions of a certain trigger class. The CTP sends a L0 trigger signal (also called L0a, *a* for "*after* the CTP") to the corresponding read-out detectors in the trigger cluster(s). The L0 level has a latency of  $1.2 \mu\text{s}$  (from the interaction to the arrival of the L0 trigger signal to the read-out detectors).
- The L1 trigger inputs are sent to the CTP by detectors such as the TRD, ZDC and EMCAL (neutral-jet trigger) after the online calculation of some characteristic of the event. The CTP makes a decision and sends a L1 trigger signal, which arrives to the read-out detectors with a latency of  $\sim 6.5 \mu\text{s}$ . This latency is caused by the computation time in the TRD and EMCAL and the propagation times to the ZDC. The L0 and L1 trigger signals trigger the buffering of the event data in the detector FEE. If the L1 trigger signal does not arrive on time to the read-out detectors they ignore the event.
- The L2 decision is taken after  $\sim 100 \mu\text{s}$  (corresponding to the drift time of the TPC). The High Level Trigger system (HLT) is able to take more refined trigger decisions by means of an online pre-analysis of the data. It is also in charge of compressing the TPC data without loss of physical information. During Run 1, all events with L1 were accepted by L2.

There are a number of reasons why the CTP do not generate the L0 signal (CTP vetoes). Some examples are: there are at least one detector in a cluster which is busy; the L0 trigger input does not match with a bunch crossing (this is used to suppress the background); the past-future protection (if a collision happens within the TPC drift time, the event is not taken to avoid pile up); or the downscaling of a certain trigger class to allow more DAQ bandwidth for rare events.

---

<sup>6</sup>A "trigger input" is the signal from the triggering detector to the CTP. We call "trigger signal" the signal from the CTP to the read-out detector. Actually the CTP sends the signal to the detector Local Trigger Unit (LTU) which is the interface between the read-out detector and the CTP.



### 2.3.2 Data Acquisition (DAQ)

The goal of the ALICE DAQ system is to carry out the dataflow from the detector up to the data storage. The DAQ dataflow starts at the detector FEE. The data are then transferred to a farm of computers, the Local Data Concentrator (LDC), where the different data fragments corresponding to the information of one event are checked for data integrity, processed and assembled into sub-events. The sub-events information is sent to the Global Data Collector computers (GDC), which build the events combining the information of several LDCs. The Global Data Storage Servers (GDS) store the data. Finally the data are migrated to the CERN computing centre, and duplicated to some Tier 1s computing centres, where they become available for the offline reconstruction.

### 2.3.3 Reconstruction

Once the raw data is written by the DAQ into a disk buffer at the CERN computing center, the data is copied to permanent tapes and, in parallel, a first pass processing is performed. During the first pass reconstruction, high-precision alignment and calibration data are produced. The detector alignment and calibration data are stored in the Offline Condition Data Base (OCDB). With the data reconstruction information, a first set of Event Summary Data (ESD) is produced. Moreover, a filtering of the data in the ESDs for specific analyses can be done to produce the first Analysis Object Data (AOD). The feedback derived from the first pass, including analysis, is used to tune the code for the second pass processing.

## 2.4 Data sample selection

The analysis in this thesis is based on data collected at the beginning of 2013: p-Pb and Pb-p collisions at  $\sqrt{s_{NN}} = 5.02$  TeV, and end of 2012: pp 8 TeV, periods LHC12h and LHC12i, restricted to the runs triggered by the VZERO.

The data passed the standard quality checks for the detectors considered in the analysis (V0, SPD, muon tracking, trigger chambers and ZDC for p-Pb periods). The runs considered as good for muon analysis are listed in the Run Condition Table in Monalisa. Details on the run list selection are given in [229, 230].

Different triggers were activated during data taking. The Minimum Bias (MB) trigger is defined as the coincidence of signals in the VZERO-A (trigger input name: 0V0A) and VZERO-C (trigger input name: 0V0C) detectors synchronized with the passage of the colliding particles (p or Pb) bunches, and is called CINT7<sup>7</sup>. The chosen data taking periods<sup>8</sup> are rare trigger periods (MB trigger is downscaled), which are LHC13d, LHC13e (p-Pb) and LHC13f (Pb-p). The MB period LHC13c (p-Pb) has been used for crosschecks. During the periods we are focusing on (LHC12h and LHC12i for pp, LHC13d and LHC13e for p-Pb and

<sup>7</sup>Generically the coincidence between the signals of the two sides of the VZERO is called V0AND.

<sup>8</sup>The data taking periods naming convention is "LHC+year+letter".

LHC13f for Pb-p collisions), the MB trigger was downscaled at the L0 level to allow more DAQ bandwidth for the rare triggers. For the muon data-taking the following triggers were also defined:

- CMSL: Single muon low- $p_T$  (single muon with  $p_T^\mu \geq 0.5$  GeV/c)
- CMSH: Single muon high- $p_T$  (single muon with  $p_T^\mu \geq 4$  GeV/c)
- CMUL: Unlike sign di-muon low- $p_T$  (muon pair with opposite charge and each muon  $p_T^\mu \geq 0.5$  GeV/c)
- CMLL: Like sign di-muon low- $p_T$  (muon pair with same charge and each muon  $p_T^\mu \geq 0.5$  GeV/c)

The corresponding L0 trigger inputs are named replacing the "C" with "0". (i.e. 0MSL, 0MSH, 0MUL and 0MUH). The muon unlike trigger used in this analysis is called CMUL7 and is defined as the coincidence of a 0MUL trigger input with 0V0A and 0V0C inputs. A physics selection (PS) consisting of timing cuts on the signals from the VZERO and the ZDC to reduce the beam induced background is applied to the events. The amount of background events in the data sample after the application of this cut is negligible. The counts on each trigger class considered in this analysis, for PS selected events, are listed in Tab. 2.2. The V0AND cross section is measured by van der Meer scans resulting in  $2.09 \pm 0.07$  b in p-Pb configuration,  $2.12 \pm 0.07$  b in the Pb-p one [231], and  $55.74 \pm 0.46$  mb in pp [232]. Using the di-muon trigger normalisation factors in Sec. 6.1.4, the total integrated luminosities can be computed. They result to be  $5.01 \pm 0.17$  nb<sup>-1</sup> in p-Pb,  $5.81 \pm 0.18$  nb<sup>-1</sup> in Pb-p, and  $587.12 \pm 29.36$  nb<sup>-1</sup> in pp.

## 2.5 Muon Tracks selection

The selection applied to single muon and unlike sign di-muon tracks in the spectrometer is:

- Single muons:  $-4 < \eta_\mu < -2.5$ , to ensure that muons are in the acceptance of the spectrometer.
- Required matching of both of the tracker tracks with the trigger tracks.
- $17.6 < R_{abs} < 89.5$  cm, where  $R_{abs}$  is the radial transverse position of the muon tracks at the end of the absorber. This cut removes tracks crossing the thicker part of the absorber.
- P×DCA<sup>9</sup> cut. This cut removes fake tracks (negligible in p-Pb) and tracks from beam-gas interactions.

---

<sup>9</sup>P stands for the track momentum.

- $J/\psi$  level:  $-4 < y_{J/\psi} < -2.5$ , only  $J/\psi$  within the acceptance of the spectrometer are selected.

Period	Trigger name	Trigger description	Trigger count
LHC12h+i	CMSL7-S-NOPF-ALLNOTRD	Single muon low- $p_T$ ( $p_T^\mu \geq 1$ GeV/c)	1736761
LHC12h+i	CMSL7-S-NOPF-MUON	Single muon low- $p_T$ ( $p_T^\mu \geq 1$ GeV/c)	628091
LHC12h+i	CMUL7-S-NOPF-MUON	Dimuon low- $p_T$ (both muons with $p_T^\mu \geq 1$ GeV/c)	1880234
LHC12h+i	CINT7-S-NOPF-ALLNOTRD	Minbias (VZERO AND)	22152459
LHC13c (run 195644)	CINT7-B-NOPF-ALLNOTRD	Minbias (VZERO AND)	9778644
LHC13d+e	CMSL7-B-NOPF-MUON	Single muon low- $p_T$ ( $p_T^\mu \geq 0.5$ GeV/c)	14812244
LHC13d+e	CMUL7-B-NOPF-MUON	Dimuon low- $p_T$ (both muons with $p_T^\mu \geq 0.5$ GeV/c)	9274006
LHC13d+e	CINT7-B-NOPF-ALLNOTRD	Minbias (VZERO AND)	3720572
LHC13f	CMSL7-B-NOPF-MUON	Single muon low- $p_T$ ( $p_T^\mu \geq 0.5$ GeV/c)	26323858
LHC13f	CMUL7-B-NOPF-MUON	Dimuon low- $p_T$ (both muons with $p_T^\mu \geq 0.5$ GeV/c)	20906188
LHC13f	CINT7-B-NOPF-ALLNOTRD	Minbias (VZERO AND)	4215581

Table 2.2: Triggers used, one way or another, in this analysis. CMUL triggers were the primary ones used to measure the  $J/\psi$ . The other triggers were used for normalization purposes mainly. Events in this table have passed only Physics Selection cut. Note that the name of the trigger classes includes the trigger name but also bunch crossing features (i.e. "B" meaning beam-beam, "S" meaning beam-satellite), CTP vetoes (i.e. NOPF meaning no past-future protection activated) and trigger cluster name (i.e. MUON which contains SPD, MTR and MCH).



## **Part II**

# **Charged particle multiplicity measurement**



## SPD ACCEPTANCE $\times$ EFFICIENCY MULTIPLICITY CORRECTION METHOD

The charged-particle multiplicity is the number of primary charged particles produced in the collision. Primary particles are defined as prompt particles produced in the collision, including decay products, except those from weak decays of strange particles. In order to study the global properties of pp, p-A and A-A collisions, it is essential the measurement of the pseudorapidity density of charged particles  $dN_{ch}/d\eta$ . Furthermore, an estimate of the initial energy density of the system produced in A-A collisions can be obtained from  $dN_{ch}/d\eta$ . The pseudorapidity density is the average number of particles produced in an  $\eta$  region. In this chapter the  $dN_{ch}/d\eta$  is measured using data from the Silicon Pixel Detector (SPD). The primary goal is to obtain an estimator of  $dN_{ch}/d\eta$  to classify the events to later study the  $J/\psi$  production dependence on the pseudorapidity density of charged particles.

The SPD data has to be corrected to get the number of primary charged particles from the reconstructed tracks. The correction method presented in this chapter includes detector tracking efficiency, acceptance losses as well as other effects like generation of secondary particles in the detector or combinatorial background. For the measurement of the  $dN_{ch}/d\eta$  distribution it is also necessary to correct by the event selection efficiency. These corrections are obtained from MC simulations. A similar procedure as the one used in [233–241] is used to correct the data from the SPD. The method used there is intended to be used to measure event-averaged quantities, like the charged particle pseudorapidity density distribution  $dN_{ch}/d\eta(\eta)$ . In this chapter we perform a similar implementation but we apply it in an event-by-event way, to study if such a correction would be suitable to obtain an estimator of the charged particle multiplicity of individual events. In order to cross-check the method implementation of this thesis within an ALICE muon analysis framework, the  $dN_{ch}/d\eta(\eta)$  distribution in p-Pb collisions is measured and compared to that in [239].

### 3.1 SPD vertex and tracking

The starting point on the ALICE tracks reconstruction, both for the central barrel and Forward Muon Spectrometer tracking, is the determination of the SPD vertex. In this section we focus on giving a summary on the SPD vertex and tracks reconstruction. The SPD vertex is estimated using the correlation between the SDP clusters<sup>1</sup> information (which mainly correspond to reconstructed particle hits) reconstructed on the two layers of the SPD. There are two algorithms in ALICE to reconstruct the SPD vertex. The 3D-vertexer, which is able to reconstruct the  $x$ ,  $y$  and  $z$  vertex positions. The reconstruction efficiency and resolution of the 3D-vertexer depends on the charged particle multiplicity, and it is typically about 0.3 mm both in the longitudinal and perpendicular direction to the beam axis. If the 3D-vertexer does not find a vertex (mostly for low multiplicity events) the 1D-vertexer is used to determine only the  $z$  position (from the intersection of one or few tracklets with the beam axis ) and the  $x$  and  $y$  coordinates are taken from the run average. In case of finding several possible interaction vertexes, the primary vertex is chosen as the one with the biggest number of SPD tracklets contributing to the vertex measurement (called contributors from now on). More information about the vertex reconstruction algorithms can be found in [242].

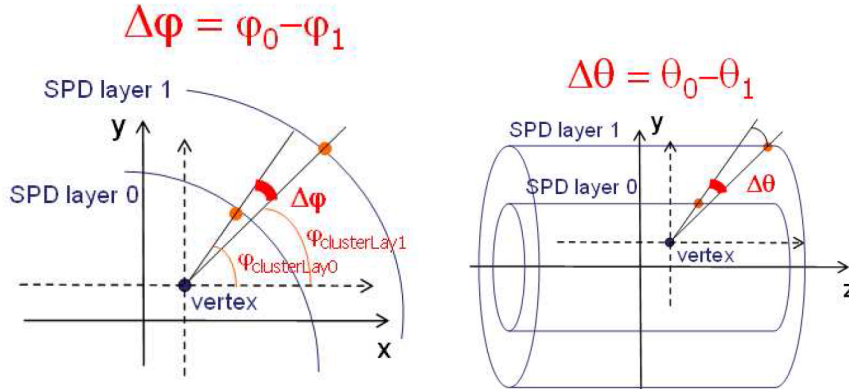


Figure 3.1: Sketch to illustrate the calculation of  $\Delta\phi$  and  $\Delta\theta$  used for the tracklet reconstruction. [243]

Then the tracklets reconstruction is performed using the SPD vertex information as starting point. The SPD tracklets are line segments built using the SPD clusters at the two layers of the detector and the vertex position. Using the primary vertex position as origin, a straight line to a cluster in the inner layer is considered. Then the difference in the azimuthal ( $\Delta\phi$ ) and polar ( $\Delta\theta$ ) angles between the considered cluster in the inner layer and the clusters in outer layer is computed as seen in Fig. 3.1. A 80 mrad and 25 mrad cut-off is applied on  $\Delta\phi$  and  $\Delta\theta$  respectively. The cut on the azimuthal angles would reject charged particles with a transverse momentum below 30 MeV/c but in practice, the transverse

<sup>1</sup>Group of one or more hits in adjacent pixels



momentum cut-off is determined by particle absorption in the detector material and is about 50 MeV/c. Furthermore, in order to reject combinatorial background tracklets, the reconstructed tracklet is the candidate passing a  $\chi^2$  requirement in  $\Delta\varphi$  and  $\Delta\theta$ . If more than one cluster in the outer SPD layer match the cluster in the inner one, only the combination with the smallest  $\chi^2$  is kept, so each cluster in the inner layer can be associated to a tracklet only once. The procedure is repeated for each cluster in the inner layer.

Note here that, when the information of TPC, ITS or both is available, the primary vertex can be reconstructed using the tracks of these detectors reaching resolutions of typically 0.1 mm in the longitudinal ( $z$ ) direction and 0.05 mm in the transverse direction to the beam<sup>2</sup>. Further information on the SPD tracklets and global tracks (TPC+ITS) reconstruction can be found in [205, 240, 243, 244].

## 3.2 SPD status and run variations

Due to several reasons, not all the SPD pixels or modules are used during the data-taking or for the data reconstruction<sup>3</sup>. As an example, noisy pixels (those which provide a signal even without a particle hit) and dead pixels (those which do not provide a signal) are removed from the data-analysis by a specific algorithm. Also, some SPD modules are not included during the data-taking due to reduced cooling performance.

The effect of these dead regions of the detector is a reduced acceptance of the SPD. In the top panels of Fig. 3.2 the maps of the dead modules in the inner (left) and outer (right) SPD layers during the first runs of the Pb-p (LHC13f) data-taking period are shown as a function of the SPD  $z$ -vertex position ( $z_v$ ) and the azimuthal angle  $\varphi$ . At the bottom panel of Fig. 3.2 the reconstructed number of tracklets as a function of  $z_v$  and  $\varphi$  is presented (note that the  $x$ -axis coordinate in the top plots corresponds to  $-z_v$ ). The effect of the dead zones is clearly seen on the reduced number reconstructed tracklets at the  $\varphi$  regions corresponding to the dead modules of the SPD.

Furthermore, the status of the SPD in terms of number and location of dead zones may vary among runs. In Fig. 3.3, we present the number of inactive SPD modules in the inner and outer layers as a function of run number during the p-Pb data-taking periods. The SPD modules configuration is very stable during the p-Pb periods, except for one run where two modules in the outer layer are lost. The weight of that run on the total p-Pb statistics is small so this variation is ignored and the two p-Pb periods (LHC13d and LHC13e) are treated as a single one in what the SPD concerns. At the beginning of the Pb-p data-taking the status of the SPD was the same as in p-Pb. However, there are two active modules less at the end of the Pb-p period, which implies a variation of the SPD acceptance. The run by run variations need to be taken into account when correcting the SPD number of tracklets,

<sup>2</sup>In any case the SPD-only vertex is always available.

<sup>3</sup>This information is stored in the OCDB (see Sec. 2.3.3) to be used at the reconstruction level.

so the Pb-p period is divided in two parts with equal modules status to get the corresponding corrections for the SPD data.

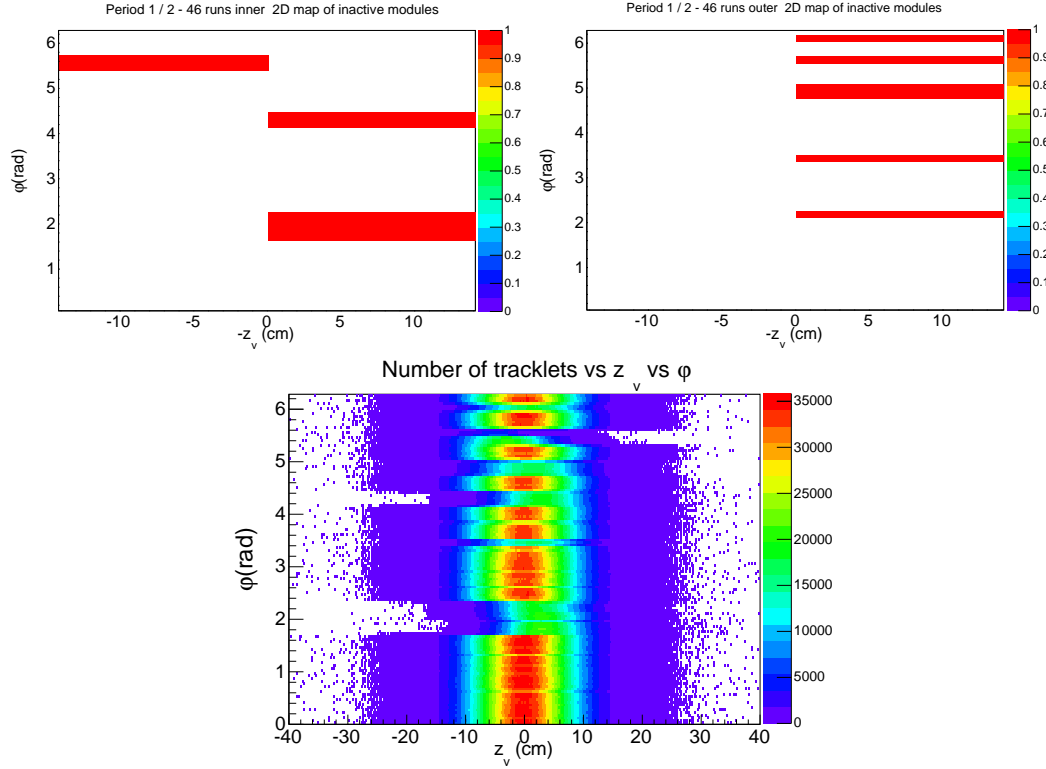


Figure 3.2: Top: SPD inactive modules in the inner (left) and outer (right) layers during the first runs of LHC13f data-taking period as a function of the  $z$ -vertex position ( $-z_v$ ) and  $\phi$ . Bottom: Number of reconstructed SPD tracklets as a function of  $z_v$  and  $\phi$ .

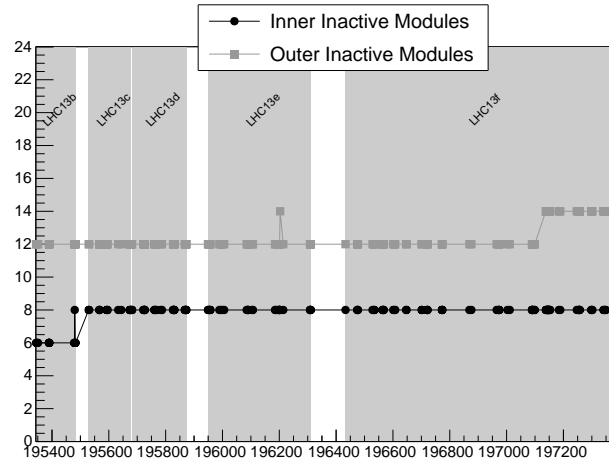


Figure 3.3: SPD inactive modules in the inner and outer layers during p-Pb runs. LHC13b, LHC13c, LHC13d and LHC13e correspond to p-Pb and LHC13f to Pb-p beam configurations.

### 3.3 Event selection for multiplicity determination

Only events passing the physics selection (see 2.4) conditions are kept. For the multiplicity analysis, since the tracklets reconstruction and correction (see Sec. 3.4) rely on the accurate determination of the SPD vertex, a series of vertex-based cuts on the events have to be imposed (we call these cuts vertex "Quality Assurance" or vertex QA). First of all the events are required to have a reconstructed SPD vertex. This selects about 99.15% of the MB events in p-Pb (LHC13d+e)<sup>4</sup>. The first quality requirement for the events with a vertex is to have a number of contributors ( $n_{contrib}$ ) to the SPD vertex bigger than zero, since zero and negative values correspond to events where the vertexer algorithms fail due to the absence of SPD clusters or the impossibility of building suitable tracklets. It is also needed to have a relatively precise location of the vertex position, which depends on the vertexer algorithm used and the number of contributors. The number of events classified in type of SPD vertexer used, for the CINT7 and CMUL7 samples in the LHC13d+e data-taking periods are shown in Fig. 3.4. The events reconstructed with the 1D-vertexer represent a 3.4% (0.4%) of the CINT (CMUL) data sample. The found difference is due to the average multiplicity being bigger for CMUL than CINT events, as it is shown later in this thesis. This makes the efficiency of the 3D-vertexer bigger for CMUL events. Since the vertex resolution of the 1D-vertexer is worse than that of the 3D-vertexer, it is necessary to require a resolution better than 0.25 cm for events which vertex has been reconstructed with the 1D-vertexer. This cut removes about 0.4 % of the CINT events and a negligible fraction of the CMUL ones. The evolution of the SPD  $z$ -vertex resolution with the number of contributors can be seen in Fig. 3.5 (top left).

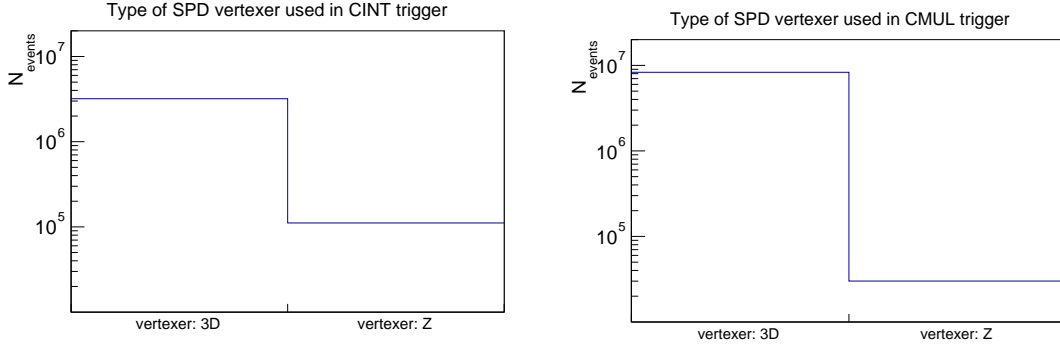


Figure 3.4: Number of events classified depending on the vertexer type used to reconstruct the SPD vertex for CINT (left) and CMUL events (right) in LHC13d+e.

In other multiplicity analyses, like the one in [240], a further requirement to the event vertex is applied. As discussed in Sec. 3.1 the vertex reconstructed using the information of the full ITS (ITS-only-tracks) or the ITS+TPC (global tracks), when available, is more

<sup>4</sup>In the following only the numbers for LHC13d+e are given but very similar results are obtained for LHC13f.

accurate than the SPD one. The primary vertex of the event,  $z_v^p$ , is defined as the most accurate one. Therefore, a further consistency requirement on the event should be imposed on the difference between the primary and SPD vertex position, consisting on a cut on the difference between the  $z$ -coordinate of the primary vertex and the SPD primary vertex ( $z_v^{SPD}$ )<sup>5</sup> not bigger than 0.5 cm<sup>6</sup>. In Fig. 3.5 (top right) it can be seen how the bigger the number of contributors the smaller the difference between the primary and SPD  $z$ -vertex position due to resolution improvement.

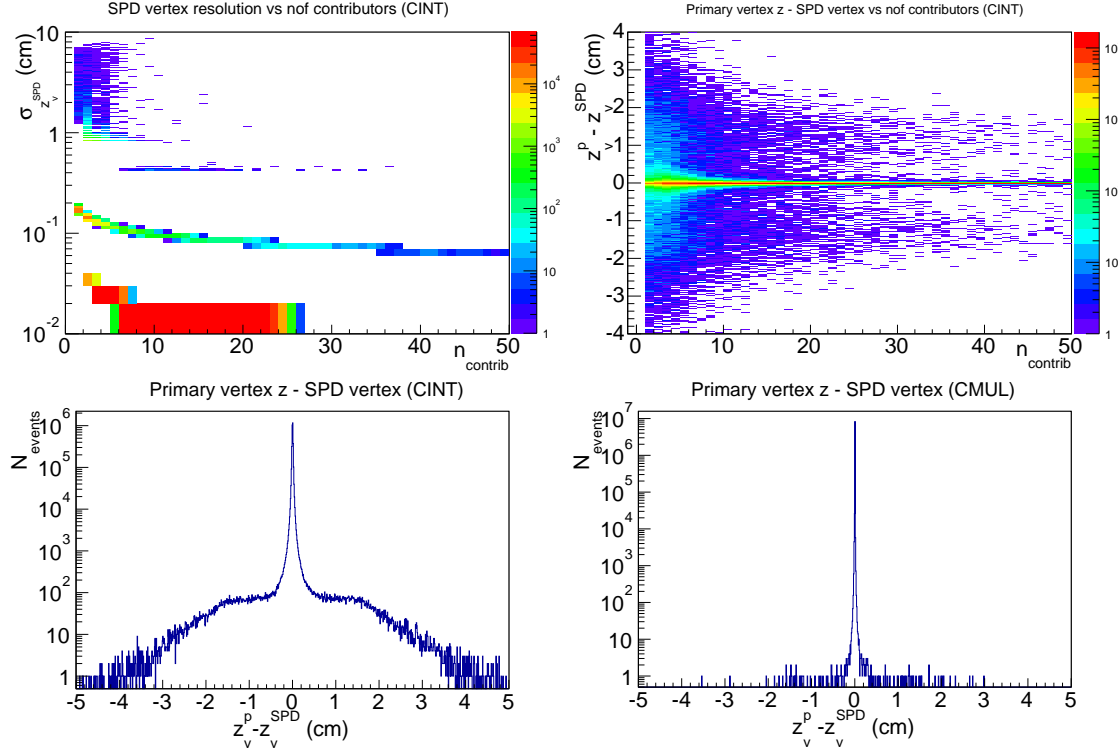


Figure 3.5: Top left: Evolution of the SPD  $z$ -vertex resolution as a function of the number of contributors for CINT events in LHC13d+e. Top right:  $z$ -vertex position difference between the primary and the SPD vertexes as a function of the contributors for CINT 7 events in LHC13d+e. Bottom:  $z$ -vertex position difference between the primary and the SPD vertexes distribution for CINT (left) and CMUL (right) events in LHC13d+e.

However due to the trigger configuration during the data taking periods considered in this analysis, the trigger cluster for muon events has only the SPD as read-out detector but not the rest of the ITS nor the TPC<sup>7</sup>. On the contrary, for the minimum bias trigger cluster the full ITS is included in the read-out detectors. In Fig. 3.5 the difference between the primary and SPD vertex ( $z_v^p - z_v^{SPD}$ ) distribution is shown. From the CINT figure it can be

<sup>5</sup>The notation of the SPD vertex is changed from  $z_v$  to  $z_v^{SPD}$  for more clarity now

<sup>6</sup>This distance is chosen to be compatible with the Distance of Closest Approach between a track and the  $z$ -vertex ( $DCA_z$ ) used to select tracks

<sup>7</sup>Since the TPC is slower and not needed for muon analyses

seen that a cut  $|z_v^p - z_v^{SPD}| < 0.5$  cm would remove a 0.7% of the CINT events. Nevertheless, as can be seen for the CMUL trigger, there are some events for which the primary vertex is different from the SPD one. It has been found that those events correspond to CMUL events which have triggered also the CMSL trigger, which belongs to a trigger cluster where the ITS is included as read-out detector. These events correspond to a very small fraction of the CMUL events (0.5%). Therefore the ITS vertex information is not present for the whole CMUL data sample and consequently, the cut is only applied to the MB data sample and not the di-muon one. This would bias the di-muon events normalisation factors (Sec. 6.1.4) and therefore this cut is not applied in this analysis.

Finally a last cut on the  $z_v^{SPD}$  position<sup>8</sup> of the events is applied. Depending on the  $\eta$  range which want to be probed, the vertex position has to be constrained to  $|z_v| < z_0$  in order to keep a reasonably good acceptance of the SPD when counting the tracklets to estimate the multiplicity. In this analysis two different  $z_0$  ranges are used: 10 and 18 cm, depending on the purpose. The SPD  $z$ -vertex distribution and the lines representing the different cuts are shown in Fig. 3.6 for p-Pb. The selection  $|z_v| < 18$  cm removes a 0.2% of the events while  $|z_v| < 10$  cm removes about 9% of the events.

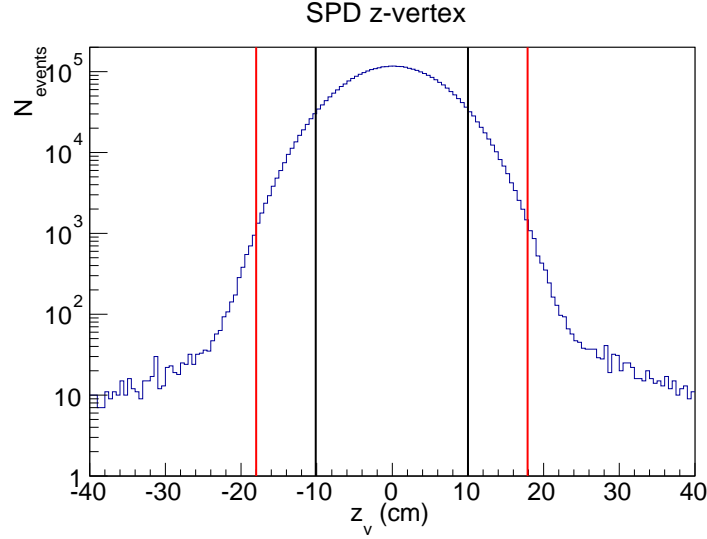


Figure 3.6: LHC13d+e SPD  $z$ -vertex distribution. The lines represent the  $|z_v| < 10$  cm (black) and  $|z_v| < 18$  cm (red) cuts.

The applied cuts for the multiplicity analysis are summarised here:

- Only events with a reconstructed SPD vertex are kept
- Only events which SPD vertex has  $n_{contrib} > 0$  are kept
- Only events with vertex reconstructed with the SPD 1D-vertexer which resolution is better than 0.25 cm ( $\sigma_{z_v^{SPD}} < 0.25$  cm) are kept

<sup>8</sup>The SPD  $z$ -vertex position is denoted again as  $z_v$  in the following

- Only events with SPD vertex reconstructed within  $|z_v| < z_0$  are kept.

These event cuts are also applied when analysing simulated events. In addition to the latter event cuts, only Non-Single Diffractive (NSD) events are selected in simulations. This choice is motivated by the fact that the MB trigger in p-Pb collisions data-taking selects NSD events with a 99.2 % efficiency with a negligible contamination of Single Diffractive (SD) and ElectroMagnetic (EM) events, as stated in [239]. In addition, during this chapter we only deal with MB events both in data and simulation.

### 3.4 SPD acceptance×efficiency correction

The multiplicity measurement is based on a SPD tracklets analysis. In order to correct the measured tracklets by SPD acceptance losses, pixels' efficiency and tracklet-to-particle effects (described later in this section), the SPD acceptance×efficiency ( $\mathcal{A} \times \mathcal{E}$ ) is needed. To determine it, a p-Pb simulation using the DPMJET generator [245] is used. The computations of this chapter are performed through the analysis of the DPMJET MC productions LHC13b2\_efix1, runs 195593 and 195644 (p-Pb); and LHC14k2 runs 196601, 196972, 197152 and 197348 (Pb-p).

The SPD  $z$ -vertex position where the events are reconstructed (or generated) is binned, as well as the  $\eta$  coordinate ( $\eta = \eta_{lab}$ ) of the tracklets ( $\Delta\eta = 0.1$ ,  $\Delta z_v = 0.25$  cm). 2D histograms in  $(\eta_i, z_{vj})$  bins are filled with the number of generated primary charged particles and the number of reconstructed tracklets for MB events passing the cuts specified in Sec. 3.3. In Fig. 3.7 the results obtained with a simulation of one run for the generated primary charged particles (left) and the reconstructed tracklets are presented. The curves represent the SPD acceptance of the two layers as a function of  $z_v$ . The effect of the limited SPD acceptance is observed as well as the acceptance effect of the dead pixels. The fact that there are tracklets reconstructed beyond the SPD acceptance is due to the vertex distribution in the transverse plane, which was not taken into account to calculate the acceptance curves, and resolution effects of the reconstructed event vertex and tracklet  $\eta$ .

The curves which define the acceptance of the inner (I) and outer (O) SPD layers as a function of  $z_v$  on the left (L) side ( $z_v < 0$ ) and right (R) side ( $z_v > 0$ ) are defined by:

$$(3.1) \quad \eta_{L(R)}^{I(O)}(z_v) = -\ln \left( \tan \left( \frac{\theta_{L(R)}(z_v, r_{I(O)})}{2} \right) \right)$$

where  $r_{I(O)}$  denotes the radius of the corresponding SPD layer (3.9 and 7.6 cm for the inner and outer layers respectively).  $\theta_{L(R)}(z_v, r_{I(O)})$  are the angles between the beam axis and the line formed by the interaction vertex  $z_v$  with the right (R) and left (L) edges of the SPD layers, which are defined as:

$$(3.2) \quad \theta_L(z_v, r_{I(O)}) = \begin{cases} \arctan(r_{I(O)} / (-d_z - z_v)) & : z_v < -d_z \text{ cm} \\ \pi - \arctan(r_{I(O)} / (d_z + z_v)) & : z_v \geq -d_z \text{ cm} \end{cases}$$

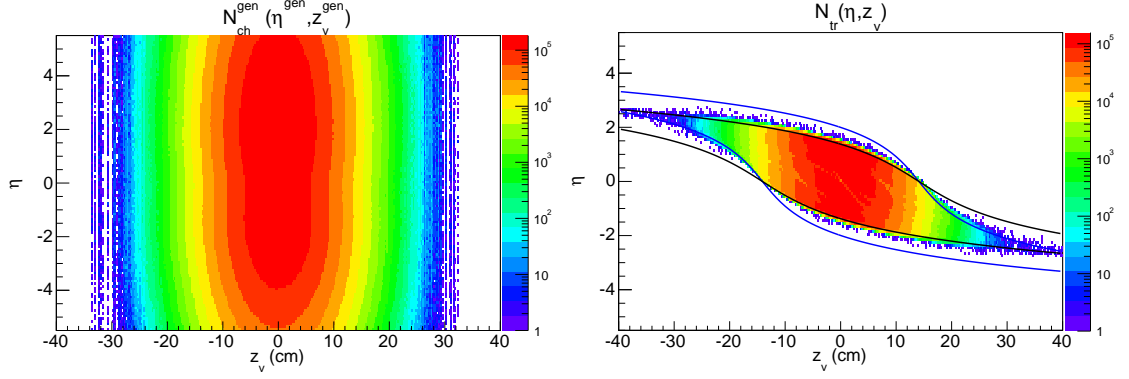


Figure 3.7: Left: generated primary charged particles as a function of event generated  $z$  position and particle  $\eta$ . Right: Reconstructed tracklets as a function of the event reconstructed  $z_v$  position and tracklets  $\eta$ . The curves represent the  $\eta$  of the SPD layers' extremes seen from a given vertex  $z_v$  (Blue: inner layer, Black: Outer layer), Eqs. 3.2 and 3.3.

$$(3.3) \quad \theta_R(z_v, r_{I(O)}) = \begin{cases} \arctan(r_{I(O)}/(d_z - z_v)) & : z_v < d_z \text{ cm} \\ \pi - \arctan(r_{I(O)}/(z_v - d_z)) & : z_v \geq d_z \text{ cm} \end{cases}$$

where  $d_z = 14.1$  cm is the SPD coverage along the  $z$ -axis from the interaction point ( $z = 0$ ). These curves represent the limit  $\eta$  range that can be studied with the SPD with events reconstructed at a given  $z_v$  position. These curves are used in order to optimise the  $\eta$  range studied in the  $dN_{ch}/d\eta$  computation.

Using the generated and reconstructed 2D information in Fig. 3.7, the two-dimensional  $(\eta, z_v)$  SPD  $\mathcal{A} \times \mathcal{E}$  is determined as:

$$(3.4) \quad \mathcal{A} \times \mathcal{E}(\eta, z_v) = \frac{N_{tr}(\eta, z_v)}{N_{ch}^{gen}(\eta^{gen}, z_v^{gen})},$$

where  $N_{tr}(\eta, z_v)$  is the total number of reconstructed tracklets in a given  $(\eta, z_v)$  bin and  $N_{ch}^{gen}(\eta^{gen}, z_v^{gen})$  the corresponding number of generated primary charged particles. Using the reconstructed  $\eta$  and  $z_v$  coordinates for the number of tracklets, and the generated coordinates for the generated primary charged particles in eq. 3.4, allows to partially account for reconstruction resolution effects in the correction.

The inverse of the resulting SPD  $\mathcal{A} \times \mathcal{E}(\eta, z_v)$  (correction matrix) for the p-Pb periods is presented in Fig. 3.8. The effects of the acceptance losses due to dead pixels can be clearly observed in the regions where the inverse of the correction becomes bigger. The characteristic shape in  $(\eta, z_v)$  of the regions where the  $\mathcal{A} \times \mathcal{E}(\eta, z_v)$  is worse, is the result of missing SPD modules in the inner and outer layers of the detector (Fig. 3.2).

The simulations used for the correction computation are performed using the DPMJET generator. They provide a realistic description of the charged particle multiplicity,  $\eta$  and

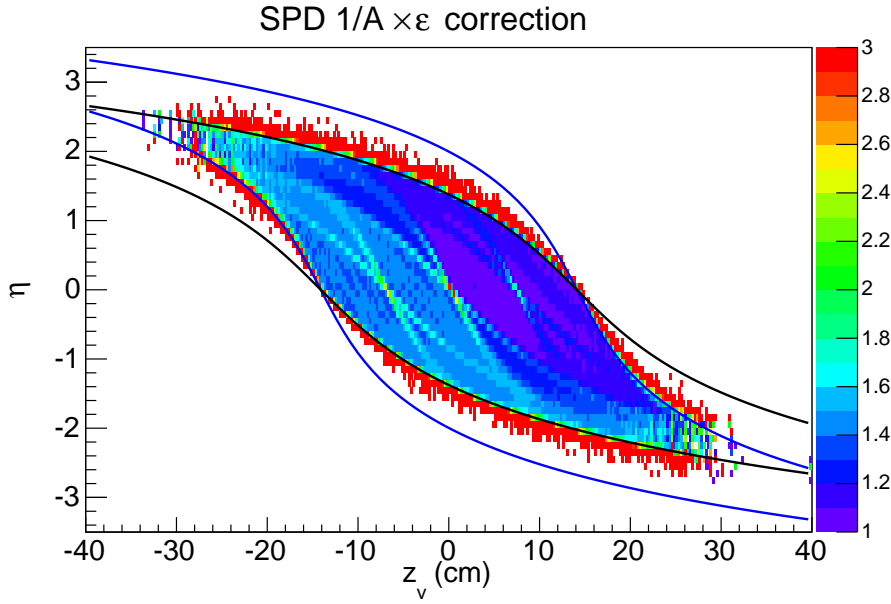


Figure 3.8: SPD  $1/\mathcal{A}\times\epsilon(\eta, z_v)$  obtained with DPMJET simulation for p-Pb . The curves represents the  $\eta$  of the SPD layers' extremes seen from a given vertex  $z_v$  (Blue: inner layer, Black: Outer layer).

$p_T$  distributions of charged particles. We therefore consider that the simulation reproduces at first order the tracklet-to-particle effects: particles with  $p_T$  below 50 MeV/c which are absorbed by the detector material and not reconstructed by the tracklets algorithm, combinatorial background tracklets, contribution from strange weak decays and secondary particles produced in the detector (like  $\gamma$ -conversions). Possible variations of these effects in the simulation with respect to the data are treated as systematic uncertainties. Furthermore, the tracklet-to-particle corrections may also depend on other variables like particle transverse momentum ( $p_T$ ), azimuthal angle ( $\phi$ ), charge, relative abundances of particle species, or multiplicity. These variables are integrated in the correction in Eq. 3.4. The effect of this integration is in principle considered to be small and a systematic uncertainty can be assigned. Nevertheless, we show in Sec. 3.9 that using a multiplicity averaged correction has an effect that must be corrected when studying multiplicity differential observables.

In Fig. 3.9 the ratios of the SPD  $\mathcal{A}\times\epsilon$  in p-Pb and Pb-p are shown for the first (left) and second parts (right) of the Pb-p period. The ratio of the corrections in p-Pb and first part of Pb-p periods is unity for most of the  $(\eta, z_v)$  range, except for those regions where the statistics is low. This means that the impact of the  $\eta$  dependence of the input charged particle distribution on the correction is small, since the p-Pb and Pb-p distributions are completely symmetric one with respect to the other. On the contrary the ratio of the corrections in p-Pb and second part of Pb-p periods shows a difference of 2-4% due to the loss of two SPD modules. Therefore two different SPD corrections are used depending on the run number when analysing the Pb-p period.



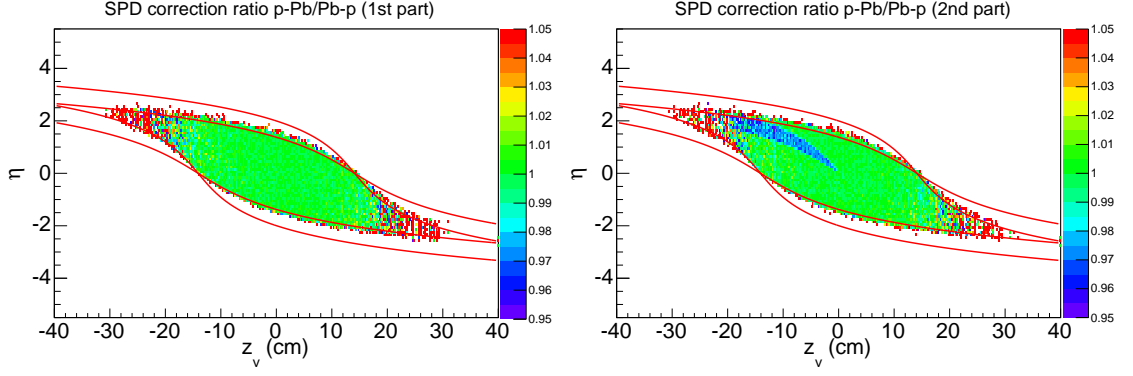


Figure 3.9: SPD  $\mathcal{A}\times\epsilon$  ratio to compare the corrections of p-Pb periods with the first (left) and second (right) parts of the Pb-p data-taking periods.

Fake tracklets can be reconstructed from clusters in the two SPD layers that fulfil the reconstruction algorithm conditions to form a tracklet, but are not coming from the same charged particle (combinatorial background tracklets). The contribution of these tracklets to the total tracklets multiplicity can be estimated from simulation. Each generated primary particle in the simulation has a label. The hits left by a particle in the pixels of each SPD layer, are labeled with the same label as the particle. Therefore, if the MC labels of the clusters used to reconstruct a tracklet are different, the tracklet is identified as a combinatorial background. In order to estimate the presence of such tracklets in the sample, the fraction of combinatorial background tracklets in  $(\eta, z_v)$  bins is presented in Fig. 3.10. The background contribution to the total reconstructed tracklets is between 0.5% and 3.5% for the ranges considered in this analysis ( $|\eta| < 2$ ,  $|z_v| < 18$  cm).

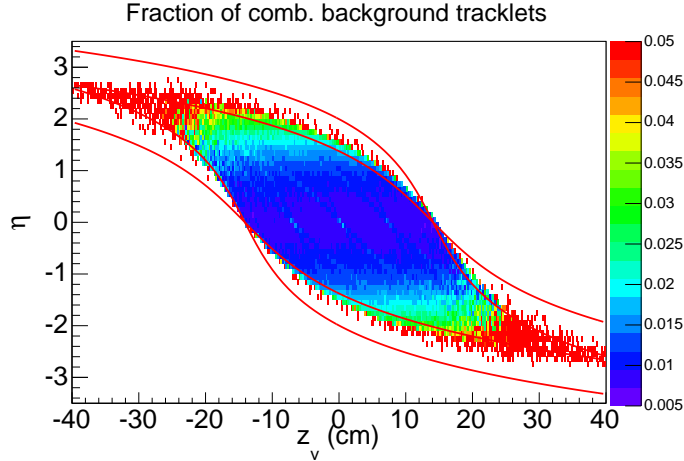


Figure 3.10: Fraction of combinatorial background tracklets contributing to the total reconstructed tracklets. The fraction is below 3.5% for the  $\eta$  and  $z_v$  ranges considered in this analysis.

In Fig. 3.11 we observe a variation of the fraction of combinatorial background tracklets

with the global tracklets multiplicity, with respect to the integrated value. The amount of fake tracklets is rising at high multiplicities. This is explained by the fact that the more clusters available to build tracklets, the bigger the possibility to have fakes from wrong clusters combinations. This affects the SPD  $\mathcal{A}\times\epsilon$  correction as we show later.

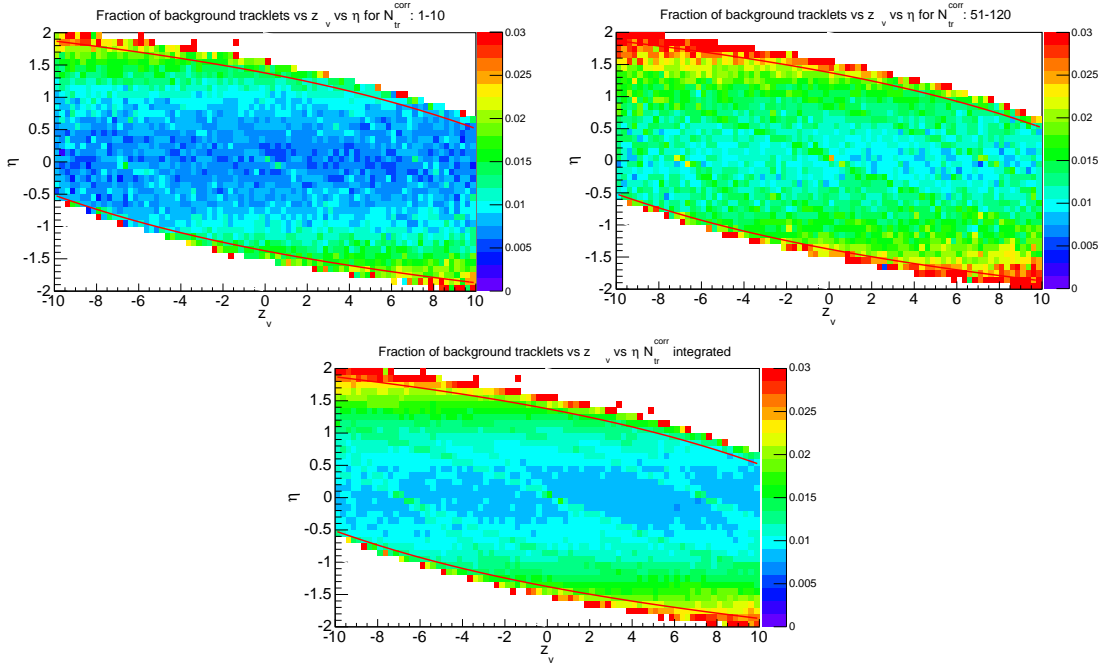


Figure 3.11: Combinatorial background fraction variation for two multiplicity intervals (top). Multiplicity integrated combinatorial background fraction (bottom). The red lines represent the acceptance limits of the SPD.

It is important to be sure that the simulation statistics is enough to be able to neglect the statistical uncertainty of the correction matrix with respect to the other uncertainties. In order to compute the statistical uncertainty of the correction, the properties of the binomial distribution are used. The variance of a binomial-distributed variable  $X$  ( $X \sim B(N,p)$ , the probability of getting  $n$  successes in  $N$  trials with a success probability  $p$ ) is:

$$(3.5) \quad Np(1-p)$$

so the variance of  $X/N$  is:

$$(3.6) \quad \frac{p(1-p)}{N}$$

Let us consider now the calculation of an efficiency  $\epsilon$ .  $N_{tr}$  out of  $N_{ch}^{gen}$  "events" are reconstructed ( $N_{tr}$  successes out of  $N_{ch}^{gen}$  trials). The probability for a generated particle to

be reconstructed is:

$$(3.7) \quad \varepsilon = \frac{N_{tr}}{N_{ch}^{gen}}$$

So  $N_{tr}$  follows a binomial distribution with success probability  $p \approx N_{tr}/N_{ch}^{gen}$ , in the limit of large  $N_{ch}^{gen}$ . Consequently, using Eq. 3.6, the uncertainty on the efficiency  $\varepsilon$  is:

$$(3.8) \quad \sigma_\varepsilon = \sqrt{\frac{\varepsilon(1-\varepsilon)}{N_{ch}^{gen}}}$$

Note here that this error estimation is only valid in the case of the correction without secondaries and combinatorial background, since their number is not binomially distributed. However, for the purposes of this thesis we consider that the contribution of these sources is small, so Eq. 3.8 is used. In [246] the amount of secondaries was estimated by simulation to be 2.8%(+30% syst), and the average contribution of the combinatorial background 1.1%(+30%), in p-Pb collisions. The statistical error on the correction matrix is shown in Fig. 3.12. The error is well below 1% for  $|\eta| < 0.5$  and  $|z_v| < 10$  cm, and it goes beyond 1% for  $z_v > 15$  cm. We show in Sec. 3.10 that the different sources of systematic uncertainty contribute to the measured average  $dN_{ch}/d\eta$  value with 1 to 3 %. Accordingly, we conclude that the statistical uncertainty do not play a significant role on the total uncertainty and therefore it is not taken into account.

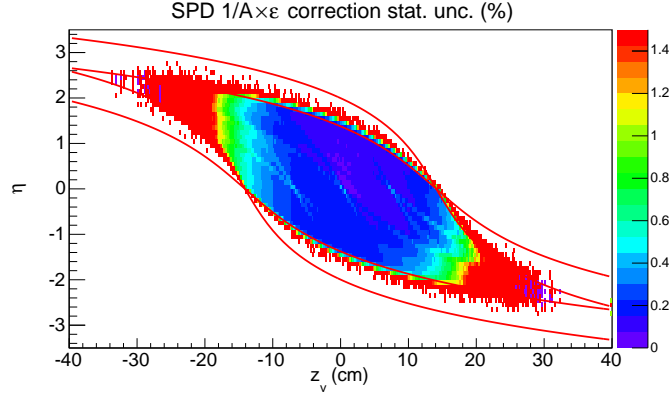


Figure 3.12: Statistical uncertainty of the  $1/\mathcal{A} \times \varepsilon(\eta, z_v)$  correction

### 3.5 Implementation of the correction method

In this section the SPD  $\mathcal{A} \times \varepsilon$  correction method used to estimate the charged particle multiplicity from the SPD tracklets, is explained in detail. The use of an  $\mathcal{A} \times \varepsilon$  correction is justified when computing event-averaged quantities. This is because the correction itself is

an event average of the different effects. As an example, one can consider the computation of the average number of charged particles from the average number of reconstructed tracklets in a given  $(\eta, z_v)$  bin, in a certain event sample.

Since the goal of this thesis is to obtain an *event-by-event* multiplicity estimator, the SPD  $\mathcal{A}\times\mathcal{E}$  correction is applied to each individual event. The correctness of this method is evaluated later. In order to do this, for each event the  $\eta$  coordinate is discretized in bins of size 0.1 pseudorapidity units, which are denoted by  $\eta_i$ . An event reconstructed at a given  $z_v^0$  can have a certain *tracklets configuration* in terms of the number of tracklets reconstructed in each  $\eta_i$  bin,  $n_{tr}^{\eta_i}$ , i.e.  $\widehat{N}_{tr} = \{n_{tr}^{\eta_i}\}$ . The number of reconstructed tracklets for that event is simply  $N_{tr} = \sum_{\eta_i} n_{tr}^{\eta_i}$ . The  $\mathcal{A}\times\mathcal{E}$  correction is therefore applied bin by bin in  $\eta_i$ :

$$(3.9) \quad n_{tr}^{corr, \eta_i} = n_{tr}^{\eta_i} \cdot \frac{1}{\mathcal{A}\times\mathcal{E}(\eta_i, z_v^0)},$$

and the resulting number of corrected tracklets for the event is  $N_{tr}^{corr} = \sum_{\eta_i} n_{tr}^{corr, \eta_i}$ . This correction gives the number of corrected tracklets of an 'average event' with the configuration of the current event.

Due to resolution effects there are tracklets which are reconstructed outside the acceptance of the SPD. Besides, the acceptance varies with the  $z_v$  position. In order to obtain a correct number of corrected tracklets, the  $\eta$  range has to be restricted to be within the acceptance of the SPD. Therefore, only  $\eta$  bins fully inside the range given by Eq. 3.1 are considered. Moreover, inside the acceptance of the detector there are also dead zones but, again due to resolution effects, there are tracklets reconstructed inside. In order to avoid these regions, bins where  $1/\mathcal{A}\times\mathcal{E}(\eta, z_v) > 2.5$  are also rejected (i.e. regions where the  $\mathcal{A}\times\mathcal{E}$  is smaller than 40%). To use the result from this correction as an event-by-event multiplicity estimator, the rapidity coverage must be the same for every event independently on its  $z_v$  position, and must be always within the acceptance of the SPD. Consequently, to fulfil these conditions the chosen estimator is the number of corrected tracklets in  $|\eta| < 0.5$ , and the events have to be reconstructed within  $|z_v| < 10$  cm.

In order to see how the correction affects the measured tracklets, the correction method is applied to the same simulation from which the correction has been obtained. The number of reconstructed tracklets in  $|\eta| < 0.5$  for events with  $|z_v| < 10$  cm is shown in Fig. 3.13 (left) as a function of the generated primary charged particles. This is the so-called detector's *response matrix*,  $\mathcal{R}_{N_{tr} N_{ch}}$ . It gives the conditional probability that an event with true multiplicity  $N_{ch}$  is measured with  $N_{tr}$  multiplicity. We can see that the slope of the  $N_{tr}$ - $N_{ch}$  correlation is smaller than 1 and that  $N_{tr}$  is systematically smaller than  $N_{ch}$ , which reflects the loss of the SPD acceptance and efficiency. The average measured multiplicity is about 0.75 times the true multiplicity. Likewise, the number of corrected tracklets is also drawn as a function of the generated primary particles event by event in Fig. 3.13 (right) (we call it  $\mathcal{A}\times\mathcal{E}$  corrected detector's response matrix). After correction, the correlation  $N_{tr}^{corr}$ - $N_{ch}$  is globally closer to 1 and the dispersion is more symmetric around the mean than before. After the use

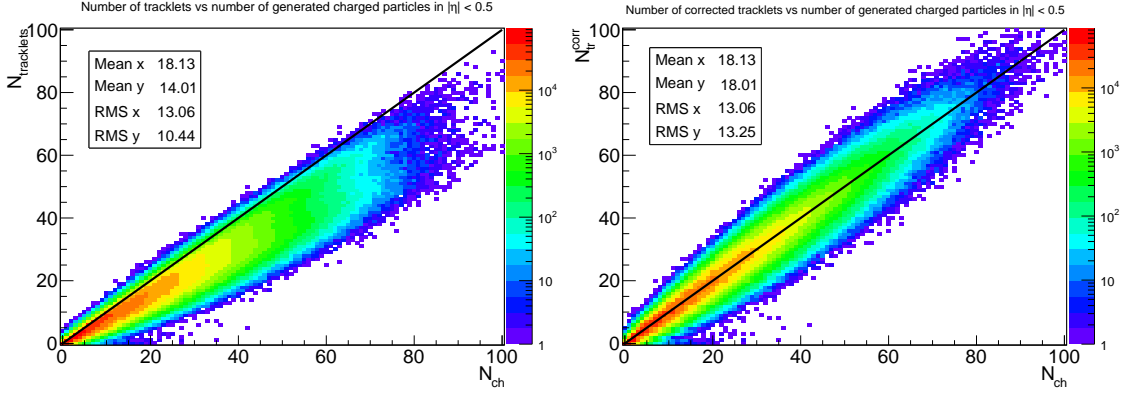


Figure 3.13: Left: Number of tracklets as a function of generated particles in  $|\eta| < 0.5$  for events with  $|z_v| < 10$  cm. Right: Corrected number of tracklets as a function of the generated charged particles. The black lines represent the line  $N_{tr} = N_{ch}$  and  $N_{tr}^{corr} = N_{ch}$  respectively.

of the  $\mathcal{A} \times \mathcal{E}$  correction, the average measured multiplicity ( $\langle N_{tr}^{corr} \rangle$ ) is closer to the mean number of generated charged particles ( $\langle N_{ch} \rangle$ ). This means that after this correction the  $\langle N_{tr}^{corr} \rangle$  is a good estimator of the  $\langle N_{ch} \rangle$ . The remaining dispersion is an effect of the fact that the efficiency and acceptance losses affect the resolution in the detection of the number of charged particles, and it cannot be corrected. Even with a perfect detector, there would be a certain dispersion due to the tracklet-to-particle effects, like secondaries and combinatorial background. These effects that cannot be accounted for individual events but only in average. As a consequence, several events with different true  $N_{ch}$  multiplicities are reconstructed with the same measured  $N_{tr}^{corr}$  multiplicity.

After the SPD 2D  $\mathcal{A} \times \mathcal{E}$  correction a correlation between the corrected tracklets and the generated charged particles is clearly observed, and the dispersion is reasonably narrow. This means that the number of corrected tracklets is also a good candidate for an event-by-event multiplicity estimator. To test the validity of the implementation of the method, the pseudorapidity density and multiplicity distributions are measured in the following. They are also compared with published results when available.

### 3.6 Charged particle pseudorapidity density distribution measurement

In this section we describe how the charged particle pseudorapidity density  $dN_{ch}/d\eta(\eta)$  is determined from the number of reconstructed tracklets. We use the event-by-event correction method described in the previous section. The event-averaged number of corrected tracklets

for a certain pseudorapidity bin  $\eta_i$  is determined as:

$$(3.10) \quad \langle N_{tr}^{corr} \rangle(\eta_i) = \frac{\sum_{j=1}^{N_{events}^{\eta_i}} n_{tr,j}^{corr,\eta_i}}{N_{events}^{\eta_i}}$$

where  $N_{events}^{\eta_i}$  is the number of events contributing to the bin  $\eta_i$ .<sup>9</sup>  $n_{tr,j}^{corr,\eta_i}$  denotes the  $i$ -th component of the tracklets configuration ( $n_{tr}^{corr,\eta_i}$ , Eq. 3.9) of the  $j$ -th event contributing to the  $\eta_i$  bin under consideration.

We can compare our event-by-event definition in Eq. 3.10, with the one used in [239, 240]. There, 2D histograms with the number of effective events contributing to a  $(\eta_i, z_v^j)$  bin  $(N_{events}(\eta_i, z_v^j))^{10}$ , and the total number of tracklets ( $N_{tr}(\eta_i, z_v^j)$ ) are used. The event-averaged number of corrected tracklets for a certain pseudorapidity bin  $\eta_i$  is determined in that case as:

$$(3.11) \quad \langle N_{tr}^{corr} \rangle(\eta_i) = \frac{\sum_{z_v^j} N_{tr}(\eta_i, z_v^j) \cdot \frac{1}{\text{Acc} \times \epsilon(\eta_i, z_v^j)}}{\sum_{z_v^j} N_{events}(\eta_i, z_v^j)}$$

We show later that our *event-by-event* definition in Eq. 3.10 gives equivalent results to the *event-averaged* one in Eq. 3.11.

In order to maximise the  $\eta$  range studied, keeping a reasonable coverage for the extremes of the distribution, the events are selected to have a SPD vertex in  $|z_v| < 18$  cm and the pseudorapidity is limited to  $|\eta| < 2$ . To ensure that for every event we consider tracklets reconstructed within the acceptance of the detector, Eq. 3.1 is used to constrain the  $\eta$  range for each event.

From Fig. 3.13 right, we can extract that  $\langle N_{tr}^{corr} \rangle = \langle N_{ch} \rangle$ . We assume that the same holds as a function of  $\eta$ , so the event averaged pseudorapidity density distribution can be calculated as:

$$(3.12) \quad \left\langle \frac{dN_{ch}}{d\eta} \right\rangle(\eta) = \frac{\langle N_{tr}^{corr} \rangle(\eta)}{\Delta\eta}$$

where  $\Delta\eta = 0.1$  is the bin width. And  $\langle N_{tr}^{corr} \rangle(\eta)$  is computed using Eq. 3.10.

As a self-consistency check (closure test), the method has been applied to the simulation itself. In Fig. 3.14 we show the reconstructed and generated values of the  $dN_{ch}/d\eta(\eta)$  distributions for the selected data sample. A very good agreement (within 0.2%) between the two distributions is found.

---

<sup>9</sup>Events reconstructed at  $z_v$ 's such as the SPD acceptance covers the full  $\eta$  range of the bin.

<sup>10</sup>We call them effective events in the sense that  $\sum_{\eta_i, z_v^j} N_{events}(\eta_i, z_v^j)$  is not the total number of events. This is because an event at a given  $z_v^j$  can contribute to several  $\eta_i$  bins. Note that  $\sum_{z_v^j} N_{events}(\eta_i, z_v^j)$  equals  $N_{events}^{\eta_i}$  in Eq.3.10

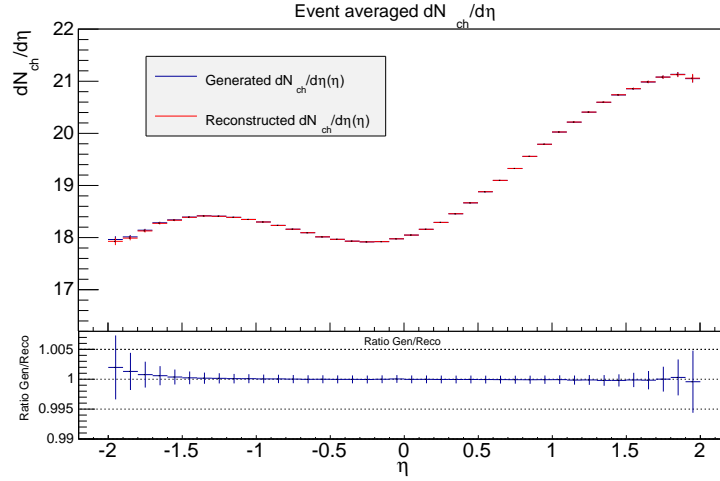


Figure 3.14: Comparison between generated and reconstructed  $dN_{ch}/d\eta(\eta)$  for selected events, obtained with the p-Pb MC simulation.

Then the method has been applied to data. In Fig. 3.15 (left) the  $dN_{ch}/d\eta$  distribution for p-Pb (LHC13c) is calculated for three different  $\eta$ - $z_v$  cuts. The distributions are the same in the overlapping region. In order to check how the chosen  $z_v$  to probe a certain  $\eta$  influences the result, the  $dN_{ch}/d\eta$  distribution for several  $z_v$  ranges and  $0 < \eta < 1$  are shown in Fig. 3.15 (right). There are differences up to 2.6% in the  $dN_{ch}/d\eta$  value depending on the vertex region used for the calculation. These variations are caused by the SPD  $\mathcal{A} \times \mathcal{E}$ . As we can see in Fig. 3.8, the range  $0 < z_v < 5$  cm is in a region where the SPD acceptance is better than in the range  $-5 < z_v < 0$  since the correction is very close to one. These variations have to be taken into account in the systematic uncertainty computation of the  $dN_{ch}/d\eta$  distribution for each  $\eta$  bin.

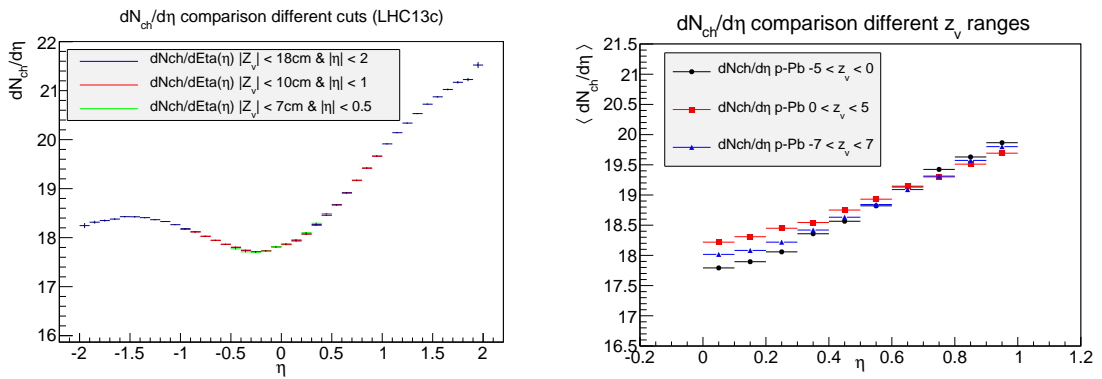


Figure 3.15:  $dN_{ch}/d\eta(\eta)$  for several  $z_v$ -  $\eta$  cuts in p-Pb.

To be sure that our implementation of the correction method is correct, the  $dN_{ch}/d\eta(\eta)$  distributions obtained in this analysis are compared with the distribution in [239]. In Fig.3.16 we present the comparison of the obtained distributions in this thesis for p-Pb rare

trigger periods LHC13d+e (the ones used for the  $J/\psi$  analysis in the following chapters), and the p-Pb minimum bias run period LHC13c, with the one in [239]. It is important to take into account in the comparison, that the results shown for this analysis are obtained for physics selected events with a SPD vertex passing the QA cut, and the published results are for NSD events. So the event selection efficiency correction still remains to be applied to our results to obtain the NSD distribution. This correction accounts for events with no tracklets as we show in Sec. 3.7. However, an already good agreement within the uncertainties is reached with the LHC13c result. The fact that the LHC13d+e result is slightly higher could be due to a higher pile-up rate for the rare trigger periods than for the MB one (see Tab. 4.6).

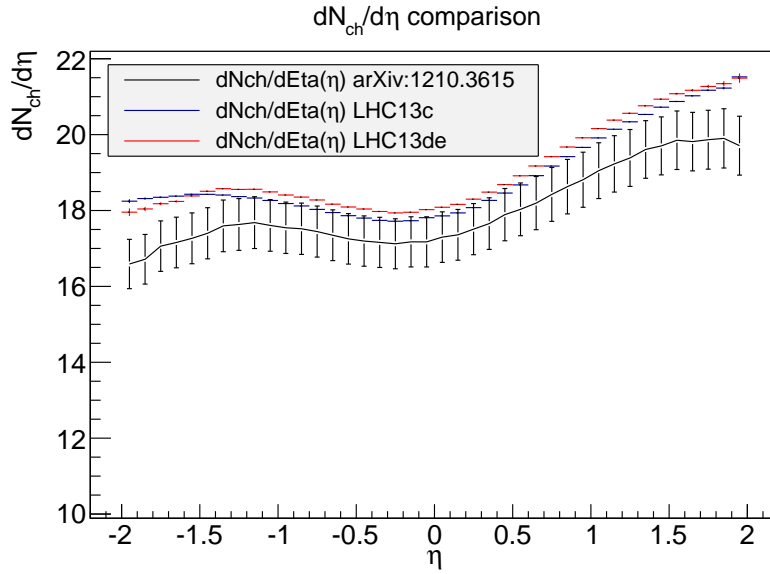


Figure 3.16:  $dN_{ch}/d\eta(\eta)$  results from this analysis (MB events passing QA vertex cuts) for several p-Pb data taking periods compared with the result in [239] (NSD events).

Another cross-check that can be done, is to divide the data sample into event classes based on cuts on the total charge deposited in the VZERO-A detector. Then the values of the average  $dN_{ch}/d\eta$  in  $|\eta| < 0.5$  for each event class are calculated and compared to those obtained in [247]. The results for the corresponding fractions of the data sample in each event class are listed in Tab. 3.1. Note that the results obtained in this thesis have no estimate of uncertainties. This comparison is done only as a cross-check, so we do not compute the systematic uncertainties in VZERO event classes. In this case, neither the published values nor the ones obtained in this analysis are corrected by event selection efficiency<sup>11</sup>. The results obtained here are in very good agreement with the published ones, reaffirming the validity of the present implementation of the multiplicity correction method.

We now present the comparison of the result obtained in p-Pb with the one in Pb-p. In Fig.3.17 (left) the result for the two p-Pb periods considered here is shown together with the

<sup>11</sup>This correction is not needed since it is only applicable for events with zero multiplicity (see Sec. 3.7)



Event class	VZERO-A range (a.u.)	$\langle dN_{ch}/d\eta \rangle$ ([247])	$\langle dN_{ch}/d\eta \rangle$ (this thesis)
0-5 %	> 227	$45 \pm 1$	45.0
5-10 %	187-227	$36.2 \pm 0.8$	36.3
10-20 %	142-187	$30.5 \pm 0.7$	30.6
20-40 %	89-142	$23.2 \pm 0.5$	23.4
40-60 %	52-89	$16.1 \pm 0.4$	16.2
60-80 %	22-52	$9.8 \pm 0.2$	9.9
80-100 %	< 22	$4.4 \pm 0.1$	4.5

Table 3.1: Comparison of the average  $dN_{ch}/d\eta$  in VZERO-A event classes published in [247] and obtained in this thesis for p-Pb (LHC13d+e). This comparison is done only as a cross-check, so the systematic uncertainties in VZERO event classes are not computed for the results in this thesis.

Pb-p result from the LHC13f data-taking period. As we can see, the distribution in Pb-p is the mirror-reflected distribution in p-Pb respect to an axe at  $\eta = 0$ , *i.e.*  $(dN_{ch}/d\eta)_{pPb}(\eta) = (dN_{ch}/d\eta)_{Pbp}(-\eta)$ . This is better observed when performing an  $\eta$  flip ( $\eta \rightarrow -\eta$ ). This is shown in Fig. 3.17 (right).

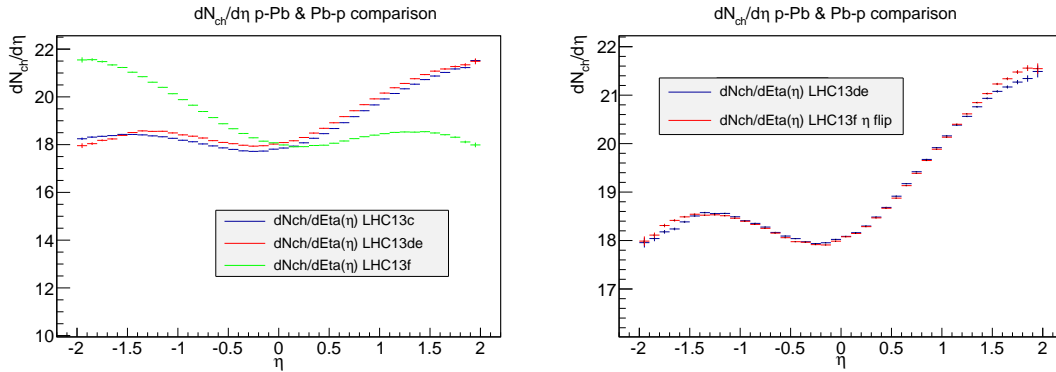


Figure 3.17:  $dN_{ch}/d\eta(\eta)$  results from this analysis for several p-Pb periods compared with the Pb-p result.

### 3.7 Event selection efficiency correction

The event selection used in the analysis rejects MB events with no SPD vertex or with SPD vertex that do not pass the vertex QA (see Sec. 3.3). The multiplicity measured in the previous section corresponds only to the selected data sample. Our goal is to measure the multiplicity of NSD events. For that, the contribution to the multiplicity of the MB rejected events and the NSD events that do not trigger the MB, have to be taken into account. In this section we study the influence on the measured event-averaged multiplicity of the vertex

cuts and MB selection. We compute the NSD selection efficiency of the MB trigger and applied event selection.

From the number of selected events obtained with different cuts in the DPMJET simulation, shown in Tab. 3.2, the MB trigger efficiency for selection of NSD events can be calculated. The MB trigger selects 98.9% of the generated NSD events, which is within 0.3% agreement with the value of 99.2% published in [239]. For consistency with other analyses, and due to the fact that the VZERO efficiency is very stable among data-taking periods, the published value is used in the following.

The effects of the event selection on the measured multiplicity, and the applied corrections are:

**Vertex position  $|z| < z_0$ :** The requirement of  $|z| < z_0$  does not need any correction, since the properties of the events, multiplicity in this case, do not depend on the interaction vertex of the collision. Events out-of-range can be safely removed without affecting the multiplicity computation.

**Vertex requirement and vertex QA:** The rejection of these events removes contributions with zero or small number of tracklets biasing the multiplicity measurement. The distributions shown in Fig. 3.17 are not the distributions for a data sample of NSD events but a subsample of it. In order to obtain a correct estimation of the NSD event-averaged charged particle multiplicity, we need to correct by the event selection efficiency. The event-averaged number of corrected tracklets of MB events,  $\langle N_{tr}^{corr} \rangle_{MB}$ , can be written as:

$$(3.13) \quad \begin{aligned} \langle N_{tr}^{corr} \rangle_{MB} = & \epsilon_{SPDQA} \cdot \langle N_{tr}^{corr} \rangle_{measured} + \\ & \epsilon_{\overline{SPD}} \cdot \langle N_{tr}^{corr} \rangle_{\overline{SPD}} + \epsilon_{SPD\overline{QA}} \cdot \langle N_{tr}^{corr} \rangle_{SPD\overline{QA}} \end{aligned}$$

where we have separated the contributions from different MB event subsamples, that we detail in the following<sup>12</sup>. The MB-physics selected (MB-PS) fraction of events with SPD vertex and passing the vertex QA (the subsample used in the analysis), is denoted by  $\epsilon_{SPDQA}$ . The MB-PS fraction of events without SPD vertex is denoted by  $\epsilon_{\overline{SPD}}$ . The corresponding fraction of events with SPD vertex but not passing the vertex QA, is  $\epsilon_{SPD\overline{QA}}$ .  $\langle N_{tr}^{corr} \rangle_{measured}$  is the event-averaged number of corrected tracklets measured with the event cuts applied in the analysis.  $\langle N_{tr}^{corr} \rangle_{\overline{SPD}}$  and  $\langle N_{tr}^{corr} \rangle_{SPD\overline{QA}}$  are the the event-averaged number of corrected tracklets for events without SPD vertex, and events with SPD vertex that not pass the vertex QA requirements respectively.

The Eq. 3.13 can be modified taking into account several considerations. The events with no reconstructed SPD vertex have by definition 0 reconstructed tracklets ( $\langle N_{tr}^{corr} \rangle_{\overline{SPD}} = 0$ ). The fraction of events used for the measurement can be written as:

$$(3.14) \quad \epsilon_{SPDQA} = 1 - \epsilon_{\overline{SPD}} - \epsilon_{SPD\overline{QA}}$$

---

<sup>12</sup>Note that all the event fractions,  $\epsilon$ , that we handle are with respect to the MB physics selected event sample

Accordingly:

$$(3.15) \quad \langle N_{tr}^{corr} \rangle_{MB} = (1 - \epsilon_{\overline{SPD}} - \epsilon_{SPD\overline{QA}}) \cdot \langle N_{tr}^{corr} \rangle_{measured} + \epsilon_{SPD\overline{QA}} \cdot \langle N_{tr}^{corr} \rangle_{SPD\overline{QA}}$$

In the previous expression, the contribution of all the physics selected events which trigger the MB is included. In order to obtain the event-averaged number of corrected tracklets for NSD events, we need also to include the contribution from those events not selected by the MB trigger. We consider that the NSD events which do not trigger the MB would not have a reconstructed SPD vertex (*i.e.* zero tracklets). Therefore,  $\epsilon_{\overline{SPD}}$  represents only a fraction of the NSD events without SPD vertex. Consequently the NSD  $\langle N_{tr}^{corr} \rangle$  can be written as:

$$(3.16) \quad \langle N_{tr}^{corr} \rangle_{NSD} = (1 - \epsilon_{\overline{SPD}}/\epsilon' - \epsilon_{SPD\overline{QA}}) \cdot \langle N_{tr}^{corr} \rangle_{measured} + \epsilon_{SPD\overline{QA}} \cdot \langle N_{tr}^{corr} \rangle_{SPD\overline{QA}}$$

where  $\epsilon'$  is the selection efficiency for events without SPD vertex, that we define in the following. In order to estimate  $\epsilon'$ , the same MC productions used to get the SPD corrections are employed. For this, we need to determine the fraction of the MB event sample that represents the amount of generated NSD events which vertex is not reconstructed by the SPD ( $\epsilon_{\overline{SPD}}^{NSD}$ ). Also, we need to know the MB fraction of events with no SPD vertex ( $\epsilon_{\overline{SPD}}^{MB}$ , which is the MC equivalent to our measured  $\epsilon_{\overline{SPD}}$ ). The MB selection efficiency for events without SPD vertex is then determined as  $\epsilon' = \epsilon_{\overline{SPD}}^{MB}/\epsilon_{\overline{SPD}}^{NSD}$ . This procedure is the same as the one used in [239]. The results for the different MC productions are listed in Tab. 3.2. As we can observe the obtained probability of selecting an event without a primary vertex is 18% in p-Pb and Pb-p. This result differs from the 41% in [239]. The obtained fraction of NSD events without vertex,  $\epsilon_{\overline{SPD}}^{NSD}$ , is very similar to the 1.43% found in [239]. However, the fraction of events without vertex which are selected,  $\epsilon_{\overline{SPD}}^{MB}$ , was found to be 0.58%, which differs by a 45% with our value.

	p-Pb	Pb-p
# generated events ( $N_g$ )	5705400	12883200
# NSD events ( $N_{nsd}$ )	5549268	12531473
# NSD events & MB trig. ( $N_s$ )	5486768	12390010
# NSD events & MB trig. & $SPD_v$ ( $N_{sv}$ )	5472183	12357254
# events w/o vtx ( $\epsilon_{\overline{SPD}}^{NSD} = (N_{nsd} - N_{sv})/N_s$ )	1.40%	1.41%
# events w/o vtx & MB trig ( $\epsilon_{\overline{SPD}}^{MB} = (N_s - N_{sv})/N_s$ )	0.26%	0.26%
$\epsilon' (\epsilon_{\overline{SPD}}^{MB}/\epsilon_{\overline{SPD}}^{NSD})$	0.18	0.18

Table 3.2: Number of events passing different event cuts in simulation and selection efficiency for NSD events without SPD vertex ( $\epsilon'$ ) for different MC productions.

Then we assume that the selection efficiency for events without vertex is the same in data and MC, including a systematic uncertainty of 31.70% [248], so data  $\epsilon' = 0.18 \pm 0.06$ .

This  $\epsilon'$  is then applied to the fraction of events without vertex found in data to obtain the total fraction of events without vertex ( $\epsilon_{\overline{SPD}}/\epsilon'$ ).

The tracklets distribution of events not passing the vertex QA (leading to  $\langle N_{tr}^{corr} \rangle_{SPD\overline{QA}}$ ) has been studied to have an idea of its contribution to the total multiplicity. We have observed that the average number of tracklets in  $|\eta| < 0.5$  of these events is  $\sim 0.7$ . Due to the 2.5 threshold in the  $1/\mathcal{A} \times \epsilon$  correction, the average corrected number of tracklets can be at most  $\langle N_{tr}^{corr} \rangle_{SPD\overline{QA}} = 0.7/0.4 = 1.75$ . However, due to the small amount of events not passing the vertex QA (0.32% of the MB sample), their contribution to the total multiplicity is negligible, so we can safely neglect the second term in Eq. 3.16. The NSD event-averaged corrected tracklets multiplicity is then:

$$(3.17) \quad \langle N_{tr}^{corr} \rangle_{NSD} = (1 - \epsilon_{\overline{SPD}}/\epsilon' - \epsilon_{SPD\overline{QA}}) \cdot \langle N_{tr}^{corr} \rangle_{measured}$$

where  $1 - \epsilon_{\overline{SPD}}/\epsilon' - \epsilon_{SPD\overline{QA}}$  is the NSD event selection efficiency of the MB trigger and event selection applied in the analysis.

Finally, using the fractions of events passing the different cuts in data and the obtained efficiency for events without vertex in Tab. 3.2<sup>13</sup>, the NSD event selection efficiency in Eq. 3.17 can be computed. The results are listed in Tab. 3.3.

System	$\epsilon_{SPDQA}$ (Eq. 3.14)	$\epsilon_{\overline{SPD}}$	$\epsilon_{\overline{SPD}}/\epsilon'$	$\epsilon_{SPD\overline{QA}}$	$1 - \epsilon_{\overline{SPD}}/\epsilon' - \epsilon_{SPD\overline{QA}}$
p-Pb	98.83%	0.85%	4.72%	0.32%	$0.950 \pm 0.031$
Pb-p	98.83%	0.86%	4.78%	0.30%	$0.949 \pm 0.031$

Table 3.3: Event fractions with respect to MB physics selected events in p-Pb, and Pb-p collisions real data. The NSD event selection efficiency of the MB trigger and event selection ( $1 - \epsilon_{\overline{SPD}}/\epsilon' - \epsilon_{SPD\overline{QA}}$ ) is also shown. For an explanation on the uncertainty see Sec. 3.10

Assuming that the correction factors in Tab.3.3 do not vary with  $z_v$ , the  $dN_{ch}/d\eta(\eta)$  distributions are corrected with them. As it is observed in Fig. 3.18, after correction for vertex reconstruction efficiency of the result obtained in this thesis, the obtained  $dN_{ch}/d\eta(\eta)$  distribution for NSD events is in very good agreement with the ALICE published result [239]. The result of this thesis lacks of a systematic uncertainty study since this measurement is not the main goal of this work. However, since the event generator and transport code are the same as for the published data, and the SPD conditions very similar, the magnitude of the uncertainties would be similar to that of the published result.

In Fig. 3.19 the results of the  $dN_{ch}/d\eta(\eta)$  distributions for NSD events in p-Pb and Pb-p collisions are shown together. Note that this is the first measurement of the Pb-p distribution. The obtained averaged values of the charged particle pseudorapidity density in  $|\eta| < 0.5$  for NSD events are  $\langle dN_{ch}/d\eta \rangle_{pPb} = 17.15$  and  $\langle dN_{ch}/d\eta \rangle_{PbP} = 17.12$  (the statistical

<sup>13</sup>Note that our value of  $\epsilon_{\overline{SPD}}$  in data differs from the one in [239] (1.46%). This result is consistent with the difference found also in simulation (Tab. 3.2)

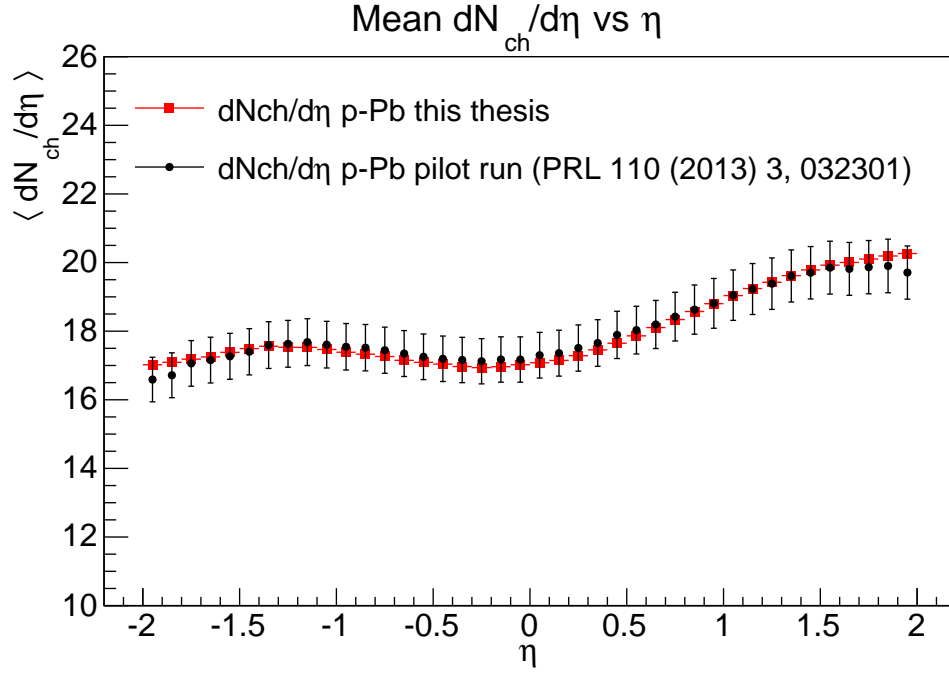


Figure 3.18:  $dN_{ch}/d\eta(\eta)$  distribution for NSD events in p-Pb collisions at  $\sqrt{s_{NN}} = 5.02$  TeV measurement from this thesis compared to ALICE publication result [239].

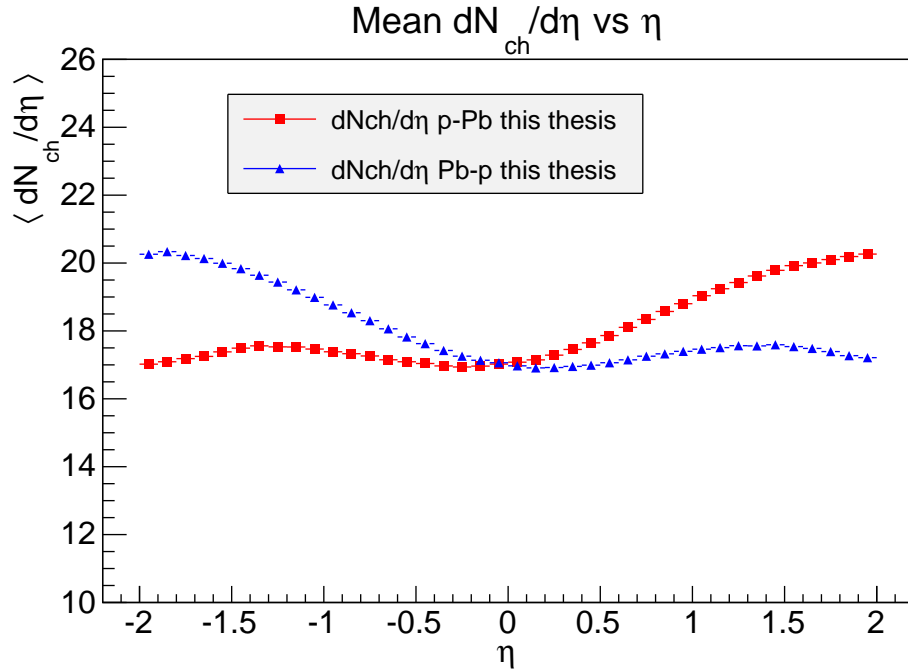


Figure 3.19:  $dN_{ch}/d\eta(\eta)$  distribution for NSD events in p-Pb and Pb-p collisions at  $\sqrt{s_{NN}} = 5.02$  TeV measurement from this thesis.

uncertainties are negligible), which are in very good agreement with the published value of  $\langle dN_{ch}/d\eta \rangle = 17.35 \pm 0.01$  (stat.)  $\pm 0.67$  (syst.) [239].

### 3.8 Charged particle distribution measurement

In this section the charged particle probability distribution  $P(N_{ch})$  is determined from the distribution of corrected tracklets in  $|\eta| < 0.5$  for events with  $z_v < 10$  cm. The SPD  $\mathcal{A} \times \mathcal{E}$  correction is applied event by event in  $\eta$  bins as in Eq. 3.9. For each event, the total number of corrected tracklets in  $|\eta| < 0.5$  is taken and the distribution is built.

The obtained result in the p-Pb simulation for the reconstructed  $N_{tr}^{corr}$  and the generated  $N_{ch}$  distributions are shown in Fig. 3.20. As can be observed, the corrected reconstructed distribution does not reproduce the generated one. At zero multiplicity the difference reaches 40%. This is because when there are no reconstructed tracklets, a simple  $\mathcal{A} \times \mathcal{E}$  correction does not work. Then, for multiplicities between 2 to 50, the generated distribution is in average reproduced, but there are big fluctuations (10-20%) from bin to bin. These fluctuations are a product of the resolution of the correction and the integer nature of the number of tracklets. Due to the limited statistics in the simulation, the  $\mathcal{A} \times \mathcal{E}$  is binned in ranges much bigger than the resolution of the detector. As a consequence, for every event in a given  $z_v^j$  bin with the same tracklets configuration  $\widehat{N}_{tr}$  (only  $\eta$  is known), the correction is the same hence the resulting  $N_{tr}^{corr}$  is also the same even if the true multiplicity is not. For example, consider a single bin where the correction is 1.33. An event reconstructed with 1 tracklets has, after correction, 1 corrected tracklets. But an event with 2 reconstructed tracklets has 3 corrected tracklets, producing a defect of events in the bin of 2 corrected tracklets. This situation could be improved (but not solved) if the region corresponding to the bin could be better resolved and be divided in 4 bins, where it could be that 3 bins were 100% efficient and the other 0%. At high multiplicities the  $N_{tr}^{corr}$  distribution is shifted to higher multiplicities with respect to the generated one, so the method is not able to reproduce the true distribution at these multiplicities.

We know from the  $\mathcal{A} \times \mathcal{E}$  corrected detector's response matrix in Fig. 3.13 that the mapping  $N_{tr}^{corr} \rightarrow N_{ch}$  is not  $1 \rightarrow 1$ . There is a certain dispersion, so events reconstructed with a certain number of corrected tracklets  $N_{tr}^{corr} = 0$  come from events with a true  $N_{ch}$  with a certain probability distribution  $\tilde{P}_0(N_{ch})$ . This distribution probability corresponds to a  $N_{tr}^{corr}$  slice in the detector's response matrix. It can be interpreted as the conditional probability distribution for an event to have a true multiplicity  $N_{ch}$ , having measured  $N_{tr}^{corr} = 0$ . The correction as it is being applied now (only SPD  $\mathcal{A} \times \mathcal{E}$ ), corresponds to do the following assignment for each event in a multiplicity bin  $i$ :  $N_{ch} = N_{tr}^{corr} = i$ . However, this is like assuming that the  $N_{tr}^{corr} = i$  matches with the mean value of the probability distribution  $\tilde{P}_i(N_{ch})$  corresponding to the  $i$ -th  $N_{tr}^{corr}$  slice,  $\langle N_{ch} \rangle_i$ . An example of these distributions can be observed in Fig. 3.21 for several different  $N_{tr}^{corr}$  slices in the  $\mathcal{A} \times \mathcal{E}$  corrected detector's response matrix. If one compares the  $N_{tr}^{corr} = i$  value in each bin with the corresponding  $\langle N_{ch} \rangle_i$ ,

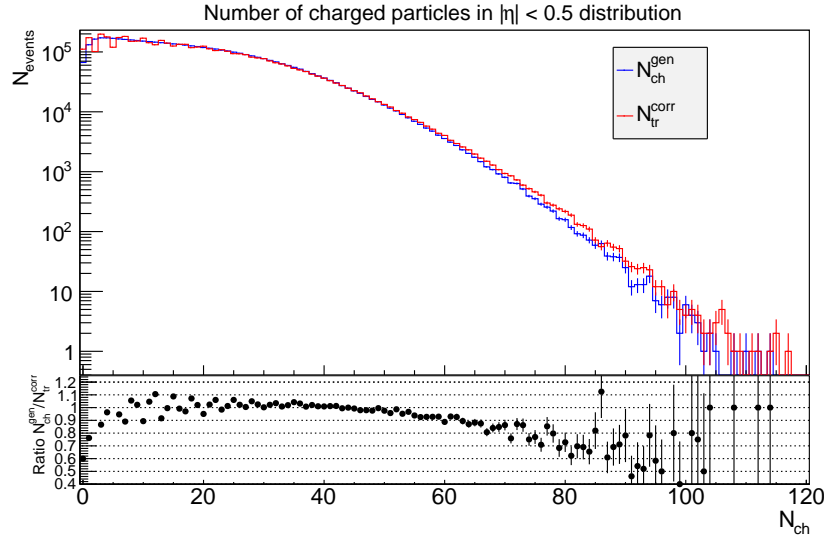


Figure 3.20:  $N_{tr}^{corr}$  distribution (red) in p-Pb simulation compared to the generated  $N_{ch}$  distribution (blue) and its ratio.

it can be seen that there is a difference which can explain the behaviour observed in Fig. 3.20. For the bin  $N_{tr}^{corr} = 0$  the  $\langle N_{ch} \rangle_i$  is bigger than  $N_{tr}^{corr} i$ . This explains the excess of events in that multiplicity bin, since some of those events should be spread through the following bins. The results for the bins  $N_{tr}^{corr} = 19$  and 39 explain the relative good agreement of the multiplicity distributions at mid multiplicities. Then for the bin  $N_{tr}^{corr} = 59$ , the difference with  $\langle N_{ch} \rangle_i$  reaches 3.9%, which explains the shift to higher multiplicities in Fig. 3.20.

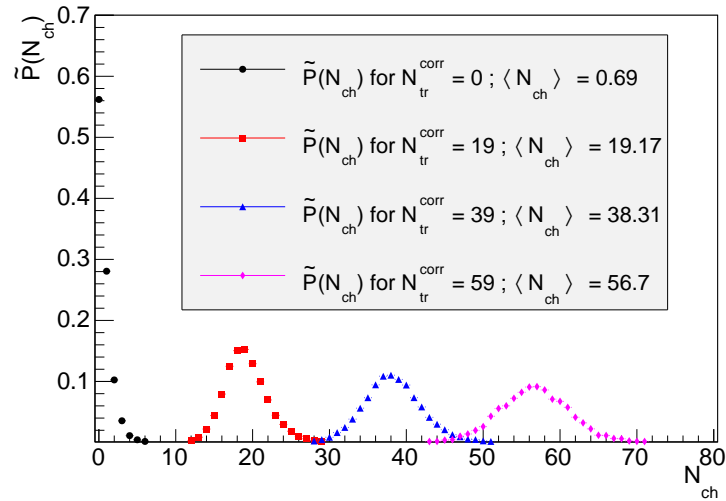


Figure 3.21:  $\tilde{P}_i(N_{ch})$  distribution for several  $N_{tr}^{corr}$  bins. The mean  $N_{ch}$  value of each distribution is written on the legend for comparison with the corresponding  $N_{tr}^{corr}$ .

Altogether this behaviour could be explained by a variation of the tracklet-to-particle

correction with the multiplicity. The applied correction is multiplicity-averaged. However, effects like secondaries or combinatorial background vary with the multiplicity of the collision, as was shown in Fig. 3.11. Even kinematical variables such as the transverse momentum distribution of the charged particles could vary with multiplicity (as they indeed do, [7]), affecting also the acceptance. In Fig. 3.22 we show the ratios of the SPD  $\mathcal{A}\times\mathcal{E}$  correction integrated in multiplicity, over the correction computed in two different multiplicity bins. It can be seen that the tracklet-to-particle correction varies with multiplicity. The correction is bigger than the multiplicity-averaged correction at low multiplicity (Fig. 3.22 right,  $z_v < 0$ ) and smaller at higher multiplicities (Fig. 3.22 left,  $z_v < 0$ ). This could explain the results previously observed. The solution to improve the description of the true multiplicity could be the use of a multiplicity differential SPD  $\mathcal{A}\times\mathcal{E}$  correction. Note here that the word *improve* is used, since the multiplicity dependent correction would not solve the fluctuations problem. This problem is briefly discussed at the end of this section. However, these fluctuations could be dealt with when using the  $\mathcal{A}\times\mathcal{E}$  corrected tracklets as event multiplicity estimator for the  $J/\psi$  studies, by slicing event samples in wide enough multiplicity ranges. In order to compute such a correction, a simulation with high multiplicity events enhancement would be required. Due to the present lack of statistics at high multiplicity, it is not possible to compute a differential SPD  $\mathcal{A}\times\mathcal{E}$  correction in multiplicity, and it is left for future works. A workaround to reproduce the true multiplicity distribution was tried instead, as we explain in the following.

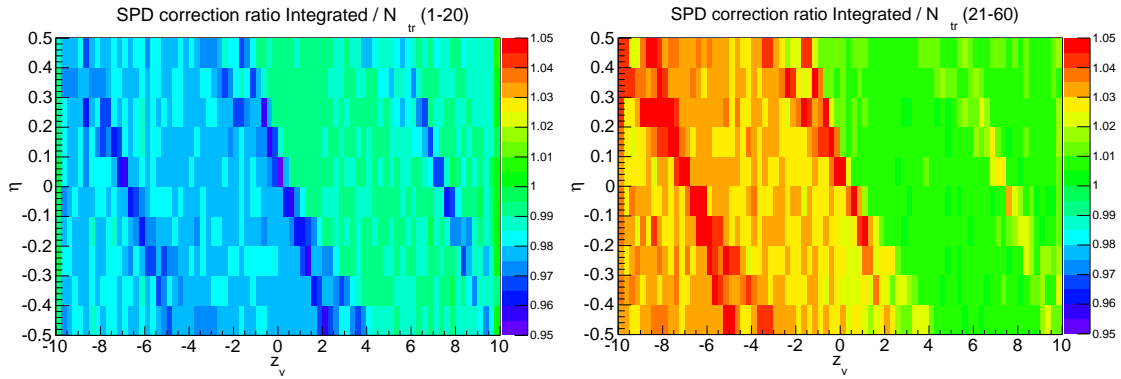


Figure 3.22: p-Pb SPD  $\mathcal{A}\times\mathcal{E}$  ratio of the integrated correction over the correction computed with events having  $N_{tr} = 1 - 20$  (left) and  $N_{tr} = 21 - 60$  (right) in  $|\eta| < 0.5$ .

In order to improve the charged particle distribution measurement, the  $\tilde{P}_i(N_{ch})$  distributions obtained from the  $\mathcal{A}\times\mathcal{E}$  corrected detector's response matrix are used to re-distribute the events. This is performed by randomly assigning a  $N_{ch}$  to each measured event with  $N_{tr}^{corr}_i$  following the  $\tilde{P}_i(N_{ch})$  distribution. The multiplicity re-distribution is applied event-by-event during the analysis, after the correction by SPD  $\mathcal{A}\times\mathcal{E}$ . This can help to get rid off the bin by bin fluctuations in the distribution at low multiplicity, and also to take into account the variations of the tracklet-to-particle effects with multiplicity. The validity of this event



multiplicity re-distribution must be considered very carefully for the reasons that we discuss later.

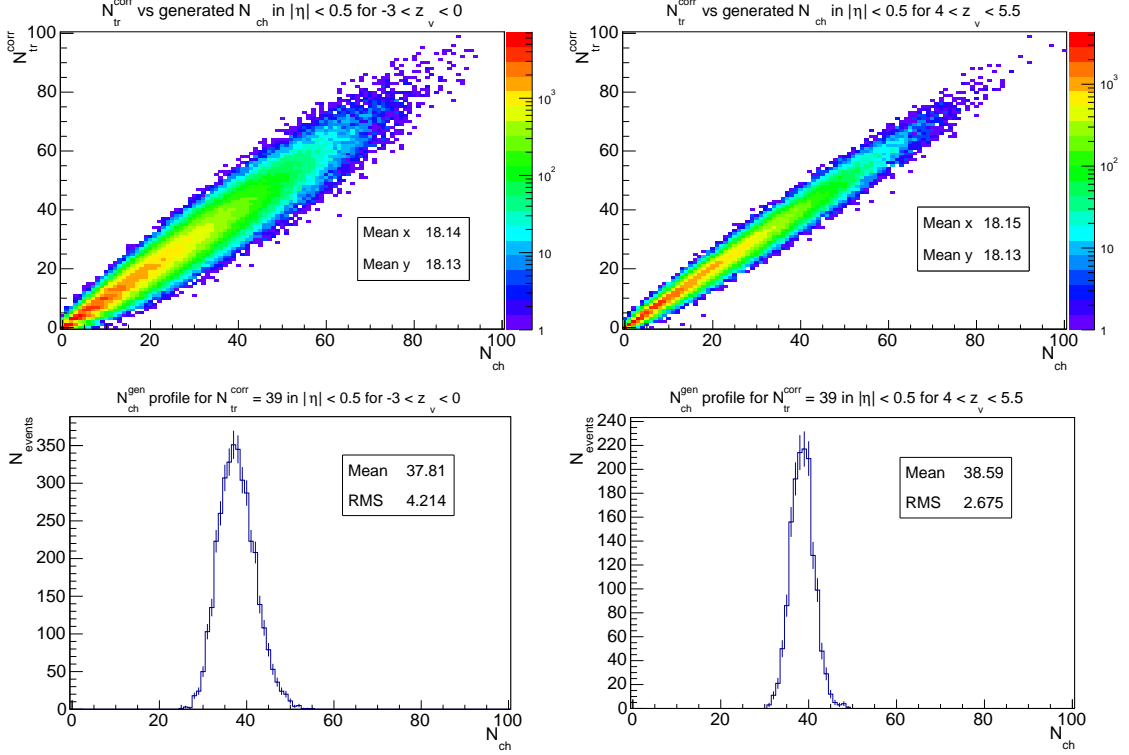


Figure 3.23: Illustration of the variation of the multiplicity resolution with  $z_v$  due to  $\mathcal{A} \times \mathcal{E}$  variations. The plots to the left are the  $N_{tr}^{corr}$  as a function of generated  $N_{ch}$  (top) and the  $\tilde{P}_{39}(N_{ch})$  distribution (bottom) for events with  $-3 < z_v < 0$ . The plots to the right are the equivalent to the left ones but for events with  $4 < z_v < 5.5$ .

As a first approach, two known details are not taken into account: first, the fact that the multiplicity resolution is worse for those regions of the detector where the SPD  $\mathcal{A} \times \mathcal{E}$  is lower (Fig. 3.23). The  $\tilde{P}_{39}(N_{ch})$  is a 36% wider for  $z_v$  ranges where the  $\mathcal{A} \times \mathcal{E}$  is worse, and also the  $\langle N_{ch} \rangle$  are different by 2%. This means that a particular  $\mathcal{A} \times \mathcal{E}$  corrected detector's response matrix should be used for different  $z_v$  regions. But for now, a  $z_v$ -integrated one is used as first approximation. Second, the probability distributions  $\tilde{P}_i(N_{ch})$  should be taken for single  $N_{tr}^{corr}$  bins. Due to the limited statistics in the simulation, we are forced to merge several  $N_{tr}^{corr}$  bins at high multiplicity to avoid fluctuations. Another solution would be to parametrize the distributions by performing a fit to the slices. Again, as a first approximation, the following binning is taken for the probability distributions:

- $0 \leq N_{tr}^{corr} \leq 70$  :  $\tilde{P}_{(N_{tr}^{corr})_i}(N_{ch})$  where  $(N_{tr}^{corr})_i = 0 \dots 49$  (70 bins)
- $71 \leq N_{tr}^{corr} \leq 80$  :  $\tilde{P}_{(N_{tr}^{corr})_i - ((N_{tr}^{corr})_i + 1)}(N_{ch})$  where  $(N_{tr}^{corr})_i = 71 \dots 79$  (5 bins)
- $81 \leq N_{tr}^{corr} \leq 100$  :  $\tilde{P}_{81-100}(N_{ch})$  (1 bin)

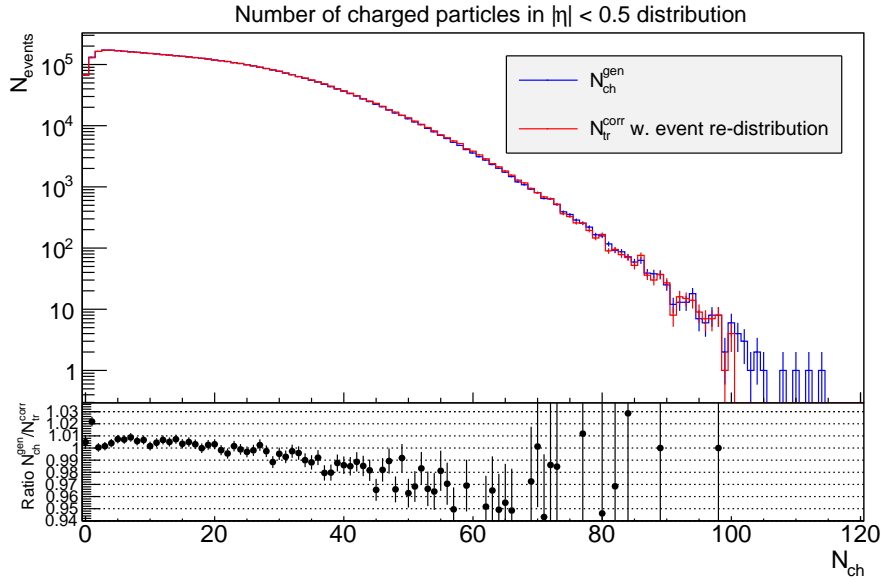


Figure 3.24: Comparison of generated  $N_{ch}$  distribution (blue) and  $N_{tr}^{corr}$  with event multiplicity re-distribution measured distribution (red).

The result is presented in Fig. 3.24, where we compare the generated true multiplicity distribution with the reconstructed one with the applied event multiplicity re-distribution. After the event-redistribution, the bin-to-bin fluctuations have disappeared. Furthermore the measured distribution is in good agreement with the generated one up to  $N_{ch} \approx 40$ , with deviations of 1-2%. This is a huge improvement since before the multiplicity re-distribution the differences reached up to 40%. However, for  $N_{tr}^{corr} > 45$  the ratio of the generated and measured distributions deviates from unity as a consequence of the approximations made. Again, the 5% deviation after re-distribution constitutes a great improvement compared to the former 30%. This effect comes from the poor determination of the  $\tilde{P}_i(N_{ch})$  distributions at high multiplicity due to the lack of statistics. There is also an effect on the probability distributions due to the merging of several bins. To improve the multiplicity distribution measurement we should use bins of one corrected tracklet in order to do not bias the result. For this we would need a parametrisation of the distributions at high multiplicity.

As we already anticipated, the validity of the multiplicity re-distribution must be carefully considered. The issue is that the probability distributions  $\tilde{P}_i(N_{ch})$  used in this method are dependent on the true multiplicity distribution simulated, hence the the measured multiplicity distribution is model dependent. This is the reason why this method works fairly well when applied on the same simulation used to get the detector's response matrix. However, it only works on data when the simulated distributions are close to the ones we want to measure. In such case it would be possible to do the measurement and estimate a systematic uncertainty by using variations of the simulated distribution to get the variations on the  $\tilde{P}_i(N_{ch})$  probability distributions.

However, another methods that can be used for the measurement of the multiplicity

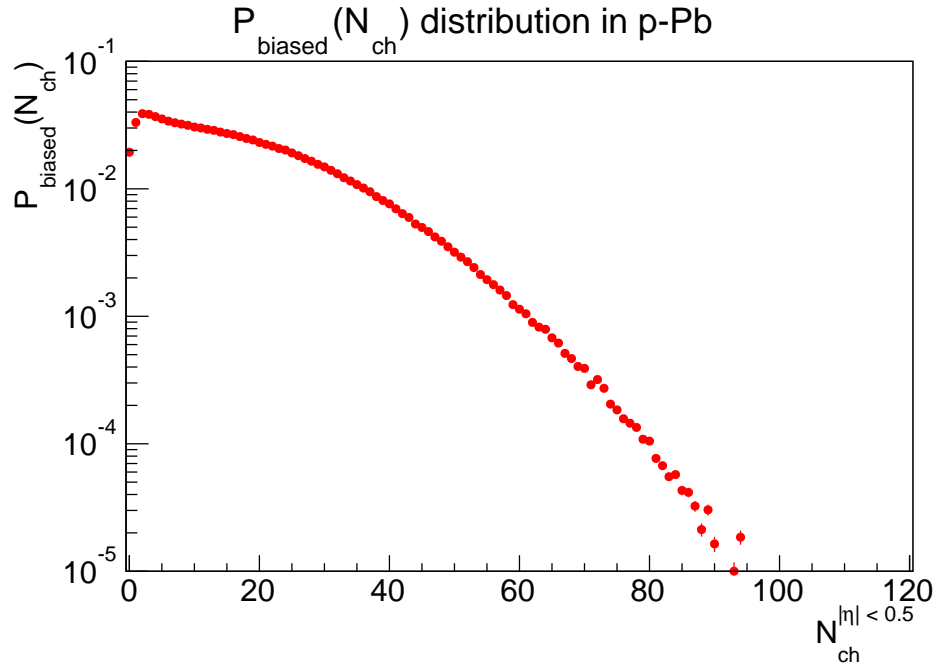


Figure 3.25: Biased multiplicity distribution  $P_{biased}(N_{ch})$  measured in p-Pb collisions at  $\sqrt{s_{NN}} = 5.02$  TeV.

distribution already exist, the so called unfolding methods [249, 250]. These methods use the  $\hat{P}_j(N_{tr})$  distributions, which represent the conditional probability of an event with true multiplicity  $N_{ch}$  to be reconstructed with a certain number of tracklets. The probability distributions  $\hat{P}_j(N_{tr})$  are only dependent on the detector simulation, but not on the simulated distribution, and therefore they can yield model independent solutions. These methods are not further discussed here since they are out of scope of the main goal of this work (and they are not applicable in an event-by-event way), but can be consulted in [240, 241].

The result of the multiplicity distribution in p-Pb data using the  $\mathcal{A} \times \mathcal{E}$  corrected tracklets and the event multiplicity re-distribution is shown in Fig. 3.25. The biases introduced in this measurement as a result of the model dependence of the correction method are still unknown. A dedicated study using several simulated distributions would be needed but could not be carried out during this thesis due to the limited time. In order to make explicit the presence of possible biases in the measured multiplicity distribution, it is called  $P_{biased}(N_{ch})$ .

### 3.9 Use of the SPD $\mathcal{A} \times \mathcal{E}$ corrected tracklets as multiplicity estimator

Since our primary objective is to use this  $\mathcal{A} \times \mathcal{E}$  correction method to obtain an *event-by-event* multiplicity estimator and study  $J/\psi$  production correlation with that multiplicity, we need to ensure that the method fulfils certain conditions. For now, even though the solution is model

dependent, we focus on the result obtained using the event multiplicity re-distribution. First we need to determine how the application of the event multiplicity re-distribution affects the multiplicity resolution. In Fig. 3.26 (left) the  $\mathcal{A}\times\mathcal{E}$  corrected detector's response matrix after the application of event multiplicity re-distribution is shown. If we compare it with the one in Fig. 3.13 (right) we observe how the resolution on the event-by-event multiplicity determination is worse by a 20-30%, since the dispersion is bigger after the re-distribution. However there still exist a correlation between  $N_{tr}^{corr}$  and  $N_{ch}$  so the number of corrected tracklets can be used as multiplicity estimator. Note that the multiplicity re-distribution of the events would not be needed if we had applied a multiplicity dependent  $\mathcal{A}\times\mathcal{E}$  correction and therefore the resolution would remain unchanged.

To perform the  $J/\psi$  study, the data sample is divided in multiplicity slices (bin lower edges:  $N_{tr}^{corr} = 1, 9, 14, 17, 21, 25, 33, 39, 45, 55, 75$ ) and the average values of the studied observables are given as a function of the average multiplicity in each bin. Therefore, the next step on the validation of the considered estimator is to determine if it is able to assign the correct average charged particle multiplicity to each corrected tracklets bin  $i$  (i.e.  $\langle N_{tr}^{corr} \rangle_i = \langle N_{ch} \rangle_i$ ). To do so, the p-Pb simulation is used again. First, the measured  $N_{tr}^{corr}$  distribution shown in Fig. 3.26 (right) is divided in  $N_{tr}^{corr}$  bins, and the average values in each bin,  $\langle N_{tr}^{corr} \rangle_i$ , are computed. Then, the  $\mathcal{A}\times\mathcal{E}$  corrected detector's response matrix, shown in Fig. 3.26 (left), is also divided in the same  $N_{tr}^{corr}$  bins. Then each bin is projected over the  $N_{ch}$  axis, and the  $\langle N_{ch} \rangle_i$  value is obtained from the mean value of the projected distribution.

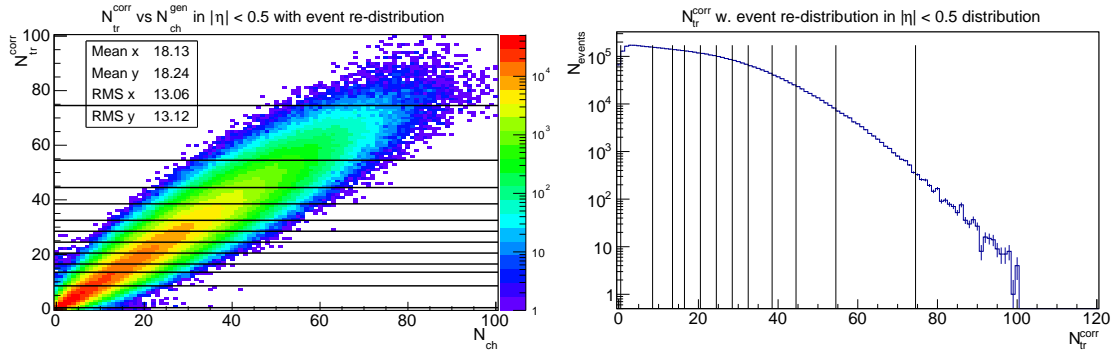


Figure 3.26: Left: Number of corrected tracklets with event multiplicity re-distribution as a function of the generated charged particles in p-Pb simulation. Right:  $N_{tr}^{corr}$  distribution obtained in the p-Pb simulation. The horizontal (left) and vertical (right) lines represent  $N_{tr}^{corr}$  bin limits.

The values of  $\langle N_{tr}^{corr} \rangle_i$  and  $\langle N_{ch} \rangle_i$  are compared in Fig. 3.27. In the left plot the mean values are directly shown while in the right plot their ratios are shown for each multiplicity bin. It can be observed how the measured average values are deviated from the generated ones by  $\sim 8\%$  in the extreme multiplicity bins and less than 5 % for the rest of the range. This is a reasonable agreement and this difference could be either corrected for or added as

systematic uncertainty on the bin average multiplicity measurement. The agreement could be improved by sharpening the description of the  $\tilde{P}_i(N_{ch})$  used to re-distribute the events. Again, it is worth to note that these differences would probably not be present if we had used a multiplicity dependent  $\mathcal{A} \times \mathcal{E}$  correction.

Note here that, provided the bin-to-bin fluctuations in the  $\mathcal{A} \times \mathcal{E}$  corrected distributions could be avoided by using wide enough multiplicity slices, the simple  $\mathcal{A} \times \mathcal{E}$  correction method could be used as multiplicity estimator. Then, the differences between  $\langle N_{tr}^{corr} \rangle_i$  and  $\langle N_{ch} \rangle_i$  could be corrected using the simulation information (see Sec. 4.3).

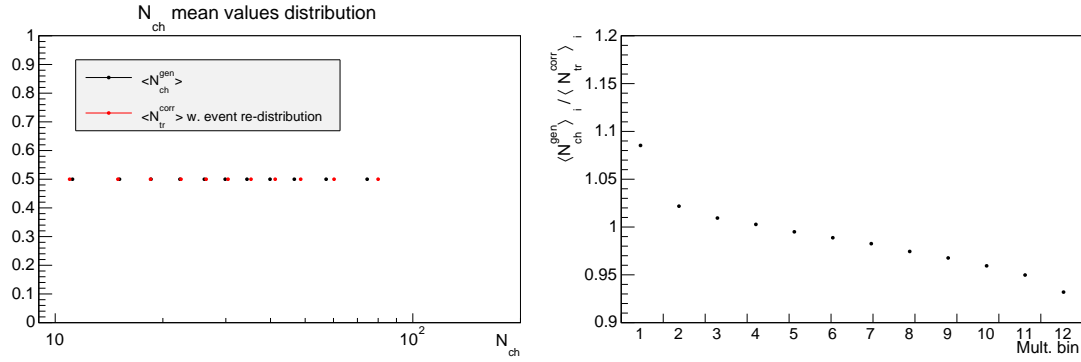


Figure 3.27: Number of corrected tracklets as a function of the generated charged particles.

It has been shown that correcting the tracklets of individual events by the SPD  $\mathcal{A} \times \mathcal{E}(\eta, z_v)$  allows to measure not only event-averaged quantities like the  $dN_{ch}/d\eta(\eta)$  distribution, but also the  $P_{biased}(N_{ch})$  distribution and also to obtain a multiplicity estimator to study particle production properties as a function of the event charged particles. Still, before this method can be used in a reliable way, several issues should be addressed:

1. Event multiplicity re-distribution using  $\tilde{P}_i(N_{ch})$  distributions is model dependent and also worsens the global multiplicity resolution. The inclusion of the variations of the tracklet-to-particle corrections with multiplicity in the SPD  $\mathcal{A} \times \mathcal{E}$  correction may make the event multiplicity re-distribution unnecessary to improve the description of the  $N_{ch}$  distribution (except fluctuations). Another advantage is that the global resolution would remain unchanged, and would probably improve the precision on the determination of the average  $N_{ch}$  corresponding to a  $N_{tr}^{corr}$  bin. In this case it would be necessary to study the influence of the bin to bin fluctuations observed in the multiplicity distributions when performing multiplicity slices to study  $J/\psi$  production. Furthermore, it would reduce the systematic uncertainties on the  $dN_{ch}/d\eta(\eta)$  distribution measurement.
2. The variations of the multiplicity resolution with  $z_v$  may introduce a bias in the selected event sample in a multiplicity bin. This can be seen in Fig. 3.23: the average  $N_{ch}$  is different for the same  $N_{tr}^{corr}$  bin, depending on the  $z_v$  region where the events

are reconstructed. It is necessary to find a procedure to equalise the resolution along  $z_v$  (see Sec. 4.2).

These constraints, and the fact that the MC simulations for the Pb-p data-taking period were not available during the development of the work done for this chapter, are the reasons that made the use of the SPD  $\mathcal{A}\times\epsilon$  corrected tracklets not the best option to be used as a multiplicity estimator to study the  $J/\psi$  production for the work of this thesis. This method is proposed for further development in future works.

Alternatively, a data-driven correction method has been used. This method was used for the ALICE measurement of  $J/\psi$  production in pp collisions at 7 TeV as a function of relative charged particle multiplicity,  $dN_{ch}/d\eta/\langle dN_{ch}/d\eta\rangle$ . The data-driven approach was only suitable for the relative multiplicity measurement. However it has the advantage, under certain conditions, of not requiring MC simulations. The following chapter is dedicated to the study and improvement of the data-driven correction method.

### 3.10 Systematic uncertainties on $dN_{ch}/d\eta(\eta)$ measurement

The procedure to compute the systematic uncertainty on the overall-averaged charged particle multiplicity measurement in p-Pb collisions,  $dN_{ch}/d\eta(\eta)$  is detailed in [239, 246, 248]. Since the same event generator and transport code are used for the MC simulations employed to obtain the multiplicity correction in this analysis, and the collision system and data taking conditions are similar, the magnitude of the uncertainties for this analysis is also similar. Details on other sources that are common for every analysis in ALICE can be also found in [237]. The main aspects of its computation are explained here again for completeness, but are not recalculated:

- The MB data sample contamination from background events was estimated to be negligible from control triggers on non-colliding bunches.
- The uncertainties on the detector material budget could lead to a misestimation of the secondary particles produced due to interaction with the detector. The density of the material types of the detector were varied resulting in a negligible systematic uncertainty on the multiplicity measurement.
- The alignment of the detectors is taken into account in the simulations. The uncertainty on the SPD alignment is very small so its effect on the multiplicity is negligible compared to other sources of uncertainty.
- Tracklets selection uncertainty are estimated by performing variations on the reconstruction cuts corresponding to the spatial resolution of the detector. Again a negligible effect is found.

- The cuts used for the tracklets determination select particles with a  $p_T$  above 50 MeV/c, while particles below are mostly absorbed by the detector material. These particles are not reconstructed as tracklets but count on the generated primary charged particles used for the efficiency determination. Therefore this effect is already included in the correction. The uncertainty on this effect was computed by varying the amount of undetected particles below 50 MeV/c by 50%, obtaining a 1% uncertainty on the resulting  $dN_{ch}/d\eta$  measurement.
- The combinatorial background tracklets and contribution of strange weak decays are also included in the correction. However, the simulation does not reproduce well the combinatorial and secondary tracks from weak decays resulting in a 0.3% and 0.9 % uncertainties respectively. These are determined from the comparison in data and simulation of the tracklet residual distributions, in which the tails are dominated by combinatorial background and secondaries.
- Since the particle species composition is not exactly known, the uncertainty corresponding uncertainty was determined by varying the relative abundances of pions, kaons and protons by a factor 2 in the simulation, obtaining a 1% uncertainty.
- The uncertainty on the SPD acceptance was determined from the change on multiplicity at a given  $\eta$  by varying the range of the  $z$ -vertex position (see Fig. 3.15 left). This uncertainty was estimated to be 1.5%.
- Since the  $\mathcal{A} \times \mathcal{E}$  correction varies with multiplicity, the results obtained for multiplicity averaged quantities (i.e.  $dN_{ch}/d\eta(\eta)$ ) are also dependent on the simulated multiplicity distributions used to get the correction. Depending on the shape of the simulated distribution, more or less weight in the averaged correction is given to the tracklet-to-particle effects in a certain multiplicity range. The variations on the multiplicity correction using different event generators (DPMJET and HIJING [251]) were estimated to be  $\sim 1\%$ .
- Finally, the MB trigger and event selection efficiency uncertainty for NSD events was estimated to be 3.1%. For this, a sample of events collected with the ZNA trigger with an offline selection on the deposited energy was used. This value includes also the uncertainty of using different MC generators mentioned above.

The total systematic uncertainty for  $\langle dN_{ch}/d\eta \rangle$  was obtained by summing all these contributions in quadrature, obtaining a 3.8% value.

For the multiplicity distribution measurement it is needed also to include the uncertainty of the method used (unfolding, event-multiplicity re-distribution), but these uncertainties are not discussed here since we do not aim to obtain a final result for this measurement.





## DATA-DRIVEN MULTIPLICITY CORRECTION METHOD

The goal of this chapter is to obtain a multiplicity estimator which allows to classify events in terms of their relative charged particle pseudo rapidity density, defined as  $dN_{ch}/d\eta/\langle dN_{ch}/d\eta \rangle$ . The method proposed in the previous chapter to use the absolute measurement of the event pseudo rapidity density as multiplicity estimator, resulted not to be reliable enough for the time being, and further developments would be needed. Meanwhile, a one dimensional data-driven correction method is proposed. The method is based on the use of the mean raw number of reconstructed SPD tracklets as a function of the interaction  $z$ -vertex,  $\langle N_{tr} \rangle (z_v)$ . This approach has been already used for the  $J/\psi$  measurements in [8], although some modifications are done here with respect to the former implementation (see [111]).

The basis of the data-driven correction is to equalise the SPD efficiency along the  $z$ -vertex direction. It corrects event multiplicities by the efficiency loss of the detector with respect to a reference region. However, this correction alone is not able to take into account tracklet-to-particle corrections or to correct for the global efficiency loss of the detector. In order to get rid of these effects, the multiplicity obtained with this method is normalised by the multiplicity averaged over events, to get an estimation of  $dN_{ch}/d\eta/\langle dN_{ch}/d\eta \rangle$ . In the cases where this approach is valid, the use of a MC simulation is not needed, reducing the time and difficulty of the multiplicity estimation.

However, when the tracklet-to-particle effects vary with multiplicity, they do not cancel out on the  $dN_{ch}/d\eta/\langle dN_{ch}/d\eta \rangle$  calculation. In this case, this approach is not reliable and the measurement have a large systematic uncertainty. The modifications developed during this thesis are important when the tracklet-to-particle corrections vary with multiplicity, and specially when a thin binning is to be used. They allow a more precise estimation of the event multiplicity, reducing and controlling the resolution biases, as well as reducing the systematic uncertainty of the multiplicity measurement.

## 4.1 Basics of the correction method

The method that is used in this chapter for the event relative charged particle multiplicity determination, is a 1D  $\mathcal{A} \times \mathcal{E}$ -like *data-based* correction for the measured number of tracklets. The tracklets used as multiplicity estimator are selected in the pseudorapidity range  $|\eta| < 1.0$ . In order to have a reasonable SPD acceptance for this  $\eta$  range, the event SPD  $z$ -vertex position has to be constrained to  $|z_v| < 10$  cm. The MC simulations used for the different studies of this chapter are the same productions used for the previous one.

As an illustrative example, in Fig. 4.1 (top) we show for a p-Pb MC sample, the mean number of generated primary charged particles,  $\langle N_{ch}^{gen} \rangle$  ( $|\eta| < 1$ ), and the mean reconstructed tracklets per event,  $\langle N_{tr} \rangle$  ( $|\eta| < 1$ ), as a function of the event interaction  $z$ -vertex coordinate ( $z_v$ ). Since the physical properties of the events do not change with the position where the events have been reconstructed, a flat  $\langle N_{tr} \rangle(z_v) = \langle N_{ch}^{gen} \rangle$  would be expected in presence of a detector with no inactive areas and a homogeneous efficiency. As a result of the SPD inefficiencies and acceptance losses due to inactive modules during the data-taking (see Sec. 3.2), the  $\langle N_{tr} \rangle(z_v)$  is smaller than the generated and is not flat as observed in Fig. 4.1 (top). The drop on the distribution for  $|z| \geq 5.5$  cm is explained by the fact that the chosen  $\eta$  range to count the tracklets begins to be out of the acceptance of the SPD (Eq. 3.2 and 3.3).

An  $\mathcal{A} \times \mathcal{E}$  correction as a function of  $z$ -vertex would be simply  $\mathcal{A} \times \mathcal{E}(z_v) = \langle N_{tr} \rangle(z_v) / \langle N_{ch}^{gen} \rangle$ , as proposed in the previous chapter. Since the goal is to compute relative multiplicities and try to not depend on MC simulations (see section 4.3 for a detailed discussion), a relative correction is proposed. The correction procedure uses the measured  $\langle N_{tr} \rangle(z_v)$  distribution itself and is based on choosing a  $\langle N_{tr} \rangle(z_v^0)$  value as a reference. Then the number of tracklets for each event reconstructed at a given  $z$ -vertex position,  $N_{tr}(z_v)$ , is corrected by the average fraction of missing tracklets at the interaction vertex  $z_v$  with respect to the reference value:

$$(4.1) \quad N_{tr}^{corr}(z_v) = N_{tr}(z_v) \frac{\langle N_{tr} \rangle(z_v^0)}{\langle N_{tr} \rangle(z_v)}$$

In this section the reference  $z_v^0$  used, is such as  $\langle N_{tr} \rangle(z_v^0) = \max(\langle N_{tr} \rangle(z_v))$ . This correction provides the event tracklets multiplicity as if the SPD efficiency was constant with  $z_v$ , and equal to the detector efficiency at  $z_0$ . After this correction the  $N_{tr}^{corr}(z_v)$  distribution is flat, but since the correction uses as reference a region of the SPD where the efficiency is not 100%, it happens that  $\langle N_{tr}^{corr} \rangle(z_v) < \langle N_{ch}^{gen} \rangle$ , Fig. 4.1 (top). In Fig. 4.1 (bottom), the  $N_{tr}$ ,  $N_{ch}^{gen}$  and  $N_{tr}^{corr}$  distributions are shown. We observe also that the  $N_{tr}^{corr}$  distribution is different from the generated one, Fig. 4.1 (bottom). The correction by the missing tracklet-to-particle effects can be overcome by using this method to compute relative multiplicities. If these effects are constant with multiplicity they vanish on the ratio  $N_{tr}^{corr} / \langle N_{tr}^{corr} \rangle$ . In this way, the method does not require a MC to account for the efficiency loss at  $z_v^0$  and the rest of tracklet-to-particle effects. Nevertheless, we discuss in section 4.3 to what extent this is

valid, since we already know from the results in previous chapter that the tracklet-to-particle effects indeed vary with the tracklets multiplicity (Fig. 3.11).

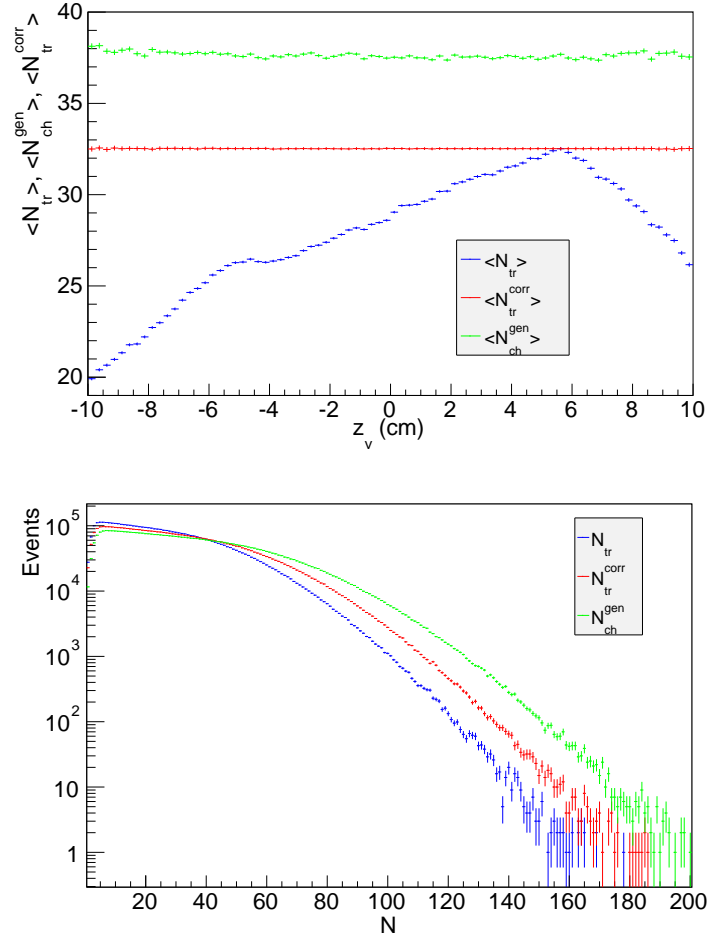


Figure 4.1: Top: Generated event-averaged number of charged particles, reconstructed event-averaged number of tracklets and corrected event-averaged number of tracklets (Using  $\max(\langle N_{tr} \rangle(z_v))$  as reference) as a function of  $z$ -vertex position. Bottom: Generated charged particle distribution, reconstructed tracklets distribution and corrected tracklets distribution.

In addition, due to the integer nature of the number of tracklets and that the correction factor in eq. 4.1 is always the same for events reconstructed at the same interaction  $z$ -vertex, some structures are observed in the  $N_{tr}^{corr}$  distribution as were also seen in Fig. 3.20. When using the correction in this way to perform studies of observables as a function of multiplicity, these structures in the multiplicity distribution can affect the mean multiplicity determination of each subsample if the chosen binning is too thin.

In order to deal with these issues the correction factor can be randomised with a certain dispersion. We denote by  $\Delta N$  the average number of missing/excess tracklets of an event

reconstructed at  $z_v$  with respect to the average tracklets of events reconstructed at a given reference.  $\Delta N$  can be estimated by taking the difference between the number of corrected tracklets with Eq. 4.1 and the measured tracklets:

$$(4.2) \quad \Delta N = N_{tr}(z_v) \frac{\langle N_{tr} \rangle(z_v^0) - \langle N_{tr} \rangle(z_v)}{\langle N_{tr} \rangle(z_v)}$$

Then the correction is generated randomly with a Poisson distribution centered at  $|\Delta N|$ , and the number of corrected tracklets is given by:

$$(4.3) \quad N_{tr}^{corr}(z_v) = N_{tr}(z_v) + \Delta N_{rand}$$

where  $\Delta N_{rand}$  is taken to be positive if the mean number of tracklets at a given  $z$ -vertex is bigger than that at the reference value  $z_v^0$ , or negative in the opposite case. In this way we can add/remove the missing/excess tracklets in a  $z$ -vertex position with respect to the reference value. This is used to equalise the multiplicity along  $z$ -vertex. The  $\langle N_{tr}^{corr} \rangle(z)$  distribution remains flat, and the structures that appeared in Fig. 3.20 in the  $N_{tr}^{corr}$  distribution, are not present when using Eq. 4.3 (Fig. 4.1 bottom). This was the approach used in [111], with the choice of the reference  $\langle N_{tr} \rangle(z_v^0) = \max(\langle N_{tr} \rangle(z_v))$ .

We show in section 4.2 how the Poisson distribution can be used not only to flatten the  $N_{tr}^{corr}$  distribution but also, if wisely employed, to equalise the SPD resolution along  $z$ -vertex direction<sup>1</sup>. The choice of a Poissonian distribution can be justified by the fact that distribution of the number of missing tracklets with respect to the generated number of charged particles ( $N_{ch}^{gen} - N_{tr}$ ) at a given  $z$ -vertex, can indeed be approximatively described by a Poissonian distribution as shown in Fig. 4.2.

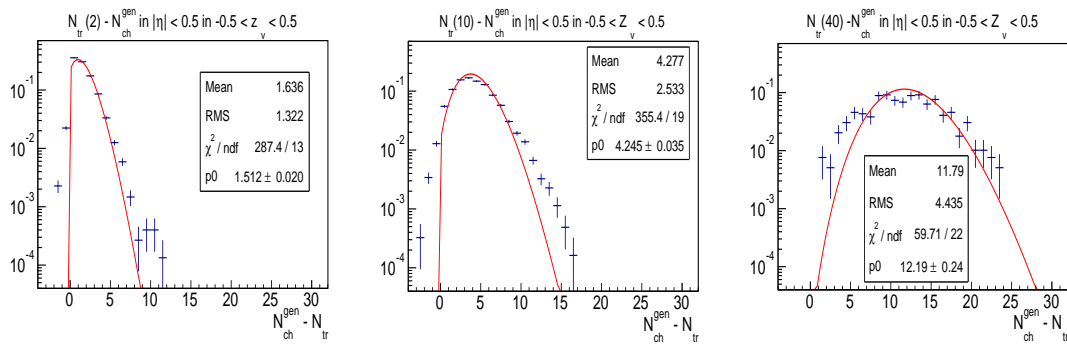


Figure 4.2: Poisson fits of the number of missing tracklets with respect to the generated number of charged particles distribution, at a given  $z$ -vertex for events with 2 (left), 10 (middle) and 40 (right) reconstructed tracklets.  $p_0$  is the mean of the Poisson distribution found by the fit.

<sup>1</sup>the variation of multiplicity resolution with the vertex position was shown in Fig. 3.23

It can be proven that any choice of the reference value  $z_v^0$  leads to a flat  $\langle N_{tr}^{corr} \rangle(z)$  distribution. However in the following subsection a study on the reference choice is presented. We show that there are arguments which make a choice better than the others in terms of equalisation of the event multiplicity resolution as a function of  $z_v$ . Besides, the event multiplicity given by this method is not a measurement of the actual charged particle multiplicity, since it has been corrected by the efficiency loss with respect to the reference value, where the SPD efficiency is not necessarily 100%. It is then necessary to account for the efficiency loss at the reference value  $z_v^0$  and the other tracklet-to-particle corrections, which are treated in section 4.3.

Note that the data-driven correction used here is not able to correctly reproduce the "bin 0" (events with no tracklets detected in the interval  $|\eta| < 1$ ). These events have a null correction, remaining always with zero corrected tracklets when they could come from higher multiplicities. Consequently, this "bin 0" is not taken into account in the multiplicity analyses.

## 4.2 Choice of the reference value

Due to the SPD efficiency variations with  $z_v$ , the resolution of the determination of the event multiplicity varies with  $z_v$  (Fig. 3.23). The Poissonian distribution used to randomise the multiplicity correction introduces an additional dispersion (spread out of the  $N_{tr}^{corr}$ - $N_{ch}$  correlation) to the events reconstructed away of the reference value  $z_v^0$ . This leads to a further loss of resolution in the multiplicity determination. Therefore, the choice of the reference value  $\langle N_{tr} \rangle(z_v^0)$  has to be done wisely in order to not worsen more the resolution in the regions of the detector where the efficiency is already low. The goal of the studies presented in this section is to determine the best reference value  $z_v^0$  for the multiplicity correction.

In order to perform particle production studies as a function of event multiplicity, the event sample is sliced in multiplicity bins<sup>2</sup>. It is then necessary to ensure that the selected subsample in a given  $N_{tr}^{corr}$  bin has the same properties in terms of the true multiplicity, independently on the  $z_v$  positions where the events are reconstructed. The true multiplicity distribution in a  $N_{tr}^{corr}$  bin might be different for samples of events reconstructed at different  $z_v$  regions, due to the differences in the SPD efficiency. As was observed in Fig. 3.23, the event dispersion is bigger in regions of the detector where the efficiency is lower. This results on a smaller resolution, and hence the selected data sample for a given  $N_{tr}^{corr}$  bin in each region is also different, introducing a bias in the multiplicity measurement.

The Poissonian smearing is able to account for dispersion differences with respect to the reference value. With the proper choice of the reference in the correction, this method allows to get a uniform dispersion along  $z$ -vertex. Three possible reference choices have

<sup>2</sup>Note that for the checks performed in this section on MC events, the binning is not the same as the one used for the actual analysis

been made in order to compare the resulting dispersion differences in  $z$ -vertex:  $\langle N_{tr} \rangle(z_v^0) = \min(\langle N_{tr} \rangle(z_v)), \max(\langle N_{tr} \rangle(z_v))$  and  $\text{mean}(\langle N_{tr} \rangle(z_v))$ .

In Fig. 4.3, the dispersion  $N_{tr}^{corr} - N_{ch}^{gen}$  at three different  $z$ -vertex regions for the three reference choices is presented for simulated events. As can be seen, choosing the minimum as reference, the dispersion is roughly the same for every  $z_v$ . This is because the fraction of missing tracklets with respect to the reference value is very small for events reconstructed at  $z_v$  positions with a similar efficiency to that of the reference value (Eq. 4.2). As a consequence, the additional dispersion introduced by the correction method for events reconstructed there, is very small. In this case the additional multiplicity dispersion is applied to the events in more efficient regions of the detector. This degrades the resolution to get it similar to that at the less efficient regions. For the other reference choices, the Poissonian smearing leave unchanged the dispersion in the most efficient regions of the SPD, enlarging it for less efficient regions. The choice of the *max* and *mean* as references, increase the differences of resolution along the detector and thereby the bias.

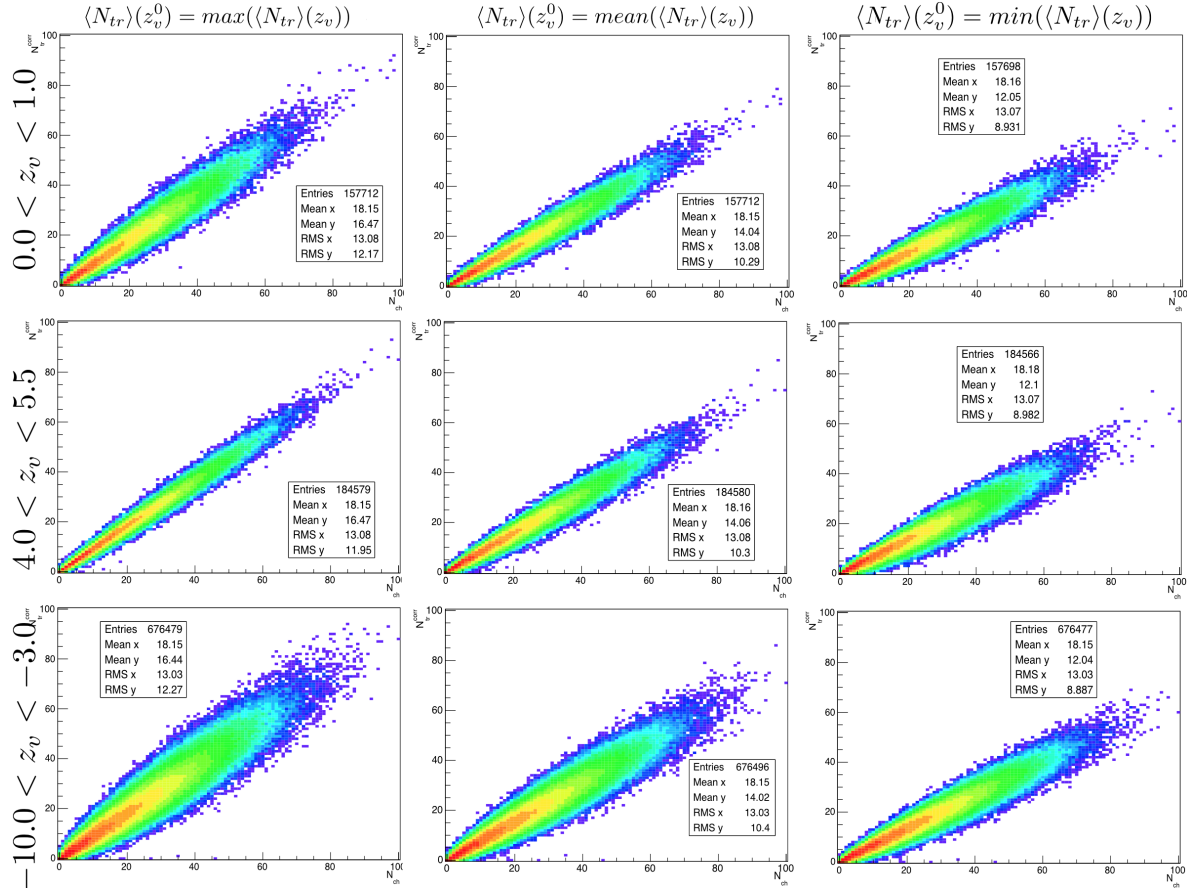


Figure 4.3:  $N_{tr}^{corr}$  as a function of  $N_{ch}^{gen}$  scatter plots. The results are shown for three reference choices:  $\langle N_{tr} \rangle(z_v^0) = \max(\langle N_{tr} \rangle(z_v))$  (left column),  $\text{mean}(\langle N_{tr} \rangle(z_v))$  (middle column) and  $\min(\langle N_{tr} \rangle(z_v))$  (right column), and three different  $z_v$  regions (from top to bottom).

Another way to observe the effect of the reference choice on the data sample selection in multiplicity bins, is the dispersion plot as a function of  $z$ -vertex of the number of generated charged particles corresponding to each  $N_{tr}^{corr}$  bin. As can be seen in Fig. 4.4, choosing the minimum as reference, the dispersion is the same no matter where the events are reconstructed, and hence the selected data sample in a multiplicity bin is uniform in  $z$ -vertex. However, with the other reference choices the dispersion is smaller for regions of the detector where the efficiency is bigger ( $z_v > 0$ ), resulting in non uniformities in the selected data sample along  $z$ -vertex.

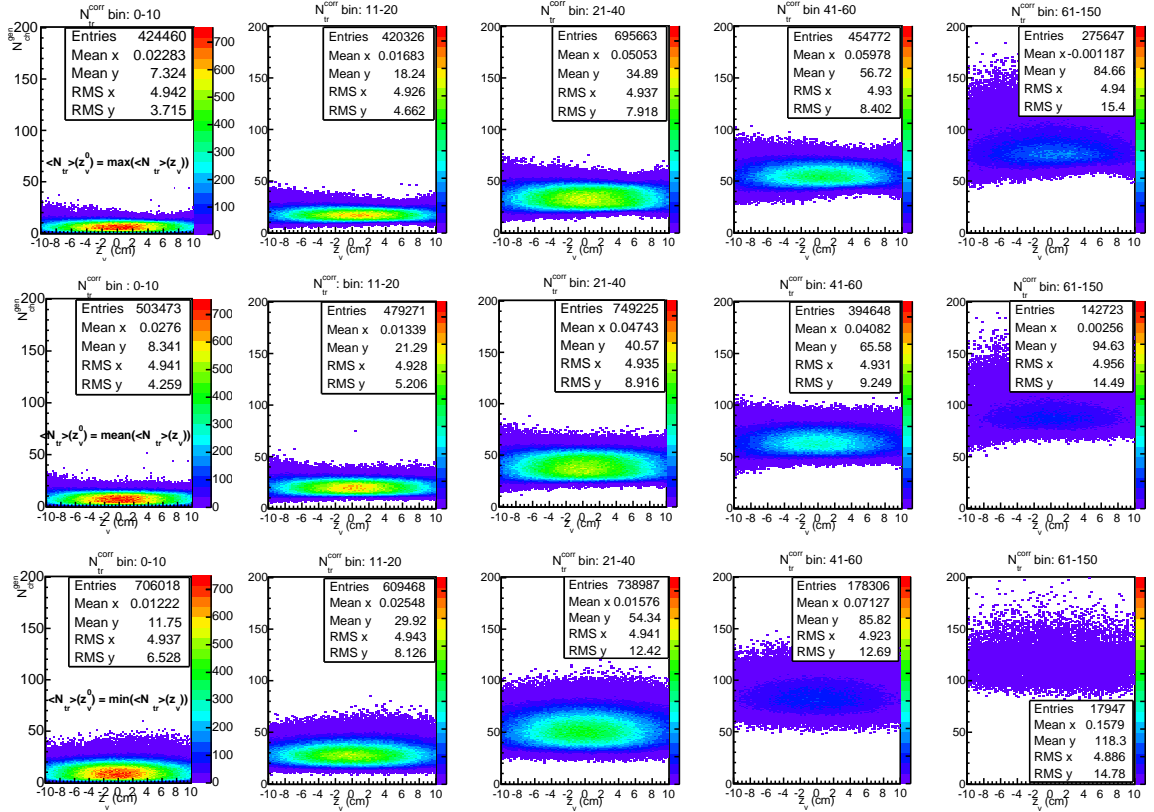


Figure 4.4: Number of generated charged particles in  $N_{tr}^{corr}$  bins (from left to right) as a function of  $z_v$  scatter plots for three reference choices:  $\langle N_{tr} \rangle(z_v^0) = \max(\langle N_{tr} \rangle(z_v))$  (top row),  $\langle N_{tr} \rangle(z_v) = \text{mean}(\langle N_{tr} \rangle(z_v))$  (middle row) and  $\langle N_{tr} \rangle(z_v) = \min(\langle N_{tr} \rangle(z_v))$  (bottom row).

A more clear way to observe the reference choice effect is the average number of generated charged particles,  $\langle N_{ch}^{gen} \rangle$ , as a function of  $z$ -vertex in  $N_{tr}^{corr}$  multiplicity bins. The results for the different reference choices are presented in Fig. 4.5. The distribution is flatter for all the multiplicity bins when choosing the minimum as reference than for other reference choices.

However, there is one drawback of this choice of reference for the correction. When choosing the minimum, we are always removing tracklets to the events to equalize the efficiency along  $z_v$ . Due to this correction, some events can end up with zero tracklets, and thereby not be used in the analysis. In Fig. 4.6, the number of measured tracklets is

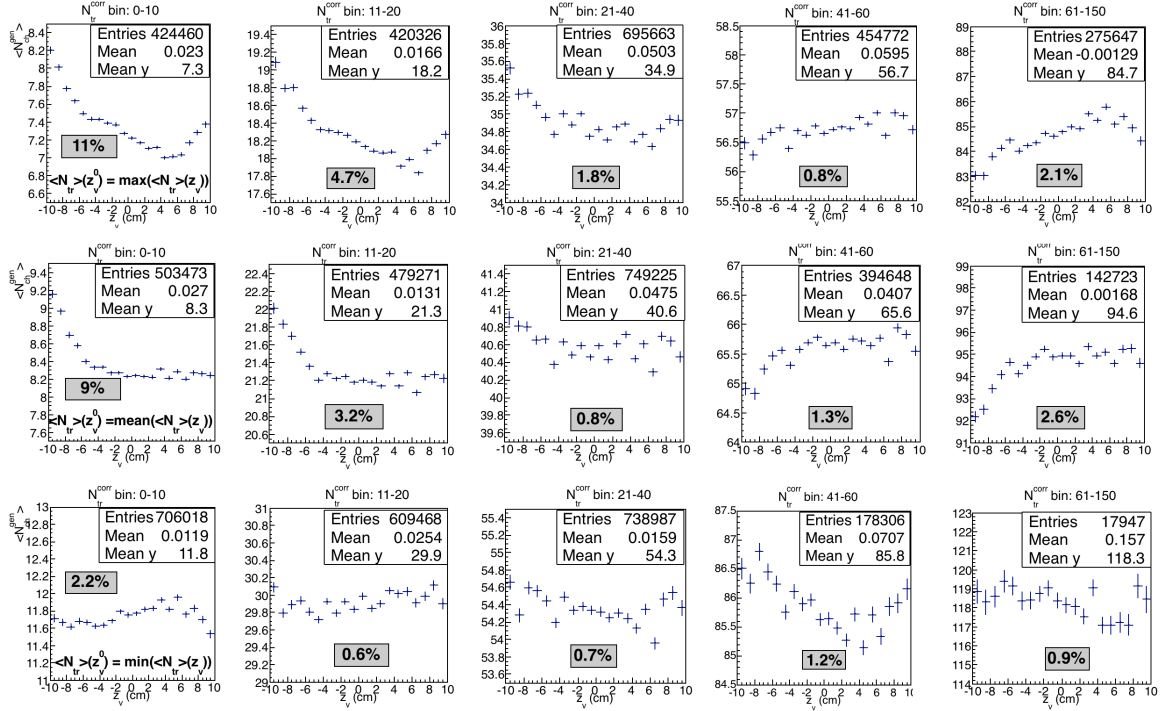


Figure 4.5: Average number of generated charged particles in  $N_{tr}^{corr}$  bins (from left to right) as a function of  $z_v$  for three reference choices:  $\langle N_{tr} \rangle(z_v^0) = \max(\langle N_{tr} \rangle(z_v))$  (top row),  $\text{mean}(\langle N_{tr} \rangle(z_v))$  (middle row) and  $\min(\langle N_{tr} \rangle(z_v))$  (bottom row). The values in the grey boxes are the maximum deviations respect to  $\langle N_{ch}^{gen} \rangle$ .

compared before (blue) and after correction (red) for CINT and CMUL triggers in LHC13d+e data.

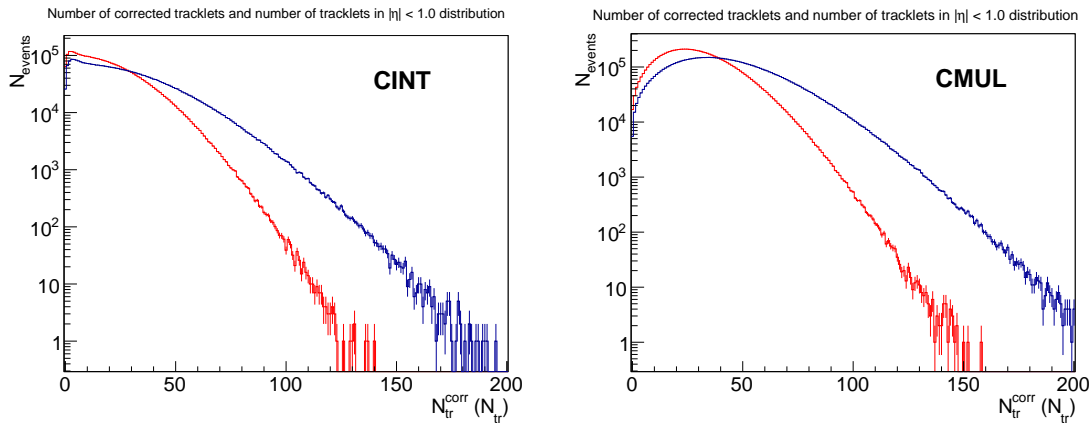


Figure 4.6: Reconstructed (blue) and corrected (red) tracklets distributions in LHC13d+e data for CINT (left) and CMUL (triggers).



We observe how after correction, the distribution is shifted to lower multiplicities, and there are more events in the bin for zero tracklets which are not used in the multiplicity differential analysis. The fraction of events which end up in the zero tracklets bin after the correction is 1.2% and 0.1% for the CINT and CMUL event samples respectively. Since this thesis is focused in the study of  $J/\psi$  production, which is based on the CMUL trigger, this effect play a negligible role. However it can be important in MB-based analysis which require a lot of statistics. Note here also that for the analysis, the data sample is selected up to 140 corrected tracklets (despite of the CMUL distribution reaches 150). This is done to have enough MB statistics in the last bin to compute the corresponding MB average multiplicity (see Sec. 4.3). This removes a 0.08% of the CMUL events which has also a negligible effect on the analysis.

This study allows to conclude that the reference choice is not arbitrary. The best choice to make for the analysis in this thesis is the  $z_v^0$  value such as  $\langle N_{tr}(z_v^0) \rangle = \min(\langle N_{tr} \rangle(z))$ . With that choice, the Poissonian smearing serves to equalise the multiplicity resolution along the  $z$ -vertex direction. In this way, the selected data sample in the multiplicity bins is independent on the event interaction  $z$ -vertex position.

### 4.3 $dN_{ch}/d\eta/\langle dN_{ch}/d\eta \rangle$ axis construction from $N_{tr}^{corr}$

The  $N_{tr}^{corr}$  obtained with this method is not the actual measurement of the charged particle multiplicity as it has been already said. In order to obtain a  $N_{ch}$  estimation, we need to correct by the efficiency loss at the reference  $z_v^0$  and by the other tracklet-to-particle corrections. For this we need to know the correlation of the event-averaged number of corrected tracklets in a certain multiplicity range with the number of primary charged particles. Since the effects of the efficiency variations and resolution with the  $z$ -vertex position have been already corrected, it is enough to use a  $z$ -vertex averaged correction. This correction can be obtained from a MC analysis, computing the correlation between  $N_{tr}^{corr}$  and the generated  $N_{ch}^{gen}$  by means of the  $\bar{\alpha} = N_{ch}^{gen}/N_{tr}^{corr}$  factor. The  $\bar{\alpha}$  factor represents the average tracklet-to-particle effect when the whole SPD efficiency is that of the reference value  $z_v^0$ . It is obtained from a linear fit of the  $N_{ch}^{gen}$  vs.  $N_{tr}^{corr}$  distribution.

In order to obtain the multiplicity coordinate where a given observable value has to be located, the starting point is the MB  $N_{tr}^{corr}$  distribution. The distribution is divided in the same multiplicity bins used to analyse the observable, as it is shown in Fig. 4.7 (top), and the mean number of corrected tracklets is computed for each bin  $i$ :  $\langle N_{tr}^{corr} \rangle_i$ . Then the corresponding value of the event-averaged charged particle multiplicity density in that bin can be computed as follows:

$$(4.4) \quad \langle dN_{ch}/d\eta \rangle_i = \frac{\langle N_{tr}^{corr} \rangle_i \cdot \alpha_i}{\Delta\eta}$$

where  $\alpha_i$  is obtained from the  $N_{tr}^{corr}$ - $N_{ch}^{gen}$  correlation in the given bin (Fig. 4.7 bottom) and  $\Delta\eta = 2$  for events with selected tracklets in  $|\eta| < 1$ .

To get the relative charged particle multiplicity density,  $dN_{ch}/d\eta/\langle dN_{ch}/d\eta \rangle$ , the bin  $\langle dN_{ch}/d\eta \rangle_i$  has to be divided by the event averaged charged particle multiplicity. The event averaged charged particle multiplicity can be obtained using eq. 4.4 to correct the event-average  $N_{tr}^{corr}$ , using the multiplicity averaged  $\bar{\alpha}$  value (global fit (black line) in Fig. 4.7 bottom). In the case where  $\alpha_i = \bar{\alpha}$  the relative multiplicity in a bin  $i$  is simply:

$$(4.5) \quad \left( \frac{dN_{ch}/d\eta}{\langle dN_{ch}/d\eta \rangle} \right)_i = \frac{\langle N_{tr}^{corr} \rangle_i}{\langle N_{tr}^{corr} \rangle}$$

where  $\langle N_{tr}^{corr} \rangle$  is the event-averaged multiplicity of non-single diffractive (NSD) events (see section 4.6). The equality  $\alpha_i = \bar{\alpha}$  implies that the missing efficiency with respect to the reference  $z_v^0$  and the remaining tracklet-to-particle effects (like, for example, the amount of combinatorial background tracklets) are constant with multiplicity. If the equality holds, the relative multiplicity estimation with the data-driven correction method does not need a simulation at all. In previous pp analysis, this assumption has been made for the correction factors and a systematic uncertainty of 4% was added to account for the variations of  $\bar{\alpha}$  with multiplicity [8, 111]. In this analysis the validity of this choice for p-Pb collisions has been revisited using MC data.

In order to test the approach in Eq. 4.5, we have obtained the event-averaged number of reconstructed charged particles in simulation using a constant  $\alpha$  (fit of the whole distribution in Fig. 4.7 (bottom)),  $\langle N_{ch} \rangle_i = \bar{\alpha} \cdot \langle N_{tr}^{corr} \rangle_i$ . To compute the  $\langle N_{ch} \rangle_i^{gen}$  corresponding to a  $N_{tr}^{corr}$  bin, we divide the  $N_{ch}^{gen}$  vs.  $N_{tr}^{corr}$  distribution in  $N_{tr}^{corr}$  bins as shown in Fig. 4.7 (bottom). Then each bin is projected over the  $N_{ch}^{gen}$  axis, and the  $\langle N_{ch} \rangle_i^{gen}$  value is obtained from the mean value of the projected distribution. The results for the p-Pb simulation are shown together in Fig. 4.8. In the right panel of Fig. 4.8 we see that there is a difference between the generated and reconstructed  $\langle N_{ch} \rangle_i$ , which reaches 17 % for the first multiplicity bin. This difference is considered too large to not be corrected for. It is therefore necessary to use different factors for each multiplicity bin. The variation of the  $\alpha$  factors with multiplicity means that the tracklet-to-particle corrections of the SPD vary with multiplicity (we indeed already know it from the results in Chap. 3).

The solution to take this effect away is to use a different  $\alpha_i$  factor for each bin. To get the correction factors, the linear fit of the  $N_{ch}^{gen}$ - $N_{tr}^{corr}$  distribution is performed in multiplicity bins fixing the origin to 0. In Fig. 4.7 (bottom) the individual bin fits and a profile of the distribution are also shown. We observe how the individual bin fits describe much better the variation of the  $N_{ch}^{gen}$ - $N_{tr}^{corr}$  distribution with multiplicity than the global fit. As it can be seen in Fig. 4.9, using a bin by bin correction factor, the reconstructed  $\langle N_{ch} \rangle_i$  values are in much better agreement with the generated values than using a global factor (Fig. 4.8 right).

However there is still a difference of 3.2% (3.6% in the Pb-p case) on the first multiplicity bin. It comes from the deviation of the fit in the first bin from the profile result at

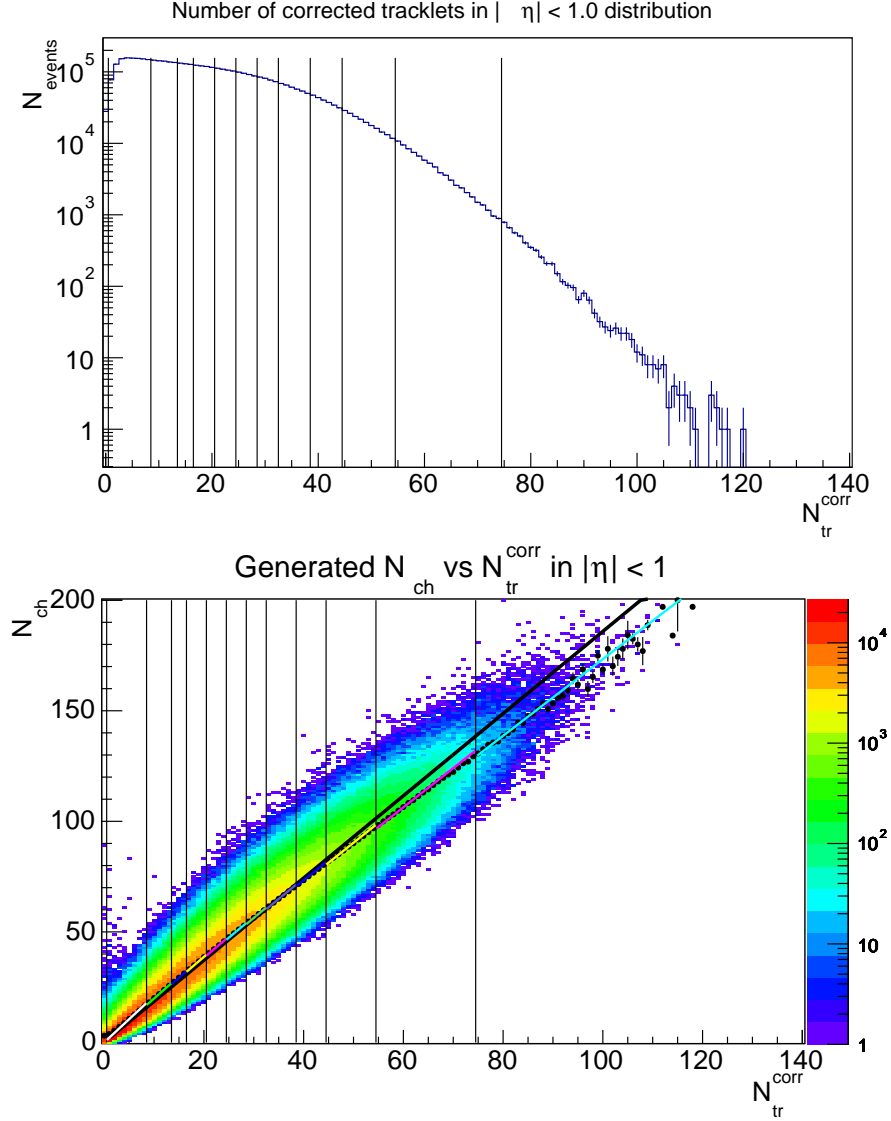


Figure 4.7: Top: Corrected tracklets distribution in LHC13b2\_efix1 MC. Vertical lines delimit the multiplicity bins chosen for the analysis. Bottom: Generated  $N_{ch}$  vs  $N_{tr}^{corr}$  scatter plot. Vertical lines delimit the multiplicity bins chosen for the analysis. The fits are used to get the global  $\alpha$  correction (black line) and the bin by bin ones (coloured lines). The black dots are the profile of the scatter plot.

low multiplicity in Fig. 4.7 (bottom). This is because at very low tracklets multiplicity the correction procedure is delicate, and the data-driven correction has more issues reproducing this bin. In fact, the data-driven correction is not able to correct events with zero reconstructed tracklets. This affects the first multiplicity bin since these events have a small true multiplicity. We therefore add an *ad hoc* term,  $\hat{\epsilon}$ , to correct by this effect in the first bin, by doing  $\alpha_1 \rightarrow \alpha_1(1 + \hat{\epsilon})$ . In this case  $\hat{\epsilon}$  takes the value 0.033 (0.034) for p-Pb (Pb-p). After this, the difference between the generated and measured  $\langle N_{ch} \rangle_i$ , stays below 0.1%. Similar results

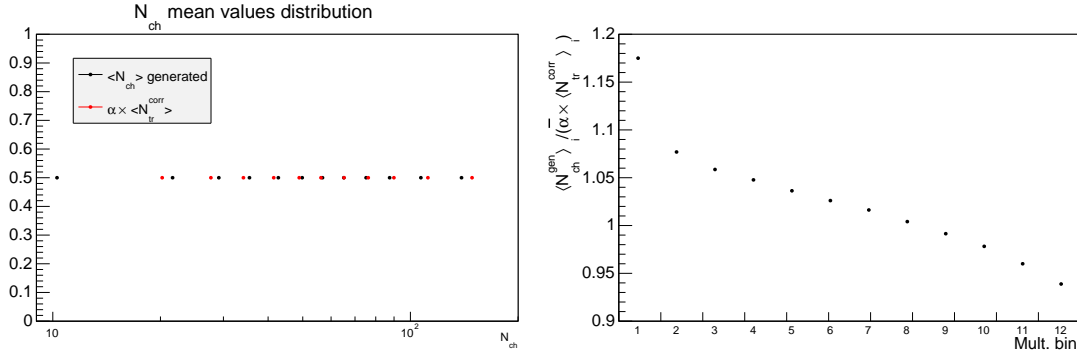


Figure 4.8: Left: Comparison of generated  $\langle N_{ch} \rangle$  and reconstructed  $\langle N_{ch} \rangle$  (obtained as  $\bar{\alpha} \times \langle N_{tr} \rangle$ ) bin by bin. Right: Ratio of the number of generated charged particles and corrected number of tracklets corrected by the missing efficiency through the global  $\bar{\alpha}$  factor.

have been obtained for the Pb-p MC production.

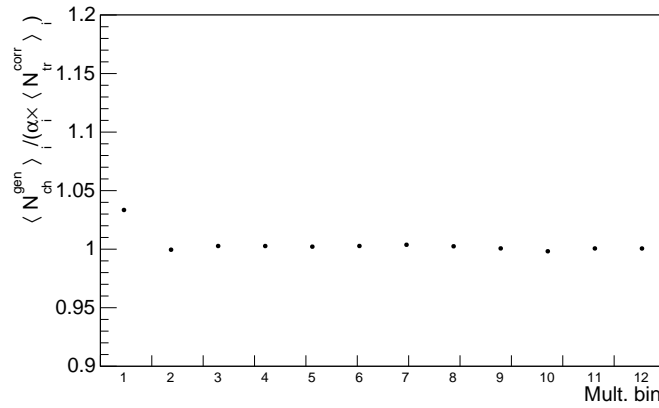


Figure 4.9: Ratio of the number of generated charged particles and corrected number of tracklets corrected by the missing efficiency through the bin by bin  $\alpha$  factors.

It is important to note that, since the  $\alpha$  factors are obtained directly from the correlation between the generated primary charged particles and the reconstructed corrected tracklets using the same method as in data, the correction also takes into account the tracklet-to-particle effects. These effects are averaged over  $z$ -vertex position and for a given multiplicity range. The validity of this  $\alpha$  factors for the correction of the data relies in the good description of these effects in data by the MC. The MC description of the tracklets distributions behaviour obtained in data (due to input  $dN_{ch}/d\eta(\eta)$  and detector) are discussed in Sec. 4.5 and the systematic uncertainties linked to deviations from data are studied in Sec. 4.7.

Finally, the relative charged particle multiplicity density is computed as:

$$(4.6) \quad \left( \frac{dN_{ch}/d\eta}{\langle dN_{ch}/d\eta \rangle} \right)_i = \frac{\langle N_{tr}^{corr} \rangle_i \cdot \alpha_i / \Delta\eta}{\langle dN_{ch}/d\eta \rangle},$$

where  $\langle dN_{ch}/d\eta \rangle = 17.64 \pm 0.01$  (stat.)  $\pm 0.68$  (syst.) (for  $|\eta| < 1$ ) is the overall-averaged (event,  $\eta$  and  $z_v$  -averaged) charged particle pseudo rapidity density, obtained integrating in  $\eta < 1$  [239]. The  $\alpha_i$  factors are obtained using the DPMJET MC productions LHC13b2\_efix1 (p-Pb) and LHC13k2\_fix (Pb-p). The values obtained for  $\langle N_{tr} \rangle(z_v^0) = \min(\langle N_{tr} \rangle(z))$  can be found in Tab. 4.1. We observe that the factors differ about 2% between the p-Pb and Pb-p MC. This is somehow expected since the reference value for the correction differs also by the same amount. This is already an indication that these factors have a weak dependence on the shape of the input  $dN_{ch}/d\eta(\eta)$  distribution. This is further discussed in Sec. 4.7. It is important to note here that there are several additional considerations to make in order to correctly obtain the corrections from the MC which are discussed in Sec. 4.5.

$N_{tr}^{corr}$ bin	$\alpha_i$ (p-Pb)	$\alpha_i$ (Pb-p)
Integrated	$1.859 \pm 0.004$	$1.898 \pm 0.004$
1 - 8	$2.10$ (2.17) $\pm 0.04$	$2.15$ (2.22) $\pm 0.04$
9 - 13	$1.99 \pm 0.03$	$2.03 \pm 0.03$
14 - 16	$1.95 \pm 0.03$	$2.00 \pm 0.03$
17 - 20	$1.93 \pm 0.02$	$1.98 \pm 0.02$
21 - 24	$1.91 \pm 0.02$	$1.95 \pm 0.02$
25 - 28	$1.89 \pm 0.02$	$1.93 \pm 0.02$
29 - 32	$1.88 \pm 0.01$	$1.91 \pm 0.01$
33 - 38	$1.85 \pm 0.01$	$1.89 \pm 0.01$
39 - 44	$1.83 \pm 0.01$	$1.86 \pm 0.01$
45 - 54	$1.81 \pm 0.01$	$1.84 \pm 0.01$
55 - 74	$1.772 \pm 0.004$	$1.802 \pm 0.004$
75 - 140	$1.733 \pm 0.004$	$1.761 \pm 0.004$

Table 4.1: Correction factors to go from  $\langle N_{tr}^{corr} \rangle_i$  to  $\langle N_{ch} \rangle_i$  in multiplicity bins for  $\langle N_{tr} \rangle(z_v^0) = \min(\langle N_{tr} \rangle(z))$ . The errors are the statistical errors from the fits. The values in parentheses for the first bin correspond to the value corrected by  $\hat{\epsilon}$ . Note that multiplicity slices, contain the extremes of the ranges indicated in the left column. See Sec. 4.5 for the considerations needed to compute these factors in simulation.

The study we have presented in this section, shows that the approach used in [8, 111] for the pp collisions analysis, Eq. 4.5, is not applicable for the analysis in p-Pb collisions. The use of Eq. 4.4 and the explained procedure for the multiplicity definition, achieve a more precise estimation of the multiplicity than the one used in the pp analysis. It also reduces considerably the systematic uncertainty. Note that in pp collisions, effects like combinatorial background tracklets are smaller than in p-Pb collisions due to the lower multiplicities. Therefore the approach in Eq. 4.5 could be kept in pp with reasonable systematic uncertainties. In the p-Pb case a multiplicity dependent correction is needed, so does the usage of MC simulations, which hinder the analysis. Consequently a systematic

uncertainty related to the use of a correction extracted from MC has also been considered.

On the other hand, the use of a MC simulation has also the advantage of enabling the possibility to measure the absolute charged particle multiplicity  $dN_{ch}/d\eta$ , through Eq. 4.4. However this requires a separated treatment of the systematic uncertainties, as we do in Sec. 4.7. This allows us to study the  $J/\psi$  production as a function of the absolute and relative multiplicity in the following chapters.

#### 4.4 Equalization of p-Pb and Pb-p multiplicity estimation

This analysis is based on p-Pb and Pb-p rare trigger periods so there might be some differences in the bias introduced by the trigger on each period, which may affect the multiplicity estimation if not treated properly. Besides, the status of the SPD varies among periods as was seen in Fig. 3.3. Another factor to consider is whether the CMUL or MB  $\langle N_{tr}^{corr} \rangle(z_v)$  distributions are used to correct the multiplicity. In order to ensure a consistent multiplicity estimation between both collision systems, these issues have to be addressed.

In Fig. 4.10 (left), the comparison of the event-averaged number of tracklets vs  $z$ -vertex distributions in MB and CMUL triggers for data p-Pb and Pb-p periods is shown. The ratio is flat with bin-to-bin fluctuations smaller than 1.5%. Since the data-driven multiplicity correction method is based on relative variations among  $z$ -vertex, both distributions can be used in an equivalent way to correct the multiplicity. Nevertheless, the statistics in the CMUL distribution is higher than in the MB one. Therefore, we use the CMUL distribution in the correction procedure.

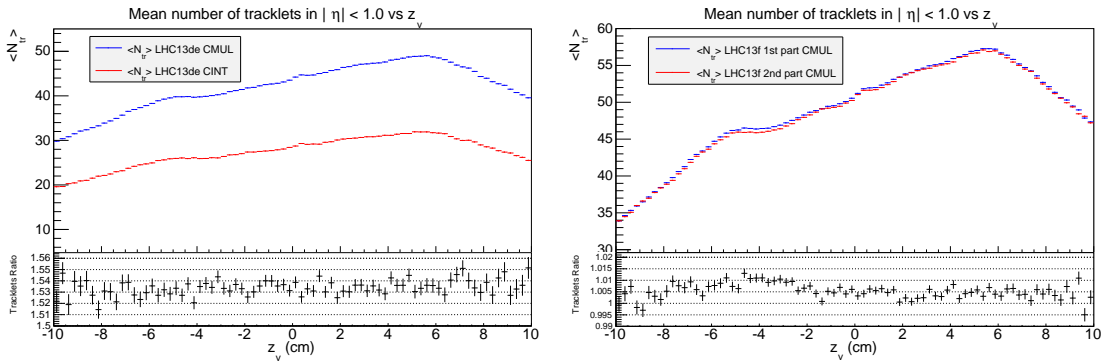


Figure 4.10: Left: Comparison of  $\langle N_{tr}^{corr} \rangle(z)$  for MB and CMUL triggers in p-Pb data. Right: Comparison of the two subperiods in Pb-p data for CMUL trigger.

In order to deal with the SPD status variations, the p-Pb period (meaning LHC13d and e together) is analysed as a whole and the Pb-p period is split in two subperiods depending on the SPD conditions (the full period is analysed together but the corresponding multiplicity correction is assigned depending on the run number). The first part of the LHC13f period has the same detector conditions as LHC13d+e periods which allow to study the variations due to the different charged particle distributions. The changes in the

SPD status can also be observed by comparing the  $\langle N_{tr}^{corr} \rangle(z)$  distributions among the two Pb-p subperiods. In Fig. 4.10 (right) a small difference on the  $\langle N_{tr}^{corr} \rangle(z)$  can be observed due to the loss of 4 SPD modules (see Fig. 3.3). The difference reaches a maximum of 1.3% around  $z_v \sim -4.5$ . Consequently, each distribution is used to correct its corresponding subperiod. In order to arrive to a common definition of multiplicity within the Pb-p period independently on the SPD status, the reference  $z_v^0$  for the correction has to be chosen so that  $\langle N_{tr} \rangle_{\text{subperiod1}}(z_v^0) = \langle N_{tr} \rangle_{\text{subperiod2}}(z_v^0)$ . Fortunately, this condition is satisfied at  $z_v^0 = z_v^{0'} = -10$  cm where  $\langle N_{tr} \rangle(z_v)$  is also at its minimum value for both subperiods. In this way the latter condition and  $\langle N_{tr} \rangle(z_v^0) = \min(\langle N_{tr} \rangle(z_v))$  are simultaneously fulfilled.

The next step is to verify if the event-averaged number of reconstructed tracklets as a function of the interaction vertex is the same among the two collision systems under the same detector conditions. In Fig. 4.11, the event-averaged number of tracklets vs  $z$ -vertex is shown for the data p-Pb period and the first part of the Pb-p period for MB and CMUL triggers. As can be observed, for the MB trigger the ratio of the two distributions is quite flat and close to one, with variations up to 2% in the  $z$ -vertex regions where the SPD acceptance is smaller. In  $z$ -vertex regions where the SPD covers the range  $|\eta| < 1$ , the difference is about 0.5-1%. This result gives an idea of the variations of the SPD  $\mathcal{A} \times \mathcal{E}(z_v)$  due to the different charged particle  $\eta$  distributions<sup>3</sup>. Therefore the reference of  $N_{tr}^{corr}$  for MB events is similar for both collision systems, allowing to use the same multiplicity binning definition. For the CMUL trigger, the LHC13f distribution is shifted about 14% to higher values (Fig. 4.11). This indicates that the bias introduced by the CMUL trigger is different among the two collision systems. However, the ratio of the distributions is quite flat and a 2% variation is observed in the SPD regions with less acceptance, as for the MB trigger.

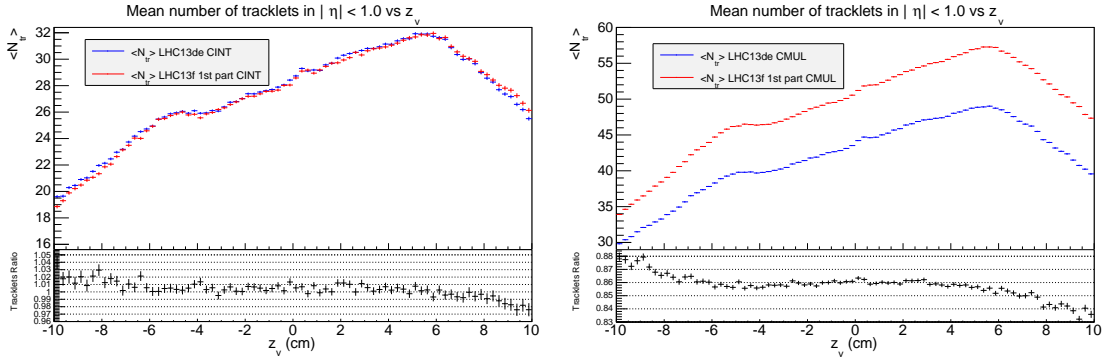


Figure 4.11: Comparison of the event-averaged tracklets vs  $z_v$  for MB (left) and CMUL (right) triggers in p-Pb and first part of Pb-p data periods.

In Tab. 4.2 the average tracklets multiplicity at the chosen reference region of the SPD ( $z_v^0 = -10$  cm) for the CMUL distribution are shown for p-Pb and Pb-p periods. These are the values used for the multiplicity correction. After the correction, the MB  $\langle N_{tr}^{corr} \rangle$  presented in

<sup>3</sup>Remember from Fig. 3.17 right, that both collision systems have the same overall-averaged number of charged particles but their distributions in  $\eta$  are  $(dN_{ch}/d\eta)_{pPb}(\eta) = (dN_{ch}/d\eta)_{PBp}(-\eta)$

Period	$\langle N_{tr} \rangle(z_v^0)$ (CMUL)	$\langle N_{tr}^{corr} \rangle$ (MB)
p-Pb	29.82	19.33
Pb-p	33.91	18.82

Table 4.2: Reference multiplicity values in p-Pb and Pb-p and obtained mean multiplicities in the selected MB data sample for this analysis.

Tab. 4.2 is obtained. It is worth to note here that the MB  $\langle N_{tr}^{corr} \rangle$  are slightly different due to the acceptance variation of the SPD at  $z_v^0$  among p-Pb and Pb-p collisions. If the simulations are able to reproduce the data behaviour, the  $\bar{\alpha}$  factors should be such as at the end  $\langle N_{ch} \rangle$  is the same in p-Pb and Pb-p collisions. Another option would have been to choose a reference such as  $\langle N_{tr} \rangle_{p-Pb}(z_v^0) = \langle N_{tr} \rangle_{Pb-p}(z_v^0)$  (where  $z_v^0$  can also be equal to  $z_v^0$ ) for MB events. In this case similar  $\alpha$  factors from simulations would be obtained, but the condition of the minimum would not be fulfilled introducing a bias in the multiplicity measurement with  $z$ -vertex.

## 4.5 Considerations for the computation of the $\alpha$ factors in MC

In order to correct the obtained  $N_{tr}^{corr}$  in data by the efficiency loss at  $z_v^0$ , a MC simulation analysis is used to obtain the  $\alpha$  factors. In this section, we discuss the additional considerations needed to apply the multiplicity correction in simulation in a consistent way with the data. This is crucial to compute correctly the  $\alpha$  factors in Tab. 4.1.

First of all, the same event cuts and correction procedure as in data are applied to simulated events in order to obtain the  $N_{ch}^{gen}$ - $N_{tr}^{corr}$  correlation. Note here that only generated events which pass the cuts after reconstruction are kept, so the correction factors do not account for event selection efficiency. These effects were already calculated in Sec.3.7 and are taken into account in Sec. 4.6.

To make consistent corrections in data and MC, the reference value to correct the MC has to be chosen in a specific way with respect to the data reference. It is important to take into account that the status of the detector should be properly simulated, but the input charged particle distribution could be different in data and MC. Therefore, we must not choose the reference regarding  $\langle N_{tr} \rangle$  but the  $z_v^0$  position. The reason for this is that if the input charged particle distributions in MC are different from those in data, the same  $\langle N_{tr} \rangle$  values in data and MC correspond to a different  $z_v^0$ . This means that indeed the reference (detector region) is not the same in data and MC. This choice would lead to a wrong  $N_{ch}$ - $N_{tr}^{corr}$  relation.

Let us illustrate this with a simple example: suppose that the efficiency of the detector is 100% for  $z < 0$  and 50% for  $z > 0$ , the same in data and MC. The event-averaged number of charged particles is constant along  $z$ -vertex, being  $\langle N_{ch} \rangle = 10$  for data and  $\langle N_{ch} \rangle_{MC} = 5$  for MC. In such a case, the event-averaged number of measured tracklets would be 10 for



$z < 0$  in data (5 in MC) and 5 for  $z > 0$  in data (2.5 in MC). If we choose as reference  $N_{tr} = 5$ , that would correspond to  $z_v^0 > 0$  in data and  $z_v^0 < 0$  in MC. After applying the multiplicity correction one would obtain  $\langle N_{tr}^{corr} \rangle(z) = 5$  for both data and MC. Consequently, the correction factor extracted from MC would be  $\langle N_{ch} \rangle_{MC} / \langle N_{tr}^{corr} \rangle_{MC} = 1$ , which would lead to a measured  $\langle N_{ch} \rangle$  for data equal to 5, which is wrong.

We have therefore to choose the same  $z_v^0$  in data and MC. The reference values ( $z_v^0 = -10$  cm) used for MC multiplicity correction in p-Pb and Pb-p periods are shown in Tab. 4.3.

Period	$\langle N_{tr}^{corr} \rangle(z_v^0)$ (MB)
p-Pb	19.38
Pb-p	18.98

Table 4.3: Reference multiplicity values for correction in MC for p-Pb and Pb-p.

In addition, we need to ensure that the MC reproduces the behaviour of the detector in data. To test this, several cross-checks are performed in the following. In Fig. 4.12 (left) the event-averaged number of tracklets as a function of  $z$ -vertex is drawn for the first and second subperiods of the Pb-p MC production. The same difference as in Fig. 4.10 (right) is observed due to the loss of 4 SPD modules. If we compare the p-Pb MC production and the first subperiod of the Pb-p one, Fig. 4.12 (right) we observe again the same behaviour as in Fig. 4.11 (left) for data. From this, it can be concluded that the simulation reproduces well the detector behaviour. The comparison between the data and simulation distributions is performed in Fig. 4.13, for similar detector conditions. The number of reconstructed tracklets as a function of  $z$ -vertex in data and MC is compatible within 1% difference. This result reassures that the simulation describes well the SPD data behaviour.

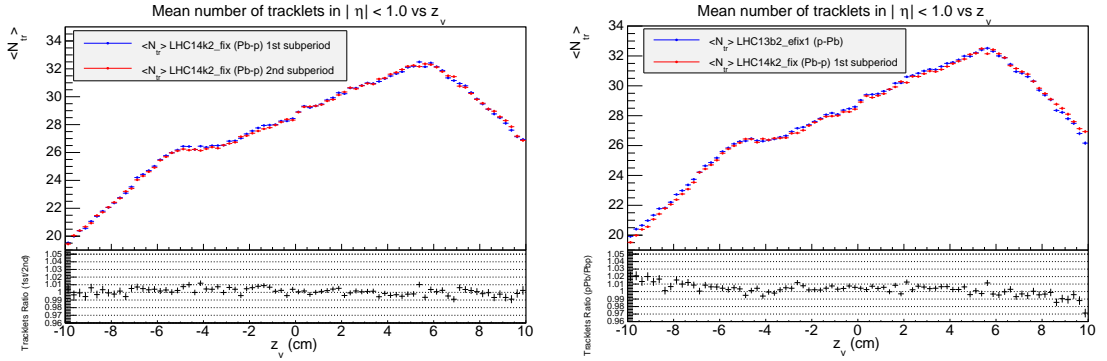


Figure 4.12: Left: Event-averaged number of tracklets as a function of  $z$ -vertex for the first and second subperiods of the Pb-p MC production. Right: Comparison of p-Pb and Pb-p (first subperiod)  $\langle N_{tr} \rangle(z_v)$  MC distributions.

As in data, a different multiplicity correction for each SPD configuration during the Pb-p runs has to be used. We use only two MC runs for each Pb-p subperiod, since the statistics is large enough. The MB statistics in each MC run in these simulations is not proportional to

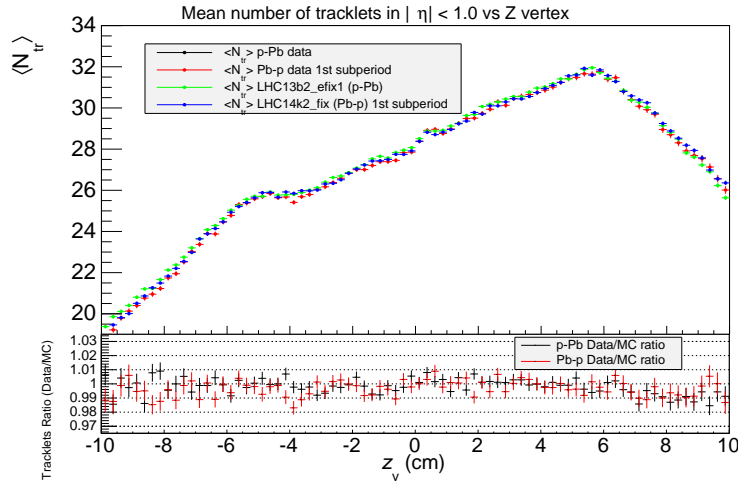


Figure 4.13: Event-averaged number of tracklets as a function of  $z$ -vertex for data and simulated events in p-Pb and first subperiod of Pb-p.

the corresponding runs in data. Therefore, the events on each MC run have to be properly weighted in order to get a correct description of the measured distributions in data. The corresponding fraction of the used MC sample, which represent each MC subperiod  $i$ , has to be determined. It has been verified that the corrections obtained from runs belonging to the same SPD subperiod are completely equivalent, so no additional weighting of each run within a MC subperiod is needed. Then we need to determine the weight of each subperiod in data with respect to the total MB data sample. Therefore the weight to apply to the MC events belonging to a subperiod  $i$  is:

$$(4.7) \quad w^i = \frac{(N_{MB}^i / N_{MB}^{total})_{MC}}{(N_{MB}^i / N_{MB}^{total})_{data}},$$

where  $N_{MB}^{total}$  is the total number of MB events in the full data period, and the total number of events in the MC considered runs. In this way, the fraction of the MC statistics contained in the run (numerator), is weighted by the corresponding fraction of the statistics of this run in the data (denominator). The corresponding values and the subperiods weights are presented in tab. 4.4.

Suberiod	$(N_{MB}^i / N_{MB}^{total})_{MC}$	$(N_{MB}^i / N_{MB}^{total})_{data}$	w
1	50.48%	59.46%	1.1779
2	49.52%	40.54%	0.8186

Table 4.4: MC weights for the two SPD subperiods in Pb-p.

## 4.6 $\langle dN_{ch}/d\eta \rangle$ computation

Taking into account the event selection efficiency correction calculated in Sec. 3.7, the overall-averaged charged particle multiplicity can be calculated with the data-driven correction method. The  $\langle N_{tr}^{corr} \rangle_{NSD}$  can be obtained by correcting the  $\langle N_{tr}^{corr} \rangle$  value in Tab. 4.2 (which is the equivalent to  $\langle N_{tr}^{corr} \rangle_{measured}$  in Sec. 3.7) with the factors in Tab. 3.3. Then by means of Eq. 4.4 and the  $\bar{\alpha}$  correction factor from Tab. 4.1, the  $(dN_{ch}/d\eta)_{NSD}$  is estimated.

The results for p-Pb and Pb-p collisions are listed in Tab. 4.5. The obtained values for the overall-averaged charged particle pseudo-rapidity density are compatible within uncertainties with the value in [239]. This shows that the data-driven method, combined with a further correction to account for tracklet-to-particle effects computed in simulation, is able to give a good estimation of the absolute charged particle pseudo rapidity density.

System	$\langle N_{tr}^{corr} \rangle_{NSD}$	$\langle dN_{ch}/d\eta \rangle$
p-Pb	$18.36 \pm 0.01$ (stat.)	$17.07 \pm 0.01$ (stat.) $\pm 0.68$ (syst.)
Pb-p	$17.86 \pm 0.01$ (stat.)	$16.95 \pm 0.01$ (stat.) $\pm 0.68$ (syst.)

Table 4.5: Measured overall-averaged charged particle pseudo-rapidity density in p-Pb and Pb-p. The systematic uncertainty on the  $\langle dN_{ch}/d\eta \rangle$  value is 4% (see Sec.4.7)

## 4.7 $\langle dN_{ch}/d\eta \rangle_i$ systematic uncertainty

The systematic uncertainties of the charged particle pseudorapidity density measurement discussed in Sec. 3.10 are valid for the multiplicity integrated analysis. Some of the effects could be different for different multiplicity ranges. Therefore, the uncertainty on the charged particle multiplicities in each multiplicity range  $i$ ,  $\langle dN_{ch}/d\eta \rangle_i$  should, in principle, be recalculated following the procedures explained in Sec. 3.10 for each multiplicity interval using the method employed in this analysis. These effects are related mainly to the simulations used to get the corrections. Our data-driven method is an approximation of the SPD  $\mathcal{A} \times \mathcal{E}$  correction, so these uncertainties need to be taken into account in the multiplicity measurement (the  $\alpha$  factors are calculated using the same simulations). In addition, we need to add the uncertainties related to our data-driven approach.

For the results in this thesis, we assume that the uncertainty related to simulation effects of the average multiplicity in each multiplicity bin, is equal to the one of the overall average multiplicity, 2.5% (which results from adding in quadrature the contributions in Sec. 3.10, except the NSD selection uncertainty). Due to the correlation of the integrated and bin multiplicities, some of the uncertainties should partially cancel on the ratio when calculating the relative multiplicity. However, the level of correlation is difficult to determine. Due to the correlation, the uncertainty on the ratio has to be smaller than the individual uncertainties. As an upper limit, we consider that the uncertainty on the ratio is equal to

the uncertainty on the overall average multiplicity. This results in a 3.8% uncertainty for the relative multiplicity in each bin.

In addition to the uncertainties already discussed, those related to the data-driven method used in this analysis must also be taken into account. In the data-driven method, the  $\eta$  variations of the SPD efficiency are not taken into account and the tracklet-to-particle corrections are integrated along  $z$ -vertex and  $\eta$ . These variations might have an impact on the calculated  $\alpha$  factors to compute  $\langle dN_{ch}/d\eta \rangle_i$  from the  $\langle N_{tr}^{corr} \rangle_i$ . In order to estimate the related uncertainty we use the comparison of the p-Pb and Pb-p data results shown in Fig. 4.11. The difference between the average number of tracklets in p-Pb and Pb-p under the same SPD conditions was determined to be about 0.5-1%. This allows to estimate an uncertainty of 1% due to the variations of the  $\eta$  distribution and the fact that the data-driven correction is integrated on  $\eta$ . Besides, the uncertainty on the fits to obtain the correction factors, is included as systematic uncertainty. This uncertainty is between 0.2% (at high multiplicity) and 2% (at low multiplicity) as extracted from Tab. 4.1.

The event cuts applied to the analysis can also have an impact on the measured average multiplicities in the multiplicity slices. This is studied in a dedicated subsection (Sec. 4.7.1), resulting in a 1% systematic uncertainty for the first multiplicity bin, and negligible for the rest of the bins.

The pile-up might also change the obtained  $\langle N_{tr}^{corr} \rangle$ , specially in the highest multiplicity bins. In addition, the correction for each event has a random component, so an uncertainty due to multiplicity bin-flow should also be ascribed. The uncertainties related to these two sources are estimated in dedicated subsections (Sec. 4.7.2 and 4.7.3) resulting to be negligible for the multiplicity estimation.

The data-driven method related uncertainties are added in quadrature to the simulation uncertainty of the relative measurement (3.8%), obtaining a systematic uncertainty of the relative charged particle multiplicity of 4 - 4.5% depending on the multiplicity bin. For the absolute multiplicity, the data-driven related uncertainties are added in quadrature to the simulation related uncertainty of the absolute multiplicity (2.5%), to get an uncertainty of 2.7- 3.5%. For the  $\langle dN_{ch}/d\eta \rangle$  uncertainty, we get 4% by adding in quadrature the 3.8% computed in Sec. 3.10 to the data-driven related uncertainties (due to the  $\eta$  distribution variations and  $\bar{\alpha}$  fit).

#### 4.7.1 Event selection efficiency uncertainty

The event selection used in this analysis rejects mainly events with a small amount of tracklets (Sec. 3.3). The possible biases and corrections for the overall-averaged measurements were already discussed in Sec. 3.7. In this section we focus on how these requirements can affect the measured average multiplicity in multiplicity slices.

The multiplicity slices do not contain events with no reconstructed tracklets in the range  $|\eta| < 1$ , so the MB event selection efficiency (see Sec. 3.10) is not relevant here. On the other hand, the vertex QA (see Sec. 3.7) removes mainly events at very low multiplicities, as

observed in Fig. 3.5. It is then important to take into account the possible effect of removing these events in the average multiplicity, especially in the first multiplicity bin. In Fig. 4.14 the comparison of the  $N_{tr}$  distribution for events passing and not passing the vertex QA is shown for CINT and CMUL triggers. In the first multiplicity slice (1 - 8)<sup>4</sup>, the number of events which do not pass the vertex QA, represents a fraction of 0.9% (0.5%) with respect to the number of selected events (the ones with vertex and passing the vertex QA) in the CINT (CMUL) triggered data sample. This fraction is negligible for higher multiplicities. It can be observed on the ratios in Fig. 4.14, that the events not passing the QA are mainly located at  $N_{tr} = 1$  and  $N_{tr} = 2$ <sup>5</sup>.

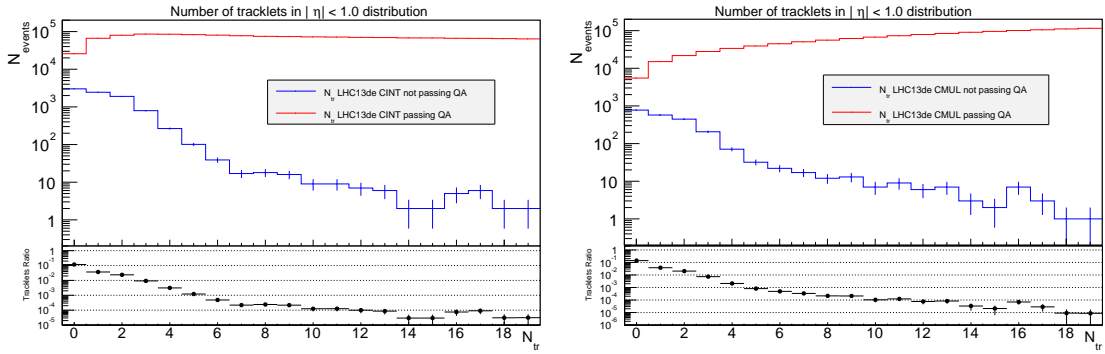


Figure 4.14: Number of reconstructed tracklets distribution in LHC13d+e period for events passing and not passing the vertex QA for CINT (left) and CMUL (right) trigger.

From the result in Fig. 4.14 we can conclude that the event selection effect is only appreciable in the first multiplicity slice. The effect of removing the events not passing the QA changes the average tracklets multiplicity of the first slice by 0.4%. Since the events not passing the QA can not be properly corrected in data, we can not know the effect on the corrected multiplicity. From Fig. 4.6 (left) it can be extracted that the average tracklets multiplicity in the first multiplicity slice decreases by 2.2% after applying the multiplicity correction. We assume that the effect on the average corrected multiplicity in the first multiplicity slice, of including the events not passing the QA is  $0.4\% \times 2.2\%$ . Since this is only a guess of the actual effect, we do not correct for it and a systematic uncertainty of 1% is considered.

#### 4.7.2 Contribution from pile-up events

When several interactions take place during the integration time of the read-out detectors, these interactions are not registered as several events but as one single event, called a pile-up event. The bunch spacing was 200 ns during 2013 p-Pb taking periods. Two types

<sup>4</sup>The extremes of the multiplicity range are *included* in the slice

<sup>5</sup>The events not passing the vertex QA represent a fraction of 4% (4%) of the events passing the cut in the bin of  $N_{tr} = 1$ , 3% (2%) in the bin of  $N_{tr} = 2$  and less than 1% in higher multiplicity bins, for the CINT (CMUL) trigger

of pile-up ought to be considered: in- (same bunch crossing) and out-of (different bunch crossings) bunch pile-up. The V0 detector, which provides the MB trigger signal, has an integration time  $< 25$  ns, the muon trigger has a decision time of  $\sim 25$  ns and the SPD has a read-out time of  $\pm 150$  ns<sup>6</sup>. This implies that the data samples considered here are not sensitive to different bunch crossing pile-up events hence only pile-up from the same bunch crossing is considered.

It can be assumed that the number of inelastic collisions in a bunch crossing follows a Poisson distribution, so the probability of having  $n$  collisions in an event is:

$$(4.8) \quad P(n) = \frac{\mu^n \cdot e^{-\mu}}{n!},$$

where  $\mu$  represents the mean number of collisions per bunch crossing.

$$(4.9) \quad \mu = \frac{\sigma \cdot \mathcal{L}}{N_b \cdot f_{LHC}}$$

$\sigma$  is the inelastic cross section and  $\mathcal{L}$  is the LHC instantaneous luminosity thus the numerator of Eq. 4.9 is the number of interactions per unit of time. The denominator of Eq. 4.9, is the maximum rate of bunch crossings, which is given by the product of the number of bunches in the LHC ring,  $N_b$ , and the LHC revolution frequency  $f_{LHC}$  (11.245 kHz).

In practice, the probability to have at least one trigger of type "trigg", can be expressed as the ratio of the trigger rate ( $Rate_{trigg}$ ) and the bunch crossing rate:

$$(4.10) \quad P_{trigg}(n \geq 1) = \frac{Rate_{trigg}}{N_b \cdot f_{LHC}},$$

since  $Rate_{trigg} \leq N_b \cdot f_{LHC}$ . In the specific case of the MB trigger CINT, the probability of having at least one MB collision selected by the physics selection is:

$$(4.11) \quad P_{CINT}(n \geq 1) = \frac{PS_{CINT} \cdot L0bRate_{CINT}}{N_b \cdot f_{LHC}},$$

where  $PS_{CINT}$  is the fraction of good MB events selected by the physics selection on the recorded events, and  $L0bRate_{CINT}$  is the L0b CINT (MB) trigger rate (see Sec. 2.3.1). The probability to have zero collisions,  $P(0)$ , is  $1 - P(n \geq 1)$ . Using the latter expression and Eq. 4.8 for  $n = 0$ , the mean number of collisions per bunch crossing can be extracted:

$$(4.12) \quad \mu = -\ln\left(1 - \frac{PS_{CINT} \cdot L0bRate_{CINT}}{N_b \cdot f_{LHC}}\right)$$

The  $L0bRate_{CINT}$  can be extracted from the OCDB scalers (see Sec. 2.4) in order to compute the  $\mu$  value. In Tab. 4.6, the period averaged  $\langle\mu\rangle$  values are listed for each collision system analysed.

<sup>6</sup>This means that when a trigger signal is received in the SPD a window of  $\pm 150$  ns is opened

System	$\langle \mu \rangle$	$P(n \geq 1)$	$P(n \geq 2)$
p-Pb (LHC13c*)	0.003	0.30%	$4.5 \cdot 10^{-4}\%$
p-Pb (LHC13d+e)	0.038	3.73%	0.0704%
Pb-p	0.043	4.21%	0.0898%

Table 4.6: Average mean number of collisions per bunch crossing  $\langle \mu \rangle$  in p-Pb (LHC13c MB (\* means that the value is only for the run analysed in this thesis) and LHC13d+e rare trigger periods), and Pb-p collisions. Probabilities to have at least one ( $P(n \geq 1)$ ) or at least two ( $P(n \geq 2)$ ) collisions, according to the poisson distribution.

The correct estimation of the event multiplicity from the SPD tracklets relies on the SPD ability to identify multiple collisions in the event. The intrinsic SPD vertex resolution in the  $z$ -vertex direction is given by  $\sigma_z \approx 900/N_{tr}^{0.7} \mu\text{m}$  for low multiplicity ( $N_{tr} \sim 10$ ) [8]. The event cuts performed in this analysis select mostly events with at least two tracklets, so the worse resolution of a reconstructed vertex is of the order of  $\sigma_z \sim 550 \mu\text{m}$ . Remember that when several vertexes are reconstructed in a bunch crossing, the primary vertex is selected as the one with the highest tracklet multiplicity. This introduces a bias in the measured multiplicity distribution shifting the distribution to higher values. The cuts applied in the tracklets algorithm in [243] correspond to a maximum separation from the interaction vertex of, at most,  $|\Delta z| < 1 \text{ cm}$ . If two or more collisions in the event happen to be closer than that distance, their tracklets are merged in a single collision. In this case the event tracklets are the sum of the tracklets of the piled-up collisions, resulting in a further bias to higher multiplicities of the event multiplicity estimation.

The probability of occurrence of a pile-up event that cannot be resolved by the SPD is given by:

$$(4.13) \quad P_{SPD} = P(n \geq 2) \cdot Q(|\Delta z| < 1 \text{ cm}),$$

where  $P(n \geq 2)$  is the probability of having at least two collisions and  $Q(|\Delta z| < 1 \text{ cm})$  represents the probability of having a distance between two of the collision vertexes smaller than  $1 \text{ cm}$ <sup>7</sup>. This probability is very small for the data taking periods analysed here ( $< 0.1\%$ , see Tab. 4.6), which allows to treat the effect of pile-up in SPD tracklets based multiplicity measurements as a systematic uncertainty only.

In order to estimate this effect on the multiplicity measurement, a toy MC has been developed in this thesis to reproduce the main features of the pile-up. This toy MC uses as input the corrected tracklets distribution of a low pile-up p-Pb period (LHC13c), and the SPD vertex distribution of the period which we want to reproduce. We generate  $N_{events}$  MC (bunch crossings). For each event, the steps followed are:

<sup>7</sup>We do not compute  $Q(|\Delta z| < 1 \text{ cm})$  in this thesis. In [111], the value  $Q(|\Delta z| < 0.8 \text{ cm})$  was estimated to be 7.04%. We will use this values to estimate the order of magnitude of  $P_{SPD}$  in this thesis.

- For each event randomly generate  $n_{collisions}$  (interactions) according to a Poisson distribution centered at  $\langle \mu \rangle$ . Only those events with  $n_{collisions} > 0$  (MB events) are considered in the following steps
- Assign randomly to each collision  $i$  ( $i = 1..n_{collisions}$ ) in the event a pair  $\{z_v^i, N_{tr}^{corr,i}\}$  as follows:
  - $z_v^i$ : Generated from the data  $z_v^{SPD}$  distribution as the one in Fig. 4.15 (left)
  - $N_{tr}^{corr,i}$ : Generated from the data  $N_{tr}^{corr}$  distribution as the one in Fig. 4.15 (right)
- Search of pile up collisions for each event: If two collisions  $i$  and  $j$  in an event have vertex positions such as  $|z_v^i - z_v^j| < 1$  cm, they are merged into a single collision. The  $N_{tr}^{corr}$  of the piled-up collisions are summed, and the vertex position of the resulting collision is set as the one with highest tracklet multiplicity
- Selection of event primary vertex and multiplicity as the one of the collision with the highest tracklet multiplicity
- Events with primary  $|z_v| > 10$  cm are rejected.

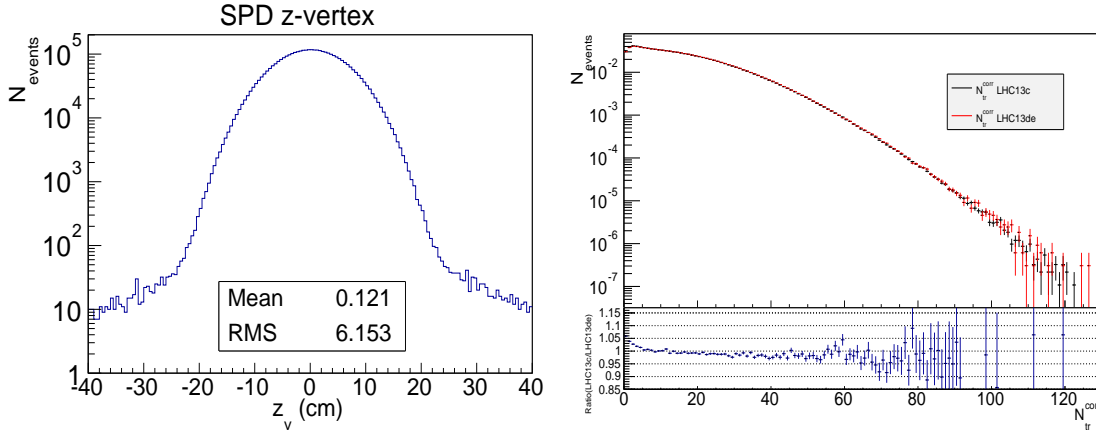


Figure 4.15: Left: SPD  $z_v$  distribution for LHC13d+e periods. Right: LHC13c and LHC13d+e number of corrected tracklets distribution comparison.

Following these steps, a sample of MC MB events is generated, and by comparing its corrected tracklets distribution with the input one, the effect of the pile-up in the multiplicity measurement can be estimated.

First of all, the data results of the self-normalized corrected tracklets distributions in LHC13d+e and LHC13c (low pile-up period) are compared (Fig. 4.15 (right)). At low multiplicity a smaller fraction of events in the LHC13d+e distribution is observed, while at high multiplicity there is a shift towards higher multiplicities though the effect is small. This could be explained by the selection of the collision with highest number of tracklets



as main collision, and also the merging of low multiplicity events into higher multiplicity ones. In order to corroborate this and to study the impact of each effect on the multiplicity distribution, we try to reproduce the features observed in the data with the toy MC.

To begin with, the toy MC is run with the vertex merging algorithm switched off. This allows to study the effect of having several collisions per bunch crossing and choosing the one with the highest number of tracklets as main collision. The fraction of MB events with more than one collision ( $f_{MB}(n > 1)$ ) can be calculated as:

$$(4.14) \quad f_{MB}(n > 1) = \frac{1 - P(0) - P(1)}{1 - P(0)} = \frac{P(n \geq 2)}{P(n \geq 1)}$$

which according to the Poisson distribution (Tab. 4.6) is 1.9% and 2.1% in p-Pb and Pb-p collisions. With the toy MC, we have obtained that the fraction of MB events with more than one collision is  $\sim 1.9\%$  and  $\sim 2.0\%$  in p-Pb and Pb-p collisions, in good agreement with the expectations from the Poisson distribution. In Fig. 4.16 (left) the comparison between the reference tracklets and the MC result for the  $\langle \mu \rangle$  corresponding to p-Pb and Pb-p periods is shown. The effect observed in data (Fig. 4.15 right) is qualitatively well reproduced already without the vertex merging.

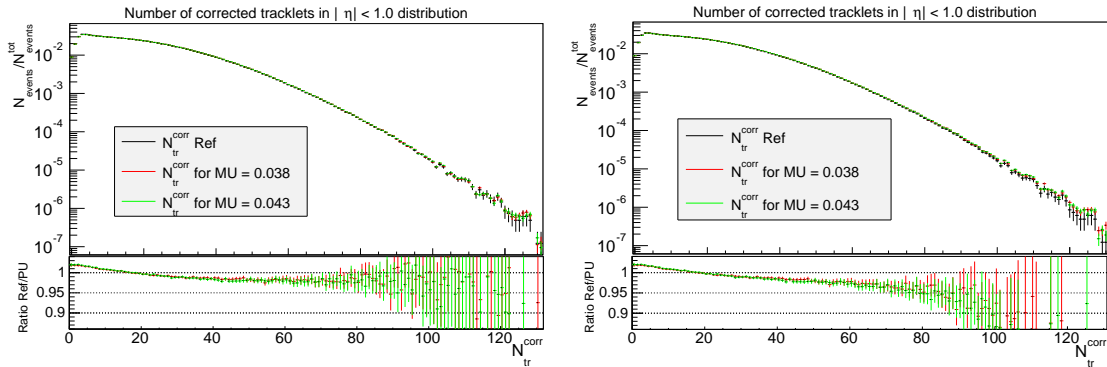


Figure 4.16: Reference corrected tracklets distribution compared with the resulting distribution for the  $\langle \mu \rangle$  factors corresponding to p-Pb and Pb-p periods and its ratio. Left: the vertex merging algorithm is switched off; the observed effect is only due to the choice of the main collision. Right: the vertex merging algorithm is switched on; the observed effect results from the two biases present in data.

As a next step, the vertex merging algorithm is switched on in the MC. The fraction of events with a merged vertex ( $P_{SPD}/P(n \geq 1) \sim 0.14\%$ , eq.4.13) is about 0.17% and 0.18% in p-Pb and Pb-p, which is a negligible contribution as expected. The multiplicity distribution results for the two  $\langle \mu \rangle$  values (p-Pb (LHC13d+e) and Pb-p) are presented in Fig. 4.16 (right). The effect of the merging moves events from low multiplicity to higher multiplicities. The effect is not noticeable at low multiplicity, since the amount of events is higher there. On the contrary, the effect is clearly visible at high multiplicity, where the amount of events is much

smaller. Comparing the left and right panels of Fig. 4.16, we observe that the ratio of the reference multiplicity distribution and the pile-up one is smaller towards high multiplicity with the vertex merging than without it.

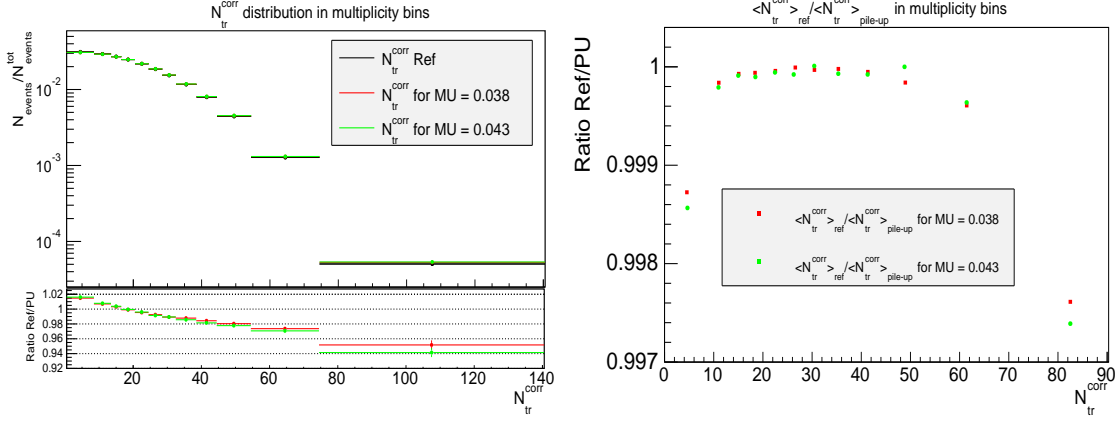


Figure 4.17: Left: Fraction of events in the pile-up distributions (in multiplicity bins) with respect to the reference distribution. Right:  $\langle N_{\text{tr}}^{\text{corr}} \rangle$  ratios of the pile-up over reference values in multiplicity bins.

The effect of pile-up at low multiplicity ( $N_{\text{tr}}^{\text{corr}} \sim 1$ ) mentioned earlier is less accentuated in the MC results ( $\sim 2\%$ ) than in data ( $\sim 4\%$ ). This is probably an effect due to the fact that we consider the vertex resolution as constant with the number of tracklets in the toy MC. In reality, the vertex resolution is worse at low multiplicities, which may contribute to a higher pile-up probability at these multiplicities. However, the toy MC qualitatively reproduces the pile-up effect. At high multiplicity the ratio of the input data distribution and the MC result is quite similar to the one observed in Fig. 4.15 (right).

In order to estimate how the pile-up affects the measurement of  $dN_{\text{ch}}/d\eta$  in each multiplicity bin, the input (low pile-up) and output (toy MC generated)  $N_{\text{tr}}^{\text{corr}}$  distributions are binned. The fraction of events coming from a merging of two or more collisions in each multiplicity bin ( $N_{\text{p.u.}}^{\text{bin}_i} / N_{\text{total}}^{\text{bin}_i}$ ) is presented in Tab. 4.7. The amount of pile-up events becomes relevant only for the last three multiplicity bins.

In addition, the fraction of events in each bin in p-Pb is shown in Fig. 4.17 (left) for the reference and pile-up distributions together with its ratio. This allows a better quantification of the pile-up effect for each bin. The difference varies from 1.7% less events in the first bin of the pile-up distribution, up to 5% (6% in Pb-p) more events in the last bin. This includes the effects of the main collision selection and vertex merging. Furthermore the mean value of  $N_{\text{tr}}^{\text{corr}}$  in each bin is computed. The ratio between the mean values of the pile-up distributions and the reference one are shown in Fig. 4.17 (right). The maximum deviation of the mean value in the bins is 0.15% in the first bin and 0.25% in the last multiplicity bin for p-Pb and Pb-p. The effect is negligible for the rest of the bins. Therefore, we conclude that the pile-up has a negligible effect on the mean multiplicity measurement compared to other sources of

uncertainty. Consequently, no uncertainty is considered due to the pile-up on the estimation of the multiplicity in each bin.

$N_{tr}^{corr}$ bin	Pile-up fraction (p-Pb)	Pile-up fraction (Pb-p)
1 - 8	0.02 %	0.02 %
9 - 13	0.06 %	0.07 %
14 - 16	0.10 %	0.10 %
17 - 20	0.12 %	0.13 %
21 - 24	0.16 %	0.16 %
25 - 28	0.20 %	0.21 %
29 - 32	0.24 %	0.25 %
33 - 38	0.31 %	0.33 %
39 - 44	0.43 %	0.45 %
45 - 54	0.62 %	0.64 %
55 - 74	1.21 %	1.27 %
75 - 140	3.72 %	4.02 %

Table 4.7: Fraction of pile-up events in multiplicity bins obtained with the toy MC. Note that multiplicity slices, contain the extremes of the ranges indicated in the left column

### 4.7.3 Multiplicity bin-flow

The correction to the number of tracklets is randomised following a Poissonian distribution centered in the average number of missing/excess tracklets (Eq. 4.2). In this section, we use this randomisation to estimate the variations of the average multiplicity in each slice. These variations are due to the intrinsic limitations of the multiplicity determination for individual events. Setting a different seed for the random number generator used to assign the multiplicity correction to the events, we can study the effect of the variations on the correction for each event. Due to the correction variations, an event can be put in a different multiplicity bin between two executions of the analysis task (*multiplicity bin-flow*). The effect on the  $\langle N_{tr}^{corr} \rangle$  in each multiplicity bin due to multiplicity bin-flow is studied by comparing the obtained values for different executions.

As an example, the variations of the number of CMUL events in multiplicity bins in the Pb-p period for eight different execution test are shown in Fig. 4.18. The figure shows the relative difference between the most different results ( $\Delta_{max}$ ), the mean value (red line) Eq. B.1, the error on the mean (dotted line) Eq. B.2 and the  $1-\sigma$  dispersion among the values ( $\sigma$ ) Eq. B.4. It is observed that the variation in the number of events in the bins is very small ( $\leq 0.1\%$ ), so we do not expect a big effect on the obtained multiplicities. In Fig. 4.19 the corresponding result of the variation of the  $\langle N_{tr}^{corr} \rangle$  in each multiplicity bin can be seen. Indeed, the variations are always much smaller than  $0.1\%$ . We can therefore conclude that

the bin-flow effect on the bin  $\langle N_{tr}^{corr} \rangle$  is negligible. Similar results are obtained for the p-Pb periods.

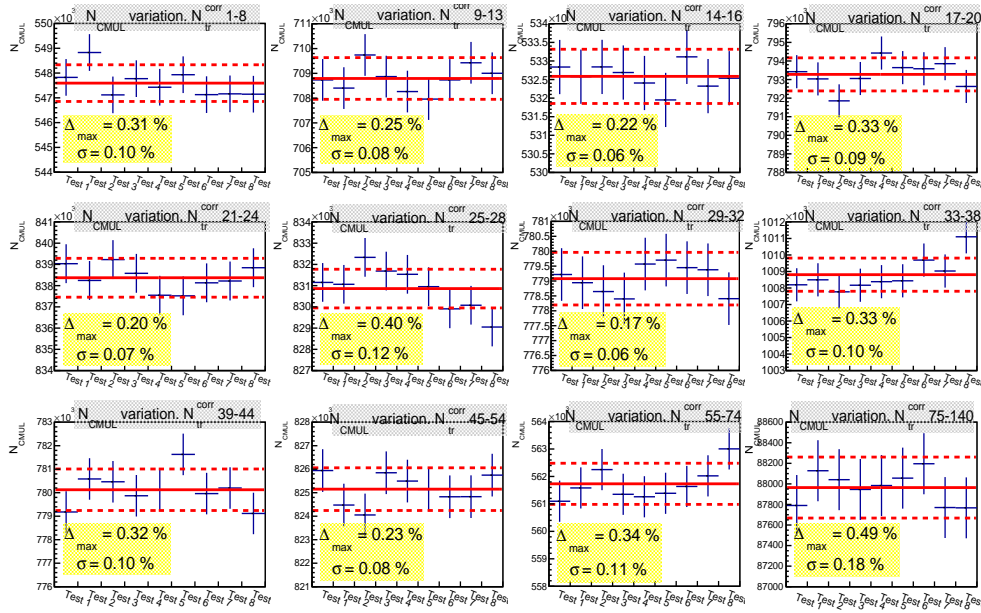


Figure 4.18: Variation on the number of di-muon events in each multiplicity bin due to bin-flow. Each point correspond to a different execution of the task.

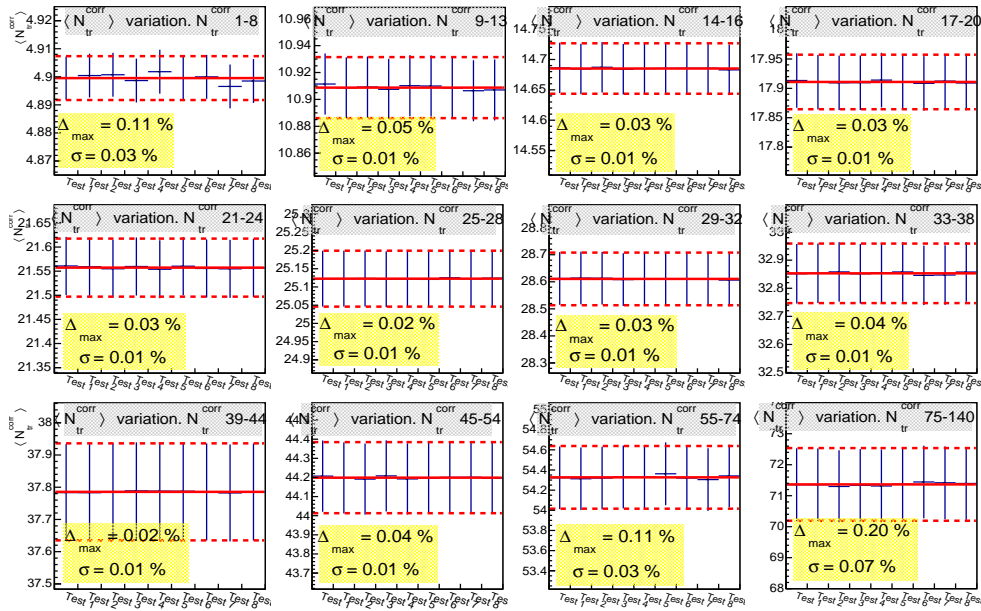


Figure 4.19: Variation on  $\langle N_{tr}^{corr} \rangle$  in each multiplicity bin due to bin-flow. Each point correspond to a different execution of the task.

## 4.8 Multiplicity results

Following the method described in this chapter, we have computed the average multiplicities (absolute and relative) corresponding to the multiplicity bins that will be used for the  $J/\psi$  analyses in the following chapters. The resulting values for the multiplicity axis in p-Pb and Pb-p collisions are summarised in Tab. 4.8 and Tab. 4.9 respectively.

$N_{tr}^{corr}$ bin	$\langle N_{tr}^{corr} \rangle$ (p-Pb)	$dN_{ch}/d\eta$ (p-Pb)	$dN_{ch}/d\eta/\langle dN_{ch}/d\eta \rangle$ (p-Pb)
1 - 8	4.42	$4.79 \pm 0.17$	$0.27 \pm 0.01$
9 - 13	10.96	$10.91 \pm 0.37$	$0.62 \pm 0.03$
14 - 16	14.98	$14.61 \pm 0.45$	$0.83 \pm 0.03$
17 - 20	18.46	$17.82 \pm 0.53$	$1.01 \pm 0.04$
21 - 24	22.46	$21.45 \pm 0.64$	$1.22 \pm 0.05$
25 - 28	26.44	$24.99 \pm 0.75$	$1.42 \pm 0.06$
29 - 32	30.44	$28.61 \pm 0.86$	$1.62 \pm 0.06$
33 - 38	35.32	$32.68 \pm 0.98$	$1.85 \pm 0.07$
39 - 44	41.30	$37.78 \pm 1.13$	$2.14 \pm 0.08$
45 - 54	48.83	$44.19 \pm 1.32$	$2.51 \pm 0.10$
55 - 74	61.36	$54.30 \pm 1.63$	$3.08 \pm 0.12$
75 -140	82.57	$71.43 \pm 2.14$	$4.05 \pm 0.16$

Table 4.8: Multiplicity absolute and relative axes from  $N_{tr}^{corr}$  in p-Pb (LHC13d+e). Only systematic errors are shown, statistical ones are negligible. Note that multiplicity slices, contain the extremes of the ranges indicated in the left column

For future reference during the discussion of the results in this thesis, it is interesting to know the fraction of the MB cross section in each multiplicity bin. The MB cross section fractions in each multiplicity bin  $i$  ( $N_{MB}^i/N_{MB}^{tot}$ ) used in this thesis are shown in Tab. 4.10 for p-Pb and Pb-p data samples.

$N_{tr}^{corr}$ bin	$\langle N_{tr}^{corr} \rangle$ (Pb-p)	$dN_{ch}/d\eta$ (Pb-p)	$dN_{ch}/d\eta/\langle dN_{ch}/d\eta \rangle$ (Pb-p)
1 - 8	4.40	$4.88 \pm 0.17$	$0.28 \pm 0.01$
9 - 13	10.96	$11.13 \pm 0.39$	$0.63 \pm 0.03$
14 - 16	14.98	$14.98 \pm 0.45$	$0.85 \pm 0.03$
17 - 20	18.46	$18.27 \pm 0.55$	$1.04 \pm 0.04$
21 - 24	22.45	$21.89 \pm 0.66$	$1.24 \pm 0.05$
25 - 28	26.44	$25.52 \pm 0.76$	$1.45 \pm 0.06$
29 - 32	30.44	$29.07 \pm 0.87$	$1.65 \pm 0.06$
33 - 38	35.31	$33.37 \pm 1.00$	$1.89 \pm 0.08$
39 - 44	41.28	$38.39 \pm 1.15$	$2.18 \pm 0.09$
45 - 54	48.81	$44.90 \pm 1.35$	$2.54 \pm 0.10$
55 - 74	61.26	$55.14 \pm 1.65$	$3.12 \pm 0.12$
75 -140	82.25	$72.38 \pm 2.17$	$4.10 \pm 0.16$

Table 4.9: Multiplicity absolute and relative axes from  $N_{tr}^{corr}$  in Pb-p (LHC13f). Only systematic errors are shown, statistical ones are negligible. Note that multiplicity slices, contain the extremes of the ranges indicated in the left column

$N_{tr}^{corr}$ bin	$N_{MB}^i/N_{MB}^{tot}$ (p-Pb)	$N_{MB}^i/N_{MB}^{tot}$ (Pb-p)
0	1.94%	2.09%
1 - 8	26.39%	27.04%
9 - 13	14.34%	14.56%
14 - 16	7.92%	8.00%
17 - 20	9.64%	9.73%
21 - 24	8.46%	8.50%
25 - 28	7.20%	7.18%
29 - 32	5.95%	5.84%
33 - 38	6.74%	6.53%
39 - 44	4.55%	4.32%
45 - 54	4.20%	3.87%
55 - 74	2.36%	2.08%
75 -140	0.30%	0.24%

Table 4.10: MB cross section fractions in each multiplicity bin  $i$  ( $N_{MB}^i/N_{MB}^{tot}$ ) used in this analysis in p-Pb and Pb-p data samples.

## **Part III**

# **$J/\psi$ production measurement**





## MUON SPECTROMETER TRACKING EFFICIENCY

The ALICE Muon Spectrometer is specifically designed to measure single and di-muon spectra to study open heavy flavours (D and B mesons), quarkonia (charmonium and bottomonium) and low-mass vector mesons ( $\phi$ ,  $\omega$  and  $\rho$ ) production via the muon decay channel. The reliability of the measurements depends to great extent on the precise knowledge of the detector acceptance times efficiency ( $\mathcal{A} \times \mathcal{E}$ ) of its tracking and trigger chambers. Those are necessary to correct the data taken by the detector for its limited acceptance and efficiency in order to obtain correct values of the production cross sections. The studies performed in this chapter are valid for all the data taken by the spectrometer during the 2013 p-Pb data taking periods.

In this chapter we begin by summarising the basics of the track reconstruction with the muon spectrometer and its acceptance times efficiency determination, to then focus specifically on the single muon tracking efficiency determination from the data. The spectrometer  $\mathcal{A} \times \mathcal{E}$  used to correct the data, is determined by mean of specific Monte Carlo (MC) simulations of the detector, comparing the reconstructed distributions with the simulated ones. Therefore it is crucial to ensure that these simulations reproduce the real conditions of the spectrometer during the data-taking and its evolution with time. In order to verify this, a method to measure the tracking efficiency from the reconstructed tracks is used [111, 252]. This method exploits the redundancy between the detection planes of the spectrometer to determine the efficiency of a given chamber. By comparing the results obtained performing the measurement in data and simulation it is possible to cross-check the validity of the simulation and assess a systematic uncertainty to the  $\mathcal{A} \times \mathcal{E}$  corrections.

## 5.1 Muon Spectrometer track reconstruction

In this section we summarise the main steps of the tracking algorithm, which combines the clusters information of the muon spectrometer chambers in order to build the track candidates. The algorithm begins the reconstruction process in the last two stations (4 and 5) of the spectrometer, since they are exposed to lower particle multiplicities than those closer to the interaction point. The reconstruction method is based on a Kalman filter. The followed steps are [253–255]:

1. The track candidates are built in station 5 by combining the information of the clusters in the two chambers. The initial candidates are line segments joining clusters. For each candidate the local position, direction and impact parameter to the collision vertex (measured with the SPD) are computed, together with their associated uncertainties. Only the candidates within the acceptance of the detector are kept. Also the track candidates are extrapolated to the vertex position through the magnetic field to estimate their momentum using the Lorentz-law<sup>1</sup>. The candidates not passing an initial momentum cut are rejected. The same procedure is performed in station 4. The primary track candidates of station 5(4) are extrapolated to station 4(5). The algorithm looks for at least one compatible cluster in the other station to validate the candidate and the track parameters and covariances of parameters are recalculated. If several compatible clusters are found in the same chamber the track is duplicated to consider all the possibilities.
2. The candidates sharing the same clusters are removed as well as those with impact parameter and momentum out of the given limits.
3. The tracks are propagated to stations 3, 2 and 1, taking into account the effect of the magnetic field (and the multiple Coulomb scattering in the detector material for the covariance of parameters). The algorithm looks for at least one compatible cluster in each station. At each step the candidate parameters are recalculated and only candidates passing the cuts on impact parameter and momentum are kept. If several compatible clusters are found in the same chamber the track is duplicated to consider all the possibilities.
4. Tracks sharing one or more clusters in the last three stations are removed, keeping the candidate with the largest number of clusters or the lowest  $\chi^2$  (goodness of the reconstructed track) in case of equality.
5. The remaining tracks are matched with the trigger tracks to identify the muon(s) which made the trigger.

---

<sup>1</sup>The magnetic field is perpendicular to the tracks

6. The last step is to extrapolate the reconstructed tracks to the collision vertex reconstructed by the SPD. In the process the track parameters are corrected for energy loss and multiple scattering in the front absorber.

The final track parameters are stored in output files to be used in the analysis. These parameters allow, among other things, to compute the invariant mass of the di-muon pairs assuming that the tracks correspond to muons ( $m_1 = m_2 = m_\mu$ ):

$$(5.1) \quad m_{12} = \sqrt{2m_\mu^2 + 2(E_1 E_2 - p_1 p_2 \cos(\theta_{12}))}$$

## 5.2 Muon Spectrometer acceptance and efficiency

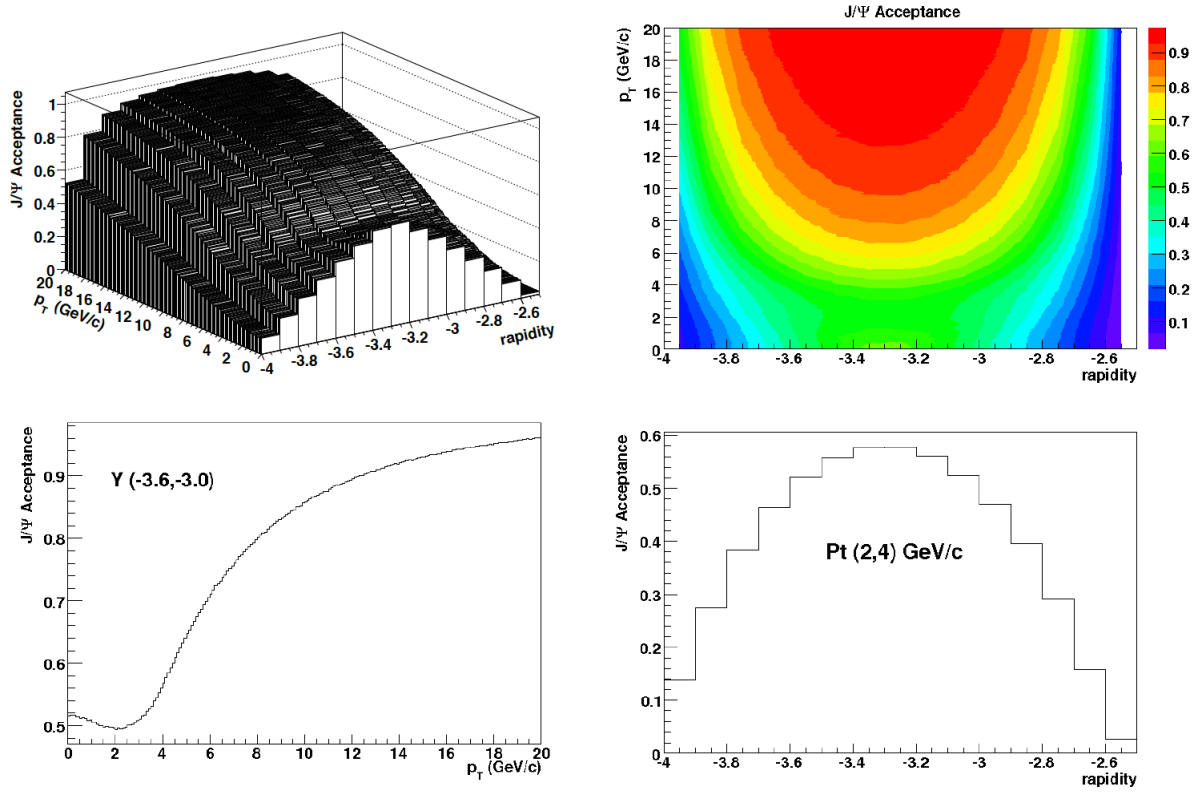
### 5.2.1 Acceptance

The acceptance of the detector is defined as the ratio of the number of muons produced within the angular coverage of the detector ( $N_{acc}$ ) and the total number of produced muons ( $N_{prod}$ ). It gives the fraction of muons which can be, a priori, reconstructed. However this is true for single muons, but when dealing with di-muon pairs coming from a particle decay (i.e.  $J/\psi$ ) the acceptance depends on the particle rapidity, transverse momentum and polarization. It can happen that one or the two muons of a  $J/\psi$  produced within the angular coverage of the spectrometer ends up outside the detection window.

In Fig. 5.1 the  $J/\psi$  acceptance calculated in [117] with the PYTHIA 6.2 event generator is presented as an example. The acceptance decreases in the rapidity regions close to the edges of the detector, since the probability to detect both decay muons, emitted back-to-back in the  $J/\psi$  rest frame, decreases. For fixed rapidity, the acceptance increases with the  $J/\psi$  transverse momentum, since at high  $p_T$  the decay muons tend to be collinear to the  $J/\psi$  direction.

### 5.2.2 Efficiency

The spectrometer efficiency contains the tracking and trigger efficiencies. In the realistic simulations, the actual status of the tracking chambers during the data taking is reproduced by mean of the calibration (pedestals, gains, capacitances and High Voltages (HV)) and alignment objects stored in the OCDB (see Sec. 2.3.3). Furthermore, the intrinsic efficiency of the trigger chambers is calculated from real data using a method developed in [256]. The method allows the computation of efficiency maps for the trigger chambers. These efficiency maps are also used in the simulation to compute the spectrometer efficiency. The spectrometer efficiency for the  $J/\psi$  measurement, corresponds to the number of reconstructed  $J/\psi$  compared to that produced within the spectrometer acceptance.


 Figure 5.1:  $J/\psi$  acceptance as a function of  $p_T$  and  $y$ . [117].

### 5.2.3 Acceptance $\times$ Efficiency determination

The particle distribution we intend to measure can be expressed as:

$$(5.2) \quad \frac{d^2 N(p_T, y)}{dp_T dy} = \frac{1}{\mathcal{A}(p_T, y) \times \varepsilon(p_T, y)} \frac{d^2 N_{rec}(p_T, y)}{dp_T dy}$$

where  $\mathcal{A}(p_T, y)$  stands for the spectrometer acceptance and  $\varepsilon(p_T, y)$  is the efficiency. The product of the acceptance times efficiency,  $\mathcal{A} \times \varepsilon(p_T, y)$ , is obtained from realistic simulations by comparing the reconstructed to the simulated distributions, using the same track selection than the one used in data (see Sec. 2.5).

The problem is that the  $\mathcal{A} \times \varepsilon(p_T, y)$  corrections depend on the simulated distributions, and therefore we need to know a priori the distributions we want to measure. In order to circumvent this issue an iterative technique is used [117]. The following steps are performed:

1. A first estimation of the  $\mathcal{A} \times \varepsilon(p_T, y)^0$  is calculated by simulating a guessed distribution (using a functional form reproducing the measurements at other energies [257]).
2. The  $\mathcal{A} \times \varepsilon(p_T, y)^0$  is used to correct the actual data and get a first estimation of the physics distribution. The physics distribution is fitted.

3. The first simulated distribution is compared to the fit of the physics distribution. A weight,  $\omega(p_T, y)$  is computed from the ratio of the distributions.
4. The weight is applied to each simulated particle in the step 1 to get a new efficiency  $\mathcal{A} \times \varepsilon(p_T, y)^i$ . We go back to step 3 and repeat the process until the simulated (weighed) and corrected physics distributions match (the weight converges). This step avoids to repeat the simulation at each iteration, saving a great amount of computing time.

After this iterative procedure, the parameters of the true distribution are known. We use them to produce a new simulation from which the product of the spectrometer's acceptance times efficiency  $\mathcal{A} \times \varepsilon$  is calculated to correct the data.

### 5.3 Tracking efficiency estimation from reconstructed tracks

In order to verify the realism of the simulations used to compute the spectrometer  $\mathcal{A} \times \varepsilon$ , a method to measure the intrinsic chamber's efficiency from the reconstructed tracks has been developed [111, 252]. This method is based on the tracking algorithm properties. The tracking algorithm requires only one cluster per station in stations 1, 2 and 3 and three clusters in the last two stations. Assuming that the efficiency of one chamber is independent on the others, it is possible to exploit the redundancy between the chambers in the stations to determine the efficiency of a given chamber.

An sketch of the arrangement in stations of the spectrometer chambers and the possible responses of a station to a track are illustrated in Fig. 5.2. The track can have a cluster in both chambers ( $N_{i-j}$ ), a cluster either in chamber  $i$  or  $j$  ( $N_{i-0}$  and  $N_{0-j}$ ), or the track does not fulfil the tracking conditions so it can not be reconstructed ( $N_{0-0}$ ). The total number of tracks crossing the station ( $N_{tot}$ ) is :

$$(5.3) \quad N_{tot} = N_{i-j} + N_{i-0} + N_{0-j} + N_{0-0}$$

Considering that the efficiency of chamber  $i$  ( $\varepsilon_{Ch\ i}$ ) is independent of the efficiency of chamber  $j$  ( $\varepsilon_{Ch\ j \neq i}$ ),  $N_{i-j}$ ,  $N_{i-0}$  and  $N_{0-j}$  can be expressed as a function of the total number of tracks crossing the station:

$$(5.4) \quad N_{i-j} = \varepsilon_{Ch\ i} \cdot \varepsilon_{Ch\ j} \cdot N_{tot}$$

$$(5.5) \quad N_{i-0} = \varepsilon_{Ch\ i} \cdot (1 - \varepsilon_{Ch\ j}) \cdot N_{tot}$$

$$(5.6) \quad N_{0-j} = (1 - \varepsilon_{Ch\ i}) \cdot \varepsilon_{Ch\ j} \cdot N_{tot}$$

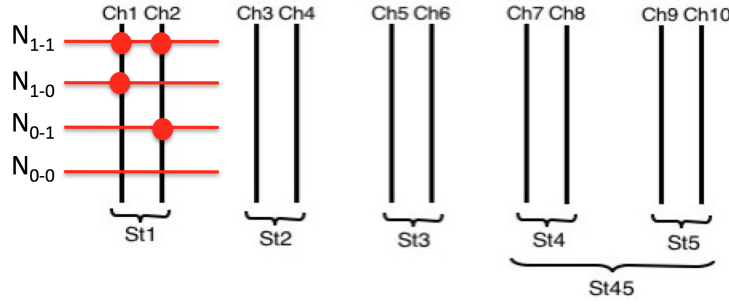


Figure 5.2: Sketch showing the arrangement of the chambers into stations and the possible responses of one station to a track.

Since  $N_{0-0}$  is not measured, the total number of tracks is unknown. However if the chambers efficiency is not zero, the previous equations can be combined to compute  $\varepsilon_{\text{Ch } i}$  and  $\varepsilon_{\text{Ch } j}$ :

$$(5.7) \quad \varepsilon_{\text{Ch } i} = \frac{N_{i-j}}{N_{i-j} + N_{0-j}}$$

$$(5.8) \quad \varepsilon_{\text{Ch } j} = \frac{N_{i-j}}{N_{i-j} + N_{i-0}}$$

For the three first stations the efficiency of a chamber can be measured using the reconstructed tracks for which the other chamber has responded. Following the same recipe, the efficiency for the last four chambers can be computed using tracks for which the other three chambers have responded.

This procedure can be applied also to compute the efficiency of a certain region of a chamber, like a Detection Element (DE), Bus Patch (BP), PCB or MANU. These substructures in the chambers can be seen in Fig. 5.3. The numbering of the DEs is: DE number = Chamber number + DE number in the chamber. The counting of DEs inside the chamber starts at the right hand side of the chamber and continues anti-clockwise.

The individual chamber efficiencies can be combined to compute the efficiency of each station. In the case of the first three stations, the efficiency is defined as the probability for a muon to be detected by at least one of the two chambers:

$$(5.9) \quad \varepsilon_{\text{St } 1(2)(3)} = 1 - (1 - \varepsilon_{\text{Ch } 1(3)(5)})(1 - \varepsilon_{\text{Ch } 2(4)(6)})$$

For the last two stations the efficiency has to be calculated as a whole due to the tracking algorithm requirements. This efficiency is the probability that a muon is detected by at least



Figure 5.3: Visualization of chamber 6 showing its different substructures: DE (red), PCB (blue), BP (green) and MANU (yellow).

three out of the four chambers in the stations:

$$(5.10) \quad \varepsilon_{\text{St } 4-5} = \prod_{i=7}^{i=10} \varepsilon_{\text{Ch } i} + \sum_{i=7}^{i=10} \left( (1 - \varepsilon_{\text{Ch } i}) \prod_{j=7, j \neq i}^{j=10} \varepsilon_{\text{Ch } j} \right)$$

Finally the overall tracking efficiency for single muons can be estimated as:

$$(5.11) \quad \varepsilon_{\text{tracking}} = \varepsilon_{\text{St } 1} \cdot \varepsilon_{\text{St } 2} \cdot \varepsilon_{\text{St } 3} \cdot \varepsilon_{\text{St } 4-5}$$

## 5.4 Biases of the efficiency estimation from reconstructed tracks

It is important to note that the chambers single muon tracking efficiency measured with this method, is intrinsically biased due to non-uniformities on the efficiency within the chamber themselves. For now, we only measure the average efficiency per chamber, or at most DE by DE. This means that we can miss local correlations between the chambers. In addition, the average efficiency measured for a chamber is modified by the local variation of the efficiency of the other chambers. Two different correlation effects can take place: correlation and anti-correlation effects.

In Fig. 5.4 an illustration of the possible correlation effects is shown. Let us suppose that we want to measure the efficiency of a DE in chamber 1. As we see, at both the left and the right hand side panels, there is a half of the DE which is not working (grey shaded area) and the other half which is working. If we assume that the working area has an efficiency of 100%, the true average efficiency of the chamber would be 50%. Now, we use the method to measure the efficiency to illustrate how the efficiency of the chamber 2, can change the

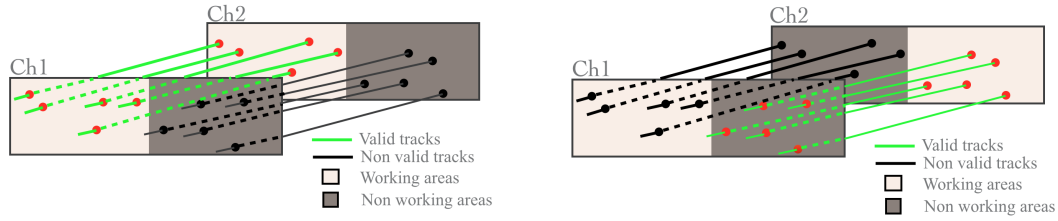


Figure 5.4: Sketch of a CDA (left) and ACDA (right) (see text for details) to illustrate the bias on the efficiency measurement from reconstructed tracks.

measurement of the efficiency of chamber 1. The left panel shows the case of a dead area in chamber 2, in front of the dead area in chamber 1, a Correlated Dead Area (CDA). As we see, there are only 5 tracks (out of 10) which are detected by chamber 2, so only 5 tracks available for the measurement. Chamber 1 detects the 5 tracks available for the measurement so the measured efficiency is 100%. A CDA thus leads to an overestimation of the efficiency. On the right panel the efficiency of chamber 2 has changed with respect to chamber 1. Now the dead areas in the chambers are crossed, which is called Anti-Correlated Dead Area (ACDA). In this case there are also 5 tracks for the measurement from which chamber 1 detects none. The method yields a measured efficiency of 0% for chamber 1. Therefore, the ACDA leads to an underestimation of the efficiency. These examples allow to show that as soon as the redundancy in the measurement is broken, the method fails.

These effects make this method unreliable to measure the absolute efficiency of the spectrometer. The correlation effects could be reduced by computing the efficiency not chamber by chamber but for DEs, MANUs or PADs. Then we could construct an efficiency map for each chamber and use it on the specific simulations ( $J/\psi$ ,  $\Upsilon$ , ...) to compute the spectrometer's efficiency. However, this measurement is limited by the statistics and the problem of measuring the efficiency for those regions in front of dead zones.

In [111, 258, 259] the effects of CDAs were corrected for, to get a better estimation of the tracking efficiency and of the related systematic uncertainties. This is not done in this thesis because the dead zones have been studied in detail, and carefully reproduced in simulation, as is described in the following section. Therefore, the same biases affect the measurement in both data and simulation, and the differences directly provide a good estimate of the systematic uncertainty on the description of the detector.

## 5.5 Efficiency studies for p-Pb data-taking periods

In this section we present the different studies performed on the data, and the comparison with the results from simulations to test the validity of the detector description. These studies are based on those made for previous pp and Pb-Pb data taking periods in [111, 258, 259]. In addition, in this thesis the efficiency as a function of the run number is also studied



chamber by chamber and DE by DE, which allows a better identification of the runs where the detector had issues. The starting point is the measurement of the single muon tracking efficiency in data using the reconstructed tracks. In the following subsection we show an example of a study to identify the issue causing an apparent loss of efficiency. Then the results found in data are compared to those in MC.

### 5.5.1 Efficiency computation in data

The results shown here are intended to illustrate some of the issues faced when computing the efficiency from the reconstructed tracks. First of all, the overall single muon tracking efficiency,  $\varepsilon_{tracking}$ , is studied as a function of run for the data-taking period LHC13e in Fig. 5.5 (top). We have spotted three suspicious runs for which the efficiency drops significantly (196091, 196105 and 196107). In order to identify the source of the problem, the individual chamber efficiency,  $\varepsilon_{Ch\ i}$  is also studied as a function of run. The responsible for the efficiency loss are identified to be the chambers 3 and 4, where a drop is also observed (Fig. 5.5, bottom panels).

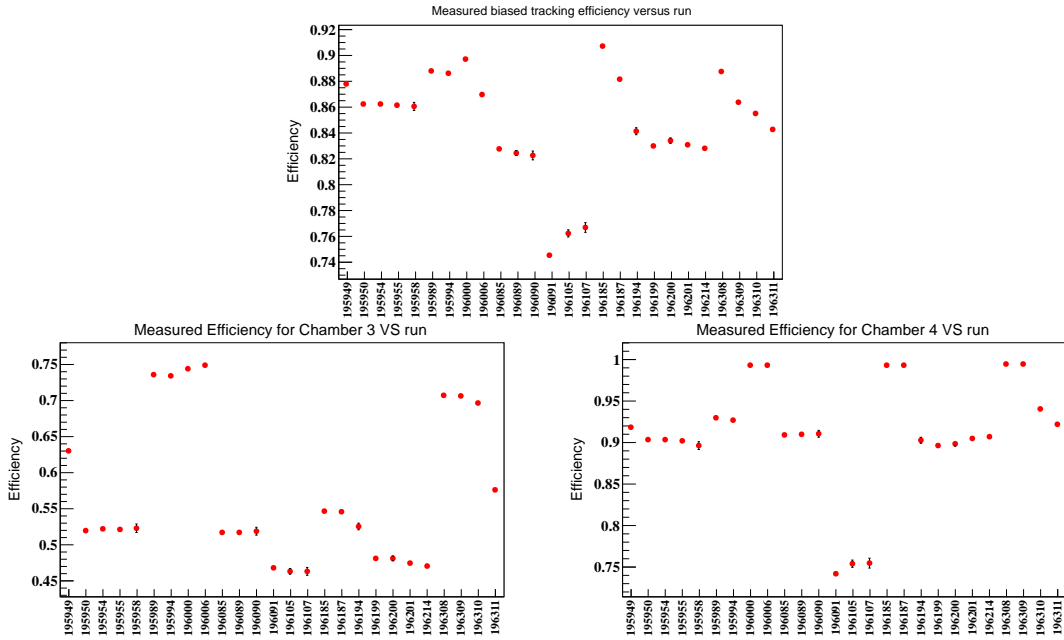


Figure 5.5: Top: Measured single muon tracking efficiency as a function of run number for data-taking period LHC13e. Bottom: Measured single muon tracking efficiency for chambers 3 (left) and 4 (right) as a function of run for the same period.

The run dependence of the efficiency is then studied for each DE of these two chambers. A large anti-correlation for DE 0 and 1 is observed for these three runs, as shown in Fig. 5.6, which causes an artificial reduction of the measured efficiency. Thanks to the redundancy of the detection planes in the stations, there are efficient DEs in front of the dead ones. The tracks can be actually reconstructed hence the station is in reality more efficient than what

is measured with this method. This anti-correlation effect can be also seen in Fig. 5.7 where the status map<sup>2</sup> for these two chambers is shown for run 196091. This is an example of the bias on the efficiency measurement with the reconstructed tracks. However, this bias is expected to be the same when measuring the efficiency in data and MC, so we are more interested in their comparison than in the individual results.

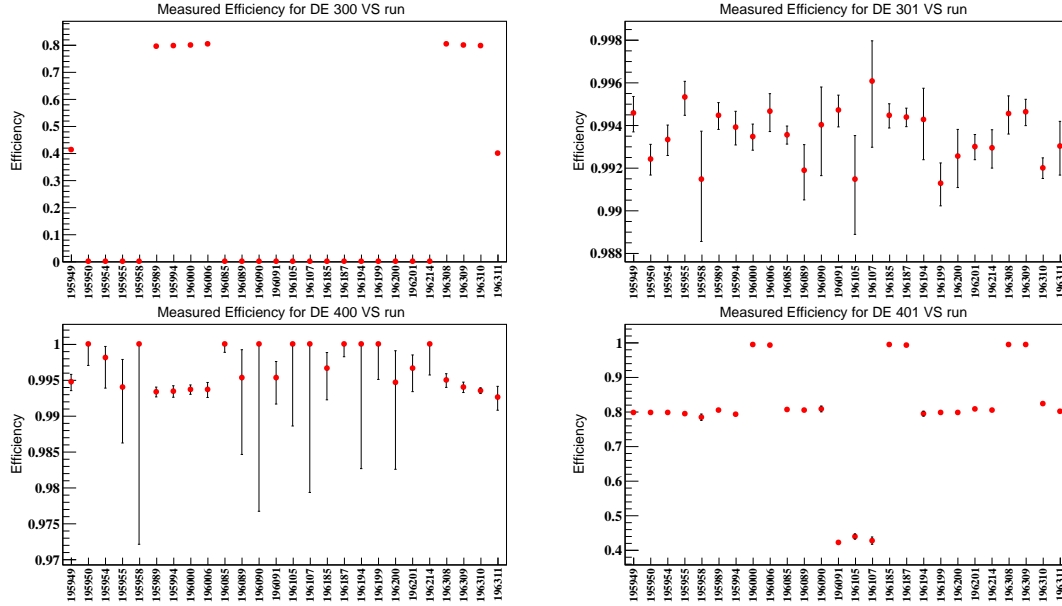


Figure 5.6: Measured single muon tracking efficiency for DEs 300, 301, 400 and 401 as a function of run for the LHC13e period.

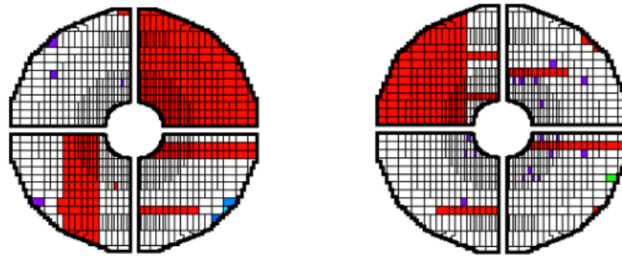


Figure 5.7: Status map at MANU level showing the dead zones (red) in chambers 3 (left) and 4 (right) during run 196091 of the LHC13e period.

<sup>2</sup>The status map, is a map of the chambers that contains the global status (*good/bad*) at the pad level. It is computed during the digitization of the raw data using informations like pedestal, gain and HV values during the run

### 5.5.2 Comparison data-MC efficiency results

In this section we compare the results obtained in data with the ones in simulation. As an example, we focus on the results obtained for LHC13f period. In Fig. 5.8 the efficiency results for data and MC are shown together with the ratio, as a function of run number, of the azimuthal angle ( $\phi$ ), rapidity ( $y$ ) and transverse momentum ( $p_T$ ) of the muons. In general we observe that the efficiency is very variable along the period. The variation of the efficiency as a function of  $\phi$  and  $y$  may indicate the presence of low efficient regions in the detector, while the  $p_T$  dependence is quite flat. In general, the shape of the measured efficiency in data is more or less well reproduced by the simulation but its magnitude is not. The efficiency is systematically lower in data than in MC. The differences reach about 16% in the run by run efficiency, between 5 to 12% in rapidity, around 9% as a function of  $p_T$  and up to 27% for some  $\phi$  regions. This means that the MC is not reproducing well the detector behaviour in data and specially some regions of the detector. To further investigate these issues we need to study the efficiency chamber by chamber and DE by DE to identify the problematic regions in a similar way as was done in Sec. 5.5.1.

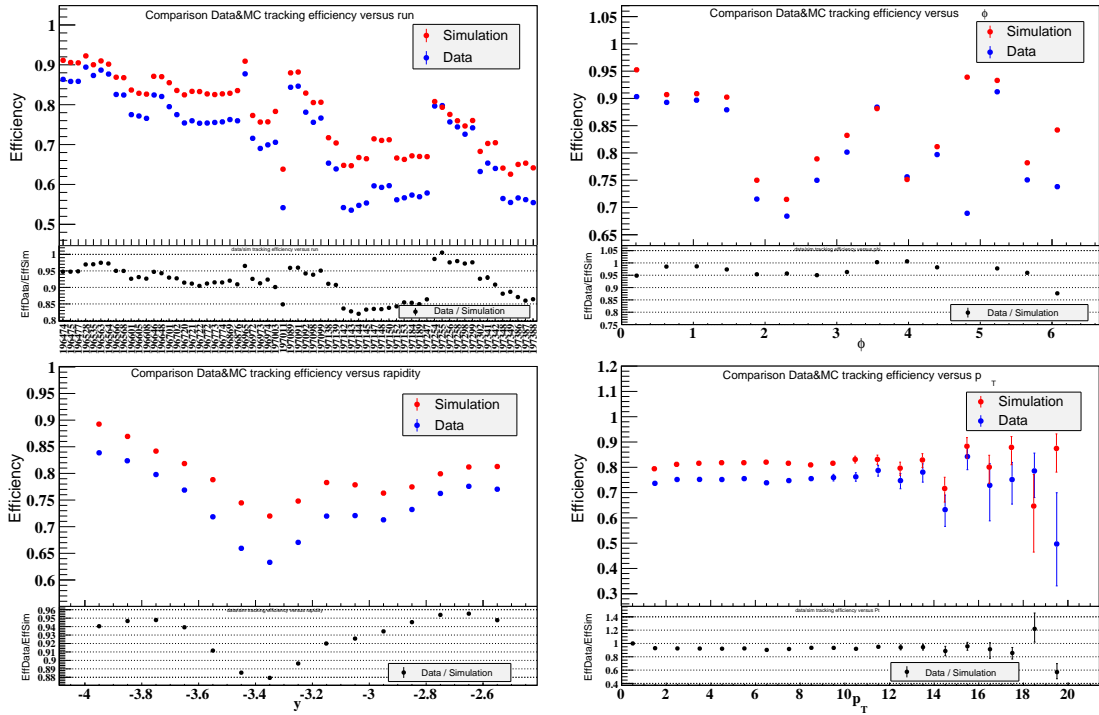


Figure 5.8: Single muon tracking efficiency results from reconstructed tracks in data and MC for LHC13f period as a function of run number (top left),  $\phi$  (top right), rapidity (bottom left) and  $p_T$  (bottom right).

In order to illustrate the issues found during the comparison study, we have selected chamber 10 among the problematic chambers, since it contains several of the issues we have faced. The measured efficiency of chamber 10 as a function of run number and the average

measured efficiency in data and MC during the LHC13f period as a function of DE are shown in Fig. 5.9. During this study we have considered as problematic those DEs for which the difference between data and MC was bigger than 5%. In the figure the DEs under study are marked with coloured squares to allow a more visual comparison with the subsequent plots. Each colour correspond to a DE number: 1010 (red), 1011 (green), 1018 (blue) and 1025 (yellow). The difference between data and MC is also indicated, and it reaches up to 34%.

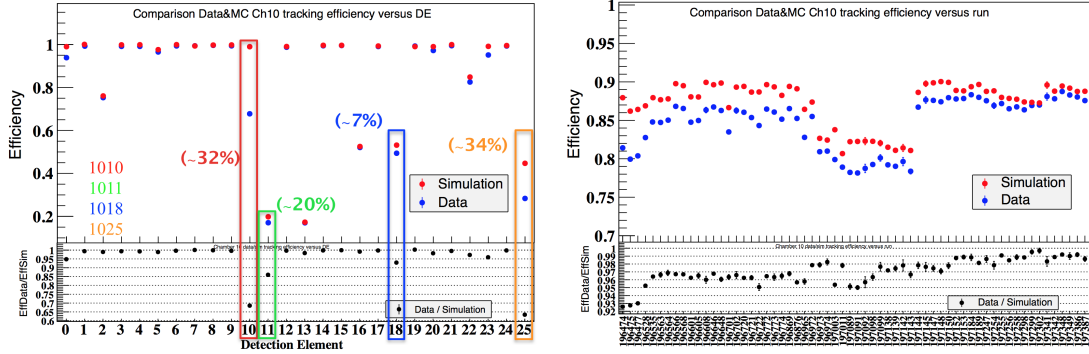


Figure 5.9: Left: Chamber 10 average measured single muon tracking efficiency during LHC13f period as a function of DE. The problematic DEs are highlighted with coloured squares. Right: Chamber 10 measured single muon tracking efficiency as a function of run during LHC13f period.

After studying the DEs efficiency in chamber 10 for the LHC13f runs, the run 196474 has been chosen in order to compare the cluster maps<sup>3</sup>, between data and MC. The results are shown in Fig. 5.10, and the problematic DEs are marked with the same colour coding as before. The cluster map for the data shows a PCB in DE 1010 which is dead but was included in the reconstruction for the MC. After revision of the status map of the concerned runs it was observed that the PCB was marked as *good* during those runs. This means that there was a problem with that PCB during the data-taking that was not spotted online. In the case of DE 1011, we could not identify a difference which could be the responsible of the 20% difference. However, if the cluster map for data and MC is examined for the other chambers in the last two stations, we observe an ACDA in chamber 8 for that DE in data (the data taking algorithm requires at least 3 clusters in the last 4 chambers, so to measure efficiency in chamber 10, the chambers 7, 8 and 9 must have responded). This ACDA is not present in the MC, due to a PCB which was not taking data but is not marked as *bad* in the status map. This is causing an artificial loss of efficiency in data, but it is not reproduced in MC. The problematic PCB is marked in black in Fig. 5.11. Finally for DEs 1018 and 1025 a clear reason for the discrepancy was not found, since the difference could not be ascribed to a precise substructure of the detector.

<sup>3</sup>Cluster Map is a 2-D map (x,y) of the spatial coordinates of the reconstructed clusters in the chambers

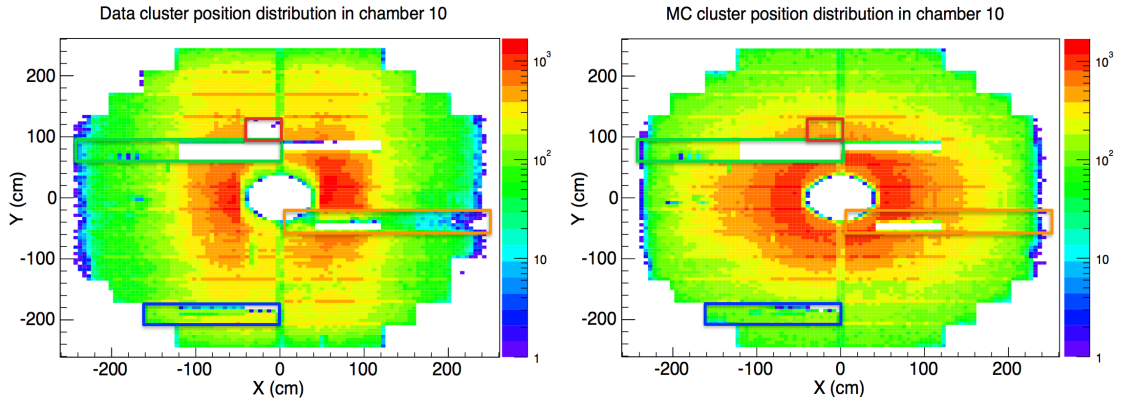


Figure 5.10: Chamber 10 cluster map reconstructed in data (left) and MC (right). The problematic DEs are highlighted with coloured squares following the same convention as in Fig. 5.9.

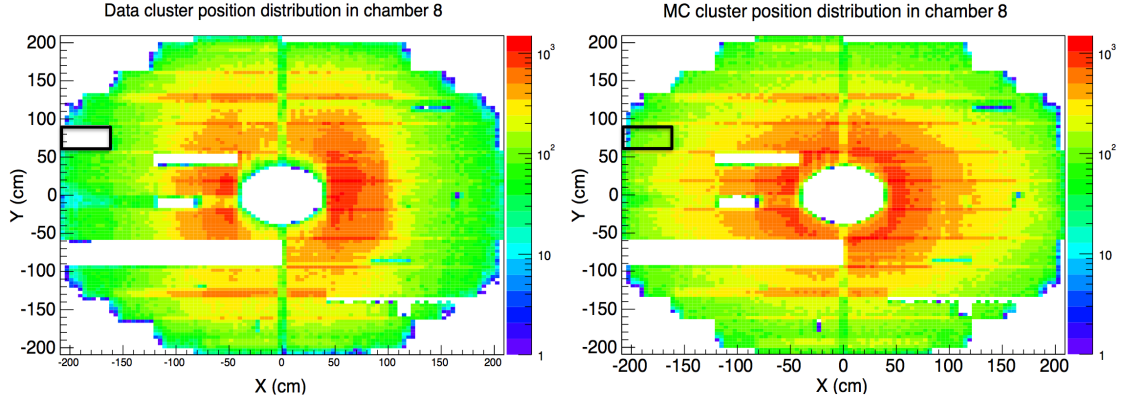


Figure 5.11: Chamber 8 cluster map reconstructed in data (left) and MC (right). The dead PCB (only in data) which causes the ACDA in chamber 10 is highlighted with a black square.

Every chamber has been studied run per run in order to be able to spot these problems for the three p-Pb data-taking periods studied in this thesis. In order to improve the description of the detector in the simulations, the cases like the *bad* status PCBs in DE 1010 and 811 which were not spotted online have to be taken into account. For this purpose, another object is included in the OCDB, the *reject list*. The information of *bad* status regions of the detector not included in the status map, are included for each run and each chamber into the reject list. This information is used at the reconstruction, in both simulation and data, in addition to the status map. For the case of other DEs like 1018 and 1025, the difference between data and MC could have been included as a detection probability ( $P \in (0,1)$ ) in the reject list. However, for the time being only the well defined problematic regions of the detector are removed (*i.e.*  $P = 0$ ) from the reconstruction to see if the agreement is good enough. The problems spotted in this study happen during all the periods used for the  $J/\psi$  analysis in

p-Pb collisions (LHC13d, LHC13e and LHC13f) so the same reject list can be used in addition to the status map. This reject list is shown in Fig. 5.12.

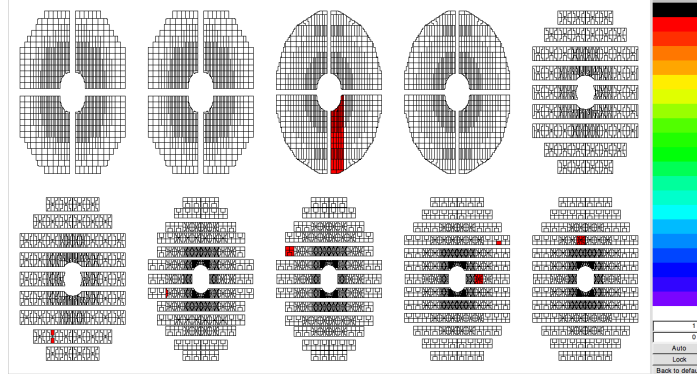


Figure 5.12: Reject List used in reconstruction for the LHC13d, LHC13e and LHC13f p-Pb periods.

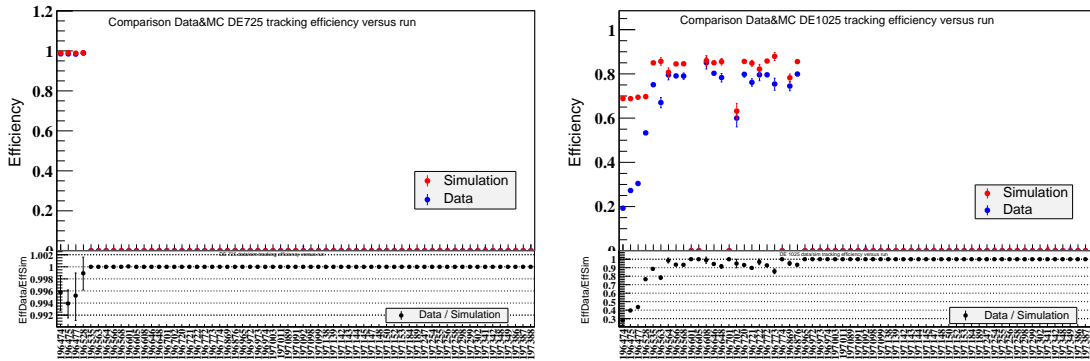


Figure 5.13: Comparison of the measured single muon tracking efficiency in data and MC as a function of run number in period LHC13f for DEs 725 (left) and 1025 (right).

Another kind of problem found during this study can be illustrated by looking at DE 725 during the LHC13f period. The measured efficiency for this DE is 30% lower in data than in MC. However, when trying to identify for which runs this chamber was not well reproduced in Fig. 5.13 (left), it can be seen that the MC reproduces well the data measurement for every run. The explanation of this effect is found in the fact that DE 1025 is badly described in MC during the four first runs of the period, when the DE 725 is working, as seen in Fig. 5.13 (right). This is an integration problem due to the way of calculating the period averaged efficiency, which uses the tracks of every run in the period. To measure the efficiency of DE 725, we must select the tracks for which the chambers 8, 9 and 10 responded. Since the DE 1025 is less efficient in data than in MC in the first four runs, less tracks are used on data than in MC from these runs (where the DE 725 is well functioning compared to the rest of the period, where this DE is off). Integrating this way, more weight is given to the rest of the period in data, and the measured efficiency of DE 725 is artificially smaller than in MC.

The solution to this issue is to compute the efficiency run by run first, and then compute the period average by properly weighting the efficiency of each run. This is now implemented in the latest version of the muon tracking efficiency code in AliROOT.

### 5.5.3 Comparison data-MC efficiency results with reject list

A new MC simulation was performed including the information of the reject list. The efficiency measurements were performed on this simulation and the comparison with the data and the previous simulation results is shown in Fig. 5.14. As can be seen, the simulation with the reject list describes much better the efficiency results obtained in data than the one obtained only with the status map.

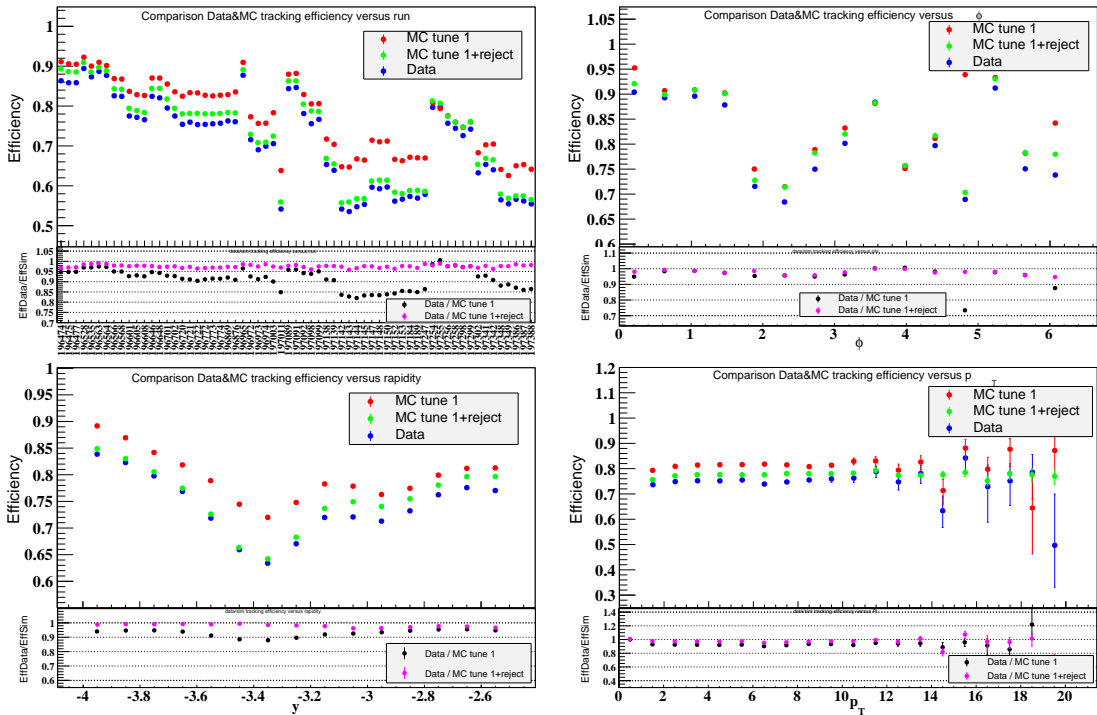


Figure 5.14: Single muon tracking efficiency results from reconstructed tracks for LHC13f period. The plots show the comparison of the data measurements with the realistic simulation with and without the reject list. The efficiency is shown as a function of run number (top left),  $\phi$  (top right),  $y$  (bottom left) and  $p_T$  (bottom right).

With the new simulation, the differences as a function of run number are at most 4%. For the  $\phi$  distribution there are still some regions where the difference is about 5% due to some DEs that could not be completely reproduced in the simulation. For the  $p_T$  distribution a great improvement is observed, and now the difference is at most 2%. The same happens for the rapidity distribution where the discrepancies reach only 3.5%. At this point we have considered that the differences found in the detector description in simulation are acceptable, so the status map and reject list built from this study are used for the simulations used



to compute the  $\mathcal{A} \times \varepsilon$  corrections. A systematic uncertainty to account for these residual differences is evaluated in Sec. 5.5.4.

#### 5.5.4 Single muon tracking efficiency systematic uncertainty estimation

The average result of the spectrometer biased tracking efficiency for single muons in LHC13d, LHC13e and LHC13f periods is approximately 90%, 85% and 74% respectively. The remaining differences found in Sec. 5.5.3 between the efficiency results in data and MC are used as estimation of the systematic uncertainty on the tracking efficiency of single muons due to the detector description. The resulting overall uncertainties were found to be 2% (3%) for p-Pb (Pb-p) periods. These uncertainties are considered as uncorrelated as a function of rapidity and  $p_T$ .

#### 5.5.5 From single muon to $J/\psi$ tracking efficiency systematic uncertainty estimation

In order to propagate the uncertainty of the single muon tracking efficiency to the  $J/\psi$  detection, we would need to take into account the correlated dependence on  $p_T$ ,  $y$  and  $\phi$  of the two decay muons, and also that it might be different between  $\mu^+$  and  $\mu^-$ . Then a new realistic simulation for  $J/\psi$  could be performed by using the single muon systematic uncertainty as an additional detection probability. The  $J/\psi$  uncertainty could then be calculated by comparing the results between the standard realistic simulation and the one with the additional detection probability.

The correlated dependence of the muon tracking efficiency on the muon kinematics, charge and run number is studied by computing the efficiency maps  $(y, \phi)^4$  in data and MC for different  $p_T$  ranges, for positive and negative muons separately (period averaged), and for two different runs. The results in Fig. 5.15 show the period averaged efficiency maps as a function of  $\phi$  and  $y$  in polar coordinates for  $p_T > 1$  GeV/c (left) and  $p_T > 3$  GeV/c (right) obtained in data (top) and MC (bottom). Similar results are shown in Fig. 5.16 for positively charged muons (left) and negatively charged muons (right), and in Fig. 5.17 for two runs. As we can see in the figures, the efficiency strongly depends on  $\phi$  and  $y$ , but also on  $p_T$ , the muon charge and run number. The MC reproduces well the efficiency variations observed in data, except for some regions.

In order to quantify the variations of the systematic uncertainty on the single muon tracking efficiency with  $p_T$ ,  $y$ , muon charge and run, we perform the ratio of the efficiency maps. In Fig. 5.18 the ratios of data over MC for the different  $p_T$  cuts, muon charge and run number are shown. Despite these variations are pretty stable as a function of one single variable (Fig. 5.14), due to the correlation and anti-correlation effects previously discussed, we observe large local fluctuations in the ratios of the efficiency maps. Therefore these ratios

<sup>4</sup>Each bin covers 0.1 pseudorapidity units and 0.41 radians.



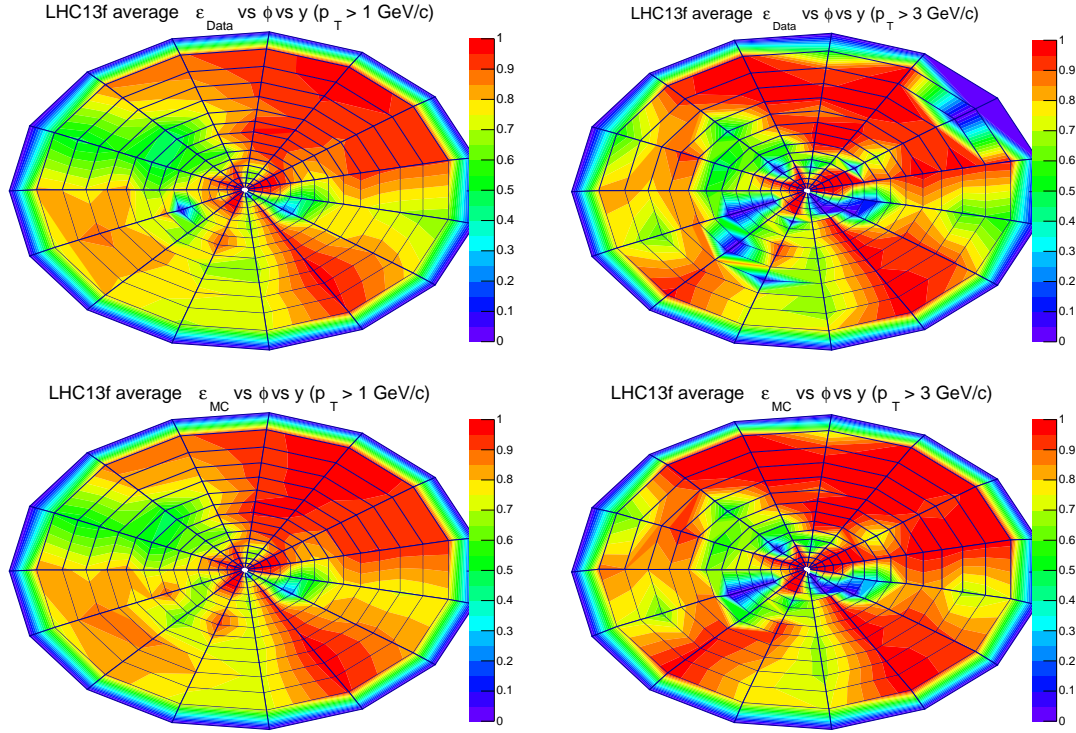


Figure 5.15: Single muon efficiency polar maps ( $y, \phi$ ), for two different  $p_T$  cuts,  $p_T > 1$  GeV/ $c$  (left) and  $p_T > 3$  GeV/ $c$  (right). The top plots show the efficiency maps for data, and the bottom ones the corresponding maps for MC.

are locally very biased, so the propagation of the single muon uncertainty to the  $J/\psi$  detection cannot be done reliably in the way we proposed.

For now it is better to trust the overall magnitude of the measured efficiencies. Consequently, to estimate the uncertainty associated to the  $J/\psi$  tracking efficiency, the effect of the two muons is finally considered as uncorrelated, and the average values for single muons in Sec. 5.5.4 are used. Therefore the systematic uncertainty due to the detector description on the tracking efficiency for  $J/\psi$  detection is simply taken as twice that of single muons. The resulting uncertainty is 4% (6%) for p-Pb (Pb-p), and it is considered as uncorrelated in  $p_T$  and  $y$ .

To summarise, in the tracking efficiency studies performed in this thesis we have introduced the usage of a reject list in order to improve the description of the detector in the MC. This has allowed to obtain a more precise  $\mathcal{A} \times \epsilon$  correction for the data taken by the spectrometer in the 2013 p-Pb data taking periods, and a reduction of the associated systematic uncertainty with respect to previous studies. This uncertainty has then been evaluated for single muons, and propagated to di-muon tracking. The resulting uncertainties for the single muon and di-muon detection are summarised in Tab. 5.1.

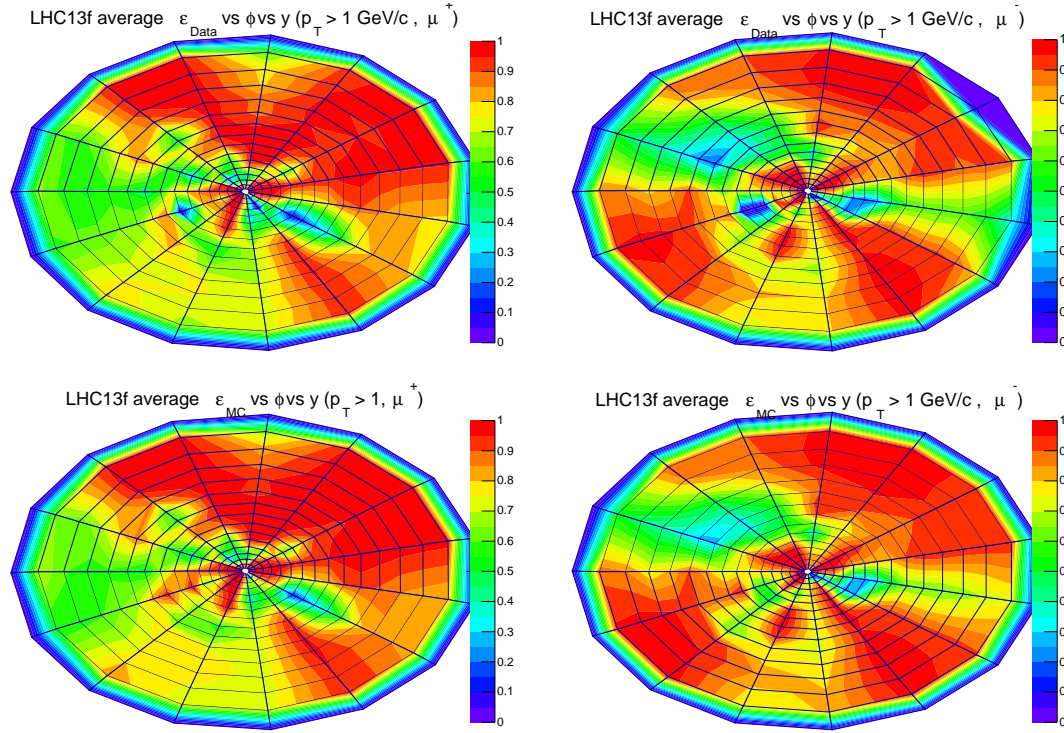


Figure 5.16: Single muon efficiency polar maps ( $y, \phi$ ) (for  $p_T > 1 \text{ GeV}/c$ ) for  $\mu^+$  (left) and  $\mu^-$  (right). The top plots show the efficiency maps for data, and the bottom ones the corresponding maps for MC.

	single- $\mu$	di- $\mu$
Syst. unc. p-Pb	2%	4%
Syst. unc. Pb-p	3%	6%

Table 5.1: Tracking efficiency systematic uncertainties for single muons and di-muons in 2013 p-Pb collisions.

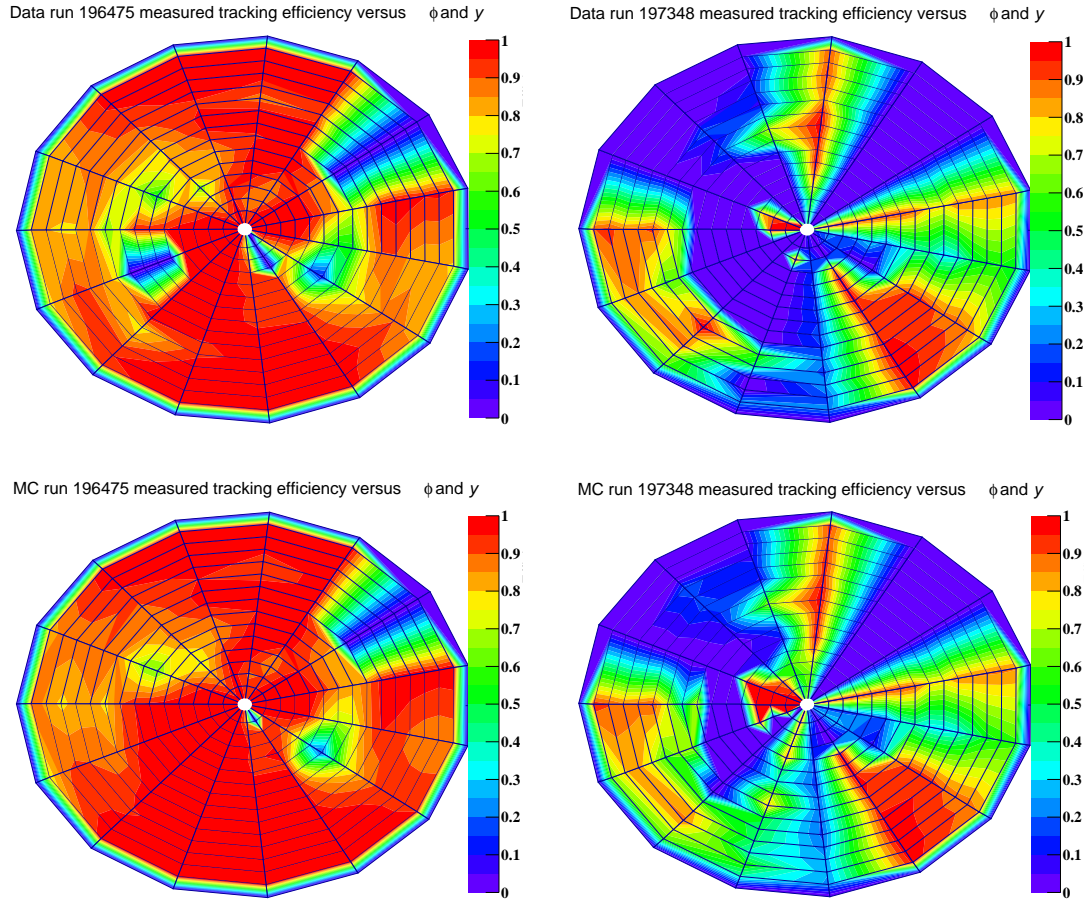


Figure 5.17: Single muon efficiency polar maps ( $y, \phi$ ) for run 196485 (left) and run 197348 (right). The top plots show the efficiency maps for data, and the bottom ones the corresponding maps for MC.

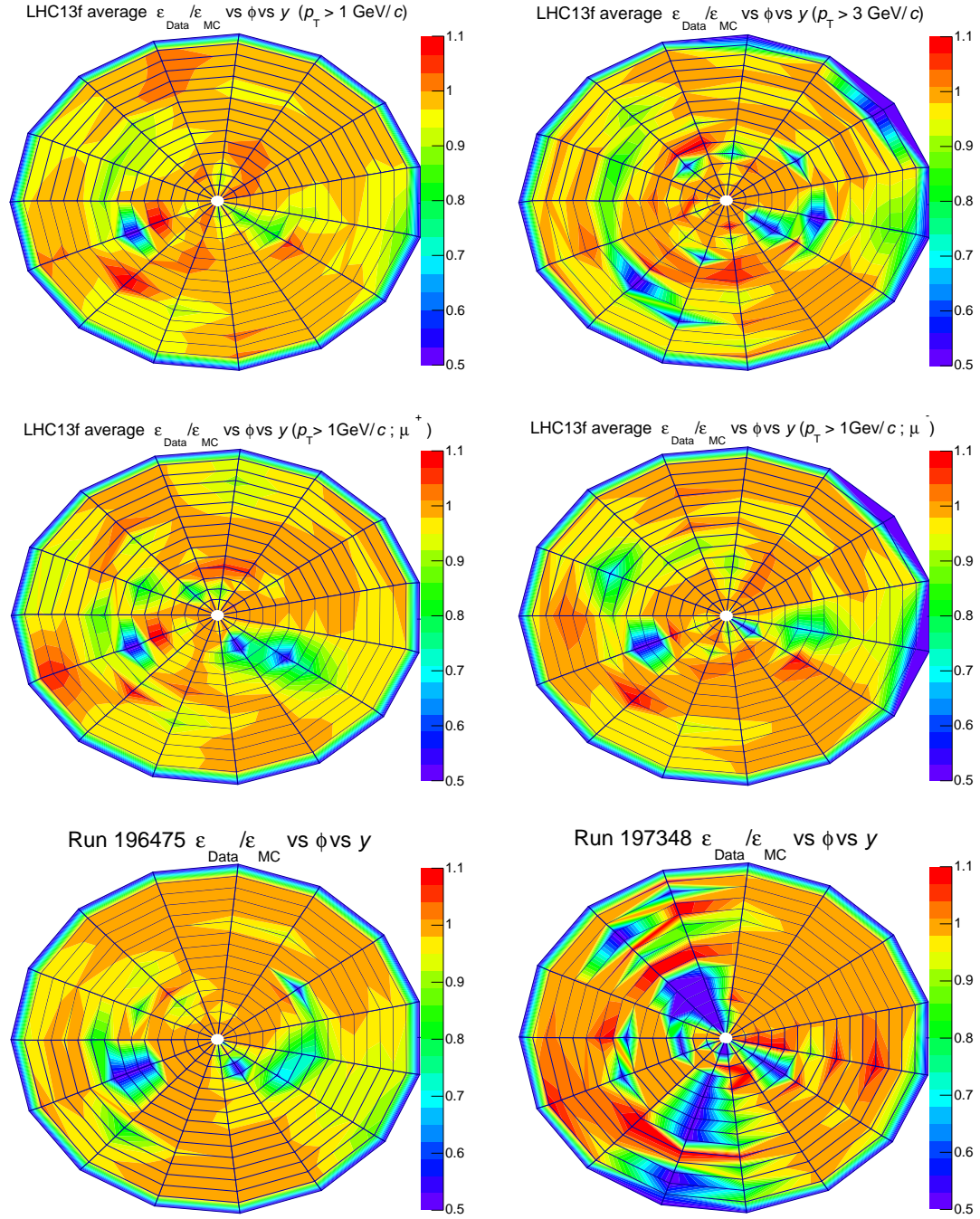


Figure 5.18: Ratio data over MC of the  $(y, \phi)$  efficiency maps in polar coordinates. The two top plots show the variation of the ratio with the  $p_T$  range under consideration. The two middle plots show the variation with the sign of the muon charge. The two bottom plots show the variation of the ratio with the run.



**$J/\psi$  YIELD MEASUREMENT**

In this thesis, the main objective is to study the correlation of the  $J/\psi$  production properties with the charged particle multiplicity of the events. In order to estimate the event multiplicity, the data-driven method developed in Chap. 4 is used. We are specially interested on multiplicities several times bigger than the minimum bias one, where collective-like effects might be observed already in p-Pb collisions. The study of  $J/\psi$  production at high multiplicities can also help to discern among the available theoretical models of Cold Nuclear Matter (CNM) effects.

This chapter is devoted to the  $J/\psi$  yield measurement. The main goal is to obtain a relative measurement,  $Y^{J/\psi}/\langle Y^{J/\psi} \rangle$  to study its evolution with the relative charged particle pseudorapidity density. The relative analysis allows to cancel out some of the multiplicity correlated uncertainties, as well as to ease the comparison of results among different collision systems and center-of-mass energies. In addition, we perform the absolute measurement, which requires a different treatment of the systematic uncertainties.

The  $J/\psi$  are measured in the di-muon decay channel with the ALICE muon spectrometer. The usual procedure to measure the  $J/\psi$  yield is to extract the number of  $J/\psi$  from the measured invariant mass spectra in a certain kinematical range. Then, the number of  $J/\psi$  is corrected by the spectrometer  $\mathcal{A} \times \epsilon$  computed for the same range. In this thesis, we use a different approach. The muon spectrometer 2D  $\mathcal{A} \times \epsilon(p_T, y)$  correction is applied to each di-muon pair prior to build the invariant mass spectra, and therefore the corrected signal shapes can be directly extracted from the spectra.

In this chapter we describe the 2D  $\mathcal{A} \times \epsilon(p_T, y)$  correction method,  $J/\psi$  signal extraction, calculation of the di-muon event normalization factor and the evaluation of the systematic uncertainties. We show that this correction method yields equivalent results to the usual one, but is less sensitive to the uncertainties of the input distributions used in the simulations employed to calculate the  $\mathcal{A} \times \epsilon$  correction, reducing the associated systematic uncertainty.

## 6.1 $J/\psi$ yield measurement

The  $J/\psi$  MB yield is the number of  $J/\psi$  produced per MB collision, and is obtained in the following way:

$$(6.1) \quad Y^{J/\psi} = \frac{N_{J/\psi}^{corr}}{BR_{J/\psi \rightarrow \mu^+ \mu^-} \cdot N_{MB}}$$

where  $N_{J/\psi}^{corr}$  is the number of  $J/\psi$  extracted and corrected by the muon spectrometer  $\mathcal{A} \times \mathcal{E}$ ,  $N_{MB}$  is the equivalent number of MB events corresponding to the di-muon triggered (CMUL) event sample and  $BR_{J/\psi \rightarrow \mu^+ \mu^-}$  is the  $J/\psi$  branching ratio to muons, which is equal to  $(5.961 \pm 0.033)\%$  [33].

The usual technique to extract the number of  $J/\psi$  (see for example [3]), consist of the following: The  $J/\psi$  candidates are obtained by combining pairs of opposite charge muons passing the track selection in Sec. 2.5. The invariant mass spectra for a certain kinematical region,  $\Delta x_k$  ( $x_k = p_T, y, \dots$ ), are constructed by selecting the pairs with the desired kinematics. We extract the number of  $J/\psi$  in a given kinematical range from the corresponding invariant mass spectrum,  $N_{J/\psi}(\Delta x_k)$ . To correct  $N_{J/\psi}(\Delta x_k)$  by the spectrometer  $\mathcal{A} \times \mathcal{E}$ , we compute it in the kinematical range where we measure the  $J/\psi$ ,  $\mathcal{A} \times \mathcal{E}(\Delta x_k)$ , and we correct the measurement by doing:

$$(6.2) \quad N_{J/\psi}^{corr}(\Delta x_k) = \frac{N_{J/\psi}(\Delta x_k)}{\mathcal{A} \times \mathcal{E}(\Delta x_k)}$$

A novel technique has been developed in this thesis to take into account the spectrometer  $\mathcal{A} \times \mathcal{E}$ . The correction is computed differentially in the relevant  $J/\psi$  kinematical variables with the highest possible granularity. In our case, a 2D  $J/\psi$   $\mathcal{A} \times \mathcal{E}(p_T, y)$  correction has been computed. In order to build the invariant mass spectra, the correction is applied directly to each  $J/\psi$  candidate according to its kinematics. The number of corrected di-muon pairs in each invariant mass bin  $i$  of the spectrum is given by:

$$(6.3) \quad n_i^{corr} = \sum_{j=1}^{n_i} \frac{1}{\mathcal{A} \times \mathcal{E}(p_T^j, y^j)}$$

$n_i$  is the number of entries (di-muon pairs) contributing to the  $i$ -th invariant mass bin, and  $p_T^j$  and  $y^j$  are the transverse momentum and rapidity of the  $j$ -th pair contributing to the bin. The number of corrected  $J/\psi$ ,  $N_{J/\psi}^{corr}$ , is obtained directly from the corrected spectrum. This technique has some advantages with respect to the usual one, that we discuss in detail later. We show that this technique reduces the impact of the possible variations of the input distributions used in MC simulations to get the  $\mathcal{A} \times \mathcal{E}$ , hence reducing the associated systematic uncertainty on the  $J/\psi$  signal extraction.

The resulting spectrum is parametrised by fitting it with a superposition of a  $J/\psi$  and  $\psi(2S)$  signals plus a background shape. The number of  $J/\psi$  are obtained by integrating

the obtained signal shape. Since the signal tails are covered by the background, the tail parameters of the signal functions cannot be deduced from the data themselves. The tail parameters have to be therefore tuned on a  $J/\psi$  MC simulation and then fixed in the fitting procedure on data (Sec. 6.1.1). Then the  $\mathcal{A} \times \epsilon$  corrected number of  $J/\psi$  is obtained directly from the integral of the signal shape.

The analysis is performed integrated in multiplicity ( $\langle Y_{J/\psi} \rangle$ ) and sampling the events in the same multiplicity bins  $i$  as the ones used in Chap. 4 ( $Y_{J/\psi}^i$ ). It is important to note here that in the following, two different event selections are used for the integrated and multiplicity differential analyses. For the integrated analysis, physics selected events (Sec. 2.4) are considered with no further event cuts. For the multiplicity differential analysis, in addition to the physics selection, all the vertex requirements mentioned in Sec. 3.3 are also applied in order to obtain a reliable estimation of the event multiplicity. The relative  $J/\psi$  yield is also measured,  $Y_{J/\psi}^{R,i} = Y_{J/\psi}^i / \langle Y_{J/\psi} \rangle$ . For the absolute and relative measurements, a different treatment of the systematic uncertainties computation is needed, as we show in Sec. 6.3.

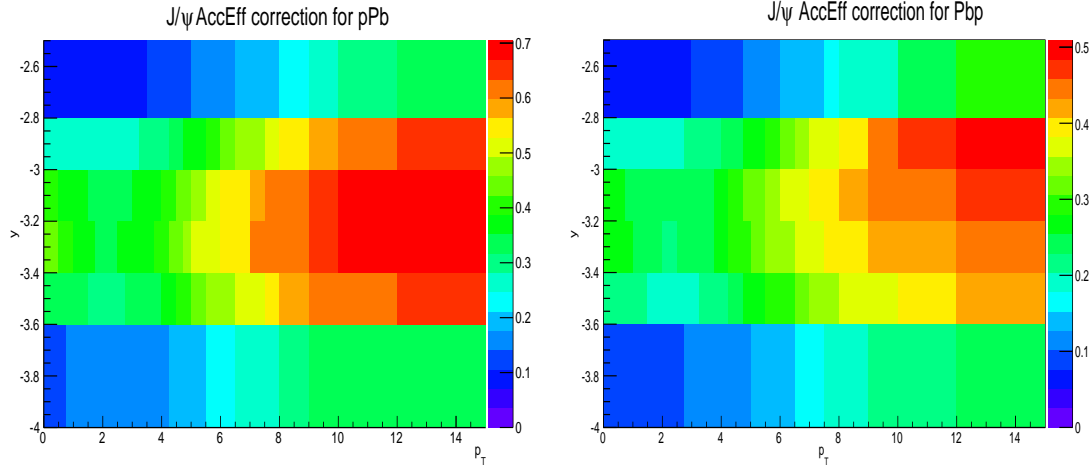
### 6.1.1 $J/\psi$ $\mathcal{A} \times \epsilon$ correction

In order to correct the muon data taken by the spectrometer  $\mathcal{A} \times \epsilon$ ,  $J/\psi$  2D  $\mathcal{A} \times \epsilon$  corrections in  $(p_T, y)$  bins have been computed using the same simulations as the ones used in [3]. These are run-per-run simulations with a number of events proportional to the di-muon triggers found in data. They are performed using a pure signal parametrisation that reproduces the measured  $J/\psi$   $p_T$  and  $y$  distributions as explained in Sec. 5.2. The  $J/\psi$  polarisation is assumed to be zero and the events are generated at a fixed vertex position. GEANT3 [260] is used for the propagation of the muons from the decay of the generated  $J/\psi$ , through the detector.

The spectrometer  $J/\psi$   $\mathcal{A} \times \epsilon$  in a given  $(p_T, y)$  bin is calculated as the ratio of the reconstructed number of  $J/\psi$ , using the same di-muon selection as for data (Sec. 2.5), over the generated ones in the corresponding bin in generated coordinates:

$$(6.4) \quad \mathcal{A} \times \epsilon(p_T, y) = \frac{N_{J/\psi}^{reco}(p_T, y)}{N_{J/\psi}^{gen}(p_T^{gen}, y^{gen})}$$

In this way, the  $\mathcal{A} \times \epsilon$  takes partially into account  $p_T$  and  $y$  resolution effects. The binning is determined based on the available statistics in the simulations, and is such as the statistical error is below 1% at low  $p_T$  and in the central rapidity region of the spectrometer. The statistical error reaches 3-4% for the last  $p_T$  bins and the edges of the spectrometer rapidity. In this region, the di-muon statistics in real data is small anyway, so the effect of the statistical error have a small weight in the analysis. Therefore, the statistical uncertainty on the  $\mathcal{A} \times \epsilon$  is considered negligible in the analysis with respect to the other sources of uncertainties. The results for these corrections are shown in Fig. 6.1 for each considered period.


 Figure 6.1:  $J/\psi$   $\mathcal{A} \times \mathcal{E}$  for LHC13d+e (left) and LHC13f (right) periods

The  $\mathcal{A} \times \mathcal{E}$  correction in  $(p_T, y)$  is more precise than a one-dimensional correction. Since it is less averaged than a one-dimensional correction, it takes into account more accurately the variations of the efficiency among the different regions of the spectrometer. Therefore, the possible variations of the input distributions (we have a limited knowledge of the true distributions) used to estimate the correction, have a smaller impact on the result. In consequence, the  $\mathcal{A} \times \mathcal{E}(p_T, y)$  has a smaller associated systematic uncertainty than a one-dimensional or integrated correction, as we show in Sec. 6.3.4.

### 6.1.2 Computation of signal tails parameters

Since the signal tails are hidden by the background, we can only study the tails shape in simulations. The observed asymmetry and deviation from a gaussian behaviour of the signal tails are caused by the muons multiple scattering and energy loss in the front absorber. Therefore we parametrize the tails in pure signal simulations and the parameters are then fixed in the fitting procedure on data.

Furthermore, the number of corrected  $J/\psi$  is extracted directly from the  $\mathcal{A} \times \mathcal{E}$  corrected spectrum, so it is mandatory to study how the correction affects the reconstructed data in simulation in order to properly tune the signal shape parameters. This study has to be performed, not only on  $J/\psi$  simulations but also on  $\psi(2S)$  simulations, since a priori, it is not known how the  $J/\psi$   $\mathcal{A} \times \mathcal{E}$  could affect the  $\psi(2S)$  signal extraction. Therefore, the 2D  $J/\psi$   $\mathcal{A} \times \mathcal{E}$  correction has been applied to the pure signal simulations in the same way as is done in real data, Eq. 6.3.

First of all, the variation of the reconstructed signal in simulation for  $J/\psi$  and  $\psi(2S)$  has been studied. The corrected and raw spectra obtained from simulation for  $J/\psi$  and  $\psi(2S)$  are shown in Fig. 6.2 and Fig. 6.3 respectively. The signal shape changes a bit between the raw (blue dots) and corrected (red dots) spectra. The raw and corrected spectra in simulation



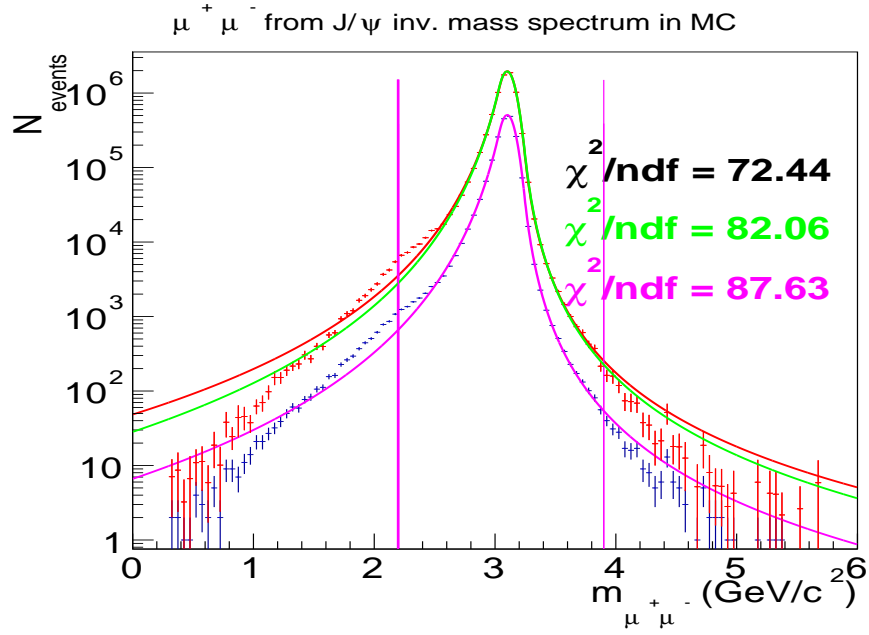


Figure 6.2: Tail fits tests for  $J/\psi$  on pure signal simulation using an Extended Crystal Ball function. The figure shows: raw  $J/\psi$  spectrum (blue dots),  $\mathcal{A} \times \mathcal{E}$  corrected spectrum (red dots), raw spectrum fit (magenta line), corrected spectrum fit (green line) and corrected spectrum fit using the tails parameters extracted from the raw spectrum (black line). The vertical lines delimit the fitting range.

are fitted using an Extended Crystal Ball (CB2) function (see appendix B in [261]) with all the parameters free. The number of  $J/\psi$  and  $\psi(2S)$  are obtained by integrating the obtained signal shapes. It has been checked that the number of extracted particles is consistent whether we use the raw spectrum correcting by the integrated  $\mathcal{A} \times \mathcal{E}$ , or the  $\mathcal{A} \times \mathcal{E}$  corrected spectrum.

Moreover, to study the relevance of extracting the signal parameters from the corrected simulation several tests have been done. A set of tail parameters is obtained from the raw spectra and a second one from the  $\mathcal{A} \times \mathcal{E}$  corrected spectra. As it is observed in Tab. 6.1, the parameters' values change. Then, the tails obtained from the raw spectra are used to fit the  $\mathcal{A} \times \mathcal{E}$  corrected ones. In order to determine how the changes in the parameters affect the number of extracted particles, the fractions of the number of total particles found in the core of the CB2 function, and the left and right tails are presented in Tab. 6.2 for three cases: raw spectrum with free tails, corrected spectrum with free tails and corrected spectrum fitted with the tail parameters extracted from the raw spectrum. The fraction of the particles in the different regions of the signal varies with the tail parameters. In contrast, the number of total extracted  $J/\psi$  and  $\psi(2S)$  differ only by  $< 0.3\%$  and  $\sim 0.6\%$  respectively, when using the "corrected" or "uncorrected" sets of tails in the  $\mathcal{A} \times \mathcal{E}$  corrected spectra, leading to the conclusion that the use of one or another set of signal tails has a

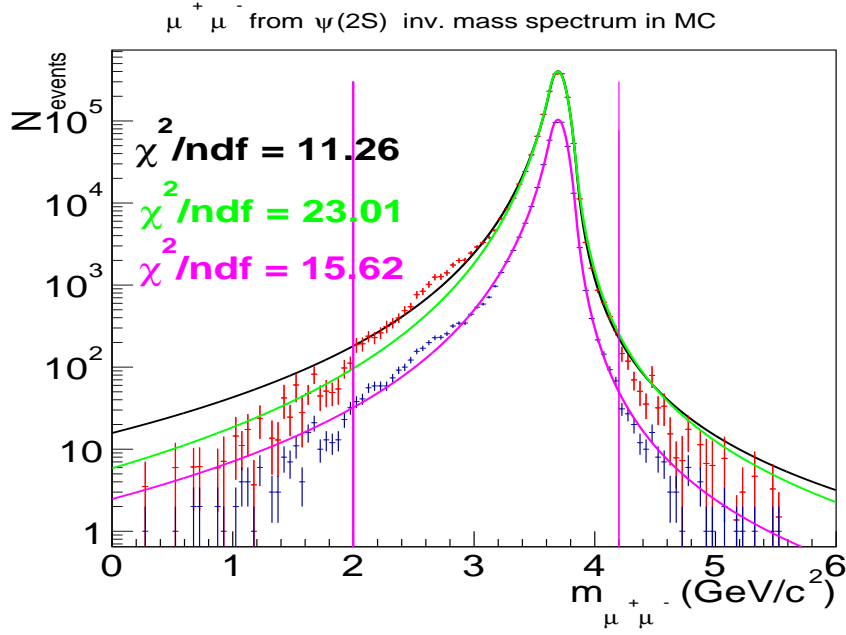


Figure 6.3: Tail fits tests for  $\psi(2S)$  on pure signal simulation using an Extended Crystal Ball (CB2) function. The figure shows: raw  $\psi(2S)$  spectrum (blue dots),  $\mathcal{A} \times \epsilon$  corrected (using  $J/\psi$  correction) spectrum (red dots), raw spectrum fit (magenta line), corrected spectrum fit (black line) and corrected spectrum fit using the tails parameters extracted from the corrected  $J/\psi$  spectrum (green line). The vertical lines delimit the fitting range.

negligible effect. Nevertheless, the tails tuned on the  $\mathcal{A} \times \epsilon$  corrected simulation are used in the analysis for the sake of consistency. In addition, the  $\psi(2S)$  corrected spectrum has been fitted also with the set of tails parameters obtained from the  $J/\psi$  spectrum. The effect results to be negligible in simulation.

	$J/\psi$ raw	$J/\psi$ corrected	$\psi(2S)$ raw	$\psi(2S)$ corrected
$\alpha_l$	$1.046 \pm 0.004$	$1.032 \pm 0.004$	$1.048 \pm 0.004$	$1.02 \pm 0.004$
$n_l$	$4.17 \pm 0.03$	$3.89 \pm 0.04$	$3.49 \pm 0.04$	$3.32 \pm 0.04$
$\alpha_u$	$2.25 \pm 0.01$	$2.28 \pm 0.01$	$2.34 \pm 0.01$	$2.41 \pm 0.01$
$n_u$	$3.08 \pm 0.05$	$2.91 \pm 0.05$	$2.88 \pm 0.05$	$2.55 \pm 0.05$

Table 6.1: Extended Crystal Ball tails parameters extracted from pure signal  $J/\psi$  and  $\psi(2S)$  simulations

Furthermore, the importance of using different sets of tails for  $J/\psi$  and  $\psi(2S)$  has also been studied on data. For that, the signal extraction on the integrated spectra of LHC13d+e periods has been done in two ways: first,  $J/\psi$  tails parameters tuned on simulation are used in the  $J/\psi$  and  $\psi(2S)$ ; and second,  $J/\psi$  and  $\psi(2S)$  tails parameters tuned independently in their respective simulations are used. The difference on the  $J/\psi$  signal extraction in the

	$J/\psi$ raw - free tails	$J/\psi$ corrected - free tails	$J/\psi$ corrected - raw tails
$\frac{N_{part(core)}}{N_{tot}}$	$73.01 \pm 0.11 \%$	$71.82 \pm 0.11\%$	$73.02 \pm 0.11\%$
$\frac{N_{part(left\ tail)}}{N_{tot}}$	$25.18 \pm 0.16 \%$	$26.44 \pm 0.16 \%$	$25.08 \pm 0.16 \%$
$\frac{N_{part(right\ tail)}}{N_{tot}}$	$1.81 \pm 0.49 \%$	$1.73 \pm 0.49 \%$	$1.81 \pm 0.49 \%$

Table 6.2: Fraction of  $J/\psi$  in the core and tails of the signal in simulation.

two tests is at the permil level, so  $\psi(2S)$  tails parameters play a negligible role on the  $J/\psi$  extraction, and hence the set of tails obtained from the  $J/\psi$  simulation is used for both  $J/\psi$  and  $\psi(2S)$  signals.

A different parametrisation has also been used to try to better reproduce the tails behaviour found in the simulated data. The second function used here is the "NA60 function" (NA60) (see appendix B in [261]). The result obtained in the fitting procedure of the  $J/\psi$  signal in simulation is shown in Fig. 6.4. The shape of the tails is better reproduced with the NA60 than with the CB2 function. However, the fraction of the total  $J/\psi$  in the spectrum recovered by each function is in both cases bigger than 99%. Since the shape of the signal and tails depend on how well the detector effects are reproduced by the simulation, both functions are used for the signal extraction in the data analysis to account for possible variations.

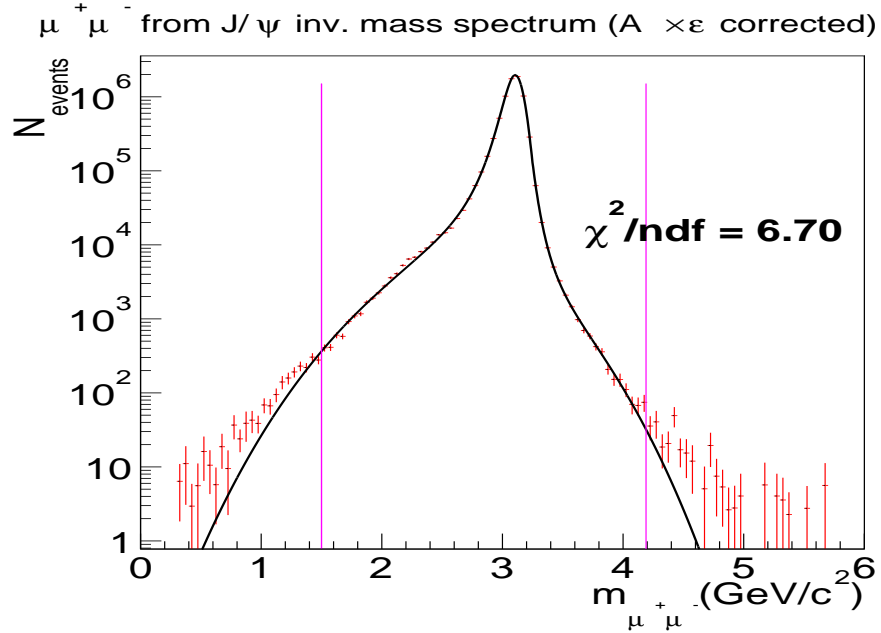


Figure 6.4: Tail fits for  $J/\psi$  on pure signal simulation using a NA60 function. The figure shows the  $J/\psi$   $\mathcal{A} \times \epsilon$  corrected spectrum (red dots) and its fit. The vertical lines delimit the fitting range.

### 6.1.3 $J/\psi$ signal extraction

In order to extract the  $\mathcal{A} \times \mathcal{E}$  corrected number of  $J/\psi$  the corrected di-muon invariant mass spectra are fitted with several sets of functions. Two different signal shapes have been used: CB2 and NA60 functions. The tail parameters are obtained from simulation and fixed in the fitting procedure as seen in Sec. 6.1.2. The functions used to parametrize the background are: a variable Width Gaussian (VWG), and a second order polynomial times exponential (Pol2 $\times$ Exp). Two fitting ranges are also used (2.0-5.0 GeV/ $c^2$  and 2.2-4.7 GeV/ $c^2$ ).

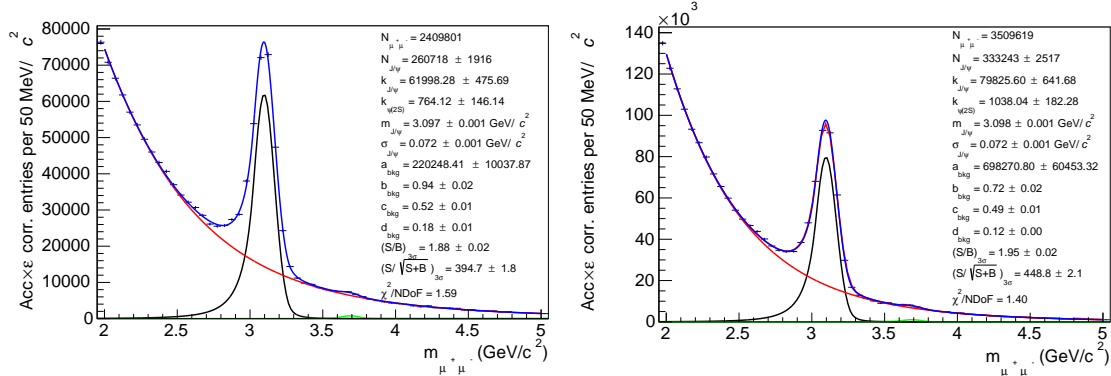


Figure 6.5: Example of signal extraction for the integrated invariant mass spectra in p-Pb (left) and Pb-p (right) for a fit combination choice (CB2+VWG+Range= 2.0 – 5.0+ $\sigma_{\psi(2S)}$  =  $0.9 \cdot \sigma_{J/\psi}$ ).

Since the signal-to-background ratio in the  $\psi(2S)$  region is too small, the  $\psi(2S)$  mass,  $m_{\psi(2S)}$ , and width,  $\sigma_{\psi(2S)}$ , have to be bounded to that of the  $J/\psi$  in the following way:

$$(6.5) \quad m_{\psi(2S)} = m_{J/\psi} + (m_{\psi(2S)}^{PDG} - m_{J/\psi}^{PDG}); \sigma_{\psi(2S)} = \sigma_{J/\psi} \times f$$

where PDG denotes Particle Data Group values [33]. The factor  $f$  for the  $\psi(2S)$  width can take the values 0.9, 1.0 and 1.1, which cover the possible variations of the values observed in simulation.

Note here that even though the  $\psi(2S)$  signal is parametrized, the number of  $\psi(2S)$  cannot be extracted from the obtained shape. This is because the spectrum has been corrected with the  $J/\psi$   $\mathcal{A} \times \mathcal{E}$ , which is different from the  $\psi(2S)$  one. Therefore, with the technique used in this thesis, we need to correct the spectrum with the  $\mathcal{A} \times \mathcal{E}$  of the particle to be extracted, and we just parametrize the other contributions.

As was shown in  $J/\psi$  Pb-Pb ALICE analyses [205], the shape of the signal does not change with the event multiplicity (correlated to the event centrality in Pb-Pb collisions). Consequently, it can be safely assumed that the shape is the same for every multiplicity bin also in p-Pb collisions. Thus the tails used for the different multiplicity bins are those obtained from the integrated MC spectrum.

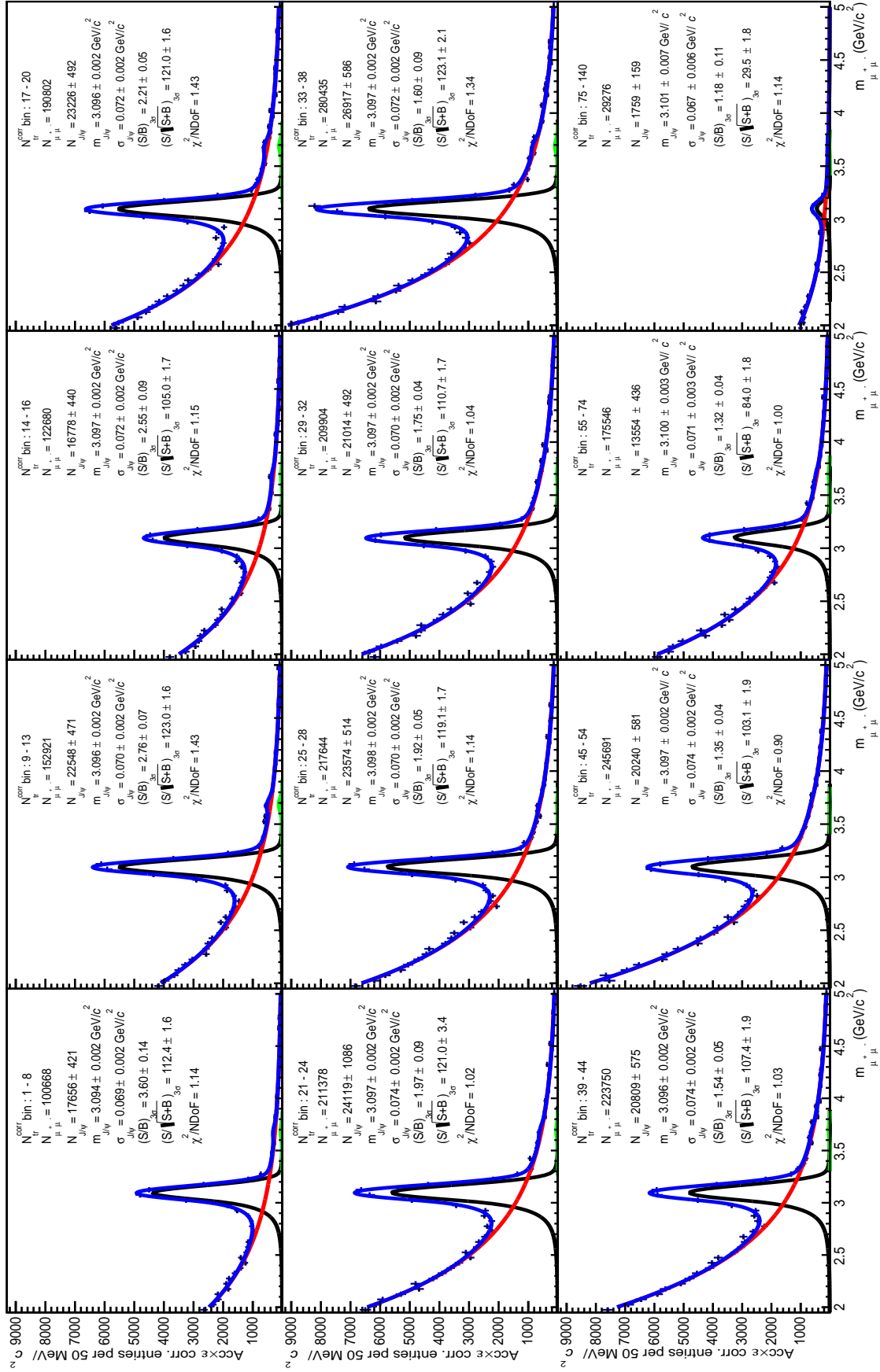


Figure 6.6: Example of signal extraction for the multiplicity bins invariant mass spectra in p-Pb for a fit combination choice (CB2+VWG+Range= $2.0 - 5.0 + \sigma_{\psi(2S)} = 0.9 \cdot \sigma_{J/\psi}$ ).

The integrated fit spectra in p-Pb and Pb-p, and those in multiplicity (data-driven  $N_{tr}^{corr}$ ) bins for the fit combination CB2+VWG+Range =  $2.0 - 5.0 + \sigma_{\psi(2S)} = 0.9 \cdot \sigma_{J/\psi}$  are shown in Fig. 6.5 and Fig. 6.6. The extracted  $J/\psi$  invariant mass value is in very good agreement with that of the PDG ( $m_{J/\psi}^{PDG} = 3096.916 \pm 0.011 \text{ MeV}/c^2$ ) and the signal width is  $\sim 72 \text{ MeV}/c^2$ , in good agreement with previous analyses. Both values are very stable among multiplicity bins and the fits  $\chi^2$  values are always around 1. The signal over background ratio in a three sigma range around the  $J/\psi$  peak is between 1.18 (high multiplicity) and 3.60 (low multiplicity) depending on the multiplicity bin considered.

The last multiplicity bin lacks statistics, so the fits in this bin have to be treated carefully. In order to test if the  $\chi^2$  fits give correct results for the extracted number of  $J/\psi$  in this bin, likelihood fits have also been used. The results of the number of extracted  $J/\psi$  are the same, with less than 0.4% difference, with the  $\chi^2$  or likelihood fits for the higher statistics multiplicity bins. For the last multiplicity bin the difference is 4%, which is not significant taking into account that the statistical errors given by the fits are about 10% in this bin. The statistical errors given by the likelihood fits are, by far, much bigger than the ones given by the  $\chi^2$ . This is because the MINOS minimisation technique of ROOT MINUIT minimiser [262] is known to give incorrect errors for likelihood fits in weighted histograms. Therefore only  $\chi^2$  fits are used for every multiplicity bin.

Finally, a test to verify the equivalence of the  $\mathcal{A} \times \mathcal{E}$  corrected  $N_{J/\psi}$  extracted from the raw spectra and from the  $\mathcal{A} \times \mathcal{E}$  corrected ones has also been performed on data. The result shows that the extraction differs in  $< 0.3\%$  for the total (multiplicity integrated) number of  $J/\psi$ .

The results of the absolute  $J/\psi$  extraction are listed in Tab. 6.3 for p-Pb and Pb-p data-taking periods. The values shown are the resulting average of the signal extraction tests in Sec. 6.3.1. A cross-check of the validity of our results is performed in App. C, by comparing with the results in [3] and [261].

#### 6.1.4 Di-muon trigger event normalisation

In Sec. 2.4 we mentioned that the CMUL trigger, used to take the data for quarkonium measurements in the di-muon channel, has implicit the MB trigger condition. However, the CINT7 (MB) trigger was downscaled during the data taking to allow more DAQ bandwidth for the rare triggers (such as the CMUL). To calculate the  $J/\psi$  MB yield, we need to determine the equivalent number of MB events corresponding to our muon triggered data sample. For this, it is necessary to calculate the di-muon trigger event normalisation factor  $F_{norm}$ . Then, the equivalent number of MB events ( $N_{MB}$ ) corresponding to the analysed CMUL sample ( $N_{CMUL}$ ) is:

$$(6.6) \quad N_{MB} = F_{norm} \times N_{CMUL}$$

The computation of the  $F_{norm}$  directly from the ratio of measured MB events to the

$N_{tr}^{corr}$ bin	LHC13d+e (p-Pb)	LHC13f (Pb-p)
Integrated	$(26.07 \pm 0.20 \text{ (stat.)} \pm 0.10 \text{ (sys.)}) \cdot 10^4$	$(33.42 \pm 0.26 \text{ (stat.)} \pm 0.13 \text{ (sys.)}) \cdot 10^4$
0.5 - 8.5	$(18.59 \pm 0.54 \text{ (stat.)} \pm 0.08 \text{ (sys.)}) \cdot 10^3$	$(17.15 \pm 0.50 \text{ (stat.)} \pm 0.11 \text{ (sys.)}) \cdot 10^3$
8.5 - 13.5	$(22.29 \pm 0.56 \text{ (stat.)} \pm 0.13 \text{ (sys.)}) \cdot 10^3$	$(22.64 \pm 0.57 \text{ (stat.)} \pm 0.04 \text{ (sys.)}) \cdot 10^3$
13.5 - 16.5	$(16.99 \pm 0.45 \text{ (stat.)} \pm 0.15 \text{ (sys.)}) \cdot 10^3$	$(18.72 \pm 0.62 \text{ (stat.)} \pm 0.18 \text{ (sys.)}) \cdot 10^3$
16.5 - 20.5	$(23.02 \pm 0.71 \text{ (stat.)} \pm 0.13 \text{ (sys.)}) \cdot 10^3$	$(26.45 \pm 0.67 \text{ (stat.)} \pm 0.03 \text{ (sys.)}) \cdot 10^3$
20.5 - 24.5	$(23.92 \pm 0.69 \text{ (stat.)} \pm 0.10 \text{ (sys.)}) \cdot 10^3$	$(31.16 \pm 0.96 \text{ (stat.)} \pm 0.17 \text{ (sys.)}) \cdot 10^3$
24.5 - 28.5	$(23.85 \pm 0.77 \text{ (stat.)} \pm 0.19 \text{ (sys.)}) \cdot 10^3$	$(29.82 \pm 0.99 \text{ (stat.)} \pm 0.37 \text{ (sys.)}) \cdot 10^3$
28.5 - 32.5	$(21.24 \pm 0.76 \text{ (stat.)} \pm 0.08 \text{ (sys.)}) \cdot 10^3$	$(28.88 \pm 0.91 \text{ (stat.)} \pm 0.08 \text{ (sys.)}) \cdot 10^3$
32.5 - 38.5	$(27.84 \pm 0.85 \text{ (stat.)} \pm 0.13 \text{ (sys.)}) \cdot 10^3$	$(37.71 \pm 0.99 \text{ (stat.)} \pm 0.15 \text{ (sys.)}) \cdot 10^3$
38.5 - 44.5	$(20.08 \pm 0.62 \text{ (stat.)} \pm 0.10 \text{ (sys.)}) \cdot 10^3$	$(29.51 \pm 0.94 \text{ (stat.)} \pm 0.09 \text{ (sys.)}) \cdot 10^3$
44.5 - 54.5	$(21.03 \pm 0.65 \text{ (stat.)} \pm 0.20 \text{ (sys.)}) \cdot 10^3$	$(30.35 \pm 0.86 \text{ (stat.)} \pm 0.13 \text{ (sys.)}) \cdot 10^3$
54.5 - 74.5	$(13.08 \pm 0.58 \text{ (stat.)} \pm 0.07 \text{ (sys.)}) \cdot 10^3$	$(22.43 \pm 0.75 \text{ (stat.)} \pm 0.18 \text{ (sys.)}) \cdot 10^3$
74.5 - 140.5	$(1.65 \pm 0.23 \text{ (stat.)} \pm 0.04 \text{ (sys.)}) \cdot 10^3$	$(3.38 \pm 0.31 \text{ (stat.)} \pm 0.08 \text{ (sys.)}) \cdot 10^3$

Table 6.3: Extracted number of  $J/\psi$  (from the  $\mathcal{A} \times \mathcal{E}$  corrected spectra) in p-Pb and Pb-p periods for one of the execution tests with the nominal  $\mathcal{A} \times \mathcal{E}$  correction (see Sec. 6.3). The systematic uncertainty is the one related to the signal extraction only (see Sec. 6.3.1).

measured MB events in coincidence with a L0 trigger input 0MUL:

$$(6.7) \quad F_{norm} = \frac{N_{MB}}{N_{MB \& 0MUL}}$$

is affected by a large statistical uncertainty, due to the low MB statistics. To overcome this issue, two different techniques have been used in p-Pb collisions analyses (see for example [261]). Nevertheless, the method which consist on using the L0b trigger scalers can not be used here to compute the  $F_{norm}$  in multiplicity bins, since they have no information of the event multiplicity. Consequently, from the methods used in [261], only the offline method in two steps is used here:

$$(6.8) \quad F_{norm}^{offline,i} = \frac{N_{CMSL}^i}{N_{CMSL \& 0MUL}^i} \times \frac{N_{CINT7}^i}{N_{CINT7 \& OMSL}^i} \times F_{pile-up}^i$$

where  $i$  denotes a certain run and  $F_{pile-up}^i$  is the pile-up correction factor for the run  $i$ , which is defined as:

$$(6.9) \quad F_{pile-up}^i = \frac{\mu^i}{P^i(n \geq 1)} = \frac{\mu^i}{1 - e^{-\mu^i}}$$

where  $\mu^i$  is the mean number of collisions per bunch crossing for a run  $i$  that was defined in Eq. 4.12, and  $P^i(n \geq 1)$  is the probability of having at least one collision per bunch crossing

defined in Eq. 4.11. This method can also be used equivalently to compute the multiplicity differential normalisation factor for the each multiplicity slice  $j$ ,  $F_{norm}^{offline, bin_j}$ . As an example, the multiplicity integrated  $F_{norm}^{offline}$  evolution as a function of the run number, and that of a multiplicity bin in Pb-p are shown in Fig. 6.7. The normalisation factor varies from run to run. In order to obtain a correct estimation, these variations have to be taken into account in the global  $F_{norm}^{offline}$  computation. The  $F_{norm}^{offline}$  used when analysing the whole period is correspondingly computed as the weighted average of the run-by-run factors:

$$(6.10) \quad F_{norm}^{offline} = \frac{\sum_{i=1}^{n_{runs}} F_{norm}^{offline, i} \cdot N_{CMUL7}^i}{\sum_{i=1}^{n_{runs}} N_{CMUL7}^i}$$

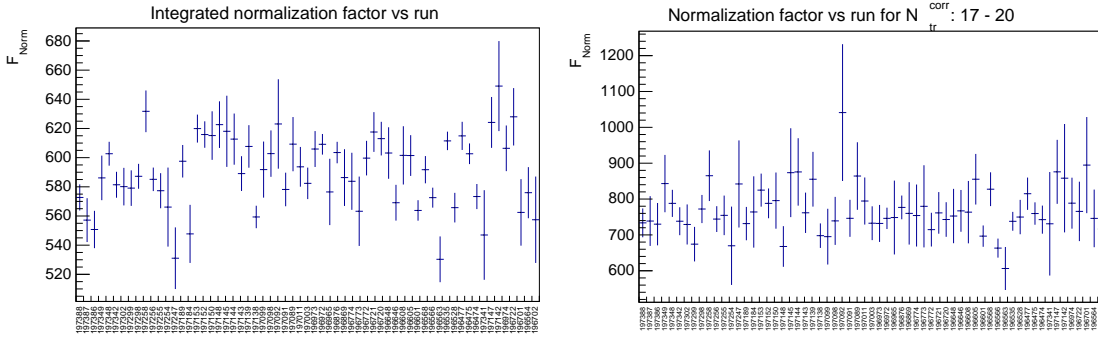


Figure 6.7: Di-muon trigger normalisation factor in Pb-p as a function of run. Left: Integrated in multiplicity. Right: Multiplicity bin  $N_{tr}^{corr}$  17-20.

The event cuts used for the computation of the integrated and multiplicity differential  $F_{norm}^{offline}$  are the same as those used for the yield extraction. For the integrated analysis, no cut on the vertex is needed. For this reason the integrated normalisation factor is computed using only the physics selection cut for the events. The results obtained for the integrated  $F_{norm}^{offline}$  (LHC13f and LHC13d+e) together with the results from [263] are listed in Tab. 6.4. A very good agreement between results is observed.

Period	$F_{norm}^{offline}$ (this thesis)	$F_{norm}^{offline}$ ([263])
LHC13d+e	$1123.71 \pm 4.52$	$1124.00 \pm 4.99$
LHC13f	$588.60 \pm 1.55$	$588.52 \pm 2.65$

Table 6.4: Global  $F_{norm}^{offline}$  pile-up corrected integrated values and comparison with [263]. The uncertainty on the result of this analysis is only the statistical one. The systematic uncertainty is discussed in Sec. 6.3.3

The results for the normalisation factor obtained in multiplicity bins are shown in Tab. 6.5. Note that the global pile-up correction factor in Eq. 6.9 has also been applied to the



$N_{tr}^{corr}$ bin	$F_{norm}^{offline}$ (pile-up corr.) (p-Pb)	$F_{norm}^{offline}$ (pile-up corr.) (Pb-p)
0.5 - 8.5	$4337.87 \pm 64.61$	$3555.97 \pm 37.91$
8.5 - 13.5	$1865.62 \pm 27.40$	$1526.55 \pm 15.19$
13.5 - 16.5	$1419.32 \pm 25.34$	$982.58 \pm 11.04$
16.5 - 20.5	$1136.92 \pm 15.64$	$748.66 \pm 6.94$
20.5 - 24.5	$932.09 \pm 12.77$	$560.91 \pm 5.01$
24.5 - 28.5	$802.47 \pm 10.84$	$444.01 \pm 3.97$
28.5 - 32.5	$700.40 \pm 12.00$	$358.43 \pm 3.31$
32.5 - 38.5	$629.01 \pm 8.17$	$284.92 \pm 2.34$
38.5 - 44.5	$545.47 \pm 8.40$	$224.35 \pm 2.10$
44.5 - 54.5	$487.62 \pm 14.39$	$174.77 \pm 1.61$
54.5 - 74.5	$413.03 \pm 8.65$	$121.18 \pm 1.38$
74.5 - 140.5	$336.56 \pm 18.03$	$79.76 \pm 2.52$

Table 6.5:  $F_{norm}^{offline}$  pile-up corrected in multiplicity bins for p-Pb and Pb-p. The uncertainty on the result of this analysis is only the statistical one. The systematic uncertainty is discussed in Sec. 6.3.3

multiplicity bins. The variation of the fraction of pile-up events in multiplicity bins has not been taken into account. We proceeded this way in order to obtain a consistent number of events after the correction on the integrated and multiplicity differential analysis. This can be justified by the fact that the pile-up effect is small and that the correction factors are very close to 1 (1-3% deviations). The pile up fraction effect is treated as a systematic uncertainty on the measured yield in Sec. 6.3.6.

A second method to estimate the normalisation factor in multiplicity bins has also been used. It is based on rescaling the integrated global normalisation factor, calculated with the offline method, with the ratio of the fraction of MB events to the fraction of di-muon events in each multiplicity slice:

$$(6.11) \quad F_{norm}^{resc;bin_j} = F_{norm}^{offline} \frac{N_{MB}^{bin_j}/N_{MB}}{N_{CMUL}^{bin_j}/N_{CMUL}}$$

This method has the advantage of having a smaller statistical error than the offline method. The values yielded by this method are slightly different than the offline method values. The reason for this difference is that the event selection affects differently the event samples used. Hence, the normalisation factor used in the analysis is the unweighted average of the  $F_{norm}^{bin_j}$  given by the two methods. The difference between the mean and the values is used as systematic uncertainty. More details are given in Sec. 6.3.

## 6.2 Event selection efficiency correction

The yields computed with the ingredients included so far, are relative to MB collisions passing the event selection. In order to obtain the  $J/\psi$  production rate in non-single diffractive (NSD) collisions, the efficiency of the applied cuts and the MB trigger efficiency have to be accounted for. In this section we discuss the need of applying an efficiency correction or not for each cut applied to the analysed events:

**Vertex position  $|z_v| < 10$  cm:** The requirement of  $|z_v| < 10$  cm does not need an efficiency correction, since the  $J/\psi$  yield and multiplicity (the actual values, not the raw measured ones) do not depend on the interaction vertex of the collision. This affects in the same way the number of extracted  $J/\psi$  and the number of MB events, so the effect vanishes on the yield.

**Vertex requirement:** For the analysis in multiplicity bins, the cuts on SPD vertex are necessary to insure a correct multiplicity computation for the events. As already discussed, since the first multiplicity bin starts at one measured tracklet in  $|\eta| < 1$ , when slicing in multiplicity bins, the SPD vertex requirement is implicit. As considered in Sec. 3.7, the MB trigger efficiency is 100% for NSD events with a reconstructed vertex, so no correction associated to this cut is needed. For the integrated analysis, since no vertex cuts or tracklets requirements are performed, the efficiency of the MB trigger to select NSD collisions is needed. As found in [239], the fraction of NSD events selected by the MB trigger and passing the physics selection is  $\epsilon_{MB}^{NSD} = 99.2\%$ . Consequently, the multiplicity integrated  $J/\psi$  yield is given by:

$$(6.12) \quad \langle Y^{J/\psi} \rangle_{NSD} = \frac{N_{J/\psi}^{corr, tot}}{BR_{J/\psi \rightarrow \mu^+ \mu^-} \cdot N_{MB} / \epsilon_{MB}^{NSD}}$$

where  $N_{J/\psi}^{corr, tot}$  denotes the total  $\mathcal{A} \times \epsilon$  corrected number of  $J/\psi$  in the data sample used for the multiplicity integrated analysis.

**Vertex QA:** As mentioned in Sec. 4.7.1, the QA vertex selection removes events with low tracklets multiplicity, which has an influence on the mean value of the multiplicity in the first multiplicity bin. Consequently, this also has an impact on the number of extracted  $J/\psi$  at low multiplicity. In the case of no correlation of the QA vertex selection cut with the  $J/\psi$  production, no correction would be needed neither in the multiplicity nor in the number of extracted  $J/\psi$ . However, one could think on the case that the QA removes, for example, only low multiplicity events without  $J/\psi$ . In this case the impact on the number of extracted  $J/\psi$  would not be compensated by the variation of the average multiplicity in the slice and a correction would be needed.

This effect should be studied in simulation<sup>1</sup>, but we have no simulations which provide enough  $J/\psi$  statistics correlated to the underlying event to do such a study. Nevertheless,

<sup>1</sup>It could also be done in data by studying the yield with or without the vertex QA selection, but the uncertainties of the signal extraction would shade this effect

the effect is expected to be small, since the fraction of MB events removed by the vertex QA selection in the first multiplicity bin is 0.9% (negligible at higher multiplicities), as found in Sec. 4.7.1. In the case where the vertex QA selection would only remove low multiplicity events without  $J/\psi$ , the number of  $J/\psi$  would remain unchanged with or without the cut but the number of MB events in the first bin would be 0.9% bigger. This would make the yield a 0.9% smaller in the first multiplicity bin when including the events not passing the vertex QA. In the case where the events removed by the vertex QA had always a  $J/\psi$ , there would be no effect on the yield. Therefore, the maximum effect of the vertex QA selection on the yield in the first multiplicity bin is 0.9%.

If we consider the relative yield, we need to take into account that the effect of the vertex QA is correlated between the numerator and denominator. The fraction of total MB events removed by the vertex QA selection was determined to be  $\sim 0.3\%$  in Sec. 3.7. Consequently, this partially compensates the effect on the first bin, producing a variation of 0.6% on the relative yield. The variation on the relative yield in higher multiplicity bins would be 0.3% at most due to the total MB events variation.

Since we do not know the  $J/\psi$  production in events not passing the vertex QA, we cannot correct by this selection. A systematic uncertainty of 0.6% is assigned to the relative yield in the first multiplicity bin, and 0.3% for the rest of the bins. For the absolute yield measurement, there is no compensation in the first bin, so a 0.9% uncertainty is assigned. There is no effect on higher multiplicity bins, so no associated uncertainty.

### 6.3 Systematic uncertainties

The main objective of this chapter is to measure relative yields. In this measurement, some of the systematic uncertainties, present in the absolute measurement, cancel in the ratios. The relative yield can be expressed for each multiplicity bin  $i$  as follows (using Eq. 6.12 and 6.6):

$$(6.13) \quad \frac{(dN_{J/\psi}/dy)^i}{\langle dN_{J/\psi}/dy \rangle} = \frac{Y_{J/\psi}^i}{\langle Y_{J/\psi} \rangle} = \frac{N_{J/\psi}^{corr, i}}{N_{J/\psi}^{corr, tot}} \times \frac{F_{norm}}{F_{norm}^i} \times \frac{N_{CMUL}}{N_{CMUL}^i} \times \frac{1}{\epsilon_{MB}^{NSD}}$$

Note that the branching ratio and its uncertainty cancel on the ratio. In fact, all the systematic uncertainties which are correlated between the integrated and multiplicity differential yields cancel on the ratios at first order. Only the uncorrelated uncertainties remain. Since the tracking, trigger and trigger-tracker matching efficiencies do not depend on the event multiplicity in Pb-Pb collisions (within the multiplicities obtained in this analysis) [205], we have no reason to think that this is different in p-Pb collisions. It is therefore considered that the corresponding systematic uncertainties cancel in the  $N_{J/\psi}$  ratio.

However, the  $J/\psi$   $p_T$  distribution changes with the multiplicity, which might imply a variation of the spectrometer  $\mathcal{A} \times \epsilon$ . Besides, the uncertainty on the correction for the

multiplicity estimation might produce bin-flow, changing the obtained result in each bin. The fit combination used to extract the signal can influence the result in a different way for the integrated and bin by bin results. On the normalisation factor  $F_{norm}$  side, the systematic uncertainty is extracted from the computation with two different methods and the possible variations due to the bin-flow. A systematic uncertainty due to the pile up is also assigned. Finally, the effect of the systematic uncertainty on the MB trigger efficiency for NSD events is added as a global uncertainty. Every effect mentioned here is treated in a dedicated subsection below.

The systematic uncertainty for the different quantities in Eq. 6.13 is determined from a series of  $n_{tests}$  tests in a given multiplicity bin  $i$ . The values of the quantities are taken as the average in Eq. B.1, the statistical uncertainty is the error on the average in Eq. B.2 and the systematic uncertainty is the  $1-\sigma$  dispersion of the different tests, Eq. B.4. When computing the systematic uncertainties for the relative yield, we take into account the correlation of the quantities in Eq. 6.13 within the systematic tests, by estimating the uncertainty directly on the ratio.

### 6.3.1 Signal extraction uncertainty

In this section we evaluate the systematic uncertainty on the extraction of the number of  $J/\psi$ . We focus on the computation for the ratio  $N_{J/\psi}^{R, i} = N_{J/\psi}^{corr, i} / N_{J/\psi}^{corr, tot}$ , but the procedure is similar for the absolute measurement. The signal shape does not change with the event multiplicity as was shown in Pb-Pb [205]. It is considered that the same is true in p-Pb collisions. Therefore, the systematic uncertainty in the  $N_{J/\psi}$  ratio only comes from the background parametrization. To study this source of uncertainty, a series of  $n_{tests}$  tests have been performed. In these tests the signal shape (tail parameters and the factor  $f$  in  $\sigma_{\psi(2S)}$ ) is the same in the numerator and denominator. Only the components of the fits which affect the background are allowed to be different between the numerator and the denominator: the background parametrization itself and the fitting range. These variations imply a total of 96 tests per bin (24 fit combinations per bin (integrated)  $\times$  2 bkg. shape variations  $\times$  2 fitting range variations).

The final values of the  $\mathcal{A} \times \mathcal{E}$  corrected number of  $J/\psi$  in a multiplicity bin  $i$ , are computed as the average of the values obtained for each fit combination (combination signal+background +range+ $\sigma_{\psi(2S)}$ ). However, for the relative yield, the ratio bin/integrated quantity is performed for each test  $j$ . The average of the ratios is then calculated. In this way, we account for the correlation between the integrated and bin number of  $J/\psi$  within the  $j$ -th test. The

Eq. B.1 in this case can be written as<sup>2</sup>:

$$(6.14) \quad \langle N_{J/\psi}^R \rangle^i = \left\langle \frac{N_{J/\psi}^{corr, i}}{N_{J/\psi}^{corr, tot}} \right\rangle = \frac{1}{n_{tests}} \times \sum_{j=1}^{n_{tests}} \left( \frac{N_{J/\psi}^{corr, i}}{N_{J/\psi}^{corr, tot}} \right)_j$$

where  $n_{tests} = 24$  is the number of fit combinations keeping the same signal shapes and their parameters for the integrated (denominator) and bin (numerator) extraction. The statistical uncertainty is the error on the average in Eq. B.2 and Eq. B.3 and the systematic uncertainty is the  $1\text{-}\sigma$  dispersion of the different tests, Eq. B.4.

For the absolute signal extraction,  $N_{J/\psi}^{corr, tot}$  and  $N_{J/\psi}^{corr, i}$ , the average values and uncertainties are computed in a similar way. However, in this case there is no restriction on the possible fit combinations used for the tests.

As an instance, the  $N_{J/\psi}^{R, i}$  results are shown in Fig. 6.8 as a function of the test for one multiplicity bin in p-Pb. Each point is the computed ratio with the statistical error (Eq. B.3). The red solid line is the unweighted mean of all the values (Eq.6.14) and the dotted red line is the  $1\text{-}\sigma$  dispersion of all the tests (Eq.B.4), which represents the signal extraction systematic uncertainty in the bin. As can be observed the values are always compatible among them and with the mean value. Most of them lay within the found systematic uncertainty.

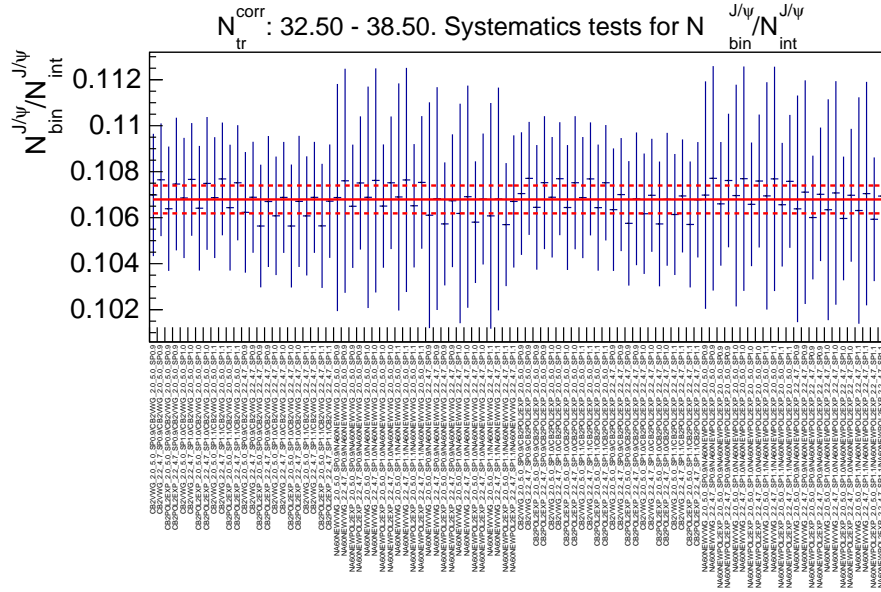


Figure 6.8: Example of signal extraction test set for the relative yield systematic uncertainty in a multiplicity bin in p-Pb. The red solid line is the unweighted mean of all the values (Eq.6.14) and the dotted red line is the  $1\text{-}\sigma$  dispersion of all the tests (Eq.B.4), which represents the signal extraction systematic uncertainty in the bin.

<sup>2</sup>Note that the unweighted mean is used. As explained in App. B, we do not know a priori if the number of  $J/\psi$  extracted from a test is closer to the actual value than the others

In Fig. 6.9 the resulting relative signal extraction systematic uncertainties for each multiplicity bin in p-Pb and Pb-p are shown. The uncertainty is usually smaller than 1%, except for the last multiplicity bin, where it reaches about 2.4%. Note that these are typical values, but the multiplicity bin-flow can make them change from execution test to execution test (Sec. 4.7.3), as we explain below.

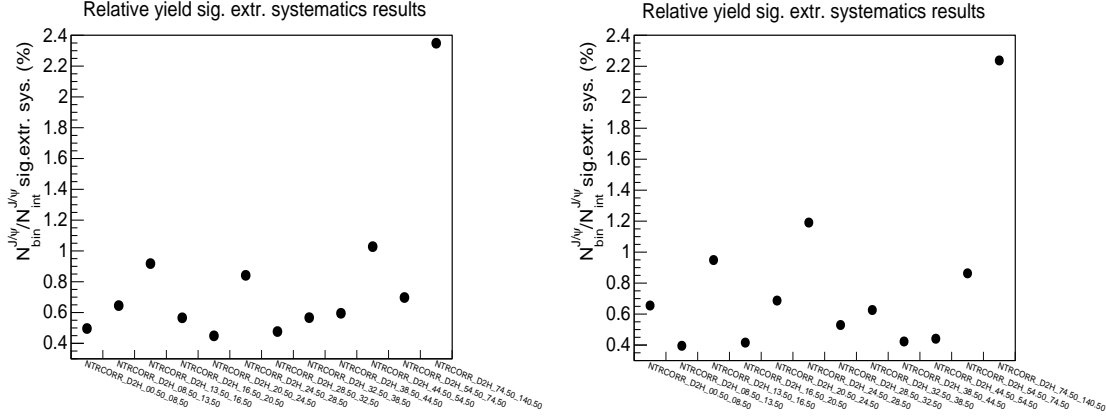


Figure 6.9: (Left) Relative signal extraction systematic uncertainty in multiplicity bins in p-Pb. (Right) Relative signal extraction systematic uncertainty in multiplicity bins in Pb-p. These values are for one single execution of the multiplicity analysis. See also Fig. 6.10 for the final values.

In order to take into account the possible variations due to multiplicity bin-flow, the obtained signal extraction systematic uncertainty for each bin is represented as a function of the series of execution tests (different executions of the analysis task). These execution tests are obtained changing the seed of the random number generator for the multiplicity correction (Sec. 4.7.3). The results are shown for p-Pb in Fig. 6.10. The figure shows the relative difference between the most different results ( $\Delta_{max}$ ), the mean value (red line) and the  $1\text{-}\sigma$  dispersion among the values ( $\sigma$ ). The value of the uncertainty is quite variable from test to test in the same bin. This is because small changes on the data sample in a bin can make a series of signal extraction tests to converge to rather different values. In the end, the signal extraction systematic uncertainty for each bin is taken as the average value of the tests in each bin (red line). The signal extraction systematic uncertainty ranges between 0.6% and 2% in p-Pb depending on the multiplicity bin. Similar results are obtained in Pb-p.

### 6.3.2 Tails variation uncertainty

As discussed in previous  $J/\psi$  analyses in p-Pb, the uncertainty on the absolute signal extraction due to the limited knowledge of the tails is estimated to be  $\sim 2\%$ , by using several sets of tails to extract the  $J/\psi$  signal. The same value is used for the absolute yield results obtained here.

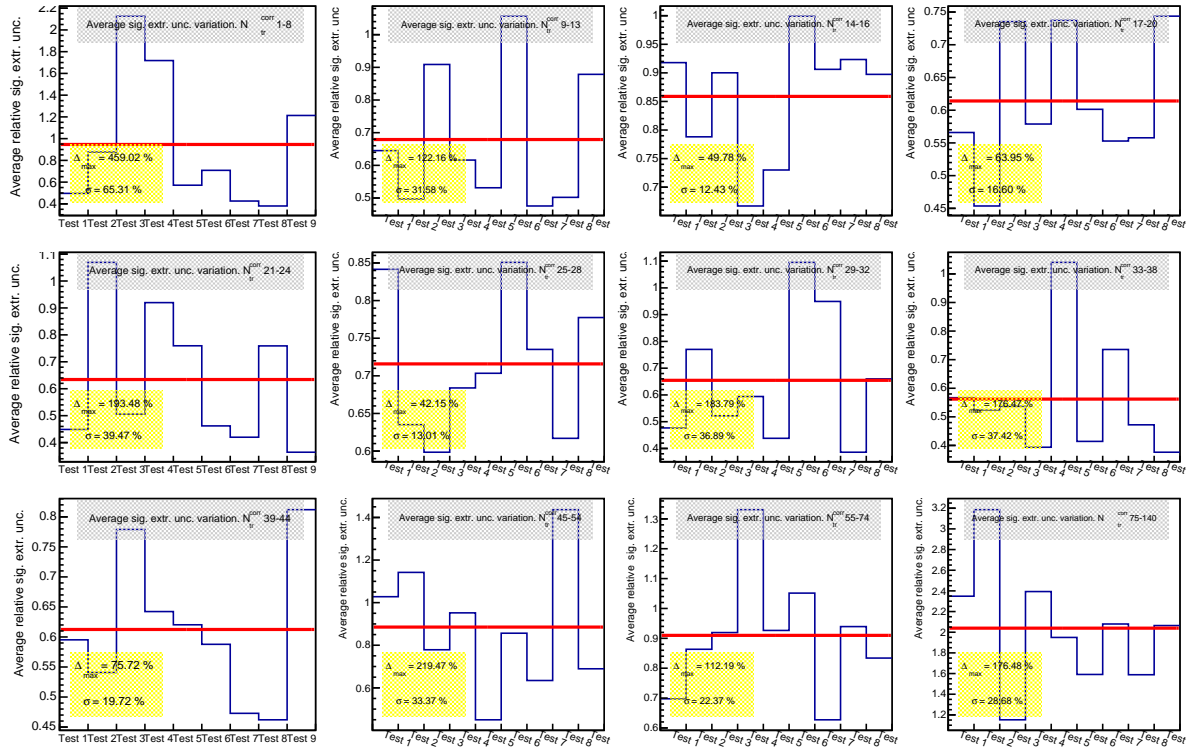


Figure 6.10: Relative signal extraction systematic uncertainty variations due to bin-flow in multiplicity bins in p-Pb. Each value in a bin corresponds to the result of a set of signal extraction tests (as in Fig. 6.9) obtained in a execution test. The figure shows the relative difference between the most different results ( $\Delta_{max}$ ), the mean value (red line) and the 1- $\sigma$  dispersion among the values ( $\sigma$ ).

But in the case of the relative number of  $J/\psi$ , since the signal is known to remain the same in the integrated and in multiplicity bins, most of this effect should vanish on the ratio. However there is a correlation between the amount of  $J/\psi$  in the signal tails and the amount of background di-muons in that region. Since the background parametrization can be different for the integrated and multiplicity bin spectra, it is necessary to study the effect of using different sets of tails on the relative number of  $J/\psi$ . This study is currently ongoing, but we consider that the effect is small. However in order to be conservative, a systematic uncertainty of 1% due to this effect is considered for the results in this thesis.

### 6.3.3 Di-muon trigger event normalisation uncertainty

The systematic uncertainty on the integrated  $F_{norm}$  was already computed in [263]. It was found to be 1% and this is the value that is used here as well for the integrated di-muon trigger event normalisation factor.

As explained in Sec. 6.1.4, two methods to compute the  $F_{norm}$  in multiplicity bins have

been used. The final value of the  $F_{norm}$  in multiplicity bins which we use to compute the yields, is the unweighted average of the values given by the two methods. The systematic uncertainty on the computation method in a multiplicity bin is given by the difference between the average and the individual values of the two methods. The differences are typically between 1% and 4% at low and high multiplicities respectively. These values are used as systematic uncertainty on the  $F_{norm}^i$  computation for the absolute yield values.

For the relative yield we are interested in the ratio of the integrated and multiplicity differential  $F_{norm}$ . Therefore, we need to correctly combine the integrated and differential systematic uncertainties. For this it is required to know the level of correlation between both quantities. The systematic uncertainty on the relative normalization factor  $F_{norm}^{R,i} = F_{norm}^i / F_{norm}$  can be estimated as follows. If we compute the relative number of MB events using  $F_{norm}^{resc}$  (Eq. 6.11), the systematic uncertainty on the integrated  $F_{norm}$  ( $F_{norm}^{offline}$ ) would vanish on the ratio. If we assume the same level of correlation between the integrated and bin  $F_{norm}$  with the offline method, the uncertainty of the integrated value also vanishes. Therefore, we consider that only the systematic uncertainties mentioned above due to the computation method in the multiplicity bin  $i$ , remain on the  $F_{norm}^{R,i}$  computation.

As already mentioned, the bin-flow effect changes the events entering in a given multiplicity bin. It was shown in Sec. 4.7.3 that this effect is smaller than 0.2% in terms of the number of di-muon events in a bin. Nevertheless this variation can go in opposite directions for the different triggered samples used when computing the  $F_{norm}$ . This may cause bigger variations in the number of equivalent MB events in a bin than those observed for the number of di-muon events. In Fig. 6.11 the variation of the number of MB events as a function of the different execution tests is shown. The figure shows also the relative difference between the most different results,  $\Delta_{max}$ , the mean value (red line), the error on the mean (dotted line) and the 1- $\sigma$  dispersion among the values  $\sigma$ . The variations are small but still bigger than those of the number of di-muon events for the reason previously stated. The variations of the number of equivalent MB events are between 0.3% and 2.1% depending on the multiplicity bin considered. This uncertainty is included in the one estimated in section 6.3.5, by computing the bin-flow variations directly on the relative yield itself.

### 6.3.4 Uncertainty on the input MC distributions for $\mathcal{A} \times \mathcal{E}$ computation

The changes on the  $p_T$  and  $y$  distributions with multiplicity can result in changes on the spectrometer  $\mathcal{A} \times \mathcal{E}$ , which are not taken into account using a single correction. Ideally the measured  $p_T$  and  $y$  distributions should be extracted for each multiplicity bin and used as input in the MC simulations to compute the corresponding  $\mathcal{A} \times \mathcal{E}$  correction. However, if the changes on the distributions with multiplicity are not big this may not be necessary, specially using a 2-D  $\mathcal{A} \times \mathcal{E}$  correction. The more differential the  $\mathcal{A} \times \mathcal{E}$  correction the less sensitive it is to changes on the input distributions. Negligible changes on the 2D  $\mathcal{A} \times \mathcal{E}$  are expected due to changes on the distributions, and thereby no changes on the signal extraction with multiplicity. However these changes might be noticeable when using an integrated





$N_{tr}^{corr}$ bin	$N_{J/\psi}^{raw}/\mathcal{A}\times\mathcal{E}$	$N_{J/\psi}^{corr}$
0.5 - 8.5	$18358 \pm 377$	$18668 \pm 458$
8.5 - 13.5	$21753 \pm 418$	$22203 \pm 523$
13.5 - 16.5	$16695 \pm 385$	$16928 \pm 464$
16.5 - 20.5	$23473 \pm 456$	$23017 \pm 549$
20.5 - 24.5	$24273 \pm 476$	$23939 \pm 579$
24.5 - 28.5	$23298 \pm 461$	$23754 \pm 588$
28.5 - 32.5	$21419 \pm 460$	$21220 \pm 552$
32.5 - 38.5	$27623 \pm 534$	$27699 \pm 676$
38.5 - 44.5	$20309 \pm 456$	$20154 \pm 578$
44.5 - 54.5	$20924 \pm 480$	$20760 \pm 593$
54.5 - 74.5	$13233 \pm 397$	$12995 \pm 497$
74.5 - 140.5	$1723 \pm 148$	$1603 \pm 174$

Table 6.6: p-Pb  $J/\psi$  extraction from raw spectra and corrected by integrated  $\mathcal{A}\times\mathcal{E}(0.252)$  compared to the result of the extraction from the  $\mathcal{A}\times\mathcal{E}$  corrected spectra for a single fit test. The uncertainties are the statistical uncertainties given by the fit.

them hard(soft)- $y$  and hard(soft)- $p_T$ ) are shown in four panels. They show the nominal  $p_T$  and  $y$  distributions together with the variations. We can also see the ratio of the corrections obtained with the nominal distributions, and the ones obtained with the varied distributions. As can be observed in the ratios, the different input distributions leave the corrections almost unchanged. The biggest differences ( $\sim 1.5\%$ ) are found in the  $(p_T, y)$  bins corresponding to a rapidity in  $-4 < y < -3.6$ . This difference is caused by the lower MC statistics in that region. Due to the lower statistics, the bins in that region are wider than the rest, and therefore the changes on the input distribution affect more the correction value. However, due to the low statistics in these bins also in data (due to low  $\mathcal{A}\times\mathcal{E}$ ), the variations on the  $\mathcal{A}\times\mathcal{E}$  correction here have a negligible effect on the total number of extracted  $J/\psi$ .

The four  $\mathcal{A}\times\mathcal{E}$  corrections have been used to correct the data and perform the full signal extraction with all the possible fit combinations tests. Then, the results are compared with the results obtained with the nominal  $\mathcal{A}\times\mathcal{E}$  correction. In Fig 6.13 the results of the integrated  $\langle N_{J/\psi} \rangle$  for the four varied  $\mathcal{A}\times\mathcal{E}$  corrections are shown in blue, and the nominal result as the red line. Each point is the average value of the results of all the fit combinations (Eq. B.1), and the error of each point is the error on the average (dotted red line for nominal value) (Eq. B.2). The figure shows the relative difference between the most different results ( $\Delta_{max}$ ), between the nominal value and the more distant value ( $\Delta_{nom}$ ) and the  $1\text{-}\sigma$  dispersion among the values ( $\sigma$ ) (Eq. B.4). The differences and dispersion are smaller than 1%. The systematic uncertainty is taken to be the maximum difference between the obtained values with different distributions. The value obtained in this thesis is 0.74%. If one compares with the value obtained in [263], 1.5%, we observe that the two-dimensional  $\mathcal{A}\times\mathcal{E}$  correction

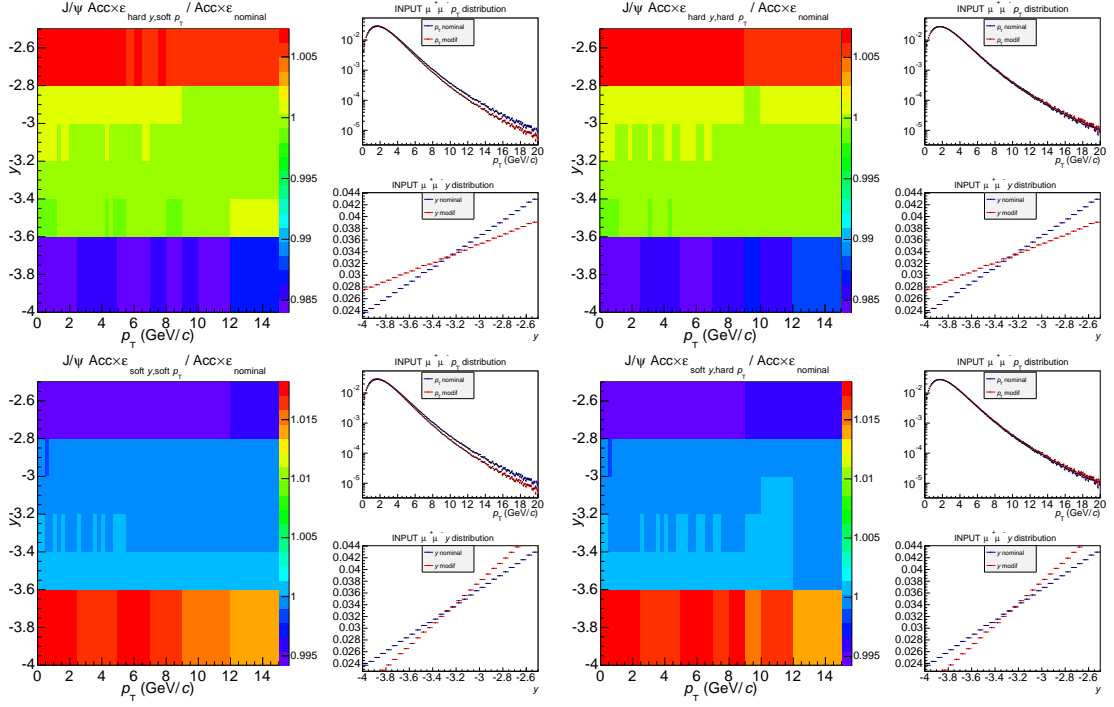


Figure 6.12:  $\mathcal{A} \times \epsilon$  variations (ratio varied over nominal correction) due to changes in the input MC distributions and the used input distributions (the blue curves represent the nominal and the red curves the varied distributions). The results are shown for four combinations of extreme variations of the  $p_T$  and  $y$  distributions: hard- $y$  and soft- $p_T$  (top left), hard- $y$  and hard- $p_T$  (top right), soft- $y$  and soft- $p_T$  (bottom left), soft- $y$  and hard- $p_T$  (bottom right).

method is less sensitive to the shape of the input distributions, which reduces the value of the associated systematic uncertainty by about 50% with respect to the use of the integrated correction.

In Fig 6.14 a similar result for the relative signal extraction in multiplicity bins,  $\langle N_{J\psi}^R \rangle^i$  (Eq. 6.14), is presented. In this case unexpectedly big differences (1-12%) are found. It turns out that the  $\mathcal{A} \times \epsilon$  is not the only responsible of these differences, but the effect of bin-flow and signal extraction are also contributing. As we show later, the effect of the  $\mathcal{A} \times \epsilon$ , bin-flow and signal extraction cannot be separated. This is treated in the following subsection.

### 6.3.5 Bin-flow uncertainty. Combination of $\mathcal{A} \times \epsilon$ , bin-flow and signal extraction uncertainties

In order to give an estimation of the multiplicity-bin-flow effect on the measured  $\langle N_{J\psi}^R \rangle^i$ , we follow the same procedure as in Sec. 4.7.3. We use the nominal  $\mathcal{A} \times \epsilon$  correction in four executions of the analysis under the same conditions (analysis facility, binning, data sample and analysis code version). The full signal extraction procedure is performed each time. As a cross-check, it has been seen that the integrated  $\langle N_{J\psi} \rangle$  is exactly the same as for the

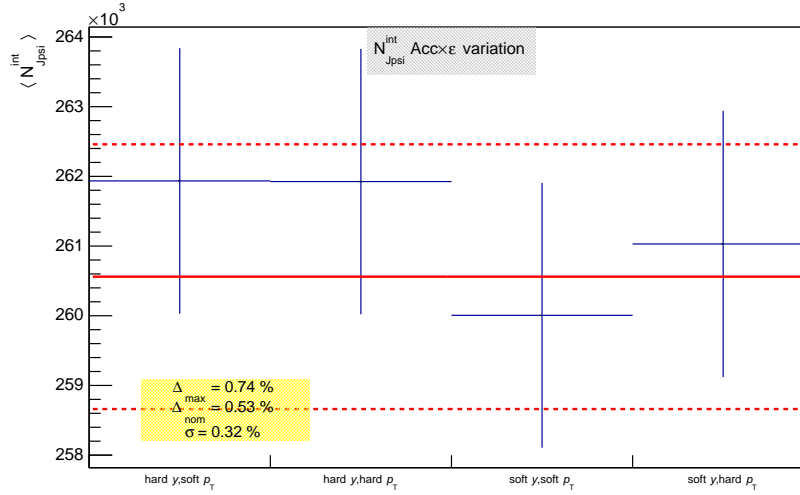


Figure 6.13: Integrated signal extraction with different  $\mathcal{A} \times \mathcal{E}$  corrections.  $\langle N_{J\psi} \rangle$  for the four varied  $\mathcal{A} \times \mathcal{E}$  corrections are shown in blue and the nominal result as the red line. The figure also shows the relative difference between the most different results ( $\Delta_{max}$ ), between the nominal value and the more distant value ( $\Delta_{nom}$ ) and the  $1\text{-}\sigma$  dispersion among the values ( $\sigma$ ) (Eq. B.4). The systematic uncertainty due to the  $\mathcal{A} \times \mathcal{E}$  is taken as  $\Delta_{max}$  which is 0.74%.

"nominal" case, in order to discard possible effects of the signal extraction procedure when the spectra are the same. The results in multiplicity bins are shown in Fig. 6.15 as a function of the tests ( $n$ -th execution). The results of each test are the blue points and the "nominal" result is the red line. Each point is the mean value of the results of all the fit combinations as in Eq. 6.14, and the point error is the error on the mean value (dotted red line for nominal value). The definitions of  $\Delta$ 's and  $\sigma$  are the same as for the  $\mathcal{A} \times \mathcal{E}$  tests.

The values of the dispersion are of the same order (or even bigger for certain bins) as the ones for the  $\mathcal{A} \times \mathcal{E}$  tests. This means that the effect of the  $\mathcal{A} \times \mathcal{E}$  variations alone is very small and it is the bin-flow, together with the fitting procedure, that is the leading source of the signal extraction variations. The explanation for this is that even if the number of events in each bin barely changes from execution to execution, the shape of the spectrum in each bin changes slightly (different  $(p_T, y)$  di-muon pairs enter in the bin). As a consequence, the fitting procedure converges to different values.

This means that the effects of the  $\mathcal{A} \times \mathcal{E}$ , signal extraction, and bin-flow have to be treated as a whole. From now on, we consider the effect of the  $\mathcal{A} \times \mathcal{E}$  negligible compared to bin-flow/signal extraction, which allow us to treat the "nominal" and  $\mathcal{A} \times \mathcal{E}$  tests in Sec. 6.3.4 in the same way as the different execution tests in this section.

In addition, to account for the bin-flow correlation effect between the  $\langle N_{J\psi}^R \rangle^i$  and number of equivalent MB events, we cannot separate the computation of these quantities when computing the yield and its systematic uncertainty. Therefore, using Eqs. 6.13 and 6.14 the relative yield is computed for every execution test. The results of the relative yields as a

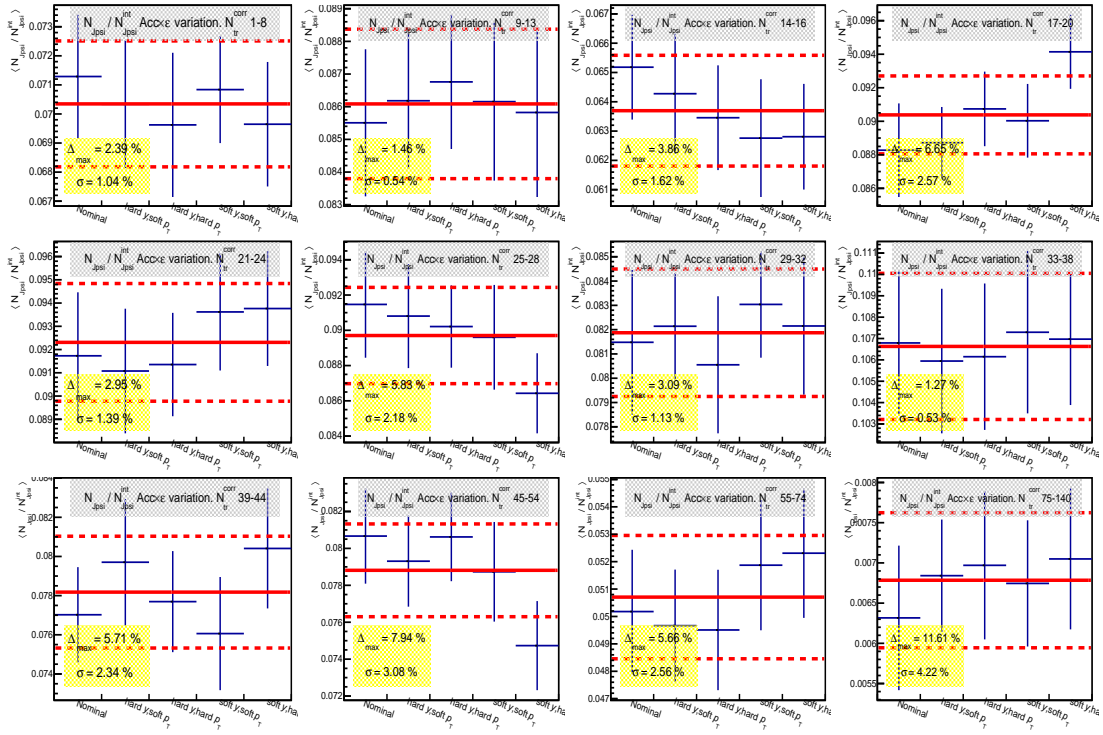


Figure 6.14: Relative signal extraction with different  $\mathcal{A} \times \epsilon$  corrections in multiplicity bins.  $\langle N_{J\psi}^R \rangle^i$  for the four varied  $\mathcal{A} \times \epsilon$  corrections are shown in blue and the nominal result as the red line. The figure also shows the relative difference between the most different results ( $\Delta_{max}$ ), between the nominal value and the more distant value ( $\Delta_{nom}$ ) and the 1- $\sigma$  dispersion among the values ( $\sigma$ ) (Eq. B.4).

function of the test, together with the mean value (red solid line), the error on the mean (dotted line) and the 1- $\sigma$  dispersion are shown in Fig. 6.16. The mean value accounts for the  $\mathcal{A} \times \epsilon$ , signal extraction and bin-flow effects, and is taken as the final value for each bin. The error on the mean is the statistical error and the 1- $\sigma$  dispersion is taken as the combined systematic uncertainty of the three effects.

Similar tests are performed on the absolute yield measurement, obtaining very similar uncertainties to the ones in the relative measurement. This is due to the fact that it is the multiplicity differential measurement which dominates the uncertainty.

However, the systematic uncertainty computed in this way takes into account only a part of the signal extraction systematic uncertainty. In these bin-flow tests, we only use the average value of the different relative signal extraction tests in Sec. 6.3.1 (Eq. 6.14). In addition, the average dispersion of the different signal extraction tests (results in Fig. 6.10) need to be taken into account. Therefore, the resulting systematic uncertainties in Fig. 6.16 are summed in quadrature to the signal extraction uncertainties in Fig. 6.10. In this way we obtain the total combined  $\mathcal{A} \times \epsilon$ , bin-flow and signal extraction systematic uncertainty. This

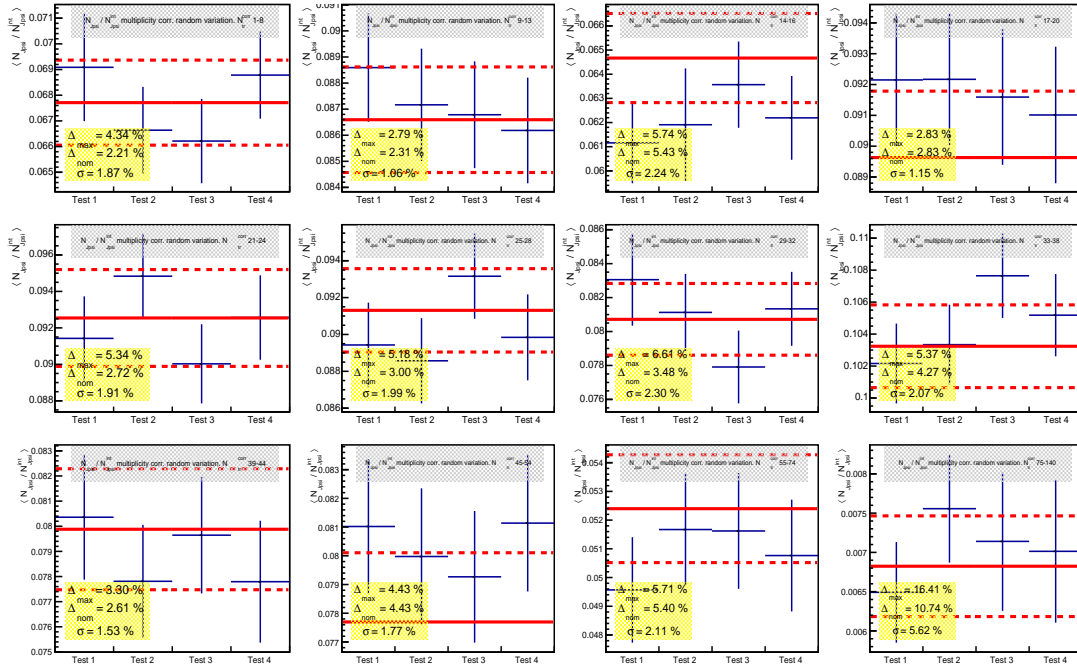


Figure 6.15: Relative number of  $J/\psi$ ,  $\langle N_{J/\psi}^R \rangle^i$ , extracted using the nominal  $\mathcal{A} \times \epsilon$  correction but four different execution of the analysis task. The result of each test are the blue points and the "nominal" result is the red line. The comparison of the results in different execution tests give an idea of the bin-flow effect on the signal extraction in each multiplicity bin.

uncertainty is the dominating one in this analysis for both relative and absolute  $J/\psi$  yield measurements.

It has been found that when taking into account additional execution tests, the obtained systematic uncertainties change by a few percent, specially in the las bin. This means that the value has not yet converged and it is necessary to add more tests to reach a stable value. This is currently being done<sup>3</sup>.

### 6.3.6 Pile-up

The toy MC used in Sec. 4.7.2 can be upgraded in order to study the pile-up effect on  $J/\psi$  production as a function of multiplicity. A pile-up free  $J/\psi$  yield as a function of multiplicity distribution is needed as input. We are going to assume that the pile-up effect on the yield is small. This allows to use the measured yield distribution as input, and study the pile-up effect on it. For each generated collision in an event with a given number of corrected tracklets, a certain number of  $J/\psi$ ,  $N_{J/\psi}^i$ , is randomly assigned in this way:

- $N_{J/\psi}^i$ : Generated with a Poissonian distribution centered at  $Y_{J/\psi}(N_{tr}^{corrected,i})$

<sup>3</sup>The reason to not merge the different sets of execution tests to compute the uncertainty is because they have slightly different event selections, which affects mainly low multiplicity.

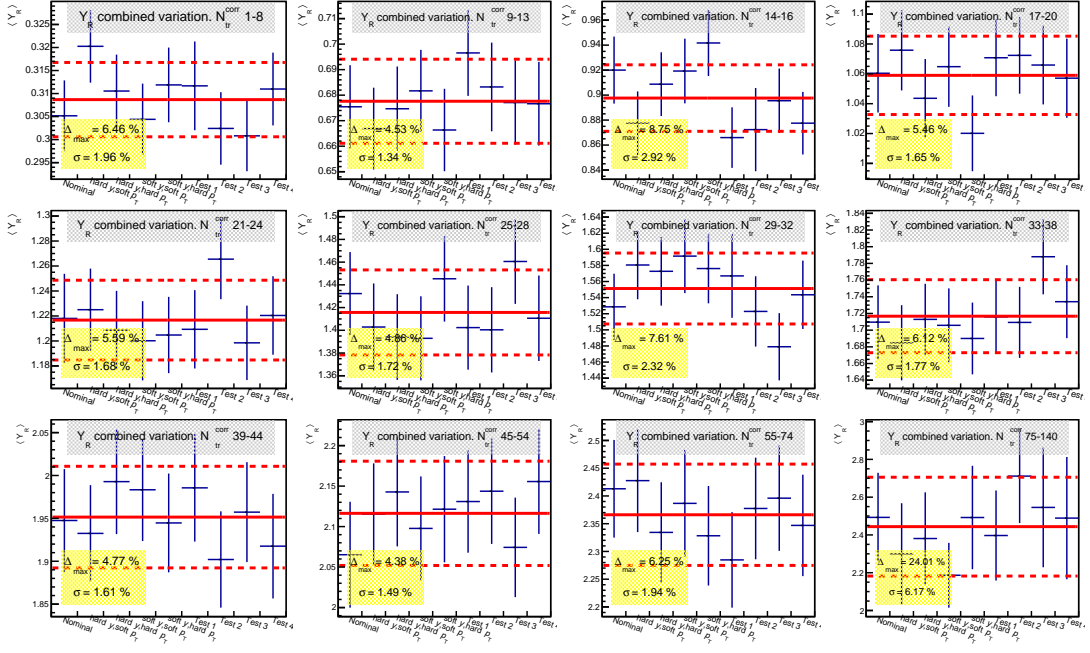


Figure 6.16: Variation on the relative yield in multiplicity bins due to bin-flow,  $\mathcal{A} \times \epsilon$  and signal extraction. The blue points are the average values of the relative yield obtained with Eqs. 6.13 and 6.14 in each execution test. The red line shows the average of the values obtained from the execution tests in each bin. The dotted line is the statistical error.  $\sigma$  is the value of the 1- $\sigma$  dispersion of the values for each execution test in a bin.

- The number of  $J/\psi$  in an event is the sum of the  $J/\psi$  in every collision of the event

This simulates the fact that in data, when a muon is measured in the spectrometer, it is not possible to distinguish if it is coming from the main vertex or from a secondary one, so all the  $J/\psi$  within the acceptance of the spectrometer are taken. This effect always tends to raise the measured  $J/\psi$  yield with respect to the true one even if the SPD is able to distinguish different collisions. In addition, the selection of the main collision as the one with the highest number of tracklets introduces also a bias in the  $J/\psi$  yield, due to the fact that we are not able to discriminate from which collision the  $J/\psi$  is coming from. But it has been measured that the yield rises with multiplicity, so the probability that the  $J/\psi$  is coming from the event with highest multiplicity is bigger. In consequence this bias is expected to be small.

In order to study the effect of the main collision determination alone, the vertex merging pile-up is switched off in the MC and only the  $J/\psi$  coming from the main collision are counted. It has been seen that this effect is indeed unobservable for the  $\langle \mu \rangle$  considered here.

The next step is to consider all the  $J/\psi$  in the event. This tends to artificially rise the  $J/\psi$  production probability per MB collision in a multiplicity bin. According to the result obtained with the toy MC, the number of MB events with a  $J/\psi$  where more than one  $J/\psi$  has been found is estimated to be  $\sim 0.02\%$  ( $0.05\%$ ) in p-Pb (Pb-p), indeed negligible. Also, the



number of MB events with a  $J/\psi$ , where the  $J/\psi$  comes from a secondary collision, has been found to be about 1.2% for the  $\langle\mu\rangle$  values and yield distributions considered here, both in p-Pb and Pb-p collisions. The reference yield (the one measured in this analysis) and the pile-up toy MC results are shown in Fig. 6.17 for p-Pb and Pb-p, together with the ratio of the reference and pile-up distributions. The points are placed at the MB  $N_{tr}^{corr}$  average value of each multiplicity bin. The effect reaches  $\sim 2\%$  in both collision systems and it always tends to raise the measured yield in a multiplicity bin as it is expected. The effect rises with multiplicity up to a maximum about  $N_{tr}^{corr} \sim 30-50$  and then it decreases with multiplicity at high multiplicity. To explain this we need to take into account the  $N_{tr}^{corr}$  distribution, together with the yield correlation with  $N_{tr}^{corr}$ . Regarding the  $N_{tr}^{corr}$  distribution, when a collision with low/mid multiplicity is selected as main collision, in case of existing secondary collisions in the event they probably have a similar multiplicity than the main one. Therefore the contributions to the yield from each collision are comparable, so the effect is sizeable. On the contrary, when a high multiplicity collision is selected as a main collision, the secondary collisions are most probably low/mid multiplicity ones. Therefore, the contribution to the yield is smaller than that of the high multiplicity collision and hence the effect is smaller. Another observation is that the dependence of the effect with multiplicity barely changes between p-Pb and Pb-p, Fig. 6.17 left and right. The reason for this is that the rise of the yield due to taking all the  $J/\psi$  in the event, depends mainly on the multiplicity distribution and the difference on the production probability between low and high multiplicity events. The difference between the yield dependence at high multiplicity in p-Pb and Pb-p is not big enough to observe a difference in this effect.

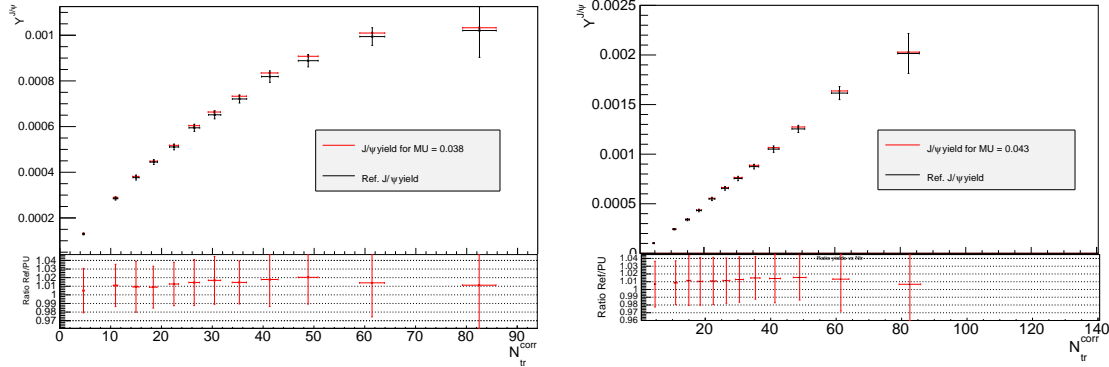


Figure 6.17:  $J/\psi$  yield as a function of number of corrected tracklets obtained from the toy MC. The vertex merging is switched off, so the observed effect is due to taking all the  $J/\psi$  in the event. The figure shows that the effect has a similar size in p-Pb (left) and Pb-p (right).

The next effect to account for is that when two or more collisions are merged, the event multiplicity is overestimated. The multiplicity of the resulting pile-up event is the sum of the multiplicities of the individual collisions. As a result, the contribution to the  $J/\psi$  yield of the merged event corresponds to the sum of the yield contributions of the individual events.



Therefore, in this case, the effect on the measured yield depends on the actual multiplicity correlation of the yield. In the following, we try to make a qualitative estimation of the effect for the different shapes of the measured yields in this thesis. We are going to separate the behaviour at low and high multiplicities. From the observed behaviour in p-Pb and Pb-p collisions, it is reasonable to assume a linear dependence of the yield with multiplicity,  $Y_{J/\psi}^{low} = a \cdot N_{tr}^{corr}$ , in the low multiplicity region. Note that in this region the effect of merging collisions is bigger. At high multiplicity different behaviours can qualitatively agree with the obtained results. Let us suppose that two low multiplicity collisions, having  $N_{tr}^{corr 1}$  and  $N_{tr}^{corr 2}$ , are merged. Then the pile-up effect on the yield at high multiplicity might be, depending on the yield dependence with multiplicity:

- a) If  $Y_{J/\psi}^{high} = a \cdot N_{tr}^{corr}$ : The effect on the measured yield at the multiplicity of the merged event is null since  $Y_{J/\psi}^{p.u} = Y_{J/\psi}^{low}(N_{tr}^{corr 1}) + Y_{J/\psi}^{low}(N_{tr}^{corr 2}) = Y_{J/\psi}^{high}(N_{tr}^{corr 1} + N_{tr}^{corr 2})$
- b) If  $Y_{J/\psi}^{high} < a \cdot N_{tr}^{corr}$ : The measured yield at the multiplicity of the merged event is bigger than the actual one since  $Y_{J/\psi}^{p.u} = Y_{J/\psi}^{low}(N_{tr}^{corr 1}) + Y_{J/\psi}^{low}(N_{tr}^{corr 2}) > Y_{J/\psi}^{high}(N_{tr}^{corr 1} + N_{tr}^{corr 2})$
- c) If  $Y_{J/\psi}^{high} > a \cdot N_{tr}^{corr}$ : The measured yield at the multiplicity of the merged event is smaller than the actual one since  $Y_{J/\psi}^{p.u} = Y_{J/\psi}^{low}(N_{tr}^{corr 1}) + Y_{J/\psi}^{low}(N_{tr}^{corr 2}) < Y_{J/\psi}^{high}(N_{tr}^{corr 1} + N_{tr}^{corr 2})$

In Fig. 6.18 the comparison between the input yield and the MC result for p-Pb (left) and Pb-p (right) are presented. In this case, for p-Pb, the effect raises the yield at the last multiplicity bins. This is an expected result since the p-Pb measurement correspond to the **b)** case mentioned earlier. It can be observed that the difference between the MC result and the input value is always less than 4%. The Pb-p situation is different from the p-Pb one since now the effect of merging collisions is not observable, leaving only the effect of taking  $J/\psi$  from secondary collisions already observed in Fig. 6.17. This corresponds to the aforementioned **a)** case.

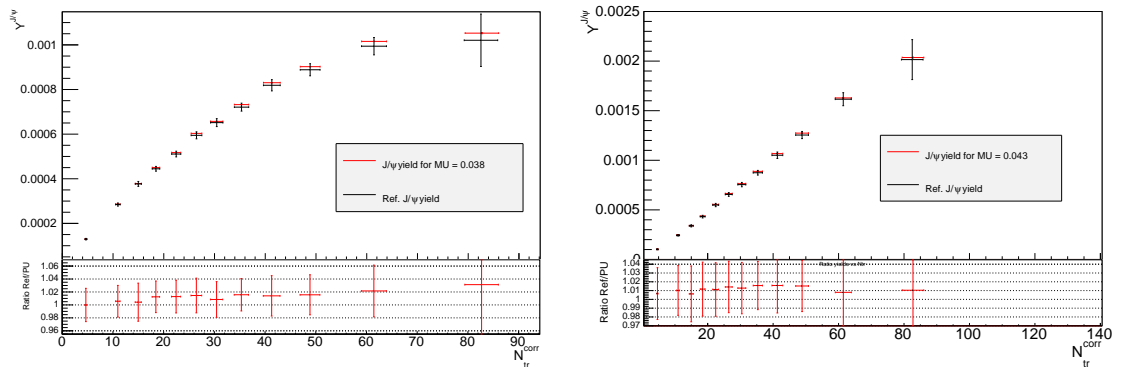


Figure 6.18:  $J/\psi$  yield as a function of number of corrected tracklets obtained from the toy MC with vertex merging and taking all the  $J/\psi$  in the event for p-Pb (left) and Pb-p (right).

Up to here, the binned yield as a function of multiplicity distributions have been used as input probability distributions. This is like assuming that the yield is constant or that it varies linearly within the multiplicity bins. This a doubtful assumption, specially in the p-Pb case. The comparison of the pile-up effect in p-Pb and Pb-p yields have shown the importance of the yield shape on the resulting effect. Consequently, in order to test different possible variations within the multiplicity bin, the input distributions are fitted with several functional forms and used as probability distributions for the generated yield. The result of the toy MC in each bin is compared with the yield function evaluated at the mean value of the MB multiplicity at each multiplicity bin. The fitting functions considered are:

1.  $f_1 = p_0 + p_1 \cdot x$
2.  $f_2 = p_0 + p_1 \cdot x + p_2 \cdot x^2$
3.  $f_3 = p_0 + p_1 \cdot x + p_2 \cdot x^2 + p_3 \cdot x^3$
4.  $f_4 = p_0 + p_1 \cdot x + p_2 \cdot x^2 + p_4 \cdot x^4$
5.  $f_{1/2} = p_0 + p_{1/2} \cdot x^{1/2}$

The results for several of these fitting functions used on p-Pb are presented in Fig. 6.19 and Tab. 6.7. Note that the fit results are performed taking into account only statistical uncertainties and not the systematic ones. The fit with the linear function  $f_1$  is limited to  $N_{tr}^{corr} = 30$ . As we can see from the result (top left), and the parameters in the table, the p-Pb yield follows approximately a linear behaviour at low multiplicity. The effect is bigger for the first multiplicity bin than with the binned distribution but approximately the same for the rest of the bins up to  $N_{tr}^{corr} = 30$ . The difference between the second ( $f_2$ ) and third ( $f_4$ ) shapes is mainly the behaviour for the last multiplicity bin. Note here that both results give very similar ratio with the reference distribution and also to the one obtained with the binned yield, except for the last bin. The fourth shape ( $f_{1/2}$ ) introduces differences both at low and high multiplicities. In this case, at high multiplicity, the ratio with the reference shape is quite similar although a bit smaller compared to that obtained with previous functions. However at low multiplicity the ratio descends to -5% due to the yield shape at very low multiplicity. In this case the yield function reaches zero at  $N_{tr}^{corr}(|\eta| < 1) > 0$ . This implies that there would not be  $J/\psi$  produced at low multiplicities, which is contrary to the observations (*i.e.*  $J/\psi$  photoproduction in Ultra Peripheral Collisions [264, 265]). Therefore the 5% variation observed with this test is not taken into account for the uncertainty estimation. Other shapes have been tested yielding similar results. Finally, we can conclude that different physically reasonable yield shapes do not produce dramatic changes on the pile-up effect. Taking the maximum possible effect within the physically reasonable cases leads to an estimation of the pile-up effect on the  $J/\psi$  yield of 1-4% in p-Pb depending on the multiplicity bin.

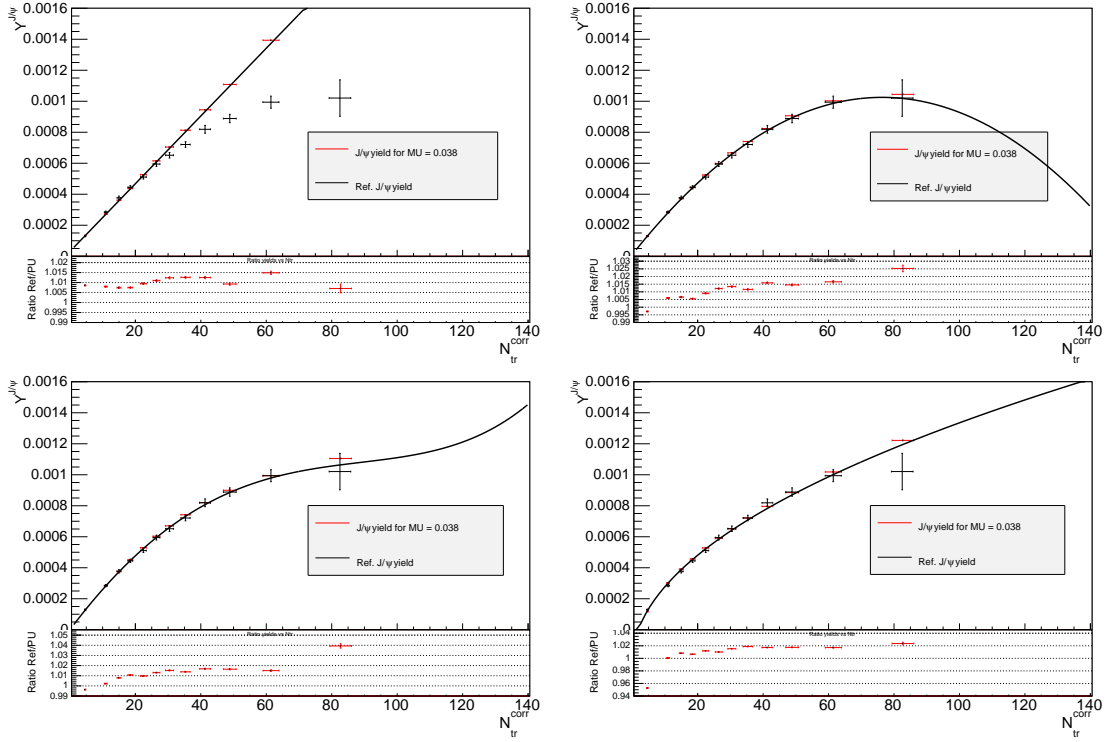


Figure 6.19:  $J/\psi$  yield as a function of number of corrected tracklets obtained from the toy MC using different parametrizations for the input yield distribution in Pb-p. Top left:  $f_1$  in the range  $N_{tr}^{corr} [1,30]$  ; Top right:  $f_2 = p_0 + p_1 \cdot x + p_2 \cdot x^2$  ; Bottom left:  $f_4 = p_0 + p_1 \cdot x + p_4 \cdot x^4$  ; Bottom right:  $f_{1/2} = p_0 + p_{1/2} \cdot x^{1/2}$

	$f_1^*$	$f_2$	$f_4$	$f_{1/2}$
$p_0$	$(3.08 \pm 0.71) \cdot 10^{-5}$	$(1.04 \pm 0.85) \cdot 10^{-5}$	$(2.81 \pm 0.08) \cdot 10^{-5}$	$(-2.11 \pm 0.13) \cdot 10^{-5}$
$p_1$	$(2.18 \pm 0.07) \cdot 10^{-5}$	$(2.65 \pm 0.10) \cdot 10^{-5}$	$(-2.15 \pm 0.31) \cdot 10^{-7}$	-
$p_2$	-	$(-1.74 \pm 0.19) \cdot 10^{-7}$	-	-
$p_4$	-	-	$(4.53 \pm 4.88) \cdot 10^{-12}$	-
$p_{1/2}$	-	-	-	$(1.54 \pm 4.03) \cdot 10^{-4}$
$\frac{\chi^2}{N_{dof}}$	1.13	0.095	0.16	0.79

Table 6.7: Fit parameters of the input  $J/\psi$  yield distributions in p-Pb (see text). \* The fitting range is restricted to  $N_{tr}^{corr} \in [0,30]$ .

The fitting results for the Pb-p case are shown in Fig. 6.20 and the fit parameters in Tab. 6.8. As can be observed in the top left panel, the linear approximation works well for the Pb-p yield along the whole multiplicity range in this analysis. However the linear yield parametrisation reaches zero for  $N_{tr}^{corr} > 0$ . The 2-nd order polynomial parametrisation,  $f_2$  seems also to fit the Pb-p result, and in this case the y-axis intercept is compatible with positive values. Again, note that the fits are performed with statistical errors only. Similar

	$f_1$	$f_2$	$f_3$	$f_4$
$p_0$	$(-2.02 \pm 0.67) \cdot 10^{-5}$	$(-9.00 \pm 9.66) \cdot 10^{-6}$	$(6.03 \pm 0.14) \cdot 10^{-6}$	$(2.11 \pm 0.09) \cdot 10^{-7}$
$p_1$	$(2.53 \pm 0.05) \cdot 10^{-5}$	$(2.32 \pm 0.14) \cdot 10^{-5}$	$(1.95 \pm 0.29) \cdot 10^{-5}$	$(1.30 \pm 0.41) \cdot 10^{-7}$
$p_2$	-	$(4.89 \pm 3.27) \cdot 10^{-8}$	$(2.27 \pm 1.26) \cdot 10^{-7}$	-
$p_3$	-	-	$(-2.02 \pm 1.36) \cdot 10^{-9}$	-
$p_4$	-	-	-	$(-1.31 \pm 0.74) \cdot 10^{-11}$
$\frac{\chi^2}{N_{dof}}$	0.49	0.29	0.07	0.08

 Table 6.8: Fit parameters of the input  $J/\psi$  yield distributions in Pb-p (see text).

conclusions as in the p-Pb case about the stability of the pile-up effect with the yield shape parametrisation can be drawn in Pb-p. The estimated effect of the pile-up on the  $J/\psi$  yield is 1-1.5% in Pb-p depending on the multiplicity bin. As we have seen, even though the  $\langle\mu\rangle$  parameter is bigger in Pb-p than in p-Pb the effect on the yield is smaller due to the closer to linear dependence with multiplicity.

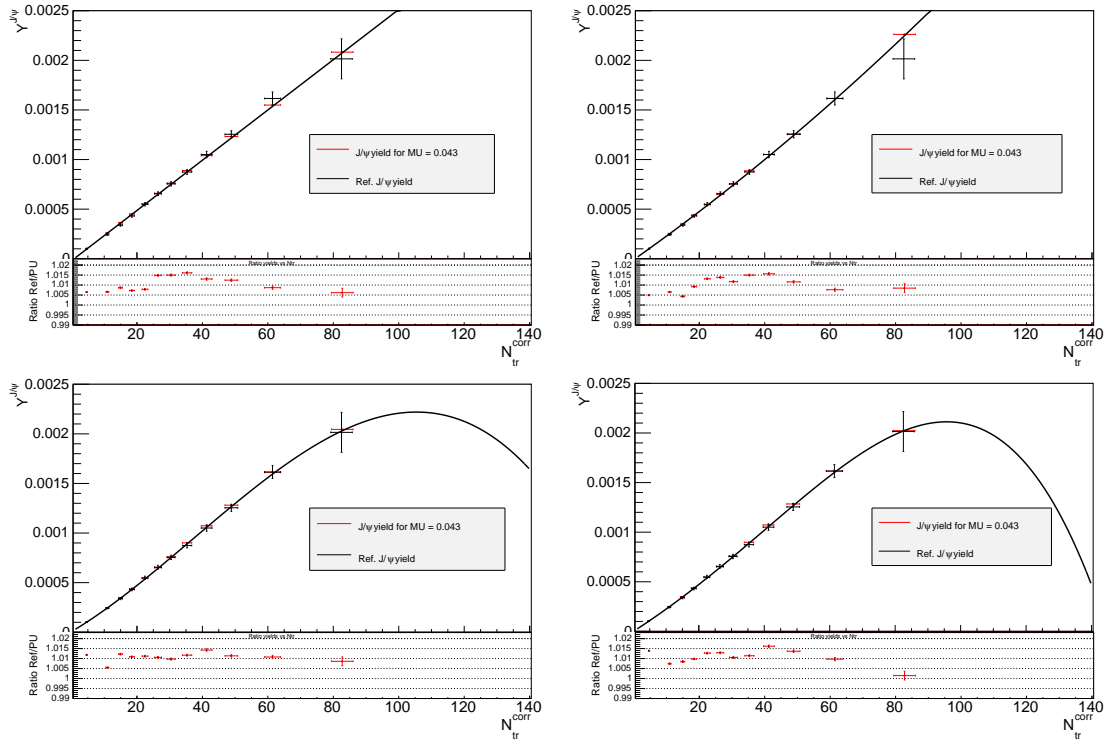


Figure 6.20:  $J/\psi$  yield as a function of number of corrected tracklets obtained from the toy MC using different parametrizations for the input yield distribution in Pb-p. Top left:  $f_1 = p_0 + p_1 \cdot x$ ; Top right:  $f_2 = p_1 \cdot x + p_2 \cdot x^2$ ; Bottom left:  $f_3 = p_0 + p_2 \cdot x^2 + p_3 \cdot x^3$ ; Bottom right:  $f_4 = p_0 + p_1 \cdot x^1 + p_4 \cdot x^4$ .

### 6.3.7 Combination of yield systematic uncertainties

As seen in previous sections, we have computed a combined  $\mathcal{A} \times \epsilon$ , signal extraction and bin-flow systematic uncertainty for the relative  $J/\psi$  yield in each multiplicity bin, the signal extraction systematic uncertainty itself due to the dispersion in the results using different fitting assumptions, the systematic uncertainty of the computation method of the relative  $F_{norm}$ , the pile-up systematic uncertainty, signal tails and vertex QA. All these effects are uncorrelated in a given multiplicity bin, hence they are added quadratically to obtain the relative yield systematic uncertainty in a multiplicity bin  $i$ . These systematic uncertainties are considered as uncorrelated between p-Pb and Pb-p collision systems. The results are shown in Tab. 6.9.

Source	p-Pb	Pb-p
Sig. Extr.	0.6-2%	0.6-2%
$F_{norm}$ method	1-4%	1-4%
$\mathcal{A} \times \epsilon$ /Sig.extr./bin-flow	1.5-6.2%	1.5-6.2%
Pile-up	1-4%	1-1.5%
Signal tails	1%	1%
Vertex QA	0.6* -0.3%	0.6* -0.3%
Total	2.4-8.7%	2.2-7.9%

Table 6.9: Relative  $J/\psi$  yield systematic uncertainties in p-Pb and Pb-p collisions. The values represent the minimum and maximum values of the uncertainties in the multiplicity bins. The uncertainties with \* are only applicable to the first multiplicity bin.

For the absolute yield measurement the uncorrelated sources of uncertainties mentioned above, calculated on the absolute yield, have to be taken into account. In addition, the multiplicity correlated uncertainties which were considered to vanish in the relative measurement (tracking, trigger and matching efficiencies and BR), have to be also taken into account. The tracking efficiency uncertainty has been computed in this thesis (Chap. 5), and the other uncertainties were computed for the analyses in [3–5]. All the uncertainties are considered as uncorrelated between p-Pb and Pb-p. The correlated uncertainties are not added to the points but reported separately. The uncertainties for the absolute measurement are listed in Tab. 6.10.

Source	p-Pb	Pb-p
Sig. Extr.	1-2.2%	1-2.2%
$F_{norm}$ method	1-4%	1-4%
$\mathcal{A} \times \epsilon / \text{Sig. extr. / bin-flow}$	1.5-6.2%	1.5-6.2%
Pile-up	1-4%	1-1.5%
Signal tails	2%	2%
Vertex QA	0.9%*	0.9%*
Total uncorr.	3.2-8.9%	3.2-8.1%
Tracking efficiency	4%	6%
Trigger efficiency	2.8%	3.2%
Matching efficiency	1%	1%
BR	0.033%	0.033%
Total corr.	5%	6.9%

Table 6.10: Absolute  $J/\psi$  yield systematic uncertainties in p-Pb and Pb-p collisions. The values represent the minimum and maximum values of the uncertainties in the multiplicity bins. The uncertainties with \* are only applicable to the first multiplicity bin.

## $J/\psi$ MEAN TRANSVERSE MOMENTUM MEASUREMENT

An important observable that carries information about the particle production mechanism, is the first moment of the transverse momentum distribution,  $\langle p_T \rangle$ . The objective of this chapter is to perform a measurement of the  $J/\psi$   $\langle p_T \rangle$  and its dependence on the event charged particle multiplicity measured at mid rapidity.

We have developed an innovative technique for the extraction of the  $J/\psi$  transverse momentum, based on the study of the di-muon mean transverse momentum invariant mass spectrum,  $\langle p_T^{\mu^+\mu^-} \rangle(m_{\mu^+\mu^-})$ . The use of the di-muon  $\langle p_T \rangle$  spectrum to extract the  $J/\psi$  average transverse momentum was first proposed in [259]. In this thesis, a correction method to account for the spectrometer  $\mathcal{A} \times \mathcal{E}$  and a full study of the systematic uncertainties on this measurement have been developed.

In order to obtain a correct value of the  $J/\psi$   $\langle p_T \rangle$  when performing the extraction from the di-muon  $\langle p_T \rangle$  spectrum, the spectrometer  $\mathcal{A} \times \mathcal{E}$  correction has to be taken into account before the extraction procedure. The same 2D  $\mathcal{A} \times \mathcal{E}(p_T, y)$  that we used to correct the di-muon invariant mass spectra in Chap. 6, is used here in a similar way.

The use of this technique to extract the  $J/\psi$   $\langle p_T \rangle$  has been motivated by the measurement as a function of charged particle multiplicity. This approach, contrary to the standard one (see for example [4, 5]), only requires to perform a data sample slicing in multiplicity, with no further slicing in  $p_T$ . Therefore, this technique is suitable to study high multiplicity regimes, where the statistics is low, with a thinner binning than with the standard procedure. It enables the study of particle production properties at higher multiplicities, which may help to better constrain the available theoretical models.

## 7.1 $J/\psi$ mean transverse momentum measurement

The technique to measure the  $J/\psi$   $\langle p_T \rangle$  consists on building the di-muon mean transverse momentum invariant mass spectrum,  $\langle p_T^{\mu^+\mu^-} \rangle(m_{\mu^+\mu^-})$ , and fit it to extract the  $J/\psi$   $\langle p_T \rangle$ . Such a spectrum is constructed as follows:

$$(7.1) \quad \langle p_T^{\mu^+\mu^-} \rangle_i^{raw} = \frac{1}{n_i} \sum_{j=1}^{n_i} p_T^j$$

where the index  $i$  denotes a given invariant mass bin,  $n_i$  is the number of di-muon pairs in that bin and  $p_T^j$  the transverse momentum of the  $j$ -th di-muon pair contributing to that bin. The error on  $\langle p_T^{\mu^+\mu^-} \rangle_i$  is given by the standard error on the mean ( $RMS/\sqrt{n_i}$ ).

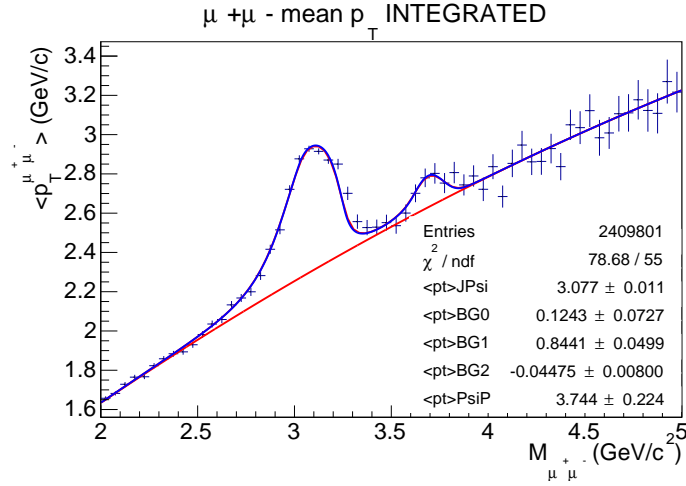
The fitting function used in this extraction is a phenomenological one. It is based on weighting the  $\langle p_T \rangle$  of each particle ( $J/\psi$  and  $\psi(2S)$ ) entering in the spectrum and the  $\langle p_T \rangle$  of the background, by the ratio of the signal over signal plus background of each particle:

$$(7.2) \quad \begin{aligned} \langle p_T^{\mu^+\mu^-} \rangle(m_{\mu^+\mu^-}) &= \alpha^{J/\psi}(m_{\mu^+\mu^-}) \times \langle p_T^{J/\psi} \rangle \\ &+ \alpha^{\psi(2S)}(m_{\mu^+\mu^-}) \times \langle p_T^{\psi(2S)} \rangle \\ &+ \left( 1 - \alpha^{J/\psi}(m_{\mu^+\mu^-}) - \alpha^{\psi(2S)}(m_{\mu^+\mu^-}) \right) \times \langle p_T^{bkg} \rangle \end{aligned}$$

where  $\alpha(m_{\mu^+\mu^-}) = S(m_{\mu^+\mu^-}) / (S(m_{\mu^+\mu^-}) + B(m_{\mu^+\mu^-}))$  ( $S$  stands for Signal and  $B$  for Background). The particle signal and background dependence with the di-muon invariant mass are extracted from the invariant mass spectrum parametrizations of Chap 6. The  $J/\psi$  and  $\psi(2S)$  average transverse momentum ( $\langle p_T^{J/\psi} \rangle$  and  $\langle p_T^{\psi(2S)} \rangle$  respectively) are considered as constant free parameters in the fit, and the background one ( $\langle p_T^{bkg} \rangle$ ) is parametrized with an *ad hoc* function. An example of this kind of spectrum is shown in Fig. 7.1. The peaks observed around the  $J/\psi$  and  $\psi(2S)$  mass mean that the particle's average transverse momenta are bigger than that of the background.

At this point, the potential of our method can be already highlighted. The standard technique to measure the  $J/\psi$   $\langle p_T \rangle$ , consist of extracting the number of  $J/\psi$  in  $p_T$  bins. Then, the obtained  $p_T$  spectrum is fitted and the  $J/\psi$   $\langle p_T \rangle$  is calculated from the resulting parametrized distribution. If we want to measure the correlation of the  $J/\psi$   $\langle p_T \rangle$  with other observable (let us say  $X$ ), it is necessary to sample the data based on that observable, and also in  $p_T$  bins. When using the technique developed in this thesis, to extract the particle  $\langle p_T \rangle$  it is only required to be able to perform the signal extraction on the observable  $X$  bins with an acceptable signal over background ratio. There is no need to perform a further  $p_T$  binning, which allows to do the analysis in thinner bins than the ones needed with a standard  $\langle p_T \rangle$  extraction procedure. We take advantage of this procedure to study the  $J/\psi$   $\langle p_T \rangle$  in the high multiplicity region. On the contrary, this method allows only to extract the moments of the  $p_T$  distribution, but no information on the distribution shape itself can be obtained.




 Figure 7.1: Raw di-muon  $\langle p_T \rangle$  invariant mass spectrum in p-Pb collisions

It should be noted that the  $\langle p_T \rangle$  value obtained in this way is not yet corrected by  $\mathcal{A} \times \mathcal{E}$ . Since, the  $J/\psi$   $\mathcal{A} \times \mathcal{E}$  depends strongly on  $p_T$ , as was shown in Fig. 6.1, the result from the fit does not yield the correct  $\langle p_T \rangle$  value. In fact, the value obtained is overestimated, since the muon spectrometer is less efficient for low  $p_T$  values. In order to correct by  $\mathcal{A} \times \mathcal{E}$ , each di-muon pair in the spectrum is weighed with the 2D  $J/\psi$   $\mathcal{A} \times \mathcal{E}(p_T, y)$  computed in Sec. 6.1.1. The corrected di-muon  $\langle p_T \rangle$  invariant mass spectrum is therefore constructed as follows:

$$(7.3) \quad \langle p_T^{\mu^+\mu^-} \rangle_i^{\mathcal{A} \times \mathcal{E} \text{ corr.}} = \frac{1}{n_i^{\text{eff}}} \sum_{j=1}^{n_i} \frac{p_T^j}{\mathcal{A} \times \mathcal{E}(p_T^j, y^j)}$$

where  $y^j$  is the rapidity of the  $j$ -th pair in a given invariant mass bin  $i$  and  $n_i^{\text{eff}}$  is the effective number of entries in the bin ( $n_i^{\text{eff}} = \sum_{j=1}^{n_i} 1/\mathcal{A} \times \mathcal{E}(p_T^j, y^j)$ ). Note that in the following the superscript " $\mathcal{A} \times \mathcal{E} \text{ corr.}$ " will be omitted for simplicity.

Consequently, the signal and background parameters have to be taken from the  $\mathcal{A} \times \mathcal{E}$  corrected invariant mass spectra. This is the reason why we performed the signal extraction on the corrected invariant mass spectra in Chap.6. In this way the corrected  $J/\psi$   $\langle p_T \rangle$  is obtained directly from the fit. An example of corrected multiplicity integrated fitted  $\langle p_T^{\mu^+\mu^-} \rangle(m_{\mu^+\mu^-})$  spectra for p-Pb and Pb-p collisions are presented in Fig. 7.2. Note here, that the value obtained for the  $\psi(2S)$   $\langle p_T \rangle$  is *not* physical, since the  $\mathcal{A} \times \mathcal{E}$  correction used is the  $J/\psi$  one. The same corrected spectrum can not be used to get simultaneously the  $J/\psi$  and  $\psi(2S)$   $\langle p_T \rangle$  values.

### 7.1.1 J/ψ mean transverse momentum extraction procedure

To perform the  $\langle p_T \rangle$  fitting procedure all the signal and background parameters are fixed to those extracted from the corresponding invariant mass spectrum in the bin (or inte-

grated). Note that since we assumed that the signal does not vary with multiplicity, the tail parameters used in the signal extraction procedure are the same for the integrated and all multiplicity bins. The  $\sigma_{J/\psi}$  ( $\sigma_{\psi(2S)}$ ) and  $m_{J/\psi}$  ( $m_{\psi(2S)}$ ) are also supposed to be the same. Nevertheless, there are small variations from bin to bin which are taken into account in the  $\langle p_T \rangle$  fits by taking the values from corresponding invariant mass spectrum in each multiplicity bin. The parameters which are meant to vary among bins are the normalisations for the  $J/\psi$  and  $\psi(2S)$  signals and background parameters which are also taken from the corresponding invariant mass spectrum.

During the fitting procedure two different functions have been used to parametrize the di-muon background  $\langle p_T \rangle$ : 2-nd order polynomial function (Pol2) and 2-nd order polynomial times exponential function (Pol2 $\times$ Exp). Two fitting ranges are also used (2.0-5.0 GeV/ $c^2$  and 2.2-4.7 GeV/ $c^2$ ) to take into account background variations. Besides, there are 24 different "signal + background" ("S + B") parametrizations for each invariant mass spectra that can be used in Eq. 7.2.

The integrated p-Pb and Pb-p di-muon  $\langle p_T \rangle$  spectra fitted with a given combination of background di-muon  $p_T$  function, fitting range and "S + B" parametrization are shown as an example in Fig. 7.2. It can be observed that the spectra are correctly reproduced by the chosen parametrisation, with a small deviation at the right hand side of the  $J/\psi$  peak ( $m_{\mu^+\mu^-} \sim m_{J/\psi}$ ). This is further discussed in Sec. 7.2.3. The results obtained with these fits are compared to those obtained in [4] in Tab. 7.1. As can be seen the obtained results are in very good agreement with the published values.

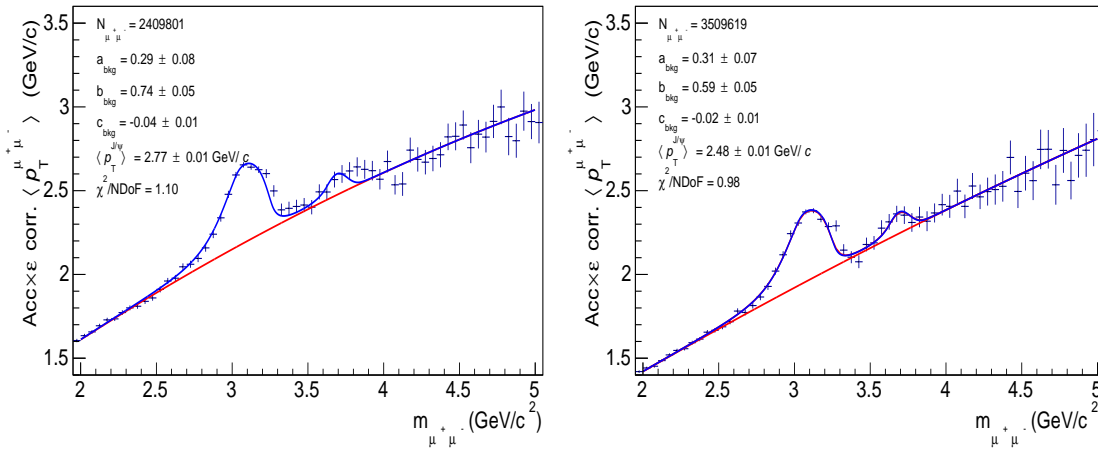


Figure 7.2: Multiplicity integrated  $\mathcal{A} \times \epsilon$  corrected di-muon  $\langle p_T \rangle$  invariant mass spectra in p-Pb (left) and Pb-p (right) collisions. The spectra are fitted with a fit combination choice (CB2+VWG+Range $^{inv.mass}=2.0-5.0+\sigma_{\psi(2S)}=1.1 \cdot \sigma_{J/\psi}$ +Pol2+Range $\langle p_T \rangle=2.0-5.0$ ) and the values of the extracted  $J/\psi$   $\langle p_T \rangle$  are shown.

The  $J/\psi$   $\langle p_T \rangle$  extraction has been performed also in multiplicity bins using the corresponding invariant mass spectra "signal + background" parametrizations. An example using

System	$\langle p_T \rangle$ (GeV/c) (this thesis)	$\langle p_T \rangle$ (GeV/c) ([4])
p-Pb	$2.77 \pm 0.01$ (stat.)	$2.77 \pm 0.01$ (stat.) $\pm 0.03$ (syst.)
Pb-p	$2.48 \pm 0.01$ (stat.)	$2.47 \pm 0.01$ (stat.) $\pm 0.03$ (syst.)

Table 7.1:  $J/\psi$  transverse momentum values in p-Pb and Pb-p collisions obtained in this thesis (for the fit combination in Fig. 7.2) compared with the ones obtained in [4].

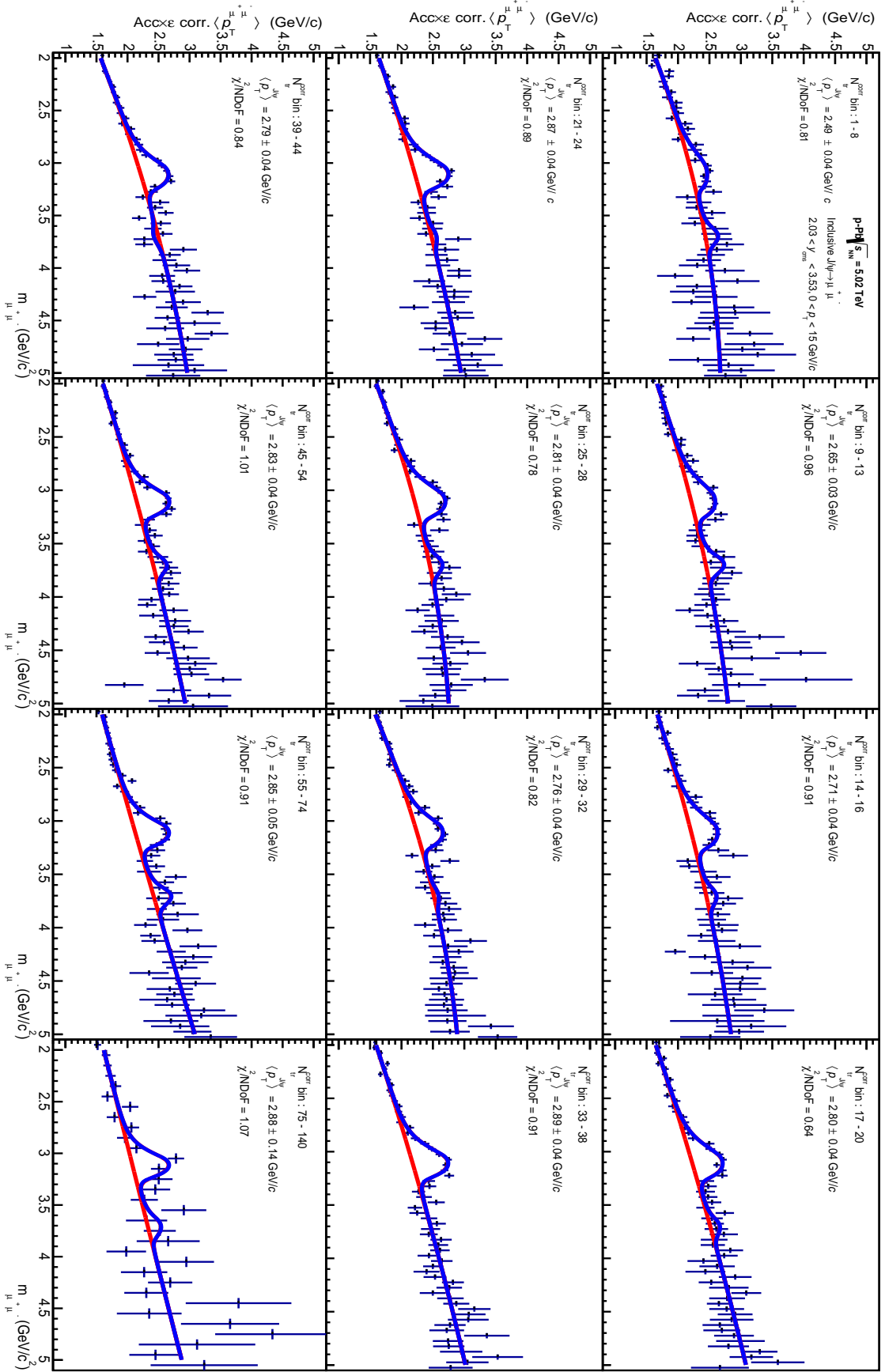
a Pol2 function to parametrize the background is shown in Fig. 7.3. A cross-check of the validity of our results is performed in App. C, by comparing with the results in [261].

## 7.2 Systematic uncertainties

The study of the systematic uncertainties, as for the number of  $J/\psi$ , is performed for the relative  $J/\psi$   $\langle p_T \rangle$  ( $\langle p_T \rangle^i / \langle p_T \rangle^{int}$ , where  $\langle p_T \rangle^i$  is the average  $J/\psi$   $p_T$  in a multiplicity bin  $i$  and  $\langle p_T \rangle^{int}$  the multiplicity integrated one), as well as for the absolute value  $\langle p_T \rangle^i$ . In the following subsections, each effect is studied in detail. The  $\langle p_T \rangle$  fitting extraction procedure uncertainties are first studied similarly to those for the signal extraction. The  $\mathcal{A} \times \mathcal{E}$ , bin-flow, and extraction uncertainties are treated as a whole as done for the relative number of  $J/\psi$ . The variations due to multiplicity bin-flow are studied by means of different execution tests (execution of the analysis task with different seeds for the multiplicity correction). The effect of pile-up on the measured value on a given multiplicity range is also studied. In addition, other sources of uncertainties, specific to the  $\langle p_T \rangle$  extraction method, are studied. These include the variation of the di-muon  $\langle p_T \rangle$  with the pair reconstructed invariant mass and the propagation of the signal extraction parameter errors from the fits on the invariant mass spectra.

### 7.2.1 $\langle p_T \rangle$ extraction uncertainty

In order to account for the variations in the obtained  $\langle p_T \rangle$  result due to the spectra parametrization, the different combinations of all the possible "S + B" parametrizations, the background di-muon  $\langle p_T \rangle$  and the different fitting ranges need to be considered on the  $\langle p_T \rangle$  extraction. These constitute a total of 96 fit combinations ( $\langle p_T \rangle$  extraction tests) for the  $\langle p_T \rangle$  extraction in each multiplicity bin (or integrated) spectrum (24 "S + B" parametrizations  $\times$  2 background di-muon  $\langle p_T \rangle$  parametrizations  $\times$  2 fitting ranges on the di-muon  $\langle p_T \rangle$  spectrum). The values of the  $\mathcal{A} \times \mathcal{E}$  corrected  $J/\psi$   $\langle p_T \rangle$  are taken as the unweighted average value of the values obtained for each  $\langle p_T \rangle$  extraction test (combination of: signal + background + inv. mass fitting range +  $\sigma_{\psi(2S)}$  + bkg  $\langle p_T^{\mu^+\mu^-} \rangle$  +  $\langle p_T^{\mu^+\mu^-} \rangle$  fitting range), Eq. B.1. The error is taken as the error on the mean, Eq. B.2, and the signal extraction systematic uncertainty is the 1- $\sigma$  dispersion in Eq. B.4 of the different results. The  $\langle p_T \rangle$  extraction systematic uncertainty for the absolute measurement of the  $J/\psi$   $\langle p_T \rangle$  take values among 0.2% and 1.3% depending on the multiplicity bin in p-Pb and Pb-p. Note that these values vary among



different executions of the task due to multiplicity bin-flow. This variation is taken into account below. For the integrated  $J/\psi$   $\langle p_T \rangle$ , the  $\langle p_T \rangle$  extraction systematic uncertainty is 0.1%.

However, a different treatment of the systematic uncertainties is needed for the relative  $J/\psi$  mean transverse momentum, as we did in the previous chapter for the relative yield. Consequently, for the relative  $\langle p_T \rangle$  extraction tests, as considered for the relative signal extraction, the correlation between the multiplicity differential and integrated values of the  $J/\psi$   $\langle p_T \rangle$  has to be taken into account when calculating the average value. In the relative signal extraction tests, the signal shape was taken as constant with multiplicity. Therefore, in the  $\langle p_T \rangle$  extraction relative tests, only the background and fitting range in the " $S + B$ " parametrizations, background di-muon  $\langle p_T \rangle$  and fitting range are allowed to be different among the numerator and denominator. This implies a total of 1536 relative  $\langle p_T \rangle$  extraction tests ( $n_{tests}$ ) per multiplicity bin (96 possible fit combinations for the numerator  $\times$  2 variations on the invariant mass signal extraction background parametrisation in the denominator  $\times$  2 variations on the invariant mass spectrum fitting range in the denominator  $\times$  2 variations on the background di-muon  $\langle p_T \rangle$  parametrizations in the denominator  $\times$  2 variations on the fitting range on the di-muon  $\langle p_T \rangle$  spectrum in the denominator). Within an execution test, the average relative  $J/\psi$   $\langle p_T \rangle$  in a multiplicity bin  $i$  is defined as:

$$(7.4) \quad \langle p_T^{J/\psi} \rangle_i^R = \left\langle \frac{\langle p_T^{J/\psi} \rangle_i}{\langle p_T^{J/\psi} \rangle^{int.}} \right\rangle = \frac{1}{n_{tests}} \times \sum_{j=1}^{n_{tests}} \left( \frac{\langle p_T^{J/\psi} \rangle_i}{\langle p_T^{J/\psi} \rangle^{int.}} \right)_j$$

where  $\langle p_T^{J/\psi} \rangle^{int.}$  is the multiplicity integrated average  $J/\psi$   $\langle p_T \rangle$ . The index  $j$  denotes each possible relative  $\langle p_T \rangle$  extraction test mentioned above. The definition of the error is given by Eqs. B.2 and B.3. The systematic uncertainty is obtained from the  $1-\sigma$  dispersion of the tests results, Eq. B.4.

The  $\langle p_T^{J/\psi} \rangle^R$  variations as a function of the different relative extraction tests are shown in Fig. 7.4 for a multiplicity bin in Pb-p as an illustrative example. The unweighted average in Eq. 7.4 and the  $1-\sigma$  dispersion are shown as the red solid and dotted lines respectively. As can be observed most of the test values lay within the found systematic uncertainty.

In Fig. 7.5 an example of the relative  $\langle p_T \rangle$  extraction systematic uncertainties for an execution test are shown as a function of multiplicity bins in p-Pb and Pb-p. The uncertainty is usually smaller than 0.5% except for the last multiplicity bin, where it reaches 1.2% in p-Pb due to the lower statistics. The uncertainties are small compared to those on the signal extraction. This reduction on the uncertainty comes from the fact that, since the  $p_T$  distribution is not extracted, the variations induced by the signal extraction are of second order in the  $\langle p_T \rangle$  extraction. These values vary among two executions of the analysis task due to multiplicity bin-flow, as we show below.

In order to take into account the possible variations due to multiplicity bin-flow in the  $\langle p_T \rangle$  extraction systematic uncertainty, the values of the obtained uncertainty for each

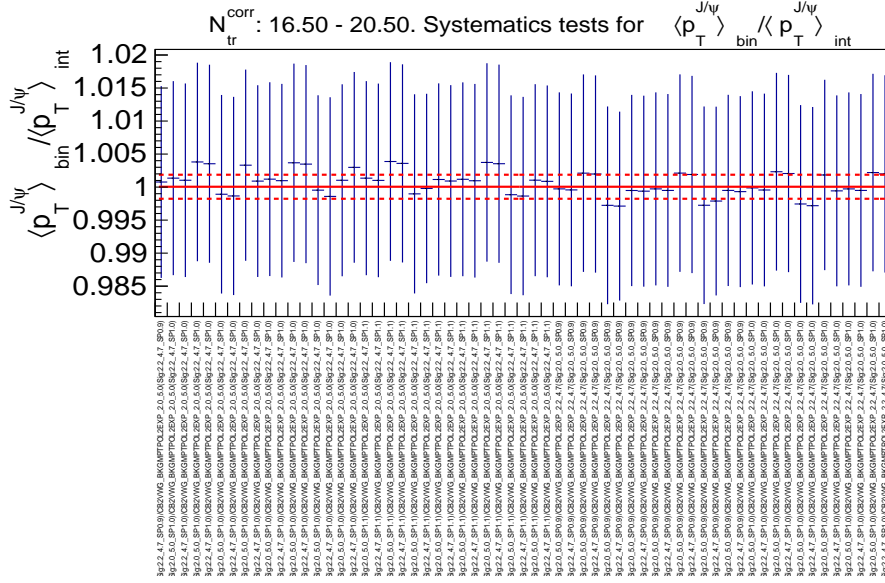
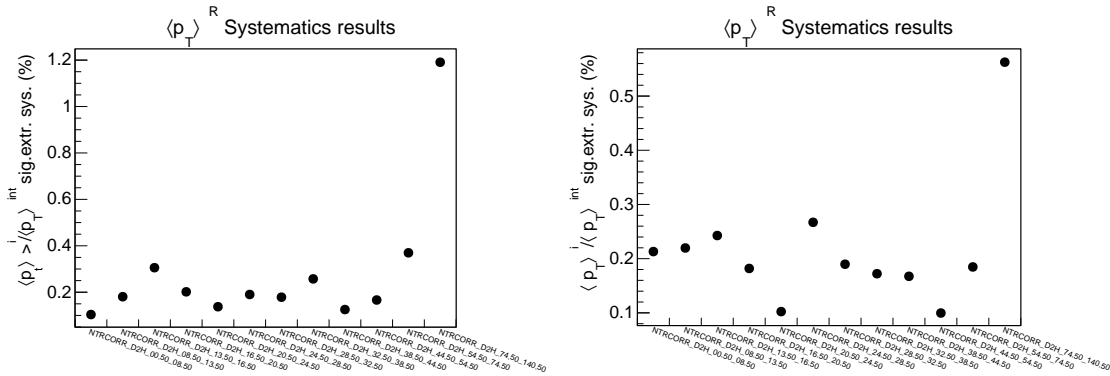


Figure 7.4: Values of  $\left( \frac{\langle p_T^{J/\psi} \rangle^i}{\langle p_T^{J/\psi} \rangle^{int}} \right)_j$  relative  $\langle p_T \rangle$  extraction tests as a function of  $j$ -th test for the  $J/\psi$   $\langle p_T \rangle$  systematic uncertainty computation in a multiplicity bin in Pb-p. The unweighted average and the  $1\text{-}\sigma$  dispersion are shown as the red solid and dotted lines respectively. The test-axis is zoomed-in to show only a fraction of the total 1536 tests.



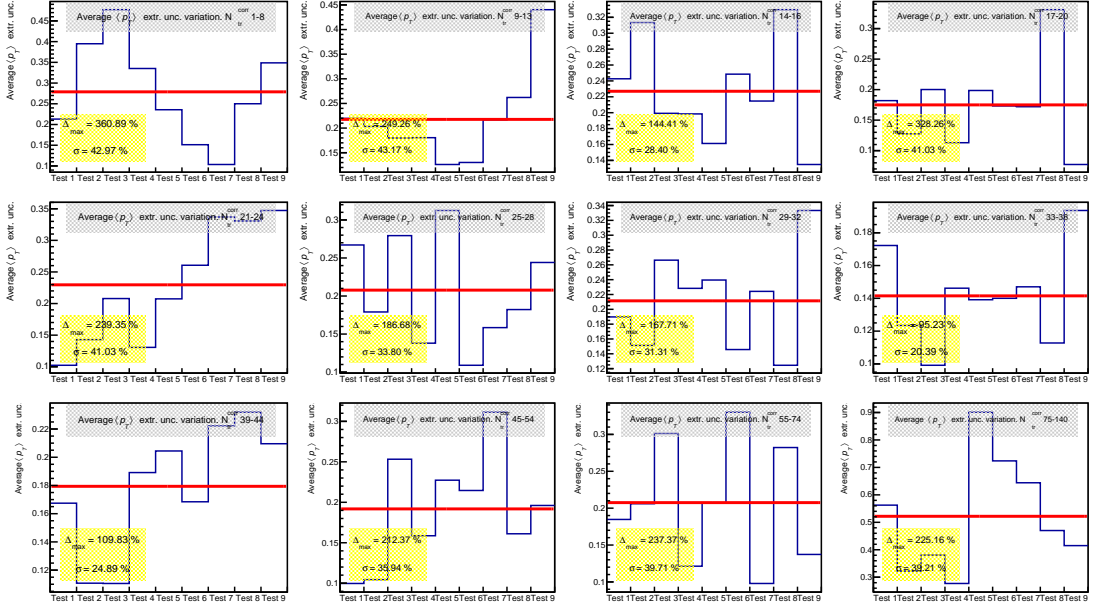


Figure 7.6: Relative  $J/\psi$   $\langle p_T \rangle$  extraction systematic uncertainty variations due to bin flow in multiplicity bins in Pb-p. Each value corresponds to the result of a set of extraction tests (Fig. 7.5) for a given execution test. The difference between the most different results ( $\Delta_{max}$ ), mean value (red line) and 1- $\sigma$  dispersion among the values are shown.

tests in each bin (red line) and it ranges between 0.15% and 0.55% in p-Pb depending on the multiplicity bin. Similar values are obtained for Pb-p.

### 7.2.2 $\mathcal{A} \times \mathcal{E}$ -Bin-flow-extraction combined effect

In this section we study the effect of the bin-flow on the obtained values of the  $J/\psi$   $\langle p_T \rangle$  in each multiplicity bin. As already seen for the yield, the measurements of an observable vary among different executions of the analysis task with different seeds for the multiplicity correction. The dispersion of the values obtained in different execution tests is used as a systematic uncertainty for this effect.

First of all, the effect of the different  $\mathcal{A} \times \mathcal{E}$  corrections due to MC input distributions variations is studied for the  $J/\psi$   $\langle p_T \rangle$ . The results obtained of the integrated  $J/\psi$   $\langle p_T \rangle$  in p-Pb with the different corrections are shown in Fig 7.7. In this case the red line is the  $\langle p_T \rangle$  value obtained with the nominal correction and the dotted line its statistical error. The results barely vary with the different corrections and the dispersion, and even the maximum variation among results, are smaller than 0.1%. A very similar value is obtained for the Pb-p  $J/\psi$   $\langle p_T \rangle$  variation. These results mean that the  $\mathcal{A} \times \mathcal{E}$  variations play a negligible role in the  $J/\psi$   $\langle p_T \rangle$  systematic uncertainty calculations.

As already shown in Sec. 6.3.5, the effect of the  $\mathcal{A} \times \mathcal{E}$ , bin-flow and  $\langle p_T \rangle$  extraction cannot be separated when dealing with multiplicity bins. In order to take them into account we

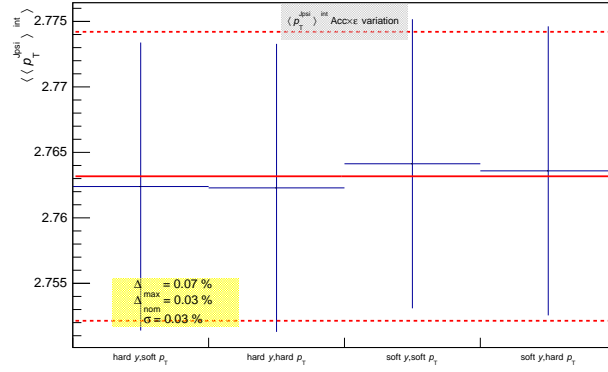


Figure 7.7: Integrated  $J/\psi$   $\langle p_T \rangle$  extraction with the four varied  $\mathcal{A} \times \epsilon$  corrections are shown in blue and the nominal result as the red line. The figure also shows the relative difference between the most different results ( $\Delta_{\max}$ ), between the nominal value and the more distant value ( $\Delta_{\text{nom}}$ ) and the 1- $\sigma$  dispersion among the values ( $\sigma$ ). The systematic uncertainty due to the  $\mathcal{A} \times \epsilon$  is  $\Delta_{\max}$  which is 0.07%

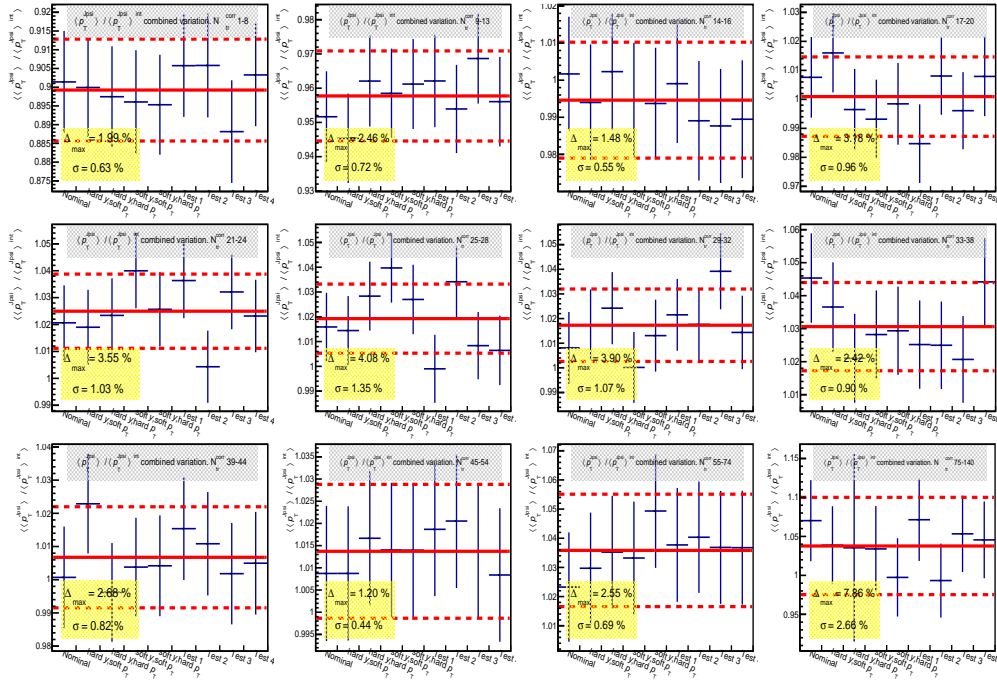


Figure 7.8: Variation on the relative  $J/\psi$   $\langle p_T \rangle$  in multiplicity bins due to bin-flow,  $\mathcal{A} \times \epsilon$  and signal extraction. The blue points are the average values of the relative  $\langle p_T \rangle$  obtained with Eq. 7.4 in each execution test. The red line shows the average of the values obtained from the execution tests in each bin. The dotted line is the statistical error.  $\sigma$  is the value of the 1- $\sigma$  dispersion of the values for each execution test in a bin.



perform the full procedure in Sec. 7.2.1 for different execution tests. The average  $\langle p_T \rangle^R$  value obtained for each multiplicity bin with Eq. 7.4 is represented as a function of the execution test. The error of each value is taken as the error on the mean. The results for the combined effects are presented in Fig 7.8. In this case the red line is the average of the values for the different execution tests, and the dotted line is the error on the mean. As we can observe, the variations of the  $\langle p_T \rangle^R$  results in multiplicity bins are smaller than the ones found for the signal extraction. The  $1-\sigma$  dispersion is around 1% except for the last bin (2.7%). The combined systematic uncertainty of the three effects is taken between 1% and 2.7%. As explained in Sec. 6.3.5, more execution tests are needed to reach the convergence. Remember that the uncertainty obtained in this way does not take into account the dispersion among the different fit combinations within a given execution test. Therefore the uncertainty obtained in Sec. 7.2.1 has to be added in quadrature to the one estimated here.

Similarly, this procedure is applied for the absolute  $J/\psi$   $\langle p_T \rangle$  extraction. The average values of the execution tests, with the obtained statistical and systematic uncertainties are shown in Tab. 7.2.

$N_{tr}^{corr}$ bin	$\langle p_T \rangle$ (GeV/c) (p-Pb)	$\langle p_T \rangle$ (GeV/c) (pPb-p)
Integrated	$2.76 \pm 0.01$ (stat.) $\pm 0.00$ (syst.)	$2.47 \pm 0.01$ (stat.) $\pm 0.00$ (syst.)
0.5 - 8.5	$2.47 \pm 0.04$ (stat.) $\pm 0.01$ (syst.)	$2.17 \pm 0.04$ (stat.) $\pm 0.02$ (syst.)
8.5 - 13.5	$2.64 \pm 0.03$ (stat.) $\pm 0.02$ (syst.)	$2.36 \pm 0.03$ (stat.) $\pm 0.01$ (syst.)
13.5 - 16.5	$2.74 \pm 0.04$ (stat.) $\pm 0.02$ (syst.)	$2.40 \pm 0.04$ (stat.) $\pm 0.02$ (syst.)
16.5 - 20.5	$2.77 \pm 0.04$ (stat.) $\pm 0.01$ (syst.)	$2.46 \pm 0.03$ (stat.) $\pm 0.02$ (syst.)
20.5 - 24.5	$2.84 \pm 0.04$ (stat.) $\pm 0.03$ (syst.)	$2.44 \pm 0.03$ (stat.) $\pm 0.02$ (syst.)
24.5 - 28.5	$2.82 \pm 0.04$ (stat.) $\pm 0.02$ (syst.)	$2.48 \pm 0.03$ (stat.) $\pm 0.02$ (syst.)
28.5 - 32.5	$2.80 \pm 0.04$ (stat.) $\pm 0.03$ (syst.)	$2.52 \pm 0.03$ (stat.) $\pm 0.02$ (syst.)
32.5 - 38.5	$2.83 \pm 0.03$ (stat.) $\pm 0.03$ (syst.)	$2.52 \pm 0.03$ (stat.) $\pm 0.02$ (syst.)
38.5 - 44.5	$2.80 \pm 0.04$ (stat.) $\pm 0.03$ (syst.)	$2.57 \pm 0.03$ (stat.) $\pm 0.02$ (syst.)
44.5 - 54.5	$2.80 \pm 0.04$ (stat.) $\pm 0.02$ (syst.)	$2.54 \pm 0.03$ (stat.) $\pm 0.02$ (syst.)
54.5 - 74.5	$2.88 \pm 0.05$ (stat.) $\pm 0.01$ (syst.)	$2.52 \pm 0.04$ (stat.) $\pm 0.04$ (syst.)
74.5 - 140.5	$2.83 \pm 0.14$ (stat.) $\pm 0.04$ (syst.)	$2.62 \pm 0.11$ (stat.) $\pm 0.08$ (syst.)

Table 7.2:  $J/\psi$   $\langle p_T \rangle$  as a function of charged particle multiplicity and multiplicity integrated in p-Pb and Pb-p collisions (incomplete syst.). Note that the systematic uncertainty due to the combined effect (no bin-flow) treated in this section is negligible for the integrated measurement.

### 7.2.3 Di-muon $\langle p_T \rangle$ variation with invariant mass

During the fitting procedure, the  $J/\psi$   $\langle p_T \rangle$  has been considered as a constant free parameter *i.e.* independent of the invariant mass. In order to study the validity of this assumption,

the reconstructed di-muon  $\langle p_T \rangle$  invariant mass spectrum has been studied in the pure  $J/\psi$  simulation used for the  $\mathcal{A} \times \mathcal{E}$  computation.

The di-muon invariant mass resolution depends on the precision in the measurement of the momentum of each muon and the angle between the two muons. There are several effects which affect the resolution of the measurements, like the event vertex determination, scatterings and energy-loss fluctuations in the muon absorber, and the precision of the tracking chambers [266]. Taking this into account we may expect a variation of the  $J/\psi$   $\langle p_T \rangle$  as a function of the invariant mass that needs to be quantified.

In the following, the results obtained with the p-Pb simulation are presented and discussed. Similar results have been found in the Pb-p simulation but they are not shown here. The  $\langle p_T \rangle$  of the  $J/\psi$  input distribution in the p-Pb simulation is  $\langle p_T \rangle_{input}^{J/\psi} = 2.81 \text{ GeV}/c$ . The reconstructed data in the simulation is corrected by  $\mathcal{A} \times \mathcal{E}$  as explained in Sec. 7.1. The result of the reconstructed  $\langle p_T \rangle$  of di-muon pairs from  $J/\psi$  decays as a function of invariant mass is shown in Fig. 7.9 for the p-Pb MC simulation. As we can observe the reconstructed  $\langle p_T \rangle$  spectrum is not constant as already expected.

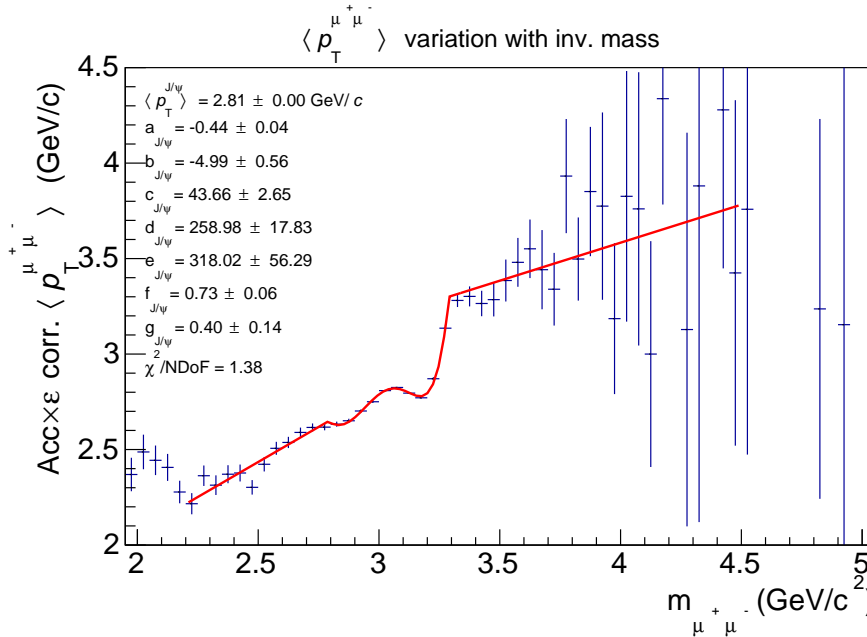


Figure 7.9:  $\mathcal{A} \times \mathcal{E}$  corrected reconstructed di-muon  $\langle p_T \rangle$  from  $J/\psi$  decays invariant mass spectrum in MC for p-Pb. The red line is the fit using Eq. 7.2.3.

In order to parametrise this variation we fit the obtained  $\langle p_T \rangle^{\mu^+ \mu^-}(m_{\mu^+ \mu^-})$ . A polynomial

piecewise function has been used based on the definition of  $h(m_{\mu^+\mu^-}) = a_0 + \sum_{i=1}^5 a_i \cdot (m_{\mu^+\mu^-} - m_{J/\psi})$ :

(7.5)

$$\langle p_T^{J/\psi} \rangle(m_{\mu^+\mu^-}) = \begin{cases} h(2.79) + a_6 \cdot (m_{\mu^+\mu^-} - 2.79) & m_{\mu^+\mu^-} \leq 2.79 \text{ GeV}/c^2 \\ h(m_{\mu^+\mu^-}) & 2.79 \text{ GeV}/c^2 < m_{\mu^+\mu^-} < 3.29 \text{ GeV}/c^2 \\ h(3.29) + a_7 \cdot (m_{\mu^+\mu^-} - 3.29) & m_{\mu^+\mu^-} \geq 3.29 \text{ GeV}/c^2 \end{cases}$$

This function is able to reproduce the variation of the di-muon  $\langle p_T \rangle$  in the invariant mass range 2.2-4.5  $\text{GeV}/c^2$ . In order to extract the  $J/\psi$   $\langle p_T \rangle$  value, the fitted function is evaluated at  $m_{\mu^+\mu^-} = m_{J/\psi}$  so we obtain  $\langle p_T^{J/\psi} \rangle = a_0$ . The fit result and the obtained function parameters are shown in Fig. 7.9. The obtained  $\langle p_T^{J/\psi} \rangle$  is exactly the same as the input one. In this way the input value can be recovered with high precision. However, the mean value of the histogram is 2.79  $\text{GeV}/c$ . Consequently we can estimate that the difference between considering the  $J/\psi$   $\langle p_T \rangle$  as a constant in the fitting procedure, or using a parametrisation such as the one in Eq. 7.2.3 is about 1%.

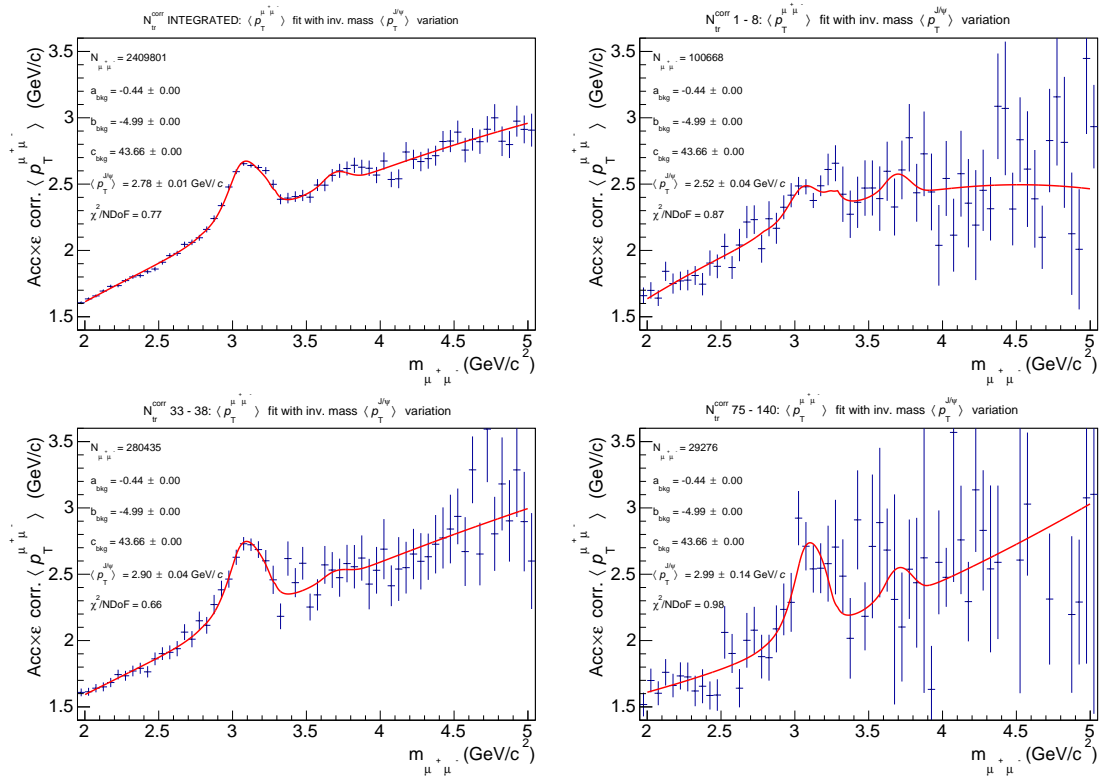


Figure 7.10:  $\mathcal{A} \times \mathcal{E}$  corrected p-Pb di-muon  $\langle p_T \rangle$  invariant mass spectrum for integrated (top left) and multiplicity bins. The  $J/\psi$   $\langle p_T \rangle$  extraction fits are performed using a parametrisation of the  $J/\psi$   $\langle p_T \rangle$  variation with the invariant mass extracted from MC.

In order to test this effect in the data di-muon  $\langle p_T \rangle$  invariant mass spectrum, the parametrisation obtained from the MC fits is used, leaving  $a_0$  as a free parameter. The

results for the p-Pb integrated and several multiplicity bins spectra with a given fit combination (CB2+VWG+Range<sup>inv.mass</sup>=2-5+ $\sigma_{\psi(2S)}$ =1.1 $\sigma_{J/\psi}$ +Pol2+Range <sup>$\langle p_T \rangle$</sup> =2-5) are shown in Fig. 7.10. If we compare the results obtained here with the ones for the same fit combination but considering the  $J/\psi$   $\langle p_T \rangle$  as constant in the fits (Fig. 7.2 and Fig. 7.3), we observe that the right hand side of the  $J/\psi$  peak is better described. This confirms that these structures observed in the di-muon  $\langle p_T \rangle$  spectra are a resolution effect. Furthermore, the  $J/\psi$   $\langle p_T \rangle$  value obtained with the MC  $\langle p_T^{J/\psi} \rangle(m_{\mu^+\mu^-})$  parametrisation is always slightly bigger as expected from the results in simulation. The differences are always smaller than 1%. Even if the variation shown in Fig. 7.9 seems big, it is only 10% in the region where the bulk of the  $J/\psi$  signal is reconstructed (2.9 - 3.3 GeV/c<sup>2</sup>) which justifies the small difference on the measured  $\langle p_T \rangle$  assuming no variation with the invariant mass. Since this variation is approximately the same in the integrated and bin-by-bin extraction, and it goes always in the direction of obtaining a higher  $\langle p_T \rangle$ , we can consider that this effect vanish on the relative  $J/\psi$   $\langle p_T \rangle$ . For the absolute  $J/\psi$   $\langle p_T \rangle$  we consider a 1% systematic uncertainty in order to be conservative.

#### **7.2.4 Propagation of signal extraction parameter errors to $\langle p_T \rangle$ extraction**

During the  $\langle p_T \rangle$  extraction procedure the  $J/\psi$  signal and background parameters obtained in the invariant mass fits were fixed in the di-muon  $\langle p_T \rangle$  fitting functions. Therefore, when extracting the  $J/\psi$   $\langle p_T \rangle$ , the possible variations due to the limited knowledge of the signal and background parameters are not taken into account.

Since some of the parameters (the ones of the invariant mass spectrum signal and background parametrizations) are common to both invariant mass and  $\langle p_T^{\mu^+\mu^-} \rangle(m_{\mu^+\mu^-})$  spectra parametrizations, the influence of the statistical errors in these parameters has been tested by performing a simultaneous (combined) fit of the invariant mass and the di-muon  $\langle p_T \rangle$  spectra. To this end, a least squares fit minimizing a common global  $\chi^2$  function is used for the invariant mass and di-muon  $\langle p_T \rangle$  spectra (based on [267]). Therefore, the possible variations of the invariant mass signal and background shapes due to their parameters' error are taken into account for the  $\langle p_T \rangle$  extraction.

Some examples of the simultaneous fits in the p-Pb spectra are shown in Fig. 7.11. In some cases, like for the last multiplicity bin, the combined fit helps to better constrain the background parameters in the invariant mass fit. However, if we compare the number of extracted  $J/\psi$  with that obtained from the individual fit ( $1802 \pm 176$ , with the same signal and background parametrization), the difference on the extracted number of  $J/\psi$  is about 2.5%. This difference is of the same order that the signal extraction uncertainty in that bin. For the rest of the bins the effect on the extracted number of  $J/\psi$  is smaller than 1%, also of the same order that the signal extraction uncertainty. The combined fit can be considered as another test for the signal extraction. Therefore the variation observed here is already

taken into account in the signal extraction systematic uncertainty estimated in the previous chapter.

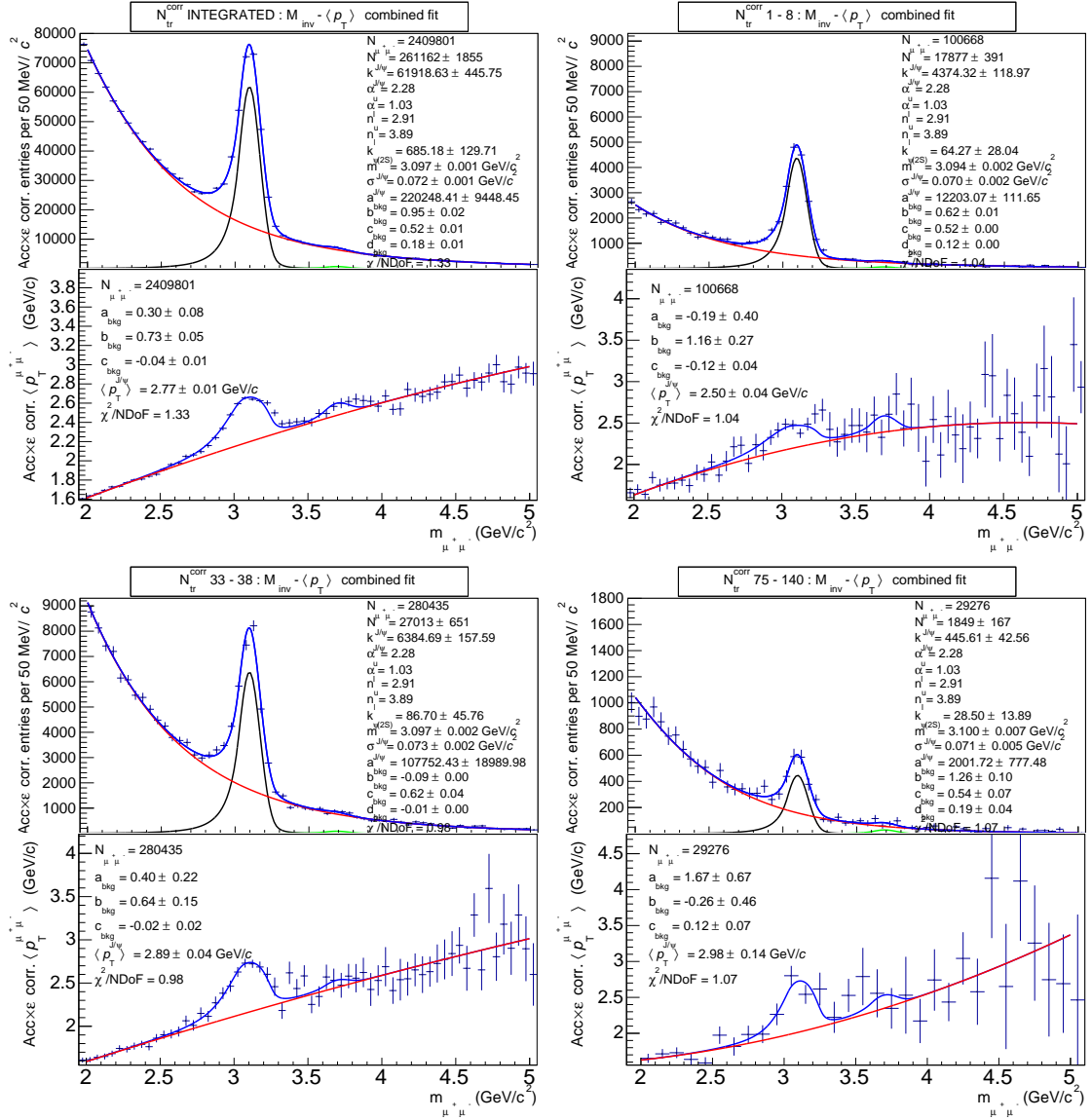


Figure 7.11: Combined fits of invariant mass and di-muon  $\langle p_T \rangle$  invariant mass spectra in p-Pb for integrated (top left) and multiplicity bins. The fit combination used is  $(CB2+VWG+Range^{inv.mass}=2-5+\sigma_{\psi(2S)}=1.1\sigma_{J/\psi}+Pol2+Range^{\langle p_T \rangle}=2-5)$ .

On the  $J/\psi$   $\langle p_T \rangle$  case, by comparing the  $\langle p_T \rangle$  values obtained with the simultaneous fit and the individual fit results with the same fit combination (Fig. 7.2 and Fig. 7.3), it can be seen that the statistical uncertainties in the signal parameters have a negligible effect in the  $J/\psi$   $\langle p_T \rangle$  extraction.

Similar conclusions can be extracted from the tests performed on the Pb-p spectra. In the view of these results, the signal and background parameters for the  $\langle p_T \rangle$  extraction tests

are kept fixed and no systematic uncertainty associated to this is therefore needed.

### 7.2.5 Pile-up contribution to $J/\psi$ $\langle p_T \rangle$ extraction

The pile-up can also affect the determination of the  $J/\psi$   $\langle p_T \rangle$  in a multiplicity bin. The effect on a given bin depends on the fraction of  $J/\psi$  in that bin which do not actually belong to it, as well as on the difference between its  $\langle p_T \rangle$  and the true  $\langle p_T \rangle$  in that bin. Using the results obtained with the toy MC developed for the multiplicity and yield pile-up effect estimation, the impact on the  $J/\psi$   $\langle p_T \rangle$  measurement can be studied.

Let us consider a multiplicity bin  $i$  with a given number of  $J/\psi$ ,  $N_{J/\psi}^i$ . A certain amount of these  $J/\psi$  are associated with pile-up events which do not belong to that bin,  $n_{J/\psi \text{ pile-up}}^i$ . The rest of the  $J/\psi$ ,  $n_{J/\psi}^i$ , do belong to that multiplicity bin. The fraction of pile-up events with a  $J/\psi$  with respect to the total number of events with a  $J/\psi$  in the multiplicity bin  $i$ , denoted here by  $\varepsilon_{J/\psi \text{ pile-up}}^i (= n_{J/\psi \text{ pile-up}}^i / N_{J/\psi}^i)$ , can be estimated with the toy MC. These fractions are presented in Tab. 7.3 for p-Pb and Pb-p collisions. The  $J/\psi$  from pile-up events in that bin, actually belong to lower multiplicity bins. The fraction of  $J/\psi$  that belongs to that bin is denoted as  $\varepsilon_{J/\psi}^i (= n_{J/\psi}^i / N_{J/\psi}^i)$ . Taking into account the measured dependence of the  $J/\psi$  yield with multiplicity<sup>1</sup>, we can estimate how the  $J/\psi$  from pile-up events affect the true transverse momentum in the bin,  $\langle p_T \rangle^i$ . The most extreme case would take place if those misplaced pile-up  $J/\psi$  actually belong to the first multiplicity bin, since the  $\langle p_T \rangle$  is the lowest in that bin. This would maximize the bias, deviating the measured  $\langle p_T \rangle_{meas}^i (= \varepsilon^i \cdot \langle p_T \rangle^i + \varepsilon_{J/\psi \text{ pile-up}}^i \cdot \langle p_T \rangle^1)$  to lower values. Consequently, the maximum variation in a multiplicity bin  $i$  of the  $\langle p_T \rangle^i$  value, due to  $J/\psi$  in pile-up events, can be calculated as follows:

$$(7.6) \quad \frac{\Delta \langle p_T \rangle^i}{\langle p_T \rangle^i} = \frac{\langle p_T \rangle^i - (\varepsilon^i \cdot \langle p_T \rangle^i + \varepsilon_{J/\psi \text{ pile-up}}^i \cdot \langle p_T \rangle^1)}{\langle p_T \rangle^i} = \varepsilon_{J/\psi \text{ pile-up}}^i \cdot \left( 1 - \frac{\langle p_T \rangle^1}{\langle p_T \rangle^i} \right)$$

The resulting differences are 0.2% (0.2%) and 0.7% (0.8%) for the two last multiplicity bins in p-Pb (Pb-p), and negligible for lower multiplicity bins. Note that this estimation is an upper limit. In order to be conservative, the found differences are added as systematic uncertainties to the last two multiplicity bins.

### 7.2.6 Combination of $J/\psi$ $\langle p_T \rangle$ systematic uncertainties

We have computed a combined  $\mathcal{A} \times \mathcal{E}$ ,  $\langle p_T \rangle$  extraction and bin-flow systematic uncertainty for the relative and absolute  $J/\psi$   $\langle p_T \rangle$  in multiplicity bins. Also the average signal extraction systematic uncertainty itself, due to the dispersion of the results using different fit combinations, has been estimated. The effect of considering the  $J/\psi$   $\langle p_T \rangle$  as a constant in the fits has been determined, as well as the impact of fixing the signal and background parameters during the fitting procedure. Finally the pile-up effect on the measurement has been also estimated to be very small.

<sup>1</sup>The  $J/\psi$   $\langle p_T \rangle$  increases with multiplicity as observed in Tab. 7.2

$N_{tr}^{corr}$ bin	$\varepsilon_{J\psi \text{ pile-up}}^i$ (p-Pb)	$\varepsilon_{J\psi \text{ pile-up}}^i$ (Pb-p)
0.5 - 8.5	0.06%	0.06%
8.5 - 13.5	0.05 %	0.06%
13.5 - 16.5	0.06 %	0.12 %
16.5 - 20.5	0.15 %	0.12 %
20.5 - 24.5	0.11 %	0.20 %
24.5 - 28.5	0.21 %	0.22 %
28.5 - 32.5	0.37 %	0.24 %
32.5 - 38.5	0.41 %	0.31 %
38.5 - 44.5	0.53 %	0.53 %
44.5 - 54.5	0.50 %	0.65 %
54.5 - 74.5	1.50 %	1.28 %
74.5 - 140.5	4.84 %	4.54 %

Table 7.3: Fraction of pile-up events with  $J/\psi$  in multiplicity bins obtained with the toy MC.

Considering the small size of the signal extraction uncertainty, and the fact that the  $J/\psi$  tails parametrisation in the signal extraction has a second order effect on the  $\langle p_T \rangle$  extraction, we can neglect possible variations of the obtained values due to this effect, both in the absolute and relative measurements.

Lastly, we need to determine if the tracking, trigger and trigger-tracker matching efficiency uncertainties have an impact on the  $\langle p_T \rangle$  measurement uncertainty or not. In Fig. 5.14, it was shown that the systematic uncertainty on the tracking efficiency can be considered as independent of the transverse momentum. This implies no effect on the  $\langle p_T \rangle$  extraction as a function of multiplicity (The  $p_T$  distribution changes with multiplicity, so a variation of the uncertainty of the tracking with  $p_T$  could have had an impact on the measurement). The systematic uncertainty due to the trigger chambers' efficiency is uncorrelated in  $p_T$ , thus no need to consider it for the  $\langle p_T \rangle$  measurement. The trigger threshold uncertainty was found to be uncorrelated with  $p_T$  ( $\sim 1\%$ ), except for  $J/\psi$  with  $p_T < 1$  GeV/ $c$  where the uncertainty is about 3%. Taking into account the average  $J/\psi$   $p_T$  found in the first bin (2.47 GeV/ $c$  in p-Pb and 2.17 GeV/ $c$  in Pb-p), we can consider this effect as negligible. Consequently, the associated systematic uncertainty is not considered. Finally, the matching efficiency uncertainty was found to be uncorrelated in  $p_T$ , and for the multiplicities reached in p-Pb collisions also uncorrelated with the multiplicity [259]. Therefore no uncertainty on the  $\langle p_T \rangle$  measurement has to be considered due to these effects.

We consider the aforementioned effects as uncorrelated in a given multiplicity bin, and hence they are added quadratically to obtain the relative  $\langle p_T \rangle$  systematic uncertainty in a multiplicity bin  $i$ . These systematic uncertainties are also considered as uncorrelated between the p-Pb and Pb-p collision systems. The results of the uncertainties entering in the relative  $J/\psi$   $\langle p_T \rangle$  measurement are shown in Tab. 7.4.

Source	p-Pb	Pb-p
Sig. Extr.	0.2-0.5%	0.2-0.5%
$\mathcal{A} \times \varepsilon / \text{Sig. extr. / bin-flow}$	0.5-2.7%	0.5-2.7%
Pile-up	0.2-0.7%*	0.2-0.8%*
Total	0.5-2.8%	0.5-2.8%

Table 7.4: Relative  $J/\psi$   $\langle p_T \rangle$  systematic uncertainties in p-Pb and Pb-p collisions. The values represent the minimum and maximum values of the uncertainties in the multiplicity bins. The uncertainties with \* are only applicable to the two last multiplicity bins.

Similarly, the uncertainties for the absolute measurement are listed in Tab. 7.5.

Source	p-Pb	Pb-p
Sig. Extr.	0.2-0.5%	0.2-0.5%
$\mathcal{A} \times \varepsilon / \text{Sig. extr. / bin-flow}$	0.5-2.7%	0.5-2.7%
Pile-up	0.2-0.7%*	0.2-0.8%*
Total	0.5-2.8%	0.5-2.8%

Table 7.5: Absolute  $J/\psi$   $\langle p_T \rangle$  systematic uncertainties in p-Pb and Pb-p collisions. The values represent the minimum and maximum values of the uncertainties in the multiplicity bins. The uncertainties with \* are only applicable to the two last multiplicity bins.



### 7.3 $J/\psi \langle p_T^2 \rangle$ measurement

The same technique as for the  $\langle p_T \rangle$  measurement can be used to measure the second moment of the  $J/\psi$  transverse momentum distribution  $\langle p_T^2 \rangle$ . In this case, we build the di-muon squared mean transverse momentum invariant mass spectrum,  $\langle p_T^{\mu^+ \mu^- 2} \rangle(m_{\mu^+ \mu^-})$  weighting each contribution by the  $J/\psi \mathcal{A} \times \epsilon$ . Similarly to the di-muon  $\langle p_T \rangle$  invariant mass spectrum:

$$(7.7) \quad \langle p_T^{\mu^+ \mu^- 2} \rangle_i^{\mathcal{A} \times \epsilon \text{ corr.}} = \frac{1}{n_i^{eff}} \sum_{j=1}^{n_i} \frac{p_T^{j 2}}{\mathcal{A} \times \epsilon(p_T^j, y^j)}$$

note that the superindex " $\mathcal{A} \times \epsilon \text{ corr.}$ " will be again omitted by simplicity. The fitting function in Eq. 7.2 can be accordingly modified:

$$(7.8) \quad \begin{aligned} \langle p_T^{\mu^+ \mu^- 2} \rangle(m_{\mu^+ \mu^-}) &= \alpha^{J/\psi}(m_{\mu^+ \mu^-}) \times \langle p_T^{J/\psi 2} \rangle \\ &+ \alpha^{\psi(2S)}(m_{\mu^+ \mu^-}) \times \langle p_T^{\psi(2S) 2} \rangle \\ &+ \left(1 - \alpha^{J/\psi}(m_{\mu^+ \mu^-}) - \alpha^{\psi(2S)}(m_{\mu^+ \mu^-})\right) \times \langle p_T^{bkg 2} \rangle \end{aligned}$$

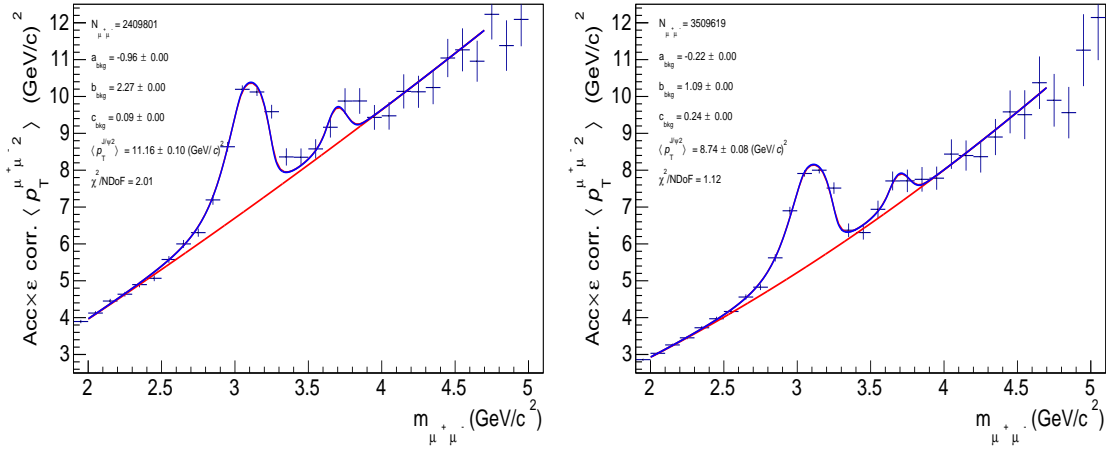


Figure 7.12: Multiplicity integrated  $\mathcal{A} \times \epsilon$  corrected di-muon  $\langle p_T^2 \rangle$  spectra in p-Pb (left) and Pb-p (right) collisions. The spectra are fitted with a fit combination choice (CB2+VWG+Range $^{inv.mass} = 2.0-5.0 + \sigma_{\psi(2S)} = 1.1 \cdot \sigma_{J/\psi} + \text{Pol2} + \text{Range}^{\langle p_T \rangle} = 2.0-5.0$ ) and the values of the extracted  $J/\psi \langle p_T \rangle$  are shown.

The same fitting procedure as for the  $\langle p_T \rangle$  is applied in this case. The integrated p-Pb and Pb-p di-muon  $\langle p_T^2 \rangle$  spectra fitted with a given combination of background di-muon  $p_T$  function, fitting range and "S + B" parametrization are shown as an example in Fig. 7.12. It can be observed that the spectra are correctly reproduced by the chosen parametrisation. The results obtained with these fits are compared to those obtained in [261] in Tab. 7.6. As can be seen both sets of values are in very good agreement.

System	$\langle p_T^2 \rangle$ (GeV <sup>2</sup> /c <sup>2</sup> ) (this thesis)	$\langle p_T^2 \rangle$ (GeV <sup>2</sup> /c <sup>2</sup> ) ([261])
p-Pb	$11.16 \pm 0.10$ (stat.)	$11.12 \pm 0.08$ (stat.) $\pm 0.21$ (syst.)
Pb-p	$8.74 \pm 0.08$ (stat.)	$8.73 \pm 0.09$ (stat.) $\pm 0.20$ (syst.)

Table 7.6:  $J/\psi$   $\langle p_T^2 \rangle$  values in p-Pb and Pb-p collisions obtained in this thesis (for the fit combination in Fig. 7.12) compared with the ones obtained in [261]. The values in this thesis are shown with statistical uncertainties only.

The  $\langle p_T^2 \rangle$  extraction has been applied also in multiplicity slices for a given fit combination. The fitted spectra are presented in Fig. 7.13. The invariant mass binning is wider than that used for the  $\langle p_T \rangle$  extraction, since the dispersion of the values in each invariant mass bin is bigger in this case. The same procedure as for the  $\langle p_T \rangle$  has to be followed to estimate the systematic uncertainties of the  $\langle p_T^2 \rangle$  measurement. However, this has not been completed for this thesis, and the results are presented with statistical uncertainties only.

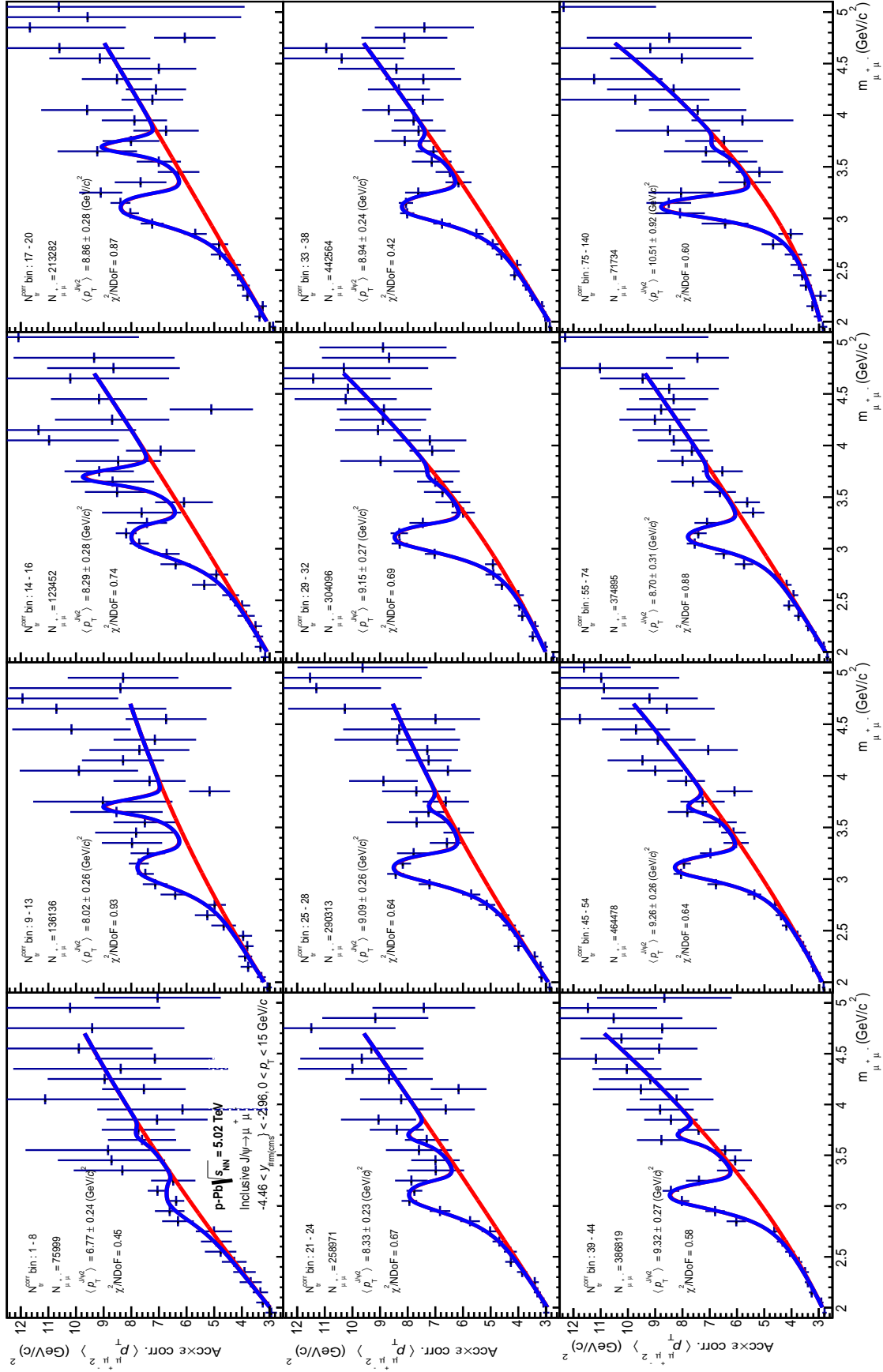


Figure 7.13:  $J/\psi \langle p_T^2 \rangle$  extraction in multiplicity bins in p-Pb for a fit combination choice (CB2+VWG+Range  $inv.mass=2.0-5.0+\sigma_{\psi(2S)}=0.9 \cdot \sigma_{J/\psi} + \text{Pol2+Range} \langle p_T \rangle = 2.0-4.7$ ).



*J/ψ* MEASUREMENTS IN PP COLLISIONS

**T**hroughout the previous chapters we have studied in detail the procedures to obtain a charged particle event multiplicity estimator and to measure the *J/ψ* yield and transverse momentum. Those studies were performed on the 2013 p-Pb data sample. However, the same techniques can be applied for the analysis of pp collisions. In this chapter we discuss the analysis performed on the 2012 pp at  $\sqrt{s} = 8$  TeV data sample.

It is important to note that, despite the fact that this chapter is the last one of the *J/ψ* analysis part of this thesis, the analysis was performed before the most recent developments explained in previous chapters (we detail the differences in the corresponding sections in this chapter). Consequently, the treatment of the multiplicity estimation and the systematic uncertainties of the results in this chapter are less refined than those in the latest p-Pb results.

The motivation to study *J/ψ* production as a function of multiplicity in pp collisions is double sided. First of all, since no cold nuclear matter effects are present in these collisions, and no hot nuclear effects are expected at low multiplicity, this measurement can provide a baseline for the interpretation of the results in p-Pb collisions. Second, the charged particle multiplicities measured in high multiplicity pp collisions, already at  $\sqrt{s} = 7$  TeV, were comparable to those measured in heavy ion collisions at lower energies, where effects ascribed to QGP formation were found [8, 9]. Therefore the search for heavy-ion like collective effects at high multiplicities is justified in pp collisions at 8 TeV [10].

## 8.1 Charged particle multiplicity estimation

One of the main differences of the analysis in this chapter with respect to the latest analyses presented in this thesis, is on the charged particle multiplicity estimator. In the present case, we choose as multiplicity estimator the number of tracklets in the pseudorapidity range  $|\eta| < 0.5$  (instead of  $|\eta| < 1$  in previous chapters)<sup>1</sup>. The correction method used to estimate the charged particle multiplicity from the measured tracklets is the data-driven method. We will show, when comparing results with different choices of the pseudorapidity ranges, that the obtained results are equivalent (see Sec. 9.1 and 9.3).

Moreover, the approach used to compute the relative charged particle multiplicity is that of Eq. 4.5 ( $dN_{ch}/d\eta/\langle dN_{ch}/d\eta \rangle = N_{tr}^{corr}/\langle N_{tr}^{corr} \rangle$ ). This only allows to compute the relative values. The reference used for the multiplicity correction was a  $z_0$  region of the SPD such as  $N_{tr}(z_0) = \max(N_{tr}(z))$ . Neither the variation of the  $\alpha$  correction with multiplicity nor the multiplicity resolution variation with  $z$ -vertex were considered at the time. Note that in this case no simulation was used to further correct the results. As it will be shown in the following chapter, the consideration of these effects changes the multiplicity estimation somewhat, but does not change the physics message sustained by the results.

In Fig. 8.1 top, the  $\langle N_{tr} \rangle$  of MB events as a function of  $z$ -vertex is shown in blue. The variations of the SPD efficiency with the vertex position can be seen. The local variations of the efficiency are observed with more detail here than when using  $|\eta| < 1$  as a multiplicity estimator (see Fig. 4.1). This is because in the case  $|\eta| < 0.5$  the integration range in pseudorapidity is smaller, thus the variations of efficiency are less averaged. The result after the correction with the data driven method is shown in red also in Fig. 8.1 top. In Fig. 8.1 bottom we show the comparison of the uncorrected number of tracklets distribution (blue) and the corrected tracklets distribution (red) for MB-triggered events.

Another difference is that the variations of the SPD detector status among different runs were not taken into account. In Fig. 8.2 the SPD inactive modules during the pp data taking periods used in this thesis are shown. As we can see, there are variations in the status of the SPD outer layer along the periods. We can distinguish three different main subperiods with 10, 14 and 16 missing modules in the outer SPD layer. As we shown in Fig. 4.10 (right), the variations in p-Pb data taking (2 modules) had an impact of about 1.3% on the average number of tracklets around the  $z_v$  region affected. In the pp case, the variations of the number of inactive modules are bigger, but the status of the SPD is not that different respect to the status in p-Pb collisions. Therefore a dramatic impact on the final result is not expected.

In addition, the treatment of the "bin 0" when slicing in multiplicity is also different in this case. The "bin 0" is included in the first bin, which introduces a bias on the result in this bin. This effect is however not expected to be big.

---

<sup>1</sup>When this analysis was performed, the multiplicity correction method using the SPD  $\mathcal{A} \times \mathcal{E}$  was being developed at the same time, hence the choice of the pseudorapidity range

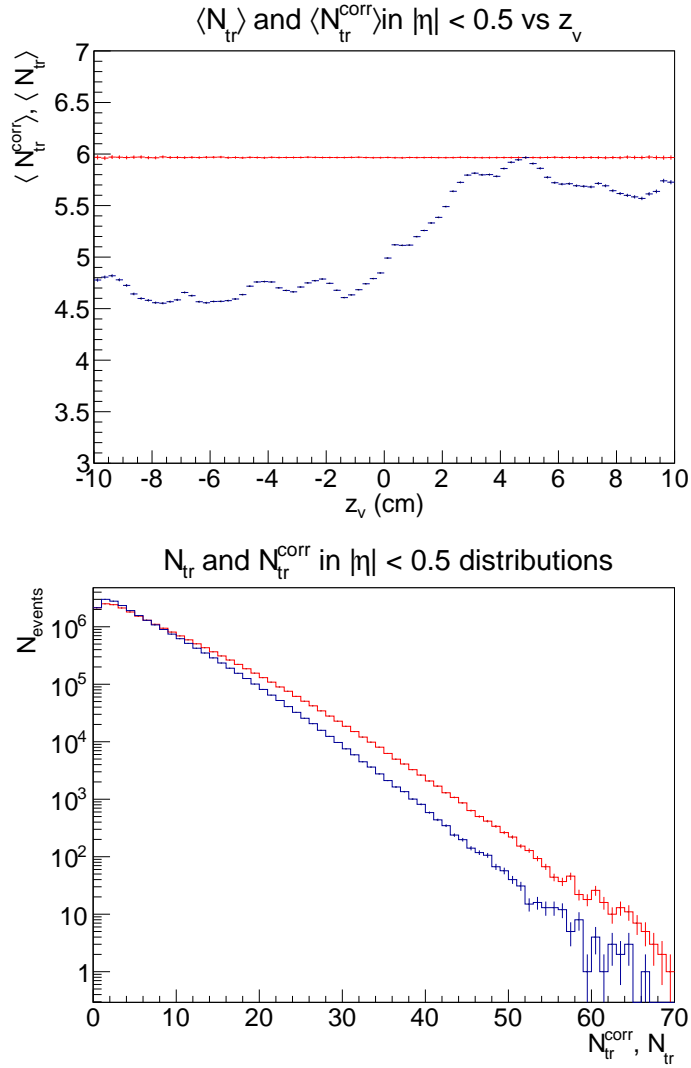


Figure 8.1: Top: Average number of tracklets (blue) and average number of corrected tracklets (red) as a function of  $z_v$  in  $|\eta| < 0.5$  for MB collisions. Bottom: Tracklets (blue) and corrected tracklets (red) distributions in  $|\eta| < 0.5$  for MB collisions.

The last difference is due to the approach used to compute the relative charged particle multiplicity. In order to obtain a correct value relative to inelastic collisions<sup>2</sup>, we need to correct the measured overall-average multiplicity in  $dN_{ch}/d\eta/\langle dN_{ch}/d\eta \rangle$ , by event selection efficiency. To account for this efficiency, we need to use an equivalent to Eq. 3.17 in order to correct the measured average number of corrected tracklets for the contribution of events without a vertex. However, this approach is valid for p-Pb collisions, since the MB selects  $\sim 99.2\%$  of NSD events, and the average multiplicity is high ( $\sim 17$ ). This means that, in the p-Pb case, considering that the 0.8% of the NSD events missed by the MB trigger have zero multiplicity is reasonable. The situation is quite different in pp collisions, since the

<sup>2</sup>Necessary, for instance, to compare with the pp results at 7 TeV in [8]

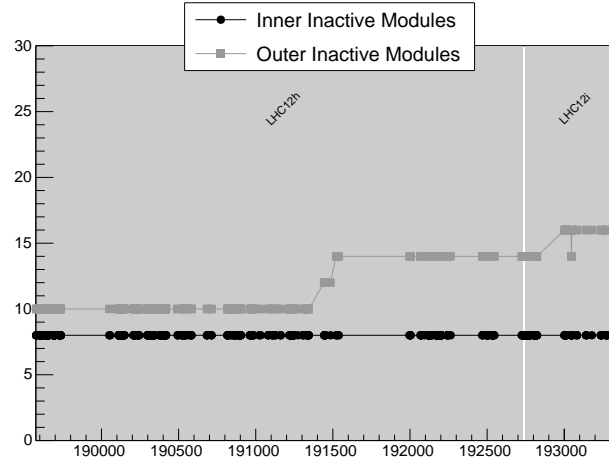


Figure 8.2: SPD inactive modules in the inner and outer layers during pp 8 TeV runs. The considered data taking periods are LHC12h and LHC12i.

average multiplicity is smaller ( $\sim 6$  [8]), and the efficiency of the MB trigger to select NSD<sup>3</sup> (inelastic<sup>4</sup>) collisions is much lower. Therefore, what we did is to correct the measured tracklets multiplicity for events not passing the selection (events without vertex or not passing the vertex QA), assuming that their average multiplicity in  $|\eta| < 0.5$  is zero (we rename it to  $\langle N_{tr}^{corr} \rangle_{measured}$ ). Then we correct for the multiplicity of events missed by the MB trigger ( $\langle N_{tr}^{corr} \rangle_{\overline{MB}}$ ):

$$(8.1) \quad \langle N_{tr}^{corr} \rangle_{inel} = \epsilon_{MB}^{inel} \langle N_{tr}^{corr} \rangle_{measured} + (1 - \epsilon_{MB}^{inel}) \langle N_{tr}^{corr} \rangle_{\overline{MB}}$$

where  $\epsilon_{MB}^{inel}$  is the MB trigger efficiency for inelastic events. The multiplicity of the events not seen by the MB trigger condition is actually unknown, so we considered two extreme cases: that their multiplicity could be as low as zero and as big as the measured multiplicity in MB bias events ( $\langle N_{tr}^{corr} \rangle_{measured}$ ). The average multiplicity  $\langle N_{tr}^{corr} \rangle_{inel}$  was taken as the average value obtained from the two extreme cases considered. The uncertainty is taken as the difference between the average and the extreme values, leading to a 15% systematic uncertainty. This is clearly an overestimation of the uncertainty, but is the best guess that could be done at that time without a simulation. The uncertainty is global but it was added to the multiplicity axis uncertainty in the plots.

<sup>3</sup>The efficiency of the MB trigger for NSD collisions in [240] for pp at 8 TeV is  $\epsilon_{MB}^{NSD} = 0.93 \pm 0.02$ , but this value was unknown at the time of this analysis.

<sup>4</sup>The efficiency of the MB trigger for pp at 8 TeV inelastic collisions was not computed at the time of this analysis so we used that at 7 TeV,  $\epsilon_{MB}^{inel} = 0.74 \pm 5\%$  [137].



## 8.2 $J/\psi$ yield and $\langle p_T \rangle$ measurement

The  $J/\psi$  yield analysis in pp is completely analogous to that in p-Pb collisions (see Sec. 6.1). The di-muon pairs entering in the analysis are weighted by the Muon Spectrometer  $J/\psi$   $\mathcal{A} \times \varepsilon$  in pp collisions shown in Fig. 8.3. This correction has been extracted from pure  $J/\psi$  signal simulations with the detector conditions of LHC12h+i periods. Equivalently, the tail parameters for the signal extraction have been tuned on the  $\mathcal{A} \times \varepsilon$  corrected simulated data.

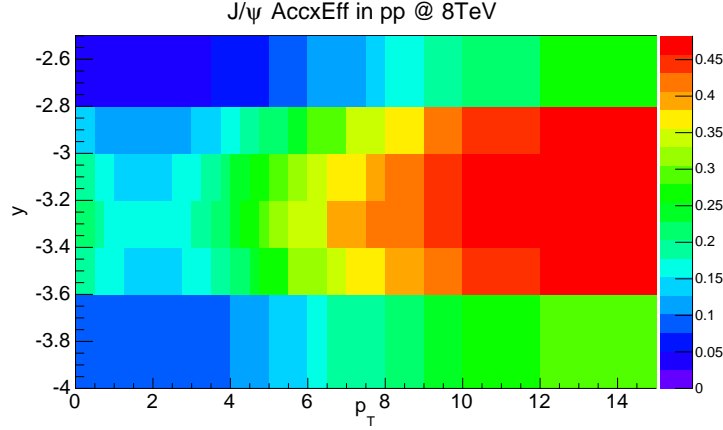


Figure 8.3:  $J/\psi$   $\mathcal{A} \times \varepsilon$  in pp collisions (LHC12h+i VZERO-triggered events).

In Fig. 8.4 we show an example of signal extraction using the fit combination (CB2+POL2EXP+Range=2.0-5.0 +  $\sigma_{\psi(2S)} = 0.9 \cdot \sigma_{J/\psi}$ ). Comparing the result in pp to that obtained in p-Pb (Fig. 6.5) we observe that the background over the left tail is much smaller in pp collisions. The signal over background ratio in the peak region is 45% higher in pp than in p-Pb collisions. This is an expected result.

In the integrated signal extraction, there is a difference at the event selection level with respect to the latest analyses in previous chapters. The same event selection was applied for the integrated and multiplicity analyses. This means that for the integrated analysis we only kept events with an SPD vertex within  $|z| < 10$  cm and passing the vertex QA. The effect on the extracted number of  $J/\psi$  and number of MB events was considered to vanish on the yield computation. The extracted inclusive  $J/\psi$  yield in MB collisions, calculated as in Sec. 6.1, is  $Y_{pp\ 8TeV}^{J/\psi} = (1.43 \pm 0.02 \text{ (stat)}) \cdot 10^{-4}$ . Note that only the uncertainties for the relative quantities are calculated in this analysis. In order to obtain a value relative to inelastic collisions we need to correct by the MB trigger efficiency. The MB trigger efficiency for inelastic events was not available at the time of this analysis, so we used the value for pp collisions at 7 TeV. This value is  $\varepsilon_{MB}^{inel} = 0.74 \pm 5\%$  [137]. This choice was justified by the stability of the V0 detectors with time. In [137], the values of the MB trigger efficiency for inelastic events are shown in Tab 3 for different energies. It can be seen that the value barely changes for pp collisions at 0.9, 2.76 up to 7 TeV.

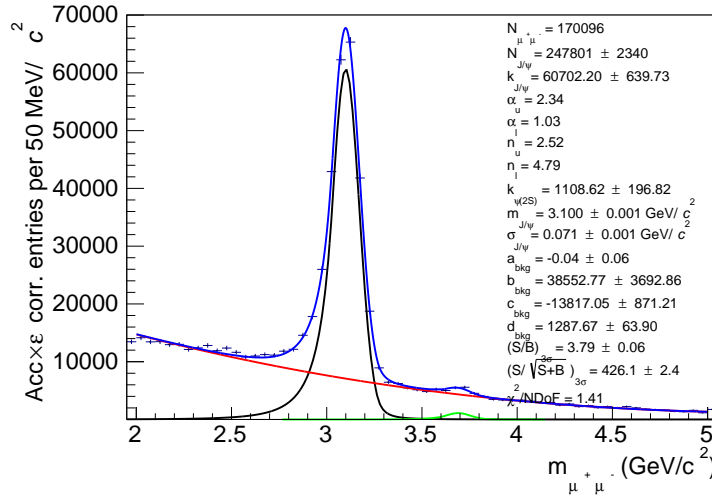


Figure 8.4: Example of signal extraction for the integrated invariant mass spectrum in pp collisions using the fit combination (CB2+POL2EXP+Range=2.0-5.0 +  $\sigma_{\psi(2S)} = 0.9 \cdot \sigma_{J/\psi}$ ).

Finally, the inclusive inelastic  $J/\psi$  production cross section is calculated as:

$$(8.2) \quad \sigma^{J\psi} = Y^{J\psi} \times \sigma_{CINT7}$$

where the MB cross section value,  $\sigma_{CINT7} = 56 \text{ mb} \pm 5\%$  was taken from [268]<sup>5</sup>. The result obtained in this thesis for the cross section of inclusive  $J/\psi$  production in pp collisions is  $\sigma_{pp \ 8TeV}^{J\psi} = 8.01 \text{ } \mu\text{b}$ . Note that no uncertainties are given on the cross section, since it is only calculated as a cross-check. We compare the results obtained in this thesis with those obtained by LHCb [269] and ALICE [270] in Tab 8.1. The results of this thesis are in agreement with both results.

System	$\sigma_{J/\psi}$ (this thesis)	$\sigma_{J/\psi}$ ([269])	$\sigma_{J/\psi}$ ([270])
pp 8 TeV	8.01 $\mu\text{b}$	$7.59 \pm 0.01 \pm 0.55 \text{ } \mu\text{b}$	$8.63 \pm 0.04 \pm 0.79 \text{ } \mu\text{b}$

Table 8.1: Integrated cross section in pp collisions at  $\sqrt{s} = 8 \text{ TeV}$  obtained in this thesis compared with the LHCb [269] and ALICE results [270]. Note that the result obtained in this thesis has no uncertainties since it is calculated as a cross-check.

The  $\langle p_T \rangle$  extraction is also applied as in p-Pb (see Sec. 7.1). In Fig. 8.5 we show an example of signal extraction using the fit combination (CB2+POL2EXP+Range<sup>inv.mass</sup>=2.0-5.0+ $\sigma_{\psi(2S)} = 1.1 \cdot \sigma_{J/\psi}$ +Pol2+Range<sup>( $p_T$ )</sup>=2.0-5.0 ). Comparing the result in pp to that obtained in p-Pb (Fig. 7.2) we observe that the  $\langle p_T \rangle$  shape of the background is also different in pp and in p-Pb collisions. The obtained value for the multiplicity integrated  $J/\psi$  transverse momentum in pp collisions is  $\langle p_T \rangle = 2.57 \pm 0.01 \text{ (stat) GeV}/c$ <sup>6</sup>.

<sup>5</sup>The latest value is  $55.74 \pm 0.46 \text{ mb}$  (see Sec. 2.4)

<sup>6</sup>Only the systematic uncertainties for the relative quantities are calculated

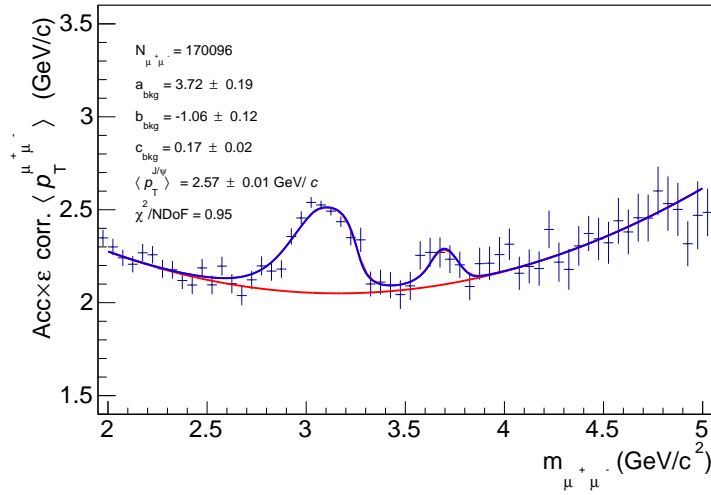


Figure 8.5: Example of signal extraction for the integrated invariant mass spectrum in pp collisions.

The relative signal extraction and relative  $\langle p_T \rangle$  extraction procedures use the same fit combination tests as those used in the p-Pb analysis (see Sec.6.3.1 and Sec.7.2.1). The procedure is applied to each multiplicity bin. The result for each multiplicity bin is computed as the average value of the results from the different fit combinations (Eq. B.1). The statistical error is the error on the average of the fit tests (Eq. B.2 and Eq. B.3) and the systematic uncertainty the  $1\sigma$  dispersion of the tests (Eq. B.4). Examples of signal extraction and  $\langle p_T \rangle$  extraction in multiplicity bins are shown in Fig. 8.6 and Fig. 8.7 respectively.

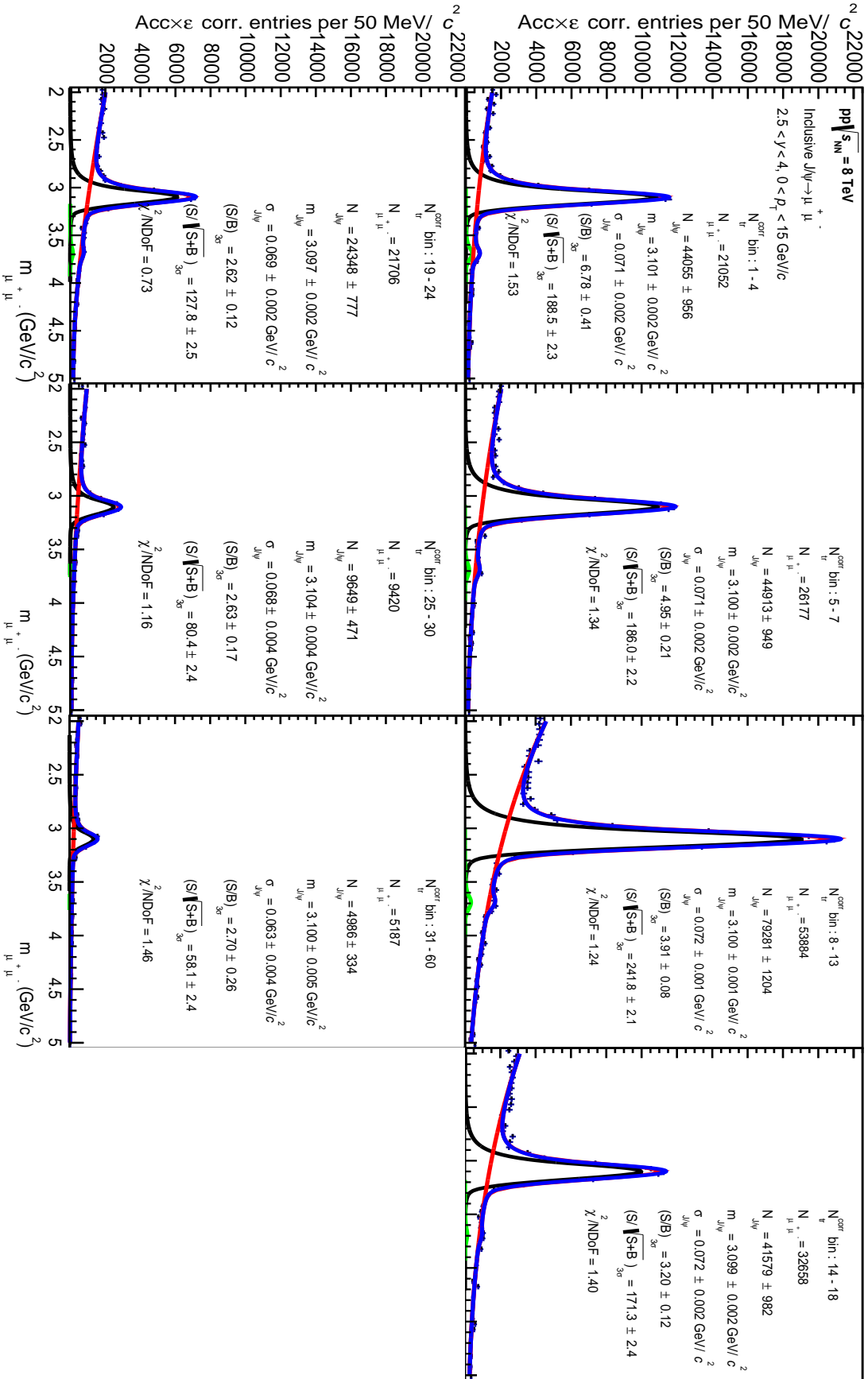
The relative yields, computed by means of Eq. 6.13, are normalised to inelastic events. Therefore the multiplicity integrated number of equivalent MB events has to be corrected by  $\epsilon_{MB}^{inel} = 0.74 \pm 5\%$  instead of the  $\epsilon_{MB}^{NSD}$  in Eq. 6.13.

### 8.3 Systematic uncertainties

The procedures to estimate the systematic uncertainties for the  $J/\psi$  measurements in the pp results are similar to those employed in previous chapters with some exceptions. In this section we only discuss those which are different, and at the end we give a summary on the systematic uncertainties. Note that in this analysis we only compute relative quantities so only the corresponding uncertainties are calculated.

We have already discussed about the uncertainty of the multiplicity axis due to the unknown multiplicity of the events not triggering the MB (Eq. 8.1), which was taken to be 15%. We consider that this uncertainty largely covers the other possible sources of uncertainty in the multiplicity measurement. The remaining differences are:

- The pile-up influence on measured yield and transverse momentum



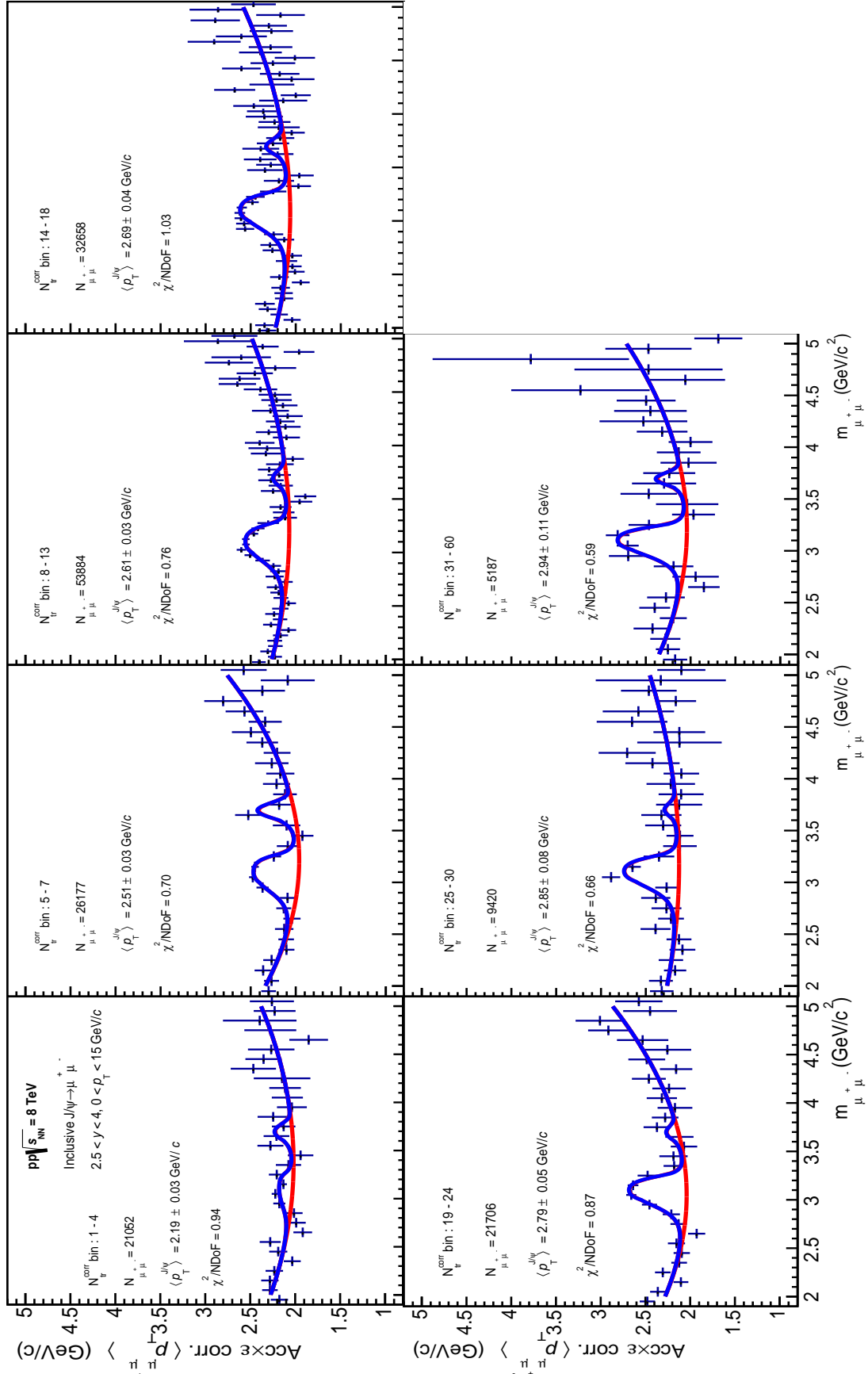


Figure 8.7:  $J/\psi$   $\langle p_T \rangle$  extraction in multiplicity bins in  $pp$  for the following fit combination choice (NA60+POL2EXP+Range $^{inv.mass}=2.0-5.0+\sigma_{\psi(2S)}=1.1\cdot\sigma_{J/\psi}$ +Pol2+Range $\langle p_T \rangle=2.0-5.0$ ).

- The treatment of the spectrometer  $\mathcal{A} \times \mathcal{E}$  uncertainty due to variations on the input distributions
- The multiplicity bin flow
- The  $\langle p_T \rangle$  uncertainties due to the variation of the transverse momentum with the invariant mass and the propagation of signal extraction parameters are combined differently

Further details on these points are given in the following sections.

### 8.3.1 Yield uncertainties

As we discuss in Sec. 9.3, the  $J/\psi$  yield correlation in pp collisions has a similar behaviour as in Pb-p collisions. Therefore, the effect of the pile-up on the measured yields is similar to that found in Pb-p. We show in Sec. 6.3.6, that the main effect in Pb-p was due to the incapability to distinguish the  $J/\psi$  produced in the main collision from those produced in secondary interactions. This effect was estimated to be at most 1.5% in Pb-p collisions. However, the average number of collisions per bunch crossing in LHC12h+i is  $\langle \mu \rangle = 0.011$ . This is  $\sim 4$  times smaller than that in Pb-p collisions. We therefore consider the effect of pile-up negligible with respect to the other uncertainties.

For this analysis, variations of the input distributions have been made to compute different  $\mathcal{A} \times \mathcal{E}(p_T, y)$  maps as done in Sec. 6.3.4. The input  $p_T$  distributions are modified to obtain an average  $p_T$  similar to that measured in the lowest and higher multiplicity bins. With these distributions, new  $\mathcal{A} \times \mathcal{E}$  corrections are computed. In Fig. 8.8, the nominal and modified distributions are shown, together with the ratio of the nominal and modified  $\mathcal{A} \times \mathcal{E}$  corrections. The variations of the modified distributions with respect to the nominal ones, are bigger than those observed in p-Pb and Pb-p collisions (Fig. 6.12). This is due to a steeper variation of the average transverse momentum in pp collisions as we already anticipated in Sec. 6.3.4. In spite of the bigger variations of the distributions, the variations observed in the  $\mathcal{A} \times \mathcal{E}$  corrections are at most 2%, very similar to that observed in the p-Pb case. Note that this difference happens in a rapidity bin where the di-muon statistics is small. Therefore this variation has a negligible influence on the results as a function of multiplicity with respect to other sources of uncertainty, as already shown in Sec. 6.3.5. This provides a further indication of the stability of the 2D  $\mathcal{A} \times \mathcal{E}$  correction method with respect to the uncertainties of the input distributions used to compute the correction.

However, the integrated  $\mathcal{A} \times \mathcal{E}$  changes up to 6% with respect to the nominal value, depending on the input distributions. To illustrate the advantages of using the 2D  $\mathcal{A} \times \mathcal{E}(p_T, y)$  correction method developed in this thesis (Eq. 6.3) with respect to the usual correction (Eq. 6.2), we compute the relative differences between the obtained number of corrected  $J/\psi$  in the first and last multiplicity bins with the two methods. In Tab. 8.2 we show the number of  $J/\psi$  extracted from the uncorrected spectra ( $N_{J/\psi}^{raw}$ ), corrected by the integrated

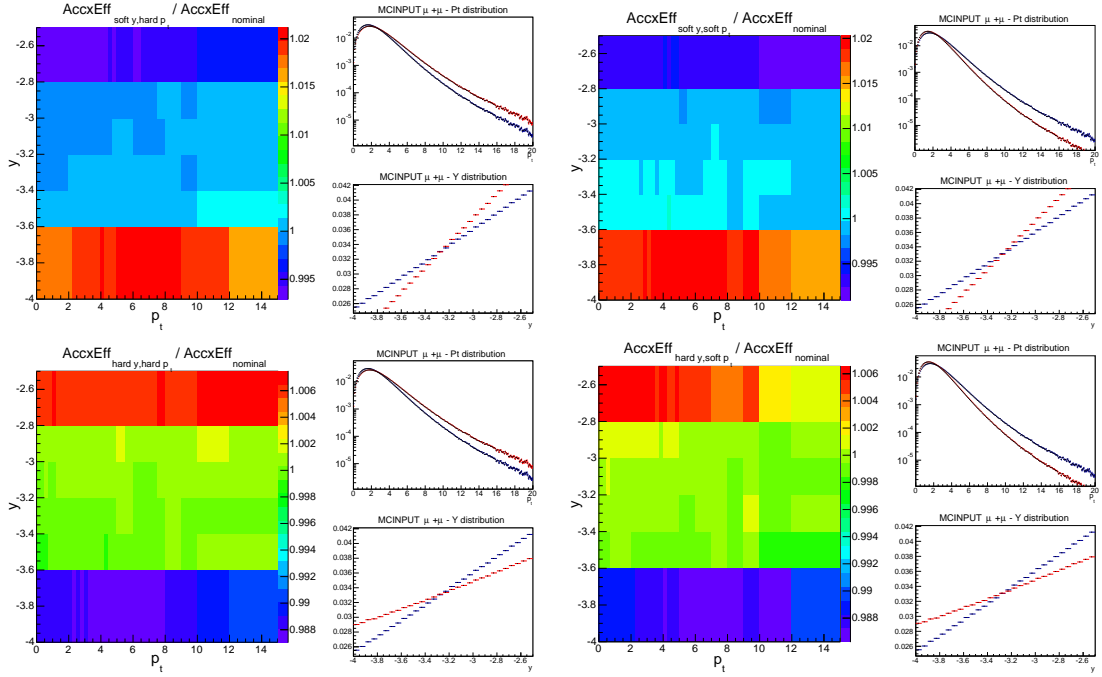


Figure 8.8:  $\mathcal{A} \times \mathcal{E}$  variations (ratio of varied over nominal correction) due to changes in the input MC distributions, and the corresponding input distributions (the blue curves represent the nominal and the red curves the varied distributions). The results are shown for four combinations of extreme variations of the  $p_T$  and  $y$  distributions: soft- $y$  and hard- $p_T$  (top left), soft- $y$  and soft- $p_T$  (top right), hard- $y$  and hard- $p_T$  (bottom left), hard- $y$  and soft- $p_T$  (bottom right).

nominal  $\mathcal{A} \times \mathcal{E}$  (12.44%). We compare them with the ones extracted from the spectra corrected by the nominal  $\mathcal{A} \times \mathcal{E}(p_T, y)$  ( $N_{J/\psi}^{corr}$ ). The relative differences are 3.4% and 9.4% for the first and last multiplicity bins respectively. Then in Tab. 8.3, we show the number of  $J/\psi$  obtained from the uncorrected spectra and corrected by the corresponding integrated  $\mathcal{A} \times \mathcal{E}$  in each bin (the  $\mathcal{A} \times \mathcal{E}$  obtained with the modified distributions that reproduce the measured average  $p_T$  in each bin) (11.80% for the first multiplicity bin and 13.25 % for the last one). They are again compared with the ones extracted from the spectra corrected by the nominal  $\mathcal{A} \times \mathcal{E}(p_T, y)$ . In this case, the relative differences are at most 2.7%. This confirms that the 2D correction method of this thesis is less sensitive to variations on the distributions used to compute the  $\mathcal{A} \times \mathcal{E}$  corrections, than the integrated correction. Therefore, the associated systematic uncertainty on the analysis in this thesis is very small with respect to the other uncertainties. On the contrary, when using the usual technique, a 6% uncertainty should be added (or a multiplicity dependent correction should be performed).

However, by the time of this analysis, we decided to be conservative and assign as systematic uncertainty of our measurement the found difference between the values obtained with the two methods. Therefore the  $\mathcal{A} \times \mathcal{E}$  uncertainty was between 3.4 and 9.4% depending

$N_{tr}^{corr}$ bin	$N_{J/\psi}^{raw}/\mathcal{A}\times\epsilon$	$N_{J/\psi}^{corr}$	Relative difference
0 - 4	$42428 \pm 740$	$43921 \pm 893$	3.4%
30 -60	$4894 \pm 364$	$5354 \pm 338$	9.4%

Table 8.2: Number of  $J/\psi$  extraction from raw spectra and corrected by integrated  $\mathcal{A}\times\epsilon$  (12.44%), compared to the result of the extraction from the  $\mathcal{A}\times\epsilon$  corrected spectra for a single fit test. The uncertainties are the statistical uncertainties given by the fit. The relative differences between the results are also shown.

$N_{tr}^{corr}$ bin	$N_{J/\psi}^{raw}/\mathcal{A}\times\epsilon$	$N_{J/\psi}^{corr}$	Relative difference
0 - 4	$44728 \pm 780$	$43921 \pm 893$	1.8%
30 -60	$5026 \pm 317$	$5354 \pm 338$	2.7%

Table 8.3: Number of  $J/\psi$  extraction from raw spectra and corrected by integrated  $\mathcal{A}\times\epsilon$  (11.80% for first bin and 13.25% for the last one), compared to the result of the extraction from the  $\mathcal{A}\times\epsilon$  corrected spectra for a single fit test. The uncertainties are the statistical uncertainties given by the fit. The relative differences between the results are also shown.

on the multiplicity bin.

Another difference on the systematic uncertainty computation is the bin flow. For this analysis, the bin flow was simply not taken into account. However, the uncertainty associated to the  $\mathcal{A}\times\epsilon$  was clearly overestimated and we consider that it covers the bin flow uncertainty.

The values of the systematic uncertainties for the relative yield are summarised in Tab. 8.4.

Source	$Y^i/\langle Y \rangle$ syst. unc.
Sig. Extr.	0.2-1.4%
$F_{norm}$ method	0.4-8%
$\mathcal{A}\times\epsilon$	2-9.4%
Pile-up	-
Total	2.1-12.4%

Table 8.4: Summary of the relative  $J/\psi$  yield systematic uncertainties in pp collisions. The values represent the minimum and maximum values of the uncertainties in the multiplicity bins.

There is an additional global uncertainty of 5% on the integrated yield due to the MB trigger efficiency for inelastic events. It is not added to the points but reported separately.

### 8.3.2 $\langle p_T \rangle$ uncertainties

For the transverse momentum, the uncertainties due to the variation of the transverse momentum with the invariant mass (see Sec. 7.2.3) and the propagation of signal extraction



Source	$p_T^i/\langle p_T \rangle$ syst. unc.
Sig. Extr.	0.1-0.5%
Pile-up	-
$\langle p_T \rangle$ extr. meth.	2%
Total	2-2.1%

Table 8.5: Relative  $J/\psi$  mean transverse momentum systematic uncertainties in pp collisions. The values represent the minimum and maximum values of the uncertainties in the multiplicity bins.

parameters uncertainties (see Sec. 7.2.4) were taken into account differently with respect to the p-Pb analysis. In order to be conservative, we kept these uncertainties as uncorrelated in the numerator and denominator of the relative measurement. This leads to an uncertainty due to both effects of 2%. For simplicity we denote this uncertainty as " $\langle p_T \rangle$  extraction method". The bin flow uncertainty was not taken into account, but it is partially covered by the  $\langle p_T \rangle$  extraction method one. The last difference is that we do not assign an uncertainty due to pile-up (see Sec. 7.2.5), but this uncertainty should be negligible in pp collisions for the reasons stated before.

The values of the systematic uncertainties for the relative transverse momentum are summarised in Tab. 8.5.



## **Part IV**

# **Results and discussion**



## EXPERIMENTAL RESULTS AND DISCUSSION

In this chapter, the results obtained from the analyses developed during this thesis are presented and discussed. The results of the  $J/\psi$  relative yield and relative  $\langle p_T \rangle$  as a function of the relative charged particle multiplicity in p-Pb collisions, were approved as "ALICE Preliminary" results in 2014 and presented at the Quark Matter conference [271, 272]. In this chapter we present an update of these results that are not yet approved by the ALICE Collaboration. These results will be part of an ALICE publication which is under preparation. Note that the updated results do not change the physics conclusions inferred from the preliminary results.

The main results of the analysis concern the measurement of the  $J/\psi$  production,  $dN_{J/\psi}/dy$ , and average transverse momentum,  $\langle p_T \rangle$ , as a function of charged particle multiplicity,  $dN_{ch}/d\eta$ , in pp collisions at  $\sqrt{s} = 8$  TeV and p-Pb collisions at  $\sqrt{s_{NN}} = 5.02$  TeV. These measurements are performed to study cold nuclear matter effects, but also to search for collective-like behaviour in high multiplicity events in small size systems. They also help to improve our understanding of quarkonium production in pp and p-Pb collisions. In order to further investigate the particle production mechanism and nuclear effects, preliminary results of the transverse momentum broadening,  $\Delta\langle p_T^2 \rangle$ , are also presented and discussed. At the end of the chapter, we present results as a function of the number of binary collisions, estimated from the charged particle multiplicity measurement. We compare with results obtained using the ALICE centrality selection in p-Pb collisions [5] (see App. A). The pros and cons of our approach are discussed.

## 9.1 Relative $J/\psi$ production and $\langle p_T \rangle$ dependence with multiplicity in p-Pb collisions at 5.02 TeV

In this section we present the results obtained in this thesis for the  $J/\psi$  relative  $dN_{J/\psi}/dy$  and relative  $\langle p_T \rangle$  as a function of the relative  $dN_{ch}/d\eta$  in p-Pb collisions at  $\sqrt{s_{NN}} = 5.02$  TeV<sup>1</sup>. In Fig. 9.1, the relative  $dN_{J/\psi}/dy$  measured in non-single diffractive (NSD) collisions at backward and forward rapidities<sup>2</sup> is shown. At low multiplicity a linear increase of the relative  $dN_{J/\psi}/dy$  is observed in both rapidity ranges. This behaviour is similar to that observed in pp collisions at 7 TeV [8, 111], where medium effects are not expected. The comparison with pp results is discussed in Sec.9.3. At higher multiplicities, the increase continues at backward rapidity, following the same pp-like behaviour. On the contrary, we measure a deviation from this behaviour at forward rapidity. A trend towards saturation at high multiplicities is observed on  $J/\psi$  p-Pb data at forward rapidity.

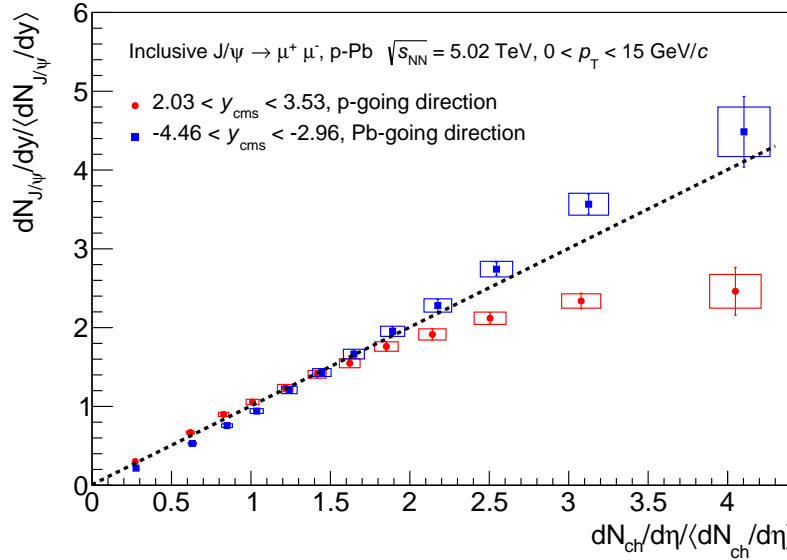


Figure 9.1:  $J/\psi$  relative  $dN_{J/\psi}/dy$  at backward (blue) and forward (red) rapidity as a function of relative charged particle multiplicity measured at mid-rapidity ( $|\eta| < 1$ ) in p-Pb collisions at  $\sqrt{s_{NN}} = 5.02$  TeV.

The relative  $J/\psi$   $\langle p_T \rangle$  as a function of the relative  $dN_{ch}/d\eta$  is presented in Fig. 9.2. An increase of the  $\langle p_T \rangle$  at low multiplicity is observed both at forward and backward rapidity. However, at multiplicities beyond the average multiplicity ( $dN_{ch}/d\eta / \langle dN_{ch}/d\eta \rangle > 1$ ), the  $\langle p_T \rangle$  shows a trend towards saturation, in the two rapidity ranges under study. In addition, the absolute value of the  $J/\psi$   $\langle p_T \rangle$  as a function of the absolute  $dN_{ch}/d\eta$  is presented in Fig. 9.3. The results show a harder  $J/\psi$   $p_T$  at forward than at backward rapidities. In pp

<sup>1</sup>The results are normalised by the corresponding multiplicity averaged quantities

<sup>2</sup>In the figures of this chapter, the label "p(Pb)-going direction" means that in the corresponding beam configuration the muon spectrometer is in the p- or Pb-going direction.

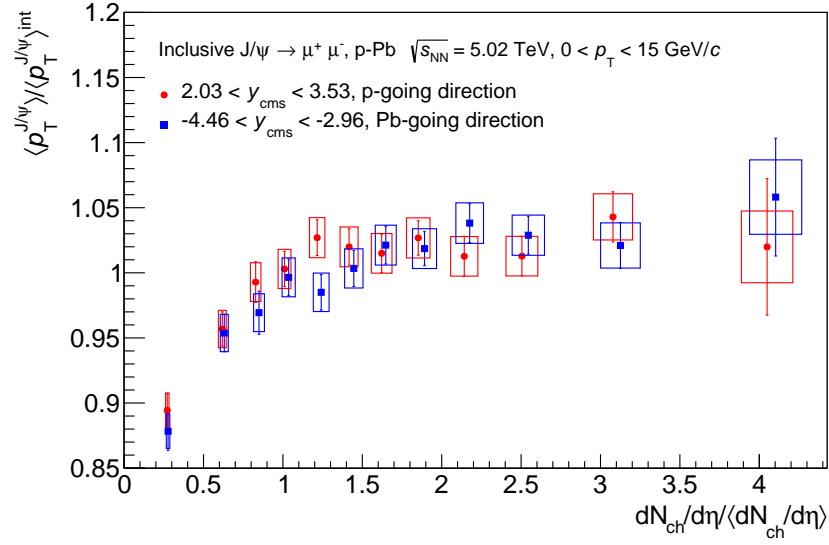


Figure 9.2:  $J/\psi$  relative transverse momentum at backward (blue) and forward (red) rapidity as a function of relative charged particle multiplicity measured at mid-rapidity ( $|\eta| < 1$ ) in p-Pb collisions at  $\sqrt{s_{NN}} = 5.02$  TeV.

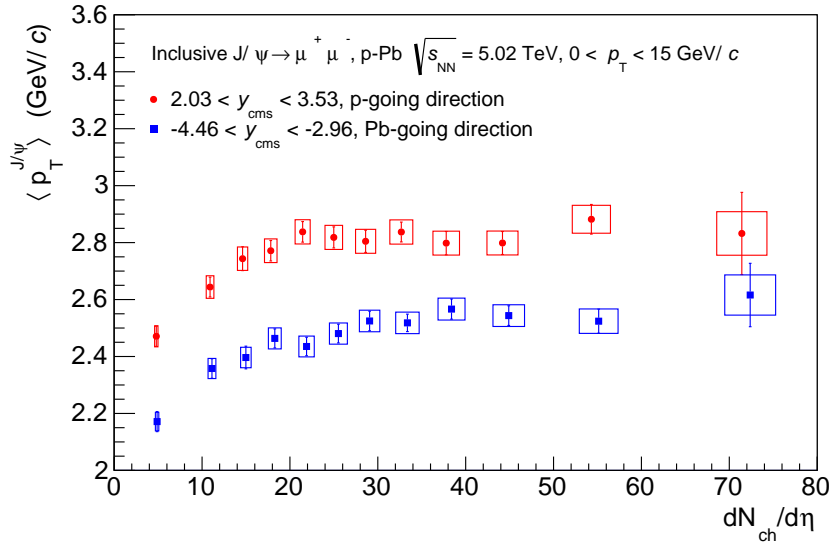


Figure 9.3:  $J/\psi$  absolute  $\langle p_T \rangle$  as a function of the absolute  $dN_{ch}/d\eta$  ( $|\eta| < 1$ ) in p-Pb collisions at  $\sqrt{s_{NN}} = 5.02$  TeV.

collisions at 7 TeV [273] it was observed that the  $J/\psi$   $\langle p_T \rangle$  decreases towards increasing  $|y|$ . This can explain a part of the effect observed here in p-Pb collisions. In addition, the measured suppression in p-Pb collisions at forward rapidity due to cold nuclear matter effects, is more important at low than at high  $p_T$  [4]. This effect contributes to the observed increase of the  $\langle p_T \rangle$  at forward rapidity with respect to backward rapidity.

The observed saturation on the  $\langle p_T \rangle$  could indicate that the production mechanism

does not vary with multiplicity. However, we cannot conclude on this point, since other effects might be at play in p-Pb collisions producing this behaviour. The  $dN_{J/\psi}/dy$  pp-like dependence at backward rapidity indicates that the used multiplicity selection is not biased by particle production not correlated with the  $J/\psi$  production (e.g. jet production). This allows to say that the observed saturation effect on the  $dN_{J/\psi}/dy$  at forward rapidity is hardly the consequence of an event selection bias. The fact that the saturation is only observed at forward rapidity points to the origin of the effect from cold nuclear matter. In case of the presence of collective effects, a variation of the  $dN_{J/\psi}/dy$  dependence at backward rapidity with respect to the pp measurement should also be observed.

The results presented here are compared to the ALICE preliminary in App. D. We found that these results do not change the physics conclusions inferred from the preliminaries. In addition, in App. E we present a comparison with the results obtained using the V0A detector to estimate the relative multiplicity. The same dependence of the  $dN_{J/\psi}/dy$  as the one in Fig. 9.1 is observed. The fact that the correlation is maintained along almost 4 pseudorapidity units provides further arguments to support that the observed effects are not a product of an event selection bias.

In App. C we compare the relative  $dN_{J/\psi}/dy$  as a function of the relative  $dN_{ch}/d\eta$  in this thesis, with the results obtained by selecting the events in centrality classes, using the energy deposited in the ZDC neutron calorimeters (ZN) [261]. The ZN selection is correlated with the geometry of the collision (impact parameter), while the  $dN_{ch}/d\eta$  one selects on the products of the collision. As we see in Figs. C.1 and C.2, with the ZN selection events with multiplicities up to 1.7 times the minimum bias average can be studied. With the  $dN_{ch}/d\eta$  selection, we can study events with 4 times the minimum bias average multiplicity. Therefore, the multiplicity selection enables the possibility to explore collision regimes not accessible with the centrality one. The saturation that we found in the relative  $dN_{J/\psi}/dy$  at forward rapidity is manifested in very rare event classes, and was not seen in the centrality analysis. To draw a conclusion on the origin of the observed effect a detailed comparison with theoretical calculations is needed. Models including cold nuclear matter effects as a function of charged particle multiplicity, are not available for the moment.

The fraction of produced charmonia to open charm can give information about medium effects. If this fraction is measured over the entire phase space, the effects of possible initial state modifications cancel out (effects before the  $c\bar{c}$  formation, such as nuclear modification of PDF or parton energy loss in the nuclear medium). Therefore deviations of this fraction from the expectations in pp collisions would indicate the presence of final state effects (effects after the formation of the  $c\bar{c}$  pair, such as energy loss in the nuclear medium or color screening in a hot medium). However there are no open charm measurements at the LHC down to  $p_T = 0$  in p-Pb collisions, so such a comparison cannot be fully performed. The comparison of the relative yield variation with relative multiplicity, for  $J/\psi^3$  and D mesons is shown anyway in Fig. 9.4 [274]. Note that the D mesons and  $J/\psi$  are measured in different rapidity ranges.

<sup>3</sup>Note that the results shown here correspond to the ALICE preliminary (see App. D)



The D mesons are measured in  $|y_{lab}| < 0.5$  while the  $J/\psi$  are measured in  $2.5 < y_{lab} < 4.0$ . The multiplicity is estimated in  $|\eta| < 1$  in both measurements. The comparison is made for D mesons measured in two  $p_T$  intervals. The bottom panels represent the uncertainty due to the feed-down subtraction of D mesons from B decays [275]. A similar trend is observed in  $J/\psi$  and D mesons at low multiplicity while the relative yield increases more rapidly for D mesons than  $J/\psi$  at high relative multiplicities.

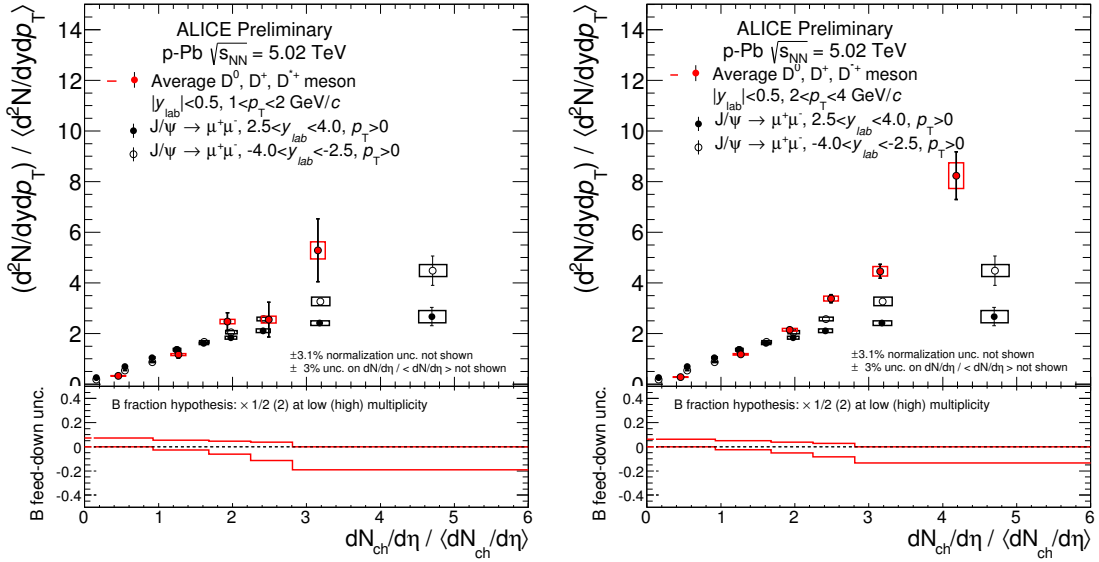


Figure 9.4: Comparison of  $J/\psi$  and D-meson relative yields as a function of the relative charged particle multiplicity in p-Pb collisions at  $\sqrt{s_{NN}} = 5.02$  TeV [274]. Note that the results shown here correspond to the ALICE preliminary (see App. D)

## 9.2 Relative $J/\psi$ production and $\langle p_T \rangle$ dependence with multiplicity in pp collisions at 8 TeV

The result obtained for the  $J/\psi$  relative  $dN_{J/\psi}/dy$  as a function of the relative  $dN_{ch}/d\eta$  in pp inelastic collisions at 8 TeV measured in this thesis is presented in Fig. 9.5. The measurement is compared with a similar one performed by ALICE in pp inelastic collisions at 7 TeV [8, 111]. The 8 TeV result is preliminary: the multiplicity needs to be better determined and the uncertainties refined (see Chap. 8). Note also that the uncertainty on the multiplicity axis is the 15 % global uncertainty due to the trigger efficiency correction (see Sec. 8.1). In this case our multiplicity measurement is performed in  $|\eta| < 1$  to match the range used in the 7 TeV measurement. We can see that a similar trend is observed on the  $J/\psi$  relative  $dN_{ch}/d\eta$  at the two energies. The  $dN_{J/\psi}/dy$  increases with multiplicity. The behaviour can be roughly considered as linear, but such an assertion needs a quantitative estimation that cannot be done reliably yet with the current status of the measurement.

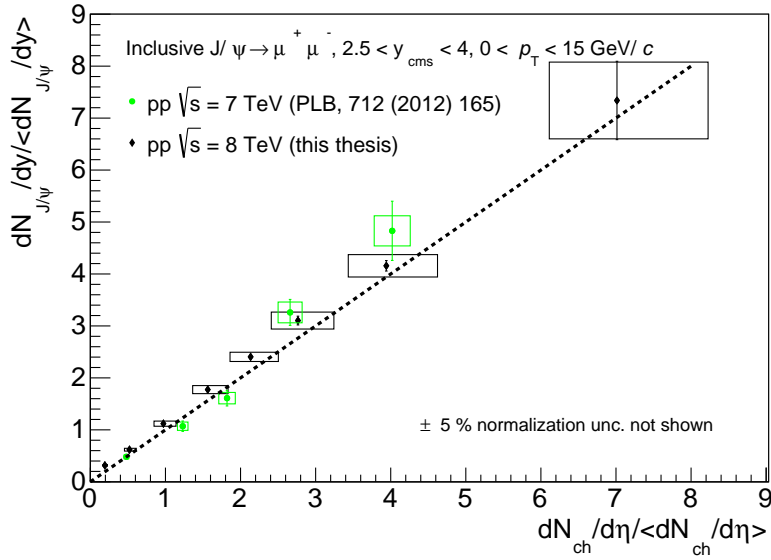


Figure 9.5: Comparison of  $J/\psi$  relative yield as a function of relative charged particle multiplicity measured at mid-rapidity ( $|\eta| < 1$ ) in  $pp$  collisions at  $\sqrt{s} = 7$  TeV [8, 111] (green) with the result in  $pp$  collisions at 8 TeV (black). The dotted line represents the linear behaviour.

Our measurement at 8 TeV, extend the previous multiplicity range at 7 TeV in [8]. This help to set further constraints to models such as the source interaction framework [116], that we show in Fig. 1.13. This is discussed in the following section.

In Fig. 9.7 we present a first measurement of the relative  $J/\psi$   $\langle p_T \rangle$  as a function of the relative  $dN_{ch}/d\eta$  in  $pp$  at 8 TeV. We observe a strong increase of the  $\langle p_T \rangle$  at low multiplicity. At high multiplicity the  $\langle p_T \rangle$  continues to rise but the increase is more gradual than at low multiplicity.

### 9.3 Comparison of $pp$ and $p$ -Pb results

The results of the  $J/\psi$  relative  $dN_{J/\psi}/dy$  in  $p$ -Pb NSD collisions and  $pp$  inelastic collisions are compared in Fig. 9.6. Note that the multiplicity measurement here is done in  $|\eta| < 0.5$ , both in  $pp$  and  $p$ -Pb collisions. The  $p$ -Pb results shown in this section correspond to the ALICE preliminaries (see App. D). A consideration we need to take into account when comparing the  $pp$  and  $p$ -Pb results, is that very different collision regimes can give rise to a similar evolution of the relative  $dN_{J/\psi}/dy$  with the relative  $dN_{ch}/d\eta$ . In  $pp$  collisions, high multiplicity events are produced by MPI in the same collision, while in  $p$ -Pb collisions these events can be produced by parton-parton interactions from different proton-nucleon collisions and/or MPI from the same proton-nucleon collision. When looking at the  $dN_{J/\psi}/dy$  comparison in  $pp$  and  $p$ -Pb collisions we observe that the  $dN_{J/\psi}/dy$  in  $p$ -Pb collisions at backward rapidity behaves as in  $pp$  collisions. However, a deviation from the  $pp$ -like behaviour, probably related to cold

nuclear matter effects, is observed in p-Pb at forward rapidity for relative multiplicities beyond 1.5-2.

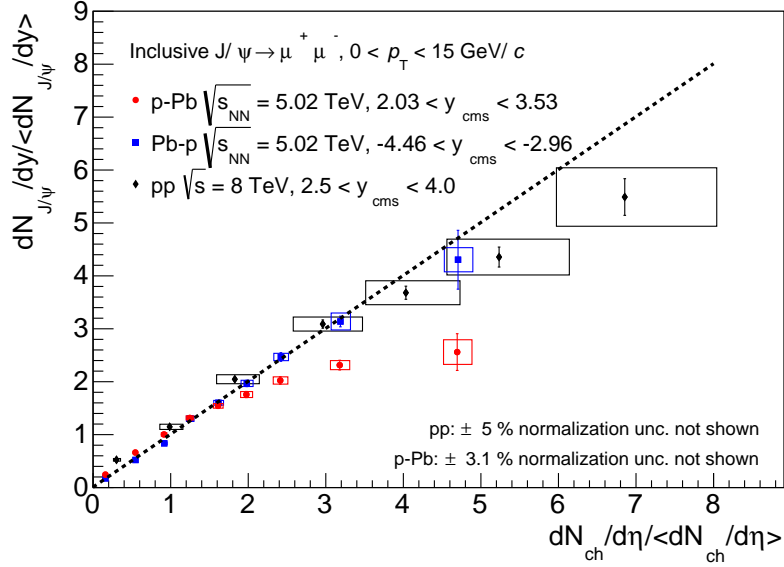


Figure 9.6: Comparison of  $J/\psi$  relative  $dN_{J/\psi}/dy$  at backward (blue) and forward (red) rapidity as a function of relative charged particle multiplicity measured at mid-rapidity ( $|\eta| < 0.5$ ) in p-Pb collisions at  $\sqrt{s_{NN}} = 5.02$  TeV (ALICE Preliminary) with the result in pp collisions at 8 TeV (black). The dotted line represents the linear behaviour.

In Fig. 1.13 we have shown the calculations of the source interaction framework [116] for the  $J/\psi$  production as a function of relative  $dN_{ch}/d\eta$ . In this model, the parton-parton interactions produce color strings (particle sources) that can interact, reducing the effective number of strings. This reduction is more important for soft than hard particle production. The model predicts a linear behaviour at low multiplicity and a quadratic one at high multiplicities. The model reproduces the relative  $dN_{J/\psi}/dy$  measured in pp collisions at 7 TeV as we mention in the previous section. The calculations for p-Pb show a stronger rise of the  $J/\psi$  relative  $dN_{J/\psi}/dy$  with the relative  $dN_{ch}/d\eta$  than that observed in pp. However, we measure the opposite effect, since a saturation of the  $dN_{J/\psi}/dy$  is observed at forward rapidity. The predictions for p-Pb collisions of the source interaction framework in [116] are in clear disagreement with the measurements performed in this thesis. Note that these calculations include no cold nuclear matter effects.

We can also compare the behaviour of the relative  $J/\psi$   $\langle p_T \rangle$  as a function of the relative  $dN_{ch}/d\eta$  in pp and p-Pb collisions. This can bring to light possible differences on the particle production mechanism or medium effects. The result is shown in Fig. 9.7. The behaviour of the relative  $J/\psi$   $\langle p_T \rangle$  is similar in pp and p-Pb collisions at low multiplicity. At high multiplicities, the relative  $J/\psi$   $\langle p_T \rangle$  in pp collisions continues to rise though a change of the slope is observed. On the contrary, hints towards saturation are observed in p-Pb collisions at high multiplicities. It is worth noting that the change on the  $\langle p_T \rangle$  slope is produced

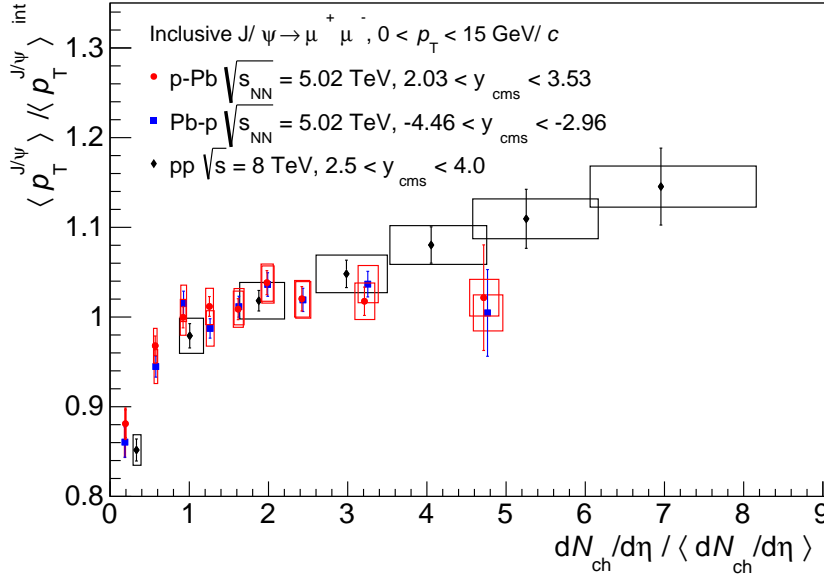


Figure 9.7: Comparison of  $J/\psi$  relative transverse momentum at backward (blue) and forward (red) rapidity as a function of relative charged particle multiplicity measured at mid-rapidity ( $|\eta| < 0.5$ ) in p-Pb collisions at  $\sqrt{s_{NN}} = 5.02$  TeV (ALICE Preliminary) with the result in pp collisions at 8 TeV (black).

at roughly the same relative multiplicity  $\sim 1$ -1.5. However with the present level of the uncertainties in the measurements, we can not conclude that the behaviour of the relative  $J/\psi \langle p_T \rangle$  in p-Pb collisions at high multiplicities is different to that in pp collisions.

Our results can be compared to those obtained for charged particles measured at mid-rapidity ( $|\eta| < 0.3$ ) in pp, p-Pb and Pb-Pb collisions [7] (Fig. 1.32). The evolution of the charged particle  $\langle p_T \rangle$  is interesting since it reveals that mechanisms such as Color Reconnections (CR) or collective hydrodynamic-type effects could be at play in particle production. A similar trend than that of charged particles in pp and p-Pb collisions, is also observed on the  $J/\psi \langle p_T \rangle$  in pp and p-Pb collisions. However, the interpretation in terms of the same hypothesis seems difficult for the  $J/\psi$  production.

#### 9.4 $p_T$ broadening as a function of charged particle multiplicity

In this section we present a preliminary analysis of the second momentum of the  $J/\psi p_T$  distribution,  $\langle p_T^2 \rangle$ . Note that the results presented here are extracted using a single fit combination and no systematic uncertainties are calculated. The transverse momentum broadening, defined as  $\Delta \langle p_T^2 \rangle = \langle p_T^2 \rangle_{pPb} - \langle p_T^2 \rangle_{pp}$ , can be used to quantify the nuclear effects on the  $J/\psi p_T$  spectrum. The results of the  $J/\psi \Delta \langle p_T^2 \rangle$  in p-Pb collisions are discussed in the following. The  $\langle p_T^2 \rangle$  values in pp collisions are  $\langle p_T^2 \rangle_{pp} (-4.46 < y_{cms} < -2.96) = 8.18 \pm 0.30$  and

$\langle p_T^2 \rangle_{pp}$  ( $2.03 < y_{cms} < 3.53$ ) =  $9.28 \pm 0.40$ , which are obtained from [5].

The  $\Delta\langle p_T^2 \rangle$  measurements at backward and forward rapidities are show in Fig. 9.8. We can see that at low multiplicity  $\Delta\langle p_T^2 \rangle$  increases with increasing multiplicity. This effect could be explained by multiple parton scattering in the nuclear medium [188, 189] or coherent parton energy loss effects [170]. Note that the  $\langle p_T^2 \rangle$  in the first bin at backward rapidity is lower than the pp value. This could be due to a different production mechanism or some effect present in p-Pb collisions<sup>4</sup>. At high multiplicities ( $dN_{ch}/d\eta > 28$ ), a very different behaviour is observed. The dependence with multiplicity of the  $\Delta\langle p_T^2 \rangle$  seems to disappear for multiplicities beyond 20-30 charged particles.

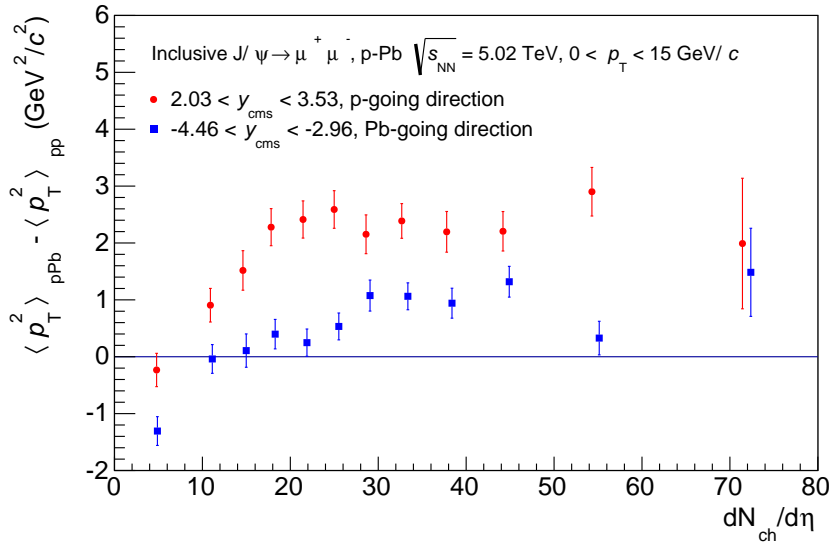


Figure 9.8:  $J/\psi$  transverse momentum broadening as a function of charged particle multiplicity ( $|\eta| < 1$ ) at forward and backward rapidity in p-Pb collisions at  $\sqrt{s_{NN}} = 5.02$  TeV.

## 9.5 $R_{FB}$ as a function of charged particle multiplicity

The nuclear modification factor, defined in Eq. 1.7, can be used to quantify nuclear effects on particle production. However, the number of binary nucleon-nucleon collisions,  $\langle N_{coll} \rangle$ , is needed for its calculation. The  $\langle N_{coll} \rangle$  can be computed assuming that the charged particle multiplicity varies monotonically with the number of participant nucleons in the collision, when events are selected according to an observable well correlated to the event geometry (see App. A). It is known that the relationship between geometry related quantities with measurable observables in p-Pb collisions introduces a certain bias on the calculations, specially when classifying events using charged particle multiplicity [55]. We can get rid of the  $\langle N_{coll} \rangle$  dependence and its uncertainty by computing the ratio of the forward and

<sup>4</sup>This effect on the first bin was also observed in [261]

backward nuclear modification factors ( $R_{\text{FB}}$ ) as a function of charged particle multiplicity. The  $R_{\text{FB}}$  is computed in this case as:

$$\begin{aligned}
 (9.1) \quad R_{\text{FB}} &= \frac{R_{pPb}(2.03 < y_{\text{cms}} < 3.53)}{R_{pPb}(-4.46 < y_{\text{cms}} < -2.96)} \\
 &= \frac{Y_{J/\psi}^{p-Pb}(2.03 < y_{\text{cms}} < 3.53)}{Y_{J/\psi}^{p-Pb}(-4.46 < y_{\text{cms}} < -2.96)} \times \frac{d\sigma_{J/\psi}^{pp}/dy(-4.46 < y_{\text{cms}} < -2.96)}{d\sigma_{J/\psi}^{pp}/dy(2.03 < y_{\text{cms}} < 3.53)}
 \end{aligned}$$

since the rapidity coverage of each measurement is of 1.5 pseudorapidity units. There are no pp measurements at 5 TeV, so the values of the pp  $J/\psi$  cross section were obtained by means of an interpolation procedure [269]. This interpolation introduces a considerable global uncertainty on the  $R_{\text{FB}}$  measurement (7.8%). Note that, to compute the dependence with multiplicity we have performed this ratio bin by bin, since the average multiplicities in each bin in the p-Pb and Pb-p measurements are compatible within uncertainties. The values of the pp cross sections are  $d\sigma_{J/\psi}^{pp}/dy(-4.46 < y_{\text{cms}} < -2.96) = 2.86 \mu\text{b} \pm 5.3\% \pm 5.5\%$  and  $d\sigma_{J/\psi}^{pp}/dy(2.03 < y_{\text{cms}} < 3.53) = 4.12 \mu\text{b} \pm 5.7\% \pm 5.5\%$ . The first uncertainty is correlated over multiplicity and the second is also correlated between rapidity intervals.

The systematic uncertainties of the absolute yields in p-Pb (Tab. 6.10), are considered as uncorrelated between forward and backward rapidity, and therefore added in quadrature (except the branching ratio, which vanishes on the ratio). The pp cross section uncertainties which are correlated between rapidity intervals vanish on the ratio. The other pp cross section uncertainties are uncorrelated over rapidity and therefore added in quadrature. Since they are correlated in multiplicity bins, the resulting uncertainty is global (shown as a red box around the unity in Fig. 9.9).

The  $R_{\text{FB}}$  as a function of charged particle multiplicity result is shown in Fig. 9.9. As already measured in [3, 261] for inclusive  $J/\psi$  production, the  $R_{\text{FB}}$  is smaller than unity. This shows that the  $J/\psi$  production is more suppressed at forward than at backward rapidity with respect to the pp expectations. The ALICE inclusive result [3] is  $R_{\text{FB}} = 0.6 \pm 0.01(\text{stat.}) \pm 0.06(\text{syst.})$ . It was computed in the forward-backward common rapidity range  $2.96 < |y_{\text{cms}}| < 3.53$ , and therefore the pp interpolation cross section and its uncertainty vanish on the ratio. Our measurement of the  $R_{\text{FB}}$  is compatible with the unity within uncertainties in the first multiplicity bin ( $dN_{ch}/d\eta \sim 4.7$ ), and decreases for increasing multiplicity reaching values down to  $0.35 \pm 0.06(\text{stat.}) \pm 0.05(\text{uc. syst.})$ .

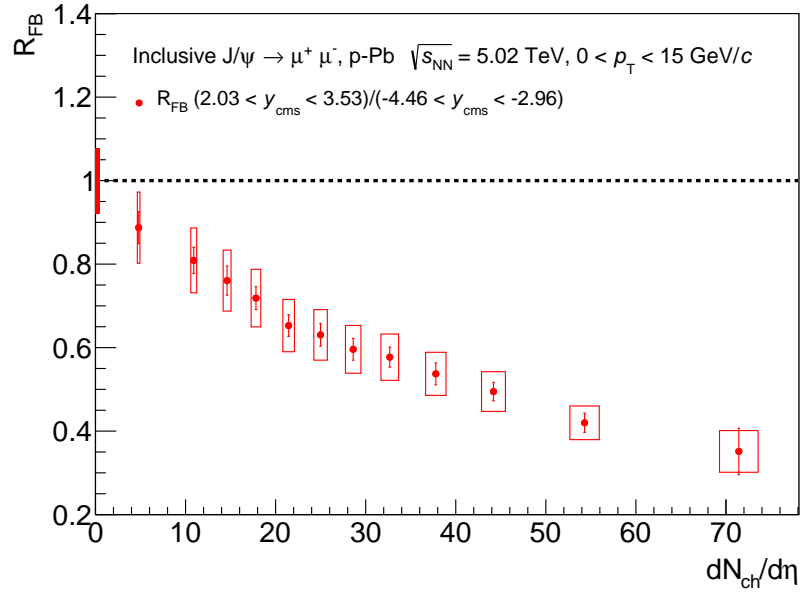


Figure 9.9:  $R_{\text{FB}}$  in p-Pb collisions at  $\sqrt{s_{\text{NN}}} = 5.02$  TeV as a function of absolute charged particle multiplicity ( $|\eta| < 1$ ). The red box around unity represents the global uncertainty.

## 9.6 Nuclear modification factor as a function of $\tilde{N}_{\text{coll}}^{\text{mult}}$

In this section we have computed the nuclear modification factor using our charged particle multiplicity event selection. In Fig. 1.27 we have shown the comparison with theoretical predictions of the  $Q_{pPb}$ <sup>5</sup>, measured as a function of  $\langle N_{\text{coll}}^{\text{mult}} \rangle$  [5, 261]. This analysis was made by selecting the events using the energy deposited in the ZN calorimeters. In each ZN event class,  $\langle N_{\text{coll}}^{\text{mult}} \rangle$  was computed using the corresponding  $\langle dN_{\text{ch}}/d\eta \rangle$  (see App. A). Therefore, regarding the comparison in App. C of the  $dN_{J/\psi}/dy$  results using the multiplicity and ZN selections, we realise that the measurement of the nuclear modification factor with the  $dN_{\text{ch}}/d\eta$  selection could help to discern among the different theoretical calculations, thanks to the extended range at high event multiplicity. However, we need to be extremely careful on the interpretation of these results.

We compute the nuclear modification factor as:

$$(9.2) \quad \tilde{Q}_{pPb}^{\text{mult}} = \frac{dN_{J/\psi}^{pPb}/dy}{\langle \tilde{T}_{pPb}^{\text{mult}} \rangle d\sigma_{J/\psi}^{pp}/dy}$$

where  $\langle \tilde{T}_{pPb}^{\text{mult}} \rangle$  is the nuclear overlap in each multiplicity event class, computed as  $\langle \tilde{T}_{pPb}^{\text{mult}} \rangle = \langle \tilde{N}_{\text{coll}}^{\text{mult}} \rangle / \sigma_{\text{NN}}^{\text{inel}}$ . The inelastic nucleon-nucleon cross section at  $\sqrt{s_{\text{NN}}} = 5.02$  TeV is  $\sigma_{\text{NN}}^{\text{inel}} = 70$  mb. Note that our variables have a *tilde* to denote that the event selection is performed

<sup>5</sup>The nuclear modification factor is denoted as  $Q_{pPb}$  to denote the presence of possible biases on the measurement, as explained in App. A

using the  $dN_{ch}/d\eta$  measured in  $|\eta| < 1$ , and their interpretation could differ from the measurements with a centrality selection. The  $\langle \tilde{N}_{coll}^{mult} \rangle$  in each multiplicity bin  $i$  is given by<sup>6</sup>:

$$(9.3) \quad \langle \tilde{N}_{coll}^{mult} \rangle_i = \langle N_{part} \rangle_{MB} \times \left( \frac{\langle dN_{ch}/d\eta \rangle_i}{\langle dN_{ch}/d\eta \rangle_{|\eta|<1}} \right) - 1$$

The MB average number of participant nucleons is  $\langle N_{part} \rangle_{MB} = 7.9 \pm 0.6$ , which implies an uncertainty of 3.4% on the  $\langle \tilde{T}_{pPb}^{mult} \rangle$ , correlated over uncertainty. The uncorrelated part of the  $\langle \tilde{T}_{pPb}^{mult} \rangle$  uncertainty is taken here as the uncertainty on the relative multiplicity in each multiplicity event class.

The results obtained in this thesis for the  $\tilde{Q}_{pPb}^{mult}$  measurement as a function of  $\langle \tilde{N}_{coll}^{mult} \rangle$  at backward and forward rapidities are shown in Fig. 9.10. The uncertainties in  $\tilde{Q}_{pPb}^{mult}$ , which are correlated over centrality (trigger, tracking and matching efficiency, branching ratio,  $\sigma_{pp}$  and the correlated part of  $\langle \tilde{T}_{pPb}^{mult} \rangle$ ), are added in quadrature into a global uncertainty (represented as a box around the unity). Our  $\tilde{Q}_{pPb}$  measurement is compared to that of [5, 261], obtained using the ALICE centrality selection in p-Pb collisions (denoted by  $Q_{pPb}$  and  $\langle N_{coll}^{mult} \rangle$ ). There is a good agreement between the measurements point by point within the uncertainties. This can be attributed to the fact that, as can be seen in Fig. A.3 in the range  $10 < N_{ch} < 30$ , the multiplicity per participant is roughly the same with the ZNA and multiplicity based event selections, so Eq. 9.3 holds for both selections in this range. The shadowing and coherent parton energy loss models [170, 186] are in fair agreement with the  $Q_{pPb}^{mult}$  results in [5]. According to our measurement, the  $\tilde{Q}_{pPb}^{mult}$  at backward rapidity is compatible with the unity, and no dependence with  $\tilde{N}_{coll}^{mult}$  is observed. The  $\tilde{Q}_{pPb}^{mult}$  trend with  $\tilde{N}_{coll}^{mult}$  differs from that observed for  $Q_{pPb}^{mult}$  with  $\langle N_{coll}^{mult} \rangle$ . At forward rapidity, the result indicates a suppression of the  $J/\psi$  production that increases with increasing  $\tilde{N}_{coll}^{mult}$ .

However, the interpretation of these results at low  $\tilde{N}_{coll}^{mult}$  is not that simple. At  $\tilde{N}_{coll}^{mult} \sim 1$  our result is 50% (35%) bigger than unity at backward (forward) rapidity. This can be explained by the drop on the multiplicity per participant that we observe in Fig. A.3, for multiplicity based event selections at very low multiplicity. Due to this effect, Eq. 9.3 is not valid for very low multiplicities.

Our measurement at high  $\tilde{N}_{coll}^{mult}$  (high multiplicity) correspond to events with big fluctuations on the number of binary nucleon-nucleon collisions and/or the number of parton-parton interactions per binary collision. Therefore, the association of multiplicity event classes with the number of binary nucleon-nucleon collisions is not straightforward. The result that we have obtained at backward rapidity can help on the interpretation of  $\tilde{N}_{coll}^{mult}$ . If we assume that the  $J/\psi$  production is proportional to the number of hard parton-parton interactions in an event, the growth of the relative  $dN_{J/\psi}/dy$  observed in Fig. 9.1 would be due to the increasing number of hard MPI. In Fig. 9.10 (top), we observe that the  $dN_{J/\psi}/dy$  at backward

<sup>6</sup> $N_{coll} = N_{part} - 1$  in pA collisions.



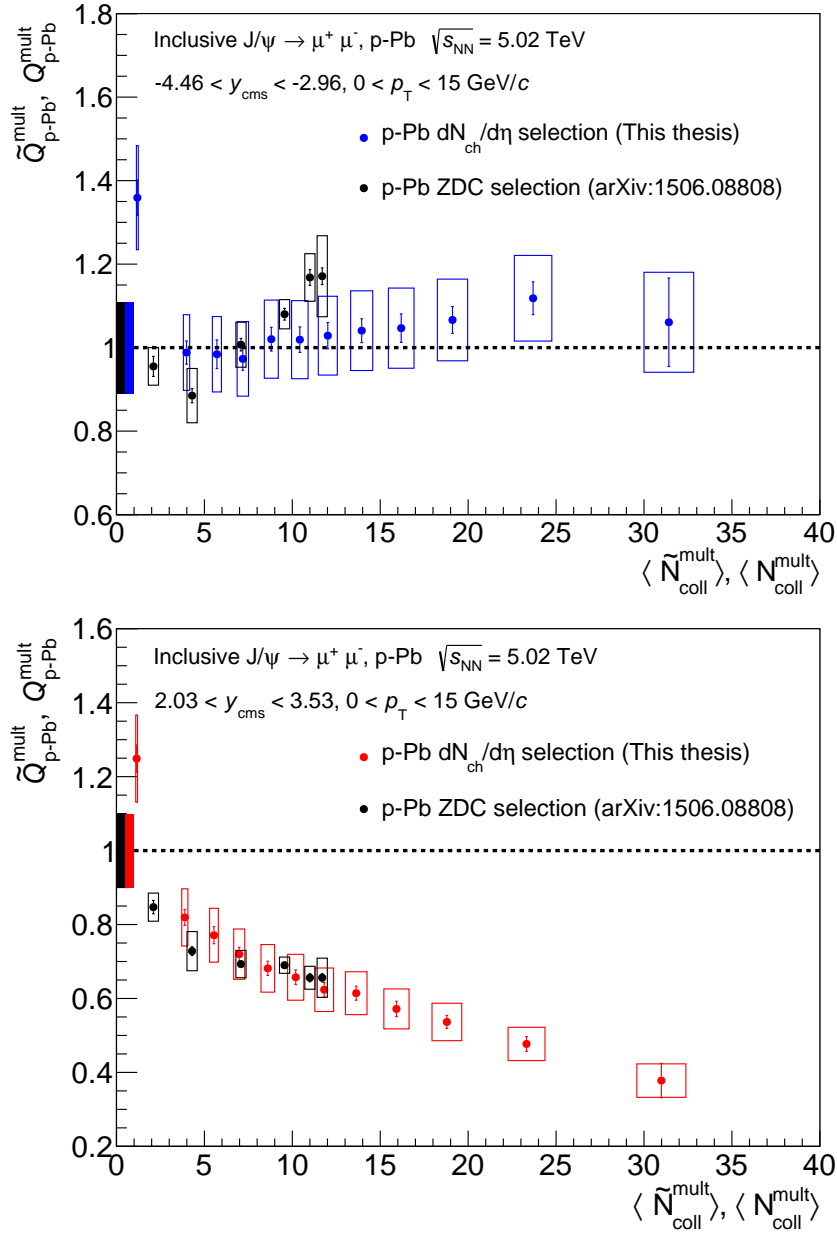


Figure 9.10:  $\tilde{Q}_{pPb}^{\text{mult}}$  as a function of  $\tilde{N}_{\text{coll}}^{\text{mult}}$  at backward (top) and forward (bottom) rapidities in p-Pb collisions at  $\sqrt{s_{\text{NN}}} = 5.02$  TeV. The results are compared to  $Q_{pPb}^{\text{mult}}$  as a function of  $N_{\text{coll}}^{\text{mult}}$  obtained using the ALICE centrality selection in p-Pb collisions [5, 261].

rapidity scales as  $\tilde{N}_{\text{coll}}^{\text{mult}}/\sigma_{\text{NN}}^{\text{inel}}$  times the pp cross section. In addition, the inclusive measurements at backward rapidity ([3, 4]) are compatible with no nuclear effects in this rapidity region. Therefore, this suggests that  $\tilde{N}_{\text{coll}}^{\text{mult}}$  is proportional the number of hard interactions. On the other hand, this implies that the charged particle multiplicity is also proportional to the number of hard interactions (or that the number of soft and hard interactions are proportional). In any case, the observed  $\tilde{Q}_{pPb}^{\text{mult}}$  scaling with  $\tilde{N}_{\text{coll}}^{\text{mult}}$  at backward rapidity, and

the fact that no nuclear effects have been observed in previous measurements in this rapidity region, suggest that  $\tilde{N}_{\text{coll}}^{\text{mult}}$  is the correct variable to scale the pp cross section when selecting events based on charged particle multiplicity. Therefore we can be confident on the results obtained at forward rapidity. The smooth increase of suppression at forward rapidity with  $\tilde{N}_{\text{coll}}^{\text{mult}}$ , suggests that the effect may be caused by a raise of the coherent parton energy loss for increasing  $\tilde{N}_{\text{coll}}^{\text{mult}}$ . This effect seems not to be expected from a shadowing point of view, since the effect due to the shadowing of the initial parton distributions due to the nuclear environment should saturate for impact parameter  $b \rightarrow 0$ .

The results presented in this section extend the present ALICE measurements in [5] and should allow to better constrain the available theoretical models.

## 9.7 $p_T$ broadening as a function of $\tilde{N}_{\text{coll}}^{\text{mult}}$

In this section, in order to compare our results of the transverse momentum broadening with those in [5, 261], we compute the  $\Delta\langle p_T^2 \rangle$  dependence with  $\tilde{N}_{\text{coll}}^{\text{mult}}$ . The results of the  $\Delta\langle p_T^2 \rangle$  as a function of  $\tilde{N}_{\text{coll}}^{\text{mult}}$  obtained with the multiplicity event selection of this thesis are shown in Fig. 9.11, together with the results in [5, 261] obtained using the ALICE centrality selection. We observe a good agreement within the uncertainties between the two measurements. Note again that our  $\tilde{N}_{\text{coll}}^{\text{mult}}$  estimation in the first multiplicity bin is not reliable. Our value of the  $\langle p_T^2 \rangle$  for  $\tilde{N}_{\text{coll}}^{\text{mult}} \sim 1$  at forward rapidity is compatible with the pp multiplicity integrated value. At backward rapidity we obtain a smaller value than in pp. The  $\Delta\langle p_T^2 \rangle$  increases with  $\tilde{N}_{\text{coll}}^{\text{mult}}$  (up to  $\tilde{N}_{\text{coll}}^{\text{mult}} \sim 12$ ) both at forward and backward rapidities. The calculations from multiple scattering [188, 189] and coherent parton energy loss [170] are in rather good agreement with the  $\Delta\langle p_T^2 \rangle$  in [5]. At forward rapidity our result of the  $\Delta\langle p_T^2 \rangle$  seems to be independent of  $\tilde{N}_{\text{coll}}^{\text{mult}}$ , for  $\tilde{N}_{\text{coll}}^{\text{mult}} > 10$ . This seems to not be the trend predicted by multiple scattering and coherent energy loss models. In the coherent energy loss framework an increase of the  $p_T$  broadening is necessary for an increase of the energy loss effect. Therefore, the interpretation of the suppression of  $\tilde{Q}_{pPb}^{\text{mult}}$  with  $\tilde{N}_{\text{coll}}^{\text{mult}}$  at forward rapidity as a coherent parton energy loss effect, would not hold at high  $\tilde{N}_{\text{coll}}^{\text{mult}}$  values. In that case another mechanism would be needed to explain the observed increasing suppression. In order to extract conclusions, the systematic uncertainties on the  $p_T$  broadening measurement and the model calculations at high  $\tilde{N}_{\text{coll}}^{\text{mult}}$  are needed. The extended  $\tilde{N}_{\text{coll}}^{\text{mult}}$  range of our measurement with respect to the present ALICE results, help to further constrain theoretical models.

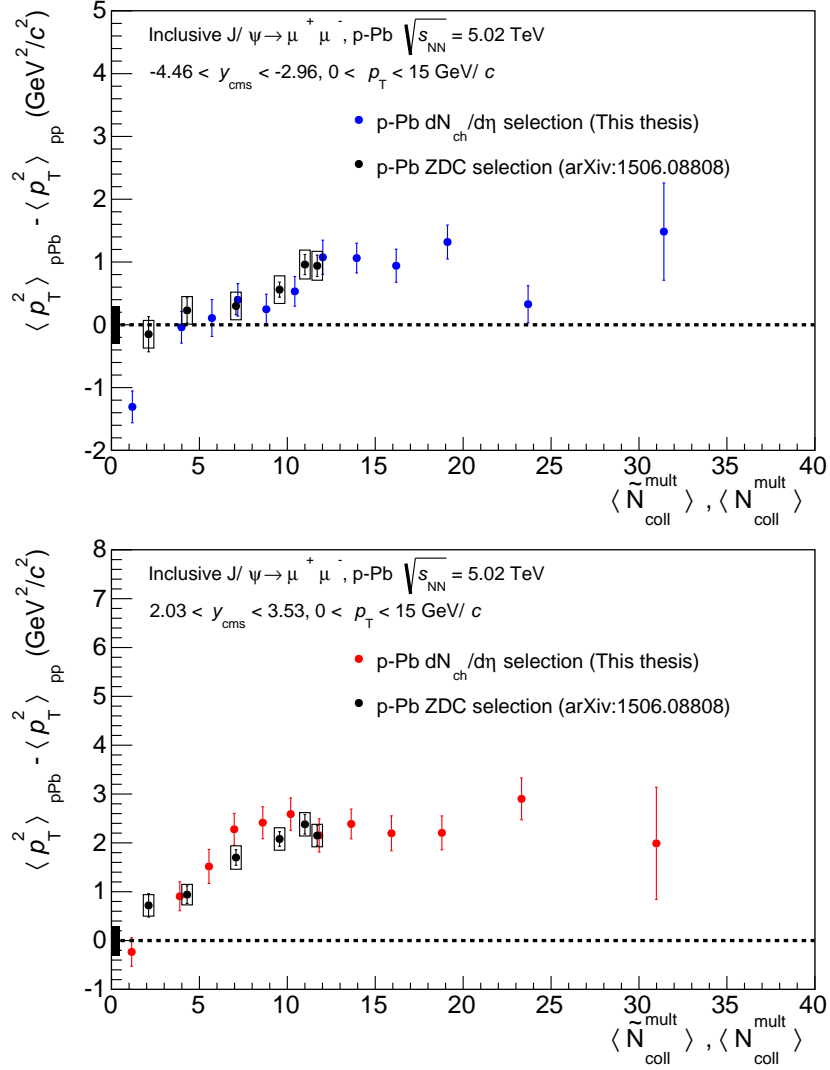


Figure 9.11:  $J/\psi$  transverse momentum broadening as a function of  $\tilde{N}_{coll}^{mult}$  at backward (top) and forward (bottom) rapidity in p-Pb collisions at  $\sqrt{s_{NN}} = 5.02$  TeV. The results are compared to those obtained as a function of  $N_{coll}^{mult}$  using the ALICE centrality selection in p-Pb collisions[5, 261].



## CONCLUSIONS AND OUTLOOK

In this thesis we have studied the evolution of the  $J/\psi$  production in pp collisions at  $\sqrt{s} = 8$  TeV and p-Pb collisions at  $\sqrt{s_{\text{NN}}} = 5.02$  TeV with the charged particle multiplicity. We have used the ALICE Muon Spectrometer for the  $J/\psi$  measurements in the di-muon decay channel, and the Silicon Pixel Detector for the event multiplicity estimation. Specific methods for the  $J/\psi$  yield,  $\langle p_T \rangle$  (and  $\langle p_T^2 \rangle$ ) and multiplicity measurements have been developed during this work. These methods improve the quality of the measurements and reduce some of the systematic uncertainties with respect to other techniques. The use of these new techniques was motivated by the study of the  $J/\psi$  production at high multiplicities. An analysis framework specific for these quarkonium analyses as a function of charged particle multiplicity has been developed during this thesis.

The studies performed on the muon tracking efficiency during the 2013 p-Pb data taking, have allowed to improve the detector description in the simulations used to correct the data taken by the spectrometer. By mean of the detailed comparison of the efficiency results in data and simulation, we have spotted the regions of the detector which were not well reproduced. These regions have been included in a reject list and new simulations have been performed using this information. This turns into a more precise correction and a reduction of the associated systematic uncertainty. These studies are an important part of all the quarkonium analyses in p-Pb collisions performed with the ALICE Muon Spectrometer.

Some of the p-Pb results presented in this thesis were approved as ALICE Preliminary results in 2014 and presented at the Quark Matter conference [271, 272]. The updated results are not yet approved by the ALICE Collaboration. They will be part of an ALICE publication which is being prepared. An ALICE internal analysis note is available.

The  $J/\psi$  pp results at 8 TeV, extend the multiplicity range studied in the previous 7 TeV analysis [8]. The measurement of the relative  $dN_{J/\psi}/dy$  in 8 TeV collisions does not show a different behaviour from that observed at 7 TeV. The  $J/\psi$   $\langle p_T \rangle$  evolution with the charged particle multiplicity in pp collisions is reported for the first time in this thesis. These results serve to set further constraints to the available theoretical models.

The p-Pb studies presented here are complementary to those performed as a function of the collision centrality in [5]. The charged particle multiplicity event selection used in this thesis has allowed to study  $J/\psi$  production in rare events at multiplicities up to four times the MB one in p-Pb collisions. A saturation effect on the  $dN_{J/\psi}/dy$  at forward rapidity, not seen in the centrality analysis, has been found in this thesis. The first measurement of

the  $J/\psi$   $\langle p_T \rangle$  evolution with the charged particle multiplicity in p-Pb collisions is presented at forward and backward rapidities. The results show a trend towards saturation at high multiplicity in both rapidity ranges. In addition, the forward to backward ratio of the nuclear modification factor has been computed. It shows a stronger suppression of the  $J/\psi$  production with respect to the pp expectations at forward than at backward rapidity. The measured suppression increases with the charged particle multiplicity. These observations can help to improve our understanding of the role of cold nuclear matter effects in p-Pb collisions. To draw conclusions on this point, the comparison of the experimental results with theoretical models is needed.

The comparison of the p-Pb and pp  $dN_{J/\psi}/dy$  results show that the  $dN_{ch}/d\eta$  dependence in p-Pb collisions at backward rapidity is similar to the one in pp collisions, while a deviation is observed at forward rapidity. This points to the presence of an effect in forward rapidity p-Pb collisions not happening in pp collisions. This effect is likely related to cold nuclear matter, since otherwise it should be also observed at backward rapidity. The  $J/\psi$   $\langle p_T \rangle$  behaviour in pp and p-Pb collisions exhibits a similar trend to that observed for charged particles in the same collision systems. The interpretation of this observation in terms of the same mechanisms for the soft and hard particle production is not evident.

To further test the presence of nuclear effects in p-Pb collisions we have presented a preliminary analysis of the  $\Delta\langle p_T^2 \rangle$  evolution with charged particle multiplicity. The results show an increase of the  $\Delta\langle p_T^2 \rangle$  with multiplicity, possibly as a consequence of multiple parton scattering in the nuclear medium or coherent energy loss effects. At high multiplicities the  $\Delta\langle p_T^2 \rangle$  seems to be independent of multiplicity.

Finally we present results as a function of  $\tilde{N}_{coll}^{mult}$ . These results extend the range studied in the ALICE centrality analysis, and are found to be in agreement with the measurements in [5, 261]. The  $Q_{pPb}^{mult}$  results presented in [5, 261] are in fair agreement with shadowing and coherent parton energy loss expectations. Our measurement of the  $\tilde{Q}_{pPb}^{mult}$  at backward rapidity shows a scaling with  $\tilde{N}_{coll}^{mult}$ . At forward rapidity the  $\tilde{Q}_{pPb}^{mult}$  shows a suppression increasing with  $\tilde{N}_{coll}^{mult}$ . The observed suppression pattern could be, in principle, understood as an increase of the coherent parton energy loss with  $\tilde{N}_{coll}^{mult}$ . Our measurements of the  $\Delta\langle p_T^2 \rangle$  evolution with  $\tilde{N}_{coll}^{mult}$  are in agreement with those in [5, 261]. We observe a trend towards saturation at high  $\tilde{N}_{coll}^{mult}$  values, not observed in the centrality analyses. This seems not to be the trend predicted by the models in [5]. This observation indicates that the interpretation of the observed suppression of the  $\tilde{Q}_{pPb}^{mult}$  at forward rapidity, as an energy loss effect, would not hold at high  $\tilde{N}_{coll}^{mult}$  values. This means that another mechanism would be needed to explain the observed suppression. A comparison with theoretical calculations at high  $\tilde{N}_{coll}^{mult}$  is needed to conclude. The extended  $\tilde{N}_{coll}^{mult}$  of this analysis may help to improve our understanding on the cold nuclear matter effects and discern among the available models.

In order to improve the results presented here, the  $J/\psi$  cross section needs to be measured in pp collisions at 5.02 TeV in order to reduce the systematic uncertainties. An interesting

measurement which can help to better understand the role of initial and final state effects in p-Pb collisions is the study of the  $\psi(2S)$  production as a function of charged particle multiplicity. The contribution to our measurement of  $J/\psi$  from B-hadron decays as a function of multiplicity is unknown. The separation of the prompt and non-prompt  $J/\psi$  production will be possible with the ALICE Muon Forward Tracker [276] which will be installed in 2018.







## CENTRALITY DETERMINATION IN ALICE

The concept of centrality in heavy-ion collisions is directly related with the impact parameter of the collisions, and is inferred by comparing the data with simulations of the collisions. In order to measure an observable as a function of collision centrality, the data sample has to be sliced using a collision geometry dependent variable. The centrality is expressed as a percentage of the total nuclear interaction cross section  $\sigma$ . The centrality percentile  $c$  of an A-A collision with an impact parameter  $b$  is defined as:

$$(A.1) \quad c = \frac{1}{\sigma_{AA}} \int_0^b \frac{d\sigma}{db'} db'$$

In the geometrical Glauber model [277], the impact parameter is directly related with other collision geometry related quantities: the number of participant nucleons  $N_{\text{part}}$  (a nucleon that undergoes one or more binary collisions), the number of spectator nucleons  $N_{\text{spec}} = 2A - N_{\text{part}}$ , where  $A$  is the number of nucleons in the nucleus, and the number of binary collisions  $N_{\text{coll}}$ .

However neither the impact parameter nor the other geometrical quantities are directly measurable. In order to estimate the collision centrality, an observable that varies monotonically with the impact parameter is needed. In Pb-Pb collisions, the charged particle multiplicity and the energy carried by particles close to the beam direction (measured as deposited energy in the ZDC calorimeters) are used as centrality estimators. The  $N_{ch}$  decreases monotonically with increasing impact parameter. However, the energy in the ZDC, which is related to the number of spectator nucleons, saturates for decreasing impact parameter<sup>1</sup>. Therefore, when using the ZDC to slice the data sample, another observable monotonically correlated with  $b$  is needed.

---

<sup>1</sup>The nuclear fragments can bound together and remain in the beam pipe. This is more likely to happen for peripheral collisions.

In Fig. A.1, the event distribution as a function of the sum of the amplitudes in the VZERO detectors in Pb-Pb collisions is shown. The Glauber Monte Carlo is used to generate events and a negative binomial distribution (NBD) is used to generate the number of particles produced per interaction [54]. The NBD-Glauber fit is shown as the red line in Fig. A.1.

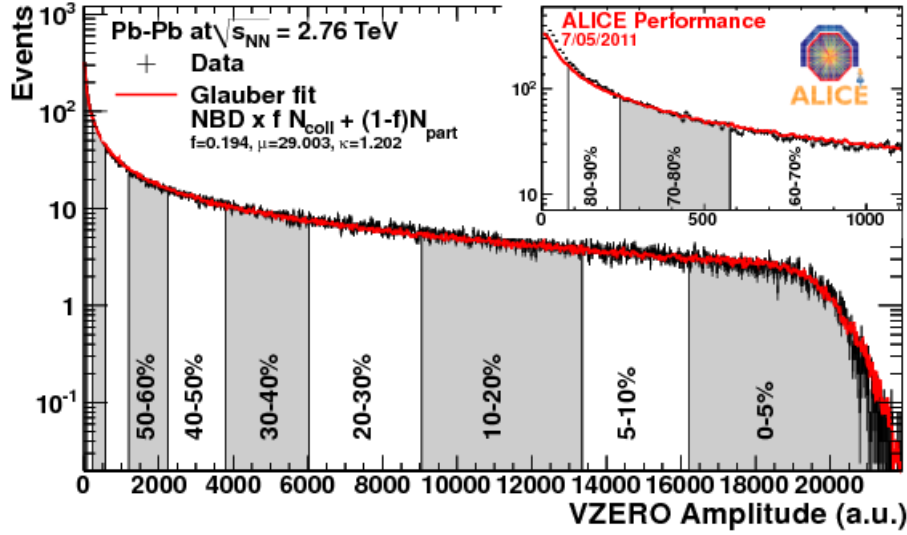


Figure A.1: Event distribution of the sum of the amplitudes of the VZERO detectors in Pb-Pb collisions. The centrality classes are shown as percentages. The red line is the fit with the NBD-Glauber fit. Figure taken from [54].

The correlation between  $N_{ch}$  (or ZDC energy) and impact parameter is good in Pb-Pb collisions (Fig. A.2 right), so it is therefore used to estimate collisions centrality in ALICE by means of the Glauber model [54]. However as discussed in [55], Glauber calculations show that in p-Pb collisions the correlation between geometrical quantities and charged particle multiplicity is bad (Fig. A.2 left). This happens due to statistical fluctuations in the particle multiplicity per nucleon-nucleon collision. Therefore when slicing the data sample using multiplicity, the sample will be biased compared to a sample defined by cuts on the impact parameter.

In order to circumvent this issue, the so called hybrid method has been developed in [55] to estimate centrality in p-Pb collisions. It consists of combining the information of the deposited energy in the ZDC neutron calorimeter (ZN energy) and charged particle multiplicity. When using the ZN energy to select events, the remnants of the collision are used, and not the products of the collision itself. Consequently this selection is not sensitive to the statistical fluctuations of the number of produced particles, so it is expected to be free of biases. Then, in order to establish a relationship between the ZN centrality event classes selected using ZN energy and the collision geometry, the correlation of the charged particle multiplicity in the ZN class with geometrical quantities is used. One of the assumptions made in [55] is that, in ZN centrality classes, the charged particle multiplicity at mid rapidity is proportional to the number of participants. The average number of binary collisions in

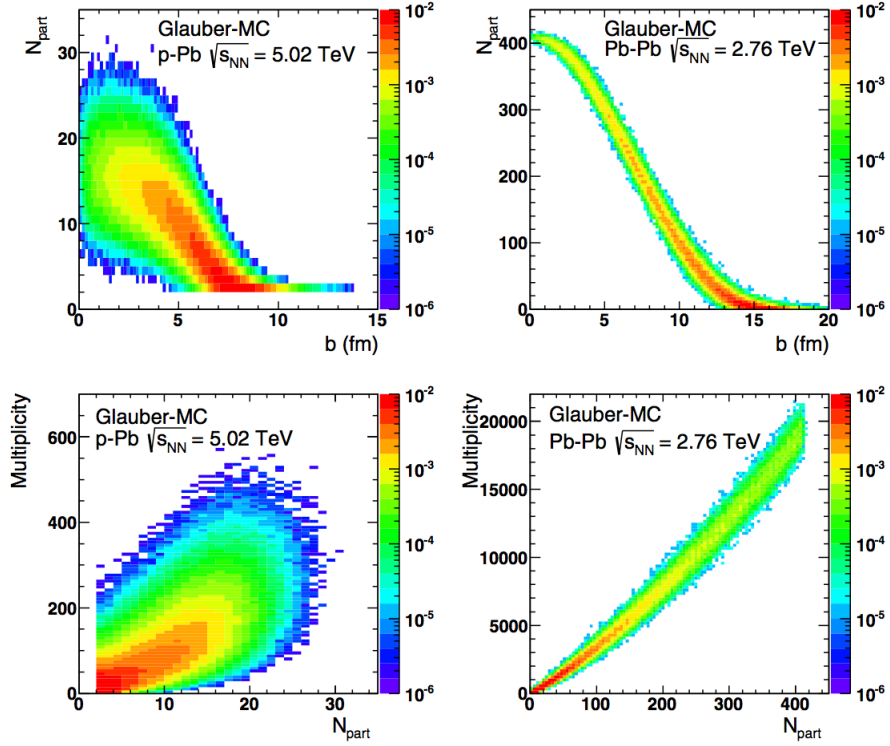


Figure A.2: Top: Scatter plot of the number of participating nucleons as a function of impact parameter in p-Pb (left) and Pb-Pb (right) collisions. Bottom: Scatter plot of the multiplicity as a function of the number of participating nucleons in p-Pb (left) and Pb-Pb (right) collisions. Figure taken from [54].

each centrality interval can be approximatively computed by scaling the minimum bias value ( $\langle N_{\text{part}} \rangle_{MB} = 7.9$ ) with the relative charged particle multiplicity at mid rapidity:

$$(A.2) \quad \langle N_{\text{part}}^{mult} \rangle_i = \langle N_{\text{part}} \rangle_{MB} \left( \frac{\langle dN_{ch}/d\eta \rangle_i}{\langle dN_{ch}/d\eta \rangle_{MB}} \right)_{-1 < \eta < 0}$$

where the index "mult" denotes the assumption made on the correlation of the multiplicity with the number of participants. Then, the number of binary nucleon-nucleon collisions can be estimated in p-Pb collisions as  $\langle N_{\text{coll}}^{mult} \rangle_i = \langle N_{\text{part}}^{mult} \rangle_i - 1$ .

In order to estimate the bias on the centrality measurement with different estimators, the ratio between the charged particle multiplicity and number of participants can be computed, by means of the Glauber model, for several event selections. The result is shown in Fig. A.3 as a function of  $N_{ch}$ . As we can observe, when using the ZNA energy selection and multiplicity on the Pb-side (open diamonds), the ratio is roughly constant with  $N_{ch}$ . However, when using selections based on particle multiplicity (multiplicity on the V0 detectors (V0A and V0M) or clusters in the first layer of the SPD (CL1)) the variation is bigger, specially at low and high multiplicity. Even when using the hybrid method to compute the nuclear

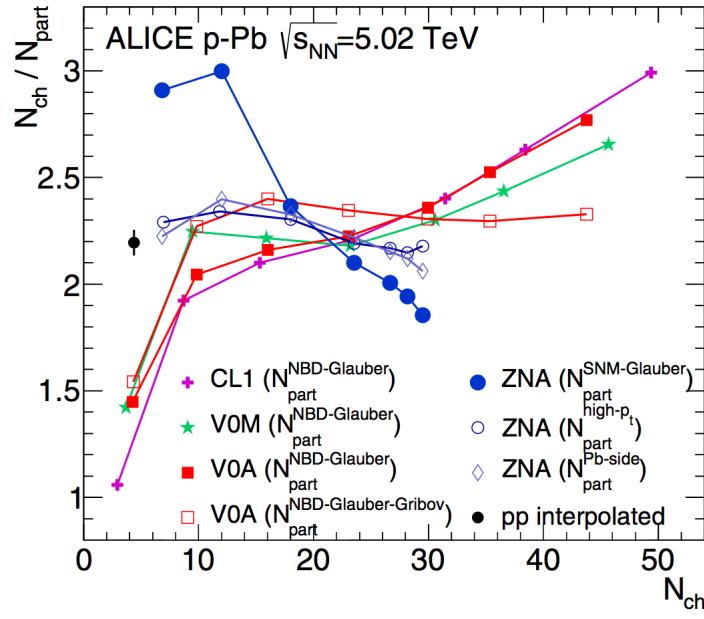


Figure A.3: Pseudorapidity density of charged particles at mid rapidity (integrated in  $-1 < \eta < 0$ ),  $N_{ch}$ , per participant nucleon as a function of  $N_{ch}$  for different centrality estimators. Figure taken from [54].

modification factor in p-Pb collisions, it will be denoted by  $Q_{pPb}$  (instead of  $R_{pPb}$ ) in order to make explicit the possible biases remaining in the measurement.

## SUMMARY OF UNCERTAINTIES FORMULAE

In this appendix we summarise the formulae used to compute the statistical and systematic uncertainties of the combination of different tests used for the extraction of various quantities in this thesis.

The average value obtained from a set of  $n_{tests}$  tests of the extraction of a quantity  $X$  is:

$$(B.1) \quad \langle X \rangle = \frac{1}{n_{tests}} \times \sum_{i=1}^{n_{tests}} X_i$$

where  $X_i$  is the value extracted from the  $i$ -th test. The statistical error of  $\langle X \rangle$  is taken as the error on the average times  $\sqrt{n_{tests}}$ <sup>1</sup>:

$$(B.2) \quad \sigma_{\langle X \rangle}^{stat} = \frac{1}{n_{tests}} \times \sqrt{n_{tests} \times \sum_{i=1}^{n_{tests}} \sigma_{X_i}^2}$$

where  $\sigma_{X_i}$  is the statistical error of the  $i$ -th test. During this thesis, the quantity  $X$  is sometimes a ratio (relative quantity) of two quantities,  $Y$  and  $Z$  ( $X = Y/Z$ ). In that case, we consider that the measurements of the two quantities in the  $i$ -th test are uncorrelated<sup>2</sup>. Consequently,  $\sigma_{X_i}$  can be written as:

$$(B.3) \quad \sigma_{X_i} = X_i \times \sqrt{\left(\frac{\sigma_{Y_i}}{Y_i}\right)^2 + \left(\frac{\sigma_{Z_i}}{Z_i}\right)^2}$$

where  $\sigma_{Y_i}$  and  $\sigma_{Z_i}$  are the errors of the measurement of  $Y$  and  $Z$  in the  $i$ -th test.

<sup>1</sup>This factor is introduced in order to avoid a dependence of the error with the number of tests

<sup>2</sup>Note that we perform the tests on relative quantities to take into account the correlation of the quantities  $Y$  and  $Z$  within a given test  $i$ . However for the computation of the ratio error we consider the two quantities as uncorrelated

The systematic uncertainty of the measurement of  $\langle X \rangle$  due to the variations among tests, is taken as the unbiased estimator of the variance:

$$(B.4) \quad \sigma_{\langle X \rangle}^{syst} = \sqrt{\frac{\sum_{i=1}^{n_{tests}} (X_i - \langle X \rangle)^2}{n_{tests} - 1}}$$

Note that no weights<sup>3</sup> (each test counts the same) are used in the computations of the mean (Eq.B.1), error on the mean (Eq.B.2), or variance values (Eq.B.4). We proceed like this since there are no arguments to support the idea that some tests are better than others, even if the yielded statistical errors are different. As an instance, in the case of the  $J/\psi$  signal extraction, we have not enough knowledge to discriminate if the number of  $J/\psi$  extracted with CB2 signal shape is closer to the actual value than the that given by the NA60 shape, no matter the size of the errors given by each parametrisation on the number of extracted  $J/\psi$ .

---

<sup>3</sup>Usually the statistical error of each measurement is used as a weight in the computation of the average



## COMPARISON OF $J/\psi$ YIELD AND $\langle p_T \rangle$ WITH OTHER ANALYSES

A verification of this analysis has been done through the comparison of the integrated cross sections with the ALICE results in [3]. These results use the standard techniques for  $J/\psi$  yield extraction. The integrated cross sections for the analysed periods are shown in Tab. C.1. A very good agreement between results is observed. Since this comparison is performed only as a cross-check, the systematic uncertainties for the cross section results of this thesis are not calculated.

System	MB Yields (this thesis)	$\sigma_{J/\psi}$ (this thesis)	$\sigma_{J/\psi}$ ([3])
p-Pb	$(4.20 \pm 0.04 \text{ (stat.)}) \cdot 10^{-4}$	$879 \mu b$	$886 \pm 48 \text{ (uc. syst)} \mu b$
Pb-p	$(4.55 \pm 0.04 \text{ (stat.)}) \cdot 10^{-4}$	$965 \mu b$	$966 \pm 70 \text{ (uc. syst)} \mu b$

Table C.1: Integrated cross section obtained in this thesis compared with the ALICE results [3]. Note that the results obtained in this thesis have no systematic uncertainties since they were calculated as a cross-check.

As a qualitative cross-check, the results of the relative yield obtained in this analysis have been compared to those obtained in [261, 278], that uses the standard techniques for  $J/\psi$  yield extraction. In addition, the ZDC detector is used as event activity estimator. The data sample is divided in event classes based on cuts on the deposited energy in the ZDC neutron calorimeters (ZN). In order to compare the results of two analyses, the corresponding  $dN_{ch}/d\eta/\langle dN_{ch}/d\eta \rangle$  values to the ZN event classes are computed. To that end, the data-driven multiplicity correction procedure has been applied in order to compute the average corrected tracklets multiplicity in each ZN bin. The relation between ZN event activity classes and  $\langle N_{tr}^{corr} \rangle$  is presented in Tab. C.2 for the fractions of the data sample in each event activity class.

ZN event class (%)	$\langle N_{tr}^{corr} \rangle$ (p-Pb)	$\langle N_{tr}^{corr} \rangle$ (Pb-p)
Integrated	16.34	16.29
0 - 5	27.54	27.78
5 - 10	26.40	26.60
10 - 20	25.06	25.07
20 - 40	22.24	21.98
40 - 60	17.07	16.64
60 - 80	11.25	10.92
80 - 100	6.63	6.47

Table C.2: Correspondence between ZN event activity classes and  $\langle N_{tr}^{corr} \rangle$ . The systematic uncertainty on the multiplicity axis were taken as the uncertainty of  $\langle dN_{ch}/d\eta \rangle$  in [239], 3.8%. The uncertainty is not shown on the table nor used in the plots.

The results presented here are part of the cross-checks that were performed for the ALICE preliminary results released in (04/2014), so neither the ZN results nor the multiplicity ones are the final values. It is also important to take into account some considerations about the comparison made here:

- The relative multiplicity  $dN_{ch}/d\eta/\langle dN_{ch}/d\eta \rangle$  is computed as following the approach in Eq. 4.5 ( $(dN_{ch}/d\eta/\langle dN_{ch}/d\eta \rangle)_i \sim \langle N_{tr}^{corr} \rangle_i/\langle N_{tr}^{corr} \rangle$ ).
- The  $z_v^0$  reference for the SPD multiplicity correction was chosen such as  $N_{tr}(z_v^0 = \max(N_{tr}(z_v)))$  so the resolution was not equalised in these results.
- The ZN analysis does not require the same vertex selection as the SPD multiplicity analysis, so the data samples are slightly different.
- The event activity selection (ZN classes or mid- $y$  multiplicity) is completely different between the two analyses. The ZN selects events using the deposited energy of the slow nucleons emitted in the nucleon fragmentation while the multiplicity selection is based on the products of the collision. This is mentioned in App. A and discussed in detail in [55].

The results of the comparison of the two analyses are shown in Fig. C.1<sup>1</sup>. As can be observed in the top panel, the results are in a good qualitative agreement. In the bottom panel a more quantitative comparison is presented. The relative yields are fitted with a third order polynomial function, and the fit results of the two analyses for the two collision systems are compared by performing the ratio. The bands in the ratio correspond to the 0.95 confidence interval in the fits. It can be seen that there is a good agreement between the analyses except at low multiplicity. This is expected, according to the results in [55],

<sup>1</sup>Note that the results in this figure are not the final results in [261] nor the final results of this thesis.



as a consequence of the multiplicity fluctuations, which are especially noticeable at low multiplicity. This is discussed in App. A. Taking into account the aforementioned caveats, we can conclude that the results obtained with both event activity estimators are in a reasonably good agreement.

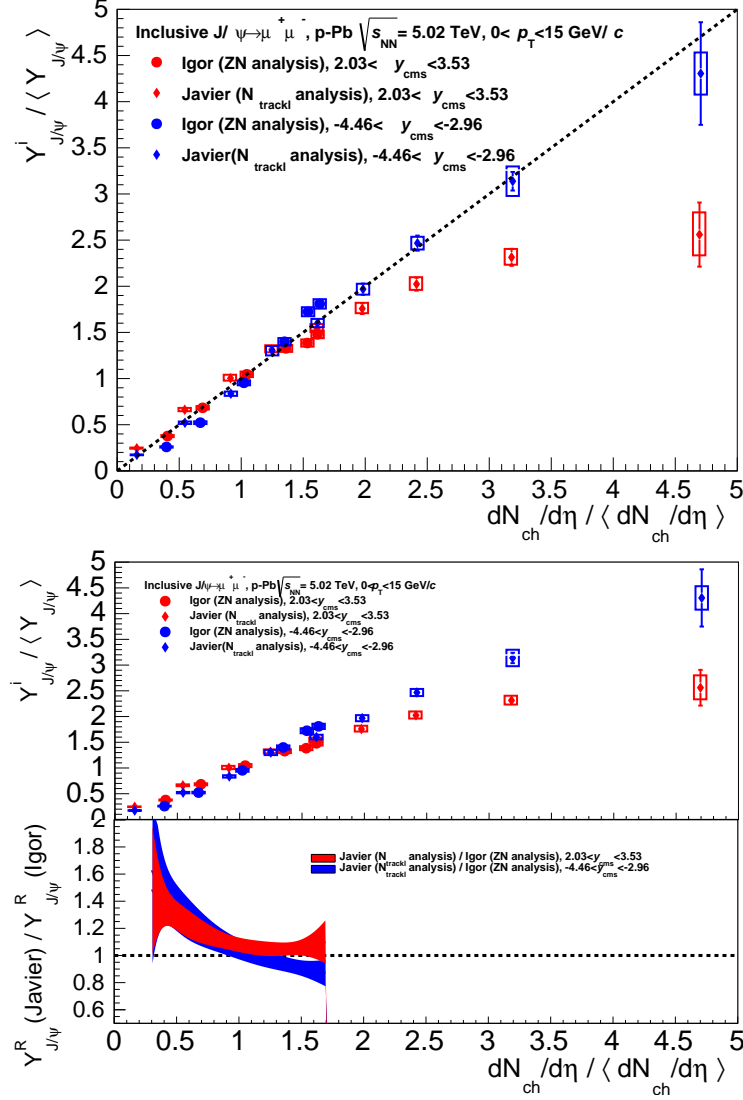


Figure C.1: Top: Relative yield comparison in p-Pb and Pb-p between  $N_{tr}^{corr}$  multiplicity estimator used in this thesis and ZN estimator used in [261]. Bottom: The relative yields are fitted with a third order polynomial function, and the fit results of the two analyses for the two collision systems are compared by performing the ratio. The bands in the ratio correspond to the 0.95 confidence interval in the fits. Note that the results in this figure are not the final results in [261] nor the final results of this thesis.

It is important to note here the advantage of using the charged particle multiplicity as estimator in terms of multiplicity range coverage. In addition, the charged particle multiplicity analysis enables the possibility to divide the event sample in bins with smaller

cross section fraction than in a centrality analysis. This can be seen by comparing the MB cross section fraction results for the bins in the multiplicity analysis in Tab. 4.10, with the ones in Tab. C.2 for the centrality analysis. This allows to study effects at very high (or very low) multiplicities, which are not observable with a centrality analysis. A clear example of this is the "saturation" effect observed in the yield obtained in this analysis at forward rapidity which is not manifested in the centrality analysis results. On the contrary, as mentioned in App. A, the multiplicity analysis has the drawback of presenting a strong bias when the results are to be correlated with the geometry of the collision [55]. Consequently the interpretation of these results has to be very carefully carried out.

Using the correspondence in Tab. C.2 we compare also the  $J/\psi$   $\langle p_T \rangle$  results as a function of multiplicity with those obtained with the ZN estimator and the standard  $\langle p_T \rangle$  extraction procedure in [261]. All the caveats mentioned before must also be taken into account for this comparison.

The results are presented in Fig. C.2. As can be observed in the top panel there is a very good qualitative agreement between the results of the two analyses. In the bottom panel a more quantitative comparison is reported. The results are fitted with a third order polynomial function, and its ratio is shown in the bottom panel. The bands represent the 0.95 level of confidence in the fits. There is a very good quantitative agreement between the  $\langle p_T \rangle$  results. This is due to the fact that the  $\langle p_T \rangle$  variation is small with multiplicity (event activity) and therefore the effect of different data sample selection in the multiplicity regions is small for the  $\langle p_T \rangle$  determination.

As for the relative  $J/\psi$  yield, we clearly observe a much wider multiplicity coverage using the number of charged particles as multiplicity estimator, enabling the observation of the  $\langle p_T \rangle$  behaviour at very high multiplicities.

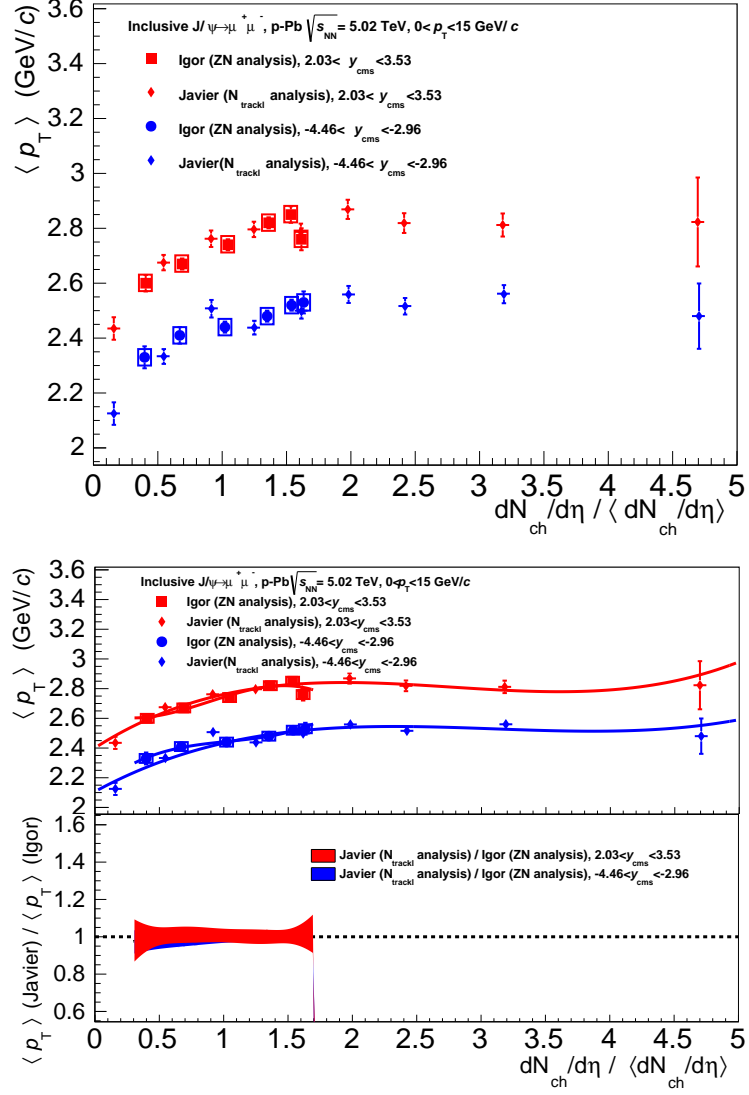


Figure C.2: Top: Absolute  $J/\psi$   $\langle p_T \rangle$  comparison in p-Pb and Pb-p between  $N_{tr}^{corr}$  multiplicity estimator used in this thesis and ZN estimator used in [261]. Bottom: The results are fitted with a third order polynomial function, and its ratio is shown in the bottom panel. The bands represent the 0.95 level of confidence in the fits. Note that the results in this figure are not the final results in [261] nor the final results of this thesis.



## COMPARISON OF UPDATED RESULTS WITH ALICE

### PRELIMINARY

In this appendix we present the ALICE Preliminary results obtained in this thesis for the  $J/\psi$  relative yield and relative average transverse momentum as a function of the relative charged particle multiplicity in p-Pb collisions at  $\sqrt{s_{NN}} = 5.02$  TeV [272]. Note that the latest improvements of the multiplicity analysis and refined systematic uncertainties computation were not yet developed by the time of the release of this results. The procedures employed are similar to those employed in the pp analysis in Chap. 8. The resulting systematic uncertainties for the preliminary results on the relative yield and average transverse momentum are listed in Tab. D.1 and Tab. D.2 respectively. The MB event selection efficiency for NSD events (NSD normalization), applied to correct the integrated yield, has a 3.1% systematic uncertainty<sup>1</sup>. It has to be taken into account for the relative yield measurement, but since it is a global uncertainty (correlated in multiplicity and between collision systems) is not added to the points but reported separately

In Fig. D.1 the inclusive relative  $J/\psi$  yield measured in p-Pb non-single diffractive (NSD) collisions at  $\sqrt{s_{NN}} = 5.02$  TeV at backward and forward rapidities as a function of the relative charged particle multiplicity measured at mid-rapidity ( $|\eta| < 0.5$ ) are shown. At low multiplicity a strong increase of the  $J/\psi$  yield is observed in both rapidity ranges. This behaviour is similar to that observed in pp collisions at 7 TeV [8, 111], where medium effects are, in principle, not expected. At higher multiplicities, the strong increase continues at backward rapidity, following the same pp-like behaviour. On the contrary, at forward rapidity a deviation from this behaviour is observed. A trend towards saturation at high multiplicities is present on  $J/\psi$  p-Pb data at forward rapidity.

---

<sup>1</sup>In the preliminary analysis we use the same selection for the integrated and multiplicity analysis, so the correction factor for NSD event selection efficiency in Tab.3.3 is applied to the integrated yield

Source	p-Pb	Pb-p
Sig. Extr.	0.8-3.3%	0.4 -1.6%
$F_{norm}$ method	0.1-4%	0.2-4%
$\mathcal{A} \times \mathcal{E}$	1.5-5%	1.5-4%
Pile-up	1-4%	1-2%
Total	2-8.2%	2-6.2%

Table D.1: Relative  $J/\psi$  yield systematic uncertainties in p-Pb collisions at forward (p-Pb) and backward (Pb-p) rapidity for the preliminary results. The values represent the minimum and maximum values of the uncertainties in the multiplicity bins.

Source	p-Pb	Pb-p
Sig. Extr.	0.1-0.4%	0.1-0.1.2%
Pile-up	-	-
$\langle p_T \rangle$ extr. meth.	2%	2%
Total	2-2.1%	2-2.3%

Table D.2: Relative  $J/\psi$  mean transverse momentum systematic uncertainties in p-Pb collisions at forward (p-Pb) and backward (Pb-p) rapidity for the preliminary results. The values represent the minimum and maximum values of the uncertainties in the multiplicity bins.

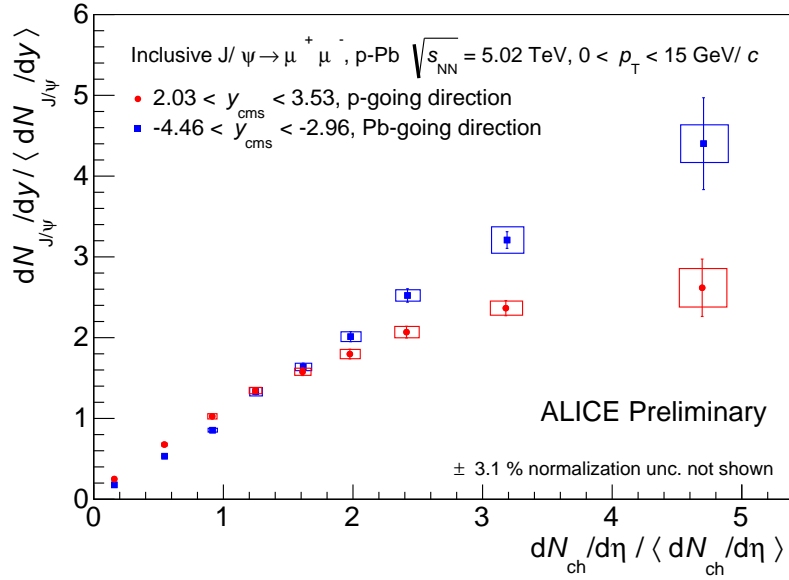


Figure D.1:  $J/\psi$  relative yield at backward (blue) and forward (red) rapidity as a function of relative charged particle multiplicity measured at mid-rapidity ( $|\eta| < 0.5$ ) in p-Pb collisions at  $\sqrt{s_{NN}} = 5.02$  TeV.

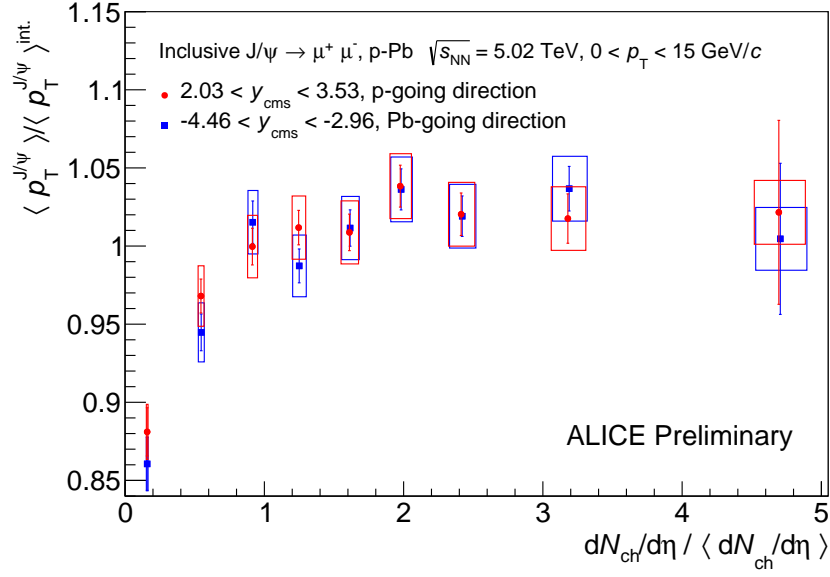


Figure D.2:  $J/\psi$  relative transverse momentum at backward (blue) and forward (red) rapidity as a function of relative charged particle multiplicity measured at mid-rapidity ( $|\eta| < 0.5$ ) in p-Pb collisions at  $\sqrt{s_{NN}} = 5.02$  TeV.

The relative average  $J/\psi$  transverse momentum as a function of the relative charged particle multiplicity is presented in Fig. D.2. An increase of the average transverse momentum at low multiplicity is observed both at forward and backward rapidity. However, at multiplicities beyond the average multiplicity ( $dN_{ch}/d\eta / \langle dN_{ch}/d\eta \rangle > 1$ ), the transverse momentum shows a trend towards saturation, also in the two rapidity ranges under study. The change on the  $\langle p_T \rangle$  slope is produced at a relative multiplicity about 1-1.5.

In the following we present the comparison between the preliminary results and the updated results presented in Chap. 9. There are several differences in the updated computation with respect to the preliminary results, which are mainly focused on the multiplicity determination and systematic uncertainties estimation. These improvements were developed and discussed in Chap. 4, 6 and 7. We summarise them here:

- Pseudorapidity range for multiplicity measurement. In preliminaries was  $|\eta| < 0.5$  while in the latest results is  $|\eta| < 1$ . The binning has been adapted to this change.
- The reference for the multiplicity correction in the preliminaries was chosen as  $\langle N_{tr}(z_0) \rangle = \max(\langle N_{tr}(z) \rangle)$ . In the latest results the reference is  $\langle N_{tr}(z_0) \rangle = \min(\langle N_{tr}(z) \rangle)$ , which removes the selection bias with  $z$ -vertex.
- A multiplicity dependent correction factor ( $\alpha_i$ ) for the average multiplicity in each slice is used in the latest results, while a constant factor was considered in the preliminary ones. This takes into account the variation of the tracklet-to-particle effects with multiplicity.

- The "bin 0" is removed from the analysis, since the correction is not able to correct the multiplicity of those events.
- Multiplicity bin flow is taken into account.
- Muon spectrometer  $\mathcal{A} \times \varepsilon$  uncertainty due to input distribution variations is computed.

In Fig. D.3, the preliminary results are compared with the latest ones implementing the improvements mentioned above. We can observe how the data points are placed at different multiplicity values, but the curves keep the same trend observed in the preliminary results. The main variations are due to the multiplicity dependent  $\alpha_i$  factors to obtain the charged particle multiplicity from the corrected SPD tracklets. The effect of this improvement pushes the data points to higher multiplicities at low multiplicity while it has the opposite effect at high multiplicity. The same conclusion can be extracted from the comparison of the  $\langle p_T \rangle$  results in Fig. D.4.

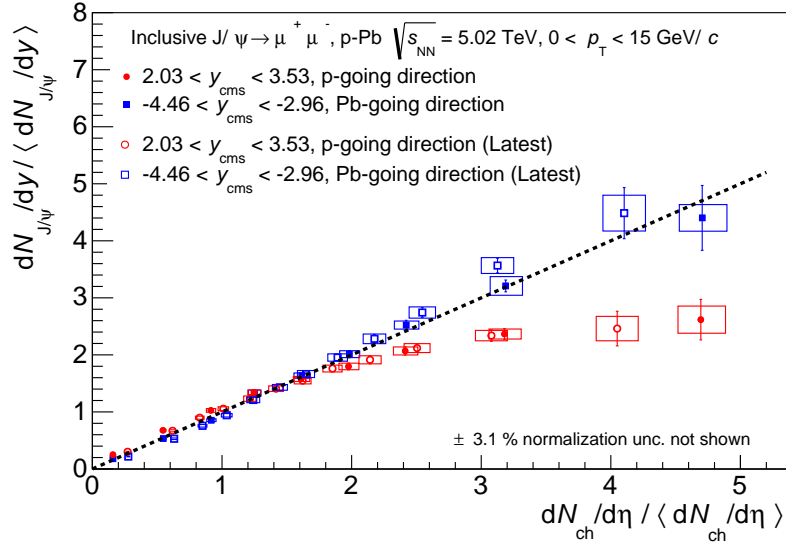


Figure D.3: Comparison between preliminary (full symbols) and latest (open symbols) results of  $J/\psi$  relative yield as a function of relative charged particle multiplicity ( $|\eta| < 0.5$  for preliminaries and  $|\eta| < 1$  for latest) in p-Pb collisions at 5.02 TeV.



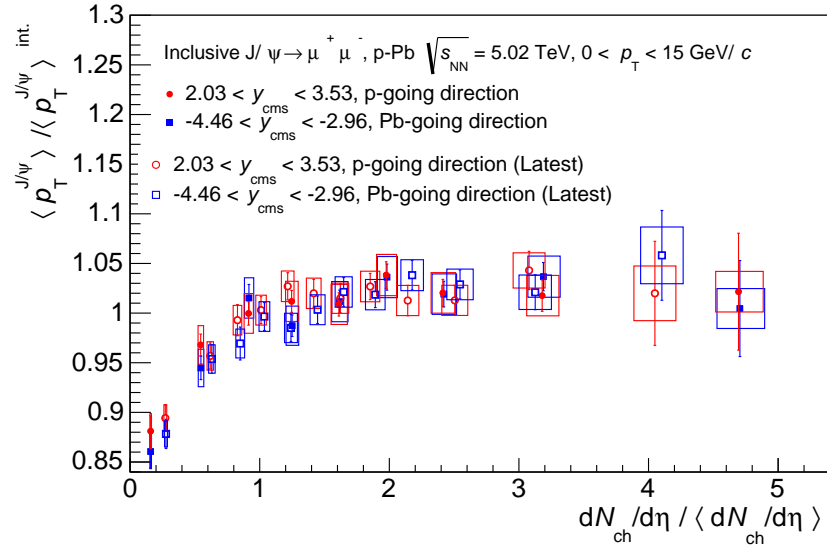


Figure D.4: Comparison between preliminary (full symbols) and latest (open symbols) results of  $J/\psi$  relative transverse momentum as a function of relative charged particle multiplicity ( $|\eta| < 0.5$  for preliminaries and  $|\eta| < 1$  for latest) in p-Pb collisions at 5.02 TeV.





## $J/\psi$ PRODUCTION DEPENDENCE WITH FORWARD RAPIDITY MULTIPLICITY

This appendix is dedicated to the study of the  $J/\psi$  yield as a function of the relative charged particle multiplicity measured with the A-side of the VZERO detector (V0A) (opposite side to the Muon Spectrometer). This study is a cross-check to observe the dependence of the measured effects on the  $J/\psi$  yield with the event multiplicity estimator. The charged particle multiplicity is not directly measured with the V0A. What we use is the V0A signal amplitude, which is proportional to the charged particle multiplicity. When using the V0A amplitude to estimate the relative multiplicity in p-Pb and Pb-p collisions, two different rapidity regions are employed ( $2.8 < |\eta_{lab}| < 5.1$ ).

In Fig. E.1 (top) we show the average V0A multiplicity ( $\langle V0A_{mult} \rangle$ ) obtained with the CMUL trigger as a function of the  $z$ -vertex in p-Pb (left) and Pb-p (right). The multiplicity is not constant with the vertex position due to the variation of the acceptance with the distance to the detector. Also, the overall multiplicity is smaller in the Pb-p than in the p-Pb configuration, since the detector is in the p-going direction. In order to equalise the multiplicity along  $z_v$  we use a similar method as for the SPD tracklets in Chap. 4. Equivalently to Eqs. 4.2 and 4.3, the corrected V0A multiplicity is given by  $V0A_{mult}^{corr}(z_v) = V0A_{mult}(z_v) + \Delta N_{rand}$ . A Poisson distribution with mean  $\Delta N$  is used to determine the missing/excess multiplicity ( $\Delta N_{rand}$ ) of an event measured at  $z_v$  with respect to a reference value in  $z_v^0$ :

$$(E.1) \quad \Delta N = V0A_{mult}(z) \frac{\langle V0A_{mult} \rangle(z_v^0) - \langle V0A_{mult} \rangle(z_v)}{\langle V0A_{mult} \rangle(z_v)}$$

In this case the reference is chosen such as  $\langle V0A_{mult} \rangle(z_v^0) = mean(\langle V0A_{mult} \rangle(z_v))$ , since the V0A resolution is not expected to vary with  $z_v$ . In this way the additional dispersion introduced by the correction is symmetric around  $z_v = 0$ . Also, no multiplicity equalisation is

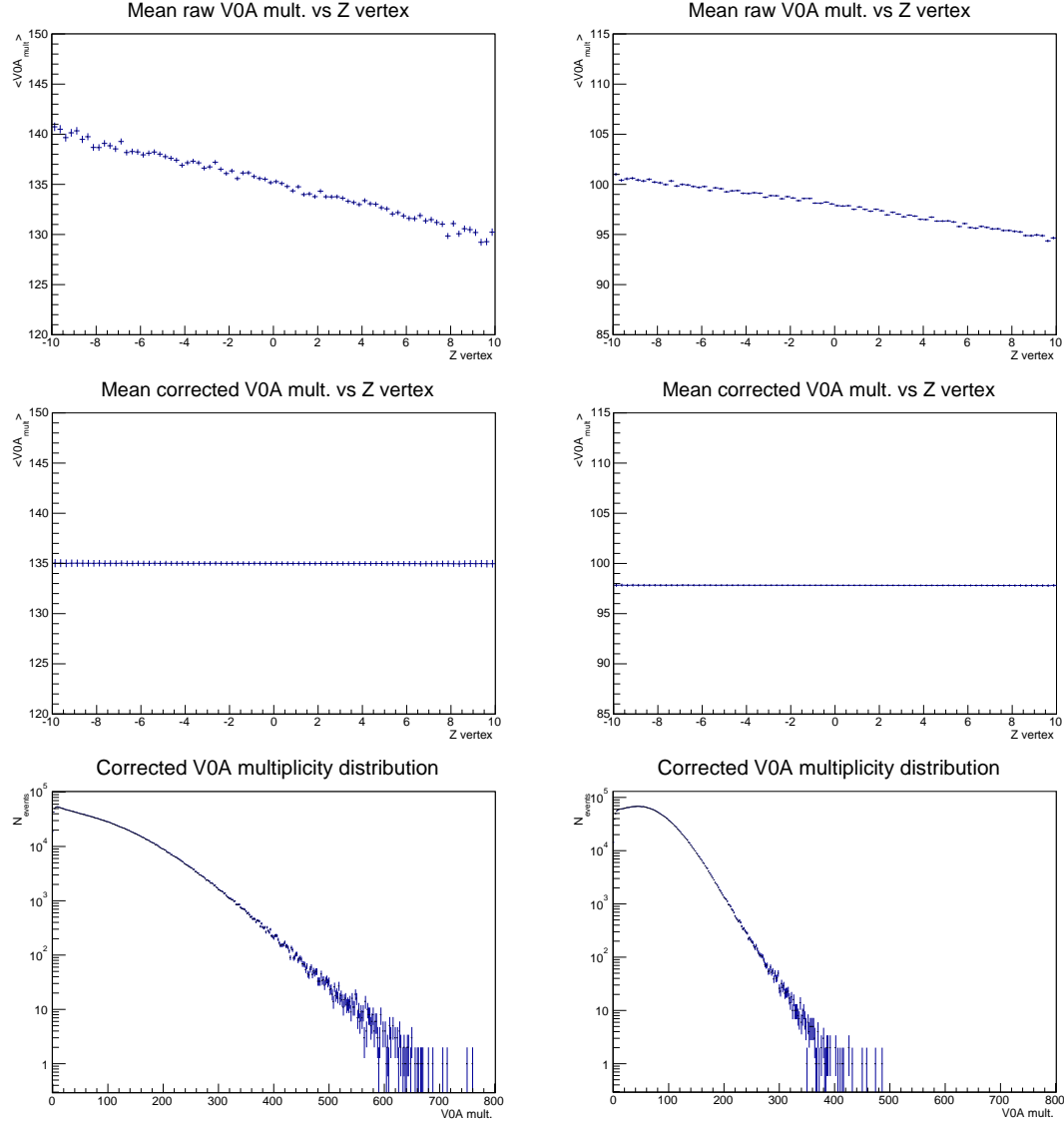


Figure E.1: Top: Raw average V0A multiplicity as a function of  $z$ -vertex in p-Pb (left) and Pb-p (right). Middle: Corrected average V0A multiplicity as a function of  $z$ -vertex in p-Pb (left) and Pb-p (right). Bottom: Corrected V0A multiplicity distribution in p-Pb (left) and Pb-p (right).

done between p-Pb and Pb-p since the V0A covers different rapidity ranges in the two beam configurations. In Fig. E.1 (middle) we show the corrected average multiplicity as a function of  $z$ -vertex, for the CMUL trigger. After the correction using Eq. E.1, the multiplicity is flat along  $z$ -vertex. In the bottom panel we show the corrected V0A multiplicity distributions in p-Pb and Pb-p, for the MB trigger. Since the distributions are different among p-Pb and Pb-p the multiplicity binning used to sample the events is different. The relative V0A multiplicity in a V0A amplitude event class is simply computed as the ratio of the average amplitude in the slice over the overall average amplitude  $\langle V0A_{mult} \rangle_i / \langle V0A_{mult} \rangle$ . We apply

no further correction for the correlation between the V0A amplitude and the number of charged particles for this cross-check.

The measured  $J/\psi$  yield in p-Pb and Pb-p collisions using the relative V0A multiplicity ( $2.8 < |\eta| < 5.1$ ) is shown in Fig. E.2, together with the result obtained using the relative  $dN_{ch}/d\eta$  measurement based on the SPD tracklets ( $|\eta| < 1$ ). The results are obtained with a single fit combination and no systematic uncertainties are calculated. The results using the V0A as multiplicity estimator are very similar to those obtained using the SPD tracklets. The saturation effect observed at forward rapidity and the linear-like increase at backward rapidity are maintained when using multiplicity estimators with a pseudorapidity gap of almost 4 units. This result provides a further argument to support that the observed effects are not simply a product of a selection bias.

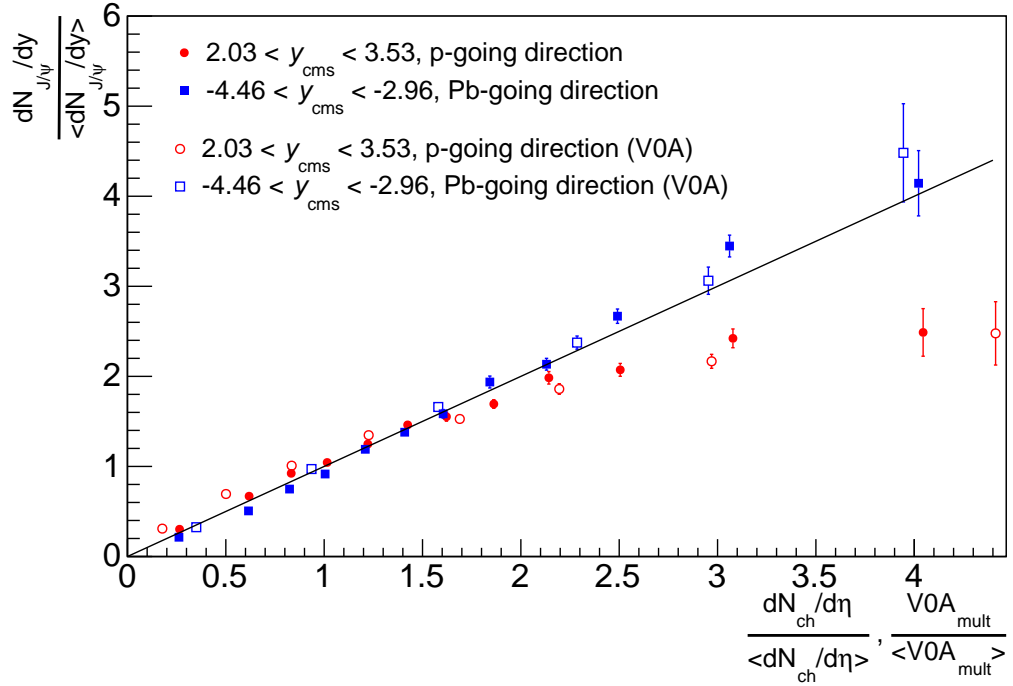


Figure E.2:  $J/\psi$  relative yield in p-Pb (red) and Pb-p (blue) collisions as a function of the relative multiplicity. Two estimators are employed: SPD tracklets (full symbols) ( $|\eta| < 1$ ) and V0A amplitude (open symbols) ( $2.8 < \eta < 5.1$ ).



# RÉSUMÉ: ÉTUDE DE LA DÉPENDANCE EN MULTIPLICITÉ DE PARTICULES CHARGÉES DE LA PRODUCTION DE $J/\psi$ DANS LES COLLISIONS P-Pb À $\sqrt{s_{\text{NN}}} = 5.02 \text{ TeV}$ ET LES COLLISIONS PP À $\sqrt{s} = 8 \text{ TeV}$ AVEC L'EXPÉRIENCE ALICE AU LHC

Dans le cadre de cette thèse, nous étudions l'évolution de la production des  $J/\psi$  à rapidité à l'avant et à l'arrière avec la multiplicité de particules chargées dans les collisions p-Pb à  $\sqrt{s_{\text{NN}}} = 5.02 \text{ TeV}$ , avec le détecteur ALICE au LHC [202]. Cette étude est complémentaire à celle effectuée en fonction de la centralité de la collision [5]. Les nouveaux résultats présentés dans cette thèse peuvent nous éclairer sur l'interaction entre les différents effets à l'oeuvre dans la matière nucléaire froide. D'autre part, les mesures des sondes molles dans des collisions p-Pb sont en bon accord qualitatif avec des calculs de modèles hydrodynamiques [6, 7], qui étaient l'explication naturelle pour les observations faites dans des collisions Pb-Pb. Ainsi, la présence d'effets collectifs dans des collisions p-Pb ne peut être exclue. Bien que les mesures inclusives des  $J/\psi$  ne montrent aucun signe de collectivité dans les collisions p-Pb, des mesures plus différentielles, notamment de la production de particules en fonction de la multiplicité de particules chargées, fournissent un moyen de signer la présence éventuelle d'effets collectifs dans l'état final. L'analyse développée dans cette thèse se concentre donc sur les événements avec une multiplicité de particules chargées élevée, dans les systèmes de petite taille (collisions p-Pb à  $\sqrt{s_{\text{NN}}} = 5.02 \text{ TeV}$  et collisions pp à  $\sqrt{s} = 8 \text{ TeV}$ ). La multiplicité de particules chargées est mesurée à l'aide du Détecteur à Pixels de Silicium (SPD) à mi-rapacité ( $|\eta| < 1$ ). Les  $J/\psi$  sont quant à eux reconstruits, dans le canal di-muon, avec le Spectromètre à Muons d'ALICE, dans le domaine de rapidité  $2.5 < |y| < 4.0$ .

Le premier chapitre est consacré à au contexte théorique et expérimental des études de quarkonium. Le Plasma de Quarks et Gluons (PQG), un état déconfiné de la matière partonique prédit par la Chromodynamique Quantique (QCD), devrait être formé dans des collisions d'ions lourds ultra-relativistes [49], puisque la matière hadronique y atteint des températures et des pressions élevées. Les quarks lourds sont produits dans les collisions partoniques primaires, et sont donc sensibles à l'ensemble de l'évolution du PQG. En conséquence, les quarkonia, états liés de paires de quarks lourds  $Q\bar{Q}$ , grâce à leur petite taille ( $< 1 \text{ fm}$ ) et une grande énergie de liaison (plusieurs centaines de MeV) sont des sondes

idéales du PQG. Il a été prédit qu'en présence d'un PQG, l'écrantage de couleur conduirait à une suppression séquentielle de la production des états quarkonium [1]. Une suppression (par rapport à la mesure dans des collisions pp à la même énergie) de la production des  $J/\psi$  a effectivement été mesurée dans des collisions Pb-Pb at  $\sqrt{s_{NN}} = 2.76$  TeV, fournissant une preuve supplémentaire de la formation d'un milieu déconfiné dans les collisions d'ions lourds ultra-relativistes. Cependant, d'autres effets comme la régénération du charmonium (dans le PQG lui-même ou à l'interface entre les phases partonique et hadronique), peuvent contribuer à la production du charmonium. La présence de ce mécanisme de régénération semble corroborée par plusieurs mesures  $J/\psi$  aux énergies du LHC (par exemple [2]).

Cependant, dans les collisions d'ions lourds, d'autres mécanismes liés aux effets initiaux et/ou à l'interaction des charmonia avec la matière nucléaire froide (par exemple l'élargissement de la distribution en  $p_T$ , le *shadowing* des gluons, ou la perte cohérente d'énergie des partons) jouent aussi un rôle dans la suppression des charmonia. L'étude des collisions proton-noyau au LHC est donc essentielle pour calibrer ces effets, afin de permettre une détermination quantitative de la suppression liée au PQG dans des collisions noyau-noyau. Comprendre les collisions p-Pb aidera à séparer les effets nucléaires froids et chauds dans les collisions Pb-Pb. Les mesures du facteur de modification nucléaire des  $J/\psi$  (Figs. 1.25 et 1.26) dans les collisions p-Pb à 5.02 TeV [3, 4] corroborent également, dans une certaine mesure, le scénario de régénération, car les modèles comprenant le *shadowing* des gluons et la perte cohérente d'énergie des partons sont en mesure de décrire les résultats p-Pb, alors qu'ils ne parviennent pas à expliquer les résultats Pb-Pb [139].

Le détecteur ALICE est décrit dans le deuxième chapitre. ALICE est l'expérience du LHC (Grand Collisionneur de Hadrons du CERN) dédiée aux ions lourds. Son objectif principal est l'étude de la physique de la matière interagissant fortement dans des collisions d'ions lourds ultra-relativistes mais elle effectue également des mesures dans les collisions pp dans le cadre de son programme de physique. L'expérience ALICE possède des détecteurs de granularité élevée pour pouvoir faire face aux hautes densités de particules secondaires produites dans les collisions Pb-Pb les plus centrales. Elle est caractérisée par un faible seuil en impulsion transverse ( $p_T \sim 0.15$  GeV/c), ainsi que par une bonne identification des particules jusqu'à 20 GeV/c. Un résumé des sujets de physique couverts par ALICE et la performance de ses détecteurs pour mesurer les différents observables est donné dans les références [203–205]. Les résultats obtenus jusqu'à présent sont disponibles dans la référence [206].

Le détecteur se compose de trois parties principales. Les détecteurs du tonneau central ( $|\eta| < 0.9$ ) sont intégrés dans un aimant solénoïdal procurant un champ magnétique  $B = 0.5$  T. Ils sont en charge de la trajectographie et de l'identification des particules chargées (ITS, TPC, TRD, TOF, HMPID) et des photons (PHOS et EMCal). Les détecteurs globaux (FMD, PMD, VZERO, TZERO et ZDC) sont quant à eux utilisés pour déclencher l'acquisition des données, caractériser les événements (centralité, plan de réaction...) et déterminer la luminosité du faisceau. Enfin, le Spectromètre à Muons ( $-4.0 < \eta < -2.5$ ), qui a son propre



---

champ magnétique dipolaire de 3 T·m, est responsable de la reconstruction des muons et de leur trajectographie. Le détecteur possède en outre un réseau de scintillateurs pour déclencher les mesures des rayonnements cosmiques (ACORDE).

Les deux principaux détecteurs utilisés dans cette thèse sont le Détecteur à Pixels de Silicium et le Spectromètre à Muons. Le Système de Trajectographie Interne (ITS) [212] couvre la région centrale des rapidités  $|\eta| < 0.9$  pour les vertex situés à  $\pm 10.6$  cm du point d'interaction le long de la direction du faisceau. Les deux premières couches de l'ITS sont des Détecteurs à Pixels de Silicium (SPD) ( $|\eta| < 1.4$ ). Les couches du SPD sont primordiales dans la détermination de la position du vertex primaire et la mesure du paramètre d'impact des traces secondaires provenant des désintégrations faibles des particules étranges, charmées et belles. Le SPD est utilisé dans cette thèse pour mesurer la multiplicité de particules chargées. Le spectromètre à muons [224, 225] est conçu pour mesurer la production de résonances via leur canal de désintégration en deux muons ( $\mu^+ \mu^-$ ) : charmonia ( $J/\psi$ ,  $\psi(2S)$ ), bottomonia ( $\Upsilon$ ,  $\Upsilon'$ ,  $\Upsilon''$ ) et mésons vecteurs de faible masse ( $\rho$ ,  $\omega$ ,  $\phi$ ). Il est également utilisé pour mesurer la production des muons simples provenant des désintégrations semileptoniques de hadrons de saveurs lourdes et des bosons  $W^\pm$  et  $Z^0$ .

Le spectromètre, d'une longueur totale de 17 m, est composé d'un système d'absorbeurs passifs, de dix plans de trajectographie de haute granularité (disposés en cinq stations), d'un aimant dipolaire, d'un mur de fer et de quatre chambres de déclenchement (disposés en deux stations).

Dans les chapitres 3 et 4, nous présentons le travail effectué dans cette thèse pour le développement de deux méthodes pour mesurer la densité moyenne en pseudorapidité de la multiplicité des particules chargées,  $\langle dN_{ch}/d\eta \rangle$ . Cette mesure est essentielle pour étudier les propriétés globales des collisions proton-proton, proton-noyau et noyau-noyau. Une estimation de  $\langle dN_{ch}/d\eta \rangle$  à partir des *tracklets* SPD est utilisée pour classer les événements afin d'étudier la dépendance de la production des  $J/\psi$  avec la multiplicité de particules chargées. Deux méthodes d'estimation différentes ont été utilisées. La première méthode est basée sur l'obtention d'une correction d'acceptance et d'efficacité ( $\mathcal{A} \times \epsilon$ ) du SPD, à partir de simulations Monte Carlo (MC). La correction prend également en compte d'autres effets comme la génération de particules secondaires dans le détecteur ou le bruit de fond combinatoire. Cette correction est appliquée événement par événement. Une étude spécifique pour vérifier si la procédure est appropriée pour obtenir un estimateur de multiplicité des événements individuels a été réalisée. Nous avons aussi mesuré la distribution  $dN_{ch}/d\eta$  en fonction de  $\eta$  dans les collisions p-Pb et Pb-p et nous l'avons comparée à celle de la référence [239]. Les résultats obtenus dans cette thèse sont en bon accord avec ceux publiés.

La seconde approche est une correction unidimensionnelle fondée principalement sur les données. La méthode est basée sur l'utilisation du nombre moyen brut de *tracklets* du SPD reconstruits en fonction de la position  $z$  du vertex d'interaction. Cette approche, déjà utilisée pour les mesures des  $J/\psi$  dans [8], a été améliorée par rapport à sa mise en oeuvre initiale [111]. Les modifications développées au cours de cette thèse impliquent l'utilisation d'une

simulation et sont importantes lorsque les corrections *tracklet*-vers-particule varient avec la multiplicité, et spécialement quand un *binning* mince doit être utilisé. Elles permettent une estimation plus précise de la multiplicité dans les événements, en contrôlant mieux les biais de résolution. Elles conduisent à la réduction de l'incertitude systématique de la mesure de multiplicité.

Le Chapitre 5 présente les études que nous avons effectuées sur l'efficacité de trajectographie du Spectromètre à Muons d'ALICE au cours de la prise des données p-Pb de 2013. La valeur  $\mathcal{A} \times \epsilon$  utilisée pour corriger les données extraites par le spectromètre est calculée au moyen de simulations spécifiques du détecteur. Le but principal des études effectuées dans ce chapitre est de s'assurer que les simulations reproduisent les conditions réelles du spectromètre lors de la prise de données, en particulier leur évolution avec le temps. Une méthode pour mesurer l'efficacité de trajectographie pour les traces reconstruites est utilisée à la fois sur des données réelles et simulées. Cette méthode exploite la redondance entre les plans de détection du spectromètre pour déterminer l'efficacité d'une chambre donnée. En comparant les résultats obtenus à partir de la mesure dans les données et dans la simulation, il est possible de vérifier la validité de la simulation et d'attribuer une incertitude systématique à la correction  $\mathcal{A} \times \epsilon$ . Au cours de cette étude, les régions qui ne sont pas correctement reproduites dans les simulations ont été incluses dans une liste de rejection. De nouvelles simulations ont été réalisées en utilisant ces informations, améliorant ainsi la description du détecteur. Cela a permis d'obtenir une correction  $\mathcal{A} \times \epsilon$  plus précise pour les données prises par le spectromètre dans les données p-Pb de 2013, et une réduction de l'incertitude systématique associée par rapport aux études précédentes. Cette correction a été utilisée dans toutes les analyses en collisions p-Pb qui utilisent le Spectromètre à Muons pour les publications d'ALICE.

Les Chapitres 6 et 7 sont consacrés à la description des analyses des  $J/\psi$  dans les collisions p-Pb menées dans cette thèse. Les mesures des  $J/\psi$  sont effectuées en fonction de la multiplicité de particules chargées déterminée au chapitre 4. L'objectif du Chapitre 6 est de mesurer le taux de production des  $J/\psi$ . Les  $J/\psi$  sont mesurés dans le canal de désintégration en deux muons avec le Spectromètre à Muons. La procédure habituelle pour mesurer le taux de production des  $J/\psi$  consiste à extraire le nombre de  $J/\psi$  partir des spectres de masse invariante mesurés dans une certaine gamme cinématique. Ensuite, le nombre de  $J/\psi$  est corrigé par la valeur d' $\mathcal{A} \times \epsilon$  du spectromètre calculée pour la même gamme. Dans cette thèse, nous avons développé une approche non-standard afin de corriger les données prises par le spectromètre à muons. Une correction bidimensionnelle  $\mathcal{A} \times \epsilon(p_T, y)$  du Spectromètre à Muons est appliquée à chaque paire de muons avant de construire les spectres de masse invariante. Les formes corrigées du signal peuvent donc être directement extraites à partir des spectres. Cette technique réduit l'incertitude systématique sur la mesure du taux de production des  $J/\psi$  due à la détermination de la correction.

Le Chapitre 7 décrit une technique innovante d'extraction de l'impulsion transverse moyenne des  $J/\psi$ ,  $\langle p_T \rangle$ , basée sur l'étude du spectre de masse invariante du  $\langle p_T \rangle$  des paires

---

de muons. Cette technique a besoin de la méthode de correction développée dans le chapitre précédent. Cette approche, contrairement à la version standard (voir par exemple [4, 5]), nécessite seulement d'effectuer un groupement (*binning*) de l'échantillon des données par classes de multiplicité, et ne nécessite pas un groupement supplémentaire par classes de  $p_T$ . En conséquence, cette technique est adaptée à l'étude des régimes à haute multiplicité, où la statistique est faible et donc à l'étude des propriétés de production des particules à des multiplicités plus élevées. En utilisant la même technique, le  $\langle p_T^2 \rangle$  des  $J/\psi$  est également extrait.

Dans le Chapitre 8, une analyse préliminaire du taux de production des  $J/\psi$  et leur  $\langle p_T \rangle$  en fonction de la multiplicité de particules chargées est effectuée dans les collisions pp à 8 TeV. La motivation pour étudier la production des  $J/\psi$  en fonction de la multiplicité dans les collisions pp est double. Tout d'abord, puisqu'aucun effet de matière nucléaire froide n'est présent dans ces collisions, et qu'aucun effet nucléaire chaud n'est attendu à faible multiplicité, cette mesure sert de base de référence pour l'interprétation des résultats dans les collisions p-Pb. De plus, les multiplicités de particules chargées mesurées en collisions pp à haute multiplicité, déjà à  $\sqrt{s} = 7$  TeV, sont comparables à celles mesurées dans les collisions d'ions lourds à des énergies plus faibles, où les effets attribués à la formation du PQG ont été trouvés [8, 9]. Par conséquent, la recherche d'effets collectifs, similaires à ceux trouvés dans des collisions d'ions lourds, en collisions pp à 8 TeV à haute multiplicités est justifiée [10].

Enfin, dans le Chapitre 9, nous présentons et discutons les résultats obtenus dans les collisions pp à  $\sqrt{s} = 8$  TeV et les collisions p-Pb et Pb-p à  $\sqrt{s_{NN}} = 5.02$  TeV, en utilisant les techniques d'analyse décrites dans les chapitres précédents. Nous sommes en mesure d'étudier les événements rares, qui représentent une infime fraction de la section efficace nucléaire en p-Pb et présentant une multiplicité de particules chargées très haute, jusqu'à quatre fois la multiplicité moyenne.

Les résultats  $J/\psi$  en pp à 8 TeV étendent la gamme de multiplicité étudiée dans l'analyse précédente à 7 TeV [8]. La mesure du taux de production relatif des  $J/\psi$  en collisions à 8 TeV montre une augmentation avec la multiplicité quasi linéaire (Fig. 9.5). Notre mesure à 8 TeV montre un comportement similaire à celui observé à 7 TeV. L'évolution de l'impulsion transverse moyenne,  $\langle p_T \rangle$ , des  $J/\psi$  avec la multiplicité de particules chargées dans les collisions pp est mesurée pour la première fois dans cette thèse (Fig. 9.7). Nous observons une forte augmentation du  $\langle p_T \rangle$  à basse multiplicité et une augmentation plus modérée aux multiplicités au delà de la multiplicité moyenne. Ces résultats servent à définir de nouvelles contraintes pour les modèles théoriques disponibles.

Les études en collisions p-Pb et Pb-p présentées ici sont complémentaires à celles réalisées en fonction de la centralité de la collision dans la référence [5]. La sélection des événements en fonction de la multiplicité de particules chargées utilisée dans cette thèse a permis d'étudier la production des  $J/\psi$  dans des événements plus rares, à des multiplicités jusqu'à quatre fois la multiplicité moyenne. Un effet de saturation du taux de production

( $dN_{J/\psi}/dy$ ) aux rapidités avant, qui n'a pas été observé dans l'analyse de centralité ni dans des collisions pp, a été mesuré dans cette thèse (Figs. 9.1 et 9.6). Cet effet est probablement lié à la matière nucléaire froide, faute de quoi il devrait être également observé aux rapidités arrière. La première mesure de l'évolution du  $\langle p_T \rangle$  des  $J/\psi$  avec la multiplicité de particules chargées dans des collisions p-Pb est présentée aux rapidités avant et arrière (Figs. 9.2 et 9.3). Les résultats montrent une tendance à la saturation du  $\langle p_T \rangle$  à une multiplicité élevée dans les deux gammes de rapidité, ce qui est qualitativement différent de l'observation faite en collisions pp (Fig. 9.7). Une explication plausible serait que les collisions multipartoniques dans les collisions pp ont lieu dans le même nucléon, et dans le cas des collisions p-Pb elles ont lieu dans des nucléons différents. Nous notons que les comportements du  $\langle p_T \rangle$  des  $J/\psi$  dans les collisions pp et p-Pb présentent une tendance similaire à celle observée pour les particules chargées dans les mêmes systèmes de collision. Cependant, l'interprétation de cette observation en faisant appel aux mêmes mécanismes pour la production de particules molles et dures n'est pas évidente. De plus, le rapport des facteur de modification nucléaire à l'avant et à l'arrière (Eq. 9.1) a été calculé (Fig. 9.9). Il montre une suppression plus forte de la production des  $J/\psi$  (par rapport aux attentes en pp) aux rapidités avant qu'aux rapidités l'arrière. Ces observations peuvent aider à améliorer notre compréhension du rôle des effets de la matière nucléaire froide dans les collisions p-Pb. En particulier, il semblerait que les effets nucléaires froids sont présents dans les  $J/\psi$  produits à l'avant dans les collisions p-Pb. Le shadowing des gluons dans le noyau peut difficilement expliquer cette effet. Pour conclure sur ce point, la comparaison des résultats expérimentaux avec des modèles théoriques spécifiques serait néanmoins nécessaire, notamment avec le modèle de perte d'énergie qui explique les données en fonction de la centralité. Cela permettrait de confirmer si ce modèle explique notre observation ou en revanche un nouvel effet nucléaire froid est à l'oeuvre.

Pour tester davantage la présence des effets nucléaires dans les collisions p-Pb nous présentons une analyse préliminaire de l'évolution de l'élargissement de la distribution en impulsion transverse ( $\Delta\langle p_T^2 \rangle$ ) avec la multiplicité de particules chargées (Fig. 9.8). Le résultat montre une augmentation du  $\Delta\langle p_T^2 \rangle$  avec la multiplicité, qui est peut-être une conséquence de la diffusion multiple des partons dans le milieu nucléaire, ou des effets cohérents de perte d'énergie. Cette observation est similaire à celle réalisée dans l'étude des  $J/\psi$  en fonction de la centralité [5]. A haute multiplicité le  $\Delta\langle p_T^2 \rangle$  semble être indépendant de la multiplicité.

Enfin, nous présentons les résultats en fonction du nombre de collisions binaires,  $\tilde{N}_{\text{coll}}^{\text{mult}}$ , où  $\tilde{N}_{\text{coll}}^{\text{mult}}$  est estimé à partir de  $dN_{ch}/d\eta$  (Eq. 9.3). Ces résultats étendent la gamme étudiée dans l'analyse de centralité ALICE [5, 261], et sont en accord avec ces mesures existantes dans la gamme commune. Les résultats du facteur de modification nucléaire,  $Q_{pPb}^{\text{mult}}$ , présentés dans [5, 261] sont en bon accord avec les attentes des modèles de *shadowing* des gluons et de perte cohérente d'énergie des partons. Notre mesure du  $\tilde{Q}_{pPb}^{\text{mult}}$  aux rapidités arrière montre qu'il varie comme  $\tilde{N}_{\text{coll}}^{\text{mult}}$  (Fig. 9.10 haut). Par contre, aux rapidités avant (Fig. 9.10 bas), le  $\tilde{Q}_{pPb}^{\text{mult}}$  montre une suppression de plus en plus forte avec  $\tilde{N}_{\text{coll}}^{\text{mult}}$  qui atteint  $\sim 0.37$ .

L'origine de cette suppression pourrait être une augmentation de la perte cohérente d'énergie des partons avec  $\tilde{N}_{\text{coll}}^{mult}$ . Nos mesures de l'évolution de l'élargissement de la distribution en impulsion transverse ( $\Delta\langle p_T^2 \rangle$ ) avec  $\tilde{N}_{\text{coll}}^{mult}$  (Fig. 9.11) sont en accord avec ceux de [5, 261] dans la gamme d'observation commune. On observe cependant une tendance à la saturation aux grandes valeurs de  $\tilde{N}_{\text{coll}}^{mult}$ , qui n'a pas été observée dans les analyses en centralité. Cela ne semble pas être la tendance prévue par les modèles dans [5]. Une comparaison détaillée avec les calculs théoriques aux grandes valeurs de  $\tilde{N}_{\text{coll}}^{mult}$  est néanmoins nécessaire pour conclure. La gamme étendue en  $\tilde{N}_{\text{coll}}^{mult}$  de cette analyse peut aider à améliorer notre compréhension des effets nucléaires froids et différencier les modèles disponibles.

En résumé, dans cette thèse nous avons étudié l'évolution de la production des  $J/\psi$  dans les collisions pp à  $\sqrt{s} = 8$  TeV et les collisions p-Pb à  $\sqrt{s_{\text{NN}}} = 5.02$  TeV avec la multiplicité de particules chargées. Nous avons utilisé le Spectromètre à Muons d'ALICE pour les mesures des  $J/\psi$  et le Détecteur à Pixels de Silicium pour l'estimation de la multiplicité. Des méthodes spécifiques pour l'étude du taux de production des  $J/\psi$ , leur  $\langle p_T \rangle$  (et  $\langle p_T^2 \rangle$ ) et des mesures de multiplicité ont été développées au cours de ce travail. Ces méthodes améliorent la qualité des mesures et réduisent certaines incertitudes systématiques par rapport à d'autres techniques. L'utilisation de ces nouvelles techniques a été motivée par l'étude de la production des  $J/\psi$  à haute multiplicité. Une structure logicielle complète pour les analyses des quarkonia en fonction de la multiplicité des particules chargées a été développée au cours de cette thèse. Dans les collisions p-Pb à l'avant nous avons mesuré des événements rares avec un grand nombre de collisions partoniques (jusqu'à deux fois le nombre maximal selon le modèle de Glauber géométrique à paramètre d'impact nul). Dans ces événements les résultats obtenus pour la production des  $J/\psi$  à l'avant montrent la présence d'effets nucléaires froids.

Certains des résultats p-Pb présentés dans cette thèse ont été approuvés en tant que résultats préliminaires d'ALICE en 2014 et présentés lors de la conférence Quark Matter [271, 272]. Les résultats mis à jour ne sont pas encore approuvés par la Collaboration ALICE. Ils feront partie d'une publication qui est en cours de préparation. Une note (interne) d'analyse est d'ores et déjà disponible.

Pour améliorer les résultats présentés ici, la section efficace de production  $J/\psi$  en collisions pp doit être mesurée à 5,02 TeV, afin de réduire les incertitudes systématiques du facteur de modification nucléaire en collisions p-Pb. Une mesure intéressante qui peut aider à mieux comprendre le rôle des effets de l'état initial et final dans des collisions p-Pb est l'étude de la production des  $\psi(2S)$  en fonction de la multiplicité de particules chargées. Cette mesure pourrait aussi être réalisée avec l'expérience CMS sur la production des  $\Upsilon$ . La contribution à notre mesure des  $J/\psi$  provenant de la décroissance des hadrons B en fonction de la multiplicité est pour l'instant inconnue. La mesure de cette contribution dans ALICE ne sera possible qu'avec le Muon Forward Tracker d'ALICE [276] qui sera installé en 2018.



## LIST OF TABLES

1.1	Charmonium states and binding energies ( $\Delta E$ ) [73]. . . . .	13
2.1	ITS detector dimensions. From [213]. . . . .	49
2.2	Triggers used, one way or another, in this analysis. CMUL triggers were the primary ones used to measure the $J/\psi$ . The other triggers were used for normalization purposes mainly. Events in this table have passed only Physics Selection cut. Note that the name of the trigger classes includes the trigger name but also bunch crossing features (i.e. "B" meaning beam-beam, "S" meaning beam-satellite), CTP vetoes (i.e. NOPF meaning no past-future protection activated) and trigger cluster name (i.e. MUON which contains SPD, MTR and MCH). . .	61
3.1	Comparison of the average $dN_{ch}/d\eta$ in VZERO-A event classes published in [247] and obtained in this thesis for p-Pb (LHC13d+e). This comparison is done only as a cross-check, so the systematic uncertainties in VZERO event classes are not computed for the results in this thesis. . . . .	83
3.2	Number of events passing different event cuts in simulation and selection efficiency for NSD events without SPD vertex ( $\epsilon'$ ) for different MC productions. . . .	85
3.3	Event fractions with respect to MB physics selected events in p-Pb, and Pb-p collisions real data. The NSD event selection efficiency of the MB trigger and event selection ( $1 - \epsilon_{\overline{SPD}}/\epsilon' - \epsilon_{SPDQA}$ ) is also shown. For an explanation on the uncertainty see Sec. 3.10 . . . . .	86
4.1	Correction factors to go from $\langle N_{tr}^{corr} \rangle_i$ to $\langle N_{ch} \rangle_i$ in multiplicity bins for $\langle N_{tr} \rangle(z_v^0) = \min(\langle N_{tr} \rangle(z))$ . The errors are the statistical errors from the fits. The values in parentheses for the first bin correspond to the value corrected by $\hat{\epsilon}$ . Note that multiplicity slices, contain the extremes of the ranges indicated in the left column. See Sec. 4.5 for the considerations needed to compute these factors in simulation. . . . .	111
4.2	Reference multiplicity values in p-Pb and Pb-p and obtained mean multiplicities in the selected MB data sample for this analysis. . . . .	114
4.3	Reference multiplicity values for correction in MC for p-Pb and Pb-p. . . . .	115
4.4	MC weights for the two SPD subperiods in Pb-p. . . . .	116
4.5	Measured overall-averaged charged particle pseudo-rapidity density in p-Pb and Pb-p. The systematic uncertainty on the $\langle dN_{ch}/d\eta \rangle$ value is 4% (see Sec.4.7) . . .	117

4.6	Average mean number of collisions per bunch crossing $\langle\mu\rangle$ in p-Pb (LHC13c MB (* means that the value is only for the run analysed in this thesis) and LHC13d+e rare trigger periods), and Pb-p collisions. Probabilities to have at least one ( $P(n \geq 1)$ ) or at least two ( $P(n \geq 2)$ ) collisions, according to the poisson distribution. . . . .	121
4.7	Fraction of pile-up events in multiplicity bins obtained with the toy MC. Note that multiplicity slices, contain the extremes of the ranges indicated in the left column . . . . .	125
4.8	Multiplicity absolute and relative axes from $N_{tr}^{corr}$ in p-Pb (LHC13d+e). Only systematic errors are shown, statistical ones are negligible. Note that multiplicity slices, contain the extremes of the ranges indicated in the left column . . . . .	127
4.9	Multiplicity absolute and relative axes from $N_{tr}^{corr}$ in Pb-p (LHC13f). Only systematic errors are shown, statistical ones are negligible. Note that multiplicity slices, contain the extremes of the ranges indicated in the left column . . . . .	128
4.10	MB cross section fractions in each multiplicity bin $i$ ( $N_{MB}^i/N_{MB}^{tot}$ ) used in this analysis in p-Pb and Pb-p data samples. . . . .	128
5.1	Tracking efficiency systematic uncertainties for single muons and di-muons in 2013 p-Pb collisions. . . . .	148
6.1	Extended Crystal Ball tails parameters extracted from pure signal $J/\psi$ and $\psi(2S)$ simulations . . . . .	156
6.2	Fraction of $J/\psi$ in the core and tails of the signal in simulation. . . . .	157
6.3	Extracted number of $J/\psi$ (from the $\mathcal{A} \times \mathcal{E}$ corrected spectra) in p-Pb and Pb-p periods for one of the execution tests with the nominal $\mathcal{A} \times \mathcal{E}$ correction (see Sec. 6.3). The systematic uncertainty is the one related to the signal extraction only (see Sec. 6.3.1). . . . .	161
6.4	Global $F_{norm}^{offline}$ pile-up corrected integrated values and comparison with [263]. The uncertainty on the result of this analysis is only the statistical one. The systematic uncertainty is discussed in Sec. 6.3.3 . . . . .	162
6.5	$F_{norm}^{offline}$ pile-up corrected in multiplicity bins for p-Pb and Pb-p. The uncertainty on the result of this analysis is only the statistical one. The systematic uncertainty is discussed in Sec. 6.3.3 . . . . .	163
6.6	p-Pb $J/\psi$ extraction from raw spectra and corrected by integrated $\mathcal{A} \times \mathcal{E}(0.252)$ compared to the result of the extraction from the $\mathcal{A} \times \mathcal{E}$ corrected spectra for a single fit test. The uncertainties are the statistical uncertainties given by the fit. . . . .	172
6.7	Fit parameters of the input $J/\psi$ yield distributions in p-Pb (see text). * The fitting range is restricted to $N_{tr}^{corr} \in [0,30]$ . . . . .	181
6.8	Fit parameters of the input $J/\psi$ yield distributions in Pb-p (see text). . . . .	182



6.9	Relative $J/\psi$ yield systematic uncertainties in p-Pb and Pb-p collisions. The values represent the minimum and maximum values of the uncertainties in the multiplicity bins. The uncertainties with * are only applicable to the first multiplicity bin. . . . .	183
6.10	Absolute $J/\psi$ yield systematic uncertainties in p-Pb and Pb-p collisions. The values represent the minimum and maximum values of the uncertainties in the multiplicity bins. The uncertainties with * are only applicable to the first multiplicity bin. . . . .	184
7.1	$J/\psi$ transverse momentum values in p-Pb and Pb-p collisions obtained in this thesis (for the fit combination in Fig. 7.2) compared with the ones obtained in [4].	189
7.2	$J/\psi \langle p_T \rangle$ as a function of charged particle multiplicity and multiplicity integrated in p-Pb and Pb-p collisions (incomplete syst.). Note that the systematic uncertainty due to the combined effect (no bin-flow) treated in this section is negligible for the integrated measurement. . . . .	195
7.3	Fraction of pile-up events with $J/\psi$ in multiplicity bins obtained with the toy MC.	201
7.4	Relative $J/\psi \langle p_T \rangle$ systematic uncertainties in p-Pb and Pb-p collisions. The values represent the minimum and maximum values of the uncertainties in the multiplicity bins. The uncertainties with * are only applicable to the two last multiplicity bins. . . . .	202
7.5	Absolute $J/\psi \langle p_T \rangle$ systematic uncertainties in p-Pb and Pb-p collisions. The values represent the minimum and maximum values of the uncertainties in the multiplicity bins. The uncertainties with * are only applicable to the two last multiplicity bins. . . . .	202
7.6	$J/\psi \langle p_T^2 \rangle$ values in p-Pb and Pb-p collisions obtained in this thesis (for the fit combination in Fig. 7.12) compared with the ones obtained in [261]. The values in this thesis are shown with statistical uncertainties only. . . . .	204
8.1	Integrated cross section in pp collisions at $\sqrt{s} = 8$ TeV obtained in this thesis compared with the LHCb [269] and ALICE results [270]. Note that the result obtained in this thesis has no uncertainties since it is calculated as a cross-check.	212
8.2	Number of $J/\psi$ extraction from raw spectra and corrected by integrated $\mathcal{A} \times \epsilon$ (12.44%), compared to the result of the extraction from the $\mathcal{A} \times \epsilon$ corrected spectra for a single fit test. The uncertainties are the statistical uncertainties given by the fit. The relative differences between the results are also shown. . .	218
8.3	Number of $J/\psi$ extraction from raw spectra and corrected by integrated $\mathcal{A} \times \epsilon$ (11.80% for first bin and 13.25% for the last one), compared to the result of the extraction from the $\mathcal{A} \times \epsilon$ corrected spectra for a single fit test. The uncertainties are the statistical uncertainties given by the fit. The relative differences between the results are also shown. . . . .	218

8.4	Summary of the relative $J/\psi$ yield systematic uncertainties in pp collisions. The values represent the minimum and maximum values of the uncertainties in the multiplicity bins. . . . .	218
8.5	Relative $J/\psi$ mean transverse momentum systematic uncertainties in pp collisions. The values represent the minimum and maximum values of the uncertainties in the multiplicity bins. . . . .	219
C.1	Integrated cross section obtained in this thesis compared with the ALICE results [3]. Note that the results obtained in this thesis have no systematic uncertainties since they were calculated as a cross-check. . . . .	249
C.2	Correspondence between ZN event activity classes and $\langle N_{tr}^{corr} \rangle$ . The systematic uncertainty on the multiplicity axis were taken as the uncertainty of $\langle dN_{ch}/d\eta \rangle$ in [239], 3.8%. The uncertainty is not shown on the table nor used in the plots. . . .	250
D.1	Relative $J/\psi$ yield systematic uncertainties in p-Pb collisions at forward (p-Pb) and backward (Pb-p) rapidity for the preliminary results. The values represent the minimum and maximum values of the uncertainties in the multiplicity bins. . . . .	256
D.2	Relative $J/\psi$ mean transverse momentum systematic uncertainties in p-Pb collisions at forward (p-Pb) and backward (Pb-p) rapidity for the preliminary results. The values represent the minimum and maximum values of the uncertainties in the multiplicity bins. . . . .	256

**TABLE****Page**

## LIST OF FIGURES

1.1	Summary table of the Standard Model elementary particles [30]. . . . .	5
1.2	Vacuum polarization Feynmann diagrams in QCD. <b>a)</b> <i>screening</i> . <b>b)</b> <i>anti-screening</i> . . . . . .	6
1.3	Summary of measurements of $\alpha_s$ as a function of the energy scale $Q$ . [33] . . . .	6
1.4	QCD phase diagram as a function of the baryon density and temperature. . . . .	8
1.5	The space-time evolution of a heavy-ion collision. The collision stages, description of QGP formation and transition to ordinary matter are described in the text. Figure taken from [52]. . . . .	10
1.6	Spectroscopic diagram for charmonium family. The bottom row shows the spin, parity and charge conjugation quantum numbers associated with the states above it [80] . . . . .	13
1.7	Heavy quark pair production at leading order through quark annihilation (left) and gluon fusion (middle and right). . . . .	14
1.8	Diagrams that contribute to $c\bar{c}$ hadroproduction via gluon fusion, at order $\alpha_s^3$ . Figure taken from [102] . . . . .	16
1.9	Left: Inclusive $J/\psi$ production cross section as a function of $p_T$ in pp collisions at $\sqrt{s} = 7$ TeV. The bands correspond to several scaled CSM calculations for direct $J/\psi$ [104]. Right: Inclusive $J/\psi$ differential production cross section as a function of $p_T$ . The band correspond to NRQCD calculations [105]. Figures taken from [103] . . . . .	17
1.10	Prompt polarization as a function of $p_T$ in $p\bar{p}$ collisions at $\sqrt{s} = 1.96$ TeV for: (a) $J/\psi$ and (b) $\psi(2S)$ . The line correspond to the $k_T$ factorization model [107] and the band to the LO NRQCD prediction [106]. Figure taken from [101] . . . . .	18
1.11	$Y(1S)$ $p_T$ differential cross section multiplied by the di-muon branching ratio $\text{Br}(Y \rightarrow \mu^+ \mu^-)$ in pp collisions at $\sqrt{s} = 7$ TeV. The maximal envelope of variation of the results due to spin-alignment uncertainty is indicated by the solid band (see [110] for details). Predictions of direct production with CSM and inclusive production with CEM are also shown. The ratio to the data is shown in the middle (CEM) and bottom (CSM) panels. Figure taken from [110] . . . . .	19
1.12	$J/\psi$ relative yield as a function of relative charged particle multiplicity measured at mid-rapidity ( $ \eta  < 1$ ) in pp collisions at $\sqrt{s} = 7$ TeV. Figure taken from [8]. . .	20

1.13	$J/\psi$ relative yield as a function of relative charged particle multiplicity measured at mid-rapidity ( $ \eta  < 1$ ) in pp collisions at $\sqrt{s} = 7$ TeV compared to prediction of the source interaction framework [116]. Figure taken from [116]	20
1.14	$J/\psi$ sequential suppression due to Debye color screening in a QPG. Figure taken from [73]	22
1.15	$J/\psi$ sequential suppression vs. regeneration: Left: $J/\psi$ survival probability. Right: $J/\psi$ transverse momentum behaviour. Figure taken from [127]	23
1.16	Left: $J/\psi$ suppression pattern measured by NA38 and NA 50 collaborations in p-A, S-U and Pb-Pb collisions as a function of the distance of nuclear matter traversed by the charmonium. The band correspond to nuclear absorption estimates. Right: $\psi(2S)$ suppression pattern. Figure taken from [134].	24
1.17	Inclusive $J/\psi$ $R_{AA}$ as a function of $\langle N_{part} \rangle$ measured in Pb-Pb collisions [65] compared to the measurement in Au-Au collisions [138]. The bottom figure shows only the ALICE (Pb-Pb) result compared to several theoretical models including recombination (see text). Figure taken from [139].	26
1.18	Inclusive $J/\psi$ $R_{AA}$ as a function of $\langle N_{part} \rangle$ measured in Pb-Pb collisions [139]. The measurement is compared to transport models (see text). Figure taken from [139].	27
1.19	Parton distribution functions at two different energy scales. The gluon and sea quark distributions are scaled by a factor 0.05 (0.01) in the left (right) plot. Figure taken from [82].	28
1.20	Illustration of $R_i^A(x, Q^2)$ parametrisation. The different parameters used for the parametrisation are also indicated. Figure taken from [143].	29
1.21	The nuclear modifications in lead for valence, sea quarks and gluons at the initial scale $Q_0^2 = 1.69 \text{ GeV}^2$ and at $Q_0^2 = 100 \text{ GeV}^2$ . The shaded areas represent the uncertainty. Figure taken from [143].	30
1.22	$J/\psi$ nuclear absorption dependence with energy. The lines represent the fits to the different nuclear absorption parametrizations. The shaded areas represent the uncertainty. Figure taken from [173].	33
1.23	$J/\psi$ nuclear modification factors ( $R_{dAu}$ ) in d-Au collisions at $\sqrt{s_{NN}} = 200 \text{ GeV}$ for (a) peripheral, (b) central, and (c) ratio of nuclear modification factors of central and peripheral collisions ( $R_{CP}$ ) as a function of rapidity. The results are compared to shadowing with nuclear break-up [143, 175] and gluon saturation models [176, 177]. Figure taken from [174].	34
1.24	$J/\psi$ nuclear modification factors ( $R_{dAu}$ ) as a function of $p_T$ for (a) backward rapidity, (b) mid-rapidity, and (c) forward rapidity in 0-100% centrality integrated d-Au collisions at $\sqrt{s_{NN}} = 200 \text{ GeV}$ . The results are compared to two theoretical models (see text). Figure taken from [178].	35
1.25	$J/\psi$ nuclear modification factor ( $R_{pPb}$ ) as a function of rapidity. The results are compared with several CNM models (see text). Figure taken from [3].	37

1.26	$J/\psi$ nuclear modification factor as a function of $p_T$ at backward (left) and forward (right) rapidity. The results are compared with several CNM models (see text). Figure taken from [4]. . . . .	37
1.27	$J/\psi$ nuclear modification factor ( $Q_{pPb}$ ) as a function of $N_{coll}^{mult}$ at backward (left), mid (middle) and forward (right) rapidity. The results are compared with several CNM models (see text). Figure taken from [5]. . . . .	38
1.28	$J/\psi$ transverse momentum broadening as a function of $N_{coll}^{mult}$ at backward (blue dots) and forward (red dots) rapidity. The results are compared with theoretical calculations (see text). Figure taken from [5]. . . . .	38
1.29	$\psi(2S)$ nuclear modification factor compared to the $J/\psi$ one. The theoretical model calculations for $\psi(2S)$ produce identical values for the coherent energy loss mechanism and a 2-3% larger result for nuclear shadowing, so only calculations for $J/\psi$ are shown. Figure taken from [190]. . . . .	39
1.30	Cross section ratio $Y(2S)/Y(1S)$ as a function of the number of measured tracks at mid rapidity $ \eta  < 2.4$ . The results for pp at 2.76 Pb-Pb at 2.76 TeV and p-Pb at 5.02 TeV are shown. Figure taken from [191]. . . . .	40
1.31	Relative $Y(1S, 2S, 3S)$ cross sections as a function of relative number of measured tracks at mid rapidity $ \eta  < 2.4$ . The results are shown for pp at 2.76 and p-Pb at 5.02 TeV collisions are shown for the three states. The measurement in Pb-Pb collisions at 2.76 is only shown for the ground state. The dotted line shows the linear behaviour. Figure taken from [191]. . . . .	41
1.32	Average transverse momentum as a function of charged particle multiplicity ( $ \eta  < 0.3$ ). Boxes represent the systematic uncertainties, and the statistical ones are negligible. Left: experimental results only. Right: experimental results compared with model predictions. Figure taken from [7]. . . . .	42
2.1	The CERN accelerator complex . . . . .	44
2.2	Schematic representation of the ALICE detector with all its sub detectors during Run1. Figure taken from [207] . . . . .	46
2.3	Schematic representation of the forward detectors. The 5 FMD rings (FMD1, FMD2 and FMD3) can be observed. The two V0 (A and C side) as well as the two T0 detectors are shown. The ITS is sketched in the centre of the figure as well as the front absorber of the Muon Spectrometer (green region). Figure taken from [208] . . . . .	47
2.4	Top: Front view of the SPD barrel and the beam pipe radius (mm). Bottom: Carbon fibre support sector. Figure taken from [213] . . . . .	49
2.5	The TPC layout. Figure taken from [215] . . . . .	50
2.6	Layout of the ALICE Muon Spectrometer. Note that the front absorber and the two first stations are inside the ALICE solenoid magnet. Figure taken from [226].	53
2.7	Layout of the Muon Spectrometer front absorber. Figure taken from [224]. . . . .	54

2.8	Sketch of the working principle of a MWPC. Figure taken from [227]. . . . .	55
2.9	Left: Picture of a quadrant design chamber. Right: Picture of a slat design chamber. Pictures taken from [202]. . . . .	55
2.10	Schematic view of a RPC cross section. Figure taken from [202]. . . . .	56
2.11	The Muon Spectrometer trigger principle. Figure taken from [224]. . . . .	57
3.1	Sketch to illustrate the calculation of $\Delta\varphi$ and $\Delta\theta$ used for the tracklet reconstruction. [243] . . . . .	66
3.2	Top: SPD inactive modules in the inner (left) and outer (right) layers during the first runs of LHC13f data-taking period as a function of the $z$ -vertex position ( $-z_v$ ) and $\varphi$ . Bottom: Number of reconstructed SPD tracklets as a function of $z_v$ and $\varphi$ . . . . .	68
3.3	SPD inactive modules in the inner and outer layers during p-Pb runs. LHC13b, LHC13c, LHC13d and LHC13e correspond to p-Pb and LHC13f to Pb-p beam configurations. . . . .	68
3.4	Number of events classified depending on the vertexer type used to reconstruct the SPD vertex for CINT (left) and CMUL events (right) in LHC13d+e. . . . .	69
3.5	Top left: Evolution of the SPD $z$ -vertex resolution as a function of the number of contributors for CINT events in LHC13d+e. Top right: $z$ -vertex position difference between the primary and the SPD vertexes as a function of the contributors for CINT 7 events in LHC13d+e. Bottom: $z$ -vertex position difference between the primary and the SPD vertexes distribution for CINT (left) and CMUL (right) events in LHC13d+e. . . . .	70
3.6	LHC13d+e SPD $z$ -vertex distribution. The lines represent the $ z_v  < 10$ cm (black) and $ z_v  < 18$ cm (red) cuts. . . . .	71
3.7	Left: generated primary charged particles as a function of event generated $z$ position and particle $\eta$ . Right: Reconstructed tracklets as a function of the event reconstructed $z_v$ position and tracklets $\eta$ . The curves represent the $\eta$ of the SPD layers' extremes seen from a given vertex $z_v$ (Blue: inner layer, Black: Outer layer), Eqs. 3.2 and 3.3. . . . .	73
3.8	SPD $1/\mathcal{A} \times \varepsilon(\eta, z_v)$ obtained with DPMJET simulation for p-Pb . The curves represents the $\eta$ of the SPD layers' extremes seen from a given vertex $z_v$ (Blue: inner layer, Black: Outer layer). . . . .	74
3.9	SPD $\mathcal{A} \times \varepsilon$ ratio to compare the corrections of p-Pb periods with the first (left) and second (right) parts of the Pb-p data-taking periods. . . . .	75
3.10	Fraction of combinatorial background tracklets contributing to the total reconstructed tracklets. The fraction is below 3.5% for the $\eta$ and $z_v$ ranges considered in this analysis. . . . .	75

3.11	Combinatorial background fraction variation for two multiplicity intervals (top). Multiplicity integrated combinatorial background fraction (bottom). The red lines represent the acceptance limits of the SPD. . . . .	76
3.12	Statistical uncertainty of the $1/\mathcal{A}\times\epsilon(\eta, z_v)$ correction . . . . .	77
3.13	Left: Number of tracklets as a function of generated particles in $ \eta  < 0.5$ for events with $ z_v  < 10$ cm. Right: Corrected number of tracklets as a function of the generated charged particles. The black lines represent the line $N_{tr} = N_{ch}$ and $N_{tr}^{corr} = N_{ch}$ respectively. . . . .	79
3.14	Comparison between generated and reconstructed $dN_{ch}/d\eta(\eta)$ for selected events, obtained with the p-Pb MC simulation. . . . .	81
3.15	$dN_{ch}/d\eta(\eta)$ for several $z_v$ - $\eta$ cuts in p-Pb. . . . .	81
3.16	$dN_{ch}/d\eta(\eta)$ results from this analysis (MB events passing QA vertex cuts) for several p-Pb data taking periods compared with the result in [239] (NSD events). . . . .	82
3.17	$dN_{ch}/d\eta(\eta)$ results from this analysis for several p-Pb periods compared with the Pb-p result. . . . .	83
3.18	$dN_{ch}/d\eta(\eta)$ distribution for NSD events in p-Pb collisions at $\sqrt{s_{NN}} = 5.02$ TeV measurement from this thesis compared to ALICE publication result [239]. . . . .	87
3.19	$dN_{ch}/d\eta(\eta)$ distribution for NSD events in p-Pb and Pb-p collisions at $\sqrt{s_{NN}} = 5.02$ TeV measurement from this thesis. . . . .	87
3.20	$N_{tr}^{corr}$ distribution (red) in p-Pb simulation compared to the generated $N_{ch}$ distribution (blue) and its ratio. . . . .	89
3.21	$\tilde{P}_i(N_{ch})$ distribution for several $N_{tr}^{corr}$ bins. The mean $N_{ch}$ value of each distribution is written on the legend for comparison with the corresponding $N_{tr}^{corr}$ . . . . .	89
3.22	p-Pb SPD $\mathcal{A}\times\epsilon$ ratio of the integrated correction over the correction computed with events having $N_{tr} = 1 - 20$ (left) and $N_{tr} = 21 - 60$ (right) in $ \eta  < 0.5$ . . . . .	90
3.23	Illustration of the variation of the multiplicity resolution with $z_v$ due to $\mathcal{A}\times\epsilon$ variations. The plots to the left are the $N_{tr}^{corr}$ as a function of generated $N_{ch}$ (top) and the $\tilde{P}_{39}(N_{ch})$ distribution (bottom) for events with $-3 < z_v < 0$ . The plots to the right are the equivalent to the left ones but for events with $4 < z_v < 5.5$ . . . . .	91
3.24	Comparison of generated $N_{ch}$ distribution (blue) and $N_{tr}^{corr}$ with event multiplicity re-distribution measured distribution (red). . . . .	92
3.25	Biased multiplicity distribution $P_{biased}(N_{ch})$ measured in p-Pb collisions at $\sqrt{s_{NN}} = 5.02$ TeV. . . . .	93
3.26	Left: Number of corrected tracklets with event multiplicity re-distribution as a function of the generated charged particles in p-Pb simulation. Right: $N_{tr}^{corr}$ distribution obtained in the p-Pb simulation. The horizontal (left) and vertical (right) lines represent $N_{tr}^{corr}$ bin limits. . . . .	94
3.27	Number of corrected tracklets as a function of the generated charged particles. . . . .	95

4.1	Top: Generated event-averaged number of charged particles, reconstructed event-averaged number of tracklets and corrected event-averaged number of tracklets (Using $\max(\langle N_{tr} \rangle(z_v))$ as reference) as a function of $z$ -vertex position. Bottom: Generated charged particle distribution, reconstructed tracklets distribution and corrected tracklets distribution. . . . .	101
4.2	Poisson fits of the number of missing tracklets with respect to the generated number of charged particles distribution, at a given $z$ -vertex for events with 2 (left), 10 (middle) and 40 (right) reconstructed tracklets. $p_0$ is the mean of the Poisson distribution found by the fit. . . . .	102
4.3	$N_{tr}^{corr}$ as a function of $N_{ch}^{gen}$ scatter plots. The results are shown for three reference choices: $\langle N_{tr} \rangle(z_v^0) = \max(\langle N_{tr} \rangle(z_v))$ (left column), $\text{mean}(\langle N_{tr} \rangle(z_v))$ (middle column) and $\min(\langle N_{tr} \rangle(z_v))$ (right column), and three different $z_v$ regions (from top to bottom). . . . .	104
4.4	Number of generated charged particles in $N_{tr}^{corr}$ bins (from left to right) as a function of $z_v$ scatter plots for three reference choices: $\langle N_{tr} \rangle(z_v^0) = \max(\langle N_{tr} \rangle(z_v))$ (top row), $\text{mean}(\langle N_{tr} \rangle(z_v))$ (middle row) and $\min(\langle N_{tr} \rangle(z_v))$ (bottom row). . . . .	105
4.5	Average number of generated charged particles in $N_{tr}^{corr}$ bins (from left to right) as a function of $z_v$ for three reference choices: $\langle N_{tr} \rangle(z_v^0) = \max(\langle N_{tr} \rangle(z_v))$ (top row), $\text{mean}(\langle N_{tr} \rangle(z_v))$ (middle row) and $\min(\langle N_{tr} \rangle(z_v))$ (bottom row). The values in the grey boxes are the maximum deviations respect to $\langle N_{ch}^{gen} \rangle$ . . . . .	106
4.6	Reconstructed (blue) and corrected (red) tracklets distributions in LHC13d+e data for CINT (left) and CMUL (triggers). . . . .	106
4.7	Top: Corrected tracklets distribution in LHC13b2_efix1 MC. Vertical lines delimit the multiplicity bins chosen for the analysis. Bottom: Generated $N_{ch}$ vs $N_{tr}^{corr}$ scatter plot. Vertical lines delimit the multiplicity bins chosen for the analysis. The fits are used to get the global $\alpha$ correction (black line) and the bin by bin ones (coloured lines). The black dots are the profile of the scatter plot. . . . .	109
4.8	Left: Comparison of generated $\langle N_{ch} \rangle$ and reconstructed $\langle N_{ch} \rangle$ (obtained as $\bar{\alpha} \times \langle N_{tr} \rangle$ ) bin by bin. Right: Ratio of the number of generated charged particles and corrected number of tracklets corrected by the missing efficiency through the global $\bar{\alpha}$ factor. . . . .	110
4.9	Ratio of the number of generated charged particles and corrected number of tracklets corrected by the missing efficiency through the bin by bin $\alpha$ factors. . . . .	110
4.10	Left: Comparison of $\langle N_{tr}^{corr} \rangle(z)$ for MB and CMUL triggers in p-Pb data. Right: Comparison of the two subperiods in Pb-p data for CMUL trigger. . . . .	112
4.11	Comparison of the event-averaged tracklets vs $z_v$ for MB (left) and CMUL (right) triggers in p-Pb and first part of Pb-p data periods. . . . .	113
4.12	Left: Event-averaged number of tracklets as a function of $z$ -vertex for the first and second subperiods of the Pb-p MC production. Right: Comparison of p-Pb and Pb-p (first subperiod) $\langle N_{tr} \rangle(z_v)$ MC distributions. . . . .	115



4.13	Event-averaged number of tracklets as a function of $z$ -vertex for data and simulated events in p-Pb and first subperiod of Pb-p. . . . .	116
4.14	Number of reconstructed tracklets distribution in LHC13d+e period for events passing and not passing the vertex QA for CINT (left) and CMUL (right) trigger. . . . .	119
4.15	Left: SPD $z_v$ distribution for LHC13d+e periods. Right: LHC13c and LHC13d+e number of corrected tracklets distribution comparison. . . . .	122
4.16	Reference corrected tracklets distribution compared with the resulting distribution for the $\langle\mu\rangle$ factors corresponding to p-Pb and Pb-p periods and its ratio. Left: the vertex merging algorithm is switched off; the observed effect is only due to the choice of the main collision. Right: the vertex merging algorithm is switched on; the observed effect results from the two biases present in data. . . . .	123
4.17	Left: Fraction of events in the pile-up distributions (in multiplicity bins) with respect to the reference distribution. Right: $\langle N_{tr}^{corr} \rangle$ ratios of the pile-up over reference values in multiplicity bins. . . . .	124
4.18	Variation on the number of di-muon events in each multiplicity bin due to bin-flow. Each point correspond to a different execution of the task. . . . .	126
4.19	Variation on $\langle N_{tr}^{corr} \rangle$ in each multiplicity bin due to bin-flow. Each point correspond to a different execution of the task. . . . .	126
5.1	$J/\psi$ acceptance as a function of $p_T$ and $y$ . [117]. . . . .	134
5.2	Sketch showing the arrangement of the chambers into stations and the possible responses of one station to a track. . . . .	136
5.3	Visualization of chamber 6 showing its different substructures: DE (red), PCB (blue), BP (green) and MANU (yellow). . . . .	137
5.4	Sketch of a CDA (left) and ACDA (right) (see text for details) to illustrate the bias on the efficiency measurement from reconstructed tracks. . . . .	138
5.5	Top: Measured single muon tracking efficiency as a function of run number for data-taking period LHC13e. Bottom: Measured single muon tracking efficiency for chambers 3 (left) and 4 (right) as a function of run for the same period. . . . .	139
5.6	Measured single muon tracking efficiency for DEs 300, 301, 400 and 401 as a function of run for the LHC13e period. . . . .	140
5.7	Status map at MANU level showing the dead zones (red) in chambers 3 (left) and 4 (right) during run 196091 of the LHC13e period. . . . .	140
5.8	Single muon tracking efficiency results from reconstructed tracks in data and MC for LHC13f period as a function of run number (top left), $\phi$ (top right), rapidity (bottom left) and $p_T$ (bottom right). . . . .	141
5.9	Left: Chamber 10 average measured single muon tracking efficiency during LHC13f period as a function of DE. The problematic DEs are highlighted with coloured squares. Right: Chamber 10 measured single muon tracking efficiency as a function of run during LHC13f period. . . . .	142

5.10	Chamber 10 cluster map reconstructed in data (left) and MC (right). The problematic DEs are highlighted with coloured squares following the same convention as in Fig. 5.9. . . . . .	143
5.11	Chamber 8 cluster map reconstructed in data (left) and MC (right). The dead PCB (only in data) which causes the ACDA in chamber 10 is highlighted with a black square. . . . .	143
5.12	Reject List used in reconstruction for the LHC13d, LHC13e and LHC13f p-Pb periods. . . . .	144
5.13	Comparison of the measured single muon tracking efficiency in data and MC as a function of run number in period LHC13f for DEs 725 (left) and 1025 (right). . .	144
5.14	Single muon tracking efficiency results from reconstructed tracks for LHC13f period. The plots show the comparison of the data measurements with the realistic simulation with and without the reject list. The efficiency is shown as a function of run number (top left), $\phi$ (top right), $y$ (bottom left) and $p_T$ (bottom right). . . .	145
5.15	Single muon efficiency polar maps ( $y, \phi$ ), for two different $p_T$ cuts, $p_T > 1$ GeV/ $c$ (left) and $p_T > 3$ GeV/ $c$ (right). The top plots show the efficiency maps for data, and the bottom ones the corresponding maps for MC. . . . .	147
5.16	Single muon efficiency polar maps ( $y, \phi$ ) (for $p_T > 1$ GeV/ $c$ ) for $\mu^+$ (left) and $\mu^-$ (right). The top plots show the efficiency maps for data, and the bottom ones the corresponding maps for MC. . . . .	148
5.17	Single muon efficiency polar maps ( $y, \phi$ ) for run 196485 (left) and run 197348 (right). The top plots show the efficiency maps for data, and the bottom ones the corresponding maps for MC. . . . .	149
5.18	Ratio data over MC of the ( $y, \phi$ ) efficiency maps in polar coordinates. The two top plots show the variation of the ratio with the $p_T$ range under consideration. The two middle plots show the variation with the sign of the muon charge. The two bottom plots show the variation of the ratio with the run. . . . .	150
6.1	$J/\psi$ $\mathcal{A} \times \epsilon$ for LHC13d+e (left) and LHC13f (right) periods . . . . .	154
6.2	Tail fits tests for $J/\psi$ on pure signal simulation using an Extended Crystal Ball function. The figure shows: raw $J/\psi$ spectrum (blue dots), $\mathcal{A} \times \epsilon$ corrected spectrum (red dots), raw spectrum fit (magenta line), corrected spectrum fit (green line) and corrected spectrum fit using the tails parameters extracted from the raw spectrum (black line). The vertical lines delimit the fitting range. . . . .	155
6.3	Tail fits tests for $\psi(2S)$ on pure signal simulation using an Extended Crystal Ball (CB2) function. The figure shows: raw $\psi(2S)$ spectrum (blue dots), $\mathcal{A} \times \epsilon$ corrected (using $J/\psi$ correction) spectrum (red dots), raw spectrum fit (magenta line), corrected spectrum fit (black line) and corrected spectrum fit using the tails parameters extracted from the corrected $J/\psi$ spectrum (green line). The vertical lines delimit the fitting range. . . . .	156

6.4	Tail fits for $J/\psi$ on pure signal simulation using a NA60 function. The figure shows the $J/\psi$ $\mathcal{A} \times \mathcal{E}$ corrected spectrum (red dots) and its fit. The vertical lines delimit the fitting range. . . . .	157
6.5	Example of signal extraction for the integrated invariant mass spectra in p-Pb (left) and Pb-p (right) for a fit combination choice (CB2+VWG+Range= 2.0 – 5.0+ $\sigma_{\psi(2S)} = 0.9 \cdot \sigma_{J/\psi}$ ). . . . .	158
6.6	Example of signal extraction for the multiplicity bins invariant mass spectra in p-Pb for a fit combination choice (CB2+VWG+Range= 2.0 – 5.0+ $\sigma_{\psi(2S)} = 0.9 \cdot \sigma_{J/\psi}$ ). . . . .	159
6.7	Di-muon trigger normalisation factor in Pb-p as a function of run. Left: Integrated in multiplicity. Right: Multiplicity bin $N_{tr}^{corr}$ 17-20. . . . .	162
6.8	Example of signal extraction test set for the relative yield systematic uncertainty in a multiplicity bin in p-Pb. The red solid line is the unweighted mean of all the values (Eq.6.14) and the dotted red line is the 1- $\sigma$ dispersion of all the tests (Eq.B.4), which represents the signal extraction systematic uncertainty in the bin. . . . .	167
6.9	(Left) Relative signal extraction systematic uncertainty in multiplicity bins in p-Pb. (Right) Relative signal extraction systematic uncertainty in multiplicity bins in Pb-p. These values are for one single execution of the multiplicity analysis. See also Fig. 6.10 for the final values. . . . .	168
6.10	Relative signal extraction systematic uncertainty variations due to bin-flow in multiplicity bins in p-Pb. Each value in a bin corresponds to the result of a set of signal extraction tests (as in Fig. 6.9) obtained in a execution test. The figure shows the relative difference between the most different results ( $\Delta_{max}$ ), the mean value (red line) and the 1- $\sigma$ dispersion among the values ( $\sigma$ ). . . . .	169
6.11	p-Pb variation on the number of equivalent MB events in multiplicity bins due to bin-flow. The figure shows the relative difference between the most different results, $\Delta_{max}$ , the mean value (red line), the error on the mean (dotted line) and the 1- $\sigma$ dispersion among the values $\sigma$ . . . . .	171
6.12	$\mathcal{A} \times \mathcal{E}$ variations (ratio varied over nominal correction) due to changes in the input MC distributions and the used input distributions (the blue curves represent the nominal and the red curves the varied distributions). The results are shown for four combinations of extreme variations of the $p_T$ and $y$ distributions: hard- $y$ and soft- $p_T$ (top left), hard- $y$ and hard- $p_T$ (top right), soft- $y$ and soft- $p_T$ (bottom left), soft- $y$ and hard- $p_T$ (bottom right). . . . .	173
6.13	Integrated signal extraction with different $\mathcal{A} \times \mathcal{E}$ corrections. $\langle N_{J/\psi} \rangle$ for the four varied $\mathcal{A} \times \mathcal{E}$ corrections are shown in blue and the nominal result as the red line. The figure also shows the relative difference between the most different results ( $\Delta_{max}$ ), between the nominal value and the more distant value ( $\Delta_{nom}$ ) and the 1- $\sigma$ dispersion among the values ( $\sigma$ ) (Eq. B.4). The systematic uncertainty due to the $\mathcal{A} \times \mathcal{E}$ is taken as $\Delta_{max}$ which is 0.74%. . . . .	174

6.14	Relative signal extraction with different $\mathcal{A} \times \mathcal{E}$ corrections in multiplicity bins. $\langle N_{J/\psi}^R \rangle^i$ for the four varied $\mathcal{A} \times \mathcal{E}$ corrections are shown in blue and the nominal result as the red line. The figure also shows the relative difference between the most different results ( $\Delta_{max}$ ), between the nominal value and the more distant value ( $\Delta_{nom}$ ) and the 1- $\sigma$ dispersion among the values ( $\sigma$ ) (Eq. B.4). . . . .	175
6.15	Relative number of $J/\psi$ , $\langle N_{J/\psi}^R \rangle^i$ , extracted using the nominal $\mathcal{A} \times \mathcal{E}$ correction but four different execution of the analysis task. The result of each test are the blue points and the "nominal" result is the red line. The comparison of the results in different execution tests give an idea of the bin-flow effect on the signal extraction in each multiplicity bin. . . . .	176
6.16	Variation on the relative yield in multiplicity bins due to bin-flow, $\mathcal{A} \times \mathcal{E}$ and signal extraction. The blue points are the average values of the relative yield obtained with Eqs. 6.13 and 6.14 in each execution test. The red line shows the average of the values obtained from the execution tests in each bin. The dotted line is the statistical error. $\sigma$ is the value of the 1- $\sigma$ dispersion of the values for each execution test in a bin. . . . .	177
6.17	$J/\psi$ yield as a function of number of corrected tracklets obtained from the toy MC. The vertex merging is switched off, so the observed effect is due to taking all the $J/\psi$ in the event. The figure shows that the effect has a similar size in p-Pb (left) and Pb-p (right). . . . .	178
6.18	$J/\psi$ yield as a function of number of corrected tracklets obtained from the toy MC with vertex merging and taking all the $J/\psi$ in the event for p-Pb (left) and Pb-p (right). . . . .	179
6.19	$J/\psi$ yield as a function of number of corrected tracklets obtained from the toy MC using different parametrizations for the input yield distribution in Pb-p. Top left: $f_1$ in the range $N_{tr}^{corr}[1,30]$ ; Top right: $f_2 = p_0 + p_1 \cdot x + p_2 \cdot x^2$ ; Bottom left: $f_4 = p_0 + p_1 \cdot x + p_4 \cdot x^4$ ; Bottom right: $f_{1/2} = p_0 + p_{1/2} \cdot x^{1/2}$ . . . . .	181
6.20	$J/\psi$ yield as a function of number of corrected tracklets obtained from the toy MC using different parametrizations for the input yield distribution in Pb-p. Top left: $f_1 = p_0 + p_1 \cdot x$ ; Top right: $f_2 = p_1 \cdot x + p_2 \cdot x^2$ ; Bottom left: $f_3 = p_0 + p_2 \cdot x^2 + p_3 \cdot x^3$ ; Bottom right: $f_4 = p_0 + p_1 \cdot x^1 + p_4 \cdot x^4$ . . . . .	182
7.1	Raw di-muon $\langle p_T \rangle$ invariant mass spectrum in p-Pb collisions . . . . .	187
7.2	Multiplicity integrated $\mathcal{A} \times \mathcal{E}$ corrected di-muon $\langle p_T \rangle$ invariant mass spectra in p-Pb (left) and Pb-p (right) collisions. The spectra are fitted with a fit combination choice (CB2+VWG+Range $^{inv.mass}=2.0-5.0+\sigma_{\psi(2S)}=1.1 \cdot \sigma_{J/\psi}$ +Pol2+Range $\langle p_T \rangle=2.0-5.0$ ) and the values of the extracted $J/\psi$ $\langle p_T \rangle$ are shown. . . . .	188
7.3	$J/\psi$ $\langle p_T \rangle$ extraction in multiplicity bins in p-Pb for a fit combination choice (CB2+VWG+Range $^{inv.mass}=2.0-5.0+\sigma_{\psi(2S)}=1.1 \cdot \sigma_{J/\psi}$ +Pol2+Range $\langle p_T \rangle=2.0-5.0$ ). . . . .	190

7.4	Values of $\left( \frac{\langle p_T^{J/\psi} \rangle_i}{\langle p_T^{J/\psi} \rangle_{int.}} \right)_j$ relative $\langle p_T \rangle$ extraction tests as a function of $j$ -th test for the $J/\psi$ $\langle p_T \rangle$ systematic uncertainty computation in a multiplicity bin in Pb-p. The unweighted average and the $1-\sigma$ dispersion are shown as the red solid and dotted lines respectively. The test-axis is zoomed-in to show only a fraction of the total 1536 tests. . . . .	192
7.5	Example of relative $J/\psi$ $\langle p_T \rangle$ extraction systematic uncertainty in multiplicity bins in p-Pb (left) and Pb-p (right). The values correspond to one single execution of the analysis task. See also Fig. 7.6 for the final values. . . . .	192
7.6	Relative $J/\psi$ $\langle p_T \rangle$ extraction systematic uncertainty variations due to bin flow in multiplicity bins in Pb-p. Each value corresponds to the result of a set of extraction tests (Fig. 7.5) for a given execution test. The difference between the most different results ( $\Delta_{max}$ ), mean value (red line) and $1-\sigma$ dispersion among the values are shown. . . . .	193
7.7	Integrated $J/\psi$ $\langle p_T \rangle$ extraction with the four varied $\mathcal{A} \times \mathcal{E}$ corrections are shown in blue and the nominal result as the red line. The figure also shows the relative difference between the most different results ( $\Delta_{max}$ ), between the nominal value and the more distant value ( $\Delta_{nom}$ ) and the $1-\sigma$ dispersion among the values ( $\sigma$ ). The systematic uncertainty due to the $\mathcal{A} \times \mathcal{E}$ is $\Delta_{max}$ which is 0.07% . . . . .	194
7.8	Variation on the relative $J/\psi$ $\langle p_T \rangle$ in multiplicity bins due to bin-flow, $\mathcal{A} \times \mathcal{E}$ and signal extraction. The blue points are the average values of the relative $\langle p_T \rangle$ obtained with Eq. 7.4 in each execution test. The red line shows the average of the values obtained from the execution tests in each bin. The dotted line is the statistical error. $\sigma$ is the value of the $1-\sigma$ dispersion of the values for each execution test in a bin. . . . .	194
7.9	$\mathcal{A} \times \mathcal{E}$ corrected reconstructed di-muon $\langle p_T \rangle$ from $J/\psi$ decays invariant mass spectrum in MC for p-Pb. The red line is the fit using Eq. 7.2.3. . . . .	196
7.10	$\mathcal{A} \times \mathcal{E}$ corrected p-Pb di-muon $\langle p_T \rangle$ invariant mass spectrum for integrated (top left) and multiplicity bins. The $J/\psi$ $\langle p_T \rangle$ extraction fits are performed using a parametrisation of the $J/\psi$ $\langle p_T \rangle$ variation with the invariant mass extracted from MC. . . . .	197
7.11	Combined fits of invariant mass and di-muon $\langle p_T \rangle$ invariant mass spectra in p-Pb for integrated (top left) and multiplicity bins. The fit combination used is $(CB2+VWG+Range^{inv.mass}=2-5+\sigma_{\psi(2S)}=1.1 \cdot \sigma_{J/\psi}+Pol2+Range^{\langle p_T \rangle}=2-5)$ . . . . .	199
7.12	Multiplicity integrated $\mathcal{A} \times \mathcal{E}$ corrected di-muon $\langle p_T^2 \rangle$ spectra in p-Pb (left) and Pb-p (right) collisions. The spectra are fitted with a fit combination choice $(CB2+VWG+Range^{inv.mass}=2.0-5.0+\sigma_{\psi(2S)}=1.1 \cdot \sigma_{J/\psi}+Pol2+Range^{\langle p_T \rangle}=2.0-5.0)$ and the values of the extracted $J/\psi$ $\langle p_T \rangle$ are shown. . . . .	203
7.13	$J/\psi$ $\langle p_T^2 \rangle$ extraction in multiplicity bins in p-Pb for a fit combination choice $(CB2+VWG+Range^{inv.mass}=2.0-5.0+\sigma_{\psi(2S)}=0.9 \cdot \sigma_{J/\psi}+Pol2+Range^{\langle p_T \rangle}=2.0-4.7)$ . . . . .	205

8.1	Top: Average number of tracklets (blue) and average number of corrected tracklets (red) as a function of $z_v$ in $ \eta  < 0.5$ for MB collisions. Bottom: Tracklets (blue) and corrected tracklets (red) distributions in $ \eta  < 0.5$ for MB collisions. . . . .	209
8.2	SPD inactive modules in the inner and outer layers during pp 8 TeV runs. The considered data taking periods are LHC12h and LHC12i. . . . .	210
8.3	$J/\psi$ $\mathcal{A} \times \epsilon$ in pp collisions (LHC12h+i VZERO-triggered events). . . . .	211
8.4	Example of signal extraction for the integrated invariant mass spectrum in pp collisions using the fit combination (CB2+POL2EXP+Range=2.0-5.0 + $\sigma_{\psi(2S)} = 0.9 \cdot \sigma_{J/\psi}$ ). . . . .	212
8.5	Example of signal extraction for the integrated invariant mass spectrum in pp collisions. . . . .	213
8.6	$J/\psi$ signal extraction in multiplicity bins in pp for the following fit combination choice (CB2+POL2EXP +Range <sup>inv.mass</sup> =2.0-5.0+ $\sigma_{\psi(2S)} = 1.1 \cdot \sigma_{J/\psi}$ ). . . . .	214
8.7	$J/\psi$ $\langle p_T \rangle$ extraction in multiplicity bins in pp for the following fit combination choice (NA60+POL2EXP+Range <sup>inv.mass</sup> =2.0-5.0+ $\sigma_{\psi(2S)} = 1.1 \cdot \sigma_{J/\psi}$ +Pol2+Range <sup><math>\langle p_T \rangle</math></sup> =2.0-5.0 ). . . . .	215
8.8	$\mathcal{A} \times \epsilon$ variations (ratio of varied over nominal correction) due to changes in the input MC distributions, and the corresponding input distributions (the blue curves represent the nominal and the red curves the varied distributions). The results are shown for four combinations of extreme variations of the $p_T$ and $y$ distributions: soft- $y$ and hard- $p_T$ (top left), soft- $y$ and soft- $p_T$ (top right), hard- $y$ and hard- $p_T$ (bottom left), hard- $y$ and soft- $p_T$ (bottom right). . . . .	217
9.1	$J/\psi$ relative $dN_{J/\psi}/dy$ at backward (blue) and forward (red) rapidity as a function of relative charged particle multiplicity measured at mid-rapidity ( $ \eta  < 1$ ) in p-Pb collisions at $\sqrt{s_{NN}} = 5.02$ TeV. . . . .	224
9.2	$J/\psi$ relative transverse momentum at backward (blue) and forward (red) rapidity as a function of relative charged particle multiplicity measured at mid-rapidity ( $ \eta  < 1$ ) in p-Pb collisions at $\sqrt{s_{NN}} = 5.02$ TeV. . . . .	225
9.3	$J/\psi$ absolute $\langle p_T \rangle$ as a function of the absolute $dN_{ch}/d\eta$ ( $ \eta  < 1$ ) in p-Pb collisions at $\sqrt{s_{NN}} = 5.02$ TeV. . . . .	225
9.4	Comparison of $J/\psi$ and D-meson relative yields as a function of the relative charged particle multiplicity in p-Pb collisions at $\sqrt{s_{NN}} = 5.02$ TeV [274]. Note that the results shown here correspond to the ALICE preliminary (see App. D) . . . . .	227
9.5	Comparison of $J/\psi$ relative yield as a function of relative charged particle multiplicity measured at mid-rapidity ( $ \eta  < 1$ ) in pp collisions at $\sqrt{s} = 7$ TeV [8, 111] (green) with the result in pp collisions at 8 TeV (black). The dotted line represents the linear behaviour. . . . .	228

9.6	Comparison of $J/\psi$ relative $dN_{J/\psi}/dy$ at backward (blue) and forward (red) rapidity as a function of relative charged particle multiplicity measured at mid-rapidity ( $ \eta  < 0.5$ ) in p-Pb collisions at $\sqrt{s_{NN}} = 5.02$ TeV (ALICE Preliminary) with the result in pp collisions at 8 TeV (black). The dotted line represents the linear behaviour. . . . .	229
9.7	Comparison of $J/\psi$ relative transverse momentum at backward (blue) and forward (red) rapidity as a function of relative charged particle multiplicity measured at mid-rapidity ( $ \eta  < 0.5$ ) in p-Pb collisions at $\sqrt{s_{NN}} = 5.02$ TeV (ALICE Preliminary) with the result in pp collisions at 8 TeV (black). . . . .	230
9.8	$J/\psi$ transverse momentum broadening as a function of charged particle multiplicity ( $ \eta  < 1$ ) at forward and backward rapidity in p-Pb collisions at $\sqrt{s_{NN}} = 5.02$ TeV. . . . .	231
9.9	$R_{FB}$ in p-Pb collisions at $\sqrt{s_{NN}} = 5.02$ TeV as a function of absolute charged particle multiplicity ( $ \eta  < 1$ ). The red box around unity represents the global uncertainty. . . . .	233
9.10	$\tilde{Q}_{pPb}^{mult}$ as a function of $\tilde{N}_{coll}^{mult}$ at backward (top) and forward (bottom) rapidities in p-Pb collisions at $\sqrt{s_{NN}} = 5.02$ TeV. The results are compared to $Q_{pPb}^{mult}$ as a function of $N_{coll}^{mult}$ obtained using the ALICE centrality selection in p-Pb collisions [5, 261]. . . . .	235
9.11	$J/\psi$ transverse momentum broadening as a function of $\tilde{N}_{coll}^{mult}$ at backward (top) and forward (bottom) rapidity in p-Pb collisions at $\sqrt{s_{NN}} = 5.02$ TeV. The results are compared to those obtained as a function of $N_{coll}^{mult}$ using the ALICE centrality selection in p-Pb collisions[5, 261]. . . . .	237
A.1	Event distribution of the sum of the amplitudes of the VZERO detectors in Pb-Pb collisions. The centrality classes are shown as percentages. The red line is the fit with the NBD-Glauber fit. Figure taken from [54]. . . . .	244
A.2	Top: Scatter plot of the number of participating nucleons as a function of impact parameter in p-Pb (left) and Pb-Pb (right) collisions. Bottom: Scatter plot of the multiplicity as a function of the number of participating nucleons in p-Pb (left) and Pb-Pb (right) collisions. Figure taken from [54]. . . . .	245
A.3	Pseudorapidity density of charged particles at mid rapidity (integrated in $-1 < \eta < 0$ ), $N_{ch}$ , per participant nucleon as a function of $N_{ch}$ for different centrality estimators. Figure taken from [54]. . . . .	246

C.1	Top: Relative yield comparison in p-Pb and Pb-p between $N_{tr}^{corr}$ multiplicity estimator used in this thesis and ZN estimator used in [261]. Bottom: The relative yields are fitted with a third order polynomial function, and the fit results of the two analyses for the two collision systems are compared by performing the ratio. The bands in the ratio correspond to the 0.95 confidence interval in the fits. Note that the results in this figure are not the final results in [261] nor the final results of this thesis. . . . .	251
C.2	Top: Absolute $J/\psi$ $\langle p_T \rangle$ comparison in p-Pb and Pb-p between $N_{tr}^{corr}$ multiplicity estimator used in this thesis and ZN estimator used in [261]. Bottom: The results are fitted with a third order polynomial function, and its ratio is shown in the bottom panel. The bands represent the 0.95 level of confidence in the fits. Note that the results in this figure are not the final results in [261] nor the final results of this thesis. . . . .	253
D.1	$J/\psi$ relative yield at backward (blue) and forward (red) rapidity as a function of relative charged particle multiplicity measured at mid-rapidity ( $ \eta  < 0.5$ ) in p-Pb collisions at $\sqrt{s_{NN}} = 5.02$ TeV. . . . .	256
D.2	$J/\psi$ relative transverse momentum at backward (blue) and forward (red) rapidity as a function of relative charged particle multiplicity measured at mid-rapidity ( $ \eta  < 0.5$ ) in p-Pb collisions at $\sqrt{s_{NN}} = 5.02$ TeV. . . . .	257
D.3	Comparison between preliminary (full symbols) and latest (open symbols) results of $J/\psi$ relative yield as a function of relative charged particle multiplicity ( $ \eta  < 0.5$ for preliminaries and $ \eta  < 1$ for latest) in p-Pb collisions at 5.02 TeV. . . . .	258
D.4	Comparison between preliminary (full symbols) and latest (open symbols) results of $J/\psi$ relative transverse momentum as a function of relative charged particle multiplicity ( $ \eta  < 0.5$ for preliminaries and $ \eta  < 1$ for latest) in p-Pb collisions at 5.02 TeV. . . . .	259
E.1	Top: Raw average V0A multiplicity as a function of $z$ -vertex in p-Pb (left) and Pb-p (right). Middle: Corrected average V0A multiplicity as a function of $z$ -vertex in p-Pb (left) and Pb-p (right). Bottom: Corrected V0A multiplicity distribution in p-Pb (left) and Pb-p (right). . . . .	262
E.2	$J/\psi$ relative yield in p-Pb (red) and Pb-p (blue) collisions as a function of the relative multiplicity. Two estimators are employed: SPD tracklets (full symbols) ( $ \eta  < 1$ ) and V0A amplitude (open symbols) ( $2.8 < \eta < 5.1$ ). . . . .	263

**FIGURE****Page**



## BIBLIOGRAPHY

- [1] T. Matsui and H. Satz, “ $J/\psi$  suppression by quark-gluon plasma formation,” *Phys. Lett.*, vol. B178, pp. 416–422, October 1986.
- [2] B. Abelev *et al.*, “ $J/\psi$  suppression at forward rapidity in Pb-Pb collisions at  $\sqrt{s_{NN}} = 2.76$  TeV,” *Phys. Rev. Lett.*, vol. 109, p. 072301, 2012.
- [3] B. Abelev *et al.*, “ $J/\psi$  production and nuclear effects in p-Pb collisions at  $\sqrt{s_{NN}} = 5.02$  TeV,” *JHEP*, vol. 1402, p. 073, 2014.
- [4] J. Adam *et al.*, “Rapidity and transverse-momentum dependence of the inclusive  $J/\psi$  nuclear modification factor in p-Pb collisions at  $\sqrt{s_{NN}} = 5.02$  TeV,” *JHEP*, vol. 06, p. 055, 2015.
- [5] J. Adam *et al.*, “Centrality dependence of inclusive  $J/\psi$  production in p-Pb collisions at  $\sqrt{s_{NN}} = 5.02$  TeV,” *arXiv: 1506.08808*, 2015.
- [6] B. Abelev *et al.*, “Long-range angular correlations on the near and away side in p-Pb collisions at  $\sqrt{s_{NN}} = 5.02$  TeV,” *Phys. Lett.*, vol. B79, pp. 29–41, 2013.
- [7] B. Abelev *et al.*, “Multiplicity dependence of the average transverse momentum in pp, p-Pb and Pb-Pb collisions at the LHC,” *Phys. Lett.*, vol. B727, pp. 371–380, 2013.
- [8] B. Abelev *et al.*, “ $J/\psi$  Production as a Function of Charged Particle Multiplicity in pp Collisions at  $\sqrt{s} = 7$  TeV,” *Phys. Lett.*, vol. B712, pp. 165–175, 2012.
- [9] B. Alver *et al.*, “Phobos results on charged particle multiplicity and pseudorapidity distributions in Au+Au, Cu+Cu, d+Au, and p+p collisions at ultra-relativistic energies,” *Phys. Rev.*, vol. C83, p. 024913, 2011.
- [10] S. Vogel, P. B. Gossiaux, K. Werner, and J. Aichelin, “Heavy Quark Energy Loss in High Multiplicity Proton Proton Collisions at LHC,” *Phys. Rev. Lett.*, vol. 107, p. 032302, 2011.
- [11] F. Halzen and A. Martin, *Quarks and leptons: an introductory course of Elementary Particle Physics*.
- [12] S. L. Glashow, “Partial-symmetries of weak interactions,” *Nuclear Physics*, vol. 22, no. 4, pp. 579 – 588, 1961.

- [13] Weinberg, Steven, “A Model of Leptons,” *Phys. Rev. Lett.*, vol. 19, no. 21, pp. 1264–1266, 1967.
- [14] A. Salam, “Weak and electromagnetic interactions,” p. 367 of *Elementary Particle Theory*, ed. N. Svartholm (Almqvist and Wiksells, Stockholm, 1969).
- [15] S. L. Glashow, J. Iliopoulos, and L. Maiani, “Weak Interactions with Lepton-Hadron Symmetry,” *Phys. Rev. D*, vol. 2, p. 1285, 1292 1970.
- [16] F. Englert and R. Brout, “Broken Symmetry and the Mass of Gauge Vector Mesons,” *Phys. Rev. Lett.*, vol. 13, no. 9, pp. 321–323, 1964.
- [17] P. Higgs, “Broken symmetries, massless particles and gauge fields,” *Physics Letters*, vol. 12, no. 2, pp. 132–133, 1964.
- [18] P. W. Higgs, “Broken Symmetries and the Masses of Gauge Bosons,” *Phys. Rev. Lett.*, vol. 13, no. 16, pp. 508–509, 1964.
- [19] G. S. Guralnik, C. R. Hagen, and T. W. B. Kibble, “Global Conservation Laws and Massless Particles,” *Phys. Rev. Lett.*, vol. 13, no. 20, pp. 585–587, 1964.
- [20] P. Higgs, “Spontaneous Symmetry Breakdown without Massless Bosons,” *Phys. Rev.*, vol. 145, no. 4, pp. 1156–1163, 1966.
- [21] T. W. B. Kibble, “Symmetry Breaking in Non-Abelian Gauge Theories,” *Phys. Rev.*, vol. 155, no. 5, pp. 1554–1561, 1967.
- [22] G. Aad *et al.*, “Observation of a new particle in the search for the Standard Model Higgs boson with the ATLAS detector at the LHC,” *Phys. Lett.*, vol. B716, pp. 1–29, 2012.
- [23] S. Chatrchyan *et al.*, “Observation of a new boson at a mass of 125 GeV with the CMS experiment at the LHC,” *Physics Letters B*, vol. 716, no. 1, pp. 30–61, 2012.
- [24] Y. Neéman, “Derivation of strong interactions from a gauge invariance,” *Nuclear Physics*, vol. 26, no. 2, pp. 0029–5582, 1961.
- [25] M. Gell-Mann, “Symmetries of Baryons and Mesons,” *Phys. Rev.*, vol. 125, no. 3, pp. 1067–1084, 1962.
- [26] B. Bjorken and S. Glashow, “Elementary particles and SU(4),” *Physics Letters*, vol. 11, no. 3, pp. 0031–9163, 1964.
- [27] O. W. Greenberg, “Spin and Unitary-Spin Independence in a Paraquark Model of Baryons and Mesons,” *Phys. Rev. Lett.*, vol. 13, no. 20, pp. 598–602, 1964.
- [28] D. J. Gross and F. Wilczek, “Asymptotically Free Gauge Theories. 1,” *Phys. Rev.*, vol. D8, pp. 3633+3652, 1973.

- 
- [29] D. J. Gross and F. Wilczek, “Asymptotically free gauge theories. II,” *Phys. Rev. D*, vol. 9, no. 4, pp. 980–993, 1974.
- [30] <http://webfest.web.cern.ch/content/standard-model-standard> infographic
- [31] H. D. Politzer, “Reliable Perturbative Results for Strong Interactions?,” *Phys. Rev. Lett.*, vol. 30, no. 26, pp. 1346–1349, 1973.
- [32] D. J. Gross and F. Wilczek, “Ultraviolet behavior of Non-Abelian Gauge theories,” *Phys. Rev. Lett.*, vol. 30, no. 26, 1973.
- [33] Particle Data Group, “<http://pdg.lbl.gov/>.”
- [34] J. Goldstone, A. Salam, and S. Weinberg, “Broken Symmetries,” *Phys. Rev.*, vol. 127, no. 3, pp. 965–970, 1962.
- [35] M. G. Alford, A. Schmitt, K. Rajagopal, and T. Schäfer, “Color superconductivity in dense quark matter,” *Rev. Mod. Phys.*, vol. 80, pp. 1455–1515, 2008.
- [36] J. C. Collins and M. J. Perry, “Superdense Matter: Neutrons or Asymptotically Free Quarks?,” *Phys. Rev. Lett.*, vol. 34, no. 21, pp. 1353–1356, 1975.
- [37] N. Cabibbo and G. Parisi, “Exponential hadronic spectrum and quark liberation,” *Physics Letters B*, vol. 59, no. 1, pp. 67–69, 1975.
- [38] C. Gattringer and C. Lang, *Quantum Chromodynamics on the Lattice: An Introductory Presentation*. Springer, 2009.
- [39] A. Chodos, R. L. Jaffe, K. Johnson, C. B. Thorn, and V. F. Weisskopf, “New extended model of hadrons,” *Phys. Rev. D*, vol. 9, no. 12, pp. 3471–3495, 1974.
- [40] Y. Nambu and G. Jona-Lasinio, “Dynamical Model of Elementary Particles Based on an Analogy with Superconductivity. I,” *Phys. Rev.*, vol. 122, no. 1, pp. 345–358, 1961.
- [41] Y. Nambu and G. Jona-Lasinio, “Dynamical Model of Elementary Particles Based on an Analogy with Superconductivity. II,” *Phys. Rev.*, vol. 124, no. 1, pp. 246–254, 1961.
- [42] P. Braun-Munzinger and J. Wambach, “The Phase Diagram of Strongly-Interacting Matter,” *Rev. Mod. Phys.*, vol. 81, pp. 1031–1050, 2009.
- [43] A. Bazavov *et al.*, “Equation of state and QCD transition at finite temperature,” *Phys. Rev.*, vol. D80, p. 014504, 2009.
- [44] F. Karsch and E. Laermann, “Thermodynamics and in medium hadron properties from lattice QCD,” *hep-lat/0305025*, 2003.

- [45] Y. Hatta and T. Ikeda, “Universality, the QCD critical / tricritical point and the quark number susceptibility,” *Phys. Rev.*, vol. D67, p. 014028, 2003.
- [46] B.-J. Schaefer and M. Wagner, “On the QCD phase structure from effective models,” *Prog. Part. Nucl. Phys.*, vol. 62, p. 381, 2009.
- [47] Z. Fodor and S. D. Katz, “Lattice determination of the critical point of QCD at finite T and mu,” *JHEP*, vol. 03, p. 014, 2002.
- [48] Z. Fodor, S. D. Katz, and K. K. Szabo, “The QCD equation of state at nonzero densities: Lattice result,” *Phys. Lett.*, vol. B568, pp. 73–77, 2003.
- [49] J. D. Bjorken, “Highly relativistic nucleus-nucleus collisions: The central rapidity region,” *Phys. Rev. D*, vol. 27, no. 1, pp. 140–151, 1983.
- [50] C.-Y. Wong, “Lectures on the Near-Side Ridge, Landau Hydrodynamics, and Heavy Quarkonia in High Energy Heavy-Ion Collisions,” *EPJ Web Conf.*, vol. 7, p. 01006, 2010.
- [51] G. Martinez, “Advances in Quark Gluon Plasma,” *arXiv: 1304.1452*, 2013.
- [52] M. Lamont, *Neutral Strange Particle Production in Ultra-Relativistic Heavy-Ion collisions at  $\sqrt{s_{NN}} = 130$  GeV*.  
PhD thesis, University of Birmingham, 2002.
- [53] U. W. Heinz, “The Little bang: Searching for quark gluon matter in relativistic heavy ion collisions,” *Nucl. Phys.*, vol. A685, pp. 414–431, 2001.
- [54] B. Abelev *et al.*, “Centrality determination of Pb-Pb collisions at  $\sqrt{s_{NN}} = 2.76$  TeV with ALICE,” *Phys. Rev.*, vol. C88, no. 4, p. 044909, 2013.
- [55] J. Adam *et al.*, “Centrality dependence of particle production in p-Pb collisions at  $\sqrt{s_{NN}} = 5.02$  TeV,” *Phys. Rev.*, vol. C91, no. 6, p. 064905, 2015.
- [56] U. W. Heinz, “The Quark gluon plasma at RHIC,” *Nucl. Phys.*, vol. A721, pp. 30–39, 2003.
- [57] R. Snellings, “Collective Expansion at the LHC: selected ALICE anisotropic flow measurements,” *J. Phys.*, vol. G41, no. 12, p. 124007, 2014.
- [58] P. Braun-Munzinger, K. Redlich, and J. Stachel, “Particle production in heavy ion collisions,” *arxiv:nucl-th/0304013*, 2003.
- [59] A. Adare *et al.*, “Detailed measurement of the  $e^+e^-$  pair continuum in  $p+p$  and Au+Au collisions at  $\sqrt{s_{NN}} = 200$  GeV and implications for direct photon production,” *Phys. Rev.*, vol. C81, p. 034911, 2010.

- 
- [60] *Measurement of Direct Photons in pp and Pb-Pb Collisions with ALICE*, vol. A904-905, 2013.
  - [61] Z. Conesa del Valle, “Vector bosons in heavy-ion collisions at the LHC,” *Eur. Phys. J.*, vol. C61, pp. 729–733, 2009.
  - [62] S. Chatrchyan *et al.*, “Study of Z production in PbPb and pp collisions at  $\sqrt{s_{NN}} = 2.76$  TeV in the dimuon and dielectron decay channels,” *JHEP*, vol. 03, p. 022, 2015.
  - [63] V. Khachatryan *et al.*, “Study of W boson production in pPb collisions at  $\sqrt{s_{NN}} = 5.02$  TeV,” *arXiv:1503.05825*, 2015.
  - [64] S. Chatrchyan *et al.*, “Jet momentum dependence of jet quenching in PbPb collisions at  $\sqrt{s_{NN}} = 2.76$  TeV,” *Phys. Lett.*, vol. B712, pp. 176–197, 2012.
  - [65] B. Abelev *et al.*, “Centrality, rapidity and transverse momentum dependence of  $J/\psi$  suppression in Pb-Pb collisions at  $\sqrt{s_{NN}} = 2.76$  TeV,” *Phys. Lett.*, vol. B734, pp. 314–327, May 2014.
  - [66] B. Abelev *et al.*, “Measurement of charm production at central rapidity in proton-proton collisions at  $\sqrt{s} = 2.76$  TeV,” *JHEP*, vol. 07, p. 191, 2012.
  - [67] A. Andronic, F. Beutler, P. Braun-Munzinger, K. Redlich, and J. Stachel, “Statistical hadronization of heavy flavor quarks in elementary collisions: Successes and failures,” *Phys. Lett.*, vol. B768, pp. 350–354, 2009.
  - [68] A. Andronic, P. Braun-Munzinger, and J. Stachel, “Thermal hadron production in relativistic nuclear collisions: The hadron mass spectrum, the horn, and the QCD phase transition,” *Physics Letters B*, vol. 673, no. 2, pp. 142–145, 2009.
  - [69] B. Abelev *et al.*, “Centrality dependence of  $\pi$ , K, p production in Pb-Pb collisions at  $\sqrt{s_{NN}} = 2.76$  TeV,” *Phys. Rev.*, vol. C88, p. 044910, 2013.
  - [70] A. Andronic *et al.*, “Heavy-flavour and quarkonium production in the LHC era: from proton-proton to heavy-ion collisions,” *arXiv:1506.03981*, 2015.
  - [71] S. Jacobs, M. G. Olsson, and C. Suchyta, “Comparing the Schrödinger and spinless Salpeter equations for heavy-quark bound states,” *Phys. Rev. D*, vol. 33, no. 11, pp. 3338–3348, 1986.
  - [72] E. Eichten, K. Gottfried, T. Kinoshita, K. Lane, and T.-M. Yan, “Charmonium: The Model,” *Phys.Rev. D17 (1978) 3090 ; Phys.Rev. D21 (1980) 313*.
  - [73] H. Satz, “Colour deconfinement and quarkonium binding,” *J. Phys.*, vol. G32, p. R25, 2006.

- [74] J. Aubert *et al.*, “Experimental Observation of a Heavy Particle  $J$ ,” *Phys. Rev. Lett.*, vol. 33, no. 23, pp. 1404–1406, 1974.
- [75] J. E. Augustin *et al.*, “Discovery of a Narrow Resonance in  $e^+e^-$  Annihilation,” *Phys. Rev. Lett.*, vol. 33, no. 23, pp. 1406–1408, 1974.
- [76] Y. Lemoigne *et al.*, “Measurement of hadronic production of the  $\chi_1^{++}(3507)$  and the  $\chi_2^{++}(3553)$  through their radiative decay to  $J/\psi$ ,” *Physics Letters B*, vol. 113, no. 6, pp. 509–512, 1982.
- [77] L. Antoniazzi *et al.*, “Measurement of  $J/\psi$  and  $\psi'$  production in 300 GeV proton, antiproton and  $\pi^{pm}$  interactions with nuclei,” *Phys. Rev. D*, vol. 46, no. 11, pp. 4828–4835, 1992.
- [78] L. Antoniazzi *et al.*, “Production of  $J/\psi$  via  $\psi'$  and  $\chi$  decay in 300 GeV/c proton- and  $\pi^\pm$ -nucleon interactions,” *Phys. Rev. Lett.*, vol. 70, pp. 383–386, 1993.
- [79] R. Aaij *et al.*, “Measurement of  $J/\psi$  production in  $pp$  collisions at  $\sqrt{s} = 7$  TeV,” *Eur. Phys. J.*, vol. C71, p. 1645, 2011.
- [80] K. Zhu, “Charmonium and Light Meson Spectroscopy,” *arXiv:1212.2169*, 2012.
- [81] A. Cooper-Sarkar and C. Gwenlan, “Comparison and combination of ZEUS and H1 PDF analyses: HERA - LHC workshop proceedings,” *arXiv: hep-ph/0508304*, 2005.
- [82] F. D. Aaron *et al.*, “Inclusive Deep Inelastic Scattering at High  $Q^2$  with Longitudinally Polarised Lepton Beams at HERA,” *JHEP*, vol. 09, p. 061, 2012.
- [83] H. Fritzsch, “Producing heavy quark flavors in hadronic collisionsâ’ A test of quantum chromodynamics,” *Physics Letters B*, vol. 67, no. 2, pp. 217–221, 1977.
- [84] J. F. Amundson, O. J. P. Eboli, E. M. Gregores, and F. Halzen, “Quantitative tests of color evaporation: Charmonium production,” *Phys. Lett.*, vol. B390, pp. 323–328, 1997.
- [85] M. Bedjidian *et al.*, “Hard probes in heavy ion collisions at the LHC: Heavy flavor physics,” *arXiv:hep-ph/0311048*, 2004.
- [86] M. Einhorn and S. Ellis, “Hadronic production of the new resonances: Probing gluon distributions,” *Phys. Rev. D*, vol. 12, no. 7, pp. 2007–20014, 1975.
- [87] S. D. Ellis, M. B. Einhorn, and C. Quigg, “Comment on Hadronic Production of Psions,” *Phys. Rev. Lett.*, vol. 36, no. 21, pp. 1263–1266, 1976.
- [88] C. E. Carlson and R. Suaya, “Hadronic production of the  $\psi/J$  meson,” *Phys. Rev. D*, vol. 14, no. 11, pp. 3115–3121, 1976.

- 
- [89] E. L. Berger and D. Jones, “Inelastic photoproduction of  $\frac{J}{\psi}$  and  $\Upsilon$  by gluons,” *Phys. Rev. D*, vol. 23, no. 7, pp. 1521–1530, 1981.
  - [90] R. Baier and R. R  ckl, “Hadronic collisions: A quarkonium factory,” *Zeitschrift f  r Physik C Particles and Fields*, vol. 19, no. 3, pp. 251–266, 1983.
  - [91] J. P. Lansberg, “Total  $J/\psi$  and Upsilon production cross section at the LHC: theory vs. experiment,” *PoS*, vol. ICHEP2010, p. 206, 2010.
  - [92] F. Abe *et al.*, “ $J/\psi$  and  $\psi^{prime}$  Production in  $p\bar{p}$  Collisions at  $\sqrt{s} = 1.8$  TeV,” *Phys. Rev. Lett.*, vol. 79, no. 4, pp. 572–577, 1997.
  - [93] J. M. Campbell, F. Maltoni, and F. Tramontano, “QCD corrections to  $J/\psi$  and Upsilon production at hadron colliders,” *Phys. Rev. Lett.*, vol. 98, p. 252002, 2007.
  - [94] N. Brambilla *et al.*, “Heavy quarkonium: progress, puzzles, and opportunities,” *Eur. Phys. J.*, vol. C71, p. 1534, 2011.
  - [95] G. T. Bodwin, E. Braaten, and G. P. Lepage, “Rigorous QCD analysis of inclusive annihilation and production of heavy quarkonium,” *Phys. Rev. D*, vol. 51, no. 3, pp. 1125–1171, 1995.
  - [96] W. Caswell and G. Lepage, “Effective lagrangians for bound state problems in QED, QCD, and other field theories,” *Physics Letters B*, vol. 167, no. 4, pp. 437–442, 1986.
  - [97] G. T. Bodwin, E. Braaten, and J. Lee, “Comparison of the color-evaporation model and the NRQCD factorization approach in charmonium production,” *Phys. Rev.*, vol. D72, p. 014004, 2005.
  - [98] G. P. Lepage, L. Magnea, C. Nakhleh, U. Magnea, and K. Hornbostel, “Improved nonrelativistic QCD for heavy-quark physics,” *Phys. Rev. D*, vol. 46, no. 9, pp. 4052–4067, 1992.
  - [99] M. Kramer, 1, “Color singlet and color octet contributions to  $J/\psi$  photoproduction,” *Nucl. Phys. Proc. Suppl.*, pp. 195–200, 1996.
  - [100] B. Gong, L.-P. Wan, J.-X. Wang, and H.-F. Zhang, “Polarization for Prompt  $J/\psi$  and  $\psi(2s)$  Production at the Tevatron and LHC,” *Phys. Rev. Lett.*, vol. 110, no. 4, p. 042002, 2013.
  - [101] A. Abulencia *et al.*, “Polarization of  $J/\psi$  and  $\psi_{2S}$  mesons produced in  $p\bar{p}$  collisions at  $\sqrt{s} = 1.96$ -TeV,” *Phys. Rev. Lett.*, vol. 99, p. 132001, 2007.
  - [102] C. Geuna,  *$J/\psi$  production in proton-proton collisions at  $\sqrt{s} = 2.76$  and 7 TeV in the ALICE Forward Muon Spectrometer at LHC*.  
PhD thesis, Universit   Paris Sud - Paris XI ; CERN-THESIS-2012-315, 2012.

- [103] B. B. Abelev *et al.*, “Measurement of quarkonium production at forward rapidity in  $pp$  collisions at  $\sqrt{s} = 7$  TeV,” *Eur. Phys. J.*, vol. C74, no. 8, p. 2974, 2014.
- [104] J. P. Lansberg, “ $J/\psi$  production at  $\sqrt{s}=1.96$  and 7 TeV: Color-Singlet Model, NNLO\* and polarisation,” *J. Phys.*, vol. G38, p. 124110, 2011.
- [105] M. Butenschoen and B. A. Kniehl, “World data of  $J/\psi$  production consolidate nonrelativistic QCD factorization at next-to-leading order,” *Phys. Rev. D*, vol. 84, no. 5, p. 051501, 2011.
- [106] E. Braaten, B. A. Kniehl, and J. Lee, “Polarization of prompt  $J/\psi$  at the Tevatron,” *Phys. Rev.*, vol. D62, p. 094005, 2000.
- [107] S. P. Baranov, “Highlights from the  $k_T$ -factorization approach on the quarkonium production puzzles,” *Phys. Rev. D*, vol. 66, no. 11, p. 114003, 2002.
- [108] B. Abelev *et al.*, “ $J/\psi$  polarization in  $pp$  collisions at  $\sqrt{s} = 7$  TeV,” *Phys. Rev. Lett.*, vol. 108, p. 082001, 2012.
- [109] R. Aaij *et al.*, “Measurement of  $J/\psi$  polarization in  $pp$  collisions at  $\sqrt{s} = 7$  TeV,” *Eur. Phys. J.*, vol. C73, no. 11, p. 2631, 2013.
- [110] G. Aad *et al.*, “Measurement of Upsilon production in 7 TeV  $pp$  collisions at ATLAS,” *Phys. Rev.*, vol. D87, no. 5, p. 052004, 2013.
- [111] M. Lenhardt, *Study of the production yield of  $J/\psi$  and single muons in collisions proton-proton with the muon spectrometer of the ALICE experiment at LHC*. PhD thesis, CERN-THESIS-2011-243 ; Université de Nantes, 2011.
- [112] T. Sjöstrand and M. van Zijl, “A multiple-interaction model for the event structure in hadron collisions,” *Phys. Rev.*, vol. D36, no. 7, pp. 2019–2041, 1987.
- [113] S. Porteboeuf and R. Granier de Cassagnac, “ $J/\psi$  yield vs. multiplicity in proton-proton collisions at the LHC,” *Nucl. Phys. Proc. Suppl.*, vol. 214, pp. 181–184, 2011.
- [114] H. Abramowicz *et al.*, “Summary of the Workshop on Multi-Parton Interactions (MPI@LHC 2012),” *arXiv:1306.5413*, 2013.
- [115] S. Porteboeuf-Houssais, “ $J/\psi$  production as a function of charged particle multiplicity in  $pp$  collisions at  $\sqrt{s} = 7$  TeV with the ALICE experiment,” *arXiv:1202.5864*, 2012.
- [116] E. G. Ferreira and C. Pajares, “High multiplicity  $pp$  events and  $J/\psi$  production at energies available at the CERN Large Hadron Collider,” *Phys. Rev. C*, vol. 86, no. 3, p. 034903, 2012.



- 
- [117] Z. Conesa del Valle, *Performance of the ALICE muon spectrometer. Weak boson production and measurement in heavy-ion collisions at the LHC*.  
PhD thesis, CERN-THESIS-2007-102; Université de Nantes ; Universitat Autònoma de Barcelona, 2007.
- [118] A. Andronic, P. Braun-Munzinger, K. Redlich, and J. Stachel, “The thermal model on the verge of the ultimate test: particle production in Pb-Pb collisions at the LHC,” *J. Phys.*, vol. G38, p. 124081, 2011.
- [119] Y.-p. Liu, Z. Qu, N. Xu, and P.-f. Zhuang, “J/psi Transverse Momentum Distribution in High Energy Nuclear Collisions at RHIC,” *Phys. Lett.*, vol. B678, pp. 72–76, 2009.
- [120] X. Zhao and R. Rapp, “Medium Modifications and Production of Charmonia at LHC,” *Nucl. Phys.*, vol. A859, pp. 114–125, 2011.
- [121] P. Debye and E. Huckel *Phys. Z.*, vol. 24, p. 185, 1923.
- [122] V. V. Dixit, “Charge Screening and Space Dimension,” *Mod. Phys. Lett.*, vol. A5, p. 227, 1990.
- [123] H. Satz, “Probing the States of Matter in QCD,” *Int. J. Mod. Phys.*, vol. A28, p. 1330043, 2013.
- [124] P. Braun-Munzinger and J. Stachel, “(Non)thermal aspects of charmonium production and a new look at J /  $\psi$  suppression,” *Phys. Lett.*, vol. B490, no. 196-202, 2000.
- [125] S. Gavin and M. Gyulassy, “Transverse-momentum dependence of j/ψ production in nuclear collisions,” *Physics Letters B*, vol. 214, no. 2, pp. 241 – 246, 1988.
- [126] J. Hüfner and P. Zhuang, “Time structure of anomalous J/ψ and ψ′ suppression in nuclear collisions,” *Physics Letters B*, vol. 559, pp. 193 – 200, 2003.
- [127] H. Satz, “Quarkonium Binding and Dissociation: The Spectral Analysis of the QGP,” *Nucl. Phys.*, vol. A783, pp. 249–260, 2007.
- [128] R. L. Thews and M. L. Mangano, “Momentum spectra of charmonium produced in a quark-gluon plasma,” *Phys. Rev.*, vol. C73, p. 014904, 2006.
- [129] A. Andronic, P. Braun-Munzinger, K. Redlich, and J. Stachel, “Statistical hadronization of charm in heavy ion collisions at SPS, RHIC and LHC,” *Phys. Lett.*, vol. B571, pp. 36–44, 2003.
- [130] P. Braun-Munzinger and J. Stachel, “Charmonium from Statistical Hadronization of Heavy Quarks: A Probe for Deconfinement in the Quark-Gluon Plasma,” *Landolt-Bornstein*, vol. 23, p. 424, 2010.

- [131] L. Yan, P. Zhuang, and N. Xu, “Competition between  $J/\psi$  suppression and regeneration in quark-gluon plasma,” *Phys. Rev. Lett.*, vol. 97, p. 232301, 2006.
- [132] S. Datta, F. Karsch, P. Petreczky, and I. Wetzorke, “Behavior of charmonium systems after deconfinement,” *Phys. Rev.*, vol. D69, p. 094507, 2004.
- [133] M. C. Abreu *et al.*, “Anomalous  $J/\psi$  suppression in Pb - Pb interactions at 158 GeV/c per nucleon,” *Phys. Lett.*, vol. B410, pp. 337–343, 1997.
- [134] C. Lourenco, “Open questions in quarkonium and electromagnetic probes,” *Nucl. Phys.*, vol. A783, pp. 451–460, 2007.
- [135] D. Kharzeev, C. Lourenco, M. Nardi, and H. Satz, “A Quantitative analysis of charmonium suppression in nuclear collisions,” *Z. Phys.*, vol. C74, pp. 307–318, 1997.
- [136] G. Borges *et al.*, “The  $J/\psi$  normal nuclear absorption,” *Eur. Phys. J.*, vol. C43, pp. 161–165, 2005.
- [137] B. Abelev *et al.*, “Measurement of inelastic, single- and double-diffraction cross sections in proton–proton collisions at the LHC with ALICE,” *Eur. Phys. J.*, vol. C73, no. 6, p. 2456, 2013.
- [138] A. Adare *et al.*, “ $J/\psi$  suppression at forward rapidity in Au+Au collisions at  $\sqrt{s_{NN}} = 200$  GeV,” *Phys. Rev.*, vol. C84, p. 054912, 2011.
- [139] J. Adam *et al.*, “Differential studies of inclusive  $J/\psi$  and  $\psi(2S)$  production at forward rapidity in Pb-Pb collisions at  $\sqrt{s_{NN}} = 2.76$  TeV,” *arXiv:1506.08804*, 2015.
- [140] E. G. Ferreira, “Charmonium dissociation and recombination at LHC: Revisiting comovers,” *Phys. Lett.*, vol. B731, pp. 57–63, 2014.
- [141] S. Forte and G. Watt, “Progress in the Determination of the Partonic Structure of the Proton,” *Ann. Rev. Nucl. Part. Sci.*, vol. 63, pp. 291–328, 2013.
- [142] J. Aubert *et al.*, “The ratio of the nucleon structure functions  $\{F_2N\}$  for iron and deuterium,” *Physics Letters B*, vol. 123, pp. 275–278, 1983.
- [143] K. J. Eskola, H. Paukkunen, and C. A. Salgado, “EPS09: A New Generation of NLO and LO Nuclear Parton Distribution Functions,” *JHEP*, vol. 04, p. 065, 2009.
- [144] K. C. W. Zhu, D.L. Xu and Z. Xu *Phys. Lett.*, vol. B317, no. 200, 1993.
- [145] K. C. W. Zhu and B. He *Nucl. Phys.*, vol. B427, no. 525, 1994.
- [146] K. C. W. Zhu and B. He *Nucl. Phys.*, vol. B449, no. 183, 1995.
- [147] W. Zhu *Phys. Lett.*, vol. B389, no. 374, 1996.

- 
- [148] K. Rith, “Present Status of the EMC effect,” *arXiv:1402.5000*, 2014.
  - [149] Y. L. Dokshitzer, “Calculation of the Structure Functions for Deep Inelastic Scattering and  $e^+ + e^-$  Anihilation by Perturbation Theory in Quantum Chromodynamics,” *Sov. Phys. JETP*, vol. 46, pp. 641–653, 1977.
  - [150] V. Gribov and L. Lipatov, “Deep inelastic e p scattering in perturbation theory,” *Sov. J. Nucl. Phys.*, vol. 15, pp. 438–450, 1972.
  - [151] G. Altarelli and G. Parisi, “Asymptotic Freedom in Parton Language,” *Nucl. Phys.*, vol. B126, p. 298, 1977.
  - [152] E. Iancu and R. Venugopalan, “The Color glass condensate and high-energy scattering in QCD,” *arXiv:hep-ph/0303204*, 2003.
  - [153] H. Weigert, “Evolution at small  $x(bj)$ : The Color glass condensate,” *Prog. Part. Nucl. Phys.*, vol. 55, pp. 461–565, 2005.
  - [154] L. McLerran, “RHIC physics: The Quark gluon plasma and the color glass condensate: Four lectures,” *arXiv:hep-ph/0311028*, 2003.
  - [155] T. Lappi and L. McLerran, “Some features of the glasma,” *Nucl. Phys.*, vol. A772, pp. 200–212, 2006.
  - [156] F. Gelis, E. Iancu, J. Jalilian-Marian, and R. Venugopalan, “The Color Glass Condensate,” *Ann. Rev. Nucl. Part. Sci.*, vol. 60, pp. 463–489, 2010.
  - [157] H. Kowalski, T. Lappi, and R. Venugopalan, “Nuclear enhancement of universal dynamics of high parton densities,” *Phys. Rev. Lett.*, vol. 100, p. 022303, 2008.
  - [158] D. Kharzeev and K. Tuchin, “Signatures of the color glass condensate in J/psi production off nuclear targets,” *Nucl. Phys.*, vol. A770, pp. 40–56, 2006.
  - [159] F. Dominguez, D. E. Kharzeev, E. M. Levin, A. H. Mueller, and K. Tuchin, “Gluon saturation effects on the color singlet J/Psi production in high energy dA and AA collisions,” *Phys. Lett.*, vol. B710, pp. 182–187, 2012.
  - [160] H. Fujii, F. Gelis, and R. Venugopalan, “Quark pair production in high energy pA collisions: General features,” *Nucl. Phys.*, vol. A780, pp. 146–174, 2006.
  - [161] H. Fujii and K. Watanabe, “Heavy quark pair production in high energy pA collisions: Quarkonium,” *Nucl. Phys.*, vol. A915, p. 123, 2013.
  - [162] Z.-B. Kang, Y.-Q. Ma, and R. Venugopalan, “Quarkonium production in high energy proton-nucleus collisions: CGC meets NRQCD,” *JHEP*, vol. 01, p. 056, 2014.
  - [163] K. Adcox *et al.*, “Suppression of hadrons with large transverse momentum in central Au+Au collisions at  $\sqrt{s_{NN}} = 130\text{-GeV}$ ,” *Phys. Rev. Lett.*, vol. 88, p. 022301, 2002.

- [164] C. Adler *et al.*, “Centrality dependence of high  $p_T$  hadron suppression in Au+Au collisions at  $\sqrt{s_{NN}} = 130\text{-GeV}$ ,” *Phys. Rev. Lett.*, vol. 89, p. 202301, 2002.
- [165] N. Armesto *et al.*, “Comparison of Jet Quenching Formalisms for a Quark-Gluon Plasma ‘Brick’,” *Phys. Rev.*, vol. C86, p. 064904, 2012.
- [166] R. Baier, Y. L. Dokshitzer, A. H. Mueller, S. Peigne, and D. Schiff, “Radiative energy loss of high-energy quarks and gluons in a finite volume quark - gluon plasma,” *Nucl. Phys.*, vol. B483, pp. 291–320, 1997.
- [167] F. Arleo, S. Peigne, and T. Sami, “Revisiting scaling properties of medium-induced gluon radiation,” *Phys. Rev.*, vol. D83, p. 114036, 2011.
- [168] F. Arleo and S. Peigne, “ $J/\psi$  suppression in p-A collisions from parton energy loss in cold QCD matter,” *Phys. Rev. Lett.*, vol. 109, p. 122301, 2012.
- [169] F. Arleo and S. Peigne, “Heavy-quarkonium suppression in p-A collisions from parton energy loss in cold QCD matter,” *JHEP*, vol. 03, p. 122, 2013.
- [170] F. Arleo, R. Kolevatov, S. Peigné, and M. Rustamova, “Centrality and  $p_T$  dependence of  $J/\psi$  suppression in proton-nucleus collisions from parton energy loss,” *JHEP*, vol. 05, p. 155, 2013.
- [171] M. L. Miller, K. Reygers, S. S. J., and P. Steinberg, “Glauber modeling in high energy nuclear collisions,” *Ann. Rev. Nucl. Part. Sci.*, vol. 57, pp. 205–243, 2007.
- [172] R. Shahoyan,  *$J/\psi$  and  $\psi^{\text{prime}}$  production in 450 GeV pA interactions and its dependence on the rapidity and  $x_F$* .  
PhD thesis, IST, 2001.
- [173] C. Lourenco, R. Vogt, and H. K. Woehri, “Energy dependence of  $J/\psi$  absorption in proton-nucleus collisions,” *JHEP*, vol. 02, p. 014, 2009.
- [174] A. Adare *et al.*, “Cold Nuclear Matter Effects on  $J/\psi$  Yields as a Function of Rapidity and Nuclear Geometry in Deuteron-Gold Collisions at  $\sqrt{s_{NN}} = 200\text{ GeV}$ ,” *Phys. Rev. Lett.*, vol. 107, p. 142301, 2011.
- [175] R. Vogt, “Shadowing and absorption effects on  $J/\psi$  production in dA collisions,” *Phys. Rev.*, vol. C71, p. 054902, 2005.
- [176] D. Kharzeev and K. Tuchin, “Signatures of the color glass condensate in  $J/\psi$  production off nuclear targets,” *Nucl. Phys.*, vol. A770, pp. 40–56, 2006.
- [177] D. Kharzeev and K. Tuchin, “Open charm production in heavy ion collisions and the color glass condensate,” *Nucl. Phys.*, vol. A735, pp. 248–266, 2004.

- 
- [178] A. Adare *et al.*, “Transverse-momentum dependence of the  $J/\psi$  nuclear modification in  $d$ +Au collisions at  $\sqrt{s_{NN}} = 200$  GeV,” *Phys. Rev. C*, vol. 87, no. 3, p. 034904, 2013.
  - [179] D. de Florian and R. Sassot, “Nuclear parton distributions at next to leading order,” *Phys. Rev. D*, vol. 69, no. 7, p. 074028, 2004.
  - [180] B. Kopeliovich *et al.*, “Nuclear suppression of : From RHIC to the LHC,” *Nuclear Physics A*, vol. 864, no. 1, pp. 203–212, 2011.
  - [181] K. B.Z. *et al.*, “ $J/\psi$  production in nuclear collisions: Theoretical approach to measuring the transport coefficient,” *Phys. Rev. C*, vol. 82, no. 2, p. 024901, 2010.
  - [182] J. W. Cronin, H. J. Frisch, M. J. Shochet, J. P. Boymond, P. A. Piroué, and R. L. Sumner, “Production of hadrons at large transverse momentum at 200, 300, and 400 GeV,” *Phys. Rev. D*, vol. 11, no. 11, pp. 3105–3123, 1975.
  - [183] E. G. Ferreira *et al.*, “Centrality, Rapidity, and Transverse-Momentum Dependence of Gluon Shadowing and Antishadowing on  $J/\psi$  Production in  $d$ -Au Collisions at  $\sqrt{s_{NN}} = 200$  GeV,” *Few Body Syst.*, vol. 53, p. 27, 2012.
  - [184] E. Ferreira *et al.*, “Cold nuclear matter effects on production: Intrinsic and extrinsic transverse momentum effects,” *Physics Letters B*, vol. 680, no. 1, pp. 50–55, 2009.
  - [185] J. L. Albacete *et al.*, “Predictions for  $p$ +Pb Collisions at  $\sqrt{s_{NN}} = 5$  TeV,” *Int. J. Mod. Phys.*, vol. E22, p. 1330007, 2013.
  - [186] R. Vogt, “Cold Nuclear Matter Effects on  $J/\psi$  and  $Y$  Production at the LHC,” *Phys. Rev.*, vol. C81, p. 044903, 2010.
  - [187] E. G. Ferreira, “Excited charmonium suppression in proton–nucleus collisions as a consequence of comovers,” *Phys. Lett.*, vol. B749, pp. 98–103, 2015.
  - [188] Z.-B. Kang and J.-W. Qiu, “Nuclear modification of vector boson production in proton-lead collisions at the LHC,” *Phys. Lett.*, vol. B721, pp. 277–283, 2013.
  - [189] Z.-B. Kang and J.-W. Qiu, “Transverse momentum broadening of vector boson production in high energy nuclear collisions,” *Phys. Rev.*, vol. D77, p. 114027, 2008.
  - [190] B. Abelev *et al.*, “Suppression of  $\psi(2S)$  production in  $p$ -Pb collisions at  $\sqrt{s_{NN}} = 5.02$  TeV,” *JHEP*, vol. 1412, p. 073, 2014.
  - [191] S. Chatrchyan *et al.*, “Event activity dependence of  $Y(nS)$  production in  $\sqrt{s_{NN}} = 5.02$  TeV  $p$ Pb and  $\sqrt{s} = 2.76$  TeV  $pp$  collisions,” *JHEP*, vol. 04, p. 103, 2014.
  - [192] P. Z. Skands, “Tuning Monte Carlo Generators: The Perugia Tunes,” *Phys. Rev.*, vol. D82, p. 074018, 2010.

- [193] T. Sjostrand, S. Mrenna, and P. Z. Skands, “A Brief Introduction to PYTHIA 8.1,” *Comput. Phys. Commun.*, vol. 178, pp. 852–867, 2008.
- [194] T. Pierog, I. Karpenko, J. M. Katzy, E. Yatsenko, and K. Werner, “EPOS LHC : test of collective hadronization with LHC data,” *arXiv:1306.0121*, 2013.
- [195] A. Ortiz Velasquez, P. Christiansen, E. Cuautle Flores, I. Maldonado Cervantes, and G. Paic, “Color Reconnection and Flowlike Patterns in  $pp$  Collisions,” *Phys. Rev. Lett.*, vol. 111, no. 4, p. 042001, 2013.
- [196] O. S. Bruning, P. Collier, P. Lebrun, S. Myers, R. Ostojic, J. Poole, and P. Proudlock, “LHC Design Report Vol.1: The LHC Main Ring,” *CERN-2004-003-V1*, 2004.
- [197] O. S. Brüning, P. Collier, P. Lebrun, S. Myers, R. Ostojic, J. Poole, and P. Proudlock, “LHC Design Report Vol.1: The LHC Infrastructure and General Services,” *CERN-2004-003-V-2*, 2004.
- [198] M. Benedikt, P. Collier, V. Mertens, J. Poole, and K. Schindl, “LHC Design Report Vol.3: The LHC Injector Chain,” *CERN-2004-003-V-3*, 2004.
- [199] G. Aad *et al.*, “The atlas experiment at the cern large hadron collider,” *JINST*, vol. 3, no. S08004, 2008.
- [200] S. Chatrchyan *et al.*, “The CMS experiment at the CERN LHC ,” *JINST*, vol. 3, no. S08004, 2008.
- [201] A. Alves *et al.*, “The LHCb experiment at the CERN LHC ,” *JINST*, vol. 3, no. S08005, 2008.
- [202] K. Aamodt *et al.*, “The ALICE experiment at the CERN LHC ,” *JINST*, vol. 3, no. S08002, 2008.
- [203] F. Carminati *et al.*, “ALICE: Physics Performance Report, Volume I,” *J. Phys.*, vol. G30, p. 1517, 2004.
- [204] B. Alessandro *et al.*, “ALICE: Physics Performance Report, Volume II ,” *J. Phys.*, vol. G32, p. 1295, 2006.
- [205] B. Abelev *et al.*, “Performance of the ALICE Experiment at the CERN LHC,” *Int.J.Mod.Phys.*, vol. A29, p. 1430044, 2014.
- [206] <http://aliceinfo.cern.ch/ArtSubmission/publications>
- [207] <http://aliweb.cern.ch/>
- [208] A. Collaboration, “ALICE Technical Design Report on Forward Detectors: FMD, T0 and V0,” *CERN-LHCC-2004-025 ; ALICE-TDR-011*, 2004.

- 
- [209] A. Collaboration, “ALICE technical design report: Photon multiplicity detector (PMD),” *CERN-LHCC-99-32 ; CERN-OPEN-2000-184*, 1999.
- [210] A. Collaboration, “ALICE: Addendum to the technical design report of the Photon Multiplicity Detector (PMD),” *CERN-LHCC-2003-038*, 2003.
- [211] A. Collaboration, “ALICE technical design report of the zero degree calorimeter (ZDC),” *CERN-LHCC-99-05*, 1999.
- [212] A. Collaboration, “ALICE technical design report of the inner tracking system (ITS),” *CERN-LHCC-99-12*, 1999.
- [213] K. Aamodt *et al.*, “Alignment of the ALICE Inner Tracking System with cosmic-ray tracks,” *JINST*, vol. 5, p. 03003, 2010.
- [214] A. Collaboration, “ALICE: Technical design report of the time projection chamber,” *CERN-OPEN-2000-183 ; CERN-LHCC-2000-001*, 2000.
- [215] J. Alme *et al.*, “The ALICE TPC, a large 3-dimensional tracking device with fast readout for ultra-high multiplicity events,” *Nuclear Instruments and Methods in Physics Research Section A: Accelerators, Spectrometers, Detectors and Associated Equipment*, vol. 622, no. 1, pp. 316–367, 2010.
- [216] A. Collaboration, “ALICE transition-radiation detector: Technical Design Report,” *ALICE-TDR-9 ; CERN-LHCC-2001-021*, 2001.
- [217] A. Collaboration, “ALICE technical design report of the time-of-flight system (TOF),” *CERN-LHCC-2000-012*, 2000.
- [218] A. Collaboration, “ALICE: Addendum to the technical design report of the time of flight system (TOF),” *CERN-LHCC-2002-016*, 2002.
- [219] A. Alici, “The MRPC-based ALICE time-of-flight detector: Status and performance,” *Nuclear Instruments and Methods in Physics Research Section A: Accelerators, Spectrometers, Detectors and Associated Equipment*, vol. 706, pp. 29–32, 2013.
- [220] A. Collaboration, “ALICE technical design report of the High Momentum Particle Identification Detector,” *CERN-LHCC-98-19*, 1998.
- [221] A. Collaboration, “ALICE technical design report of the photon spectrometer (PHOS),” *CERN-LHCC-99-04*, 1999.
- [222] A. Collaboration, “ALICE Electromagnetic Calorimeter Technical Design Report,” *CERN-LHCC-2008-014 ; ALICE-TDR-14*, 2008.
- [223] A. Fernandez *et al.*, “ACORDE a Cosmic Ray Detector for ALICE,” *arxiv:physics/060605*, 2006.

- [224] A. Collaboration, “ALICE technical design report of the dimuon forward spectrometer,” *CERN-LHCC-99-22*, 1999.
- [225] A. Collaboration, “Addendum to the ALICE technical design report of the dimuon forward spectrometer,” *CERN-LHCC 2000-046*, 200.
- [226] <https://twiki.cern.ch/twiki/bin/view/ALICE/MuonTracking>
- [227] <http://www.saha.ac.in/web/henppd-introduction-detector> working
- [228] A. Collaboration, “ALICE trigger data-acquisition high-level trigger and control system : Technical Design Report,” *ALICE-TDR-10 ; CERN-LHCC-2003-062*, 2004.
- [229] <https://twiki.cern.ch/twiki/bin/viewauth/ALICE/MuonPbQA2013>
- [230] <https://twiki.cern.ch/twiki/bin/view/ALICE/MuonppQA2012>
- [231] B. B. Abelev *et al.*, “Measurement of visible cross sections in proton-lead collisions at  $\sqrt{s_{NN}} = 5.02$  TeV in van der Meer scans with the ALICE detector,” *JINST*, vol. 9, p. P11003, 2014.
- [232] J. Adam *et al.*, “Measurement of inelastic cross section in pp collisions at  $\sqrt{s} = 8$  TeV,” *In preparation*.
- [233] D. Elia *et al.*, “Measurement of pseudorapidity density of charged particles in proton-proton collisions with the ALICE pixel detector,” *ARDA-Note-2009-004 ; ALICE-INT-2009-029*, 2009.
- [234] K. Aamodt *et al.*, “First proton-proton collisions at the LHC as observed with the ALICE detector: Measurement of the charged particle pseudorapidity density at  $\sqrt{s} = 900$  GeV,” *Eur. Phys. J.*, vol. C65, pp. 111–125, 2010.
- [235] K. Aamodt *et al.*, “Charged-particle multiplicity measurement in proton-proton collisions at  $\sqrt{s} = 0.9$  and 2.36 TeV with ALICE at LHC,” *Eur. Phys. J.*, vol. C68, no. 89-108, 2010.
- [236] K. Aamodt *et al.*, “Charged-particle multiplicity measurement in proton-proton collisions at  $\sqrt{s} = 7$  TeV with ALICE at LHC,” *Eur. Phys. J.*, vol. C68, pp. 345–354, 2010.
- [237] K. Aamodt *et al.*, “Charged-Particle Multiplicity Density at Midrapidity in Central Pb-Pb Collisions at  $\sqrt{s_{NN}} = 2.76$  TeV,” *Phys. Rev. Lett.*, vol. 105, no. 25, p. 252301, 2010.
- [238] K. Aamodt *et al.*, “Centrality Dependence of the Charged-Particle Multiplicity Density at Midrapidity in Pb-Pb Collisions at  $\sqrt{s_{NN}} = 2.76$  TeV,” *Phys. Rev. Lett.*, vol. 106, no. 3, p. 032301, 2011.



- 
- [239] B. Abelev *et al.*, “Pseudorapidity density of charged particles in  $p$ -Pb collisions at  $\sqrt{s_{NN}}=5.02$  TeV,” *Phys. Rev. Lett.*, vol. 110, no. 3, p. 032301, 2013.
  - [240] “Charged-particle multiplicities in proton-proton collisions at  $\sqrt{s} = 0.9$  to 8 TeV, with ALICE at the LHC,” *in preparation*.
  - [241] J. F. Große-Oetringhaus, *Measurement of the Charged-Particle Multiplicity in Proton-Proton Collisions with the ALICE Detector*.  
PhD thesis, CERN-THESIS-2009-033.
  - [242] E. Bruna *et al.*, “Vertex reconstruction for proton-proton collisions in alice,” *ARDA-Note-2009-002 ; ALICE-INT-2009-018*, 2009.
  - [243] D. Elia *et al.*, “The pixel detector based tracklet reconstruction algorithm in ALICE the pixel detector based tracklet reconstruction algorithm in ALICE,” *ARDA-Note-2009-005 ; ALICE-INT-2009-021*, 2009.
  - [244] A. Alkin and R. Shahoyan, “The ALICE tracking algorithms,” *In preparation*.
  - [245] S. Roesler, R. Engel, and R. J., “The Monte Carlo event generator DPMJET-III,” in *Advanced Monte Carlo for radiation physics, particle transport simulation and applications. Proceedings, Conference, MC2000, Lisbon, Portugal, October 23-26, 2000*, pp. 1033–1038, 2000.
  - [246] R. Shahoyan, “ $dN/d\eta$  measurement with SPD in pA @ 5.02 TeV,” <https://indico.cern.ch/event/210551/material-old/slides/1?contribId=1>.
  - [247] B. Abelev *et al.*, “Multiplicity Dependence of Pion, Kaon, Proton and Lambda Production in  $p$ -Pb Collisions at  $\sqrt{s_{NN}} = 5.02$  TeV,” *Phys. Lett.*, vol. B728, pp. 25–38, 2014.
  - [248] R. Shahoyan, “Summary bin0 number,” <https://indico.cern.ch/event/211632/material-old/slides/0>.
  - [249] V. Blobel *in 8th CERN School of Comp. - CSC’84, Aiguablava, Spain, 9-22 Sep. 1984, CERN-85-09, 88, (1985)*.
  - [250] G. D’Agostini, “A multidimensional unfolding method based on Bayes’ theorem,” *Nuclear Instruments and Methods in Physics Research Section A: Accelerators, Spectrometers, Detectors and Associated Equipment*, vol. 362, pp. 487 – 498, 1995.
  - [251] X.-N. Wang and M. Gyulassy, “Hijing: A Monte Carlo model for multiple jet production in pp, pA, and AA collisions,” *Phys. Rev. D*, vol. 44, no. 11, pp. 3501–3516, 1991.
  - [252] N. Le Bris, *Low momentum heavy-flavours measurements in the semi-muonic channel, and tracking efficiency of the ALICE’s muon spectrometer*.  
PhD thesis, Université de Nantes, 2009.

- [253] L. Aphecetche *et al.*, “Numerical simulations and offline reconstruction of the muon spectrometer of alice,” *ALICE-INT-2009-044*, 2009.
- [254] G. Chabratova *et al.*, “Development of the Kalman filter for tracking in the forward muon spectrometer of ALICE,” *ALICE-INT-2003-002*, 2003.
- [255] G. Chabratova *et al.*, “Further development of the Kalman filter for the muon spectrometer of ALICE and its comparison with the default method,” *ALICE-INT-2003-053*.
- [256] D. Stocco, “Efficiency determination of the Muon Spectrometer trigger chambers from real data,” *ALICE-INT-2008-004*, 2008.
- [257] F. Bossu *et al.*, “Phenomenological interpolation of the inclusive  $J/\psi$  cross section to proton-proton collisions at 2.76 TeV and 5.5 TeV,” 2011.
- [258] L. Valencia Palomo, *Inclusive  $J/\psi$  production measurement in Pb-Pb collisions at  $\sqrt{s_{NN}} = 2.76$  TeV with the ALICE Muon Spectrometer*.  
PhD thesis, CERN-THESIS-2013-377, 2013.
- [259] A. Lardeux, *Étude de la production inclusive de  $J/\psi$  dans les collisions Pb-Pb à  $\sqrt{s_{NN}} = 2,76$  TeV avec le spectromètre à muons de l’expérience ALICE au LHC*.  
PhD thesis, CERN-THESIS-2014-106 2014EMNA0129, 2014.
- [260] R. Brun, F. Carminati, and S. Giani, *GEANT Detector Description and Simulation Tool*.  
CERN, 1994.
- [261] I. Lakomov and B. Espagnon, *Mesure de la production de  $J/\psi$  en collisions p-Pb au LHC avec le spectromètre à muons d’ALICE*.  
PhD thesis, CERN-THESIS-2014-176 IPNO-14-02 ; <https://tel.archives-ouvertes.fr/tel-01085203>, 2014.
- [262] F. James and M. Winkler, *MINUIT User’s Guide*, 2004.
- [263]  $J/\psi$  p Pb analysers, “ $J/\psi$  production and nuclear effects in p-Pb Collisions at  $\sqrt{s_{NN}} = 5.02$  TeV.” ALICE Analysis Note.
- [264] B. Abelev *et al.*, “Coherent  $J/\psi$  photoproduction in ultra-peripheral Pb-Pb collisions at  $\sqrt{s_{NN}} = 2.76$  TeV,” *Phys. Lett.*, vol. B718, pp. 1273–1283, 2013.
- [265] B. B. Abelev *et al.*, “Exclusive  $J/\psi$  photoproduction off protons in ultra-peripheral p-Pb collisions at  $\sqrt{s_{NN}} = 5.02$  TeV,” *Phys. Rev. Lett.*, vol. 113, no. 23, p. 232504, 2014.
- [266] A. Collaboration, “Muon Spectrometer Technical Design Report,” tech. rep., ALICE-DOC-2004-004, 1999.
- [267] “<https://root.cern.ch/root/html/tutorials/fit/combinedfit.c.html>.”

- 
- [268] M. Fontana, “Performance and detector electronics upgrade for the ALICE muon trigger system,” *Master Thesis*, 2013.
  - [269] ALICE and L. Collaborations, “Reference  $pp$  cross-sections for  $J/\psi$  studies in proton-lead collisions at  $\sqrt{s_{NN}} = 5.02$  TeV and comparisons between ALICE and LHCb results,” *LHCb-CONF-2013-013*, *CERN-LHCb-CONF-2013-013*, *ALICE-PUBLIC-2013-002*, 2013.
  - [270] J. Adam *et al.*, “Inclusive quarkonium production at forward rapidity in  $pp$  collisions at  $\sqrt{s} = 8$  TeV,” *arXiv:1509.08258*, 2015.
  - [271] J. Martín Blanco, “ $J/\psi$  production in p-Pb collisions with ALICE at the LHC,” *Contributed talk at Quark matter 2014*: <https://indico.cern.ch/event/219436/session/17/contribution/135>.
  - [272] J. Martín Blanco, “ $J/\psi$  production in p-Pb collisions with ALICE at the LHC,” *Nuclear Physics A*, vol. 931, pp. 612–616, 2014.
  - [273] R. Aaij *et al.*, “Measurement of  $J/\psi$  production in  $pp$  collisions at  $\sqrt{s} = 7$  TeV,” *Eur. Phys. J.*, vol. C71, p. 1645, 2011.
  - [274] R. Russo, “Measurement of heavy-flavour production as a function of multiplicity in  $pp$  and p-Pb collisions with ALICE,” *Nuclear Physics A*, vol. 931, pp. 552 – 557, 2014.
  - [275] J. Adam *et al.*, “Measurement of D-meson production versus multiplicity in p-Pb collisions at  $\sqrt{s_{NN}} = 5.02$  TeV,” *In preparation*.
  - [276] The ALICE Collaboration, “Technical Design Report for the Muon Forward Tracker,” *CERN-LHCC-2015-001* ; *ALICE-TDR-018*, 2015.
  - [277] M. L. Miller, K. Reygers, S. J. Sanders, and P. Steinberg, “Glauber modeling in high energy nuclear collisions,” *Ann. Rev. Nucl. Part. Sci.*, vol. 57, pp. 205–243, 2007.
  - [278] C. Hadjidakis and I. Lakomov, “Multiplicity dependence of  $J/\psi$  production in p-Pb collisions at  $\sqrt{s_{NN}} = 5.02$  TeV.” ALICE Analysis Note.



# Thèse de Doctorat

**Javier MARTIN BLANCO**

**Study of  $J/\psi$  production dependence with the charged particle multiplicity in p-Pb collisions at  $\sqrt{s_{NN}} = 5.02$  TeV and pp collisions at  $\sqrt{s} = 8$  TeV with the ALICE experiment at the LHC**

**Étude de la dépendance en multiplicité de particules chargées de la production de  $J/\psi$  dans les collisions p-Pb à  $\sqrt{s_{NN}} = 5.02$  TeV et les collisions pp à  $\sqrt{s} = 8$  TeV avec l'expérience ALICE au LHC**

## Résumé

Une suppression de la production de  $J/\psi$  a été mise en évidence lors des collisions Pb-Pb à  $\sqrt{s_{NN}} = 2.76$  TeV, fournissant une preuve supplémentaire de la formation d'un milieu déconfiné au cours des collisions d'ions lourds ultra-relativistes, appelé Plasma de Quarks et Gluons. Par ailleurs, les collisions p-Pb à  $\sqrt{s} = 5.02$  TeV ont été étudiées au LHC afin de mesurer les effets de la matière nucléaire froide (p. ex. écrantage des gluons, perte d'énergie, absorption nucléaire). La compréhension des collisions p-Pb aidera à dissocier les effets de la matière nucléaire chaude et froide dans des collisions Pb-Pb.

Cette thèse analyse la production inclusive de  $J/\psi$  dans les collisions p-Pb et pp avec le spectromètre à muons de l'expérience ALICE. Le taux de production de  $J/\psi$  et son moment transverse moyen, ont été mesurés pour des rapidités à l'avant et à l'arrière en fonction de la multiplicité des particules chargées. Des mesures de la production de particules en fonction de la multiplicité de l'événement dans des systèmes de petite taille permettent de mettre en évidence des effets collectifs de l'état final, comme ceux observés dans les collisions Pb-Pb. L'augmentation observée, avec la multiplicité, de la production de  $J/\psi$  aux rapidités à l'arrière, est en accord avec celle mise en évidence en collisions pp. Cependant, une déviation de ce comportement pour la production de  $J/\psi$  aux rapidités à l'avant à haute multiplicité a été mesurée. Une tendance à la saturation du moment transverse moyen du  $J/\psi$  en collisions p-Pb a aussi été observée. L'origine de ces comportements, qu'ils soient liés aux effets de la matière nucléaire froide ou à la présence d'autres effets dans l'état final, n'est toujours pas connue.

## Mots clés

Plasma de Quarks et Gluons,  $J/\psi$ , Matière Nucléaire Froide, Quarkonium, p-Pb, pp, LHC, ALICE.

## Abstract

A suppression of the  $J/\psi$  production was found in Pb-Pb collisions at  $\sqrt{s_{NN}} = 2.76$  TeV, providing further evidence of the formation of a deconfined medium in ultra-relativistic heavy-ion collisions, the so-called Quark-Gluon Plasma. In addition, p-Pb collisions at  $\sqrt{s} = 5.02$  TeV have been studied at the LHC to measure cold nuclear matter effects (e.g. gluon shadowing, energy loss, nuclear absorption). Understanding p-Pb collisions will help to disentangle hot and cold nuclear matter effects in Pb-Pb collisions. Surprisingly, some observables in p-Pb collisions behave as in heavy-ion collisions where it is understood as a result of a collective expansion of the medium.

This thesis analyses inclusive  $J/\psi$  production in p-Pb and pp collisions with the ALICE muon spectrometer. The  $J/\psi$  production rate, and its mean transverse momentum, have been measured at forward and backward rapidities as a function of the charged particle multiplicity. Measurements of particle production as a function of the event multiplicity in small size systems provide a way to sign the presence of collective final state effects like those observed in Pb-Pb collisions. The observed increase of the  $J/\psi$  production at backward rapidity with multiplicity, is consistent with that observed in pp collisions. However, a deviation from this behaviour in the  $J/\psi$  production at forward rapidity at high multiplicity has been measured. A trend towards saturation has also been observed in the  $J/\psi$  mean transverse momentum in p-Pb collisions. Whether these effects can be explained by cold nuclear matter effects or by the presence of further final state effects is still unresolved.

## Key Words

Quark-Gluon Plasma,  $J/\psi$ , Cold Nuclear Matter, Quarkonium, p-Pb, pp, LHC, ALICE.